Assembly, Disassembly and Reassembly:

New synthetic approaches towards hybrid, mixed-metal and framework materials

A thesis submitted to the University of Dublin for the degree of Doctor of Philosophy

Colm Healy

School of Chemistry
University of Dublin
2017

I declare that this thesis has not been submitted as an exercise for a degree at this or any other university and that it is entirely my own work.

I agree to deposit this thesis in the University's open access institutional repository or allow the Library to do so on my behalf, subject to Irish Copyright Legislation and Trinity College Library conditions of use and acknowledgement.

_____

Colm Healy

“Geronimo”

Acknowledgements

There is an extremely long list of people who provided the help, support, encouragement, guidance and entertainment that helped get me to where I am today.

First and foremost, I would like to thank my parents for supporting me throughout my studies – none of this would have been possible without them. Thanks also to my family, Aideen, Moira, Aideen, Eoin, Clare, Tom, Jayne, Colm, Claire, and the new arrivals – Maeve, Izzy and Jamie.

I also want to thank the many friends who supported me along the way; Killian, Cat, Craig, Brian and Luke to name a few.

During my (long) time in Trinity I have been lucky to meet many wonderful people who have made my time here immensely enjoyable – among them the Werner Ladies (Bryan, Olan, Eoin and Barry), the Wolf Gang (including Adam, Debo, Paul, Friedrich, Lua, Lauren, Kevin, Rory), and many others – Ciara, Rob, Alex, Niamh, Judith, Michelle, Andy… the list goes on.

Thanks to my supervisor, Prof. Wolfgang Schmitt, for giving me the opportunity to pursue my Ph.D. Thanks also to Dr. Rachel Evans for her help and encouragement.

Scientifically, I owe a great debt to Dr. Lei Zhang and Dr. Camelia Onet. The work contained in this thesis rests heavily on the foundations that they laid during their time in the Schmitt group. Thanks to all members of the group, past and present, including the project students throughout the years.

Thanks are due to the (many) people who contributed to the crystallography in this work, Friedrich and Paul in particular. Thanks also to Swetanshu for tireless computational work, Debo for gas sorption analysis, Amal and Rory for catalytic measurements, Venky for SQUID data and Ximo for electrochemistry.

I would also like to thank the technical and support staff in the School of Chemistry for helping me throughout my time here. Particular thanks are due to Dr. Brendan Twamley for all his help with crystallography and to Dr. Gary Hessman for mass spectrometry, but also to Martin Feeney, Tom McCabe, Manuel Reuther, John O'Brien, Peter Brien, Patsy Greene, Tom Conroy, Noelle Scully, Teresa McDonnell, Sinead Boyce, the secretaries in the school office, and all of the other support staff for generally being incredibly helpful and accommodating throughout my time here.

Finally, thanks to the Irish Research Council for supporting me financially and making my research here possible.

Summary

The research presented in this thesis focuses on the synthesis of novel examples of advanced materials. The project aimed to synthesise new examples of three particular classes of materials; namely *organic-inorganic hybrid polyoxometalates* (hybrid POMs), *transition metal substituted polyoxometalates* (TMS-POMs) and *extended materials* (polymer-type and framework-type materials). The thesis explores a synthetic method based on distinct assembly, disassembly and reassembly steps to access novel examples of the target materials. This methodology represents a facile and potentially fertile alternative to the more traditional "bottom-up" synthetic pathways employed elsewhere. The resulting materials were characterised using single crystal X-ray diffraction (XRD) and a variety of complementary techniques, and their physicochemical properties were examined.

Chapter 1 summarises some of the available literature in an attempt to contextualise the work. The reader is introduced to the relevant classes of compounds and a brief overview of their properties is presented. Particular attention is paid (in generalised terms) to the synthesis and application of these compounds.

Chapter 2 introduces the assembly-disassembly-reassembly synthetic procedure that forms the core of this thesis. Some relevant literature is discussed before the general principles of the technique are outlined. The Lindqvist hexamolybdate $[Mo_6O_{19}]^{2-}$ is identified as a suitable material for this methodology, and its disassembly behaviour is examined using electrospray ionisation mass spectrometry (ESI-MS). It is demonstrated that the Lindqvist species undergoes disassembly into smaller molybdate oligomers when dissolved in methanol under ambient conditions, without applying any chemical or physical stress to the system. Cone voltage (CV) variation experiments are used to demonstrate that these oligomers are truly present in solution, and are not a result of collision-induced dissociation (CID) events within the spraying chamber of the ESI-MS instrument. Subsequent reassembly is demonstrated by addition of phosphonate ligands to the system, which results in the reassembly of the molybdate oligomers into Strandberg-type molybdate ring systems; $[TBA]_4[Mo_5O_{15}(t\text{BuPO}_3)_2]$ (**1**) and $[TDP\text{-}H_2]_2[Mo_5O_{15}(t\text{BuPO}_3)_2]$ (**2**). These phosphonate-stabilised compounds represent hybrid POM systems. The templating effects of the phosphonate ligand in reassembling these ring systems is briefly considered.

Chapter 3 extends the disassembly-reassembly methodology to mixed-metal systems, specifically copper-molybdate systems. Addition of copper salts to the reaction along with phosphonate ligands generates two mixed-metal compounds, $[TBA]_2[Mo^{VI}_6Cu^{II}_4O_{16}(OH)_2(t\text{BuPO}_3)_4(py)_2(CH_3O)_4(H_2O)]$ (**3**) and $[TBA]_2[Mo^{VI}_7Cu^{VI}_7O_{19}(OH)(CH_3O)_7(t\text{BuPO}_3)_6(py)_2]$ (**4**). These phosphonate-stabilised, copper-containing compounds represent both hybrid POMs and TMS-POMs. **3** can be formally conceptualised as a $\{Cu_4\}$ core encapsulated by two $\{Mo_3\}$ moieties in a sandwich-type motif, while **4** can be formally treated as a $\{Cu_7\}$ core encapsulated by $\{Mo_2\}$ and $\{Mo_3\}$ moieties. The $\{Mo_2\}$ and $\{Mo_3\}$ moieties are identified as arising from the disassembly of the Lindqvist hexamolybdate into dinuclear and trinuclear molybdate oligomers, as observed in chapter 2. Phosphonate templating effects are briefly considered and determined to be related to the phosphonate template effect observed in chapter 2 for compounds **1** and **2**. Additionally, the magnetic behaviour of the compounds is examined.

Chapter 4 extends the assembly-disassembly-reassembly methodology to cobalt-molybdate systems and explores a set of ligand substitution reactions to modify the properties of the resulting compounds. The mixed-metal hybrid POM compound $[TBA]_2[Mo^{VI}_{10}Co^{II}_6O_{12}(\mu\text{-}O)_{14}(\mu_3\text{-}O)_4(t\text{BuPO}_3)_6(MeCOO)_2(py)_2(H_2O)_6]$ (**5**) is generated using the disassembly-reassembly methodology. The compound is stabilised by phosphonate, carboxylate and pyridyl ligands; orthogonal substitution of these ligands results in a series of 20 further compounds being isolated with a range of steric and electronic functionalities grafted on to the cluster core *via* the supporting organic ligands. These analogues are briefly discussed and the effects that ligand substitution has on the physicochemical properties of the compounds is discussed. One example in this series is a polymer system composed of $\{Mo_{10}Co_6\}$ units connected *via* 1,4-phenylenediacetate ligands, $[TBA]_2[Mo^{VI}_{10}Co^{II}_6O_{12}(\mu\text{-}O)_{14}(\mu_3\text{-}O)_4(t\text{BuPO}_3)_6(PDA)(py)_4(H_2O)_6]$, (**25**). The phosphonate templating effect is briefly discussed again, and demonstrated to be related to the effects observed in chapters 2 and 3.

Chapter 5 extends the assembly-disassembly-reassembly methodology to manganese-molybdate systems, and explores the redox behaviour of some of the resulting compounds. The manganese analogue of compound **5**, $[TBA]_2[Mo^{VI}_{10}Mn^{II}_6O_{12}(\mu\text{-}O)_{14}(\mu_3\text{-}O)_4(t\text{BuPO}_3)_6(MeCOO)_2(py)_4(H_2O)_6]$ (**26)** is generated using the same methodology. The phosphonate and pyridyl ligands are shown to be amenable to the same simple orthogonal ligand substitution as observed in chapter 4. Moreover, the carboxylate ligands are demonstrated to arise *via in-situ* carbon-carbon bond cleavage of acetylacetonate-type ligands. Atmospheric oxygen is demonstrated to play an important role in this bond cleavage, possibly as an oxygen source for generation of the carboxylate ligands. A polymeric analogue $[TBA]_2[Mo^{VI}_{10}Mn^{II}_6O_{12}(\mu\text{-}O)_{14}(\mu_3\text{-}O)_4(t\text{BuPO}_3)_6(PDA)(py)_4(H_2O)_6]$, (**30)**, is also generated using 1,4-phenylenediacetate ligands. Modification of the reaction conditions produces an unrelated mixed-metal compound, $[ClMn_6(t\text{BuPO}_3)_8(py)_6][Mo^{VI}_2Mn^{III}_{11}O_2(\mu\text{-}O)_4(\mu_3\text{-}O)_4(\mu_4\text{-}O)_2(\mu\text{-}OH)_2(t\text{BuPO}_3)_{10}(py)_4]$ (**31**). Modifications of the reaction conditions can replace the $\{Mn_6\}$ cation with a bromide-centred analogue $[BrMn_6(t\text{BuPO}_3)_8(py)_6]^+$ (**32**) or tetrabutylammonium (**33**). Compound **33** is demonstrated to be a catalyst for the water oxidation reaction.

Chapter 6 extends some of the disassembly-reassembly concepts to metal-organic framework (MOF) materials. It is demonstrated that the chloride- and bromide- centred $[ClMn_6(t\text{BuPO}_3)_8(py)_6]^+$ and $[BrMn_6(t\text{BuPO}_3)_8(py)_6]^+$ cations from chapter 5 can be linked together *via* ditopic pyridyl linkers to generate two- or three-dimensional frameworks, $[ClMn_6(t\text{BuPO}_3)_8(bpy)_3]Cl$ (**34**), $[ClMn_6(t\text{BuPO}_3)_8(bpy)_2(H_2O)_2]Cl$ (**35**) and $[BrMn_6(t\text{BuPO}_3)_8(bpy)_3]Br$ (**36**). It is demonstrated that the addition of a competing ligand such as pyridine can displace the linker units, releasing the building units into solution. Subsequent removal of the competing ligand causes the building units to reassemble into their parent framework. Some potential applications of this effect are explored.

Chapter 7 describes the experimental details of the work carried out.

Chapter 8 provides a brief conclusion and outlines some possible directions that this research could explore in the future.

Table of Contents

Definitions

Abbreviations

(FT)IR	(Fourier Transform) Infrared Spectroscopy
(SC)XRD	(Single Crystal) X-ray Diffraction
ATR	Attenuated Total Reflectance
BVS	Bond Valence Sum
CHN	Carbon Hydrogen Nitrogen (elemental analysis)
CID	Collision-Induced Dissociation
CV	Cone Voltage
DI	Distortion Index
ESI	Electrospray Ionisation
MALDI	Matrix Assisted LASER Desorption Ionisation
MOF	Metal-Organic Framework
MS	Mass Spectrometry
POM	Polyoxometalate
PSII	Photosystem II
PXRD	Powder X-ray Diffraction
SBU	Secondary Building Unit
SQUID	Superconducting Quantum Interference Device
TGA	Thermogravimetric Analysis
TMS-POM	Transition Metal Substituted Polyoxometalate
TON	Turnover Number
UV-Vis	Ultraviolet-Visible Absorption Spectroscopy

Symbols

b	Empirical Bond Valence Sum Parameter
B_0	Idealised Bond Length
B_i	Individual Bond Length
C	Curie Constant
DI	Distortion Index
g	Landé g-Factor
k_B	Boltzman's Constant
m/z	Mass-to-Charge Ratio
N	Avogadro's Constant
R	Organic (CH-containing) Moiety
S	(Ground) Spin State
s	Seconds
T	Temperature
α_i	Individual Bond Angle (in degrees)
α_m	Average Bond Angle (in degrees)
ε	Absorption Coefficient
θ	Tetrahedral Bond Angle (in degrees)
λ	Wavelength
μ_B	Bohr Magneton
σ^2_{oct}	Bond Angle Variance
τ_4	Four-Coordinate Geometry Index
τ_5	Five-Coordinate Geometry Index
χ	Magnetic Susceptibility

Formulae

$$BVS = \sum exp \frac{(B_0 - B_i)}{b}$$

$$\sigma_{oct}^2 = \frac{1}{11}\sum_{i=1}^{12}(\alpha_i - 90°)^2$$

$$DI = \frac{1}{12\alpha_m}\sum_{i=1}^{12}|\alpha_i - \alpha_m|$$

$$\tau_4 = \frac{360° - (\alpha_1 + \alpha_2)}{360° - 2\theta}$$

$$\tau_5 = \frac{\alpha_1 - \alpha_2}{60°}$$

$$C = \chi T = \frac{N\mu_B^2}{3k_b} g^2(S)(S+1)$$

Chemicals and Chemical Moieties

Acac-H	Acetylacetone	$C_5H_8O_2$	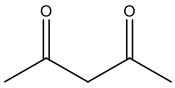
Ad	Adamantyl	$C_{10}H_{15}$	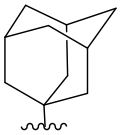
Anth	9-Anthracene	$C_{14}H_9$	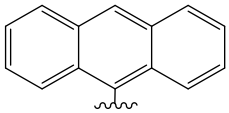
Azo	4-(Phenylazo)phenyl	$C_{12}H_9N_2$	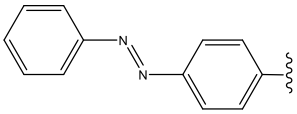
Bpy	4,4'-bipyridine	$C_{10}H_8N_2$	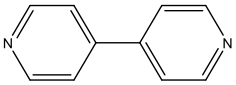
Br_2Ph	3,5-Dibromophenyl	$C_6H_3Br_2$	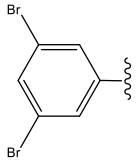
BrPh	4-Bromophenyl	C_6H_4Br	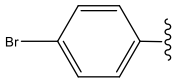
Bz	Benzyl	C_7H_7	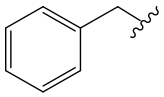
CHOPh	4-Formylphenyl	C_6H_6N	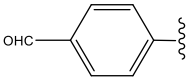
Flu	9-Fluorene	$C_{13}H_9$	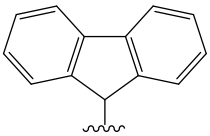
Nap	2-Naphthyl	$C_{10}H_7$	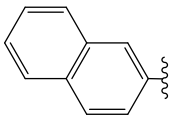
NH_2Ph	4-Aminophenyl	C_6H_6N	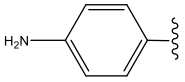
NO_2Ph	4-Nitrophenyl	$C_6H_4NO_2$	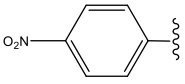
PDA-H_2	1,4-Phenylenediacetic Acid	$C_{10}H_{10}O_4$	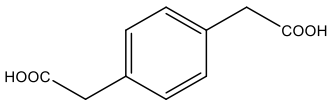
Ph	Phenyl	C_6H_5	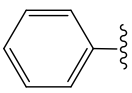

Pic	Picoline	C_6H_7N	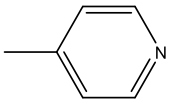
Pip	Piperazine	$C_4H_{10}N_2$	
Py	Pyridine	C_5H_5N	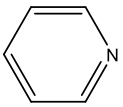
Pyr	1-Pyrene	$C_{16}H_9$	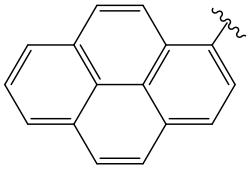
TBA	Tetrabutylammonium	$C_{16}H_{36}N^+$	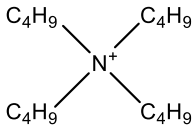
*t*Bu	*Tert*-Butyl	C_4H_9	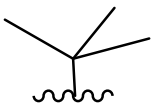
TDP	Trimethylenedipyridine	$C_{13}H_{14}N_2$	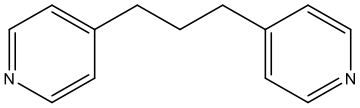
TMH-H	2,2,6,6-Tetramethylheptanedione	$C_{11}H_{20}O_2$	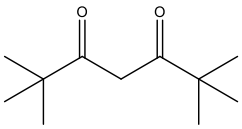
TPA-H_2	Terephthalic acid	$C_8H_6O_4$	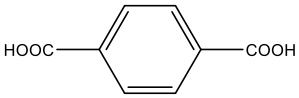
Van	4-hydroxy-3-methoxyphenyl	$C_7H_7O_2$	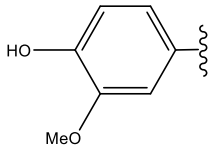

List of Compounds

1 $[pip\text{-}H_2]_4[Mo_5O_{15}(t\text{BuPO}_3)_2]$

2 $[TDP\text{-}H_2]_2[Mo_5O_{15}(t\text{BuPO}_3)_2]$

3 $[TBA]_2[Mo^{VI}_6Cu^{II}_4O_{16}(OH)_2(t\text{BuPO}_3)_4(CH_3O)_4(py)_2(H_2O)]$

4 $[TBA]_2[Mo^{VI}_7Cu^{VI}_7O_{19}(OH)(t\text{BuPO}_3)_6(CH_3O)_7(py)_2]$

5 $[TBA]_2[Mo^{VI}_{10}Co^{II}_6O_{12}(\mu\text{-O})_{14}(\mu_3\text{-O})_4(t\text{BuPO}_3)_6(MeCOO)_2(py)_2(H_2O)_6]$

6 $[TBA]_2[Mo^{VI}_{10}Co^{II}_6O_{12}(\mu\text{-O})_{14}(\mu_3\text{-O})_4(t\text{BuPO}_3)_6(MeCOO)_2(pic)_4(H_2O)_6]$

7 $[TBA]_2[Mo^{VI}_{10}Co^{II}_6O_{12}(\mu\text{-O})_{14}(\mu_3\text{-O})_4(t\text{BuPO}_3)_6(PhCOO)_2(py)_2(H_2O)_6]$

8 $[TBA]_2[Mo^{VI}_{10}Co^{II}_6O_{12}(\mu\text{-O})_{14}(\mu_3\text{-O})_4(t\text{BuPO}_3)_6(BzCOO)_2(py)_2(H_2O)_6]$

9 $[TBA]_2[Mo^{VI}_{10}Co^{II}_6O_{12}(\mu\text{-O})_{14}(\mu_3\text{-O})_4(t\text{BuPO}_3)_6(AdCOO)_2(py)_2(H_2O)_6]$

10 $[TBA]_2[Mo^{VI}_{10}Co^{II}_6O_{12}(\mu\text{-O})_{14}(\mu_3\text{-O})_4(AdPO_3)_6(MeCOO)_2(py)_2(H_2O)_6]$

11 $[TBA]_2[Mo^{VI}_{10}Co^{II}_6O_{12}(\mu\text{-O})_{14}(\mu_3\text{-O})_4(AdPO_3)_6(PhCOO)_2(py)_2(H_2O)_6]$

12 $[TBA]_2[Mo^{VI}_{10}Co^{II}_6O_{12}(\mu\text{-O})_{14}(\mu_3\text{-O})_4(AdPO_3)_6(BzCOO)_2(py)_3(H_2O)_6]$

13 $[TBA]_2[Mo^{VI}_{10}Co^{II}_6O_{12}(\mu\text{-O})_{14}(\mu_3\text{-O})_4(AdPO_3)_6(AdCOO)_2(py)_2(H_2O)_6]$

14 $[TBA]_2[Mo^{VI}_{10}Co^{II}_6O_{12}(\mu\text{-O})_{14}(\mu_3\text{-O})_4(t\text{BuPO}_3)_6(BrPhCOO)_2(py)_2(H_2O)_6]$

15 $[TBA]_2[Mo^{VI}_{10}Co^{II}_6O_{12}(\mu\text{-O})_{14}(\mu_3\text{-O})_4(t\text{BuPO}_3)_6(Br_2PhCOO)_2(py)_2(H_2O)_6]$

16 $[TBA]_2[Mo^{VI}_{10}Co^{II}_6O_{12}(\mu\text{-O})_{14}(\mu_3\text{-O})_4(t\text{BuPO}_3)_6(NO_2PhCOO)_2(py)_4(H_2O)_6]$

17 $[TBA]_2[Mo^{VI}_{10}Co^{II}_6O_{12}(\mu\text{-O})_{14}(\mu_3\text{-O})_4(t\text{BuPO}_3)_6(NH_2PhCOO)_2(py)_2(H_2O)_6]$

18 $[TBA]_2[Mo^{VI}_{10}Co^{II}_6O_{12}(\mu\text{-O})_{14}(\mu_3\text{-O})_4(t\text{BuPO}_3)_6(CHOCOO)_2(py)_2(H_2O)_6]$

19 $[TBA]_2[Mo^{VI}_{10}Co^{II}_6O_{12}(\mu\text{-O})_{14}(\mu_3\text{-O})_4(t\text{BuPO}_3)_6(VanCOO)_2(py)_4(H_2O)_6]$

20 $[TBA]_2[Mo^{VI}_{10}Co^{II}_6O_{12}(\mu\text{-O})_{14}(\mu_3\text{-O})_4(t\text{BuPO}_3)_6(NapCOO)_2(py)_2(H_2O)_6]$

21 $[TBA]_2[Mo^{VI}_{10}Co^{II}_6O_{12}(\mu\text{-O})_{14}(\mu_3\text{-O})_4(t\text{BuPO}_3)_6(AnthCOO)_2(py)_2(H_2O)_6]$

22 $[TBA]_2[Mo^{VI}_{10}Co^{II}_6O_{12}(\mu\text{-O})_{14}(\mu_3\text{-O})_4(t\text{BuPO}_3)_6(PyrCOO)_2(py)_2(H_2O)_6]$

23 $[TBA]_2[Mo^{VI}_{10}Co^{II}_6O_{12}(\mu\text{-O})_{14}(\mu_3\text{-O})_4(t\text{BuPO}_3)_6(FluCOO)_2(py)_2(H_2O)_6]$

24 $[TBA]_2[Mo^{VI}_{10}Co^{II}_6O_{12}(\mu\text{-O})_{14}(\mu_3\text{-O})_4(t\text{BuPO}_3)_6(AzoCOO)_2(py)_2(H_2O)_6]$

25 $[TBA]_2[Mo^{VI}_{10}Co^{II}_6O_{12}(\mu\text{-O})_{14}(\mu_3\text{-O})_4(t\text{BuPO}_3)_6(PDA)(py)_2(H_2O)_6]$

26 $[TBA]_2[Mo^{VI}_{10}Mn^{II}_6O_{12}(\mu\text{-O})_{14}(\mu_3\text{-O})_4(t\text{BuPO}_3)_6(MeCOO)_2(py)_4(H_2O)_6]$

27 $[TBA]_2[Mo^{VI}_{10}Mn^{II}_6O_{12}(\mu\text{-O})_{14}(\mu_3\text{-O})_4(t\text{BuPO}_3)_6(MeCOO)_2(MeOH)_4(H_2O)_6]$

28 $[TBA]_2[Mo^{VI}_{10}Mn^{II}_6O_{12}(\mu\text{-O})_{14}(\mu_3\text{-O})_4(AdPO_3)_6(MeCOO)_2(py)_4(H_2O)_6]$

29 $[TBA]_2[Mo^{VI}_{10}Mn^{II}_6O_{12}(\mu\text{-O})_{14}(\mu_3\text{-O})_4(t\text{BuPO}_3)_6(t\text{BuCOO})_2(MeOH)_4(H_2O)_6]$

30 $[TBA]_2[Mo^{VI}_{10}Mn^{II}_6O_{12}(\mu\text{-O})_{14}(\mu_3\text{-O})_4(t\text{BuPO}_3)_6(PDA)(py)_4(H_2O)_6]$

31 $[ClMn^{III}_6(t\text{BuPO}_3)_8(py)_6][Mo^{VI}_2Mn^{III}_{11}O_2(\mu\text{-O})_4(\mu_3\text{-O})_4(\mu_4\text{-O})_2(\mu\text{-OH})_2(t\text{BuPO}_3)_{10}(py)_4]$

33 $[BrMn^{III}_6(t\text{BuPO}_3)_8(py)_6][Mo^{VI}_2Mn^{III}_{11}O_2(\mu\text{-O})_4(\mu_3\text{-O})_4(\mu_4\text{-O})_2(\mu\text{-OH})_2(t\text{BuPO}_3)_{10}(py)_4]$

33 $[TBA][Mo^{VI}_2Mn^{III}_{11}O_2(\mu\text{-O})_4(\mu_3\text{-O})_4(\mu_4\text{-O})_2(\mu\text{-OH})_2(t\text{BuPO}_3)_{10}(py)_4]$

34 $[ClMn^{III}_6(t\text{BuPO}_3)_8(bpy)_3]Cl$

35 $[ClMn^{III}_6(t\text{BuPO}_3)_8(bpy)_2(H_2O)_2]Cl$

36 $[BrMn^{III}_6(t\text{BuPO}_3)_8(bpy)_3]Br$

Chapter 1

Introduction

1.1) Motivation

Some of the most intractable challenges facing the world today – changing climates, diminishing natural resources, rapidly evolving healthcare challenges – are best faced, either wholly or in part, with chemical solutions. However, in order to meet these challenges, increasingly sophisticated chemical processes will be required.

In order to develop increasingly sophisticated chemical processes, increasingly sophisticated materials with complicated architectures and combinations of diverse functionalities will be necessary. Therefore, at the beginning of this research project, our aim was to develop new examples of advanced materials.

In particular, we were interested in developing materials with combinations of distinct components. Two classes of material were identified as suitable targets:

- *Mixed-Metal Materials*
- *Organic-Inorganic Hybrid Materials*

Both of these classes of material are comprised of distinct components, with their own inherent properties, which can (at least in principle) combine into a material with more complex chemical and physical properties than their constituent parts. We were interested in developing new examples of these materials, and examining how their molecular structures influenced their bulk properties.

Furthermore, we were interested in examining how the nanoscale architecture of a material influenced these bulk properties. Two classes of material with defined nanostructures were identified as suitable targets:

- *Polymeric Materials*
- *Framework Materials*

Both of these classes of materials are comprised of multiple components in an extended architecture, which can (at least in principle) result in a material with chemical and physical properties distinct from the constituent parts. Again, we were interested in developing new examples of these materials and examining how their extended architectures influenced their bulk properties.

Over the course of the next chapter, we will introduce and discuss some examples of these classes of materials, and provide a general overview of the relevant literature. Particular attention will be paid to common structural features of these compounds, their physicochemical properties (especially those which give rise to practical applications), and the relationship between the microscopic structure and macroscopic properties. A summary of the standard synthetic methodologies used to access these compounds will also be presented. Additionally, we will consider some of the relevant analytical techniques used in this research. Finally, this chapter will discuss the specific aims and objectives of this research project.

1.2) Polyoxometalates (POMs)

Polyoxometalates (POMs) represent an important category of polymetallic molecular species. They are generally classified as clusters* of group V and VI metals (V, Nb, Ta, Mo and W) with supporting *oxo*- (O^{2-}) ligands.[1,2] More recently, POM-like *oxo*-clusters have been prepared using metals outside of this block, such as the polyoxoaurates[3] and polyoxopaladates,[4] but for the purposes of this thesis, our attention will be focused on the classical POM metals.

The metal centres in a POM (sometimes called *addenda* atoms) are generally in their highest oxidation states (+V or +VI). The supporting *oxo*-ligands play a key structural role, and can be in either bridging or terminal modes. As such, when describing POM structures it is generally convenient to envision a POM cluster as a series of corner-, edge- or face- sharing $\{MO_x\}$ polyhedra (Figure 1.2.1). In this sense, POMs are structurally similar to fragments of the parent bulk metal oxides, and indeed are sometimes used as model compounds to represent bulk oxides.[6,7]

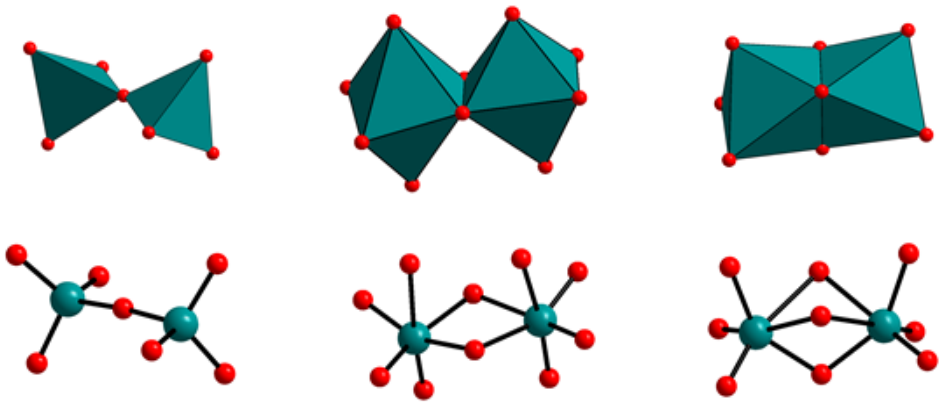

Figure 1.2.1 – Corner-, edge- and face-sharing polyhedra, and their ball-and-stick counterparts. Colour Scheme: M teal, O red.

POMs occur naturally in certain biological systems,[8] and have been investigated synthetically since the early 1800's, beginning with the work of Berzelius[9] and the development of the synthetic dyes known as "molybdenum blues".[10] However, for much of their history, it was extremely difficult to characterise their structures with certainty, as multiple structural configurations were possible for a given elemental composition.[11] Advances in single crystal X-ray diffraction studies, which have become vastly more powerful and rapid over the past 50 years or so, have aided massively in the rapid structural characterisation of novel POM systems. X-ray crystallography remains the key technique for determining the structure of a novel POM compound.

**Footnote:* The term "cluster", under the definition given by Cotton, represents molecular species with metal-metal bond character.[5] POM species generally do not display metal-metal bonds, with metal-metal interactions being mediated by *oxo*- ligands, and so should not technically be designated as clusters. However, it is common convention among POM chemists to shorten the more correct designation "*oxo*-cluster" to simply "cluster". This convention is followed in this work – hence, the use of the term "cluster" should not be construed to reflect metal-metal bond character in any of the species described in this work.

1.2.1) Synthesis and Structures

One commonly cited attractive feature of POMs is the ease with which they can be synthesised, generally employing "one-pot" aggregation and crystallisation of the target species.[12] Classical POM synthesis involves the acidification of aqueous monomeric metal oxides, which triggers polymerisation of the metal oxides (a process known as olation).[13] Olation proceeds *via* a complicated series of condensation steps (Figure 1.2.1.1). While certain details are still the subject of computational and experimental research,[14–16] the general process involves the protonation of terminal *oxo*- ligands, condensation of multiple metal-*oxo* centres, and loss of water from the structure.

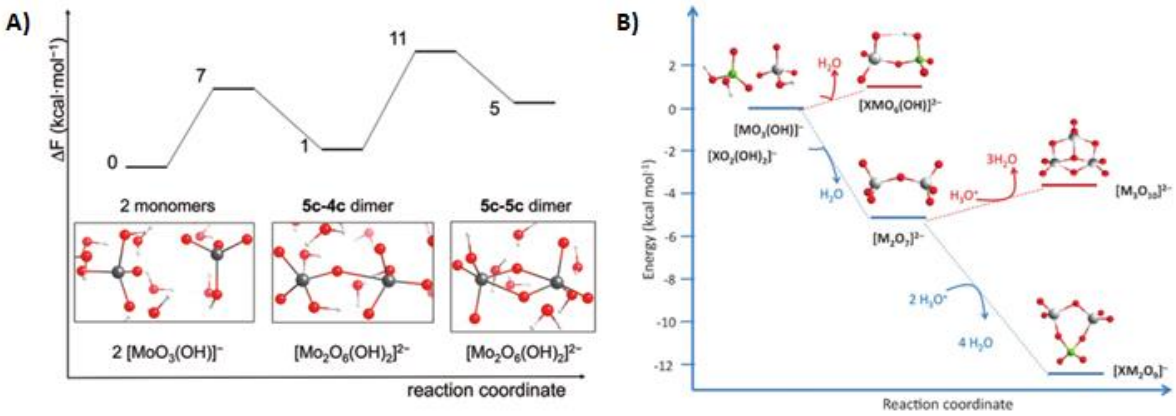

Figure 1.2.1.1 – Two proposed reaction schemes for the aggregation of simple POM systems; A) in the absence of a templating heteroatom, B) in the presence of a templating heteroatom. Reproduced from references 14 and 15, respectively.

The details of olation reactions will not be considered here. However, the overall reaction system can usually be described by fairly simple generic reaction mechanisms. The effect of template species is particularly significant, as multidentate ligands or ions with defined geometry promote certain $\{M_xO_y\}$ geometries over others, stabilising the cluster and driving equilibrium towards a given structure.[17] Two generic formulae for POM synthesis are:

$$(x)MO_4^{n-} + \{template\} \xrightarrow{2(x-1)H^+} [\{template\}M_xO_{3x+1}]^{n-} + (x-1)H_2O$$

$$(x)MO_4^{n-} + \{template\} \xrightarrow{2(x)H^+} [\{template\}M_xO_{3x}]^{n-} + (x)H_2O$$

It should be noted that these generic formulae gloss over much of the details of POM formation.[14–18] Reaction intermediates are poorly understood, often transient in nature, and generally difficult to observe experimentally. The end product of a reaction is influenced by a fine balance of myriad factors, including pH, acid type, metal species, solvent, temperature, concentration, presence of heteroatoms and the presence of ligands.[14–18] As a result, POM synthesis is sometimes considered a "black box" method, where the isolation of new compounds is largely serendipitous.[19] Nevertheless, these generic formulae are sufficient to rationalise many POM structures.

Two archetypal examples of POM species are the Lindqvist and Keggin structures. Both are synthesised *via* the acidification of monomeric metal oxide units, but their structures differ considerably due to a significant template effect.[20,21]

The Lindqvist structure is a hexametalate POM structure with the general formula $[M_6O_{19}]^{2-}$, first reported in 1952 as the tungstate, $[W_6O_{19}]^{2-}$.[22] The structure is synthesised in the absence of a templating species, fitting the generic $[\{template\}M_xO_{3x+1}]^{n-}$ formula for x = 6 and {template} = 0.[22–24] In this structure, six edge-sharing $\{MO_6\}$ octahedra share a central μ_6-O atom. Each metal centre possesses one terminal *–oxo* ligand, with twelve μ_2-O *oxo*- ligands bridging between metal centres. The structure is one of the simplest and most symmetrical available, with overall O_h symmetry (Figure 1.2.1.2).[22–24] The structure is classified as an isopolyoxometalate due to the absence of heteroatoms.

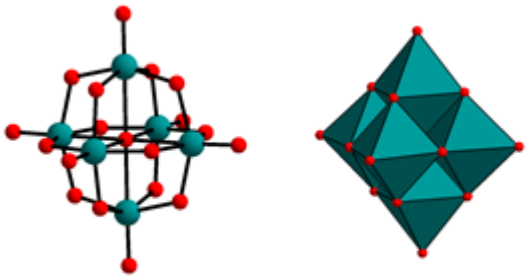

Figure 1.2.1.2 – Ball-and-stick and polyhedral representations of the Lindqvist hexametalate, $[M_6O_{19}]^{n-}$. Colour Scheme: M teal, O red.

The Keggin structure has the generic formula $[XM_{12}O_{40}]^{n-}$. First prepared by Berzelius in 1827, the structure was not finally solved until the 1930's by Keggin.[25] This structure is synthesised in the presence of a tetrahedral templating *oxo*-anion, $\{XO_4\}$, where X is usually P or Si. The structure fits the generic $[\{template\}M_xO_{3x}]^{n-}$ formula for x = 12 and {template} = $\{XO_4\}$.[25–27] In this structure, the tetrahedral *oxo*-anion coordinates to all twelve addenda atoms *via* its four O-donors, each of which coordinates to three metals in $\{M_3O_{13}\}$ units. Twenty-four of the *oxo*- ligands are bridging, while the remaining twelve are terminal.[25–27] The α-isomer of the Keggin structure retains the tetrahedral (T_d) symmetry of their central heteroatom, but four lower symmetry isomers exist which possess one or more $\{M_3O_{13}\}$ units that are twisted relative to the α-isomer (Figure 1.2.1.3).[27] The structure is classified as a heteropolyoxometalate due to the central templating heteroatom.

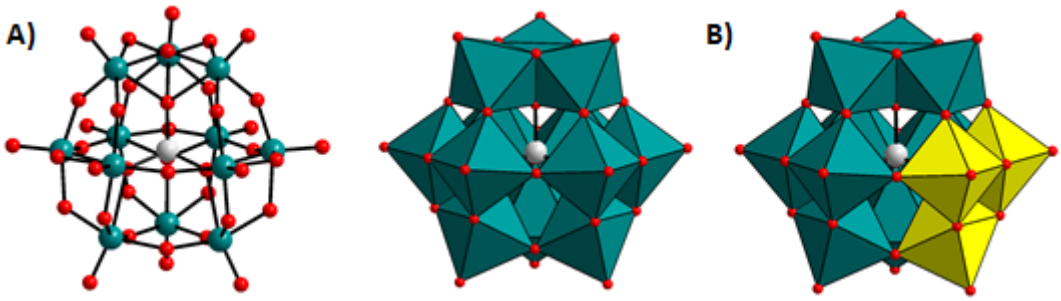

Figure 1.2.1.3 – A) Ball-and-stick and polyhedral representations of the Keggin POM, $[XM_{12}O_{40}]^{n-}$. B) The Keggin structure with one $\{M_3O_{13}\}$ unit highlighted in yellow. Colour Scheme: M teal, O red, X grey.

In addition to the template effect, a general trend in POM synthesis is that further acidification tends to produce larger clusters. In the case of molybdenum, cluster sizes have been reported ranging from relatively simple $[Mo_2O_7]^{2-}$ species up to $[H_{16}Mo_{368}O_{1032}(H_2O)_{240}(SO_4)_{48}]^{48-}$ (Figure 1.2.1.4).[28,29] Pure tungstates do not form such large clusters, with the largest reported up to 2008 being a $[P_4W_{52}O_{178}]^{24-}$ cluster,[30] but the inclusion of heteroatoms can increase tungstate cluster size, for example with the $[H_{34}W_{119}Se_8Fe_2O_{178}]^{24-}$ cluster.[31] The higher nuclearity clusters were generally produced at lower pH. Indeed, acid-driven condensation reactions can proceed to the bulk metal oxide.[32]

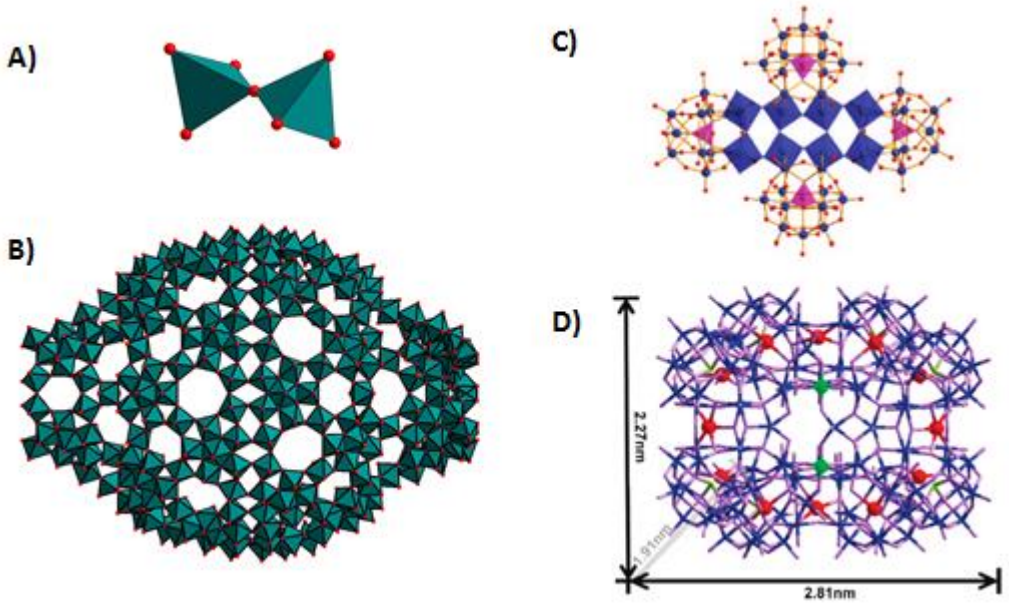

Figure 1.2.1.4 – A) The smallest molybdate cluster isolated, $[Mo_2O_7]^{2-}$. B) The largest molybdate cluster isolated, $[H_{16}Mo_{368}O_{1032}(H_2O)_{240}(SO_4)_{48}]^{48-}$. C) The largest pure tungstate species isolated, $[P_4W_{52}O_{178}]^{24-}$. D) A $[H_{34}W_{119}Se_8Fe_2O_{178}]^{24-}$ cluster that assembles around the Fe heteroatoms. C) and D) reproduced from references 30 and 31, respectively.

The work of Müller *et al* is particularly relevant here. Several gigantic molecular molybdate structures were prepared by exploiting this pH-driven aggregation effect, starting from monomeric metal oxides. One example which garnered significant attention was the $\{Mo_{154}\}$ "big wheel" species, $[Mo_{154}O_{462}H_{14}(H_2O)_{70}]^{14-}$.[33] Reported in 1995, this nanoscale molecule has a torroidal or ring shaped structure which is 3.4 nm wide (outer diameter).[33] Two related molybdate ring structures were reported in the following years – the $\{Mo_{144}\}$ structure is a smaller, defected version of the $\{Mo_{154}\}$ ring,[34] while the $\{Mo_{176}\}$ species displays an expanded ring structure of diameter 4.1 nm (outer diameter).[35] Interestingly, the $\{Mo_{176}\}$ ring cavity can be selectively "filled in" with molybdate units, creating a disc-shaped $\{Mo_{248}\}$ species (Figure 1.2.1.5).[36] This is a rare example of a larger species templating the formation of a smaller unit. Other topologies are possible, with giant spherical clusters such as the $\{Mo_{132}\}$ "keplerate" structure.[37] The largest known molybdate structure to date, $\{Mo_{368}\}$, also has a roughly spherical shape.[29]

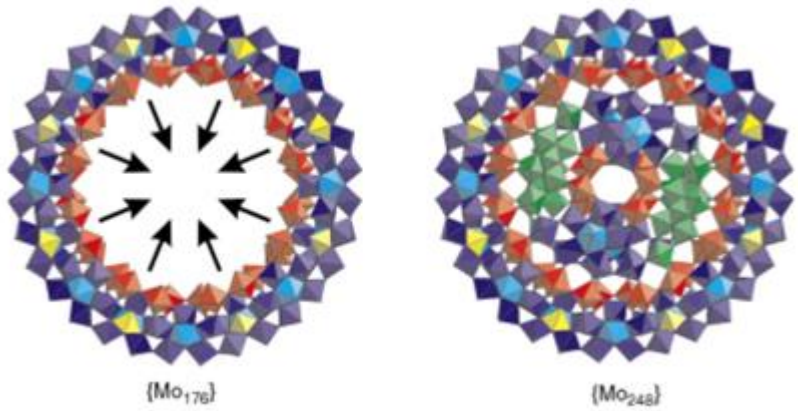

Figure 1.2.1.5 – The ring-shaped {Mo$_{176}$} structure, which can be "filled in" to generate the disk-shaped {Mo$_{248}$} structure. Reproduced from reference 36.

These structures are massive compared to most molecular structures, but are nevertheless discrete molecules with well-defined structures. Despite their size, they are relatively simple to prepare and easy to store and handle. These factors have led this class of materials to attract attention for potential application in nanostructured devices.[38,39] In one example, the {Mo$_{154}$} wheel structure can be assembled in solution into vesicle-like structures roughly 45nm in diameter.[40] In another, the {Mo$_{132}$} keplerate was used for selective host-guest chemistry.[41] Magnetic behaviour can be also imparted to the systems by introducing paramagnetic vanadium (IV) or europium (III) centres into these giant molybdate structures.[42,43]

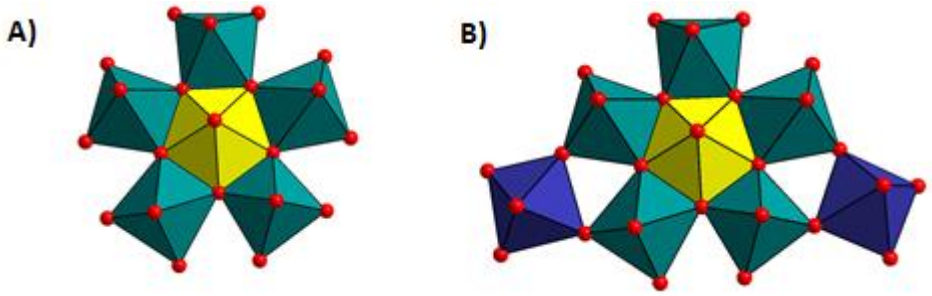

Figure 1.2.1.6 – A) the pentagonal {Mo$_6$} unit observed in many of the giant molybdate structures, with the central {MoO$_7$} unit highlighted in yellow. B) The related {Mo$_8$} unit, with the two additional {MoO$_6$} octahedra highlighted in blue.

It should be noted that these structures are difficult to predict from first principles. Instead, common structural motifs are generally extracted from the crystal structures of the isolated products.[44] In the case of these giant structures, a key structural motif is the pentagonal {Mo$_6$} molybdate unit. This consists of a central {MoO$_7$} core which shares edges with five {MoO$_6$} octahedra to produce a structural unit with C_5 symmetry (Figure 1.2.1.6).[45] Eleven of these units are present in {Mo$_{132}$}, fourteen in {Mo$_{154}$}, and sixteen in {Mo$_{176}$}. The related {Mo$_8$} unit, which is often used to describe such giant structures, can be described as this pentagonal {Mo$_6$} unit plus two additional {MoO$_6$} octahedra (Figure 1.2.1.6).[46]

Ring structures in POMs

Many POM species can be described in terms of ring structures. Ring structures generally form around a central template or templates with the generic formula $[\{template\}M_xO_{3x}]^{n-}$.

The Anderson (or Anderson-Evans) structure, $[XM_6O_{24}]^{n-}$, is a historically significant structure which follows this trend.[47] The structure is consistent with the generic formula, where the templating species is an $\{XO_6\}$ octahedron and x = 6. The structure consists of six $\{MO_6\}$ octahedra, with the octahedra sharing edges with each other in such a way as to bend around into a ring around the central templating heteroatom (Figure 1.2.1.7).[47–50] The Anderson structure can incorporate a wide variety of central heteroatoms; high-valent heteroatoms such as Te^{VI} or I^{VII} tend to produce unprotonated Anderson structures (A-type Anderson structures), while low-valent heteroatoms such as Mn^{II} or Co^{II} tend to produce structures that are protonated at the $\{XO_6\}$ oxygen atoms (B-type Anderson structures).[47–50]

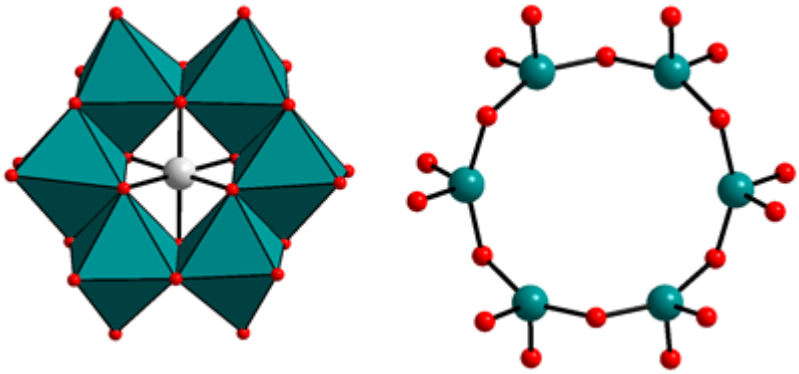

Figure 1.2.1.7 – The Anderson structure, $[XM_6O_{24}]^{n-}$, and the $\{MO_3\}_6$ ring structure with the central $\{XO_6\}$ template removed.

A noteworthy feature of the Anderson structure is that it can be supported by *tris*(alkoxide) ligands, in one of two binding motifs.[51–53] In one, two tripodal alkoxide ligands coordinate to the central heteroatom, providing the oxygen atoms for the $\{XO_6\}$ motif. In another, the tripodal ligands cap a tetrahedral cavity, bridging between the heterometal and the POM units (Figure 1.2.1.8).[51–53] Substitution on only one side of the ring is also possible.[54]

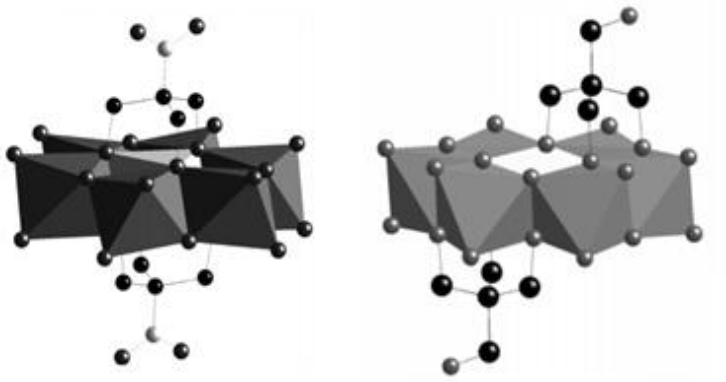

Figure 1.2.1.8 – The two binding modes of *tris*(alkoxide) ligands to Anderson-type POMs. Modified from reference 51.

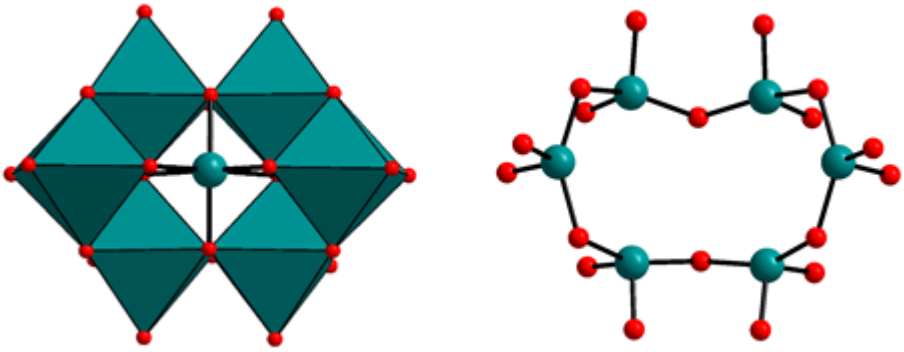

Figure 1.2.1.9 – The heptametalate structure $[M_7O_{24}]^{n-}$, and the $\{MO_3\}_6$ ring structure with the central $\{MO_6\}$ template removed.

The well-known iso-heptametalate species, $[M_7O_{24}]$, could be considered as related to the Anderson structure (Figure 1.2.1.9). This structure could be considered a six-membered $\{MO_3\}_x$ ring templated by an $\{MO_6\}$ octahedron, although it is distorted significantly from the D_{3d} symmetry of the Anderson structure.[55–58]

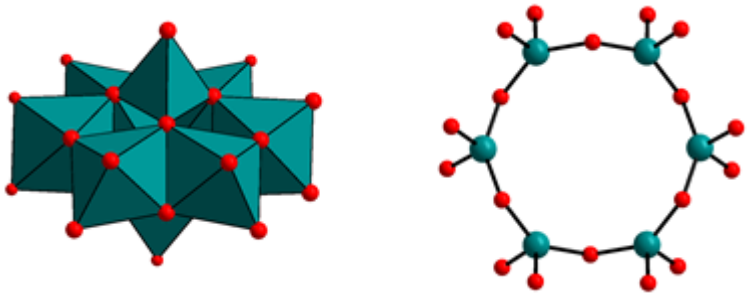

Figure 1.2.1.10 – The α-octametalate structure $[M_8O_{26}]^{n-}$, and the $\{MO_3\}_6$ ring structure with the two central $\{MO_4\}$ templates removed.

Another six membered ring system is the α-isomer of $[M_8O_{26}]^{4-}$, known as α-octametalate.[59–62] This structure is closely related to the Anderson structure, but with different templating units. In this structure, the templates are two $\{MO_4\}$ units, which cap each side of the $\{M_6O_{18}\}$ ring (Figure 1.2.1.10).[59] The $\{MO_4\}$ units both coordinate in a tripodal manner to all six of the metal centres of the ring *via* three μ_3-O ligands (a $\eta^2{:}\eta^2{:}\eta^2{:}\mu_6$ coordination mode). Of the remaining *oxo*- ligands, twelve are terminal and six bridge between metal centres in the ring.[59–62] The structure also possesses D_{3d} symmetry.

The α-octametalate is relatively unusual among POM clusters for retaining a tetrahedral coordination environment. It is more common for metal centres to expand their coordination environment to an octahedral environment upon encapsulation into a POM cluster.

A final significant POM ring structure is the Strandberg structure, $[X_2Mo_5O_{21}]^{n-}$.[63–65] Like the *α*-octamolybdate, this ring is also templated on each side by a $[XO_4]^{n-}$ tetrahedral anion (X in this case can be P, S, As or Se).[63–66] In this case, however, the ring is pentanuclear (Figure 1.2.1.11). Each anion binds to each metal centre in the ring in a $\eta^1{:}\eta^2{:}\eta^2{:}\mu_5$ coordination mode, with five bridging and ten terminal *oxo*- ligands completing the ring structure.[63–66]

Significantly, Strandberg-type ring structures can also be formed using organic ligands such as phosphonates, RPO_3.[67–69] These possess similar chemical and electronic properties to the phosphate ion, $[PO_4]^{3-}$, but contain organic moieties. A phosphonate-supported Strandberg-type ring structure was the first reported example of a hybrid POM species (*i.e.* one containing organic backbones). Many analogous compounds were subsequently reported.[67–69] The merits of hybrid POM structures will be discussed in more detail later.

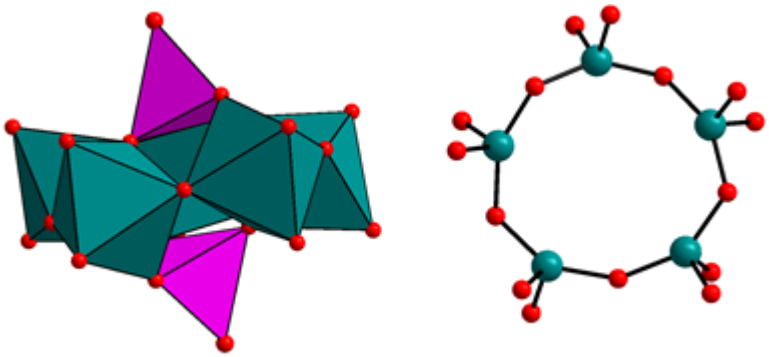

Figure 1.2.1.11 – The Strandberg structure $[M_5O_{15}(XO_4)_2]^{n-}$, and the $\{MO_3\}_5$ ring structure with the two central $\{XO_4\}$ templates removed.

Both the *α*-octamolybdate and Strandberg structures can be described as an $\{MoO_3\}_n$ ring capped on either side by two tetrahedral $\{XO_4\}$ moieties. The difference in nuclearity may be due to the different sizes of the tetrahedral template species – the tetrahedral Mo-O bonds in the *α*-octamolybdate structure are *c.* 1.7 Å,[59] while the P-O bonds in the phosphate-templated Strandberg structure are *c.* 1.5 Å,[63] promoting a smaller five-membered ring. These shorter bond lengths may preclude the formation of larger six membered rings.

Lacunary POMs

The lacunary POMs are another important subset of POM clusters. Essentially, these are structures which can be conceptualised as a "complete" POM structure (*e.g.* the Keggin structures mentioned earlier), but with one or more of the metal atoms (and any terminal *oxo*- ligands which stabilise them) removed from the structure. The resulting defect site is referred to as the "lacuna" (Figure 1.2.1.12). Some more complicated POM structures can be defined in terms of lacunary structures – for example, the common Dawson POM can be described as a dimer of two lacunary Keggin structures.[70]

Essentially, the formation of lacunary structures is a pH-driven process – if decreasing pH causes the cluster to form, then careful control of the pH can "trap" the POM at a partially formed or lacuna stage. In some cases, lacunary structures are extremely difficult to isolate, but even when obtainable they can require very precise reaction conditions to prepare (the literature procedure for one lacunary Keggin structure requires the system to be "held at pH=9.1 for sixteen minutes").[71] Nevertheless, lacunary POM structures are extremely common intermediates in the literature due to their reproducible syntheses, well-defined geometric and electronic attributes, and tendency to be highly reactive towards heterometals.

The lacuna site is essentially a cavity with multiple charged *oxo*- ligands arranged in a pre-ordered geometry that is favourable to bind metal centres in a chelating fashion. Thus, any heterometal added to the system will tend to anchor into this cavity. As such, lacunary POMs are sometimes described as "ligands" for heterometal systems.[72]

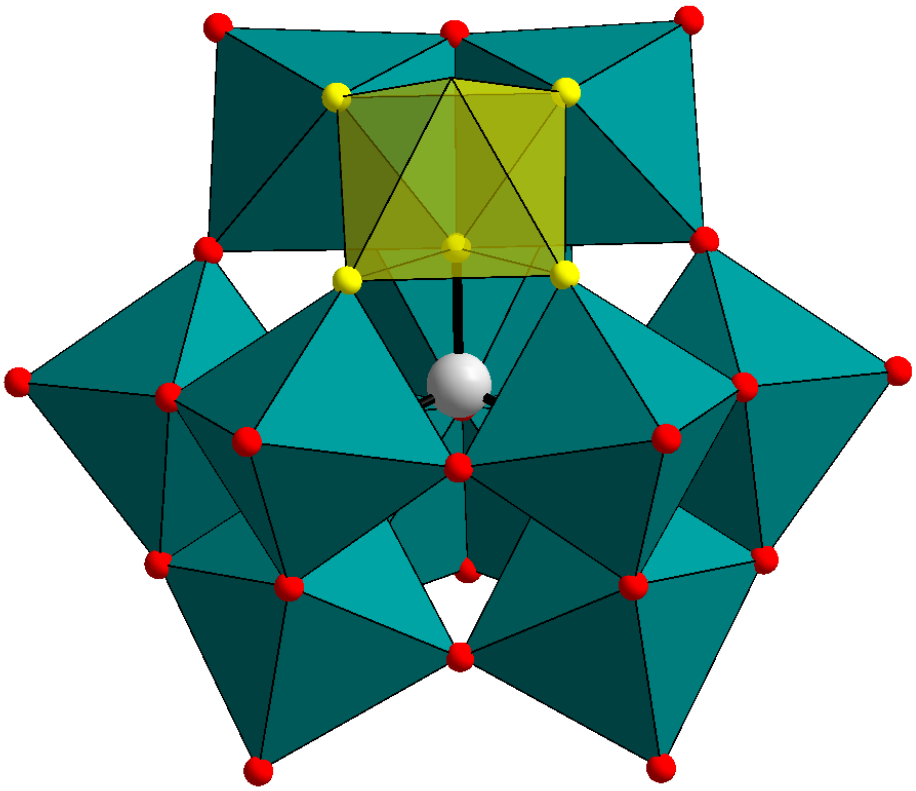

Figure 1.2.1.12 – A lacunary Keggin Structure, $[XM_{11}O_{39}]^{n-}$, with the "missing" octahedron highlighted in yellow. The five O atoms lining the lacuna (yellow) form a pre-ordered cavity to encapsulate metal centres. Colour Scheme: Mo teal, O red or yellow, X grey.

Transition Metal Substituted POMs

Transition Metal Substituted POMS (TMS-POMs) represent another important subclass of POM structures. TMS-POMs combine classical POM fragments with some other transition metal or metals to produce mixed-metal molecular species.

Synthetically, TMS-POMs can be accessed by self-assembly methods. Using lacunary POMs as precursors in these reactions lends a degree of synthetic control to these systems.[73] For example, the B-α-isomer of the trilacunary Keggin tungstate structure can be used with a variety of metals to form $\{Ni_6\}$, $\{Ni_7\}$, $\{Cu_6\}$, $\{Cu_8\}$ or $\{Fe_{13}\}$ structures (Figure 1.2.1.13).[74,75] Isomerisation of the lacunary unit can produce subtly different TMS-POM structures, for example a series of $\{Mn_3\}$-substituted tungstates with varying electrochemical and magnetic properties.[76] Extremely large clusters can be isolated with this methodology, including a $\{Mn_{40}W_{224}\}$ cluster formed from lacunary Dawson tungstates.[77] Mixed-metal species can also be generated using this approach, such as the high oxidation state $\{Mn^{IV}{}_6Ce^{IV}\}$ and $\{Mn^{IV}{}_6Ce^{IV}{}_9\}$ clusters formed from lacunary Dawson tungstates.[78,79] The motif of sandwich- or half-sandwich compounds is not universal but occurs frequently in these systems.[80]

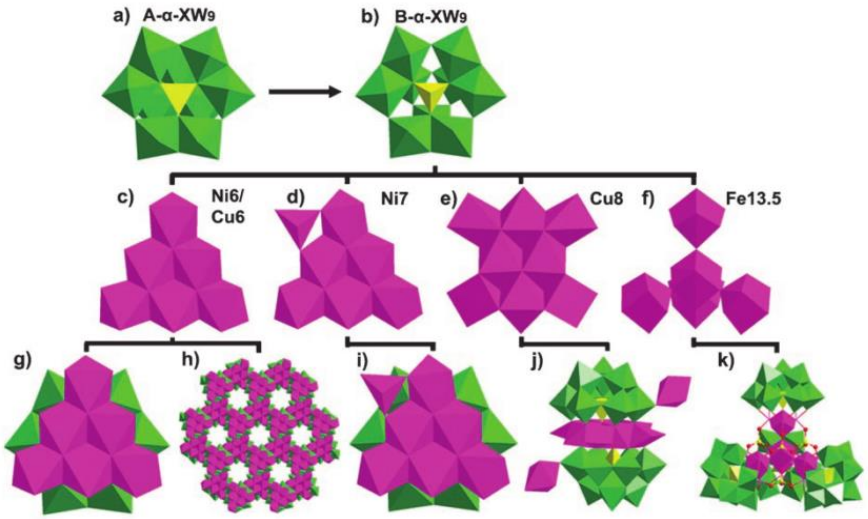

Figure 1.2.1.13 – Schematic of a lacunary Keggin cluster, B-α-$[XW_9O_{34}]^{n-}$, can be formally combined with several other heterometal clusters to generate a range of TMS-POM species. Reproduced from reference 74.

Once incorporated into the POM structure, the heterometals provide a range of functionality, most notably tuning the electronic and magnetic properties of the POM. Pure POMs are generally diamagnetic and exist primarily in their highest oxidation state, but TMS-POMs can access a much wider range of electronic states. For example, if multiple heterometals are present in the same structure, interactions between spin centres can be present, producing interesting magnetic behaviour. Examples of this type of behaviour include $[Mn_{14}O_{12}(PO_4)_4(PW_9O_{34})_4]^{31-}$ and $[Mo_{57}Cu_6(NO)_6O_{177}(H_2O)_{24}]^{24-}$, both of which display strong antiferromagnetic coupling behaviour between the paramagnetic spin centres embedded in the POM core.[81,82] Moreover, TMS-POMs can display single molecule magnet behaviour, such as in the case of a $[Mn_6O_4(H_2O)_4(SiW_9O_{34})_4]^{12-}$ cluster.[83]

Furthermore, the heterometal ligand site offers an important catalytic function, as a variety of substrates can coordinate to this site, allowing reactivity to take place that would otherwise not be possible. Examples of catalytically active TMS-POMs will be discussed in the next section.

1.2.2) Applications

POMs have attracted attention for a wide-ranging set of potential applications.[84] Practical applications for POMs include solar cells,[85] optical devices,[86] water purification,[87] sensing applications,[88] medicine,[89] magnetics[90] and electronic devices.[91] Here, we shall focus primarily on the use of POMs for catalytic purposes.

POMs are generally considered to be quite robust species. As long as structural rearrangement is not triggered by the system drifting out of a given pH range, POMs are generally capable of reversibly accepting and donating both protons and electrons without significant change to the structure of the cluster (Figure 1.2.1.1).[92] Indeed, the robustness of POMs towards changes in redox state has allowed POM solutions to be exploited as electrolytes.[93–95] Additionally, POMs can be powerful proton donors, and are sometimes referred to as "heteropolyacids" for this reason.[96] Heterogeneous POMs have therefore found use as acid catalysts in place of soluble mineral acids, for example in the acid-catalysed Friedel-Crafts acylation of benzene with benzoic anhydride to benzophenone (Figure 1.2.1.1).[97]

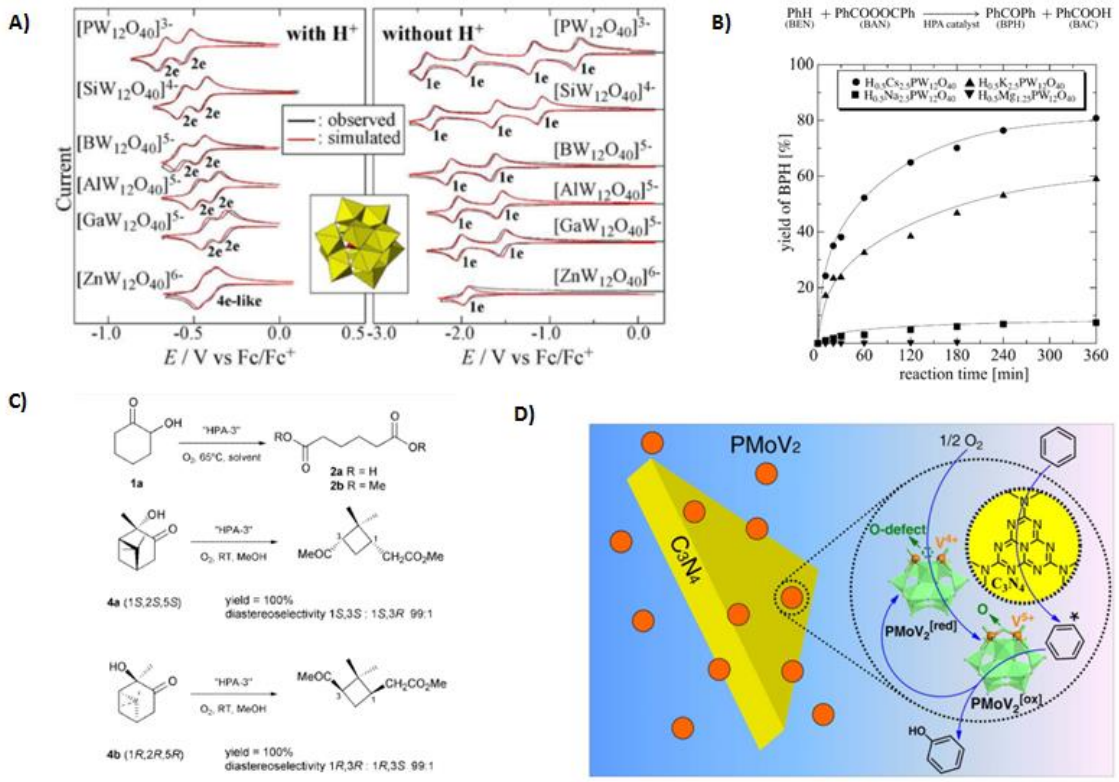

Figure 1.2.2.1 – A) Cyclic voltammagrams of several Keggin tungstates, $[XW_{12}O_{40}]^{n-}$, showing multiple reversible redox steps. B) Comparison of the kinetics of Friedel-Crafts acylation of benzene by several Keggin tungstates, $[XW_{12}O_{40}]^{n-}$. C) Some redox reactions catalysed by a mixed-metal Keggin POM, $[PV_3Mo_9O_{40}]^{6-}$, including production of adipic acid. D) Schematic of a multicomponent system that uses the mixed-metal Keggin POM $[PV_2Mo_{10}O_{40}]^{5-}$ to oxidise benzene to phenol. Modified from references 92, 97, 100 and 102.

In addition to their electron and proton transport capabilities, examples of redox catalysis using POMs are well documented. For example, $[PW_{12}O_{40}]^{3-}$ can be used to selectively oxidise alkenes to epoxides using peroxide under biphasic conditions.[98] $[PMo_{12}O_{40}]^{3-}$ can be used to oxidise alcohols to ketones using DMSO as an oxygen donor.[99] More powerful oxidation reactions by POMs include the oxidative cleavage of C-C bonds in various substituted cyclohexanes to produce the industrially relevant adipic acid by mixed-metal $[PV_3Mo_9O_{40}]^{6-}$ (Figure 1.2.1.1).[100,101] The related $[PV_2Mo_{10}O_{40}]^{5-}$ can even aerobically oxidise very inert substrates such as benzene to produce phenol in a one-step process.[102]

More recently, POMs have attracted attention for their ability to perform powerful redox reactions relevant to renewable fuel production. In particular, oxidation of biomass by Keggin-type POMs has been investigated by Neumann *et al*. The divanadate-substituted Keggin structured phosphomolybdate, $H_5[PV_2Mo_{10}O_{40}]$, was used to oxidise cellulose and hemicellulose to formic acid in a reasonable yield (Figure 1.2.2.2).[103] The pentavanadate $H_8[PV_5Mo_7O_{40}]$ was also used to perform the same reaction, this time using *in-situ* extraction of the product to improve the yield to 61% from raw beech wood.[104] The mono-, di- and tri-vanadate substituted structures were compared for their ability to oxidise glycerol to formic acid, again with good yields (~40%).[105] These processes, in conjunction with gas reforming of formic acid, are postulated to be a source of hydrogen from biomass.[103–105] Similar behaviour was exploited to generate electricity directly from biomass, by using starch to photochemically reduce $[PMo_{12}O_{40}]^{3-}$ which was subsequently re-oxidised in a fuel cell (Figure 1.2.2.2).[106]

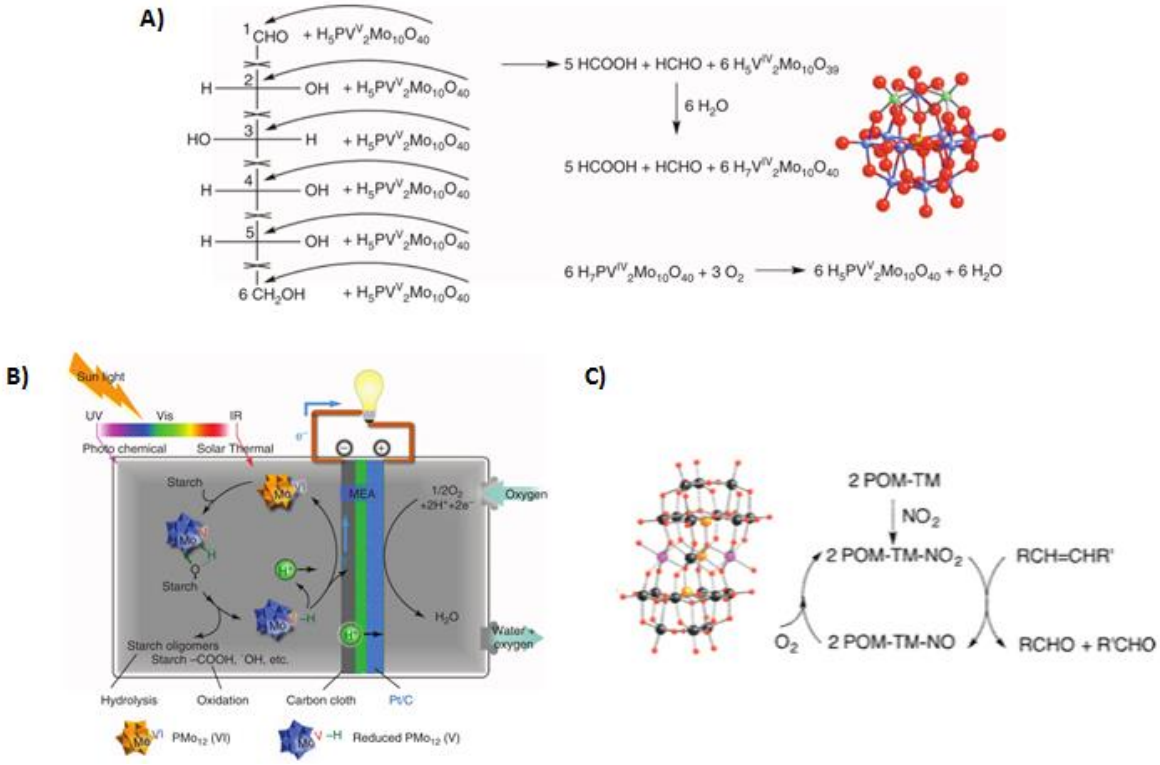

Figure 1.2.2.2 – A) The mixed-metal POM $H_5[PV_2Mo_{10}O_{40}]$, can be used to oxidise cellulose to formic acid. The reduced POM is subsequently re-oxidised by molecular oxygen to regenerate the catalytic species. B) A Schematic of direct electricity production from starch *via* reduction of the Keggin molybdate, $[PMo_{12}O_{40}]^{3-}$. C) A TMS-POM species $[Cu_2WZn(NO_2)_2(ZnW_9O_{34})_2]^{12-}$ which can cleave alkenes to the corresponding aldehydes using molecular oxygen in a two-step process. Modified from references 103, 106 and 108.

TMS-POMs also display redox activity. One series of zinc-substituted tungstates presented by Neumann *et al.* have been demonstrated to catalyse a variety of small molecule oxidations. The $[WZn_3(H_2O)_2(ZnW_9O_{34})_2]^{12-}$ species was used to oxidise primary and secondary alcohols using hydrogen peroxide.[107] The related $[Cu_2WZn(NO_2)_2(ZnW_9O_{34})_2]^{12-}$ was shown to catalytically cleave alkenes into two corresponding aldehydes with air as the oxidant, again with postulated renewable energy implications (Figure 1.2.2.2).[108] The ruthenium analogue, $[Ru_2WZn(H_2O)(OH)(ZnW_9O_{34})_2]^{12-}$ performs a milder oxidation under aerobic conditions, oxidising alkenes to the corresponding epoxides.[109]

Light, particularly UV light, can be used to promote these redox processes.[110] UV light can promote a ligand-to-metal charge transfer from a terminal *oxo*- ligand, generating a more reactive *oxo*- radical species (Figure 1.2.2.3)..[111] This effect can be used to oxidise a variety of organic substrates. In one example, chlorinated phenol pollutants were degraded using the Keggin-structured phosphotungstate, $[PW_{12}O_{40}]^{3-}$, under UV light.[112] Co-, Cu-, Ni- or Mn-substituted Keggin tungstates, $[XSiW_{11}O_{39}(H_2O)]^{6-}$, were also used to oxidatively degrade organic dyes by a similar mechanism (Figure 1.2.2.3)..[113] Primary or secondary alcohols can also be selectively dehydrogenated to aldehydes or ketones using POM species such as $[PW_{12}O_{40}]^{3-}$ under UV light.[114] In some cases, these processes can result in structural rearrangement, such as in the case of the light-induced reductive dimerization of $[V_5O_{14}]^{3-}$ to $[V_{10}O_{26}]^{4-}$, which occurs with the simultaneous oxidation of methanol to formaldehyde and subsequent re-oxidation to the $\{V_5\}$ species (Figure 1.2.2.3).[115]

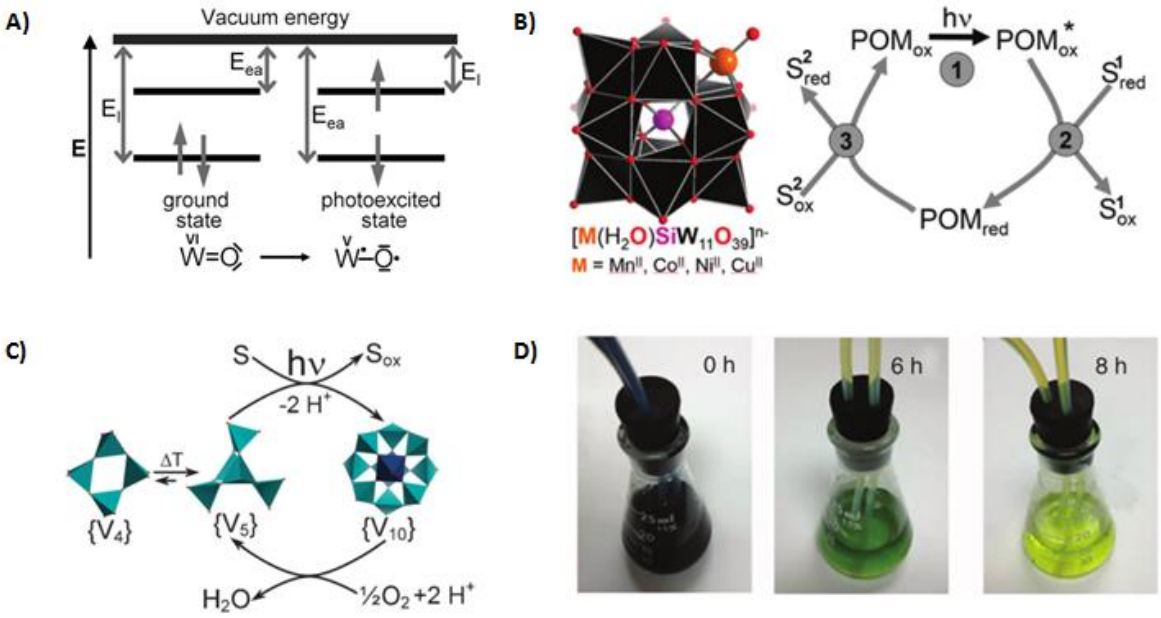

Figure 1.2.2.3 – A) Simplified molecular orbital diagram, demonstrating UV-light-induced ligand-to-metal charge transfer that generates a reactive *oxo*- radical. B) $[XSiW_{11}O_{39}(H_2O)]^{6-}$ species and a simplified scheme of their light-induced redox activity with organic substrates. C) Photoactive dimerization of the $[V_5O_{14}]^{3-}$ POM to $[V_{10}O_{26}]^{4-}$ and subsequent re-oxidation. D) Re-oxidation of reduced molybdate solutions can be monitored visually over time due to the intense colour of the reduced species. Modified from references 111, 112, 115 and 106, respectively.

POMs often react in a two-stage process, whereby the substrate is oxidised by the POM, leaving behind a reduced POM species. In the case of many molybdates, the reduced species tend to have deep blue colours, allowing redox state to be monitored visually (Figure 1.2.2.3).[116] In a second step, this reduced POM reacts with some oxidising species (such as oxygen or peroxide) to regenerate the original species.[117,118] In some systems, reduction of protons can be used to regenerate the reduced POM species, effectively extracting hydrogen from organic substrates. [119–121]

Special consideration must be given to water splitting. Significant amounts of scientific effort have been expended in recent years to improve the efficiency of the two water splitting half reactions – oxygen evolution and hydrogen evolution, respectively.[122] Oxygen evolution involves the oxidation of water (oxidation half-reaction), while hydrogen evolution involves the reduction of protons (reduction half-reaction).

Oxidation: $2H_2O \xrightarrow{catalyst} O_2 + 4H^+ + 4e^-$

Reduction: $4H^+ + 4e^- \xrightarrow{catalyst} 2H_2$

Overall: $2H_2O \xrightarrow{catalyst} O_2 + 2H_2$

If water splitting could be efficiently performed on a large scale, hydrogen could be isolated, stored, and used as fuel.[123,124] Many postulated energy economies rely on hydrogen as the energy carrier (as it is a carbon-free energy source), but it should be noted that there are other redox processes which are also chemically feasible[125,126] - water oxidation in tandem with CO_2 reduction is the process from which the biosphere derives its energy reserve, for example.[127] However, water splitting (particularly the oxidation half-reaction) is both thermodynamically and kinetically hindered, and therefore requires extremely robust and powerful redox catalysts if this method of fuel production is ever to be realised on a global scale. POMs have garnered significant attention in this regard due to their aforementioned favourable redox qualities.[128]

Water splitting can be achieved either electrochemically (using an applied voltage as the thermodynamic input) or photochemically (using a photosensitising species to provide the thermodynamic driving force). In practice, photochemical systems are often modelled by (sometimes photo-generated) sacrificial electron donors[129] or acceptors[130] to drive either the oxidation or reduction half-reaction in isolation.

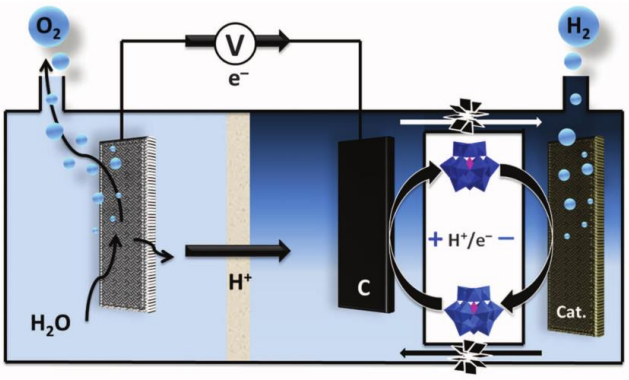

Figure 1.2.2.4 – The $[SiW12O_{40}]^{3-}$ POM can be used as a proton- and electron- carrier to in electrochemical water-splitting devices. Reproduced from reference 131.

Electrochemically, POMs can act as useful charge-transport species. For water splitting in particular, the combination of proton- and electron- storage capabilities on a single POM molecule has proved useful for electrochemical device design. In one such example, a significant rate increase in electrochemical water splitting was observed by using a silicotungstate POM, $H_6[SiW_{12}O_{40}]$, as an electron- and proton-carrier between a working carbon electrode and a platinum hydrogen evolution catalyst (Figure 1.2.2.4).[131] In another, the Keggin-structured phosphomolybdate, $H_3[PMo_{12}O_{40}]$ was used as a temporary electron- and proton-storage species, allowing the oxidation and reduction reactions to be performed at the same electrode at different times by reversing current direction.[132]

POM species are also exploited as catalytic entities for electrochemical water splitting. In such cases POM species are generally adhered to or assembled on to the surface of a suitable electrode. Optimal electronic contact between the POM species and the bulk electrode is one limiting factors in such devices. In one case, a significant increase in activity was achieved by immobilising a homogenous $[Co_9(H_2O)_6(OH)_3(HPO_4)_2(PW_9O_{34})_3]_{16-}$ catalyst in amorphous carbon paste electrodes.[133,134] Similar effects can be achieved by adhering a POM species to graphene- or carbon-nanotube modified electrodes *via* electrostatic interactions.[135,136] Embedding microcrystals of cobalt/nickel substituted tungstates $[Co_{6.8}Ni_{1.2}W_{12}O_{42}(OH)_4(H_2O)_8]$ into macroporous nickel foam electrodes has also been shown effective.[137]

(Photo)chemical water splitting using POMs as catalysts is also possible.[138] Non-POM containing water oxidation catalysts, such as the "blue dimer", $[Ru_2O(H_2O)_2(bpy)_4]^{4+}$,[139,140] are known to be susceptible to inactivation *via* oxidation of their organic components.[141] POM units are perceived to be more robust than organic components, even under the strongly oxidising reaction conditions of water oxidation, and so POM-based water oxidation catalysts have been the subject of fairly intense activity recently.

Many examples of active TMS-POM water oxidation catalysts have been reported, using a variety of transition metals. One particularly successful example is the tetraruthenate POM, $[Ru_4(H_2O)_4(\mu\text{-}O)_4(\mu\text{-}OH)_2(\gamma\text{-}SiW_{10}O_{36})_2]^{10-}$. Several studies involving the water oxidation behaviour of this POM have been reported (Figure 1.2.2.5).[142–145] This POM contains a tetraruthenium core, where the four *oxo*-bridged ruthenium centres adopt a tetrahedral arrangement. The structure can be isolated by two synthetic methods – the oxidative dimerization of a $[Ru_2(OH)_2(H_2O)_2(\gamma\text{-}SiW_{10}O_{36})]^{4-}$ precursor,[146] or by entrapping from solution a tetraruthenium species that had been previously postulated in the literature.[147] The tungstate units are dilacunary Keggin POMs, which encapsulate the transition metal core in a sandwich motif.

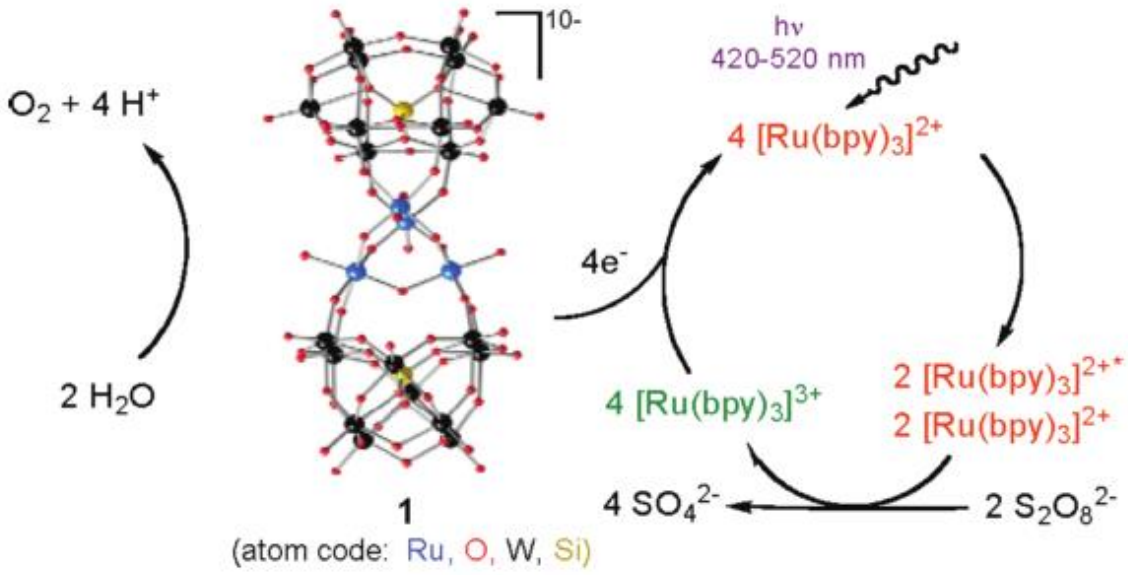

Figure 1.2.2.5 – The $[Ru_4(H_2O)_4(\mu\text{-}O)_4(\mu\text{-}OH)_2(\gamma\text{-}SiW_{10}O_{36})_2]^{10-}$ and it's photochemical reaction with a sacrificial oxidising agent to oxidise water. Reproduced from reference 145.

A manganese-containing POM, $[Mn_4O_3(CH_3COO)_3(A\text{-}\alpha\text{-}SiW9O_{34})]^{6-}$, is also a competent water oxidation catalyst. This compound consists of a trilacuanary Keggin tungstate and an *oxo*- and acetate-bridged, mixed-valent III/IV tetramanganese unit (Figure 1.2.2.6). Reported in 2014 by Kortz *et al*,[148] it was claimed that this unit bears similarity to photosystem II (PSII),[149] a ubiquitously occurring enzyme in photosynthesising plants which catalyses water oxidation. The active catalytic core in PSII is a mixed-valent tetramanganese core, analogues of which are highly prized synthetic targets.[150] A closely related POM reported in 2016 by Streb *et al.* and also claiming structural similarities to PSII, $[Mn_4V_4O_{17}(CH_3COO)_3]^{3-}$, contains a very similar manganese unit stabilised in this case by a vanadate unit (Figure 1.2.2.6).[151] Despite their structural similarities, the vanadate case was considerably more robust than the tungstate case (reported turnover numbers of approximately 1150 and 5, respectively). In both cases, the complexes are "half-sandwiches" in comparison to the more common sandwich motif.

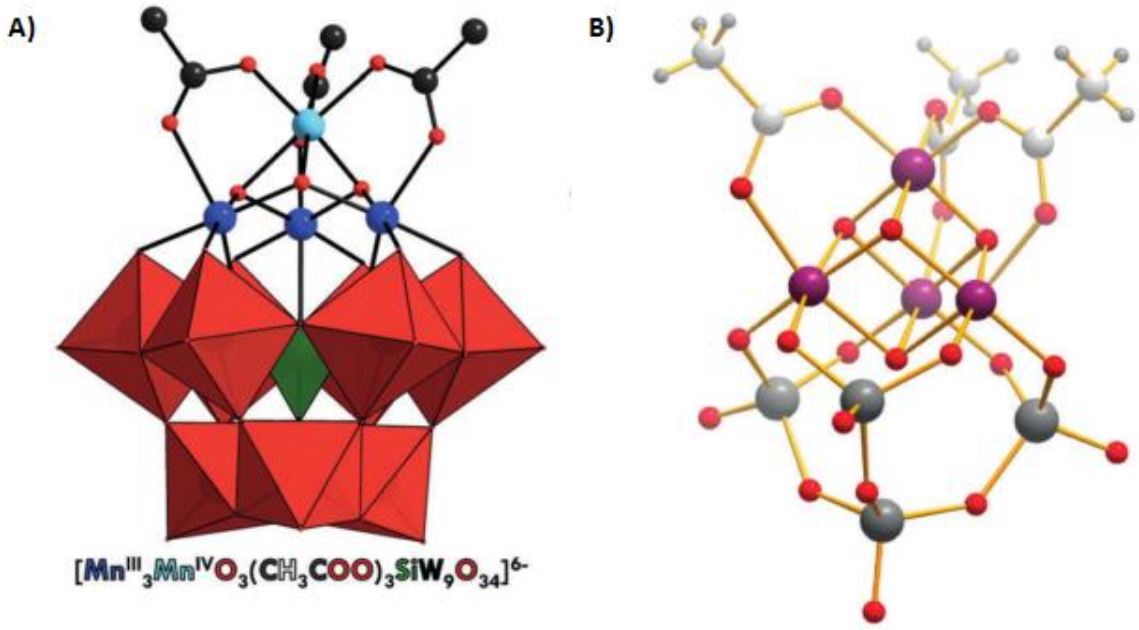

Figure 1.2.2.6 – A) The $[Mn_4O_3(CH_3COO)_3(A\text{-}\alpha\text{-}SiW9O_{34})]^{6-}$ cluster. B) The $[Mn_4V_4O_{17}(CH_3COO)_3]^{3-}$ cluster. Both contain an {Mn_4}-acetate unit and both are competent water oxidation catalysts. Reproduced from references 148 and 151, respectively.

Cobalt-containing POMs for water splitting are also reported.[152] For example, a cobalt substituted Keggin tungstate POM, $[Co_2W11O_{39}(H_2O)]^{7-}$ demonstrated photochemical water oxidation with a turnover number of 360 (Figure 1.2.2.7).[153] Two other small molecule molybdate catalysts were presented, $[CoMo_6O_{24}H_6]^{3-}$ and $[Co_2Mo_{10}O_{38}H_4]^{6-}$, with turnover numbers of approximately 110 and 160, respectively. These were unusually small compounds, indicating that high nuclearity is not necessary for catalysis.[154] Nevertheless, most Co-POM catalysts are considerably larger - the $[(Co_4(OH)_3PO_4)_4(XW_9O_{34})_4]^{n-}$ POM (where X=Si, Ge, P or As) contains 16 cobalt centres.[155] This compound was also claimed as a PSII analogue (despite not containing manganese and not being tetranuclear, see Figure 1.2.2.7). Turnover numbers were tuned only slightly by substitution of X, from roughly 20 to 40, suggesting that in this case the active metal centres are relatively insensitive to changes in the POM units.[155]

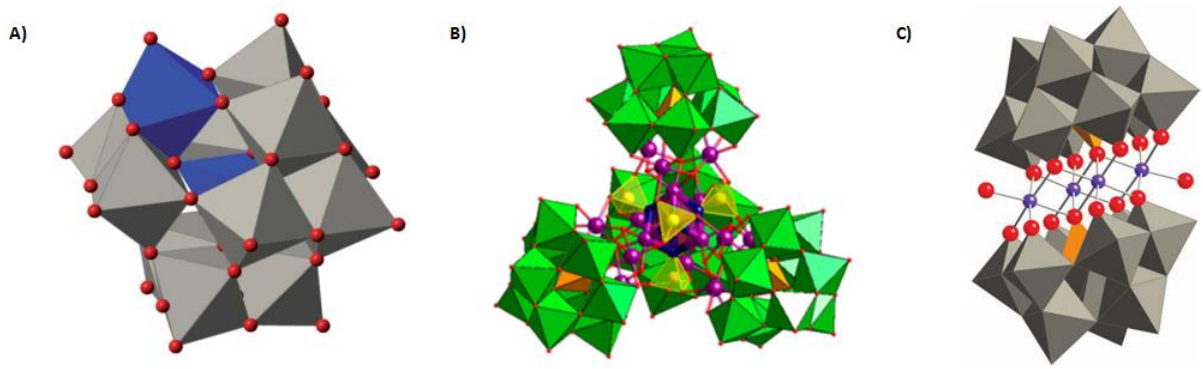

Figure 1.2.2.7 – Some Cobalt-containing POM-based water-oxidation catalysts; A) The $[Co_2W11O_{39}(H_2O)]^{7-}$ cluster. B) The $[(Co_4(OH)_3PO_4)_4(XW_9O_{34})_4]^{n-}$ cluster. C) The $[Co_4(H_2O)_2(PW_9O_{34})_2]^{10-}$ cluster. Reproduced from references 153, 155 and 156, respectively.

While much recent activity has been devoted to TMS-POMs as water splitting catalysts, it should be noted that determining the active catalytic species is not always trivial, particularly in the case of oxidation. In 2010, a $[Co_4(H_2O)_2(PW_9O_{34})_2]^{10-}$ catalyst was reported by Hill *et al.* to oxidise water (Figure 1.2.2.7).[156,157] Later studies provided evidence that the compound may in fact decompose under experimental conditions to amorphous cobalt oxides (probably *via* a homogenous Co(II) intermediate).[158,159] These studies were subsequently disputed by the authors of the original report.[160] Since then, other proposed TMS-POM water oxidation catalysts, including the structurally related $[Co_4(H_2O)_2(VW_9O_{34})_2]^{10-}$,[161] have also been demonstrated as precursors to the competent catalytic species.[162] While heterogenous transition metal oxides are catalytically attractive in their own right,[163–166] distinguishing the active catalyst from decomposition products remains challenging, and often requires significant supporting evidence.[167,168] This can be further complicated by the possibility of multiple plausible or even competing reaction pathways, which may change depending on reaction conditions.[169–175] Nevertheless, TMS-POMs remain a very promising class of catalyst for this type of reaction.

1.2.3) Limitations

One limitation on POM chemistry is that POM structures are generally extremely difficult to functionalise or modify.[176,177] This is commonly attributed to the stability of the metal-*oxo* terminal bond. This highly polarised bond has significant *d*-π double bond character and is considered highly stable, even upon redox state or protonation state changes. A typical POM cluster is surrounded by these terminal metal-*oxo* bonds, which point radially out from the cluster and "shield" the POM from structural rearrangements induced by reaction with other species. While this could be considered a positive factor in certain scenarios, it does mean that modifications to the POM structure are difficult to achieve. As a result, structural diversity in POMs is relatively limited and tends towards wholly inorganic cluster species.

In consequence, a significant amount of research effort is dedicated to producing POM structures stabilised by organic ligands. Such systems are known as hybrid systems due to the combination of organic and inorganic components.[178] In these cases the organic functional moiety effectively provides a synthetic handle for modification of the material. By changing the organic moiety but retaining the inorganic structure, functionalised POMs can be more easily modified to produce favourable material properties.[179] The advantages of such modifiable hybrid systems will be discussed further in section 1.3.

In some cases, hybrid POMs can be generated directly from using self-assembly techniques. The first reported organic derivative of a POM was a phosphonate-substituted Strandberg-type ring (Figure 1.2.1.10).[67,68] A series of related phosphonate-substituted Strandberg-type ring systems have since been prepared bearing an array of organic backbones with the general formula $[(RPO_3)_2Mo_5O_{15}]^{4-}$.[180] Polydentate ligands such as phosphonates and arsenates have been noted as suitable ligands for hybrid POM formation, as they resemble the geometry and electronic properties of metal oxide units in POMs (Figure 1.2.3.1).[181]

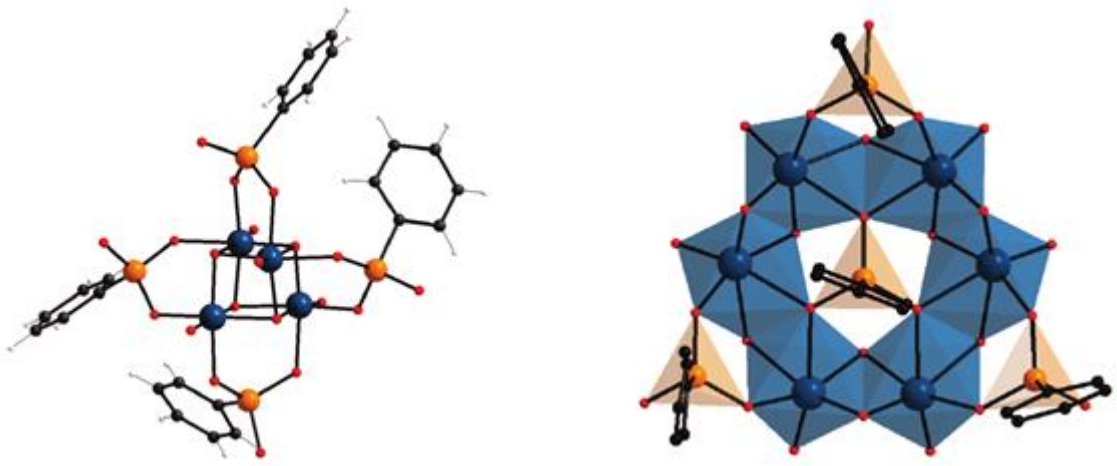

Figure 1.2.3.1 – Examples of hybrid POM structures; the cubane-shaped arsenate-substituted $[Mo^{V}_4O_8(C_5H_5AsO_3)_4]^{4-}$ and ring-shaped phosphonate-substituted POM $[Mo^{V}_6O_{12}(OH)_3(C_6H_5PO_3]^{5-}$. Modified from reference 181.

Another important example of hybrid POM systems is the Lindqvist hexamolybdate POM, $[Mo_6O_{19}]^{2-}$. *Oxo*-ligands on this cluster can be replaced by organoimido-type ligands, by exploiting coupling reactions in the presence of a powerful dehydrating agent such as Dicyclohexylcarbodiimide (DCC). [182,183] Bridging or terminal *oxo*- ligands can be replaced.[184] Various functional groups have been incorporated in this manner, including ferrocene derivatives.[185] Substituted Lindqvist structures have attracted particular attention as building units in more complicated architectures due to their high symmetry and controllable substitution (Figure 1.2.3.2).[186]

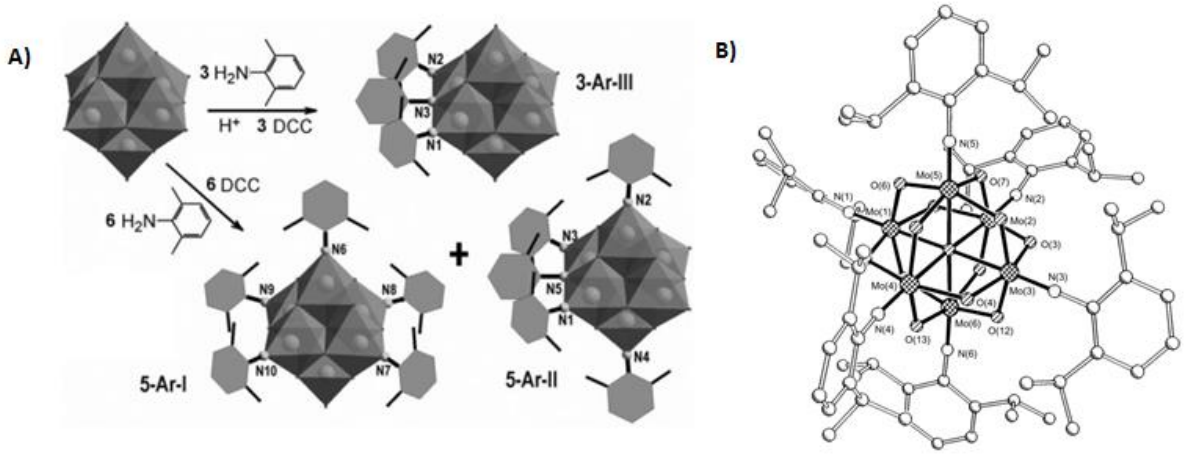

Figure 1.2.3.2 – A) Replacement of multiple terminal or bridging *oxo*- ligands on the Lindqvist hexamolybdate to generate the hybrid structures $[Mo_6O_{16}(C_8H_9N)_3]^{2-}$ and two isomers of $[Mo_6O_{14}(C_8H_9N)_5]^{2-}$. B) A hexasubstiuted Lindqvist core with all terminal *oxo*- ligands replaced, $[Mo_6O_{13}(C_{10}H_{17}N)_6]^{2-}$. Modified from references 183 and 184.

A final important example of a hybrid POM is the substituted Anderson-type molybdate, usually seen with manganese (II) as the central heteroatom.[51–53] Tripodal *tris*(alkoxide) ligands can act as supporting ligands for the Anderson cluster, in one of two binding modes. [51–53] In particular, amine-functionalised *tris*(alkoxides) have found wide use for further postsynthetic modifications of the cluster (see Figure 1.3.1).[187,188]

The Strandberg-type, Lindqvist-type and Anderson-type hybrid POMs will all be discussed further in chapter 2.

TMS-POMs offer an alternative route towards hybrid POMs (Figure 1.2.3.3). In addition to adding electronic and magnetic diversity to POM clusters, the heterometals in TMS-POMs tend not to show the same affinity for inert terminal *oxo*- ligands. As such, the heterometal offers a more versatile ligand coordination site than other metals in the cluster, allowing other, more interesting ligands to be coordinated to the cluster. For example, organoimido- ligands can be introduced into a Keggin-type tungstate *via* the substitution of one tungstate for a rhenium centre, generating $[PW_{11}O_{39}Re(NC_6H_5)]^{4-}$.[189] A related route towards hybrid POMs is to incorporate main group elements such as silicon into a POM structure. Examples include the {RSi-O-SiR} diorganosilicon derivatives of the Keggin tungstate,[190,191] which have been investigated for their self-assembly behaviour.[192]

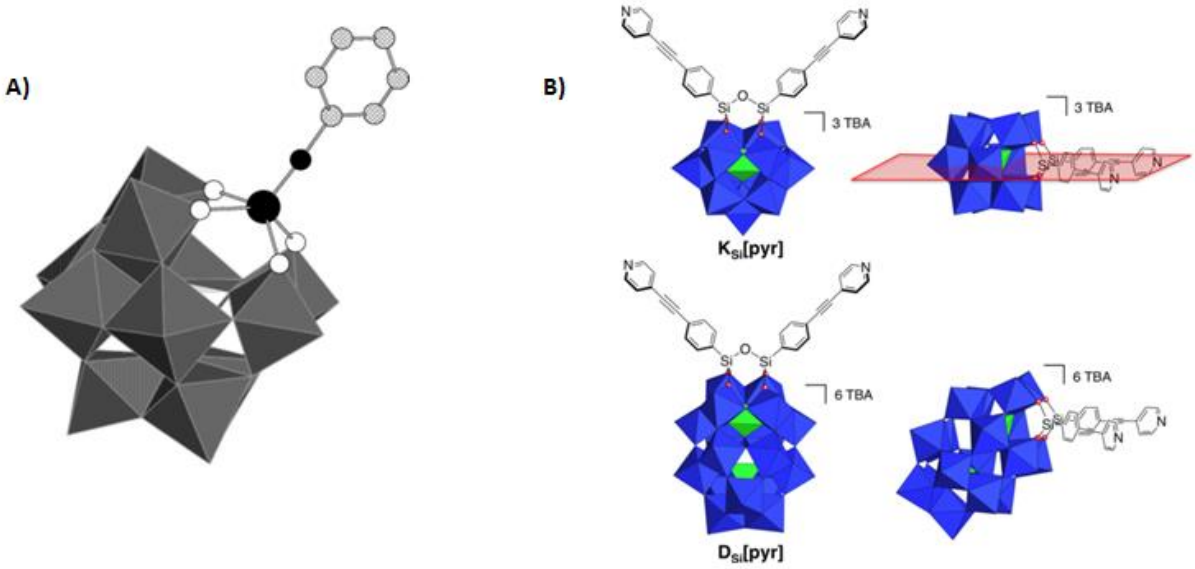

Figure 1.2.3.3 – A) An organoimido ligand can be incorporated into a Keggin-type tungstate by replacing one metal unit with a heterometal, generating $[PW_{11}O_{39}Re(NC_6H_5)]^{4-}$. B) {RSi-O-SiR} diorganosilicon derivatives of the Keggin and Dawson tungstates, and their respective geometries. Modified from references 189 and 192.

1.3) Functional Organic-Inorganic Hybrids

The term "organic-inorganic hybrid material" is an extremely broad umbrella term applied to materials on a continuum of length scales, from molecular entities through to nanocomposites through to macroscopic mixtures.[193] For our purposes, hybrid materials will be considered as any covalently-bonded compound composed of distinct inorganic moieties (*e.g.* metal-*oxo* units) and organic moieties (*e.g.* hydrocarbon units).[194] Non-covalent systems will not be discussed.[195]

In comparison to classical inorganic materials such as POMs, hybrid materials are relatively versatile in structure and function. The organic units can impart a wide range of functional properties to a material, above and beyond the metal-based properties considered in the previous section.

Organic functional groups can be used to modulate the chemical properties of the metal units in a hybrid material. Electron withdrawing or donating groups allow the electronic, magnetic or catalytic behaviour of metal centres to be modified by manipulating the amount of electron density available to the metal (*cf.* Hammett equation).[196] Moreover, these modulating groups can sometimes act as reactive chemical sites for post-synthetic modification. For example, electron donating amino functional groups can be used in condensation reactions with suitable electrophiles such as aldehydes or carboxylic acids. This has been exploited to particular effect using amine-substituted Anderson-type POMs, which can incorporate a range of functional groups *via* post synthetic amide condensation (Figure 1.3.1).[187] In one example, a Diels-Alder click reaction was used to further functionalise an amide-condensed Anderson POM with a variety of functional units.[188] Electron withdrawing halogen substituents also provide a synthetic handle for postsynthetic modification, for example in the case of a *diiodo*- substituted Lindqvist POM which was assembled into one-dimensional polymer chains.[197] A similar approach using click chemistry was used to form one-dimensional chains of a substituted Dawson unit.[198]

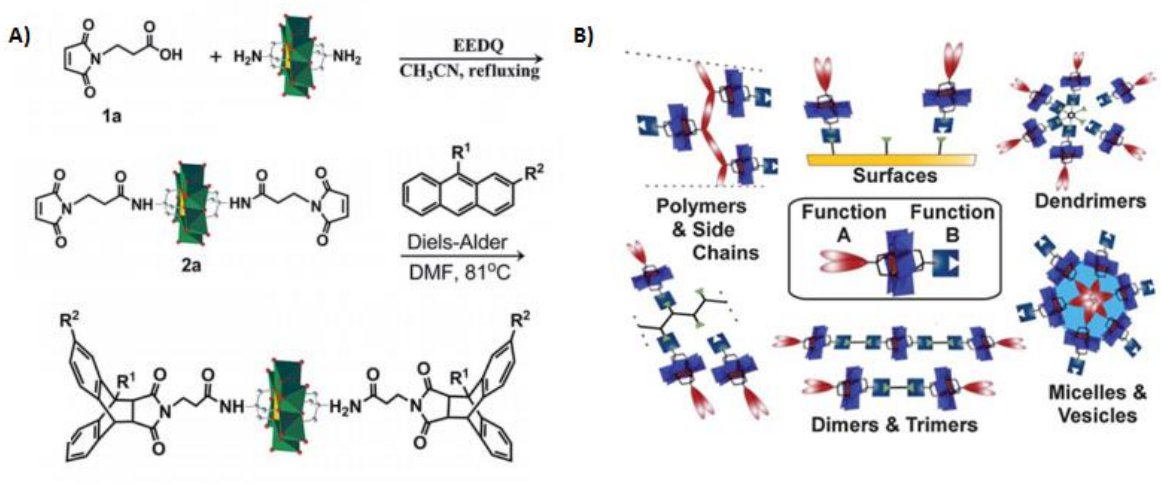

Figure 1.3.1 – A) Sequential post-synthetic modifications of the hybrid Mn-substituted Anderson POM, $[MnMo_6O_{18}((OCH_2)_3CNH_2)_2]^{3-}$ can be performed *via* amide condensation and Diels-Alder reactions. B) Schematic of some proposed uses for asymmetrically functionalised hybrid Anderson-type POMs. Modified from references 187 and 188.

Photoactive moieties are an important set of functional units that can be incorporated into hybrid materials (Figure 1.3.2). Antenna units can be used to promote electrons to higher molecular orbitals, which in turn can promote reactivity. For example, Anderson-type POMs functionalised with porphyrin moieties (*via* amide-type coupling)[199] can be used to photocatalytically reduce silver ions to nanoparticles.[200] A similar porphyrin-functionalised Dawson-type POM was used to generate a photovoltaic current.[201] Another example used fullerene moieties as sensitisers with a lacunary Keggin tungstate to induce photooxidation reactions.[202] Luminescent moieties also display interesting photophysical properties which can be modulated upon inclusion into a hybrid material. In the case of a nitroquinoline-functionalised hexamolybdate, $[Mo_6O_{18}(C_9N_3O_2H_5]$, fluorescence can be switched on or off based on pH, an effect that is attributed to the bond angle between the organic and inorganic components.[203]

Biologically relevant functional groups are also of interest. It has been shown that POM units can be functionalised with a series of biologically relevant amino acids *via* the carboxylate functionality.[204] In another example, adamantyl substituents incorporated onto a Lindqvist hexamolybdate *via* organoimido ligands were found to increase the chemotherapeutic properties of the POM.[205] A similar example used the Lindqvist hexamolybdate substituted with organic moieties to improve transport across biological membranes, and thus enhance medicinal activity.[206]

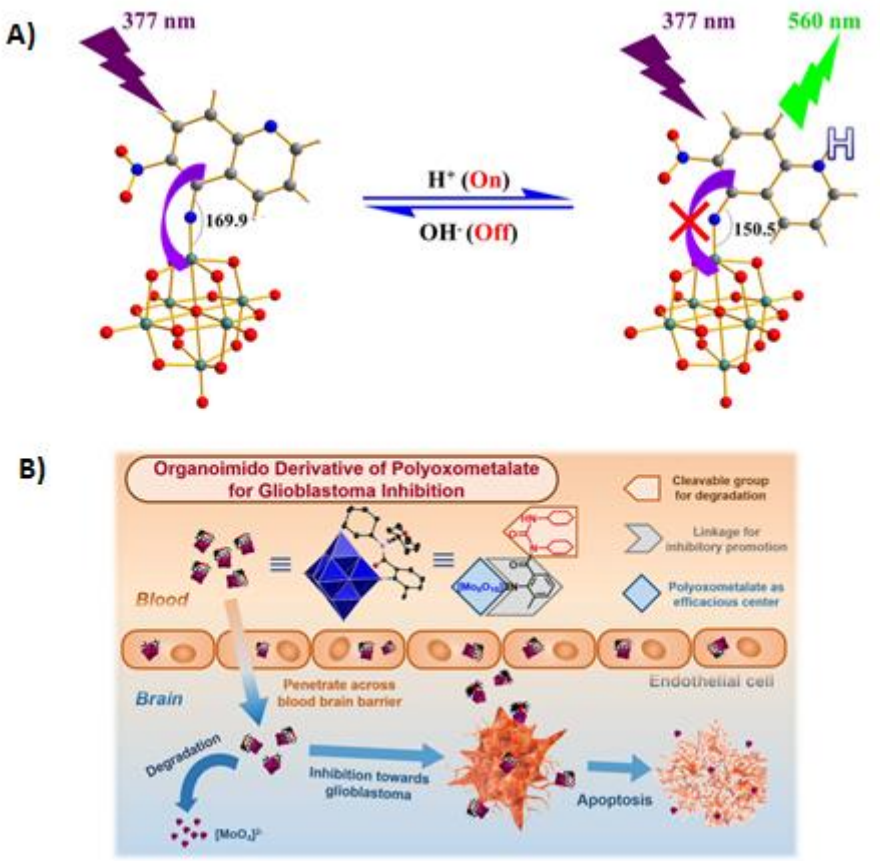

Figure 1.3.2 – Photochemical and biological activity of some hybrid POM species. A) A nitroquinoline-functionalised Lindqvist molybdate-type compound $[Mo_6O_{18}(C_9N_3O_2H_5]$, displays pH-sensitive luminescence, which is attributed to the bond angle between organic and inorganic components. B) An example of a hybrid POM that has increased medicinal activity, due to increased membrane transport capabilities imparted by the organic components. Modified from references 203 and 206.

In addition to these chemical properties imparted onto POM species by incorporating organic components, multifunctional organic groups can be used as structure-directing agents to control the microstructure of the material (Figure 1.3.3). This aggregation of zero-dimensional POM clusters into one dimensional polymers, two dimensional networks or three dimensional frameworks affects the physical and chemical properties of the resulting material.[207] One recent example formed polymer chains from Keggin tungstate units, and modified their packing structures by modifying the bridging metal units.[208] Another used ε-Keggin-type molybdates supported by isonicotinate-type ligands in combination with zinc nodes to form two extended diamondoid networks, $[PMo^{V}_{8}Mo^{VI}_{4}O_{38}(OH)_{2}(Zn)_{4}(L)_{2}]^{3-}$, where L represents isonicotinate or the phenyl-extended analogue.[209] Another example used a nickel-substituted Dawson POM linked by succinic acid into a three dimensional network.[210] The properties of extended organic-inorganic hybrid networks will be explored in more detail in the following section.

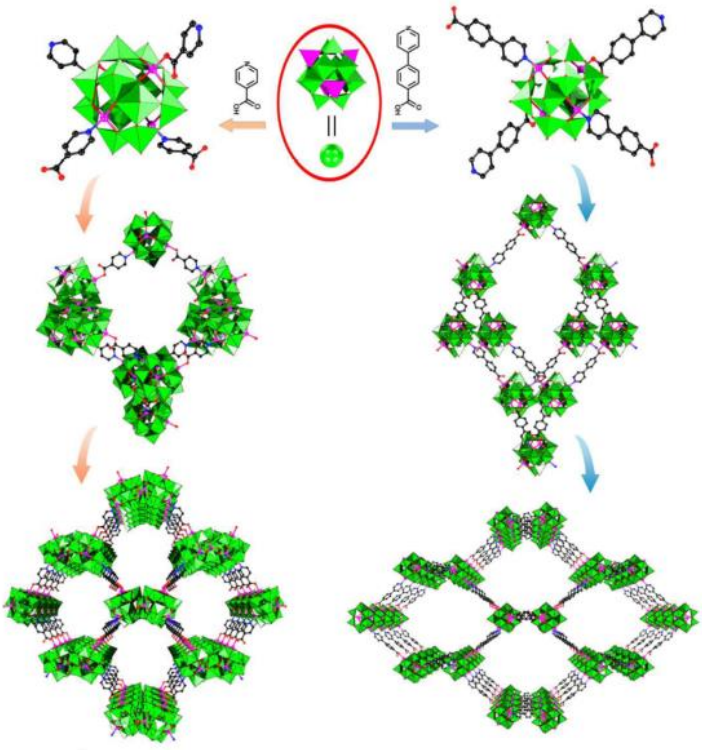

Figure 1.3.3 – The incorporation of isonicotinate-type supporting ligands onto Keggin-type molybdates in combination with zinc nodes yields two diamandoid networks, $[PMo^{V}_{8}Mo^{VI}_{4}O_{38}(OH)_{2}(Zn)_{4}(L)_{2}]^{3-}$, where L represents isonicotinate or an extended analogue. Extension of the linker ligand changes the pore size of the resulting network. Modified from reference 209.

1.4) Metal-Organic Frameworks

Metal-organic frameworks (MOFs) are an emerging class of polymeric or extended hybrid materials. Despite recent attempts to formalise the nomenclature in this relatively young and rapidly developing field of interest, the terminology is still somewhat fluid and so a strict definition of MOFs is somewhat difficult to delineate.[211,212] Structural and physicochemical features of MOFs overlap heavily with categories such as coordination polymers or zeolites, but they are generally considered as a distinct class of material.[213,214] Further complicating matters is the division of MOFs into competing subclasses,[215] as well as the sporadic application of the MOF label to compounds where metal-ligand bonds are not the primary structure directing component.[216] For the purposes of this thesis, therefore, MOFs will be considered as any covalently-bonded metal-ligand structure with repeating units that extend in two or three dimensions.

Conceptually, MOFs can be considered as repeating combinations of metal and ligand building blocks. It is common practice to reduce these building units to simple geometric shapes such as triangles, squares and octahedra (Figure 1.4.1).[217] The resulting simplified structural units are important descriptors in MOF systems where geometry and topology have a strong influence on physical properties.[218]

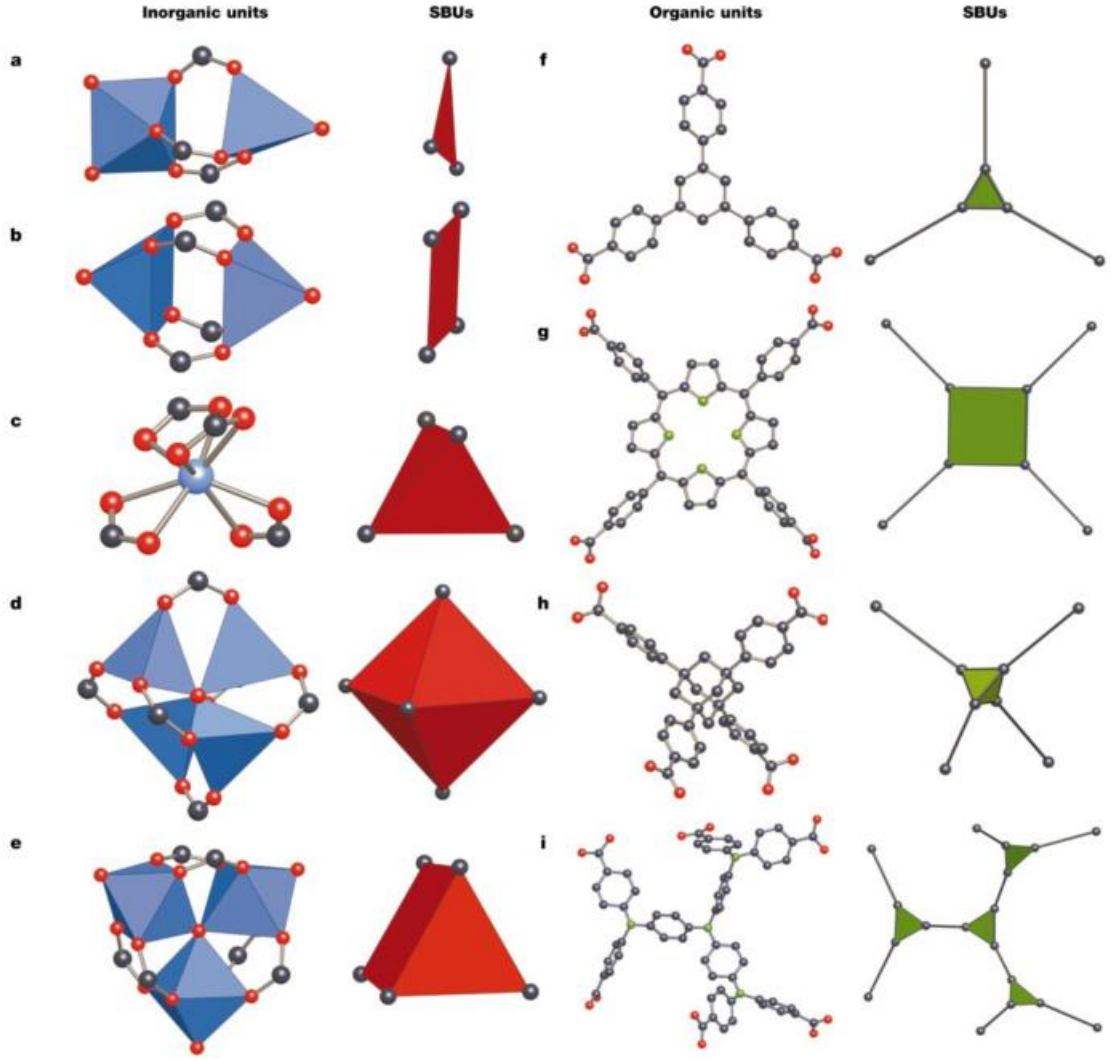

Figure 1.4.1 – Some common MOF building units and their corresponding simplified geometrical shapes. Reproduced from reference 217.

The metal building units can be single metal centres or larger clusters, and are commonly referred to as nodes or Secondary Building Units (SBUs). The organic ligand units are polytopic ligands (most commonly polycarboxylates), and are sometimes called linkers, spacers or struts. Both the node and linker tend to be structurally rigid and symmetric, as this gives rise to well defined, crystalline repeating networks which can be more easily characterised and studied.[219] MOFs are commonly labelled after the institute in which they were first produced (*cf.* the Trinity College Materials or TCM series, Figure 1.4.2).[220]

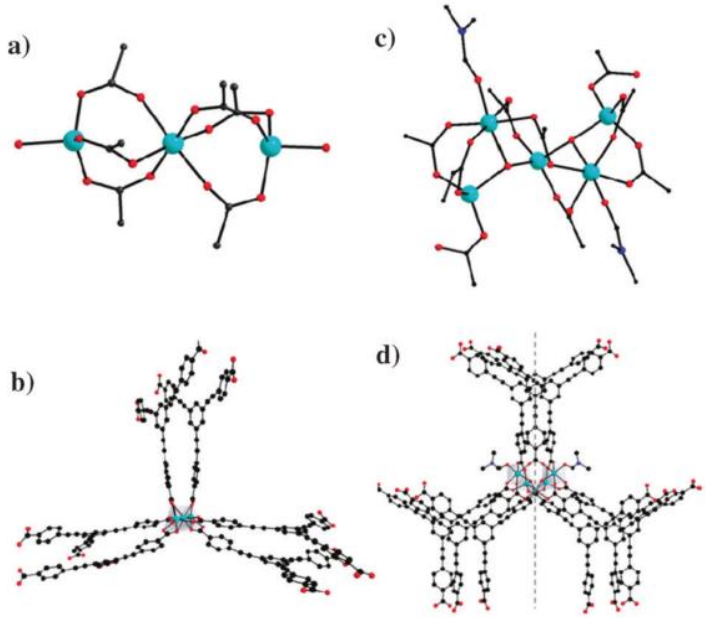

Figure 1.4.2 – a) and c) The inorganic building units in TCM-1 and TCM-2, respectively. b) and d) parts of the resulting frameworks. Reproduced from reference 220.

Historically, coordination polymers have attracted attention for centuries, with Prussian Blue dyes being used as an analytical reagent from the early 1700s onwards.[221] Zeolites are naturally occurring minerals and have been studied since at least the mid-1700s with the work of Cronstedt.[222] As with POMs, early work was somewhat hampered by the difficulty in unambiguously assigning a structure to the compound – Prussian Blue was not characterised crystallographically until the 1970s.[223] MOFs however did not emerge as a distinct class of compounds until the early 1990s, with the term MOF being coined in 1995.[224] By this time, X-ray diffraction techniques were sufficiently rapid and powerful enough to characterise a high throughput of MOF structures. The MOF literature has accordingly expanded extremely rapidly in the past decades, with single crystal X-ray being the crucial technique for determining MOF structures.[225]

Recently, related classes of compounds such as metal organic polyhedra (MOPs),[226] porous liquids,[227] liquid MOFs[228] and hybrid glasses[229] have also garnered attention, but will not be considered here.

1.4.1) Synthesis and Structures

Like with POMs, MOFs are generally synthesised by "one pot" aggregation and crystallisation.[230] Essentially, metal species are combined in solution with a suitable organic linker, and if the geometries of the building units are suitable, repeating MOF units can be formed.[231] If the metal node is a polynuclear entity, it can be added either as a discrete, pre-formed molecular entity or it can be assembled *in situ* (*e.g.* the octahedral Zn_4O unit in MOF-5[232]). The size and morphology of the particles is dependent on a fine interplay between nucleation, the amount of available building units, and the time over which the reaction takes place.[233–235]

Recently, some attention has been focused on modifying MOF properties by introducing defects (*e.g.* vacant node or linker sites) to the crystal structure.[236–238] However in the vast majority of cases, MOF research relies on the formation of suitably pristine crystals for characterisation by X-ray diffraction.[239] Therefore, standard synthetic protocols tend to employ conditions of thermodynamic control, with high temperatures and long reaction times (*c.* 150°C for five days).[240] Solvothermal conditions like these tend to promote the formation of pristine, crystalline MOFs while discouraging the formation of amorphous oligomeric materials (*cf.* Ostwald Ripening). Faster, less cost intensive synthetic methods such as mechanochemical methods[241] or rapid precipitation[242] are also possible, but less common.

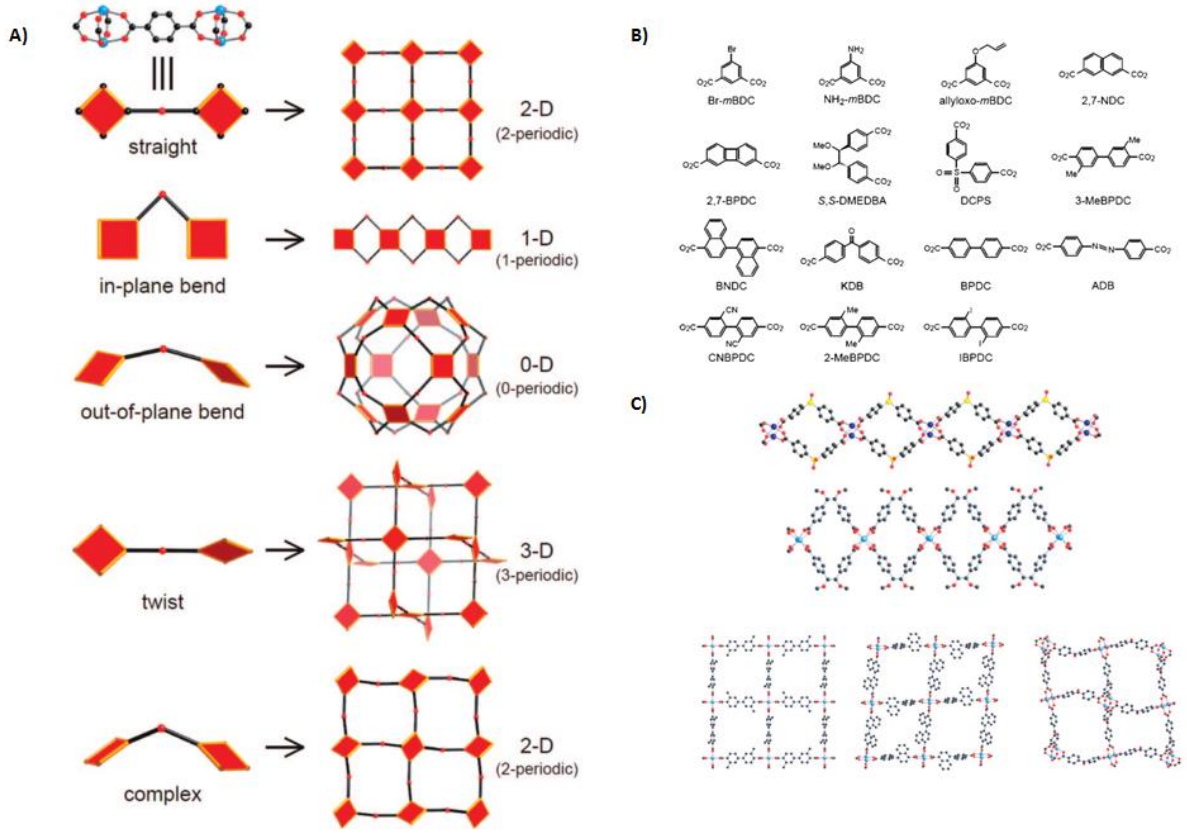

Figure 1.4.1.1 – A) Simple geometric arguments allow the dimensionality of a material to be predicted based on the geometry of the linker units. B) Some geometrically-constrained dicarboxylate linkers used to illustrate this principle. C) Representations of the resulting one- and two-dimensional materials produced. Modified from reference 246.

In contrast to POMs, whose structures are difficult to predict from first principles, MOF synthesis is comparatively rational and deliberate.[243,244] By choosing building units with rigid and well defined geometry, the structures of the products can be predicted with a reasonable degree of accuracy.[245] For example, retaining the geometry of a copper paddlewheel $\{Cu_2(RCOO)_4\}$ node and varying the geometry (twist and bend angles) of dicarboxylate linkers, a series of compounds of zero-, one-, two- or three dimensions can be formed, all of which are easy to rationalise and predict from simple geometric principles (Figure 1.4.1.1).[246]

The geometry of the building units is closely related to topology of the resulting MOF. Topologically, MOFs can be considered as simple periodic nets (Figure 1.4.1.2).[247,248] The terminology commonly used to describe MOF topology is an extension of topological classifications for inorganic solids.[249] Topologically distinct isomers can display distinct physical properties such as surface area or gas uptake. This was demonstrated by a series of chemically identical but topologically distinct frameworks, TCM-4, TCM-8 and TCM-10, which all have the formula $[Cu_3(BTEB)_2(H_2O)_2(DMF)]$ but display distinct physical properties (Figure 1.4.1.2).[250,251] Moreover, because topological nets can be deformed infinitely, series of topologically identical but chemically distinct MOFs can be prepared by replacement of linker units.[252] Most famously, this was demonstrated by the preparation of the isoreticular ("same net") IR-MOF series based on MOF-5, $[Zn_4O(terephthalate)_3]$.[253] Properties such as surface area and porosity could be modified in this series by replacing the linear terephthalate linker with longer equivalents (Figure 1.4.1.2).

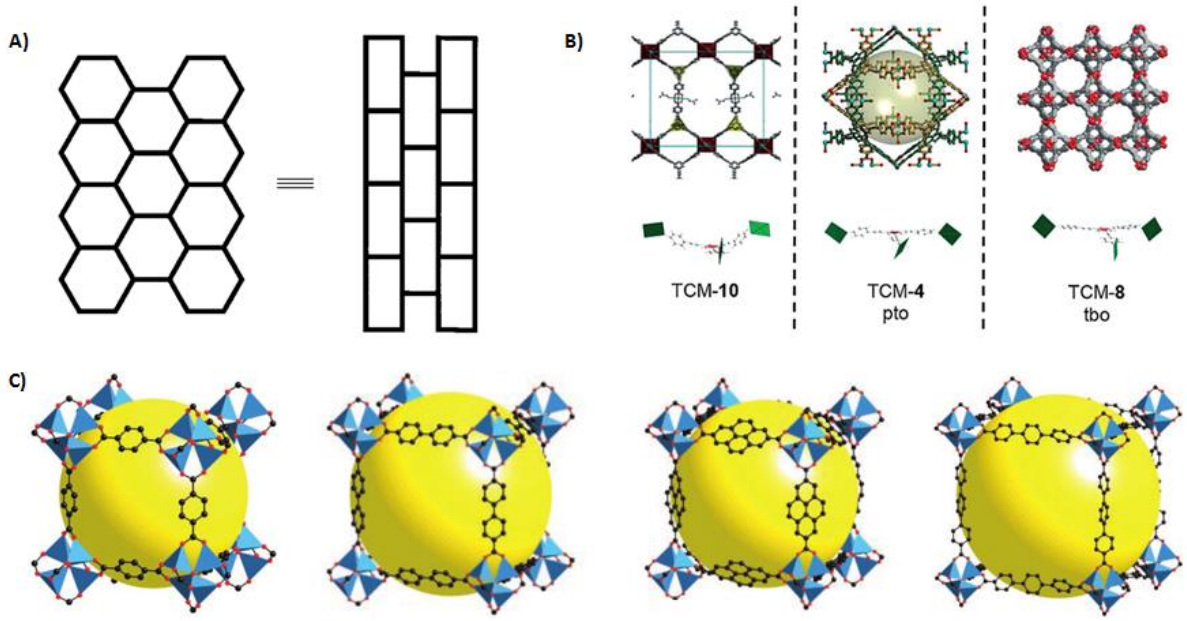

Figure 1.4.1.2 – A) Geometrically distinct forms of the same topological net (a periodic (6,3) net). B) Representations of three chemically identical but topologically distinct copper MOFs, which have the same formula $[Cu_3(BTEB)_2(H_2O)_2(DMF)]$. C) Four topologically identical but chemically distinct zinc MOFs constructed from the same $\{ZnO_4\}$ node and different ditopic carboxylate ligands. Modified from references 248, 251, and 253 respectively.

The reticular design concept can be complicated by issues such as interpenetration of multiple networks and the possibility of forming isomers or polymorphs.[254] These issues can be controlled to a certain extent by modifying intermolecular stacking and templating interactions in solution.[255–257]

Some archetypal MOF systems are shown in Figure 1.4.1.3. MOF-5 and its analogues use linear terephthalate (or similar) ligands in combination with octahedral {Zn_4O} SBUs to generate a simple cubic structure, [Zn_4O(terephthalate)$_3$].[258] UiO-66 uses the same linear linker with {Zr_6} units to generate a MOF with hierarchal pore structure, [$Zr_6O_4(OH)_4$(terephthalate)$_6$].[259] HKUST-1 is generated from the common copper paddlewheel square SBU with simple triangular trimesic acid linkers, [Cu_3(trimesate)$_2(H_2O)_3$].[260] The NOTT-112 MOF uses extended hexacarboxylate linkers with the same copper paddlewheel SBU to generate a structure with multiple pore sizes, [$Cu_3(C_{48}H_{24}O_{12})(H_2O)_3$].[261] The MIL-101 MOF uses linear terephthalate linkers with trinuclear chromium SBUs of trigonal prismatic geometry to generate a mesoporous, zeolite-like framework with hierarchal pore sizes, [Cr_3(OH)(trimesate)$_3(H_2O)_2$].[262] Zinc-imidazole frameworks (ZIFs) possess imidazolate ions that bridge between single zinc atoms, displaying zeolite-like structures, such as ZIF-8, [Zn(imidazolate)$_2$].[263]

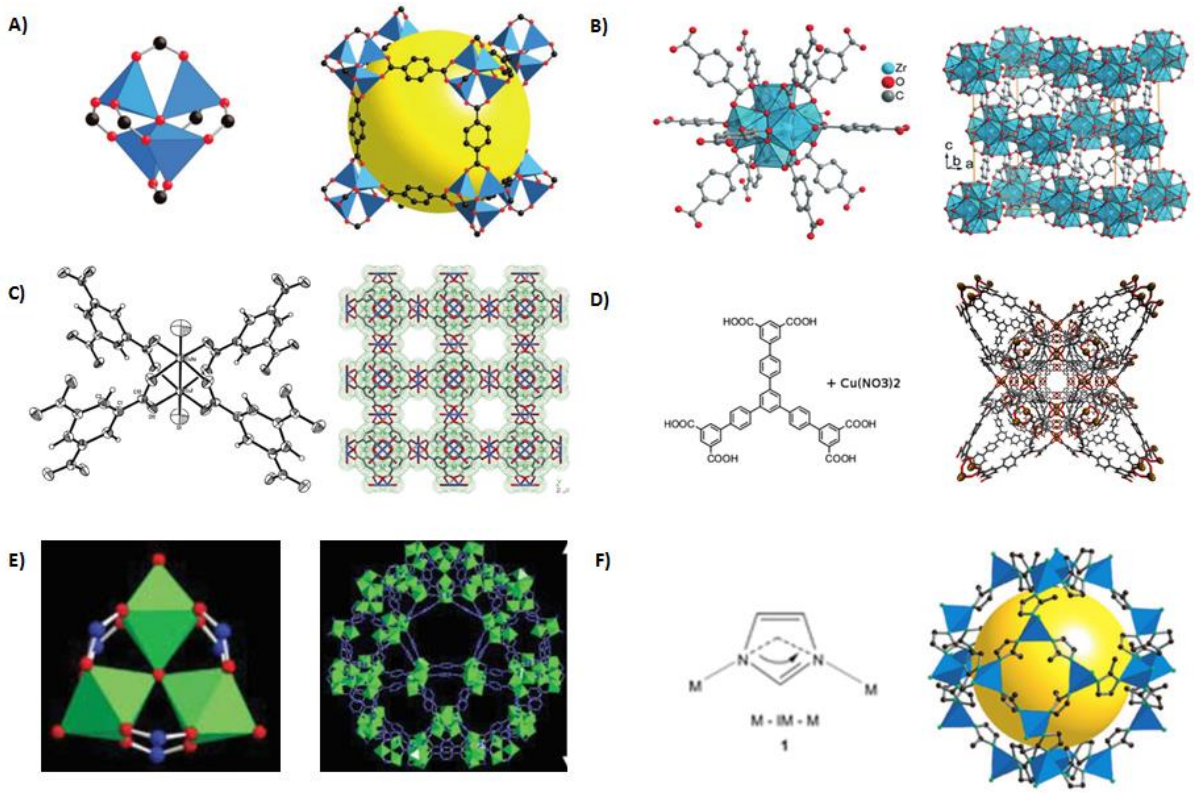

Figure 1.4.1.3 – The node or linker units alongside a portion of the parent MOF for : A) MOF-5, [Zn_4O(terephthalate)$_3$]; B) UiO-66, [$Zr_6O_4(OH)_4$(terephthalate)$_6$]; C) HKUST-1, [Cu_3(trimesate)$_2(H_2O)_3$]; D) NOTT-112, [$Cu_3(C_{48}H_{24}O_{12})(H_2O)_3$]; E) MIL-101, [$Cr_3$(OH)(trimesate)$_3(H_2O)_2$]; F) ZIF-8, [Zn(imidazolate)$_2$]. Modified from references 258-263, respectively.

1.4.2) Applications

Since their conception, numerous possible applications have been proposed for MOFs. Their mechanical properties, unusual thermal expansion behaviour and electronic properties have given rise to proposed applications in various aspects of materials science and device fabrication.[264–268] However, the vast majority of proposed applications centre on the host-guest chemistry of MOFs. Being predominantly porous materials, they can incorporate various guest molecules into their structures, giving rise to a series of separation, storage and catalysis applications.[269] Zeolites are also prized for these properties, and are used on a large scale in industrial settings.[270]

Gas storage properties of MOFs are well documented. In the confined space of MOF pores, gases form quasi-condensed phases due to the physisorption of multiple monolayers of gas molecules onto the MOF surface. Initially, the focus was on hydrogen storage as part of a hydrogen economy.[271,272] More recently, the focus has shifted somewhat to CO_2 capture to alleviate global warming concerns.[273,274] One key limitation is that the MOFs must selectively capture CO_2 at the low partial pressures commonly found in combustion exhaust. One strategy to tackle this problem is to promote stronger electrostatic interactions by incorporating functional groups like amines into the MOF, for example in the MOF-74 analogue $[Mg_2(C_{14}O_6H_6]$.[275] Another involves finely tuning the size of the MOF pores to favour the inclusion of CO_2 over other gases, for example with the SIFSIX series of MOFs (Figure 1.4.2.1).[276,277] The pore size approach can also be used to abstract ethyne from ethene using a SIFSIX MOF.[278]

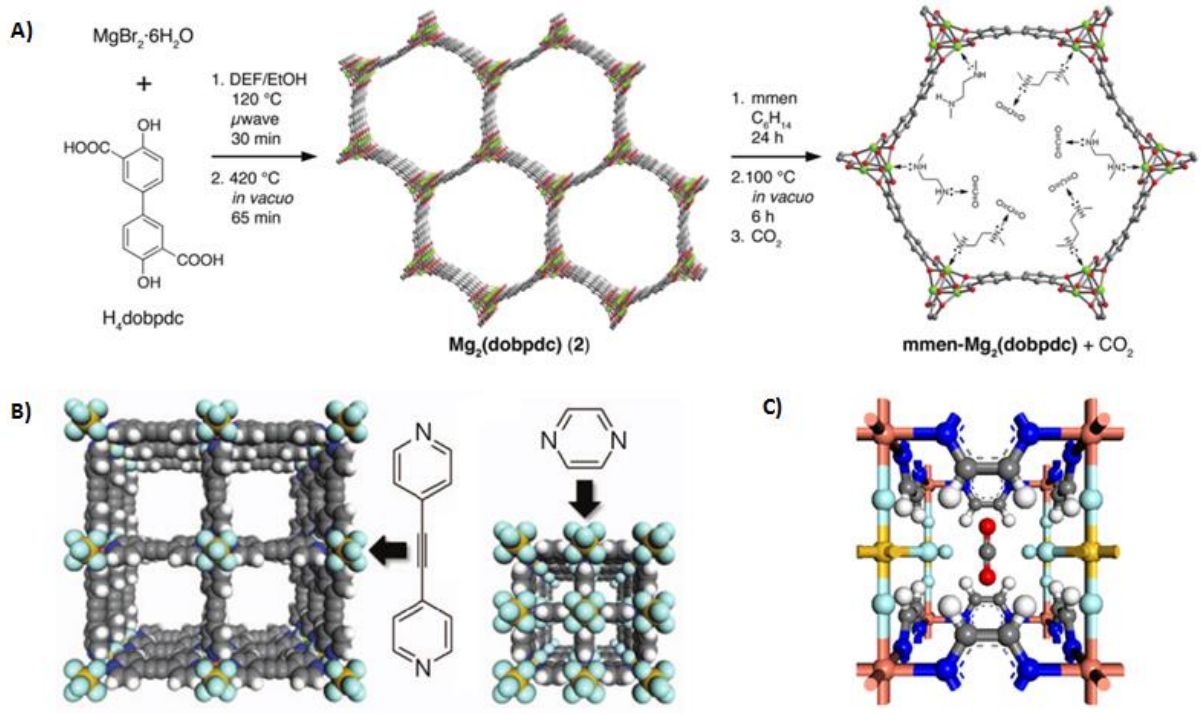

Figure 1.4.2.1 – Two strategies towards increased CO_2 uptake in MOFs; A) Incorporation of functional groups like amines can promote stronger chemisorption interactions, for example in Mg-based MOF-74, $[Mg_2(C_{14}O_6H_6]$; B) Pore sizes can be restricted to modify the physisorption interactions, for example in the SIFSIX series. C) A DFT-calculated image of a CO_2 molecule in a restricted SIFSIX MOF. Modified from references 275-277, respectively.

MOFs have also attracted attention for their ability to sequester toxic species from the environment. The zirconium-based UiO-66 MOF was shown to remove arsenic from drinking water.[279] A thiol-substituted analogue of MOF-5 was shown to sequester heavy metals such as lead and cadmium.[280] A nickel framework could exchange relatively harmless sulphate ions for toxic chromates and manganates.[281] Inclusion of a guest can also

alter the physical properties of a MOF, allowing them to be used as sensors for harmful species in the environment. For example, adsorption of gaseous nerve agents modulates the electrochemical work function of a modified UiO-66 MOF.[282] MOFs with intrinsic luminescence are particularly useful in this regard, as their luminescence can be quenched by guest molecules.[283] One recent example exploited this effect to selectively detect the explosive agent trinitrophenol (TNP) using a luminescent zinc-based MOF.[284] Another used a luminescent europium MOF to detect the presence of POM species.[285]

MOFs are catalytically interesting because their *de facto* heterogeneous nature simplifies work up significantly.[286,287] If the metal centres in the node have available labile coordination sites, catalysis can occur at these sites. One such example used a copper paddlewheel-based MOF to catalyse oxidation of alcohols *via* a peroxocopper intermediate.[288] Catalytically active entities can also be incorporated into the struts of a MOF. For example amine-based linker molecules have been shown to catalyse Knoevenagel condensation reactions.[289] Finally catalytic entities can be incorporated as guests in the pores of a MOF, including redox-active ruthenium or platinum nanoparticles.[290,291] Synergistic effects between nodes, linkers and pore guests can also be significant.[292]

POMs have been incorporated into MOF pores for catalytic purposes.[293] Electrostatic interactions between (generally negative) POMs and the (generally positive) MOF building blocks stabilise the structures and allow them to be synthesised *via* self-assembly processes.[294,295] In one case the redox activity of the Keggin phosphotungstate was enhanced by immobilisation in a modified chromium MOF based on MIL-101, with the increased activity attributed to hydrogen bonding interactions.[296] Another example used a copper-substituted phosphotungstate POM inside the copper MOF HKUST-1 to aerobically oxidise toxic mercaptans. Again, increased activity was seen, and was attributed to intermolecular interactions between the POM and the framework.[297] Another example used a Wells-Dawson POM embedded in the pores of a MOF containing photoactive Ru(bipyridine)$_3$-based linker molecules, $[P_2W_{18}O_{62}]@[Zr_6O_4(OH)_4(C_{32}H_{30}N_6O_4Ru)_6]$, to photoactively evolve hydrogen.[298] A similar example used a nickel-containing sandwich POM, $[Ni_4(H_2O)_2(PW_9O_{34})_2]^{10-}$, to the same effect (Figure 1.4.2.2).[299]

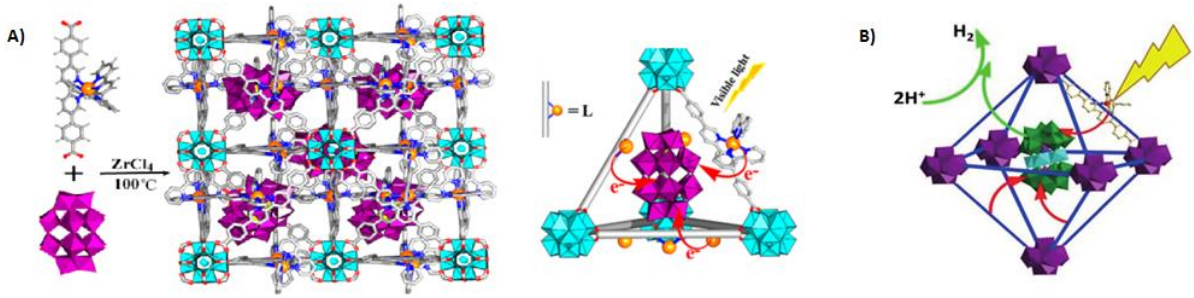

Figure 1.4.2.2 – Two examples of POM-based catalysts incorporated into photoactive MOF matrices to achieve photocatalytic hydrogen generation; A) A Dawson tungstate incorporated into a ruthenium-modified UiO-66 MOF, $[P_2W_{18}O_{62}]@[Zr_6O_4(OH)_4(C_{32}H_{30}N_6O_4Ru)_6]$; B) A Nickel-substituted sandwich-type TMS-POM incorporated into an iridium-modified UiO-66 MOF, $[Ni_4(H_2O)_2(PW_9O_{34})_2]@[Zr_6O_4(OH)_4(C_{34}H_{30}N_4O_4Ir)_6]$; Modified from references 298 and 299, respectively.

1.4.3) Limitations

Although MOFs are highly prized for their ability to incorporate guest molecules, guest absorption and release are fundamentally diffusion limited processes.[300] These processes are generally slow and gradual – in one example, diffusion of iodine guest molecules into a zinc-based MOF required *c.* 48 hours of slow diffusion before the MOF was fully loaded with guests.[300] In some cases, slow diffusion is desirable, for example in the case of drug delivery applications.[301] However, in many instances, fast release of a guest molecule is desirable.

The simplest method to drive guest molecules from their host MOF matrix is the application of heat. In one recent example, heat from sunlight was used to collect adsorbed atmospheric water from MOF-801, $[Zr_6O_4(OH)_4(fumarate)_6]$.[302] Other methods take advantage of the flexible nature of some MOFs to induce phase changes by the application of pressure, modifying guest uptake properties.[303–305] Cation exchange has also been shown to trigger extrusion of guests from the host framework.[306]

Increasingly, light-active building units have been incorporated into MOFs to modify their guest uptake.[307] *Azo-* moieties can be introduced into MOFs as part of a guest molecule, a structural part of the linker molecules, or as a side-group to the linker molecule.[308–310] In all cases, the *cis-trans* isomerisation of the *azo-* moiety under irradiation results in structural changes to the MOF that can eliminate guest molecules from the MOF.[308–310] One particularly sophisticated example used a two-layered system of "reservoir" MOF pores surrounded with a surface layer of azobenezne modified pores that serve as a "valve" to either release or retain the guest molecules (Figure 1.4.3.1).[311]

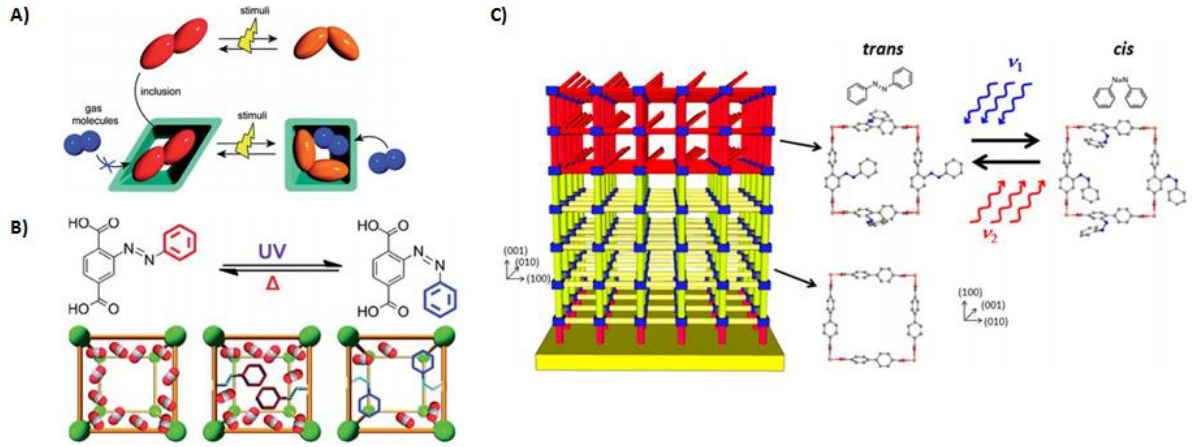

Figure 1.4.3.1 – A) Stimuli-responsive structural changes can be used to modify guest uptake into a MOF structure. B) The light-driven *cis-trans* isomerisation of azobenzene-type units can be exploited to eliminate guest molecules from the host matrix upon irradiation. C) Schematic of a two-layered "reservoir and valve"-type azobenezne-modified MOF. Modified from references 308, 309 and 311, respectively.

While these developments are promising, fast, controllable release of guest molecules from MOFs remains challenging.

1.5) Mass Spectrometry

As previously discussed, intermediates in POM synthesis can be difficult to isolate. Nevertheless, they provide valuable insights into the mechanisms of POM formation. Therefore, techniques which can identify species in solution are of considerable value. To this end, mass spectrometry (MS) represents a valuable analytical tool to monitor solution behaviour in synthetic systems.

MS analysis has been applied to numerous POM systems to understand their solution behaviour, intermediate structures, and reaction kinetics (Figure 1.5.1).[312–314] It has been shown that MS can be used to investigate POM protonation states, such as in the case of $[H_mSb_nW_{18}O_{60}]^{x-}$ Dawson clusters.[315] MS analysis can also be used to gain mechanistic insight into POM reactions, such as the aggregation and isomerisation of iron-substituted lacunary Keggin structures.[316] MS analysis also allows the kinetics of reactions to be studies, such as in the case of vanadium substitution into trilacunary Keggin tungstates.[317]

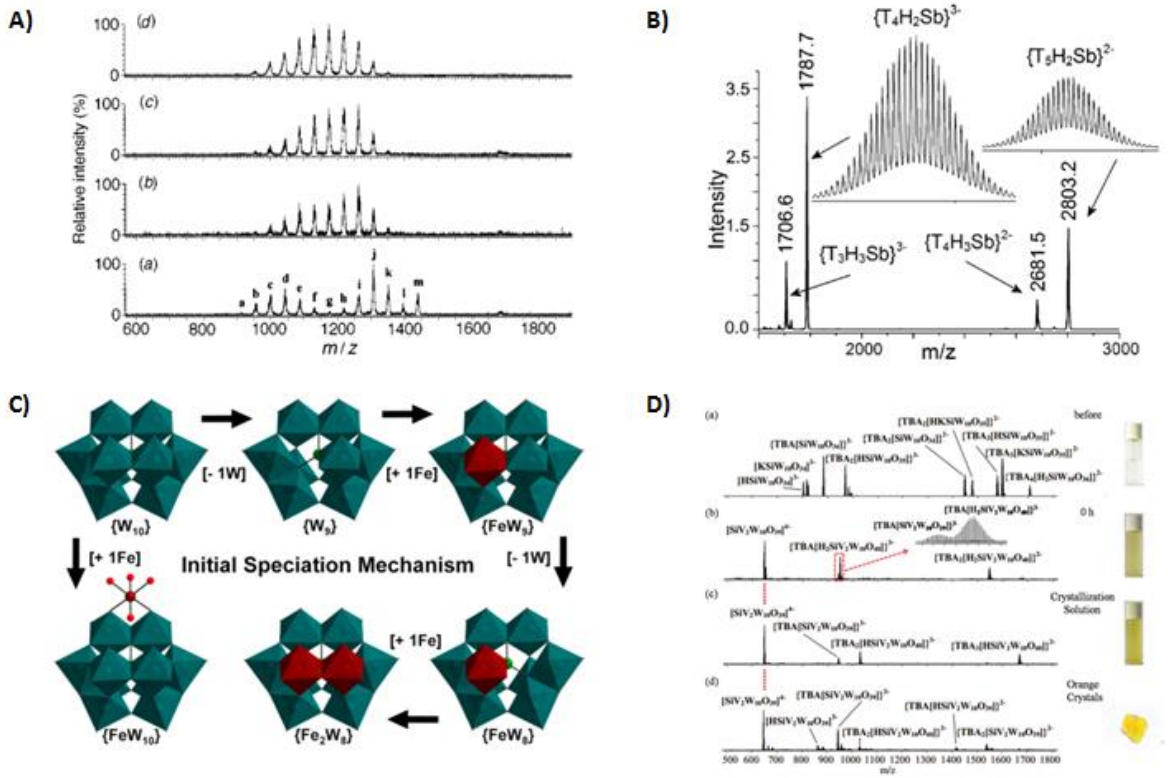

Figure 1.5.1 – Some examples of the use of mass spectrometry (MS) to analyse POM systems; A) MS analyses of mixtures of molybdate and tungstate Keggin structures, showing exchange of metal centres over time (bottom-to-top) to generate mixed metal $[HPW_nMo_{1-n}O_{40}]^{2-}$ clusters. B) MS analyses of $[H_mSb_nW_{18}O_{62}]^{x-}$ salts, showing different protonation states. C) The mechanism of iron substitution into γ-$[SiW_{10}O_{36}]^{8-}$ clusters, as elucidated my MS analyses. D) MS analyses at several stages of the reaction of lacunary Keggin POM $[SiW_{10}O_{36}]^{8-}$ to produce mixed metal $[SiV_2W_{10}O_{40}]^{6-}$. Modified from references 314-317, respectively.

A 2008 paper by Cronin *et al.* used cryospray MS to investigate the rearrangement of the Lindqvist hexamolybdate $[Mo_6O_{19}]^{2-}$ to a silver-molybdate polymer upon addition of silver fluoride to a methanol/acetonitrile solution of the POM.[318] A subsequent 2011 paper by the same group investigated the rearrangement of the α-octamolybdate $[Mo_8O_{24}]^{4-}$ cluster into a hybrid Anderson-type cluster.[319,320] These studies identified several intermediate species that will be discussed in more detail in chapter 2.

MS instruments use various methods of ionisation to transfer their analyte to the gas phase. Two such methods will be discussed here; Electrospray Ionisation (ESI-MS) and Matrix Assisted Laser Desorption Ionisation (MALDI-MS). These techniques are both noted for their wide applicability (they work with a range of volatile solvents such as methanol or acetonitrile) and relative softness compared to earlier techniques.[321,322] The type of mass analyser used is also significant, but will not be discussed here.[323]

In the ESI method, a voltage (known as the cone voltage) is applied to a capillary of the solution, causing the formation of a Taylor Cone and the ejection of microdroplets (Figure 1.5.2).[324,325] Essentially, solvent evaporation in the chamber (aided by a flow of dry gas) results in increasing charge density and "Coulomb Explosion" events, effectively ejecting any charged analyte molecules into the gas phase (although different mechanisms for ejection exist depending on the size of the molecule).[326–328]

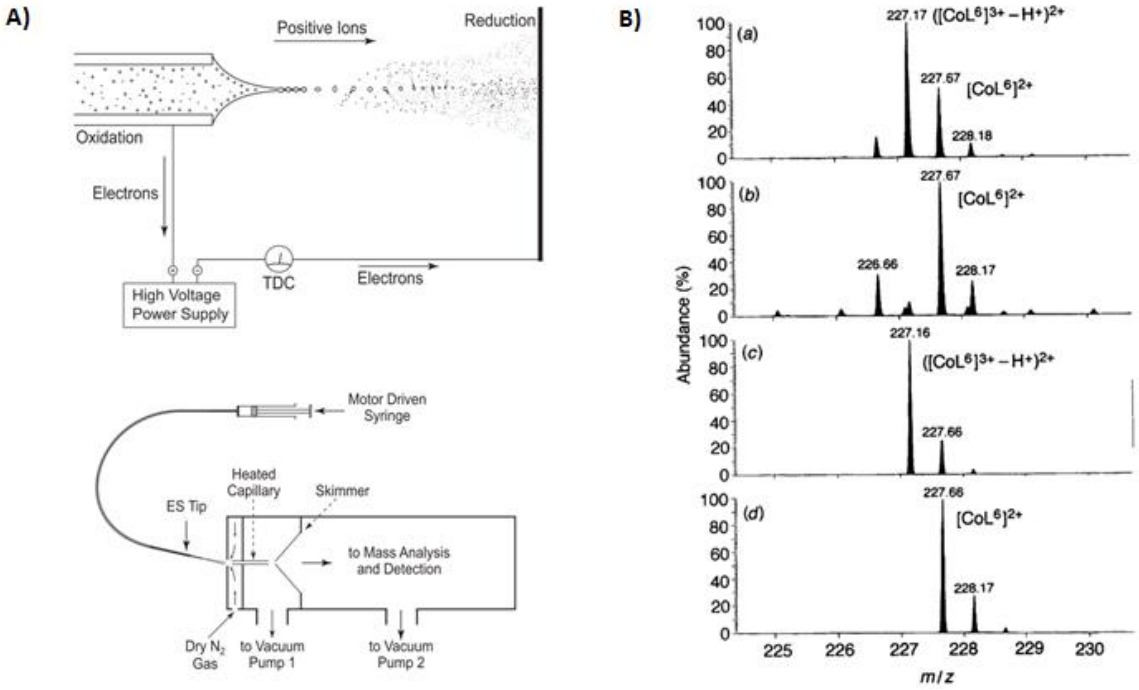

Figure 1.5.2 –A) Schematic of the Taylor Cone (under positive bias) and its position within an ESI-MS device. B) The effect of modified cone voltage (CV) on the ESI-MS analyses of a cobalt cavitand complex, $[Co(C_{22}N_6H_{48})]^{2-}$, with increased fragmentation occurring at higher CV values. Modified from references 325 and 329, respectively.

While this method is considered extremely mild and has been used to analyse very large and fragile molecules, it has been demonstrated that variation of the cone voltage does result in fragmentation of the analyte molecule (Figure 1.5.2).[329,330] Increasing the cone voltage effectively increases the kinetic energy of the analyte molecules, meaning that collisions with gas-phase solvent molecules are more likely to result in a fragmentation event (a collision induced dissociation, or CID).[331,332] This behaviour can differentiate molecules that are truly present in solution from fragments formed within the spraying chamber – signals caused by "real" species in solution diminish in intensity on increasing cone voltage, while signals due to their daughter fragments correspondingly increase in intensity. This effect has been exploited to rule out instrumental fragmentation for a series of arsonate- stabilised molybdate clusters.[181]

The MALDI method transfers the analyte to the gas phase by the application of a pulsed laser system, which causes rapid localised heating of an additive (the matrix, Figure 1.5.3) and the resulting ejection of analyte molecules into the gas phase *via* a variety of mechanisms.[333] MALDI is also considered to be a remarkably soft technique, but again instances of fragmentation have been observed.[334]

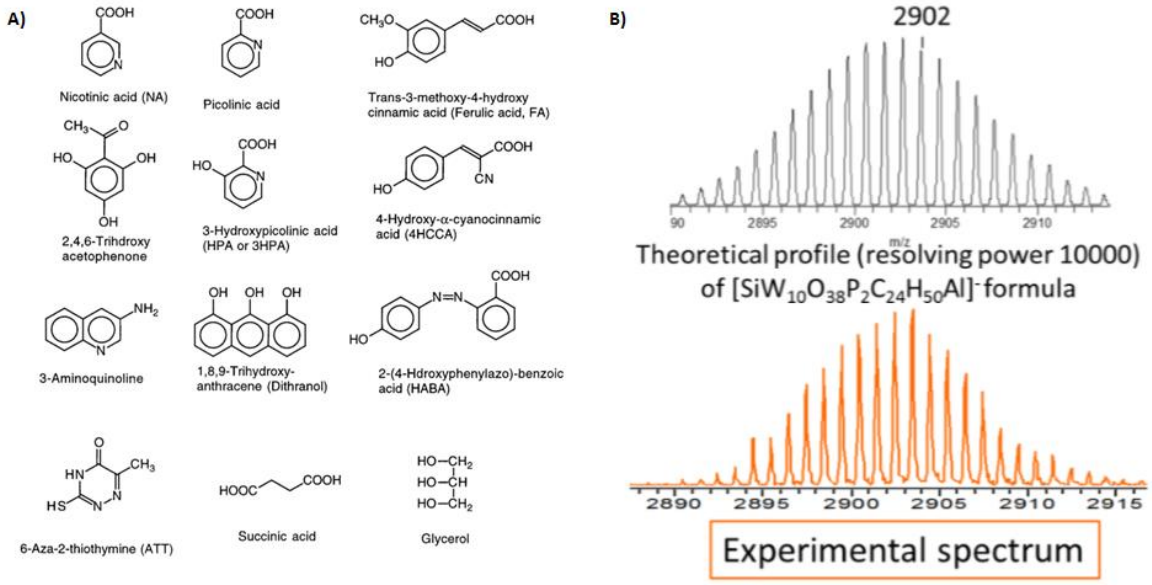

Figure 1.5.3 –A) Some compounds commonly used as matrices in MALDI-MS analyses. B) Multinuclear POM species quickly give rise to quasi-Gaussian isotopic distributions in MS analyses. Modified from references 333 and 336, respectively.

One distinctive aspect of POM clusters in MS analysis is that isotopic envelopes tend to be very broad. Molybdenum has seven naturally occurring isotopes of reasonable abundance (^{92}Mo 14.8%, ^{94}Mo 9.3%, ^{95}Mo 15.9%, ^{96}Mo 16.7%, ^{98}Mo 24.1% and ^{100}Mo 9.6%),[335,336] which when combined into polynuclear assemblies quickly give rise to quasi-Gaussian isotopic distributions (Figure 1.5.3).[337] While isotopic patterns can still be identified with reasonable certainty,[338] there is a certain degree of ambiguity for large clusters when compared to smaller species which have distinctive isotopic patterns.[339]

1.6) Aims and Objectives

The fundamental aim of this project is to develop new examples of advanced materials, such as those discussed over the course of this chapter. In particular, we were interested in accessing the following classes of materials:

- *Organic-Inorganic Hybrid POMs* (*i.e.* POM compounds supported by one or more organic ligands)
- *TMS-POMs* (*i.e.* POM compounds containing one or more heterometal atoms, particularly heterometals from the wider transition metal block that do not normally form POM compounds on their own)
- *Extended Systems* (*i.e.* Polymer or MOF-type compounds that contain repeating inorganic and organic units in extended architectures)

We were interested in accessing novel examples of these materials, investigating their structure-property relationships, and modifying the properties of the materials wherever possible. In order to access novel examples of these materials, we were interested in developing a novel synthetic approach, outside of the established synthetic approaches explored over the course of this chapter.

Therefore, the first part of this project aimed to establish a novel synthetic approach towards these classes of materials. We aimed to develop a rational synthetic strategy that would access fundamentally different intermediates than traditional methods, thereby potentially allowing access to our target compounds. This part of the project is described in **chapter 2**.

After developing a synthetic strategy, the second part of the project aimed to exploit that strategy to access our target compounds. The first objective was to obtain hybrid POMs. The aim was to synthesise novel examples of hybrid POMs by using a suitable organic ligand in the strategy developed in the first part of the project. Additionally, it was our aim to understand, insofar as was possible, the reaction mechanisms that generated the hybrid compounds. This part of the project is also described in **chapter 2**.

Having developed a strategy and demonstrated its efficacy, the third part of the project aimed to extend this methodology to hybrid TMS-POM species. The aim was to incorporate various heterometals into the synthetic strategy to generate mixed-metal compounds. Additionally, we wanted to explore how versatile the synthetic strategy was – we wanted to understand the effects that different heterometals, different ligands, and different reaction conditions would have on the applied strategy. We therefore set out to explore some of the reaction space in an attempt to understand the flexibility of the synthetic strategy, as well as generate modifications of the various TMS-POM compounds. We also wanted to explore how the structural components of the materials affected their physicochemical properties. This part of the project is explored in **chapters 3-5**, with each chapter focussing on a different heterometal.

Finally, we aimed to apply the developed principles to extended systems such as polymers and MOFs. The first objective of this part was to generate novel polymer-type compounds by using polytopic ligands in the new synthetic strategy and to investigate their structures. This part of the project is described in **chapters 4 and 5**. The final objective of the project was to develop novel MOF-type compounds using known ligands and nodes, and to apply the synthetic concepts developed to modify their properties. This part of the project is described in **chapter 6**.

In order to achieve these goals, we set out to achieve the following specific objectives:

- To analyse literature synthetic procedures and rationally develop an alternative synthetic route towards our target compounds
- To identify possible starting materials and determine if they are suitable candidates for this methodology
- To exploit the methodology to develop novel hybrid POM species
- To exploit the methodology to develop novel TMS-POM species
- To exploit the methodology to develop novel extended systems
- To determine the structure of all of the resulting compounds with appropriate analytical techniques
- To examine structural motifs present in the final products and use these to illuminate the processes by which the compounds formed
- To determine structure-property relationships in the final products and exploit them for practical purposes wherever possible

1.7) References

1 M. T. Pope and A. Müller, *Polyoxometalate Chem. From Topol. via Self-Assembly to Appl.*, 2001.

2 M. T. Pope and A. Müller, *Angew. Chem. Int. Ed.*, 1991, **30**, 34.

3 N. V Izarova, N. Vankova, T. Heine, R. N. Biboum, B. Keita, L. Nadjo and U. Kortz, *Angew. Chem. Int. Ed.*, 2010, **49**, 1886.

4 E. V Chubarova, M. H. Dickman, B. Keita, L. Nadjo, F. Miserque, M. Mifsud, I. W. C. E. Arends and U. Kortz, *Angew. Chem. Int. Ed.*, 2008, **34**, 9542.

5 F. A. Cotton, *Q. Rev. Chem. Soc.*, 1966, **20**, 389.

6 C. A. Ohlin, E. M. Villa, J. R. Rustad and W. H. Casey, *Nat. Mater.*, 2009, **9**, 11.

7 J. R. Rustad and W. H. Casey, *Nat. Mater.*, 2012, **11**, 223.

8 B. Kowalewski, J. Poppe, U. Demmer, E. Warkentin, T. Dierks, U. Ermler and K. Schneider, *J. Am. Chem. Soc.*, 2012, **134**, 9768.

9 J. Berzelius, *Poggend. Ann. Phys. Chem.*, 1826, **6**, 369.

10 A. Ure, *D. Applet. Co.*, 1844.

11 P. Gouzerh and M. Che, *l'actualite*, 2006, **298**, 1.

12 H. N. Miras, J. Yan, D. Long and L. Cronin, *Chem. Soc. Rev.*, 2012, **41**, 7403.

13 V. Sans, H. N. Miras, D. Long and L. Cronin, *Inorg. Chem.*, 2017, **56**, 5089.

14 L. Vila-Nadal, E. F. Wilson, H. N. Miras, A. Rodríguez-Fortea, L. Cronin and J. M. Poblet, *Inorg. Chem.*, 2011, **50**, 7811.

15 L. Vila-Nadal, S. G. Mitchell, A. Rodríguez-Fortea, H. N. Miras, L. Cronin and J. M. Poblet, *Phys. Chem. Chem. Phys.*, 2011, **13**, 20136.

16 P. Jiménez-Lozano, A. Solé-Daura, G. Wipff, J. M. Poblet, A. Chaumont and J. J. Carbo, *Inorg. Chem.*, 2017, **56**, 4148.

17 P. D. Beer and P. A. Gale, *Angew. Chem. Int. Ed.*, 2001, **40**, 486.

18 C. L. Hill (Editor), *Chemical Reviews Special Edition on Polyoxometalates*, 1998.

19 C. P. Pradeep, D. Long and L. Cronin, *Dalton Trans.*, 2010, **39**, 9443.

20 N. J. Hur, W. G. Klemperer and R. C. Wang, *Inorg. Synth.*, 1990, **27**, 77.

21 J. A. Dias, S. C. L. Dias, E. Caliman, J. Bartis and L. Francesconi, *Inorg. Synth.*, 2014, **36**.

22 I. Lindqvist, *Acta Crystallogr.*, 1952, **5**, 667.

23 S. Bartley, S. Bernstein and K. R. Dunbar, *Inorganica Chim. Acta*, 1993, **213**, 213.

24 P. A. Abramov, M. N. Sokolov, S. Floquet, M. Haouas, F. Taulelle, E. Cadot, E. V Peresypkina, A. V Virovets, C. Vicent, N. B. Kompankov, A. A. Zhdanov, O. V Shuvaeva and V. P. Fedin, *Inorg. Chem.*, 2014, **53**, 12791.

25 J. W. Illingworth and J. F. Keggin, *J. Chem. Soc.*, 1935, 575.

26 A. J. Bridgeman, *Chem. Phys.*, 2003, **287**, 55.

27 L. C. W. Baker and S. J. Figgis, *J. Am. Chem. Soc.*, 1970, **92**, 3794.

28 V. W Day, M. F. Fredrich, W. G. Klemperer and W. Shum, *J. Am. Chem. Soc.*, 1977, **99**, 6146.

29 A. Müller, E. Beckmann, H. Bögge, M. Schmidtmann and A. Dress, *Angew. Chem. Int. Ed.*, 2002, **41**, 1162.

30 C. P. Pradeep, D. Long, C. Streb and L. Cronin, *J. Am. Chem. Soc.*, 2008, **130**, 14946.

31 J. Yan, J. Gao, D. Long, H. N. Miras and L. Cronin, *J. Am. Chem. Soc.*, 2010, **132**, 11410.

32 J. B. Heynes and J. J. Cruywagen, *Inorg. Synth.*, 1986, **24**, 191.

33 A. Müller, E. Krickemeyer, J. Meyer, H. Bögge, F. Peters, W. Plass, E. Diemann, S. Dillinger, M. Randerath and C. Menke, *Angew. Chem. Int. Ed.*, 1995, **34**, 2122.

34 A. Müller, E. Krickemeyer, H. Bögge, M. Schmidtmann, F. Peters, C. Menke and J. Meyer, *Angew. Chem. Int. Ed.*, 1997, **36**, 483.

35 A. Müller, E. Krickemeyer, H. Bögge, M. Schmidtmann, C. Beugholt, P. Kögerler and C. Lu, *Angew. Chem. Int. Ed.*, 1998, **37**, 1220.

36 A. Müller, S. Q. N. Shah, H. Bögge and M. Schmidtmann, *Nature*, 1999, **397**, 48.

37 B. B. Sarma, L. Avram and R. Neumann, *Chem. Eur. J.*, 2016, **22**, 15231.

38 D. Long, E. Burkholder, L. Cronin and E. Burkholder, *Chem. Soc. Rev.*, 2007, **36**, 105.

39 C. Serain and A. Müller, *Acc. Chem. Res.*, 2000, **33**, 2.

40 T. Liu, E. Diemann, H. Li and A. W. M. Dress, *Nature*, 2003, **426**, 59.

41 A. Müller, L. Toma, H. Bögge, C. Schaffer and A. Stammler, *Angew. Chem. Int. Ed.*, 2005, **44**, 7757.

42 A. Müller, M. Koop, H. Bögge, M. Schmidtmann, F. Peters, P. Kögerler, *Chem. Commun.*, 1999, **3**, 1885.

43 L. Cronin, C. Beugholt, E. Krickemeyer, M. Schmidtmann, H. Bögge, P. Kögerler, T. K. K. Luong and A. Müller, *Angew. Chem. Int. Ed.*, 2002, **41**, 2805.

44 A. Müller, S. Sarkar, S. Q. N. Shah, H. Bögge, M. Schmidtmann, S. Sarkar, P. Kögerler, B. Hauptfleisch, A. X. Trautwein and V. Schünemann, *Angew. Chem. Int. Ed.*, 1999, **38**, 3238.

45 A. Müller, P. Kögerler and A. W. M. W. M. Dress, *Coord. Chem. Rev.*, 2001, **222**, 193.

46 A. Müller, P. Kögerler and C. Kuhlmann, *Chem. Commun.*, 1999, 1347.

47 H. T. Evans, *J. Am. Chem. Soc.*, 1948, **70**, 1291.

48 M. T. Pope, *Heteropoly and Isopoly Oxometaltes*, Springer-Verlag, Berlin, 1983.

49 A. Perloff, *Inorg. Chem.*, 1970, **9**, 2228.

50 K. Nomiya, T. Takahashi, T. Shirai and M. Miwa, *Polyhedron*, 1987, **6**, 213.

51 B. Hasenknopf, R. Delmont, P. Herson and P. Gouzerh, *Eur. J. Inorg. Chem.*, 2002, 1081.

52 Y. Song, N. McMillan, D. Long, S. Kane, J. Malm, M. O. Riehle, C. P. Pradeep, N. Gadegaard and L. Cronin, *J. Am. Chem. Soc.*, 2009, **131**, 1340.

53 P. R. Marcoux, B. Hasenknopf, J. Vaissermann and P. Gouzerh, *Eur. J. Inorg. Chem.*, 2003, 2406.

54 P. Wu, P. Yin, J. Zhang, J. Hao, Z. Xiao and Y. Wei, *Chem. Eur. J.*, 2011, **17**, 12002.

55 H. T. Evans, B. M. Gatehouse and P. Leverett, *J. Chem. Soc. Dalton Trans.*, 1975, 505.

56 A. Don and T. J. R. Weakley, *Acta Crystallogr. Sect. B*, 1981, **37**, 451.

57 T. Yamase and T. Ikawa, *Bull. Chem. Soc. Jpn.*, 1977, **50**, 746.

58 Y. Ohashi, K. Kanagi, Y. Sasada and T. Yamase, *Bull. Chem. Soc. Jpn.*, 1982, **55**, 1254.

59 J. Fuchs and H. Hartl, *Angew. Chem. Int. Ed.*, 1976, **15**, 375.

60 A. J. Bridgeman, *J. Phys. Chem. A*, 2002, **106**, 12151.

61 M. L. Niven, J. J. Cruywagen and J. B. B. Heyns, *J. Chem. Soc. Dalton Trans.*, 1991, 2007.

62 W. G. Klemperer and W. Shum, *J. Am. Chem. Soc.*, 1976, **98**, 8291.

63 R. Strandberg, *Acta Chem. Scand.*, 1973, 1004.

64 L. Petterson, *Acta Chem. Scand.*, 1971, **25**, 1959.

65 B. Hedman, *Acta Chem. Scand.*, 1973, **27**, 3335.

66 H. I. Buvailo, G. Makhankova, V. N. Kokozay, I. V Omelchenko, S. V Shishkina, P. Zabierowski, D. Matoga and J. Jezierska, *Eur. J. Inorg. Chem.*, 2017, **22**, 3525.

67 W. Kwak, M. T. Pope and T. F. Scully, *J. Am. Chem. Soc.*, 1975, **97**, 5737.

68 J. K. Stalick and C. Quicksall, *Inorg. Chem.*, 1976, **15**, 1577.

69 L. Yan, Z. Su, K. Tan, M. Zhang, L. Qu and R. Wang, *J. Quantum Chem.*, 2005, **105**, 37.

70 B. Dawson, *Acta Crystallogr.*, 1953, **6**, 113.

71 A. Teze and G. Herve, *Inorg. Synth.*, 1990, **27**, 85.

72 C. Rong and M. T. Pope, *J. Am. Chem. Soc.*, 1992, **114**, 2932.

73 K. Kastner, J. T. Margraf, T. Clark and C. Streb, *Chem. Eur. J.*, 2014, **20**, 12269.

74 J.-W. Zhao, H.-P. Jia, J. Zhang, S.-T. Zheng and G.-Y. Yang, *Chem. Eur. J.*, 2007, **13**, 10030.

75 S. Zheng, D. Yuan, H. Jia and G. Yang, *Chem. Commun.*, 2007, 1858.

76 R. Al-Oweini, B. S. Bassil, J. Friedl, V. Kottisch, M. Ibrahim, M. Asano, B. Keita, G. Novitchi, Y. Lan, A. Powell, U. Stimming and U. Kortz, *Inorg. Chem.*, 2014, **53**, 5663.

77 X. Fang, P. Kögerler, Y. Furukawa, M. Speldrich and M. Luban, *Angew. Chem. Int. Ed.*, 2011, **50**, 5212.

78 X. Fang and P. Kögerler, *Chem. Commun.*, 2008, 3396.

79 X. Fang and P. Kögerler, *Angew. Chem. Int. Ed.*, 2008, **47**, 8123.

80 U. Kortz, S. Isber, M. H. Dickman, D. Ravot, L. D. P. De Matie and R. V January, *Inorg. Chem.*, 2000, **34**, 2915.

81 Q. Wu, Y. Li, Y. Wang, E. Wang, Z. Zhang and R. Cle, *Inorg. Chem.*, 2009, **48**, 1606.

82 P. Kögerler and A. Müller, *J. Appl. Phys.*, 2003, **93**, 7101.

83 H. Xue, J. Zhao, R. Pan, B. Yang, G. Yang and H.-S. Liu, *Chem. Eur. J.*, 2016, **22**, 12322.

84 D. E. Katsoulis, *Chem. Rev.*, 1998, **98**, 359.

85 R. Wang, Y. Li, K. Shetye, T. Dutta, L. Jin, S. Li and Z. Peng, *Eur. J. Inorg. Chem.*, 2015, 656.

86 B. E. Papaconstantinou, *Chem. Soc. Rev.*, 1989, **292**, 1.

87 S. Herrmann, L. De Matteis, J. M. de la Fuente, S. G. Mitchell and C. Streb, *Angew. Chem. Int. Ed.*, 2017, **56**, 1667.

88 M. Ammam, *J. Mater. Chem. A*, 2013, **1**, 6291.

89 J. T. Rhule, C. L. Hill, D. A. Judd and R. F. Schinazi, *Chem. Rev.*, 1998, **98**, 327.

90 U. Kortz, A. Müller, J. van Slageren, J. Schnack, N. S. Dalal and M. Dressel, *Coord. Chem. Rev.*, 2009, **253**, 2315.

91 J. M. Clemente-Juan, E. Coronado and A. Gaita-Arin, *Chem. Soc. Rev.*, 2012, **41**, 7464.

92 K. Eda and T. Osakai, *Inorg. Chem.*, 2015, **54**, 2793.

93 L. C. W. Baker and D. C. Glick, *Chem. Rev.*, 1998, **98**, 3.

94 X. Tong and V. Thangadurai, *J. Phys. Chem. C*, 2015, **119**, 7621.

95 X. Wu, X. Tong, Q. Wu and W. Yan, *J. Mater. Chem. A*, 2014, **2**, 5780.

96 I. V. Kozhevnikov, *Chem. Rev.*, 1998, 171.

97 T. Tagawa, J. Amemiya and S. Goto, *Appl. Catal. A Gen.*, 2004, **257**, 19.

98 C. Venturello, E. Alneri and M. Ricci, *J. Org. Chem.*, 1983, **3**, 3831.

99 A. M. Khenkin and R. Neumann, *J. Org. Chem.*, 2002, **67**, 7075.

100 J. Bregeault, *Dalton Trans.*, 2003, **17**, 3289.

101 L. Aakel, F. Launay, A. Atlamsani and J. Bregeault, *Chem. Commun.*, 2001, 2218.

102 Z. Long, Y. Zhou, G. Chen, W. Ge and J. Wang, *Sci. Rep.*, 2014, **4**, 3651.

103 B. B. Sarma and R. Neumann, *Nat. Commun.*, 2014, **5**, 4621.

104 J. Reichert, B. Brunner, A. Jess and J. Albert, *Energy Environ. Sci.*, 2015, **8**, 2985.

105 J. Zhang, M. Sun and Y. Han, *RSC Adv.*, 2014, **4**, 35463.

106 W. Liu, W. Mu, M. Liu, X. Zhang, H. Cai and Y. Deng, *Nat. Commun.*, 2014, **5**, 3208.

107 D. Sloboda-Rozner, P. L. Alsters and R. Neumann, *J. Am. Chem. Soc.*, 2003, **125**, 5280.

108 A. Rubinstein, P. Jime, J. J. Carbo, J. M. Poblet and R. Neumann, *J. Am. Chem. Soc.*, 2014, **136**, 10941.

109 R. Neumann and M. Dahan, *Nature*, 1997, **388**, 353.

110 E. Papaconstantinou, *J. Chem. Soc. Commun.*, 1982, 12.

111 C. Streb, *Dalton Trans.*, 2012, **41**, 1651.

112 S. Antonaraki, E. Androulaki, D. Dimotikali, A. Hiskia and E. Papaconstantinou, *J. Photochem. Photobiol.*, 2002, **148**, 191.

113 M. Dave and C. Streb, *Dalton Trans.*, 2015, **44**, 18919.

114 C. L. Hill and D. A. Bouchard, *J. Am. Chem. Soc.*, 1985, **107**, 5148.

115 J. Forster, B. Rosner, M. M. Khusniyarov and C. Streb, *Chem. Commun.*, 2011, **47**, 3114.

116 E. Papaconstantinou, D. Dimotikali and A. Politou, *Inorganica Chem. Acta*, 1980, **46**, 155.

117 C. L. Hill and C. M. Prosser-McCartha, *Coord. Chem. Rev.*, 1995, **143**, 407.

118 R. Neumann, *Inorg. Chem.*, 2010, **49**, 3594.

119 T. Yamase, N. Takabayashi and M. Kaji, 1984, **5**, 793.

120 J. Darwent, *J. Chem. Soc. Commun.*, 1982, **14**, 789.

121 A. Ioannidis and E. Papaconstantinou, *Inorg. Chem.*, 1985, **24**, 439.

122 T. R. Cook, D. K. Dogutan, S. Y. Reece, Y. Surendranath, T. S. Teets and D. G. Nocera, *Chem. Rev.*, 2010, **110**, 6474.

123 K. S. Joya, Y. F. Joya, K. Ocakoglu and R. Van De Krol, *Angew. Chem. Int. Ed.*, 2013, **52**, 10426.

124 D. G. Nocera and M. P. Nash, *Proc. Natl. Acad. Sci. U. S. A.*, 2007, **104**, 15729.

125 J. Du, Z. Chen, C. Chen and T. J. Meyer, *J. Am. Chem. Soc.*, 2015, **137**, 3193.

126 S. Kato, J. Jung, T. Suenobu and S. Fukuzumi, *Energy Environ. Sci.*, 2013, **6**, 3756.

127 S. Sato, T. Arai and T. Morikawa, *Inorg. Chem.*, 2014, **54**, 5105.

128 H. Lv, Y. V. Geletii, C. Zhao, J. W. Vickers, G. Zhu, Z. Luo, J. Song, T. Lian, D. G. Musaev and C. L. Hill, *Chem. Soc. Rev.*, 2012, **41**, 7572.

129 Y. Pellegrin and F. Odobel, *Comptes Rendus Chim.*, 2017, **20**, 283.

130 A. R. Parent, R. H. Crabtree and G. W. Brudvig, *Chem. Soc. Rev.*, 2013, **42**, 2247.

131 B. Rausch, M. D. Symes, G. Chisholm and L. Cronin, *Science*, 2014, **345**, 1326.

132 M. D. Symes and L. Cronin, *Nat. Chem.*, 2013, **5**, 403.

133 S. Goberna-Ferron, L. Vigara, J. Soriano-Lopez and J. R. Galan-Mascaros, *Inorg. Chem.*, 2012, **51**, 11707.

134 J. Soriano-Lopez, S. Goberna-Ferron, L. Vigara, J. J. Carbo, J. M. Poblet and J. R. Galan-Mascaros, *Inorg. Chem.*, 2013, **52**, 4753.

135 X. Xing, M. Wang, R. Liu, S. Zhang, K. Zhang and B. Li, *Green Energy Environ.*, 2016, **1**, 138.

136 F. M. Toma, A. Sartorel, M. Iurlo, M. Carraro, P. Parisse, C. Maccato, S. Rapino, B. R. Gonzalez, H. Amenitsch, T. Da Ros, L. Casalis, A. Goldoni, M. Marcaccio, G. Scorrano, G. Scoles, F. Paolucci, M. Prato and M. Bonchio, *Nat. Chem.*, 2010, **2**, 826.

137 W. Luo, J. Hu, H. Diao, B. Schwarz, C. Streb and Y. Song, *Angew. Chem. Int. Ed.*, 2017, **56**, 4941.

138 M. D. Kärkäs and B. Åkermark, *Dalton Trans.*, 2016, **45**, 14421.

139 J. A. Gilbert, D. S. Eggleston, W. R. Murphy, D. A. Geselowitz, S. W. Gersten, D. J. Hodgson and T. J. Meyer, *J. Am. Chem. Soc.*, 1985, **107**, 3855.

140 S. W. Gersten, G. J. Samuels and T. J. Meyer, *J. Am. Chem. Soc.*, 1982, **104**, 4029.

141 B. Nepal and S. Das, *Angew. Chem. Int. Ed.*, 2013, **52**, 7224.

142 A. Sartorel, P. Miro, E. Salvadori, S. Romain, M. Carraro, G. Scorrano, M. Di Valentin, A. Llobet, C. Bo and M. Bonchio, *J. Am. Chem. Soc.*, 2009, 16051.

143 S. Piccinin, A. Sartorel, G. Aquilanti, A. Goldoni, M. Bonchio and S. Fabris, *Proc. Natl. Acad. Sci. U. S. A.*, 2013, **110**, 4917.

144 M. Burian, Z. Syrgiannis, G. La, F. Puntoriero, M. Natali, F. Scandola, S. Campagna, M. Prato, M. Bonchio, H. Amenitsch and A. Sartorel, *Inorganica Chim. Acta*, 2017, **454**, 171.

145 Y. V Geletii, B. Botar, P. Kögerler, D. A. Hillesheim, D. G. Musaev and C. L. Hill, *Angew. Chem. Int. Ed.*, 2008, **47**, 3896.

146 A. E. Kuznetsov, Y. V Geletii, C. L. Hill, K. Morokuma, D. G. Musaev, V. Uni and D. D. V, *J. Am. Chem. Soc.*, 2009, **131**, 6844.

147 A. Sartorel, M. Carraro, G. Scorrano, R. De Zorzi, S. Geremia, N. D. McDaniel, S. Bernhard and M. Bonchio, *J. Am. Chem. Soc.*, 2008, **130**, 5006.

148 R. Al-Oweini, A. Sartorel, B. S. Bassil, M. Natali, S. Berardi, F. Scandola, U. Kortz and M. Bonchio, *Angew. Chem. Int. Ed.*, 2014, **53**, 11182.

149 M. Suga, F. Akita, K. Hirata, G. Ueno, H. Murakami, Y. Nakajima, T. Shimizu, K. Yamashita, M. Yamamoto, H.

Ago and J. Shen, *Nature*, 2014, **517**, 99.

150 M. Wiechen, M. M. Najafpour, S. I. A. De and L. Spiccia, *Energy Environ. Sci.*, 2014, **7**, 2203–2212.

151 B. Schwarz, J. Forster, M. K. Goetz, D. Yucel, C. Berger, T. Jacob and C. Streb, *Angew. Chem. Int. Ed.*, 2016, **55**, 6344.

152 V. Artero, M. Chavarot-Kerlidou and M. Fontecave, *Angew. Chem. Int. Ed.*, 2011, **50**, 7238.

153 F. Song, Y. Ding, B. Ma, C. Wang, Q. Wang, X. Du, S. Fua and J. Song, *Energy Environ. Sci.*, 2013, **6**, 1170.

154 S. Tanaka, M. Annaka and K. Sakai, *Chem. Commun.*, 2012, **48**, 1653.

155 X. Han, Z. Zhang, T. Zhang, Y. Li, W. Lin, W. You, Z. Su and E. Wang, *J. Am. Chem. Soc.*, 2014, **136**, 5359.

156 Q. Yin, J. M. Tan, C. Besson, Y. V Geletii, D. G. Musaev, A. E. Kuznetsov, Z. Luo, K. I. Hardcastle and C. L. Hill, *Science*, 2010, **238**, 342.

157 Z. Huang, Z. Luo, Y. V Geletii, J. W. Vickers, Q. Yin, D. Wu, Y. Hou, Y. Ding, J. Song, D. G. Musaev, C. L. Hill and T. Lian, *J. Am. Chem. Soc.*, 2011, **133**, 2068.

158 J. J. Stracke and R. G. Finke, *J. Am. Chem. Soc.*, 2011, **4**, 14872.

159 M. Natali, S. Berardi, A. Sartorel, M. Bonchio, S. Campagna and F. Scandola, *Chem. Commun.*, 2012, **48**, 8808.

160 J. W. Vickers, H. Lv, J. M. Sumliner, G. Zhu, Z. Luo, D. G. Musaev, Y. V Geletii and C. L. Hill, *J. Am. Chem. Soc.*, 2013, **135**, 14110.

161 H. Lv, J. Song, Y. V Geletii, J. W. Vickers, J. M. Sumliner, D. G. Musaev, P. Ko, P. F. Zhuk, J. Bacsa, G. Zhu and C. L. Hill, *J. Am. Chem. Soc.*, 2014, **136**, 9268.

162 S. J. Folkman and R. G. Finke, *ACS Catal.*, 2017, **7**, 7.

163 M. W. Kanan and D. G. Nocera, *Science*, 2014, **321**, 1072.

164 M. Huynh, D. K. Bediako and D. G. Nocera, *J. Am. Chem. Soc.*, 2014, **136**, 6002.

165 M. Zhang, M. De Respinis and H. Frei, *Nat. Chem.*, 2014, **6**, 362.

166 L. G. Bloor, P. I. Molina, M. D. Symes and L. Cronin, *J. Am. Chem. Soc.*, 2014, **136**, 3304.

167 J. J. Stracke and R. G. Finke, *J. Am. Chem. Soc.*, 2014, **4**, 909.

168 Y. Pushkar, D. Moonshiram, V. Purohit, L. Yan and I. Alperovich, *J. Am. Chem. Soc.*, 2014, **136**, 11938.

169 Z. Chen, J. J. Concepcion, N. Song and T. J. Meyer, *Chem. Commun.*, 2014, **50**, 8053.

170 Y. Tamaki, A. K. Vannucci, C. J. Dares, R. A. Binstead and T. J. Meyer, *J. Am. Chem. Soc.*, 2014, **136**, 6854.

171 S. Guo, C. Lee, J. Zhang, A. M. Bond, Y. V Geletii and C. L. Hill, *Inorg. Chem.*, 2014, **53**, 7561.

172 P. Car, M. Guttentag, K. K. Baldridge, R. Alberto and G. R. Patzke, *Green Chem.*, 2012, **14**, 1680.

173 J. Gao, S. Cao, Q. Tay, Y. Liu, L. Yu, K. Ye, P. Choon and S. Mun, *Sci. Rep.*, 2013, **3**, 1853.

174 T. A. Betley, Q. Wu, T. Van Voorhis and D. G. Nocera, *Inorg. Chem.*, 2008, **47**, 1849.

175 R. Matheu, M. Z. Ertem, J. Benet-Buchholz, E. Coronado, V. S. Batista, X. Sala and A. Llobet, *J. Am. Chem. Soc.*, 2015, **137**, 10786.

176 A. Proust, B. Matt, R. Villanneau, G. Guillemot, P. Gouzerh and G. Izzet, *Chem. Soc. Rev.*, 2012, **41**, 7605.

177 P. Gouzerh and A. Proust, *Chem. Rev.*, 1998, **98**, 77.

178 A. Dolbecq, E. Dumas, R. Mayer and P. Mialane, *Chem. Rev.*, 2010, **110**, 6009.

179 A. Dolbecq, P. Mialane, F. Secheresse, B. Keitab and L. Nadjo, *Chem. Commun.*, 2012, **48**, 8299.

180 M. P. Lowe, J. C. Lockhart, W. Clegg and K. A. Fraser, *Angew. Chem. Int. Ed.*, 1994, **33**, 451.

181 C. I. Onet, L. Zhang, R. Clérac, J. B. Jean-Denis, M. Feeney, T. McCabe and W. Schmitt, *Inorg. Chem.*, 2011, **50**, 604.

182 Y. Huang, J. Zhang, J. Hao and Y. Wei, *Sci. Rep.*, 2016, **6**, 24759.

183 J. B. Strong, B. S. Haggerty, L. Rheingold and E. A. Maatta, *Chem. Commun.*, 1997, 1137.

184 J. Hao, Y. Xia, L. Wang, L. Ruhlmann, Y. Zhu, Q. Li, P. Yin, Y. Wei and H. Guo, *Angew. Chem. Int. Ed.*, 2008, **47**, 2626.

185 J. L. Stark, V. G. Young and E. A. Maatta, *Angew. Chem. Int. Ed.*, 1995, **34**, 2547.

186 W. Clegg, R. J. Errington, K. A. Fraser, S. A. Holmes and A. Schafer, *J. Chem. Soc. Commun.*, 1995, 455.

187 C. Yvon, A. Macdonell, S. Buchwald, A. J. Surman, N. Follet, J. Alex, D. Long and L. Cronin, *Chem. Sci.*, 2013, **4**, 3810.

188 H. Yang, M. Su, L. Ren and J. Tang, *Chem. Eur. J.*, 2013, 1381.

189 C. Dablemont, A. Proust, R. Thouvenot, C. Afonso, F. Fournier and J. C. Tabet, *Inorg. Chem.*, 2004, **43**, 3514.

190 W. H. Knoth, *J. Am. Chem. Soc.*, 1979, 759.

191 P. Judeinstein, C. Deprun and L. Nadjo, *J. Chem. Soc. Dalton Trans.*, 1991, 1991.

192 M. Piot, S. Hupin, H. Lavanant, C. Afonso, Bouteiller, A. Proust and G. Izzet, *Inorg. Chem.*, 2017, **56**, 8490.

193 C. Sanchez, B. Julia, P. Belleville and M. Popall, *J. Mater. Chem.*, 2005, **15**, 3559.

194 Z. Peng, *Angew. Chem. Int. Ed.*, 2004, **43**, 930.

195 A. Maharramov, K. Mahmudov, M. Kopylovich and A. Pombeiro, *Non-Covalent Interactions in the Synthesis and Design of New Compounds*, Wiley, 2016.

196 H. H. Jaffe, *Chem. Rev.*, 1953, 191.

197 L. Xu, M. Lu, B. Xu, Y. Wei, Z. Peng and D. R. Powell, *Angew. Chem. Int. Ed.*, 2002, **41**, 4129.

198 M.-B. Hu, N. Xia, W. Yu, C. Ma, J. Tang, Z.-Y. Hou, P. Zheng and W. Wang, *Polym. Chem.*, 2012, **3**, 617.

199 C. Allain, S. Favette, L. Chamoreau, J. Vaissermann, L. Ruhlmann and B. Hasenknopf, *Eur. J. Inorg. Chem.*, 2008, 3433.

200 D. Schaming, R. Farha, M. Goldmann, S. Lobstein, A. Giraudeau, B. Hasenknopf and L. Ruhlmann, *Langmuir*, 2010, **26**, 5101.

201 I. Azcarate, Z. Huo, R. Farha, M. Goldmann, H. Xu, B. Hasenknopf, E. Lacote and L. Ruhlmann, *Chem. Eur. J.*, 2015, **21**, 8271.

202 M. Bonchio, M. Carraro, G. Scorrano and A. Bagno, *Adv. Synth. Catal.*, 2004, **346**, 648.

203 C. Lv, K. Chen, J. Hu, J. Zhang, R. Naumaan, N. Khan and Y. Wei, *Sci. Rep.*, 2016, **6**, 27861.

204 U. Kortz, M. G. Savelieff, F. Y. A. Ghali, L. M. Khalil, S. A. Maalouf and D. I. Sinno, *Angew. Chem. Int. Ed.*, 2002, **41**, 4070.

205 S. She, S. Bian, J. Hao, J. Zhang, J. Zhang and Y. Wei, *Chem. Eur. J.*, 2014, **20**, 16987.

206 S. She, S. Bian, R. Huo, K. Chen, Z. Huang, J. Zhang, J. Hao and Y. Wei, *Sci. Rep.*, 2016, **6**, 33529.

207 H. N. Miras, L. Vila-Nadal and L. Cronin, *Chem. Soc. Rev.*, 2014, **43**, 5679.

208 M. Gu, Y. Ren, Y. Hu, M. Tang, Z. Kong, B. Yue and H. He, *Eur. J. Inorg. Chem.*, 2015, **2**, 488.

209 Y. Wang, M. Zhang, S. Li, S.-R. Zhang, W. Xie, J.-S. Qin, Z. Su and Y. Lan, *Chem. Commun.*, 2017, **53**, 5204.

210 X. Wang, S. Liu, Y. Liu, D. He, N. Li, J. Miao, Y. Ji and G. Yang, *Inorg. Chem.*, 2014, **53**, 13130.

211 S. R. Batten, N. R. Champness, X. Chen, J. Garcia-martinez, S. Kitagawa, L. Öhrström, M. O. Keeffe, M. P. Suh and J. Reedijk, *Pure Appl. Chem.*, 2013, **85**, 1715.

212 S. R. Batten, N. R. Champness, X. Chen, J. Garcia-martinez, S. Kitagawa, L. Ohrstrom, M. O'Keeffee, M. P. Suh and J. Reedijk, *CrystEngComm*, 2012, **14**, 3001.

213 D. Peralta, G. Chapalais, A. Simon-Masseron, K. Barthelet, C. Chizallet, A.-A. Quoineaud and G. D. Pirngruber, *J. Am. Chem. Soc.*, 2012, **134**, 8115.

214 K. Biradha, A. Ramanan and J. J. Vittal, *Cryst. Growth Des.*, 2009, **9**, 2969.

215 C. Janiak and J. K. Vieth, *J. New Chem.*, 2010, **34**, 2366.

216 Y. Jiao, M. Li, C. Qin and Z. Su, *CrystEngComm*, 2017, **19**, 1721.

217 O. M. Yaghi, M. O'Keeffe, N. W. Ockwig, H. K. Chae, M. Eddaoudi and J. Kim, *Nature*, 2003, **423**, 705.

218 A. Schoedel, M. Li, D. Li, M. O. Kee and O. M. Yaghi, *Chem. Rev.*, 2016, **116**, 12466.

219 B. F. Hoskins and R. Robson, *J. Am. Chem. Soc.*, 1990, **112**, 1546.

220 N. Zhu, G. Tobin and W. Schmitt, *Chem. Commun.*, 2012, **48**, 3638.

221 *Misc. Berolinensia ad Incrementum Sci.*, 1710, 377.

222 A. F. Cronstedt, *Kongl Vetenskaps Acad. Handl.*, 1756, 120.

223 H. J. Buser, D. Schwarzenbach, W. Petter and A. Ludi, *Inorg. Chem.*, 1977, **16**, 2704.

224 O. M. Yaghi and H. Li, *J. Am. Chem. Soc.*, 1995, **117**, 10401.

225 J. R. Long and O. M. Yaghi, *Chem. Soc. Rev.*, 2009, **38**, 1213.

226 J. Li, D. J. Timmons and H. Zhou, *J. Am. Chem. Soc.*, 2009, **131**, 6368.

227 N. Giri, M. G. Del Pópolo, G. Melaugh, R. L. Greenaway, K. Rätzke, T. Koschine, L. Pison, M. F. C. Gomes, A. I. Cooper and S. L. James, *Nature*, 2015, **527**, 216.

228 R. Gaillac, P. Pullumbi, K. A. Beyer, K. W. Chapman, D. A. Keen, T. D. Bennett and F. Coudert, *Nat. Mater.*, 2017, 16, 1149.

229 T. D. Bennett, J. Tan, Y. Yue, E. Baxter, C. Ducati, N. J. Terrill, H. H. Yeung, Z. Zhou, W. Chen, S. Henke, A. K. Cheetham and G. N. Greaves, *Nat. Commun.*, 2015, **6**, 8079.

230 N. Stock and S. Biswas, *Chem. Rev.*, 2012, **112**, 933.

231 M. Fujita, Y. J. Kwon, O. Sasaki, K. Yamaguchi and K. Ogura, *J. Am. Chem. Soc.*, 1995, **117**, 7287.

232 H. Li, M. Eddaoudi, M. O'Keeffe and O. M. Yaghi, *Nature*, 1999, **402**, 276.

233 H. Xu, K. Wang, M. Ding, D. Feng, H. Jiang and H. Zhou, *J. Am. Chem. Soc.*, 2016, **138**, 5316.

234 J. P. Patterson, P. Abellan, M. S. Denny, C. Park, N. D. Browning, S. M. Cohen, J. E. Evans and N. C. Gianneschi, *J. Am. Chem. Soc.*, 2015, **137**, 7322.

235 J. Huo, M. Brightwell, S. El Hankari, A. Garai and D. Bradshaw, *J. Mater. Chem. A*, 2013, **1**, 15220.

236 Z. Fang, B. Bueken, D. E. De Vos and R. A. Fischer, *Angew. Chem. Int. Ed.*, 2015, **54**, 7234.

237 D. S. Sholl and R. P. Lively, *J. Phys. Chem. Lett.*, 2015, **6**, 3437.

238 B. Tu, Q. Pang, D. Wu, Y. Song, L. Weng and Q. Li, *J. Am. Chem. Soc.*, 2014, **136**, 14465.

239 T. D. Bennett, A. K. Cheetham, A. H. Fuchs and F. Coudert, *Nat. Chem.*, 2017, **9**, 11.

240 Y. Sun and H. Zhou, *Sci. Technol. Adv. Mater.*, 2015, **16**, 11.

241 D. Crawford, J. Casaban, R. Haydon, N. Giri, T. McNally and S. L. James, *Chem. Sci.*, 2015, **6**, 1645.

242 Y. Pan, Y. Liu, G. Zeng, L. Zhao and Z. Lai, *Chem. Commun.*, 2011, **47**, 2071.

243 I. Eryazici, C. D. Malliakas, B. G. Hauser, O. K. Farha, M. G. Kanatzidis, S. T. Nguyen, R. Q. Snurr and J. T. Hupp, *Nat. Chem.*, 2010, **2**, 944.

244 G. Ferey, C. Serre, C. Mellot-Draznieks, S. Surble, J. Dutour and I. Margiolaki, *Angew. Chem. Int. Ed.*, 2004, **43**, 6296.

245 M. Eddaoudi, D. B. Moler, H. Li, B. Chen, T. M. Reineke, M. O. Keeffe and O. M. Yaghi, *Acc. Chem. Res.*, 2001, **34**, 319.

246 H. Furukawa, J. Kim, N. W. Ockwig, M. O. Keeffe and O. M. Yaghi, *J. Am. Chem. Soc.*, 2008, **130**, 11650.

247 J. V Smith, *Chem. Rev.*, 1988, **88**, 149.

248 S. R. Batten and R. Robson, *Angew. Chem. Int. Ed.*, 1998, **37**, 1460.

249 M. O'Keeffe, M. Eddaoudi, H. Li, T. Reineke and O. M. Yaghi, *J. Solid State Chem.*, 2000, **152**, 3.

250 N. Zhu, D. Sensharma, P. Wix, M. J. Lennox and T. Düren, *Eur. J. Inorg. Chem.*, 2016, 1939.

251 N. Zhu, M. J. Lennox, T. Düren and W. Schmitt, *Chem. Commun.*, 2014, **50**, 4207.

252 G. Ferey, *J. Solid State Chem.*, 2000, **152**, 37.

253 M. Eddaoudi, J. Kim, N. Rosi, D. Vodak, J. Wachter, M. O. Keeffe and O. M. Yaghi, *Science.*, 2002, **295**, 469.

254 B. Moulton and M. J. Zaworotko, *Chem. Rev.*, 2001, **101**, 1629.

255 M. Sánchez-Sánchez, N. Getachew, M. Díaz-García, Y. Chebude and I. Díaz, *Green Chem.*, 2015, **17**, 1500.

256 P. Pachfule, R. Das, P. Poddar and R. Banerjee, *Cryst. Growth Des.*, 2011, **11**, 1215.

257 C. Wang, D. Liu, Z. Xie and W. Lin, *Inorg. Chem.*, 2014, **53**, 1331.

258 R. L. Martin, L. Lin, K. Jariwala, B. Smit and M. Haranczyk, *J. Phys. Chem. C*, 2013, **117**, 12159.

259 J. H. Cavka, S. Jakobsen, U. Olsbye, N. Guillou, C. Lamberti, S. Bordiga and K. P. Lillerud, *J. Am. Chem. Soc.*,

2008, **130**, 13850.

260 S. S. Chui, S. M. Lo, J. P. H. Charmant, A. G. Orpen and I. D. Williams, *Science*, 1999, **283**, 1148.

261 D. Franz, K. A. Forrest, T. Pham and B. Space, *Cryst. Growth Des.*, 2016, **16**, 6024.

262 G. Ferey, C. Mellot-Draznieks, C. Serre, F. Millange, J. Dutour, S. Surble and I. Margiolak, *Science*, 2005, **309**, 2040.

263 K. S. Park, Z. Ni, A. P. Cote, J. Y. Choi, R. Huang, F. J. Uribe-Romo, H. K. Chae, M. O'Keeffe and O. M. Yaghi, *Proc. Natl. Acad. Sci. U. S. A.*, 2006, **103**, 10186.

264 J. C. Tan and A. K. Cheetham, *Chem. Soc. Rev.*, 2011, **40**, 1059.

265 M. Alvaro, E. Carbonell, B. Ferrer, F. X. Llabrøs and H. Garcia, *Chem. Eur. J.*, 2007, **13**, 5106.

266 S. Balestra, Bueno-Perez, S. Hamad, D. Dubbeldam, A. R. Ruiz-Salvador and S. Calero, *Chem. Mater.*, 2016, **28**, 8296.

267 A. Kondo and K. Maeda, *J. Solid State Chem.*, 2015, **221**, 126.

268 K. J. Gagnon, C. M. Beavers and A. Clearfield, *J. Am. Chem. Soc.*, 2013, **135**, 1252.

269 O. M. Yaghi, G. Li and H. Li, *Nature*, 1995, **378**, 703.

270 Z. Ghasemi, I. Sourinejad, H. Kazemian and S. Rohani, *Rev. Aquac.*, 2016, 1.

271 J. Ren, H. W. Langmi, B. C. North and M. Mathe, *Int. J. Energy Res.*, 2015, **39**, 607.

272 N. L. Rosi, J. Eckert, M. Eddaoudi, D. Vodak, J. Kim, M. O. Keeffe and O. M. Yaghi, *Science*, 2003, **300**, 1127.

273 J. Vitillo, B. Smit and L. Gagliardi, *Chem. Rev.*, 2017, **117**, 9521.

274 M. Mohamedali, D. Nath and H. Ibrahim, *Greenh. Gases*, 2016, 116.

275 T. M. McDonald, W. R. Lee, J. A. Mason, B. M. Wiers, C. S. Hong and J. R. Long, *J. Am. Chem. Soc.*, 2012, **134**, 7056.

276 P. Nugent, Y. Belmabkhout, S. D. Burd, A. J. Cairns, R. Luebke, K. Forrest, T. Pham, S. Ma, B. Space, L. Wojtas, M. Eddaoudi and M. J. Zaworotko, *Nature*, 2013, **495**, 80.

277 A. Ziaee, D. Chovan, M. Lusi, J. J. Perry, M. Zaworotko and S. A. M. Tofail, *Cryst. Growth Des.*, 2016, **16**, 3890.

278 X. Cui, K. Chen, H. Xing, Q. Yang, R. Krishna, Z. Bao, H. Wu, W. Zhou, X. Dong, Y. Han, B. Li, Q. Ren, M. J. Zaworotko and B. Chen, *Science*, 2016.

279 C. Wang, X. Liu, J. P. Chen and K. Li, *Sci. Rep.*, 2015, **5**, 16613.

280 J. Zhang, Z. Xiong, C. Li and C. Wu, *J. Mol. Liq.*, 2016, **221**, 43.

281 A. V Desai, B. Manna, A. Karmakar, A. Sahu and S. K. Ghosh, *Angew. Chem. Int. Ed.*, 2016, **55**, 7811.

282 I. Stassen, B. Bueken, H. Reinsch, J. F. M. Oudenhoven, D. Wouters, J. Hajek, V. Van Speybroeck, N. Stock, P. M. Vereecken, R. Van Schaijk, D. De Vos and R. Ameloot, *Chem. Sci.*, 2016, **7**, 5827.

283 Z. Hu, B. J. Deibert and J. Li, *Chem. Soc. Rev.*, 2014, **43**, 5815.

284 S. S. Nagarkar, B. Joarder, A. K. Chaudhari, S. Mukherjee and S. K. Ghosh, *Angew. Chem. Int. Ed.*, 2013, **52**, 2881.

285 S. Zhang, J. Yang, H. Wu, Y. Liu and J. Ma, *Chem. Eur. J.*, 2015, **21**, 15806.

286 A. H. Chughtai, N. Ahmad, H. A. Younus, A. Laypkovc and F. Verpoort, *Chem. Soc. Rev.*, 2015, **44**, 6804.

287 A. Dhakshinamoorthy, A. M. Asiri and H. Garcia, *Chem. Eur. J.*, 2016, **22**, 8012.

288 C. N. Kato, M. Hasegawa, T. Sato, A. Yoshizawa, T. Inoue and W. Mori, *J. Catal.*, 2005, **230**, 226.

289 S. Hasegawa, S. Horike, R. Matsuda, S. Furukawa, K. Mochizuki, Y. Kinoshita and S. Kitagawa, *J. Am. Chem. Soc.*, 2007, **129**, 2607.

290 F. Schröder, D. Esken, M. Cokoja, M. W. E. Van Den Berg, O. I. Lebedev, G. Van Tendeloo, B. Walaszek, G. Buntkowsky, H. Limbach, B. Chaudret and R. A. Fischer, *J. Am. Chem. Soc.*, 2008, **130**, 6119.

291 Y. K. Hwang, D. Hong, J. Chang, S. H. Jhung, Y. Seo, J. Kim, A. Vimont, M. Daturi, C. Serre and G. Førey, *Angew. Chem. Int. Ed.*, 2008, **47**, 4144.

292 Y. Huang, J. Liang, X. Wang and R. Cao, *Chem. Soc. Rev.*, 2016, **46**, 126.

293 D.-Y. Du, J.-S. Qin, S.-L. Li, Z.-M. Su and Y.-Q. Lan, *Chem. Soc. Rev.*, 2014, **43**, 4615.

294 B. J. S. Johnson, S. A. Geers, W. W. Brennessel, V. G. Young and A. Stein, *Dalton Trans.*, 2003, 4678.

295 J. Sha, J. Sun, C. Wang, G. Li, P. Yan and M. Li, *Cryst. Growth Des.*, 2012, **12**, 2242.

296 S. Abednatanzi, K. Leus, P. G. Derakhshandeh, F. Nahra, K. De Keukeleere, K. Van Hecke, I. Van Driessche, A. Abbasi, S. P. Nolan and P. Van Der Voort, *Catal. Sci. Technol.*, 2017, **7**, 1478.

297 J. Song, Z. Luo, D. K. Britt, H. Furukawa, O. M. Yaghi, K. I. Hardcastle and C. L. Hill, *J. Am. Chem. Soc.*, 2011, **133**, 16839.

298 Z. Zhang, T. Zhang, C. Wang, Z. Lin, L. Long and W. Lin, *J. Am. Chem. Soc.*, 2015, **137**, 3197.

299 X. Kong, Z. Lin, Z. Zhang, T. Zhang and W. Lin, *Angew. Chem. Int. Ed.*, 2016, **55**, 6411.

300 M. Zeng, Q. Wang, Y. Tan, S. Hu, H. Zhao and L. Long, *J. Am. Chem. Soc.*, 2010, **132**, 2561.

301 P. Horcajada, C. Serre, G. Maurin, N. A. Ramsahye, F. Balas, M. Sebban, F. Taulelle and G. Ferey, *J. Am. Chem. Soc.*, 2008, **130**, 6774.

302 H. Kim, S. Yang, S. R. Rao, S. Narayanan, E. A. Kapustin, H. Furukawa, A. S. Umans, O. M. Yaghi and E. N. Wang, *Science*, 2017, **356**, 430.

303 A. Schneemann, V. Bon, I. Schwedler, I. Senkovska, S. Kaskel and R. A. Fischer, *Chem. Soc. Rev.*, 2014, **43**, 6062.

304 A. J. Graham, D. R. Allan, A. Muszkiewicz, C. A. Morrison and S. A. Moggach, *Angew. Chem. Int. Ed.*, 2011, **50**, 11138.

305 Q. Ma, Q. Yang, A. Ghoufi, G. Férey, C. Zhong and G. Maurin, *Dalton Trans.*, 2012, **41**, 3915.

306 J. An, S. J. Geib and N. L. Rosi, *J. Am. Chem. Soc.*, 2009, **131**, 8376.

307 C. L. Jones, A. J. Tansell and T. L. Easun, *J. Mater. Chem. A*, 2016, **4**, 6714.

308 R. Lyndon, K. Konstas, B. P. Ladewig, P. D. Southon, C. J. Kepert and M. R. Hill, *Angew. Chem. Int. Ed.*, 2013, **52**, 3695.

309 N. Yanai, T. Uemura, M. Inoue, R. Matsuda, T. Fukushima, M. Tsujimoto, S. Isoda and S. Kitagawa, *J. Am. Chem. Soc.*, 2012, **134**, 4501.

310 J. Park, D. Yuan, K. T. Pham, J. Li, A. Yakovenko and H. Zhou, *J. Am. Chem. Soc.*, 2012, **134**, 99.

311 L. Heinke, M. Cakici, M. Dommaschk, S. Grosjean, R. Herges, S. Brase and C. Woll, *ACS Nano*, 2014, **8**, 1463.

312 H. N. Miras, F. Wilson and L. Cronin, *Chem. Commun.*, 2009, 1297.

313 X. Yang, T. Waters, X. B. Wang, R. A. J. O'Hair, A. G. Wedd, J. Li, D. A. Dixon and L. S. Wang, *J. Phys. Chem. A*, 2004, **108**, 10089.

314 M. J. Deery, O. W. Howarth and K. R. Jennings, *J. Chem. Soc. Dalton Trans.*, 1997, 4783.

315 D. Long, C. Streb, Y. Song, S. Mitchell and L. Cronin, *J. Am. Chem. Soc.*, 2008, **130**, 1830.

316 R. S. Winter, J. M. Cameron and L. Cronin, *J. Am. Chem. Soc.*, 2014, **136**, 12753.

317 Q. Jia, J. Cao, Y. Duan and C. Hu, *Dalton Trans.*, 2015, **44**, 553.

318 E. F. Wilson, H. Abbas, B. J. Duncombe, C. Streb, D. Long and L. Cronin, *J. Am. Chem. Soc.*, 2008, **130**, 13876.

319 E. F. Wilson, H. N. Miras, M. H. Rosnes and L. Cronin, *Angew. Chem. Int. Ed.*, 2011, **50**, 3720.

320 Y. Song, D. Long, S. E. Kelly and L. Cronin, *Inorg. Chem.*, 2008, **47**, 9137.

321 M. N. Eberlin, *Eur. J. Mass Spectrom.*, 2007, **13**, 19.

322 M. Mann, R. C. Hendrickson and A. Pandey, *Annu. Rev. Biochem.* 2001, **70**, 473.

323 C. Brunnee, *Int. J. Mass Spectrommetry Ion Process.*, 1987, **76**, 125.

324 J. F. de la Mora, *Annu. Rev. Fluid Mech.*, 2007, **39**, 217.

325 P. Kebarle and U. H. Verkerk, *Mass Spectrom. Rev.*, 2009, **28**, 898.

326 S. Nguyen and J. B. Fenn, *Proc. Natl. Acad. Sci. U. S. A.*, 2007, **104**, 1111.

327 J. F. De Mora, *Anal. Chim. Acta*, 2000, **406**, 93.

328 C. J. Hogan, J. A. Carroll, H. W. Rohrs, P. Biswas and M. L. Gross, *Anal. Chem.*, 2009, **81**, 369.

329 S. F. Ralph, M. M. Sheil, L. A. Hick, R. J. Geue and A. M. Sargeson, *J. Chem. Soc. Dalton Trans.*, 1996, 4417.

330 V. A. Pashynska, M. V. Kosevich, H. Van Den Heuvel and M. Claeys, *Rapid Commun. Mass Spectrom.*, 2006, **20**,

755.

331 W. Henderson and S. McIndoe, *Mass Spectrometry of Inorganic and Organometallic Compounds*, 2005.

332 R. B. Cole, *Electrospray Ionization Mass Spectrometry: Fundamentals, Instrumentation and Appication.*, 1997.

333 R. Zenobi and R. Knochenmuss, *Mass Spectrom. Rev.*, 1998, **17**, 337.

334 D. J. Harvey, *Mass Spectrom. Rev.*, 1999, **18**, 349.

335 D. R. Lide, *CRC Handb. Chem. Phys.*, 2006, **7**, 87.

336 J. E. Boulicault, A. Sandra and R. B. Cole, *J. Am. Soc. Mass Spectrom.*, 2016.

337 R. Colton and J. C. Traeger, *Inorganica Chem. Acta*, 1992, **201**, 153.

338 A. J. Surman, P. J. Robbins, J. Ujma, Q. Zheng, P. E. Barran and L. Cronin, *J. Am. Chem. Soc.*, 2016, **138**, 3824.

339 K. Scheubert, F. Hufsky and S. Bocker, *J. Cheminform.*, 2013, **5**, 12.

Chapter 2

Assembly, Disassembly and Reassembly

2.1) "Top-down" Synthetic Methods

Synthetic procedures for many advanced materials (such as hybrid POMs or MOFs discussed in the previous chapter) generally rely on what we term "bottom-up" methodology. These methods essentially combine metals and ligands in solution and rely on the self-assembly behaviour of the reaction system to produce a more complicated material. As an approximate rule of thumb, the number of atoms in the molecule of interest (*i.e.* the complexity of the system) is always increasing through each synthetic step; metals are assembled into complexes, complexes are assembled into polymers, polymers are cross-linked into frameworks, etc., etc. In the case of POMs, a common synthetic procedure is to assemble the monomeric metal oxide $[MO_4]^{n-}$ into a lacunary POM structure, further combine the lacunary structure with heterometals to produce TMS-POMs, and then further combine the TMS-POMs into network structures. Many examples can be found in the literature that follow this general "bottom-up" approach.[1–15]

"Top-down" synthetic methodologies are much rarer. For the purposes of this work, we are defining "top-down" methodologies as any synthetic procedure where, at some point during the reaction, a molecular precursor disassembles into smaller oligomeric species. The "top-down" label is applied here to any system where disassembly occurs, even if combinations of assembly and disassembly are taking place.

In a 2008 report, Cronin *et al.* demonstrated that combinations of "bottom-up" assembly steps with "top-down" disassembly steps can be used to generate POM structures that are inaccessible *via* bottom-up assembly alone.[16] In this procedure, a $[P_4W_{52}O_{178}]^{24-}$ cluster is assembled "bottom up" from $[WO_4]^{2-}$ monomers. This $\{W_{52}\}$ structure (the largest phosphotungstate structure reported at the time) can be described as four $\{PW_{11}\}$ lacunary Keggin structures capping a $\{W_8\}$ ladder-shaped core.[16] By dissolving the $\{W_{52}\}$ cluster and adjusting the pH, the $\{W_{52}\}$ cluster can then be sequentially decomposed into a $[P_3W_{39}O_{134}]^{19-}$ cluster and a $[P_4W_{44}O_{152}]^{24-}$ cluster (Figure 2.1.1).[16] Thus, a combination of assembly and disassembly techniques were used to access a new set of otherwise inaccessible POM clusters.

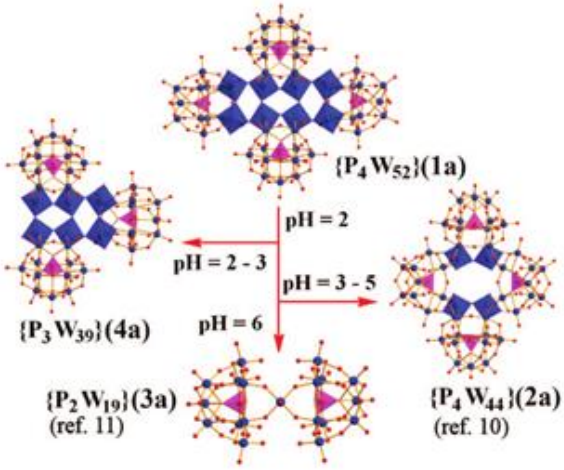

Figure 2.1.1 – Combinations of bottom-up and top-down approaches were exploited to synthesise otherwise inaccessible $[P_3W_{39}O_{134}]^{19-}$ cluster species. Colour Scheme: W blue, P pink, O red. Figure reproduced from reference 16.

Very recently, this partial disassembly approach was also used to generate an otherwise-inaccessible titanium (IV) substituted trimeric Dawson-type TMS-POM, $[Ca_7(CO_3)(OH_{22})(P_2W_{15}Ti_3O_{61})_3]^{19-}$, from a related tetrameric species, $[Ti_4(H_2O)_{12}Cl(P_2W_{15}Ti_3O_{61}H_3)_4]^{21}$ (Figure 2.1.2).[17] Another example exploited the partial disassembly of lacunary Dawson structures into lacunary Keggin structures to generate cobalt (II) or manganese (II) TMS-POM species, $[M_6(PW_6O_{26})(P_2W_{15}O_{56})_2(H_2O)_2]^{23-}$ (Figure 2.1.2).[18]

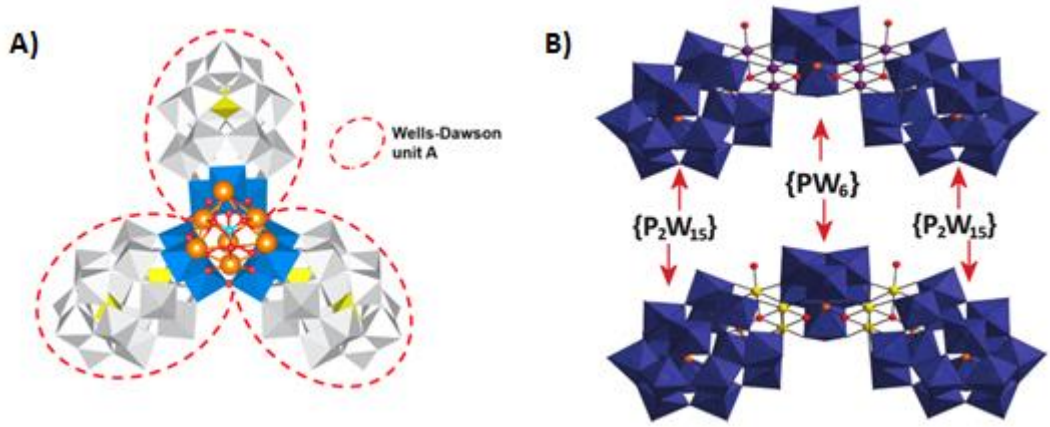

Figure 2.1.2 – A) A $[Ca_7(CO_3)(OH_{22})(P_2W_{15}Ti_3O_{61})_3]^{19-}$ trimer generated from the top-down disassembly of a tetrameric species. Colour Scheme: W grey, Ti blue, Ca orange, P yellow. Figure reproduced from reference 17. B) Two $[M_6(PW_6O_{26})(P_2W_{15}O_{56})_2(H_2O)_2]^{23-}$ species generated from the partial top-down disassembly of the Dawson tungstate. Colour Scheme: W blue, M purple or yellow, O red. Figure reproduced from reference 18.

Mechanistic studies of top-down methods have been examined in the literature before, if sporadically. In a (separate) 2008 report, Cronin *et al.* investigated the reaction of the Lindqvist hexamolybdate species, $[Mo_6O_{19}]^{2-}$, with silver fluoride.[19] This reaction had been previously reported to result in the rearrangement of the Lindqvist structure to produce one of a number of networks or frameworks based on β-octamolybdate units $[Mo_8O_{26}]^{4-}$ with silver ion linkages; $[TBA]_{2n}[Ag_2Mo_8O_{26}]_n$, $[TBA]_{2n}[Ag_2Mo_8O_{26}(CH_3CN)_2]_n$, $[HDMF]_n[Ag_3Mo_8O_{26}(DMF)_4]_n$ or $[TBA]_{2n}[Ag_2Mo_8O_{26}(DMSO)_2]_n$ can all be formed depending on reaction conditions (Figure 2.1.3).[20–22] In these structures, extended networks are produced *via* coordination of the terminal *–oxo* ligands to the silver ions to produce POM-Ag-POM linkages.

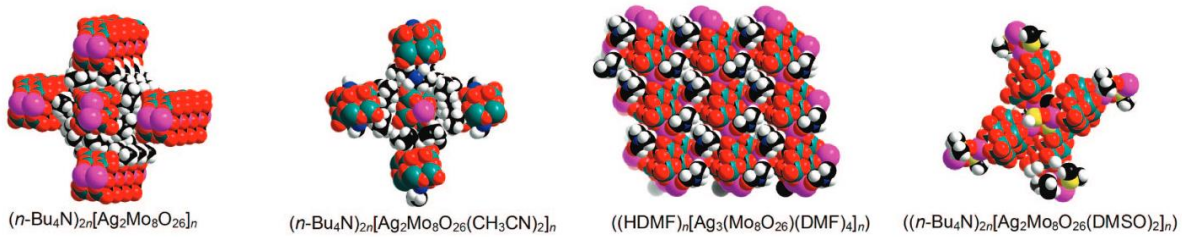

Figure 2.1.3 – $[TBA]_{2n}[Ag_2Mo_8O_{26}]_n$, $[TBA]_{2n}[Ag_2Mo_8O_{26}(CH_3CN)_2]_n$, $[HDMF]_n[Ag_3Mo_8O_{26}(DMF)_4]_n$ or $[TBA]_{2n}[Ag_2Mo_8O_{26}(DMSO)_2]_n$ structures which can be generated from the reaction of Lindqvist hexamolybdate with silver fluoride under various reaction conditions. Colour Scheme: Mo teal, Ag purple, O red, C black, H white. Figure modified from reference 19.

In this report the mechanism was identified as a top-down mechanism using cryospray ionisation mass spectrometry (CSI-MS).[19] By applying this technique to the reaction mixture, which contained $[Mo_6O_{19}]^{2-}$ and Ag^+ ions in a methanol-acetonitrile mixture, several oligomeric species were identified in solution (Figure 2.1.4). These species could only have formed *via* a top-down disassembly of the Lindqvist hexamolybdate.[19] The monoanionic species observed were divided into six classes; $[Mo_mO_{3m}]^-$ species (m=2,3,5), $[HMo_mO_{3m+1}]^-$ species (m=2-6), $[H_7Mo_mO_{3m+2}]^-$ species (m=2-6), $[H_7Mo_mO_{3m+3}]^-$ species (m=2-5), $[H_9Mo_mO_{3m+4}]^-$ species (m=2-6), $[AgMo_mO_{3m+1}]^-$ species (m=2-4);

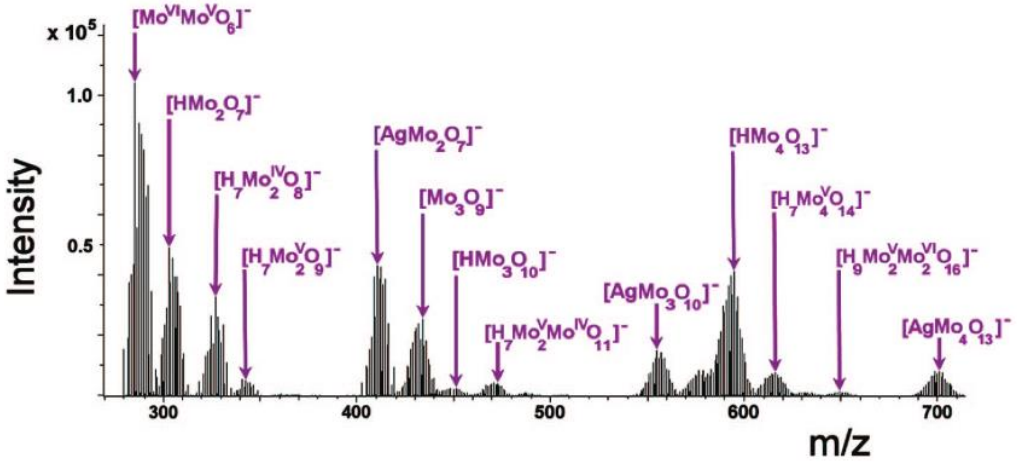

Figure 2.1.4 – A portion of the CSI-MS spectrum for the reaction mixture of Lindqvist hexamolybdate and silver fluoride in acetonitrile-methanol mixtures. Several disassembly products of the Lindqvist hexamolybdate are labelled. Figure reproduced from reference 19.

Subsequent crystallisation from this reaction mixture generated $[TBA]_{2n}[Ag_2Mo_8O_{26}]_n$. The $[Ag_2Mo_8O_{26}]^{2-}$ units were proposed to derive from assembly of the oligomeric intermediates identified in solution. The $[AgMo_2O_7]^-$ and $[AgMo_4O_{13}]^-$ species in particular were identified as key synthetic intermediates (Figure 2.1.5). Although the terminology used in the report does not explicitly acknowledge that separate disassembly and reassembly steps took place during the reaction (the process is labelled as a "rearrangement", and the intermediates as "synthons"), the report is a clear demonstration of top-down synthesis.[19] Moreover, mass spectrometry was shown to be a powerful technique in analysing top-down reaction mechanisms.

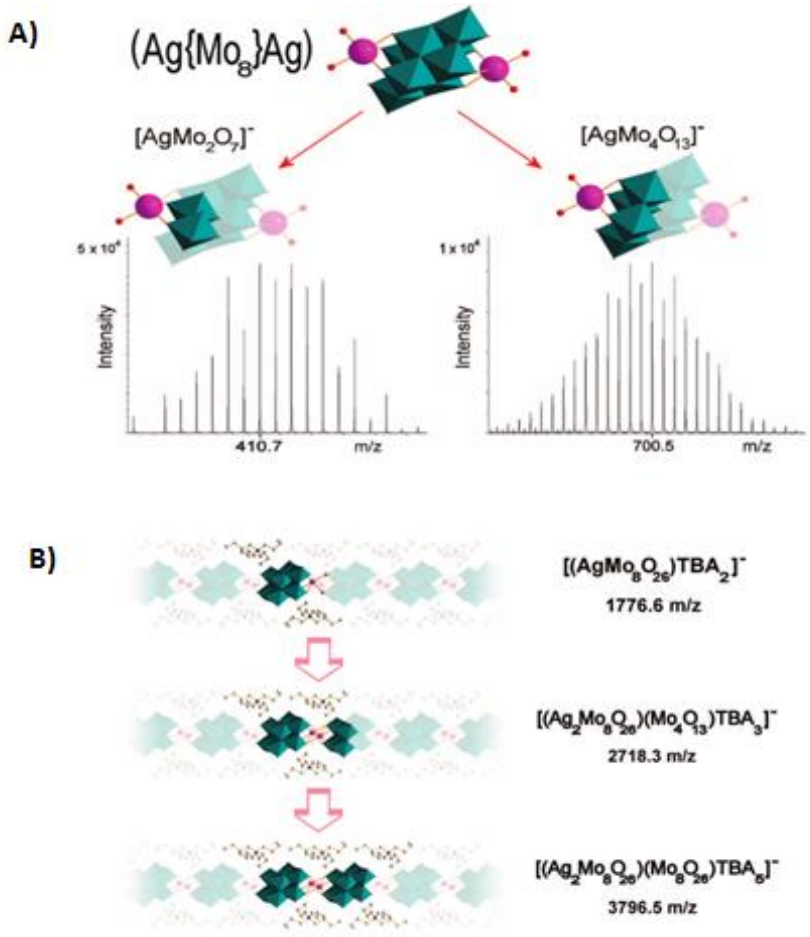

Figure 2.1.5 – A) The $[AgMo_2O_7]^-$ and $[AgMo_4O_{13}]^-$ "synthons" for the $[TBA]_{2n}[Ag_2Mo_8O_{26}]_n$ polymer, and their corresponding mass spectra. B) Schematic representing the growth of the $[TBA]_{2n}[Ag_2Mo_8O_{26}]_n$ polymer from reassembly of the oligomeric species observed in solution. Colour Scheme: Mo teal, Ag purple, O red. Figure modified from reference 19.

In a subsequent 2011 paper, Cronin *et al.* applied a similar strategy to analyse the formation of a hybrid POM species; namely the conversion of the α-octamolybdate $[Mo_8O_{26}]^{4-}$ species into the *tris*(alkoxide) supported Anderson POM structure, $[MnMo_6O_{18}((OCH_2)_3CNH_2)_2]^{3-}$.[23] This structure is related to the classical Anderson structure, where the central $\{XO_6\}$ template is provided by a manganese (III) centre supported by two *tris(*alkoxide) ligands.[24–27] This reaction was already well known,[28–35] and indeed this reaction now seems to be the standard approach to generate substituted Anderson-type POMs,[36–39] but in this report the reaction was first identified to proceed *via* a top-down process.[23]

Electrospray Ionisation Mass Spectrometry (ESI-MS) was used to analyse the reaction mixture. Two regimes were investigated – one after a short time (approx. 15 minutes) at room temperature, and one after a longer time (approx. 30 hours) at reflux. Disassembly of the octamolybdate POM and interaction with the heterometal were observed quickly, but hybrid species were observed to take longer to generate (Figure 2.1.6).[23]

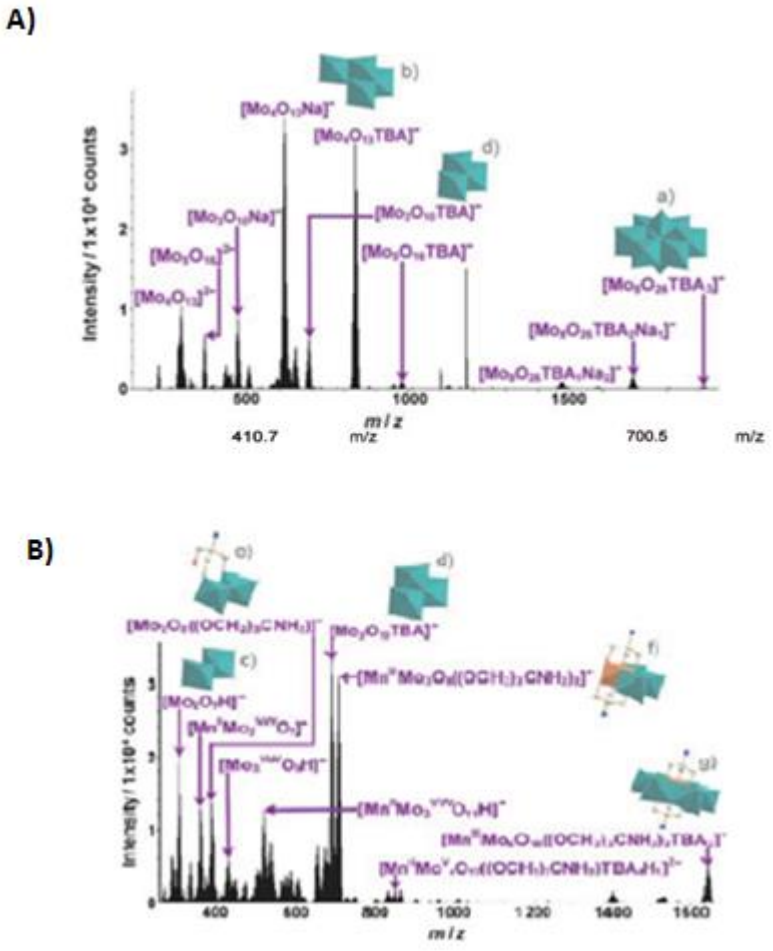

Figure 2.1.6 – A) A portion of the ESI-MS spectrum for the reaction mixture for formation of a substituted Anderson POM from the α-octamolybdate $[Mo_8O_{26}]^{4-}$ species after approx. 15 minutes reaction time. B) A portion of the ESI-MS spectrum for the same reaction after approx. 30 hours at reflux. Figure reproduced from reference 23.

By monitoring the change in ESI-MS signals over time, the authors were able to extract kinetic data about the reaction and proposed a multi-step process that proceeded *via* two convergent reaction pathways, with the disassembly of the octamolybdate to a $[Mo_4O_{13}]^{2-}$ species identified as a crucial (although not rate-determining) step (Figure 2.1.7).[23]

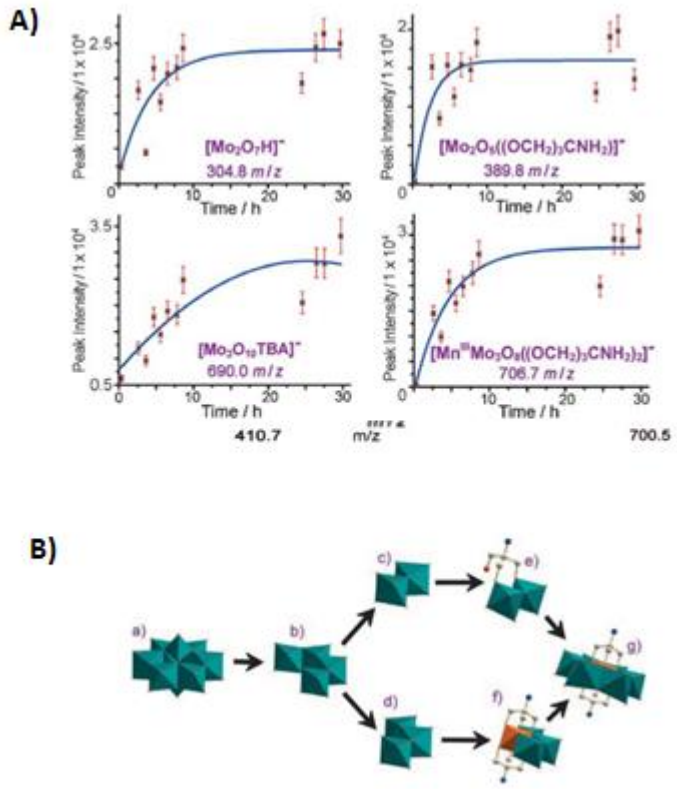

Figure 2.1.7 – A) Graphs tracking the intensity of certain signals observed in the ESI-MS analyses as a function of time. B) The proposed disassembly-reassembly mechanism for formation of a substituted Anderson POM from the α-octamolybdate. Figure reproduced from reference 23.

The reports discussed above clearly demonstrate that top-down methods can access otherwise inaccessible products, particularly when assembly and disassembly are combined in the same synthetic process.[16–18] However, despite the promising nature of this methodology, top-down synthetic procedures are vastly outnumbered by their classical bottom-up counterparts. To this day POM synthesis (in particular TMS-POM synthesis) is dominated by purely bottom-up approaches, mostly involving the lacunary method.[1–15] Top-down methods may therefore be fertile ground for the generation of new POM compounds (potentially including hybrid and TMS-POM compounds).

The 2008 and 2011 Cronin *et al.* papers discussed above lay a clear theoretical foundation for top-down mechanisms and present fairly comprehensive protocols for analysing such mechanisms.[19,23] However, the techniques were only used to retroactively analyse the mechanisms of previously reported reactions. In principle, these techniques could be used as an active tool to aid in the generation of new compounds. The techniques and protocols developed for the analysis of top-down reactions could be applied to identify conditions under which certain systems undergo disassembly.

If systems could be identified to undergo disassembly, then synthetic efforts could be concentrated on such systems to improve synthetic outcomes. Concentrating synthetic efforts on systems where disassembly is known to take place has a number of potential benefits:

- Disassembled POM oligomers are fundamentally different from both their (known) parent POM structures and from their daughter monomeric metal oxides;
- Disassembled POM oligomers are likely to be open-shell species (*i.e.* not coordinatively saturated by terminal *oxo*- ligands) and are therefore may be relatively reactive compared to the *oxo*-saturated POM clusters;
- The reaction space is fundamentally underexplored;

These considerations indicate that top-down methods may be a fertile reaction space for the isolation of new and unexpected compounds, particularly hybrid and TMS-POM species. However, to the best of our knowledge, no systematic exploration of top-down reaction spaces has been attempted.

To this end, we were interested in developing a more systematic approach towards top-down POM synthesis.

We anticipate that a successful top-down strategy towards new POM species would involve a multi-step reaction process, consisting of three distinct synthetic steps; assembly (formation of a POM cluster), disassembly (decomposition into smaller oligomers), and reassembly (reaction of oligomers with suitable reactant species) (Figure 2.1.8).

The assembly step would consist of the generating a (known) POM species *via* a bottom-up approach. Many suitable POM species could be identified and synthesised according to their literature procedures.

The disassembly step would consist of placing these precursor POMs under conditions where they undergo decomposition or disassembly reactions. This disassembly can in principle be an equilibrium process or an irreversible transformation. Ideally, disassembly should take place under the mildest possible conditions and with minimal perturbation applied to the system.

The reassembly step would consist of reacting these disassembly oligomers with suitable reactant species. To generate hybrid POMs or TMS-POMs, the reactant species would be either organic ligands, heterometals, or combinations thereof. Templating effects are likely to be highly significant during a reassembly process (as they are for bottom-up assembly processes, see chapter 1). Therefore ligands and heterometals with strong templating effects (*e.g.* polydentate ligands and transition metals, in contrast to monodentate ligands or group I ions) are expected to have a greater tendency to bias the system towards new cluster geometries.

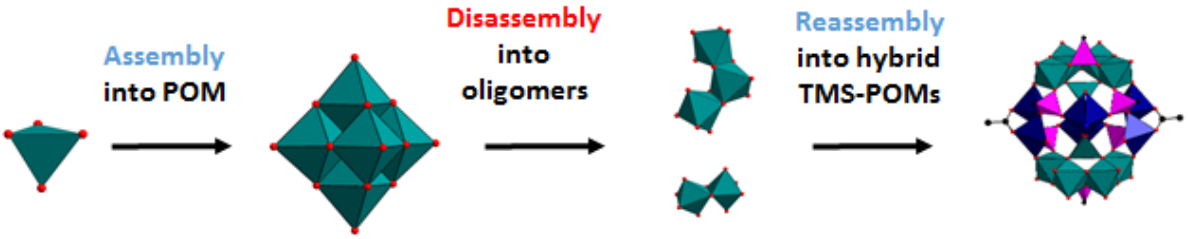

Figure 2.1.8 – Schematic of the proposed synthetic method, involving distinct assembly, disassembly and reassembly steps.

To investigate these hypotheses, we developed the following synthetic strategy:

1) Identify a suitable POM precursor
2) Screen for conditions under which disassembly oligomers can be observed
3) React these disassembly oligomers with a range of ligands and heterometals
4) Isolate and characterise the resulting products

2.2) Lindqvist Hexamolybdate (Assembly)

In order to investigate the assembly-disassembly-reassembly technique, a suitable POM precursor had to be identified. Among the many thousands of available structures, our attention was quickly drawn to the Lindqvist-structured hexamolybdate, $[Mo_6O_{19}]^{2-}$.

This structure is a hexanuclear molybdate, a "superoctahedron" of six edge-sharing $\{MoO_6\}$ octahedra around a central shared μ_6-O atom.[40–45] Twelve μ_2-O *oxo*- ligands bridge between the six metal centres, which are stabilised by an additional six terminal *oxo*- ligands. All of the metal centres are in their highest oxidation state, +VI. The structure is highly symmetric, with O_h symmetry (Figure 2.2.1).[40–45]

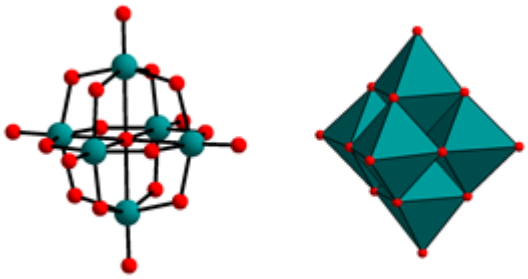

Figure 2.2.1 – Ball-and-stick and polyhedral representations of the Lindqvist hexamolybdate, $[Mo_6O_{19}]^{2-}$ Colour Scheme: Mo Teal, O red.

$[Mo_6O_{19}]^{2-}$ has a reputation as a robust anion, able to withstand quite harsh conditions - in one example, $M[Mo_6O_{19}]$ (where M is Rh(II) or Re(II)) was prepared by prolonged heating over 350° C.[41] Paradoxically, it is also recognised as a readily-modified structure. Rearrangements of the structure are well known, including rearrangements to both α- and β- isomers of the octamolybdate (Figure 2.2.2).[19,46] Indeed several structures can be isolated which contain both hexamolybdate and octamolybdate within the same structure, which can be accessed either *via* the hexamolybdate or octamolybdate.[47–50]

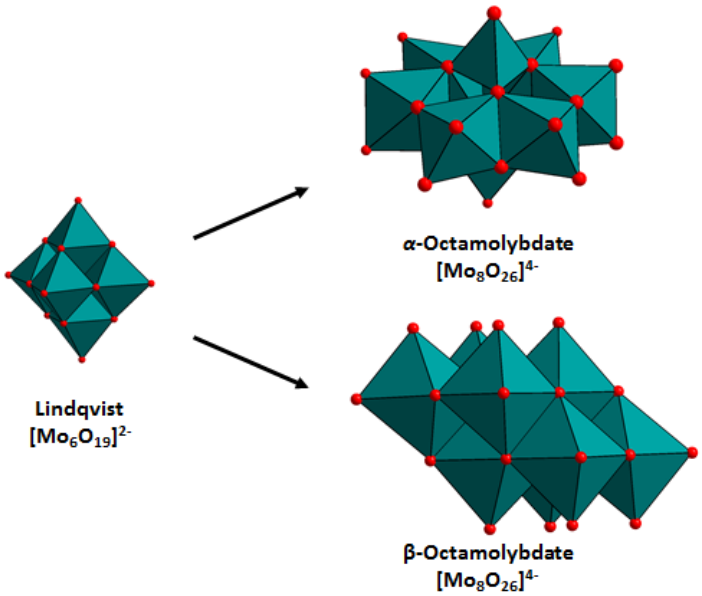

Figure 2.2.2 – Known rearrangements of the Lindqvist hexamolybdate, $[Mo_6O_{19}]^{2-}$, to the α- and β- isomers of the octamolybdate, $[Mo_8O_{26}]^{4-}$.[19,46] Colour Scheme: Mo Teal, O red.

The structure can also be readily modified by replacing one or more *oxo*- ligands. An extensive body of work by several authors has involved the replacement of *oxo*- ligands of this structure with organoimido-type ligands, usually by employing a dehydrating agent such as DCC.[51–62] Either the terminal or bridging *oxo*- ligands can be selectively replaced by altering synthetic conditions, with up to six of the terminal ligands being replaced at once (Figure 2.2.3).[51–62]

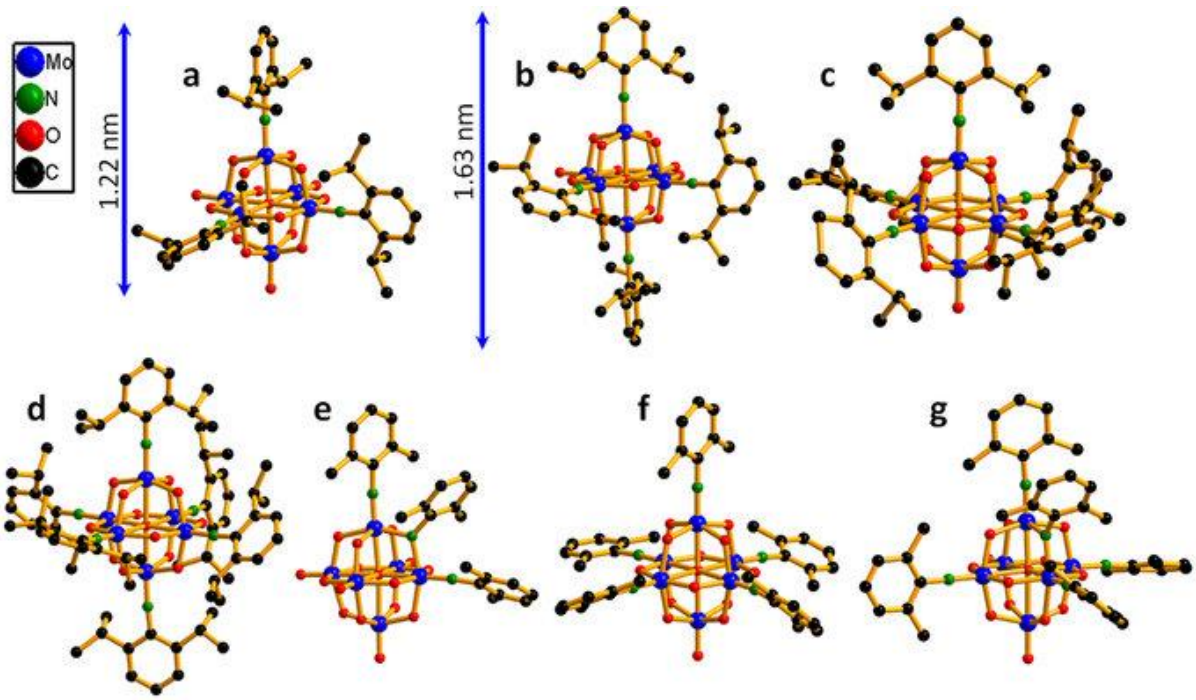

Figure 2.2.3 – Various modifications of the Lindqvist hexamolybdate, $[Mo_6O_{19}]^{2-}$, generated by substituting organoimido-type ligands in place of various terminal or bridging *oxo*- ligands. Figure reproduced from reference 51.

The Lindqvist-structured hexamolybdate POM $[Mo_6O_{19}]^{2-}$ was identified as a possible starting material for a disassembly-reassembly synthetic technique for the following reasons:

1) $[Mo_6O_{19}]^{2-}$ is a simple, reasonably small structure. Any decomposition oligomers will therefore likely be small, reactive species. This also means that decomposition should be relatively easy to study *via* mass spectrometry.[63,64]
2) The structure lacks a strongly coordinating central anion which exhibits a significant templating effect, such as phosphate. Therefore templating effects should be dominated by species subsequently added to the system.
3) The possibility of incorporating imine-type ligands into the structure allows an avenue towards modifying the starting material, introducing new ligands and possibly influencing disassembly behaviour.[51–62]
4) Rearrangements of the structure are well documented, indicating that the compound is reasonably reactive.[19,46–50]
5) The structure has been shown to undergo disassembly under certain circumstances.[19]

2.3) ESI-MS Analysis (Disassembly)

In order to investigate $[Mo_6O_{19}]^{2-}$ as a potential starting material for a disassembly-reassembly process, electrospray ionisation mass spectrometry (ESI-MS) analyses were undertaken to identify conditions under which decomposition oligomers could be observed.[19,23]

Several solvent systems were considered for studies of the disassembly process. Methanol, acetonitrile, water, DMF, DMSO (and mixtures thereof) have all been used in the conversion of $[Mo_6O_{19}]^{2-}$ to β-$[Mo_8O_{26}]^{4-}$, a reaction which (at least in some circumstances) has been demonstrated to occur *via* a top-down disassembly mechanism.[19–22] We chose methanol from this set of solvents as it is particularly amenable to study *via* ESI-MS analysis, although we anticipate that similar behaviour could in principle be observed in other solvents as well.

To this end, solid $[TBA]_2[Mo_6O_{19}]$ (where TBA represents the tetrabutylammonium cation, $(C_4H_9)_4N^+$) was added to HPLC grade methanol (*c.* 0.5 mg/ml) and sonicated for 10 minutes. The resulting suspension was filtered to remove undissolved $[TBA]_2[Mo_6O_{19}]$ and analysed by ESI-MS in negative mode. Although the hexamolybdate visually appears to be insoluble in methanol, the hexamolybdate anion could be seen in the mass spectrum, both as the monoanionic adduct with one TBA cation ($[TBA][Mo_6O_{19}]^-$, calculated mass 1112.62 *m/z*, experimental mass 1121.55 *m/z*) and as the dianionic species with no cation ($[Mo^{VI}_6O_{19}]^{2-}$, calculated mass 439.66 *m/z*, experimental mass 439.66 *m/z*) (Figure 2.3.1). This confirms that methanol is a suitable solvent for hexamolybdate chemistry.

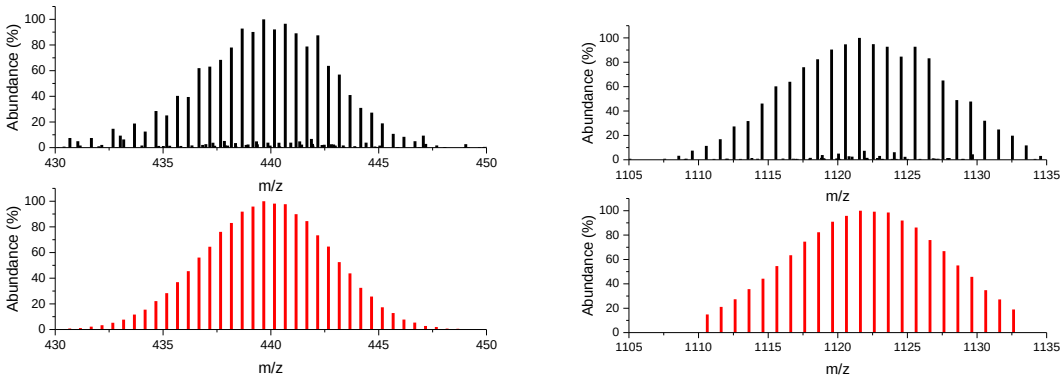

Figure 2.3.1 – ESI-MS signals for the $[Mo_6O_{19}]^{2-}$ dianion and the $[TBA][Mo_6O_{19}]^-$ monoanionic adduct, as observed in the ESI-MS analysis of a solution of Lindqvist hexamolybdate $[TBA]_2[Mo_6O_{19}]$ in methanol. Black lines represent experimental results, red lines represent simulated spectra.

More significantly, a large number of other signals were observed in solution along with the parent cluster (Figure 2.3.2 and Table 2.3.1). This large number of signals indicates that when dissolved in methanol solution and without further chemical perturbation, the Lindqvist species does disassemble into a series of smaller oligomers. These oligomers can be seen in solution along with their parent cluster.

Many of the signals can be assigned to a molecular species by comparison of the signal with a simulated molecular spectrum. This technique works very well for the low-mass molybdate oligomers, as these have distinctive isotopic abundance patterns in the mass spectrum.[63–68] However, this technique is less reliable at higher *m/z* values, as the multiple overlapping molybdenum isotopes result in extremely broad (almost Gaussian) isotopic envelope peaks.[63–68] Nevertheless, many species can be positively identified, including mononuclear, dinuclear and trinuclear species.

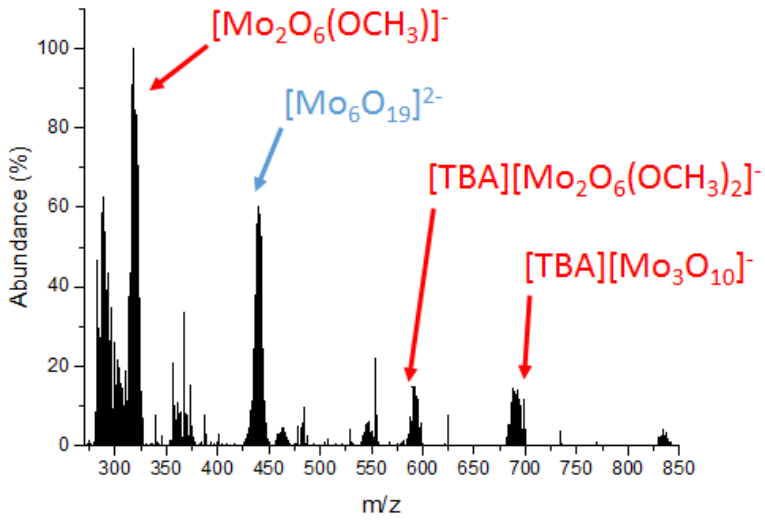

Figure 2.3.2 – Portion of the ESI-MS spectrum for a solution of Lindqvist hexamolybdate $[TBA]_2[Mo_6O_{19}]$ in methanol, highlighting the parent cluster (blue) and selected decomposition products (red).

Species	*m/z calc.*	*m/z exp.*
$[TBA][Mo_6O_{19}]^-$	*1112.62*	*1121.55*
$[TBA][Mo^{VI}_4O_{13}]^-$	*834.82*	*834.84*
$[TBA][Mo^{VI}_3O_{10}]^-$	*687.93*	*687.97*
$[TBA][Mo^{VI}_2O_6(OCH_3)_2]^-$	*592.09*	*592.10*
$[Mo^{VI}_6O_{19}]^{2-}$	*439.66*	*439.66*
$[Mo^{VI}_2O_5(OCH_3)_3]^-$	*365.84*	*365.85*
$[Mo^{VI}_2O_6(OCH_3)]^-$	*318.79*	*318.70*
$H[Mo^{V}_2O_6]^-$	*289.78*	*289.79*
$[Mo^{VI}O_3(OCH_3)]^-$	*176.90*	*176.91*
$H[Mo^{VI}O_4]^-$	*162.89*	*162.90*
$H[Mo^{IV}O_3]^-$	*146.89*	*146.90*

Table 2.3.1 – Calculated and observed *m/z* values for the species identified in the ESI-MS analyses for a solution of Lindqvist hexamolybdate $[TBA]_2[Mo_6O_{19}]$ in methanol. Signals representing the parent cluster are shaded blue.

For the mononuclear species, signals can be identified representing $H[Mo^{IV}O_3]^-$, $H[Mo^{VI}O_4]^-$ and $[Mo^{VI}O_3(OCH_3)]^{-\cdot}$ These species are small enough that the signals can be easily identified from their isotopic distribution without any ambiguity (Figure 2.3.3). The $[Mo^{VI}O_3(OCH_3)]^-$ mononuclear species is particularly abundant, dominating the mass spectrum.

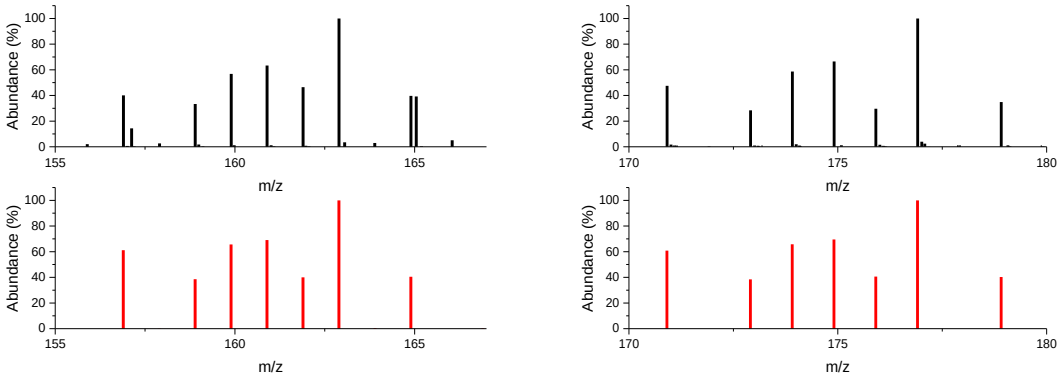

Figure 2.3.3 – Representative ESI-MS signals for mononuclear species identified in solution, $H[Mo^{VI}O_4]^-$ and $[Mo^{VI}O_3(OCH_3)]^-$. Black lines represent experimental results, red lines represent simulated spectra.

For the dinuclear species, $[TBA][Mo^{VI}_2O_6(OCH_3)_2]^-$, $[Mo^{VI}_2O_5(OCH_3)_3]^-$, $[Mo^{VI}_2O_6(OCH_3)]^-$ and $H[Mo^{V}_2O_6]^-$ can all be identified. The isotopic distributions are still distinctive enough that these species can be identified unambiguously (Figure 2.3.4).

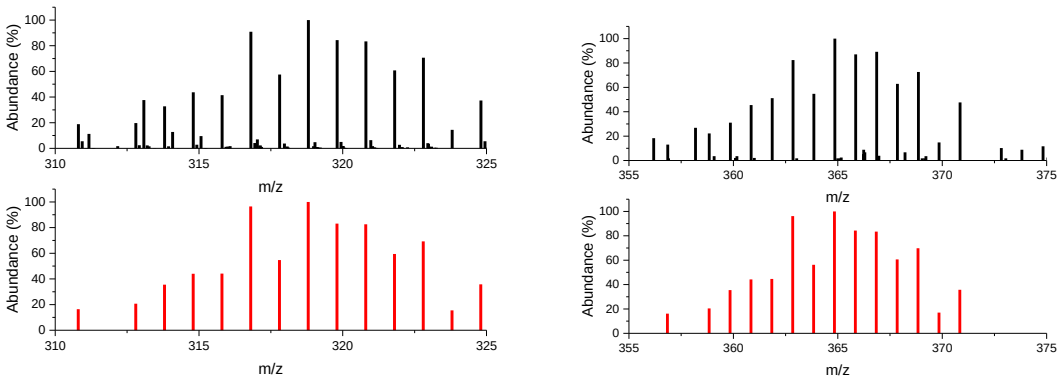

Figure 2.3.4 – Representative ESI-MS signals for dinuclear species identified in solution, $[Mo^{VI}_2O_6(OCH_3)_2]^-$ and $[Mo^{VI}_2O_5(OCH_3)_3]^-$. Black lines represent experimental results, red lines represent simulated spectra.

A trinuclear species, [TBA][$Mo^{VI}_3O_{10}$]$^-$, (calculated mass 687.93, experimental mass 687.97) can also be identified. At this point, the isotopic distributions are becoming much broader, but the species can still be identified (Figure 2.3.5). Additionally, there is a possible hint of a tetranuclear species, [TBA][$Mo^{VI}_4O_{13}$]$^-$ (calculated mass 834.82, experimental mass 834.84). However, the signal is at extremely low intensity. No signals were observed that could correspond to {Mo_5} species.

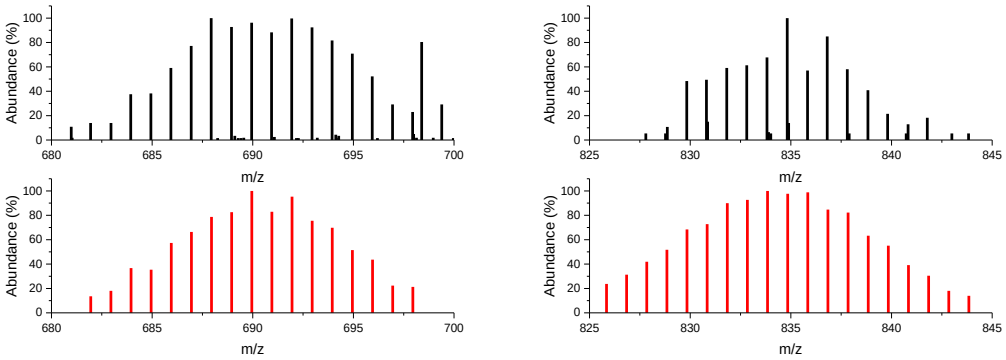

Figure 2.3.5 –ESI-MS signals for possible trinuclear and tetranuclear species identified in solution, [TBA][$Mo^{VI}_3O_{10}$]$^-$ and [TBA][$Mo^{VI}_4O_{13}$]$^-$. Black lines represent experimental results, red lines represent simulated spectra.

Cone Voltage (CV) Experiments:

The variety of molecular structures identified by ESI-MS indicated that $[Mo_6O_{19}]^{2-}$ is a promising candidate for the disassembly-reassembly technique. However, these signals can arise from two sources – "real" species in solution, or fragments that arise from collision induced dissociation (CID) of molecules within the spraying chamber.[69–73] Therefore, a series of ESI-MS experiments were conducted with varying cone voltage (CV). Signals that diminish upon increasing cone voltage are due to "real" species, signals that enhance upon increasing cone voltage are due to CID events.[69–73]

For the $H[Mo^{IV}O_3]^-$ signal, no signal can be observed at low CV values, and the intensity generally increases on increasing CV (Figure 2.3.6). Both of these facts indicate that this signal arises from CID events. This fragment may arise from gas-phase collisions of $H[Mo^{VI}O_4]^-$ and $[Mo^{VI}O_3(OCH_3)]^-$. At CV = 75 V, the signal is better represented by $[Mo^{V}O_3]^-$.

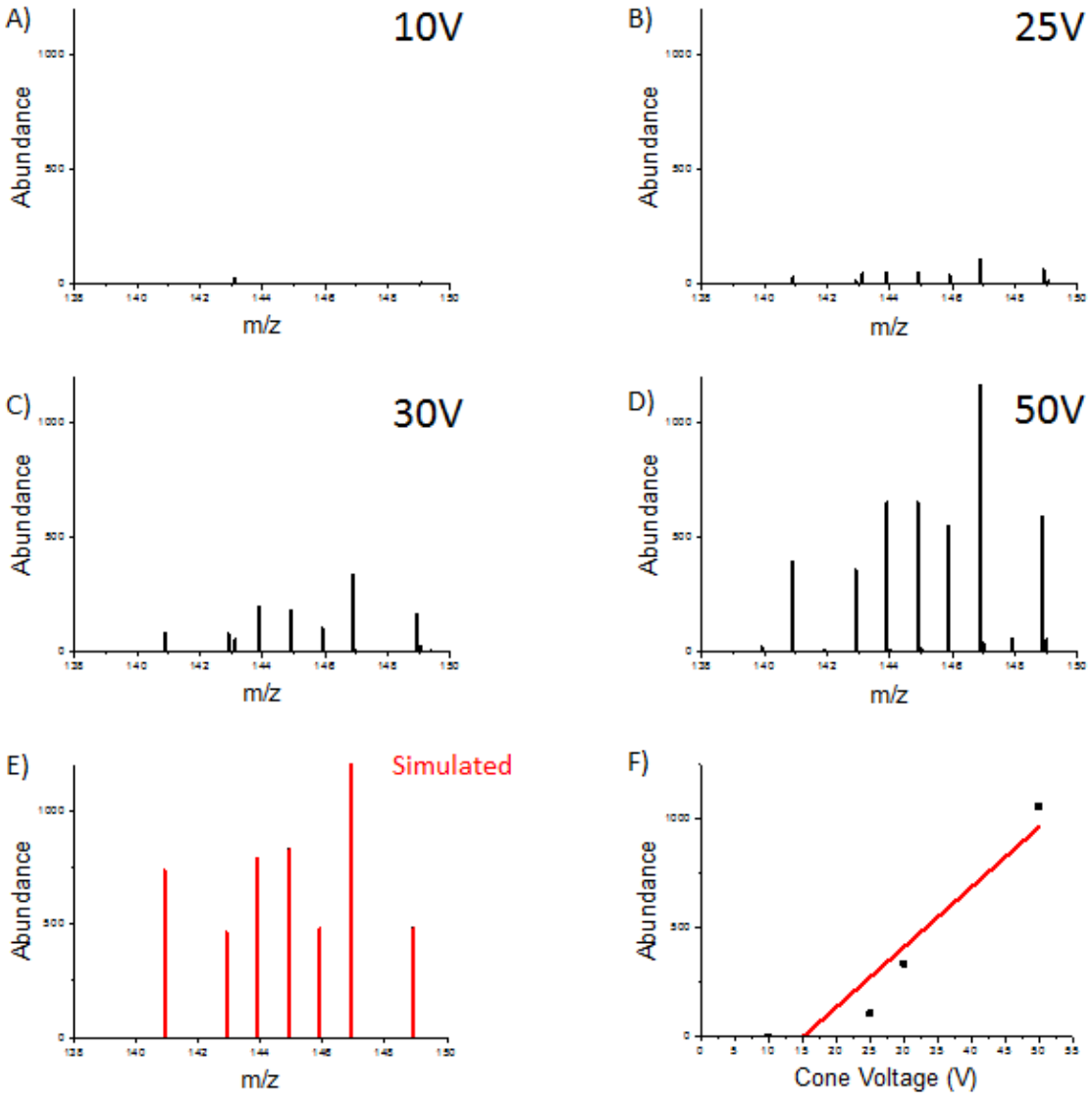

Figure 2.3.6 –ESI-MS signals for $H[Mo^{IV}O_3]^-$ at various cone voltage values: A) 10 V, B) 25 V, C) 30 V, D) 50 V. E) Simulated spectrum. F) A plot of signal intensity (highest peak) vs. cone voltage values, with a best-fit regression line drawn to act as a guide for the eye.

The $[HMo^{VI}O_4]^-$ signal shows a complicated CV dependence. The signal intensity rises to a maximum value at around CV = 30V before dropping off again (Figure 2.3.7). This can be explained by competing CID events – at intermediate CV values, increased fragmentation of this species may be compensated by the increased fragmentation of a heavier species, but at higher CV values fragmentation dominates and the signal intensity diminishes. However, the extent to which competing CID events is occurring is difficult to quantify with any accuracy. Thus, it difficult to draw definitive conclusions about this species.

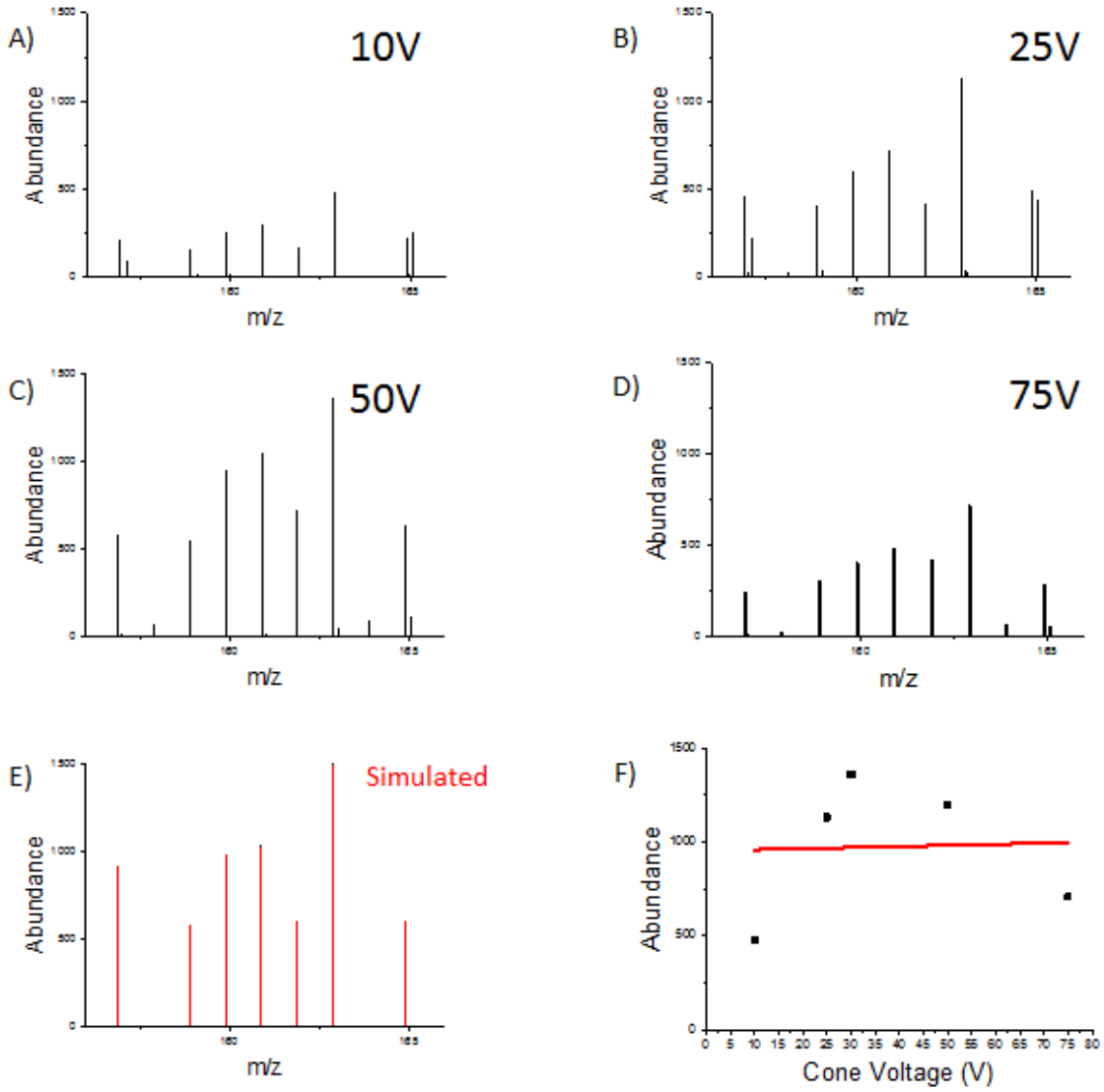

Figure 2.3.7 –ESI-MS signals for $H[Mo^{VI}O_4]^-$ at various cone voltage values: A) 10 V, B) 25 V, C) 50 V, D) 75 V. E) Simulated spectrum. F) A plot of signal intensity (highest peak) vs. cone voltage values, with a best-fit regression line drawn to act as a guide for the eye.

The $[Mo^{VI}O_3(OCH_3)]^-$ signal is present at low CV values, and the intensity gradually decreases on increasing CV, disappearing altogether at high CV values (Figure 2.3.8). This indicates that this signal arises from a "real" solution phase species. CID events involving this species probably generate $H[Mo^{IV}O_3]^-$. And $[HMo^{VI}O_4]^-$ signals.

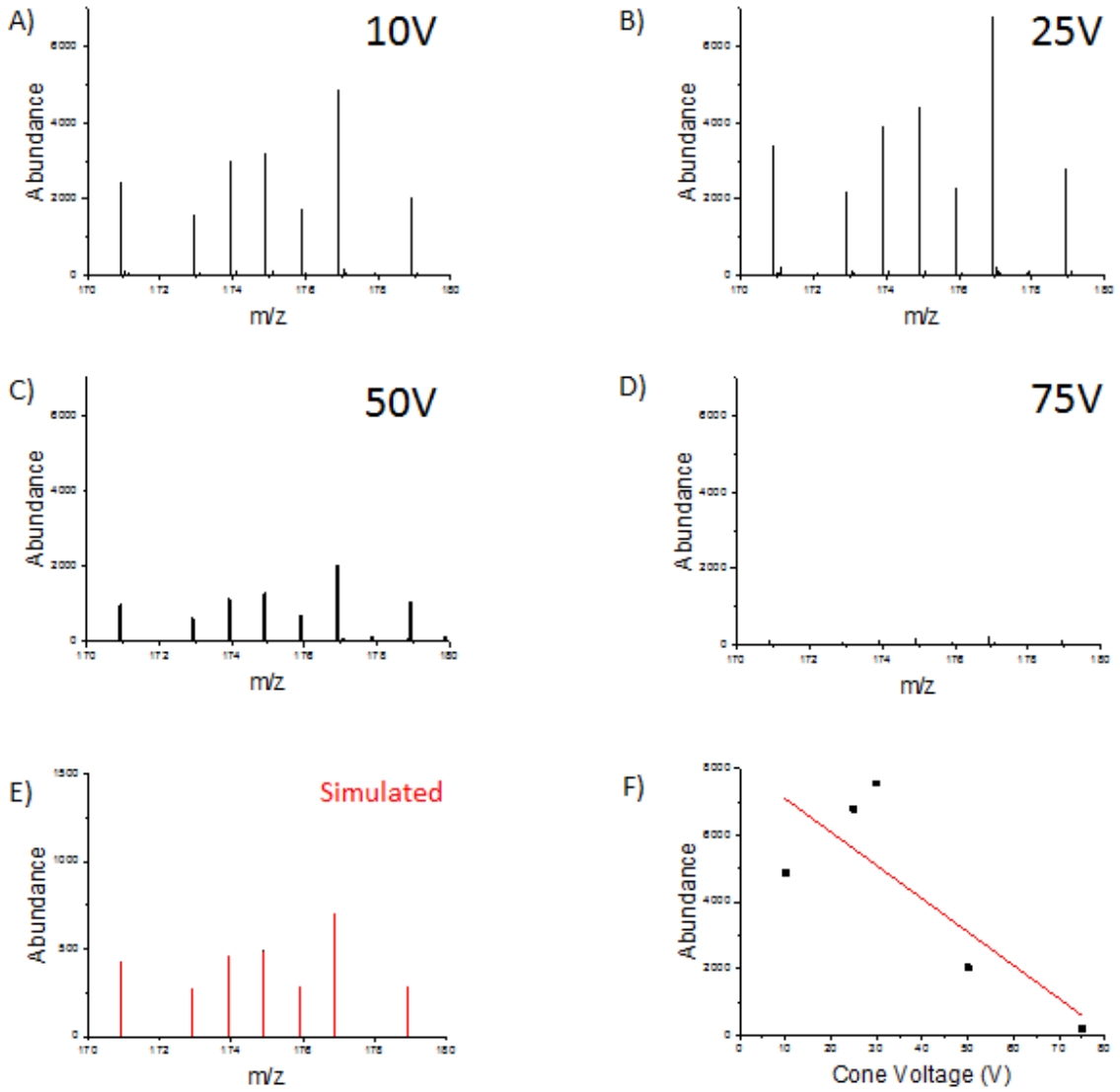

Figure 2.3.8 –ESI-MS signals for $[Mo^{VI}O_3(OCH_3)]^-$ at various cone voltage values: A) 10 V, B) 25 V, C) 50 V, D) 75 V. E) Simulated spectrum. F) A plot of signal intensity (highest peak) vs. cone voltage values, with a best-fit regression line drawn to act as a guide for the eye.

The $H[Mo^{V}_{2}O_{6}]^{-}$ is not present at low CV values, and signal intensity generally increases on increasing CV, and indicating that this signal arises from CID events (Figure 2.3.9). Gas-phase collisions of $[Mo^{VI}_{2}O_{6}(OCH_{3})]^{-}$ and $[TBA][Mo^{VI}_{2}O_{6}(OCH_{3})_{2}]^{-}$ are the likely origins of this signal. At higher CV values (75V), the signal is better described by $[Mo^{V}Mo^{VI}O_{6}]^{-}$

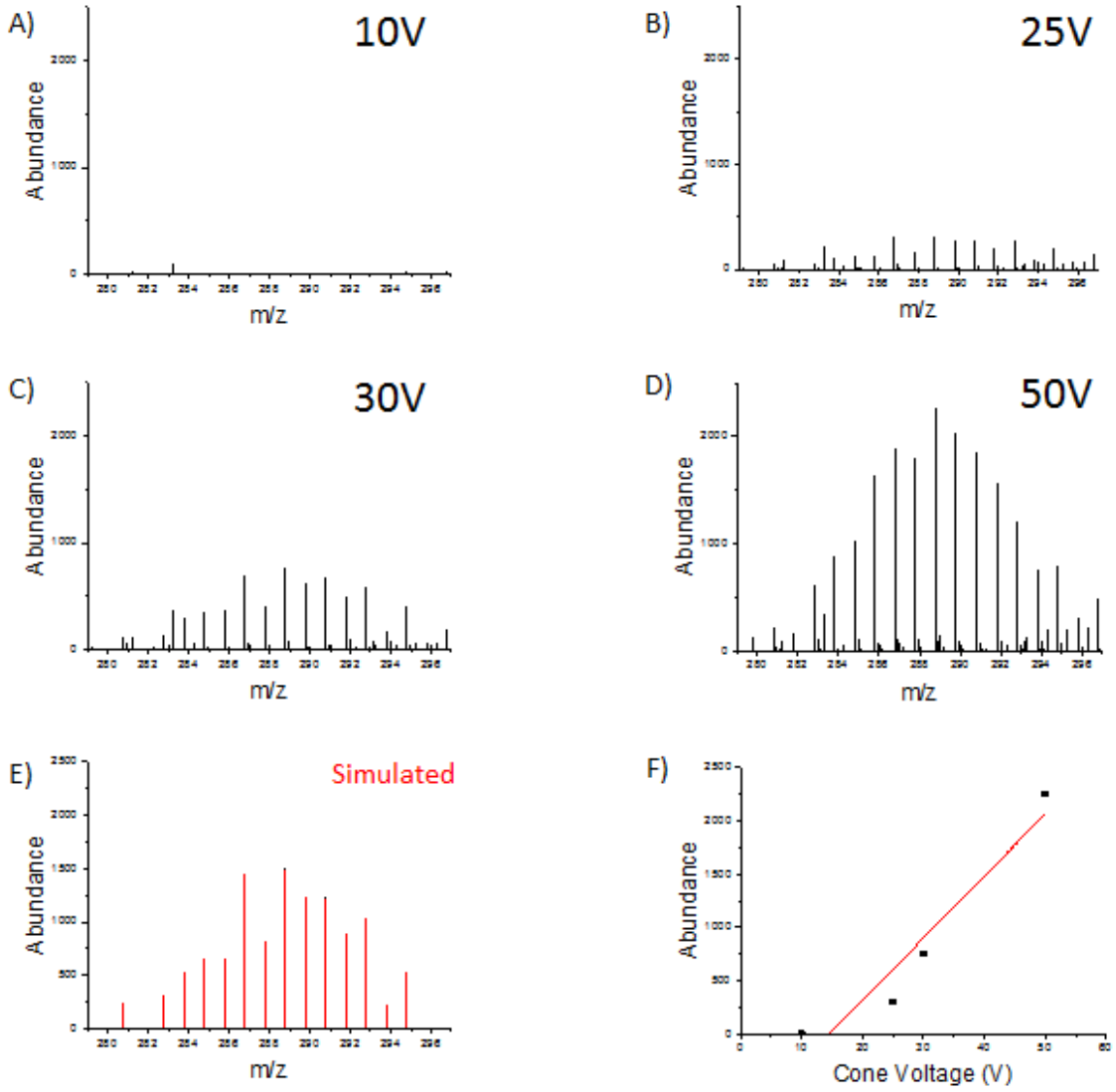

Figure 2.3.9 –ESI-MS signals for $H[Mo^{V}_{2}O_{6}]^{-}$ at various cone voltage values: A) 10 V, B) 25 V, C) 30 V, D) 50 V. E) Simulated spectrum. F) A plot of signal intensity (highest peak) vs. cone voltage values, with a best-fit regression line drawn to act as a guide for the eye.

The $[Mo^{VI}_2O_6(OCH_3)]^-$ signal is present at low CV values, and intensity diminishes at higher values, indicating that this signal arises from a "real" solution-phase species (Figure 2.3.10). CID events involving this species could generate either mononuclear or dinuclear fragments.

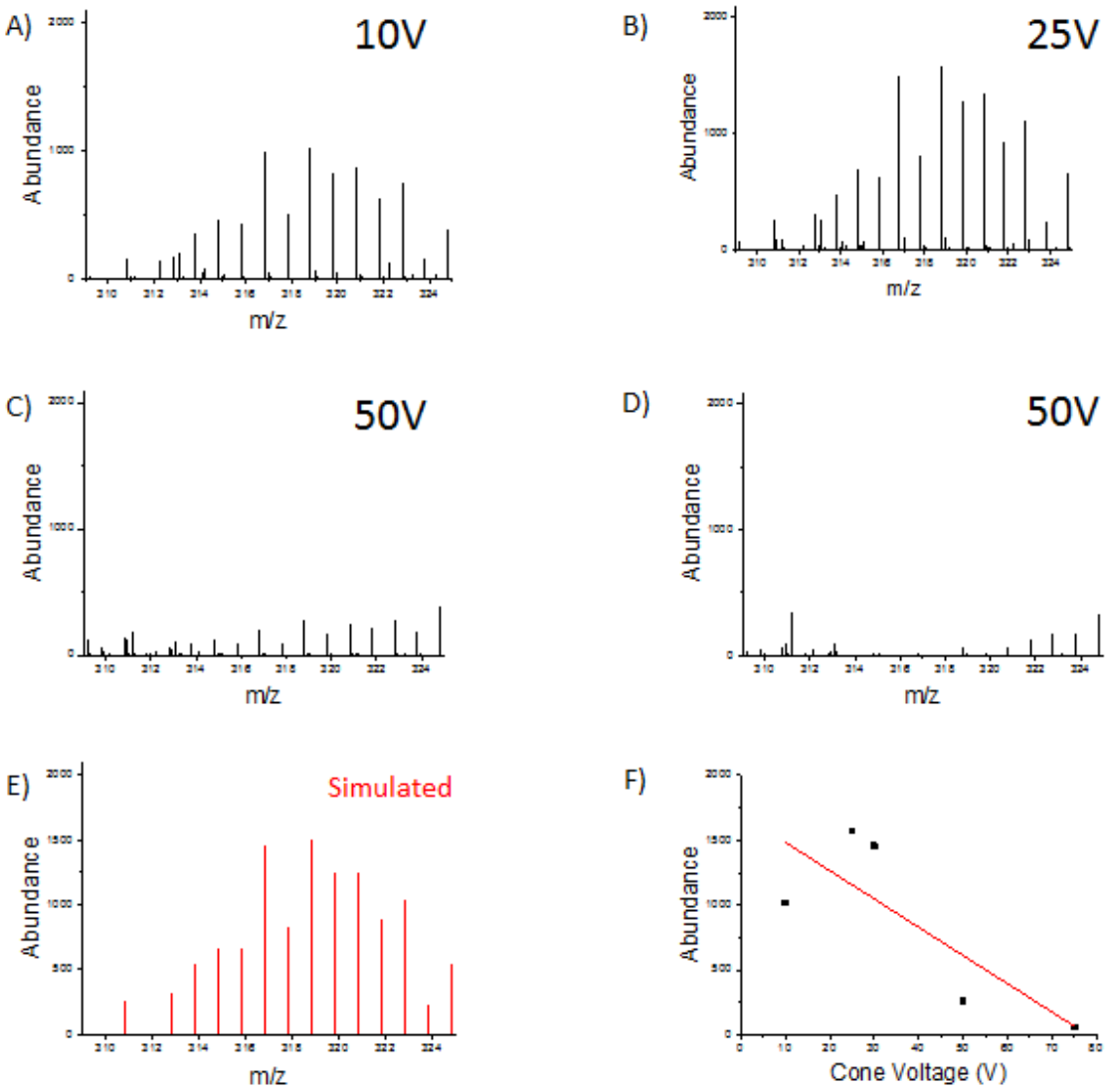

Figure 2.3.10 –ESI-MS signals for $[Mo^{VI}_2O_6(OCH_3)]^-$ at various cone voltage values: A) 10 V, B) 25 V, C) 50 V, D) 75 V. E) Simulated spectrum. F) A plot of signal intensity (highest peak) vs. cone voltage values, with a best-fit regression line drawn to act as a guide for the eye.

The $[Mo^{VI}_2O_5(OCH_3)_3]^-$ signal intensity is low, but the signal is present at low CV values and quickly vanishes on increasing CV, indicating that the signal represents a "real" solution-phase species (Figure 2.3.11). CID events involving this species could generate either mononuclear or dinuclear fragments.

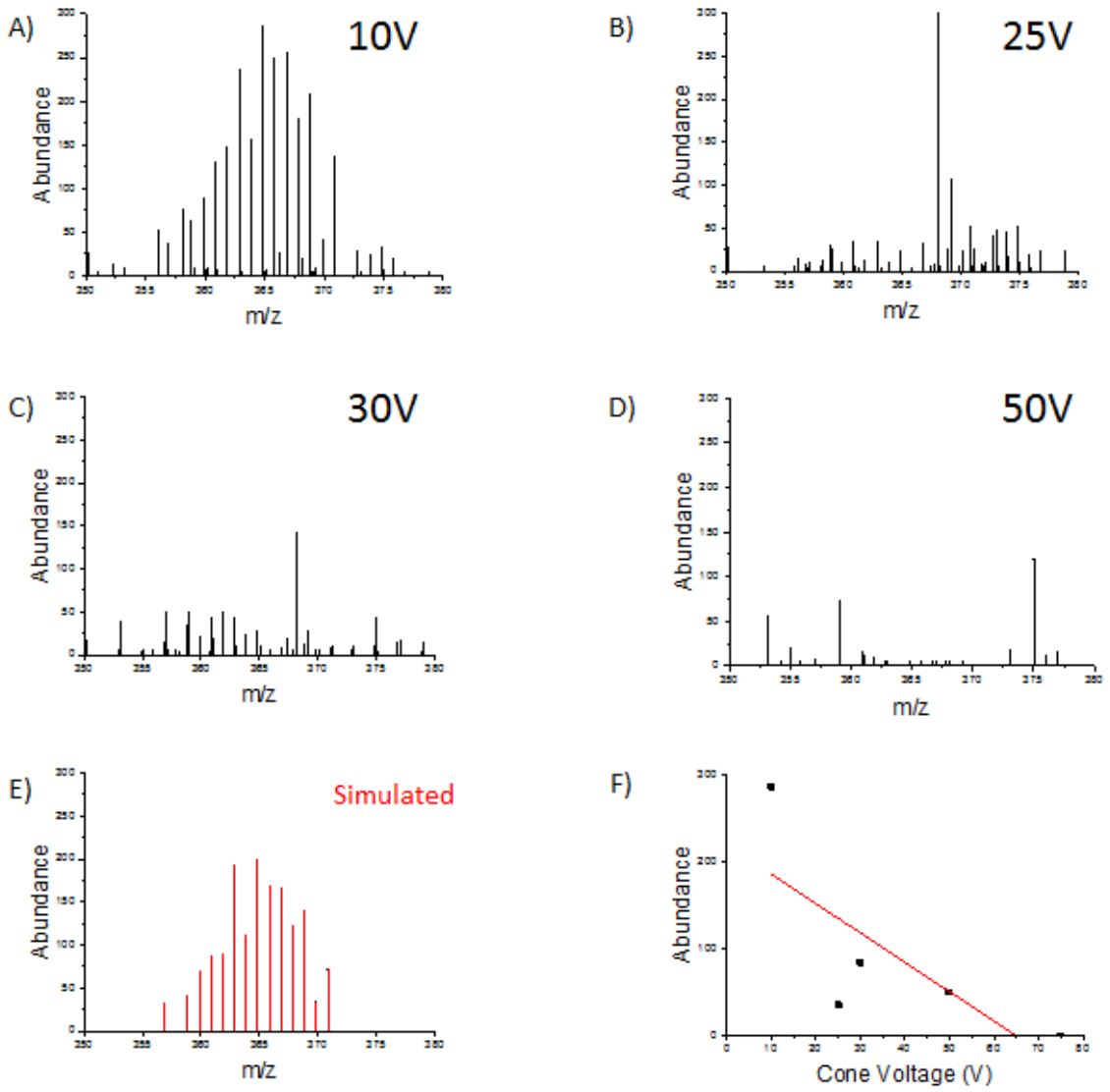

Figure 2.3.11 –ESI-MS signals for $[Mo^{VI}_2O_5(OCH_3)_3]^-$ at various cone voltage values: A) 10 V, B) 25 V, C) 30 V, D) 50 V. E) Simulated spectrum. F) A plot of signal intensity (highest peak) vs. cone voltage values, with a best-fit regression line drawn to act as a guide for the eye.

The signal for $[TBA][Mo^{VI}_2O_6(OCH_3)_2]^-$ is present at low CV values, and signal intensity decreases consistently on increasing CV, indicating that the signal represents a "real" solution-phase species (Figure 2.3.12). CID events are an unlikely source for this signal anyway, as collision events energetic enough to break metal-oxygen bonds are unlikely to leave a cation-anion adduct intact. CID events involving this species could generate either mononuclear or dinuclear fragments.

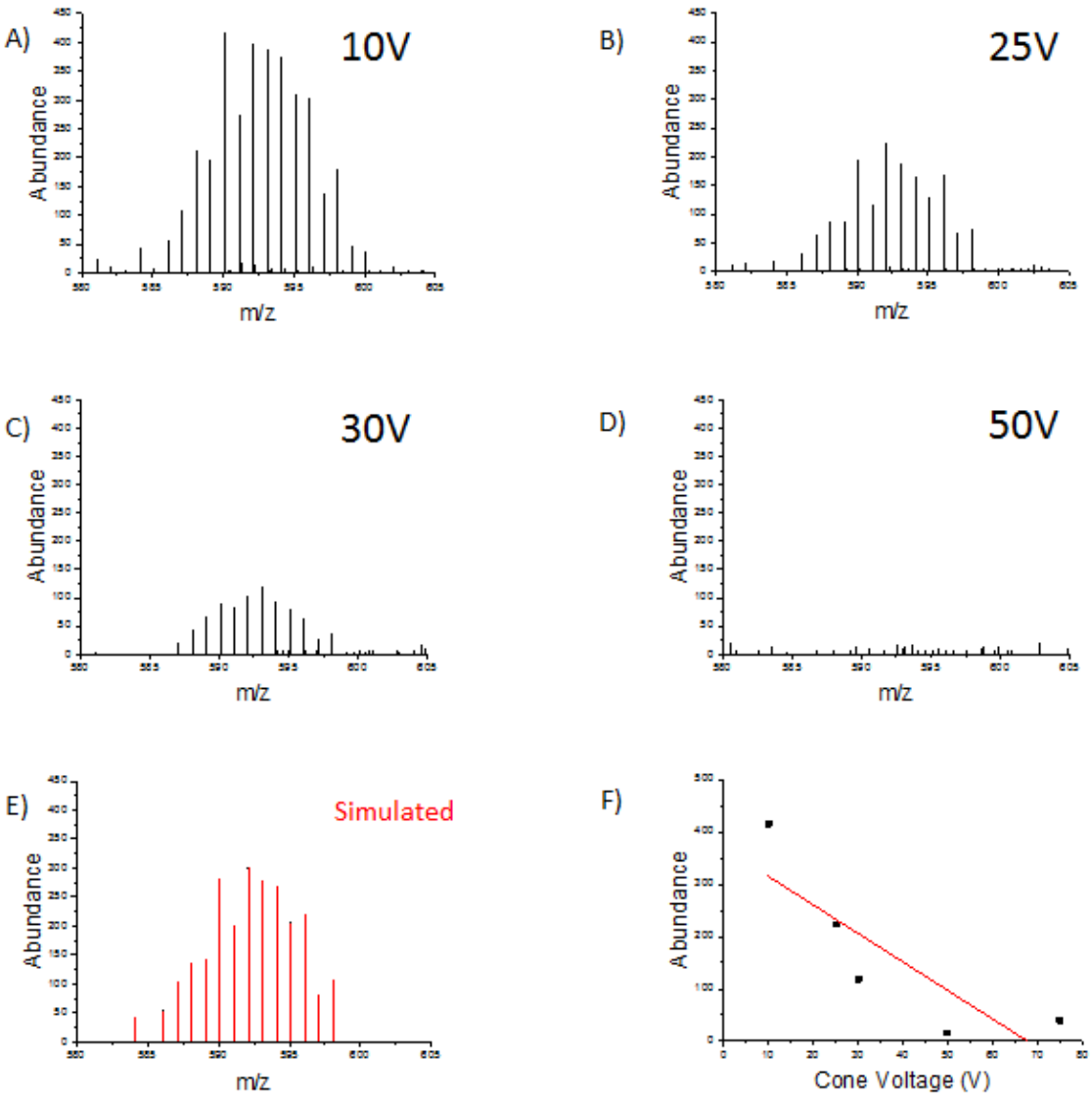

Figure 2.3.12 –ESI-MS signals for $[TBA][Mo^{VI}_2O_6(OCH_3)_2]^-$ at various cone voltage values: A) 10 V, B) 25 V, C) 30 V, D) 50 V. E) Simulated spectrum. F) A plot of signal intensity (highest peak) vs. cone voltage values, with a best-fit regression line drawn to act as a guide for the eye.

The [TBA][$Mo^{VI}_3O_{10}$]$^-$ signal has low intensity and does not display any clear trend with respect to CV (Figure 2.3.13). The presence of a very weak signal at low CV and the fact that this species is a cation-anion adduct lend support to the hypothesis that this is a real species, but the evidence is too weak to render a confident assignment of this signal.

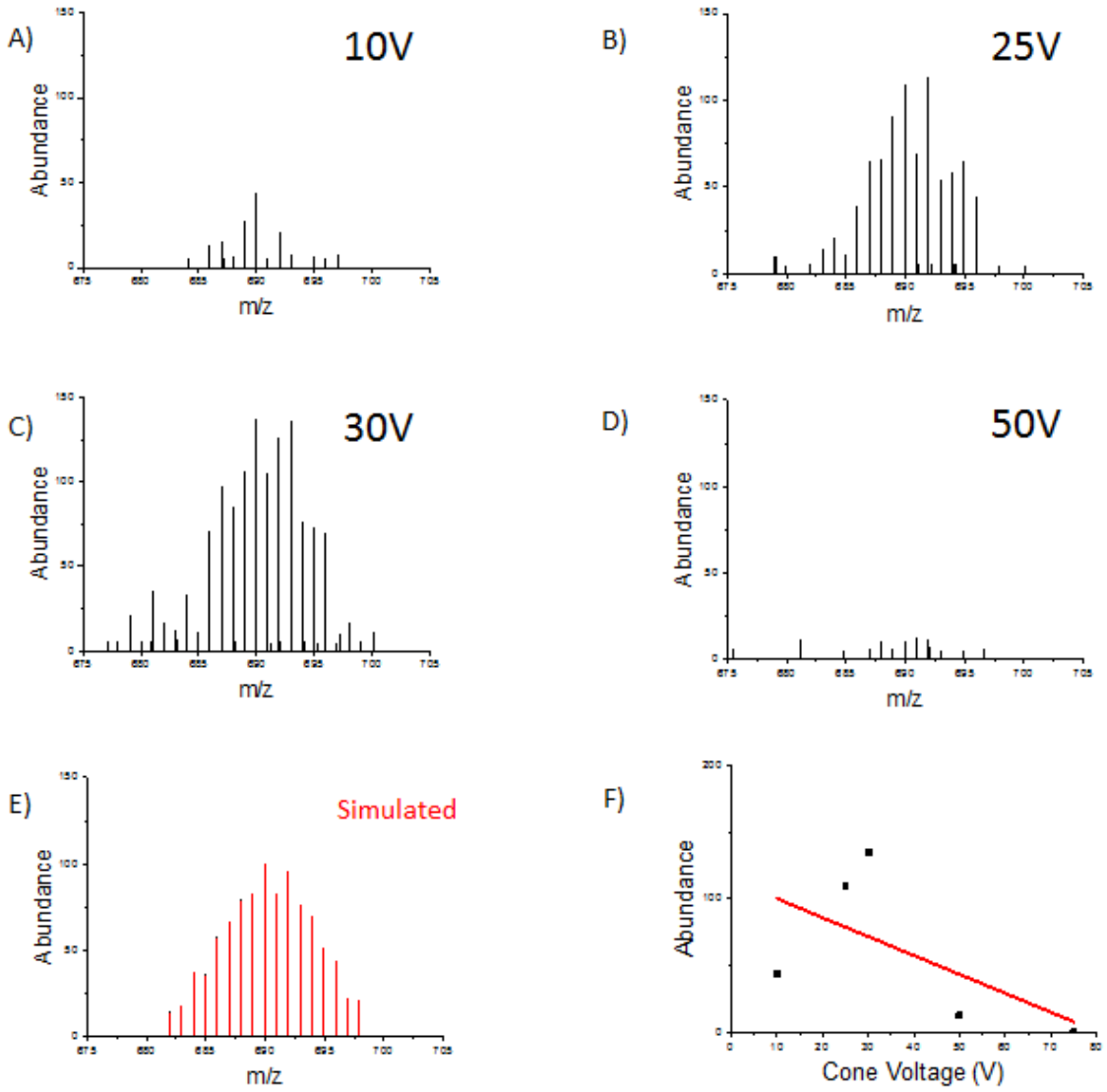

Figure 2.3.13 –ESI-MS signals for [TBA][$Mo^{VI}_3O_{10}$]$^-$ at various cone voltage values: A) 10 V, B) 25 V, C) 30 V, D) 50 V. E) Simulated spectrum. F) A plot of signal intensity (highest peak) vs. cone voltage values, with a best-fit regression line drawn to act as a guide for the eye.

The $[TBA][Mo^{VI}_4O_{13}]^-$ signal intensity is very low and does not display a clear trend with respect to CV (Figure 2.3.14). As with the previous case, the evidence here is too weak to present a definitive assignment of this species as either real or instrumentational.

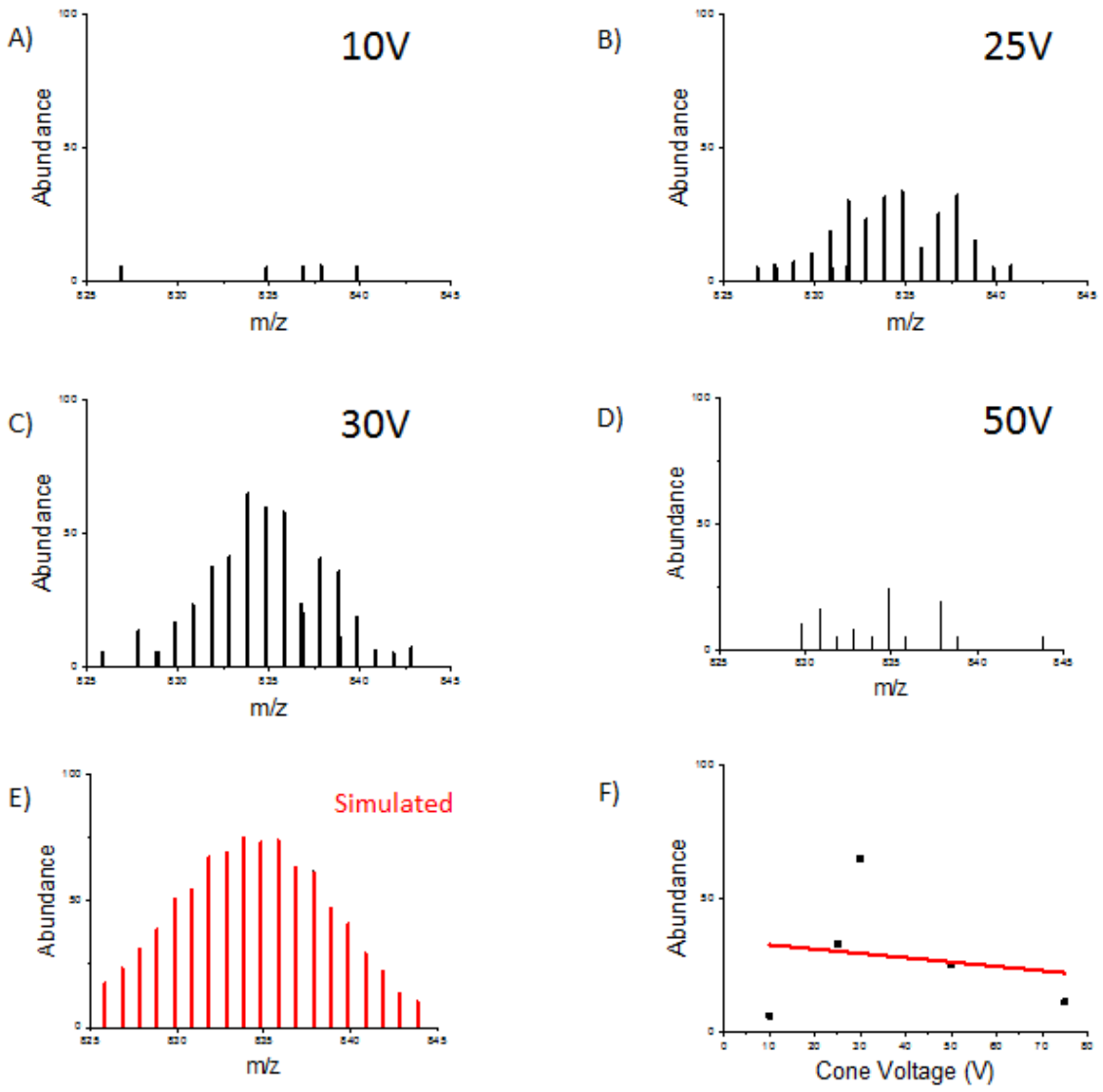

Figure 2.3.14 –ESI-MS signals for $[TBA][Mo^{VI}_4O_{13}]^-$ at various cone voltage values: A) 10 V, B) 25 V, C) 30 V, D) 50 V. E) Simulated spectrum. F) A plot of signal intensity (highest peak) vs. cone voltage values, with a best-fit regression line drawn to act as a guide for the eye.

The CV variation experiments give a significant insight into the solution behaviour of the Lindqvist hexamolybdate $[Mo_6O_{19}]^{2-}$ in methanol solution. Table 2.3.1 can be therefore be updated as follows:

Species	*m/z calc.*	*m/z exp.*
$[TBA][Mo_6O_{19}]^-$	*1112.62*	*1121.55*
$[TBA][Mo^{VI}_4O_{13}]^-$	*834.82*	*834.84*
$[TBA][Mo^{VI}_3O_{10}]^-$	*687.93*	*687.97*
$[TBA][Mo^{VI}_2O_6(OCH_3)_2]^-$	*592.09*	*592.10*
$[Mo^{VI}_6O_{19}]^{2-}$	*439.66*	*439.66*
$[Mo^{VI}_2O_5(OCH_3)_3]^-$	*365.84*	*365.85*
$[Mo^{VI}_2O_6(OCH_3)]^-$	*318.79*	*318.70*
$H[Mo^{V}_2O_6]^-$	*289.78*	*289.79*
$[Mo^{VI}O_3(OCH_3)]^-$	*176.90*	*176.91*
$H[Mo^{VI}O_4]^-$	*162.89*	*162.90*
$H[Mo^{IV}O_3]^-$	*146.89*	*146.90*

Table 2.3.2 – Species identified from the ESI-MS analyses of the Lindqvist hexamolybdate $[TBA]_2[Mo_6O_{19}]$ in methanol. Signals representing the parent cluster are shaded blue, signals arising from other species in solution are shaded green, and signals arising from CID events within the spectrometer are shaded red. Signals with some degree of ambiguity are left unshaded.

Thus, oligomeric molybdate species form *via* spontaneous disassembly of the Lindqvist hexamolybdate simply by dissolving the species in methanol. Only the parent POM cluster and a solvent were present, and no degradative processes such as heating or irradiation were applied. At least two mononuclear and three dinuclear species can be identified in solution in equilibrium with the parent POM cluster. Trinuclear and tetranuclear species may also be present. Therefore it was concluded that the Lindqvist hexamolybdate was likely to be suitable candidate for a disassembly-reassembly synthetic process.

These easily-generated oliogmeric species are in principle more reactive than their parent cluster. Addition of templating ligands or heterometals to this solution should therefore be able to trap these oligomeric fragments into new hybrid or TMS-POM architecture.

We conjecture that under a suitable templating bias, new compounds can be formed from these fragments, either *via* trapping of these fragments or *via* condensation of multiple smaller fragments under a bias applied by templating ligands. The next section will consider the reassembly of these molybdate fragments under the influence of polydentate templating ligands.

2.4) Hybrid Structures (Reassembly)

Having identified a suitable POM and a solvent system in which it disassembled, the next step towards a disassembly-reassembly synthetic procedure was to attempt to reassemble the disassembly oligomers into a new species by the addition of a suitable reactant.

Tert-butylphosphonate was identified as a potentially suitable ligand for the following reasons:

- As a polydentate ligand, it was expected to exhibit a significant templating effect; each ligand molecule can interact with multiple metal centres in solution at any given time, potentially bringing them into close enough contact for condensation to occur between metal centres (Figure 2.4.1);[74–76]
- The PO_3 unit has a similar geometry and charge to $[MoO_4]^{2-}$ species; it has been suggested in the past that this property makes phosphonates suitable ligands to generate hybrid POM species;[77–79]
- It was hypothesised that the bulky *tert*-butyl group might provide steric shielding to protect new compounds from hydrolysis, particularly during early stages of cluster formation.

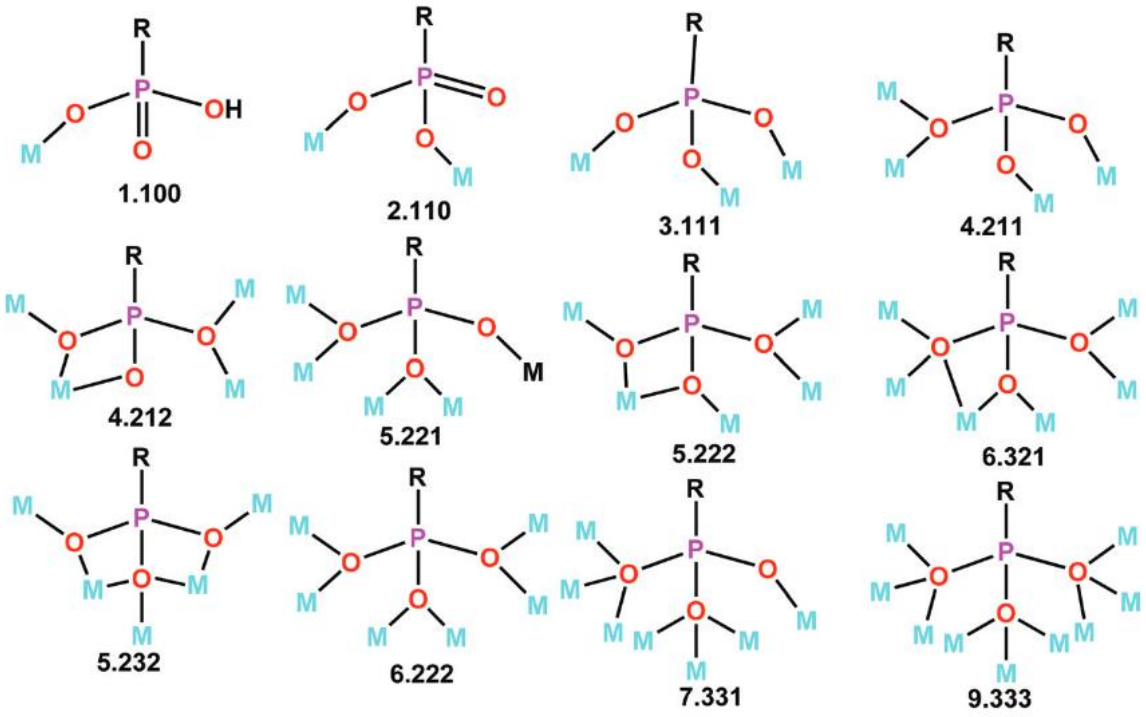

Figure 2.4.1 – Possible binding modes of phosphonate ligands. Reproduced from reference 76.

In the first instance, hybrid POM systems were targeted, on the basis that a POM-ligand system would be simpler to understand than a mixed-metal hybrid system. The simple reaction system (containing just molybdate and phosphonate ligands) was expected to generate a Strandberg-type ring structure (*c.f.* Section 1.2.1), as this is a common phosphonate-molybdate motif.[80–90] Other phosphonate-molybdate motifs are possible but rare.[91] In this structure, the phosphonate templates a five-membered ring structure (*c.f.* Figure 1.2.1.11).

*[pip-H_2]$_2$[Mo_5O_{15}(*t*$BuPO_3$)$_2$] (**1**)*

To investigate the reassembly behaviour of the oligomeric molybdate fragments with phosphonate templating ligands, *tert*-butylphosphonic acid, *t*$BuPO_3H_2$, was combined with [TBA]$_2$[Mo_6O_{19}] in methanol. Addition of piperazine to this reaction mixture resulted in the formation of an amorphous white precipitate over the course of approximately one hour. Excess starting materials were removed by washing the sample with acetonitrile. Comparison of the infrared (IR) spectrum of this powder with those of previously synthesised compounds identified the solid as containing [pip-H_2]$_2$[Mo_5O_{15}(*t*$BuPO_3$)$_2$], **(1)**, where pip represents piperazine and *t*-Bu represents the *tert*-butyl moiety.

This compound is a Strandberg-type polyanion, which was discussed in Chapter 1. The Strandberg structure is a pentanuclear ring structure, with two phosphonate ligand units binding to either side of the ring (Figure 2.4.1).[83,84] This type of polyanion was the first reported hybrid polymolybdate, and so several substitutions of the phosphonate backbone have been reported, although to the best of our knowledge **1** represents the first *tert*-butyl substituted Strandberg ring structures.[85,86] All previously reported Strandberg ring structures were synthesised *via* bottom-up approaches.[80–90]

The ring structure contains five Mo^{VI} metal centres and five μ_2-O bridging *oxo*- ligands in a ring system. Each Mo centre has two terminal *oxo*- ligands supporting the metal centre. The phosphonate ligands both bind to all five metal centres in a η^1:η^2:η^2:μ_5 coordination mode. In polyhedral representation, the structure consists of five edge-sharing {MoO_6} octahedra bent into a ring, with the two terminal {MoO_6} octahedra sharing a vertex with one another (Figure 2.4.2).

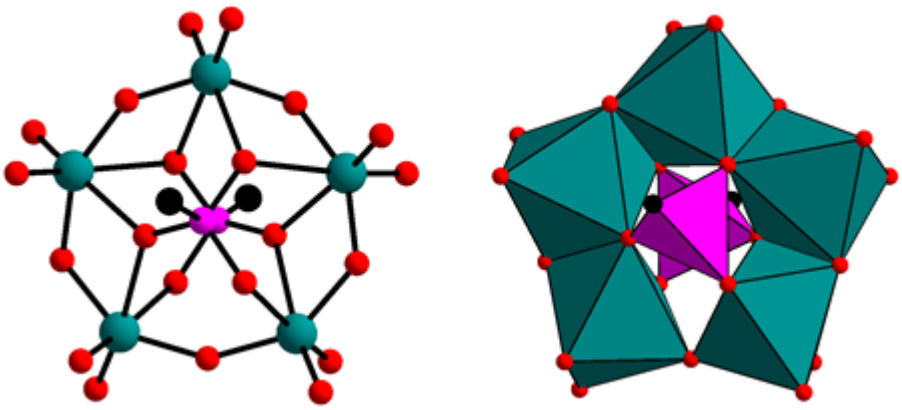

Figure 2.4.2 – The Strandberg-type ring structure, $[Mo_5O_{15}(RPO_3)_2]^{4-}$, in ball-and-stick and polyhedral representations. [pip-H_2]$_2$[Mo_5O_{15}(*t*$BuPO_3$)$_2$], compound 1, contains a *tert*-butyl-substituted analogue of this compound. Colour Scheme: Mo teal, P pink, O red, C black.

The structural characterisation for **1** is in very good agreement with the reported characterisation for analogous compounds in the literature. Kwak *et al.* present IR spectra[86] for the methyl-substituted derivative, $[Mo_5O_{15}(MePO_3)_2]^{4-}$ that are consistent with the IR spectrum for **1**•2(MeOH). (Figure 2.4.3 and Table 2.4.1).

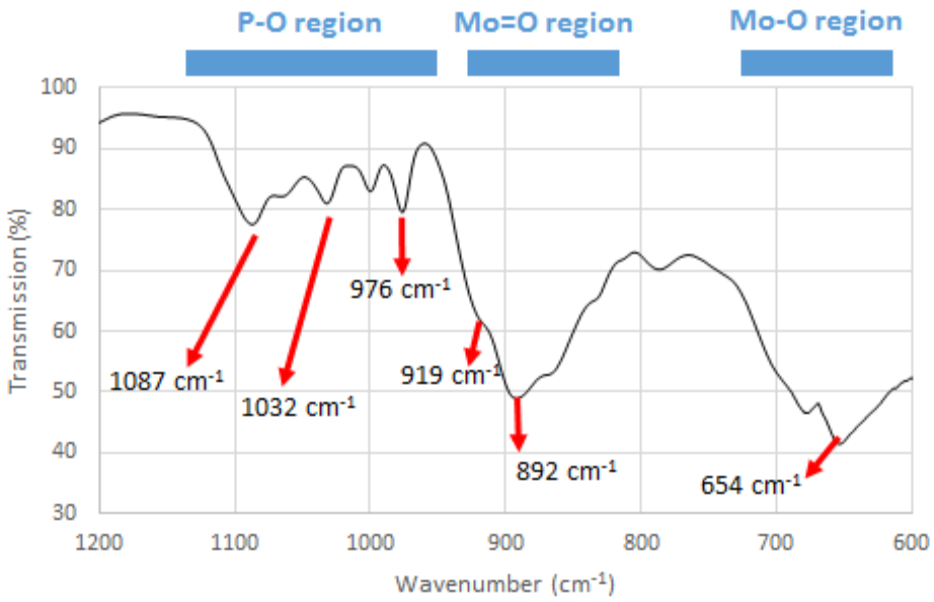

Figure 2.4.3 – A portion of the infrared (IR) absorption spectrum for $[pip\text{-}H_2]_2[Mo_5O_{15}(t\text{BuPO}_3)_2]$•2(MeOH)., compound 1•2(MeOH)..

1	$[Mo_5O_{15}(MePO_3)_2]^{4-}$	Assignment[86]
1087	1090	P-O
1032	1038	
976	982	
919 (shoulder)	920	Mo-O (terminal)
892	900	
654	660	Mo-O (bridging)

Table 2.4.1 – Comparison of the infrared absorption frequencies (cm^{-1}) for 1 and the methylphosphonate-substituted analogue as presented by Kwak *et al.*, along with the assignments proposed by Kwak.[86]

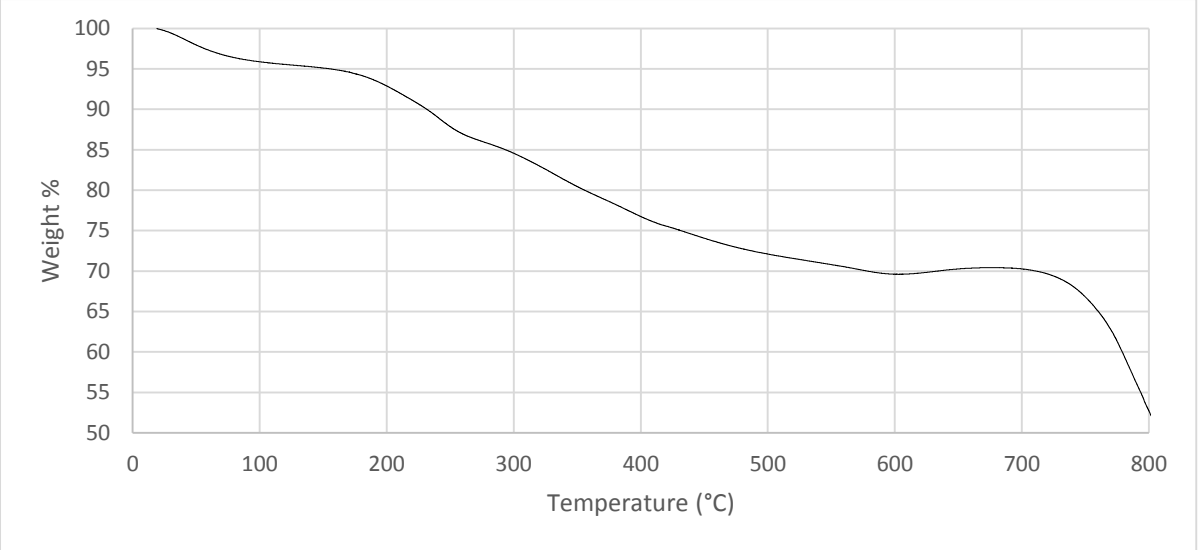

Figure 2.4.4 – The thermogravimetric analysis (TGA) for 1•2(MeOH).

The thermogravimetric analysis (TGA) indicates that **1** forms along with two constituent methanol molecules per formula unit (Figure 2.4.4). TGA analysis on the resulting white powder was consistent with this formula. The weight loss up to *c.* 100 °C is consistent with the loss of two methanol molecules per formula unit (calculated 95.1%, observed 94.8%). Subsequent heating over *c.* 200 °C results in gradual degradation of the organic components, with the weight above *c.* 700 °C being attributed to formation of dense oxide phases.

It seems reasonable to suggest that the phosphonate ligand acted as a template for the formation of this five-membered ring system. We propose that this ring structure was generated from some (unspecified) combination of the molybdate oligomers identified in Section 2.3. We know these species are present in solution, as they were observed in the ESI-MS analyses. Further, we expect the polydentate phosphonate ligand to coordinate to multiple metal centres (*c.f.* Figure 2.4.1). This may have drawn the metal centres into close enough contact for condensation to occur between adjacent metal centres, biasing the system towards the Strandberg structure. Thus, the disassembly of the Lindqvist hexamolybdate, followed by reassembly under the bias of the phosphonate template, results in the hybrid structure **1** (Figure 2.4.5)**.**

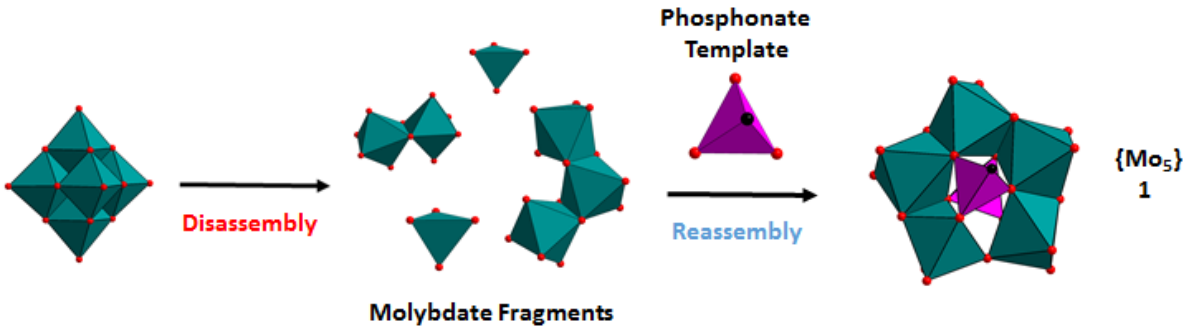

Figure 2.4.5 – The proposed disassembly-reassembly pathway, whereby the Lindqvist hexamolybdate disassembled into several oligomeric molybdate fragments, which subsequently reassembled under the influence of a phosphonate template to form the Strandberg-type ring in 1.

The tendency of oligomers to reassemble into a ring structure around tetrahedral templates is consistent with literature transformations (*e.g.* the rearrangement of the Lindqvist to the α-octamolybdate structure[46]). Assembly into a ring structure around a central template is also consistent with the top-down approaches to hybrid Anderson clusters.[28–39]

*[TDP-H_2]$_2$[Mo_5O_{15}(*t*BuPO_3)$_2$] (**2**)*

Replacement of the piperazine proton source with trimethylenedipyridine (TDP) also resulted in the formation of a white precipitate over the course of one hour. IR spectroscopic analysis (Figure 2.4.6) was applied and this solid was found to contain [TDP-H_2]$_2$[Mo_5O_{15}(*t*BuPO_3)$_2$] (**2**). This compound is also a *tert*-butylphosphonate-substituted Strandberg-type ring structure. Thus, two examples of the Strandberg ring structure can be generated using the disassembly-reassembly approach.

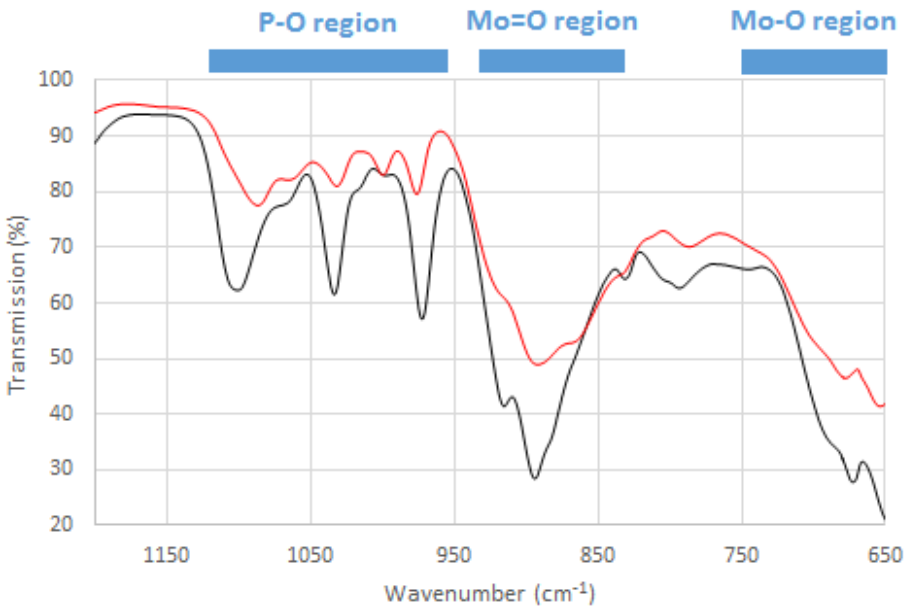

Figure 2.4.6 – Comparison of the infrared absorption frequencies (cm^{-1}) for 2•0.6(MeOH) (black) and 1•2(MeOH) (red). The similarities between the spectra indicate that they contain the same Strandberg ring motif.

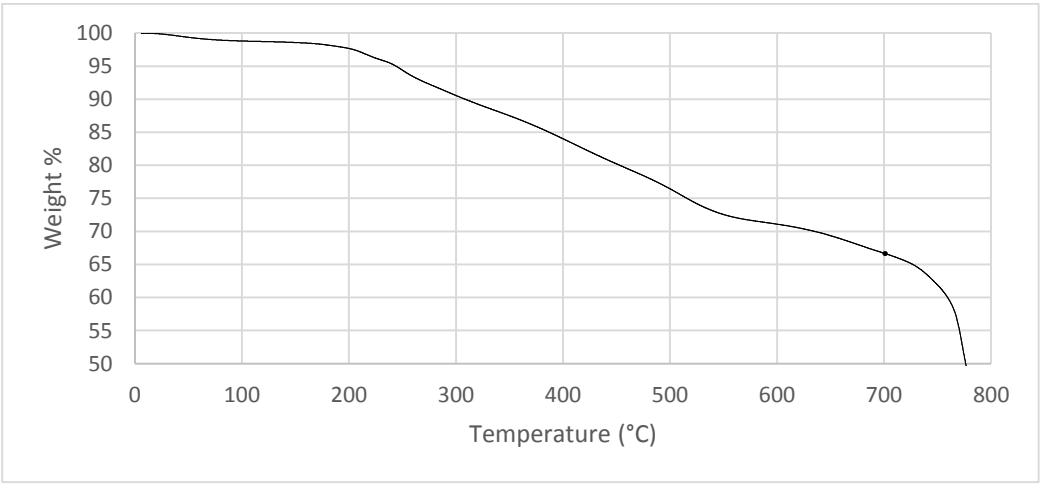

Figure 4.2.7 – The thermogravimetric analysis (TGA) for 2•0.6(MeOH).

TGA analysis indicates that **2** forms along with 0.6 methanol molecules per formula unit (calculated 98.6%, observed 98.6%). Subsequent heating over *c.* 200 °C shows a very similar decomposition behaviour to **1** (Figure 2.4.7).

2.5) Notes on the Assembly-Disassembly-Reassembly Method

Mechanism of Reassembly

We demonstrated in the previous section that molybdate oligomers form spontaneously from the Lindqvist hexamolybdate when dissolved in methanol, and conjectured that these might reassemble under suitable conditions into hybrid structures. We conjectured that the addition of phosphonate ligands would generate Strandberg-type rings. Both **1** and **2** are consistent with Strandberg-type ring systems.

The following synthetic points are worth noting:

- Combination of just *tert*-butylphosphonic acid and the Lindqvist hexamolybdate in methanol did not result in any reaction, returning only the starting materials. Therefore we can conclude that the rearrangement was not triggered by the addition of the phosphonate (*e.g. via* acid-promoted hydrolysis of the cluster)
- Piperazine and trimethylenedipyridine are both bases and N-donor ligands. However, substitution of either of these for other N-donor ligands, including pyridine (py) and picoline (pic), did not result in any reaction, despite their similarity (particularly to TDP). Therefore we can conclude that the rearrangement was not triggered simply by the addition of the N-donors (*e.g. via* base-promoted hydrolysis of the cluster)

Based on the above observations, we propose that the reaction truly does proceed *via* the (spontaneously generated) oligomeric molybdate intermediates that were observed in the previous section, and is not due to some ligand-triggered reaction (*e.g.* hydrolysis). The phosphonate ligand acts as a template for the reassembly of the oligomers, bringing molybdate oligomers into close enough contact for condensation to occur between them, but the phosphonate does not participate in the disassembly of the parent cluster.

The question remains as to why pip and TDP triggered the reaction, while similar N-donors such as py and pic did not. We attribute this to stabilisation of the end product in the solid state, rather than to some reaction in solution. It is well established that precipitation of POM compounds is highly sensitive to the presence of counterions. A common method of isolating a given POM is to add a suitable counterion to solution, resulting in the precipitation of the target compound (indeed the Lindqvist hexamolybdate was prepared in this way). In particular, pip-H_2 has previously been used as a cation for numerous Strandberg-type rings.[92–95] TDP-H_2 is less common but has also been used.[96]

Therefore, we propose that the pip-H_2 and TDP-H_2 cations represented geometrically suitable cations to the Strandberg ring structure that resulted in precipitation of an electrostatically stabilised solid state. This stable solid state provided a driving force for the reaction, sequestering the product out of solution and drawing the reaction equilibrium towards the formation of **1** and **2**. We propose that the py-H and pic-H could not generate a stable solid-state product through efficient electrostatic packing, and so the reaction equilibrium stayed on the side of the starting materials, resulting in no observable reaction.

We surmise that the presence of a templating ligand alone may be insufficient to drive reassembly in solution – there must be some stabilising influence in the final product, or else the equilibrium is not driven towards the products; hence the starting materials are recovered from the reaction mixture. The template is obviously significant, as it will dictate the form of the final product, but the final structure must be stabilised in some way relative to the parent cluster (Figure 2.5.1).

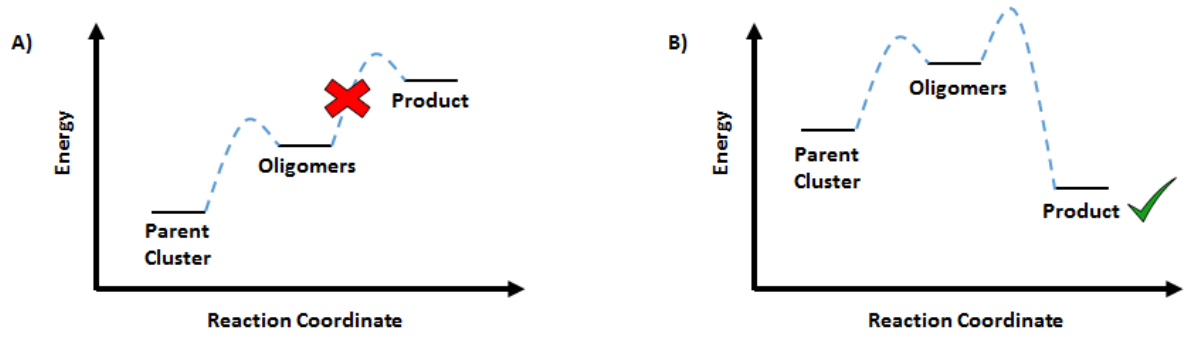

Figure 2.5.1 – Generalised energy diagrams for the disassembly-reassembly procedure. A) If the final product is not stabilised relative to the parent cluster, the equilibrium stays towards the left and the reaction might not proceed. B) If the product is stable relative to the parent cluster, the equilibrium shifts to the right and the product should form.

Solvent Choice

So far, we have considered the disassembly-reassembly procedure only in methanol. We have demonstrated that the Lindqvist hexamolybdate does disassemble spontaneously in methanol solution, and can be reassembled upon addition of a bias to generate hybrid compounds.

However, based on literature rearrangements of the Lindqvist hexamolybdate, we conjectured that acetonitrile might also be a suitable solvent for the disassembly-reassembly technique. Therefore, the syntheses of **1** and **2** were repeated using acetonitrile as the solvent. In both cases, the reaction proceeded as described above, generating white powders over the course of approximately one hour. The two powders were found to contain **1** and **2** respectively, based on IR measurements (Figures 2.5.2 and 2.5.3).

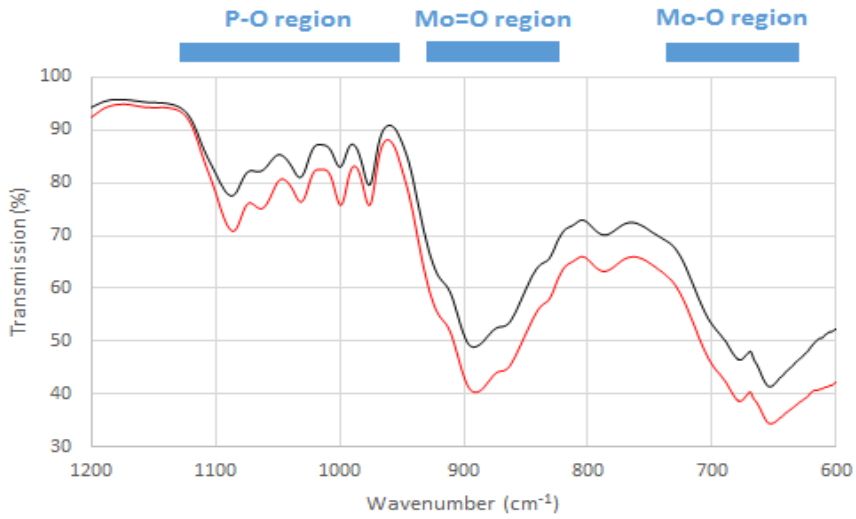

Figure 2.5.2 – Comparison of the infrared absorption frequencies (cm^{-1}) for powders containing 1, as synthesised from methanol (black) or acetonitrile (red).

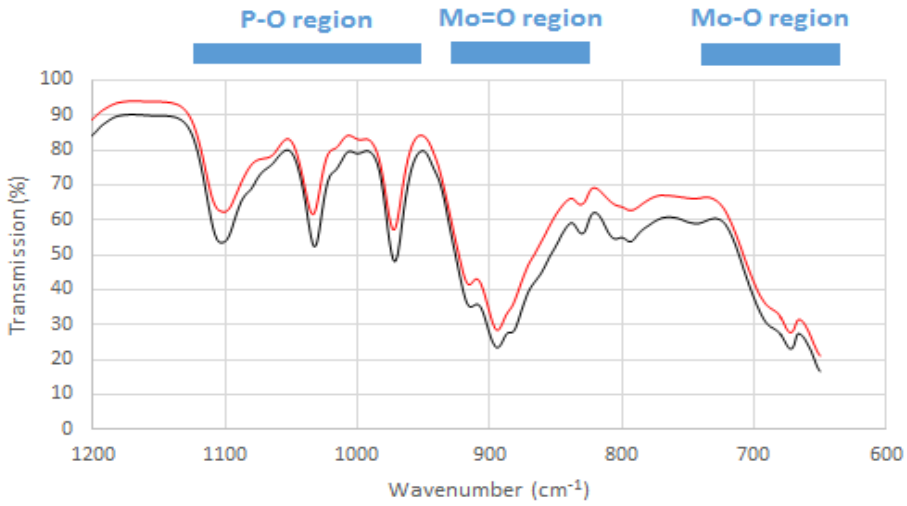

Figure 2.5.3 – Comparison of the infrared absorption frequencies (cm^{-1}) for powders containing 2, as synthesised from methanol (black) or acetonitrile (red).

Thus, acetonitrile also appears to be a suitable solvent for the disassembly-reassembly method, producing identical products to methanol as a solvent.

Moreover, after **2** was synthesised in acetonitrile, the solution was filtered and subsequently allowed to stand for several weeks. A single colourless crystal of suitable quality for analysis *via* single crystal X-ray diffraction (XRD) was obtained from this solution after approximately one month.

As anticipated, the crystal contained $[TDP\text{-}H_2]_2[Mo_5O_{15}(t\text{BuPO}_3)_2]$, **2**, along with two constituent acetonitrile molecules and two constituent water molecules. The crystal formed in the monoclinic space group *P*2/c.

The isolation of this crystal structure confirms the assignment of **1** and **2** based on their IR spectra as *tert*-butylphosphonate-substituted Strandberg-type ring systems.

The crystal structure displays an interesting packing motif in the crystalline state. Each Strandberg ring is charge-balanced by four protonated pyridyl groups, as expected, with the propylene linkages connecting the structure in to an electrostatically-bound pseudo-polymer system. Two TDP-H_2 molecules link between a pair Strandberg rings, while two more connect each pair to the neighbouring pair in a ladder motif (Figure 2.5.4). Water and acetonitrile molecules occupy the voids between each ladder-like pseudopolymer.

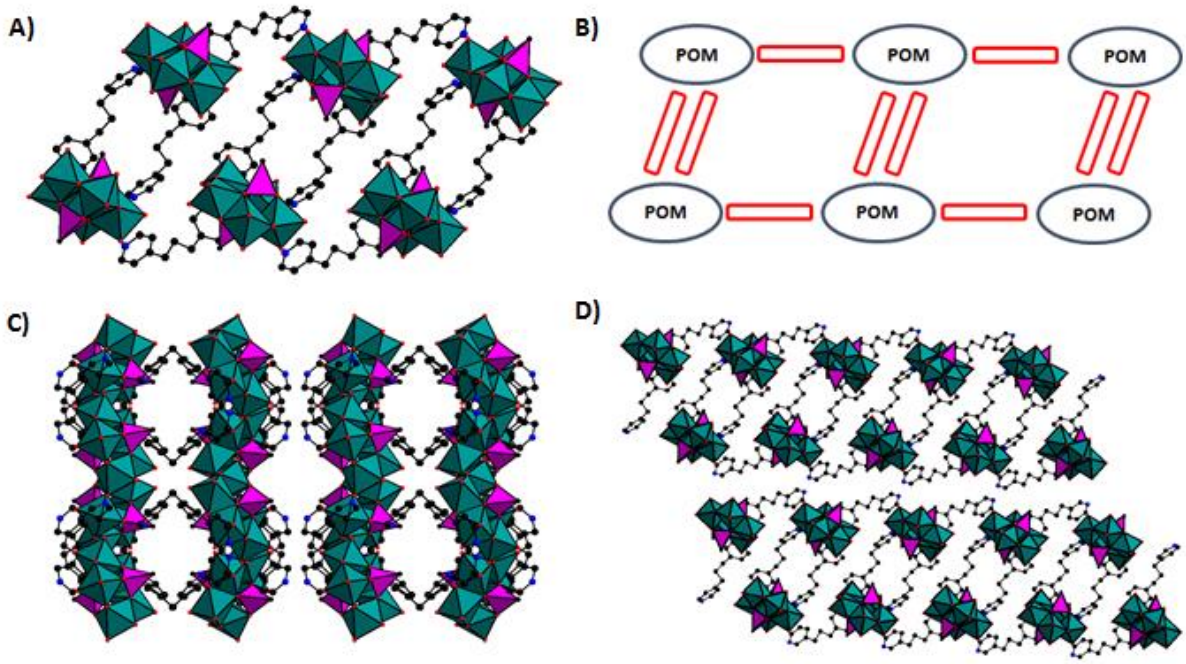

Figure 2.5.4 – A) The ladder-like repeating units in $[TDP\text{-}H_2]_2[Mo_5O_{15}(t\text{BuPO}_3)_2]$ (2), with solvent molecules removed and *tert*-butyl groups reduced to a C atom for clarity B) Schematic of the ladder-like connections, with the $[Mo_5O_{15}(t\text{BuPO}_3)_2]^{4-}$ units represented as "POM" and the protonated pyridyl ligands represented as red rectangles. C) The crystal packing of compound 2 as viewed down the crystallographic *a*-axis. D) The crystal packing of compound 2 as viewed down the crystallographic *b*-axis, showing the propagation of the ladder-like pseudopolymer units. Colour Scheme: Mo teal, P pink, O red, C black. H atoms omitted for clarity.

Given that the bulk sample of **2** precipitated over the course of about one hour whereas this crystal took approximately one month to form, we cannot necessarily conclude that the bulk sample also displays this ladder-like pseudopolymer structure (the bulk sample is completely amorphous, showing no peaks in a Powder X-ray Diffraction (PXRD) analysis). However, this crystal structure does demonstrate the type of solid-state stabilising interaction we proposed above, where the cation links between Strandberg rings to make a stable solid-state product, which pulls the equilibrium away from the parent cluster towards the new product.

Identification code	**2**•2(MeCN)•2(H_2O)
Empirical formula	$C_{152}H_{236}Mo_{20}N_{24}O_{92}P_8$
Formula weight (g/mol)	5800.32
Temperature (K)	100.15
Wavelength (Å)	1.54178
Crystal system	Monoclinic
Space group	*P*2/c
a (Å)	22.3468(7)
b (Å)	11.6096(4)
c (Å)	22.9061(7)
α (°)	90
β (°)	116.3740(10)
γ (°)	90
Volume ($Å^3$)	5324.1(3)
Z	1
Calculated density ρ_{calc} (g/cm^3)	1.809
Absorption coefficient μ (mm^{-1})	10.684
F(000)	2775.0
2Θ range for data collection (°)	7.614 to 131.722
Index ranges	$-26 \leq h \leq 26$, $-13 \leq k \leq 11$, $-26 \leq l \leq 25$
Reflections collected	30325
Independent reflections	8719 [R_{int} = 0.0457]
Data/restraints/parameters	8719/0/681
Goodness-of-fit on F^2	1.054
Final R indices [I>=2σ (I)]	R_1 = 0.0298, wR_2 = 0.0773
Final R indices [all data]	R_1 = 0.0317, wR_2 = 0.0787
Largest diff. peak and hole (e $Å^{-3}$)	0.93/-0.74

Table 2.5.1 – Crystallographic details for 2•2(MeCN)•2(H_2O)

Metal Atom	Bonded Atom	Bond Length (Å)	BVS	Oxidation State
Mo(1)	O(17)	1.7136(1)	5.914	+VI
	O(18)	1.7174(1)		
	O(8)	1.8995(1)		
	O(2)	1.9456(1)		
	O(15)	2.3037(1)		
	O(13)	2.3593(1)		
Mo(2)	O(3)	1.7005(1)	5.917	+VI
	O(23)	1.7219(1)		
	O(1)	1.9238(1)		
	O(2)	1.9586(1)		
	O(13)	2.2144(1)		
	O(16)	2.4056(1)		
Mo(3)	O(5)	1.7115(1)	6.014	+VI
	O(9)	1.7207(1)		
	O(4)	1.8982(1)		
	O(1)	1.9000(1)		
	O(16)	2.3286(1)		
	O(11)	2.3515(1)		
Mo(4)	O(6)	1.7005(1)	5.955	+VI
	O(10)	1.7144(1)		
	O(4)	1.9161(1)		
	O(7)	1.9657(1)		
	O(14)	2.1990(1)		
	O(11)	2.4320(1)		
Mo(5)	O(22)	1.6986(1)	6.026	+VI
	O(21)	1.7193(1)		
	O(8)	1.9117(1)		
	O(7)	1.9309(1)		
	O(12)	2.2174(1)		
	O(14)	2.4172(1)		

Table 2.5.2 – Crystallographically-determined bond lengths for the molybdenum centres in 2, along with their oxidation state as determined by Bond Valence Sum (BVS) analysis.

Bond lengths in **2** vary depending on the type of O-donor ligand (Table 2.5.2). Terminal *oxo*- ligands display Mo-O bond lengths around 1.7 Å, bridging *oxo*- ligands around 1.9 Å, and phosphonate O-donors display bond lengths in the 2.2-2.4 Å range. These bond lengths are all consistent with Strandberg-type ring systems in the literature.[85,86]

Bond Valence Sum (BVS) analysis is used to demonstrate the oxidation states of the metal centres based on bond length. BVS is defined as:

$$BVS = \sum exp\frac{(B_0 - B_i)}{b}$$

B_i represents a given bond length, B_o represents an idealised bond length for a given pair of atoms, and b represents an empirical constant. BVS analysis confirms that all Mo centres in **2** are in oxidation state +VI.

Given the success in generating both **1** and **2** from acetonitrile, we concluded that the reactions probably went through similar intermediates as proposed for the methanol case (*i.e.* mononuclear, dinuclear and trinuclear molybdate oligomers that reassembled into a five membered ring *via* condensation reaction under a phosphonate templating effect).

As acetonitrile is also a suitable volatile solvent for ESI analysis, we attempted to analyse possible disassembly fragments of the Lindqvist hexamolybdate in acetonitrile as well. However, $[TBA]_2[Mo_6O_{19}]$ is considerably more soluble in acetonitrile than methanol. Therefore, in simple repetitions of the ESI-MS analysis from the previous section, signals corresponding to the parent cluster dominated the spectra, and no disassembly oligomers were observed.

However, the reaction system behaves almost identically in both acetonitrile as in methanol – the reaction is not triggered by *tert*-butylphosphonate alone, nor the addition of N-donors such as pyridine or picoline, occurs over a similar timescale, and produces identical products (constituent solvents notwithstanding). These facts indicate that a very similar mechanism may occur in the acetonitrile and methanol cases. Therefore, we propose that the Lindqvist hexamolybdate also undergoes spontaneous disassembly to oligomeric molybdate species in acetonitrile, although we have no direct evidence for the existence of such oligomers.

2.6) Conclusions and Outlook

In summary, we have outlined a synthetic approach towards novel POM compounds by exploiting a "top-down" method consisting of distinct assembly, disassembly and reassembly steps.

The Lindqvist hexamolybdate was chosen as a suitable precursor POM, and was assembled from the monomeric starting material according to literature procedures.

ESI-MS analyses were used to demonstrate that the Lindqvist hexamolybdate undergoes spontaneous disassembly in methanol at room temperature without perturbing the system. Under these conditions, the parent POM species can be seen in equilibrium with a series of oligomeric molybdate species. CV variation experiments indicate that these observations are not generated *in situ* during the analysis.

Reassembly of the resulting oligomers was achieved by the addition of *tert*-butylphosphonic acid to the reaction mixture. Two substituted Strandberg-type ring systems were generated in this fashion, $[TBA]_4[Mo_5O_{15}(t\text{BuPO}_3)_2]$ (**1**) and $[TDP\text{-}H_2]_2[Mo_5O_{15}(t\text{BuPO}_3)_2]$ (**2**), depending on counterions available in the system. The phosphonate species acted as a template for a five-membered ring system, triggering reassembly of the molybdate oligomers present in solution into the product species.

Thus, the assembly-disassembly-reassembly methodology has been demonstrated to work in principle, generating two hybrid POM compounds that would normally be accessed using purely bottom-up approaches.

Having demonstrated the principle, this methodology can now be expanded to other systems. In particular, we are interested in applying this methodology towards the generation of TMS-POM species by the incorporation of heterometals into the reaction system. We anticipate that similar templating effects should be seen in mixed-metal systems, but with potentially new geometries being accessible *via* the differing coordination modes of the heterometals.

Over the next three chapters, the synthesis of TMS-POMs *via* the assembly-disassembly-reassembly methodology will be explored.

2.7) References

1 S. Xing, Q. Han, Z. Shi, S. Wang, Y. Peipei, Q. Wu and X. Li, *Dalton Trans.*, 2017, **46**, 11537.

2 D. Sloboda-Rozner, P. L. Alsters and R. Neumann, *J. Am. Chem. Soc.*, 2003, **125**, 5280.

3 Z. Zhang, J. Zhao and G. Yang, *Eur. J. Inorg. Chem.*, 2017, **3**, 3244.

4 S. Vanhaecht, T. Quanten and T. N. Parac-Vogt, *Dalton Trans.*, 2017, **46**, 10215.

5 Y. Ding, J. Peng, S. Khan and Y. Yuan, *Chem. Eur. J.*, 2017, **23**, 10338.

6 G. A. Tsigdinos and C. J. Hallada, *Inorg. Chem.*, 1968, **7**, 437.

7 L. Fan, K. Yu, J. Lv, H. Zhang, Z. Su, L. Wang, C. Wang and B. Zhou, *Dalton Trans.*, 2017, **46**, 10355.

8 K. Kastner, J. Forster, H. Ida, G. N. Newton, H. Oshio and C. Streb, *Chem. Eur. J.*, 2015, **21**, 7686.

9 T. Auvray, M.-P. Santoni, B. Hasenknopf and G. S. Hanan, *Dalton Trans.*, 2017, **46**, 10029.

10 J. Li, I. Huth, L. Chamoreau, B. Hasenknopf, E. Lacôte, S. Thorimbert and M. Malacria, *Angew. Chem. Int. Ed.*, 2009, **48**, 2035.

11 M. Piot, S. Hupin, H. Lavanant, C. Afonso, Bouteiller, A. Proust and G. Izzet, *Inorg. Chem.*, 2017, **56**, 8490.

12 X. Wang, S. Liu, Y. Liu, D. He, N. Li, J. Miao, Y. Ji and G. Yang, *Inorg. Chem.*, 2014, **53**, 13130.

13 L. Zhang, T. Cui, X. Cao, C. Zhao, Q. Chen, L. Wu and H. Li, *Angew. Chem. Int. Ed.*, 2017, **56**, 9013.

14 J. Cai, X. Zheng, J. Xie, Z. Yan, X. Kong, Y. Ren, L. Long and L. Zheng, *Inorg. Chem.*, 2017, **56**, 8439.

15 P. Huang, H. Wu, M. Huang, M. Du, C. Qin, X. Wang and Z. Su, *Dalton Trans.*, 2017, **46**, 10177.

16 C. P. Pradeep, D. Long, C. Streb and L. Cronin, *J. Am. Chem. Soc.*, 2008, **130**, 14946.

17 T. Hoshino, R. Isobe, T. Kaneko, Y. Matsuki and K. Nomiya, *Inorg. Chem.*, 2017, **56**, 9585.

18 M. Martin-Sabi, R. S. Winter, C. Lydon, J. M. Cameron, D. Long and L. Cronin, *Chem. Commun.*, 2016, **52**, 919.

19 E. F. Wilson, H. Abbas, B. J. Duncombe, C. Streb, D. Long and L. Cronin, *J. Am. Chem. Soc.*, 2008, **130**, 13876.

20 H. Abbas, A. L. Pickering, D. Long, P. Kögerler and L. Cronin, *Chem. Eur. J.*, 2005, **11**, 1071.

21 H. Abbas, C. Streb, A. L. Pickering, A. R. Neil, D. Long and L. Cronin, *Cryst. Growth Des.*, 2008, **8**, 635.

22 S. Chen, C. Lu, Y. Yu, Q. Zhang and X. He, *Inorg. Chem. Commun.*, 2004, **7**, 1041.

23 E. F. Wilson, H. N. Miras, M. H. Rosnes and L. Cronin, *Angew. Chem. Int. Ed.*, 2011, **50**, 3720.

24 H. T. Evans, *J. Am. Chem. Soc.*, 1948, **70**, 1291.

25 M. T. Pope, *Heteropoly and Isopoly Oxometaltes*, Springer-Verlag, Berlin, 1983.

26 A. Perloff, *Inorg. Chem.*, 1970, **9**, 2228.

27 K. Nomiya, T. Takahashi, T. Shirai and M. Miwa, *Polyhedron*, 1987, **6**, 213.

28 B. Hasenknopf, R. Delmont, P. Herson and P. Gouzerh, *Eur. J. Inorg. Chem.*, 2002, 1081.

29 P. R. Marcoux, B. Hasenknopf, J. Vaissermann and P. Gouzerh, *Eur. J. Inorg. Chem.*, 2003, 2406.

30 Y. Song, D. Long and L. Cronin, *Angew. Chem. Int. Ed.*, 2007, **46**, 3900.

31 Y. Song, D. Long, S. E. Kelly and L. Cronin, *Inorg. Chem.*, 2008, **47**, 9137.

32 J. Zhang, Y. Song, L. Cronin and T. Liu, *J. Am. Chem. Soc.*, 2008, **130**, 14408.

33 J. Fuchs and I. Brudgam, *Z. Naturforsch, Tl. B*, 1977, **32**, 403.

34 R. Delmont, A. Proust, F. Robert, P. Herson and P. Gouzerh, *C. R. Acad. Sci. Paris*, 2000, **3**, 147.

35 Y. Song, N. McMillan, D. Long, S. Kane, J. Malm, M. O. Riehle, C. P. Pradeep, N. Gadegaard and L. Cronin, *J. Am. Chem. Soc.*, 2009, **131**, 1340.

36 S. Schçnweiz, S. A. Rommel, J. Kübel, M. Micheel, B. Dietzek, S. Rau and C. Streb, *Chem. Eur. J.*, 2016, **22**, 12002.

37 S. Schönweiz, D. Sorsche, B. Schwarz, S. Rau and C. Streb, *Dalton Trans.*, 2017, **46**, 9760.

38 Y. Ji, J. Hu, L. Huang, W. Chen, C. Streb and Y. Song, *Chem. Eur. J.*, 2015, **21**, 6469.

39 F.-J. Yazigi, C. Wilson, D. Long and R. S. Forgan, *Cryst. Growth Des.*, 2017, **17**, 4739.

40 I. Lindqvist, *Acta Crystallogr.*, 1952, **5**, 667.

41 S. Bartley, S. Bernstein and K. R. Dunbar, *Inorganica Chim. Acta*, 1993, **213**, 213.

42 P. A. Abramov, M. N. Sokolov, S. Floquet, M. Haouas, F. Taulelle, E. Cadot, E. V Peresypkina, A. V Virovets, C. Vicent, N. B. Kompankov, A. A. Zhdanov, O. V Shuvaeva and V. P. Fedin, *Inorg. Chem.*, 2014, **53**, 12791.

43 D. Li, J. Song, P. Yin, S. Simotwo, A. J. Bassler, Y. Aung, J. E. Roberts, K. I. Hardcastle, C. L. Hill and T. Liu, *J. Am. Chem. Soc.*, 2011, **133**, 14010.

44 N. J. Hur, W. G. Klemperer and R. C. Wang, *Inorg. Synth.*, 1990, **27**, 77.

45 M. Filowitz, R. K. C. Ho, W. G. Klemperer and W. Shum, *Inorg. Chem.*, 1979, **18**, 93.

46 W. G. Klemperer and W. Shum, *J. Am. Chem. Soc.*, 1976, **98**, 8291.

47 A. Ben, J. Chékir-Mzali, K. Ezzayani, S. Freslon and M. S. Belkhiria, *Inorg. Chem. Commun.*, 2016, **70**, 56.

48 H. Zang, K. Tan, W. Guan, S. Li, G. Yang, K. Shao, L. Yan and Z.-M. Su, *CrystEngComm*, 2010, **12**, 3684.

49 Y. Shi, W. Yang, G. Xue, H. Hu and J. Wang, *J. Mol. Struct.*, 2006, **784**, 244.

50 L. Wang, P. Yin, J. Zhang, J. Hao, C. Lv, F. Xiao and Y. Wei, *Chem. Eur. J.*, 2011, **17**, 4796.

51 Y. Huang, J. Zhang, J. Hao and Y. Wei, *Sci. Rep.*, 2016, **6**, 24759.

52 J. B. Strong, B. S. Haggerty, L. Rheingold and E. A. Maatta, *Chem. Commun.*, 1997, 1137.

53 J. Hao, Y. Xia, L. Wang, L. Ruhlmann, Y. Zhu, Q. Li, P. Yin, Y. Wei and H. Guo, *Angew. Chem. Int. Ed.*, 2008, **47**, 2626.

54 J. L. Stark, V. G. Young and E. A. Maatta, *Angew. Chem. Int. Ed.*, 1995, **720**, 7.

55 W. Clegg, R. J. Errington, K. A. Fraser, S. A. Holmes and A. Schafer, *J. Chem. Soc. Commun.*, 1995, 455.

56 A. Proust, R. Thouvenot, F. Robert and P. Gouzerh, *Inorganica Chim. Acta*, 1994, **224**, 81.

57 J. L. Stark, A. L. Rheingold and E. A. Maatta, *J. Chem. Soc., Chem. Commun*, 1995, 1165.

58 A. R. Moore, H. Kwen, A. M. Beatty and E. A. Maatta, *Chem. Commun.*, 2000, **996**, 1793.

59 J. Zhang, J. Hao, Y. Wei, F. Xiao, P. Yin and L. Wang, *J. Am. Chem. Soc.*, 2010, **132**, 14.

60 Q. Li, P. Wu, Y. Xia, Y. Wei and H. Guo, *J. Organomet. Chem.*, 2006, **691**, 1223.

61 Y. Du, A. L. Rheingold and E. A. Maatta, *J. Am. Chem. Soc.*, 1992, 345.

62 M. Cortes, M. Fuentealba, C. Mazur and D. Carrillo, *J. Chil. Chem. Soc.*, 2008, **53**.

63 X. Yang, T. Waters, X. B. Wang, R. A. J. O'Hair, A. G. Wedd, J. Li, D. A. Dixon and L. S. Wang, *J. Phys. Chem. A*, 2004, **108**, 10089.

64 M. J. Deery, O. W. Howarth and K. R. Jennings, *J. Chem. Soc. Dalton Trans.*, 1997, 4783.

65 D. R. Lide, *CRC Handb. Chem. Phys.*, 2006, **7**, 87.

66 R. Colton and J. C. Traeger, *Inorganica Chem. Acta*, 1992, **201**, 153.

67 A. J. Surman, P. J. Robbins, J. Ujma, Q. Zheng, P. E. Barran and L. Cronin, *J. Am. Chem. Soc.*, 2016, **138**, 3824.

68 K. Scheubert, F. Hufsky and S. Bocker, *J. Cheminform.*, 2013, **5**, 12.

69 S. F. Ralph, M. M. Sheil, L. A. Hick, R. J. Geue and A. M. Sargeson, *J. Chem. Soc. Dalton Trans.*, 1996, 4417.

70 V. A. Pashynska, M. V. Kosevich, H. Van Den Heuvel and M. Claeys, *Rapid Commun. Mass Spectrom.*, 2006, **20**, 755.

71 W. Henderson and S. McIndoe, *Mass Spectrometry of Inorganic and Organometallic Compounds*, 2005.

72 R. B. Cole, *Electrospray Ionization Mass Spectrometry: Fundamentals, Instrumentation and Applications*, 1997.

73 C. I. Onet, L. Zhang, R. Clérac, J. B. Jean-Denis, M. Feeney, T. McCabe and W. Schmitt, *Inorg. Chem.*, 2011, **50**, 604.

74 L. Zhang, R. Clérac, P. Heijboer and W. Schmitt, *Angew. Chem. Int. Ed.*, 2012, **51**, 3007.

75 L. Zhang, R. Clérac, C. I. Onet, M. Venkatesan, P. Heijboer and W. Schmitt, *Chem. Eur. J.*, 2012, **18**, 13984.

76 D. Sahoo, R. Suriyanarayanan, R. K. Metre and V. Chandrasekhar, *Dalton Trans.*, 2014, **43**, 7304.

77 C. I. Onet, L. Zhang, R. Clérac, J. B. Jean-Denis, M. Feeney, T. McCabe and W. Schmitt, *Inorg. Chem.*, 2011, **50**, 604.

78 L. Zhang and W. Schmitt, *J. Am. Chem. Soc.*, 2011, **133**, 11240.

79 R. Villanneau, D. Racimor, E. Messner-Henning, H. Rousseliere, S. Picart, R. Thouvenot and A. Proust, *Inorg. Chem.*, 2011, **50**, 1164.

80 M. Carraro, A. Sartorel, G. Scorrano, C. Maccato, M. H. Dickman, U. Kortz and M. Bonchio, *Angew. Chem. Int. Ed.*, 2008, **47**, 7275.

81 M. P. Lowe, J. C. Lockhart, G. A. Forsyth, W. Clegg and K. A. Fraser, *J. Chem. Soc. Dalton Trans.*, 1995, 146.

82 Y. Chang and J. Zubieta, *Inorganica Chim. Acta*, 1996, **245**, 177.

83 L. Yan, Z. Su, K. Tan, M. Zhang, L. Qu and R. Wang, *J. Quantum Chem.*, 2005, **105**, 37.

84 H. I. Buvailo, G. Makhankova, V. N. Kokozay, I. V Omelchenko, S. V Shishkina, P. Zabierowski, D. Matoga and J. Jezierska, *Eur. J. Inorg. Chem.*, 2017, **22**, 3525.

85 J. K. Stalick and C. Quicksall, *Inorg. Chem.*, 1976, **15**, 1577.

86 W. Kwak, M. T. Pope and T. F. Scully, *J. Am. Chem. Soc.*, 1975, **97**, 5737.

87 B. Liu and Y. T. Ku, *Inorganica Chim. Acta*, 1989, **161**, 233.

88 T. Hori, S. Himeno and O. Tamada, *J. Chem. Soc. Dalton Trans.*, 1992, 275.

89 T. Ozeki, H. Ichida, H. Miyamame and Y. Sasaki, *Bull. Chem. Soc. Jpn.*, 1988, **61**, 4455.

90 M. P. Lowe, J. C. Lockhart, W. Clegg and K. A. Fraser, *Angew. Chem. Int. Ed.*, 1994, **33**, 451.

91 U. Kortz, J. Vaissermann, R. Thouvenot and P. Gouzerh, *Inorg. Chem.*, 2003, **42**, 1135.

92 W. T. A. Harrison, L. Dussack and A. Jacobson, *Acta Crystallogr. Sect. C*, 1997, **53**, 200.

93 W. T. A. Harrison, L. Dussack and A. Jacobson, *Acta Crystallogr. Sect. C*, 1997, **53**, 856.

94 X. Zhang, R.-Q. Fang, H. Wu and S. W. Ng, *Acta Crystallogr. Sect. E*, 2004, **60**, 171.

95 L. Paul, M. Dolai, A. Panja and M. Ali, *New J. Chem.*, 2016, **40**, 6931.

96 X. Qu, L. Xu, Y. Yang, F. Li and W. Guo, *Struct. Chem.*, 2011, **22**, 965.

Chapter 3

Hybrid Copper-Polyoxomolybdates

3.1) Copper in POM Chemistry

In the previous Chapter, we demonstrated the disassembly behaviour of the Lindqvist hexamolybdate in methanol, and exploited this behaviour to synthesise Strandberg-type hybrid POM systems.

Having demonstrated the efficacy of this disassembly-reassembly technique to generate hybrid systems, we turned our attention towards generating mixed-metal compounds. Mixed metal TMS-POM compounds can in principle display additional functionality in comparison to single metal systems.

Paramagnetic metal centres offer more interesting magnetic properties than the diamagnetic metal centres typically seen in POM clusters. Magnetic compounds have wide-ranging practical applications, including electronics, data storage and transmission, diagnostics and sensing.[1–7] Paramagnetic metal centres within a POM structure in particular can be used to study magnetic interactions of relatively isolated paramagnetic centres in defined environments.[8–16] Many examples of paramagnetic TMS-POMs have been characterised using a variety of metals, in particular in a POM-sandwich motif, including Mn, Fe, Ni, etc.[17–26]

We identified copper (II)-containing TMS-POM structures as a suitable synthetic target, for the following reasons:

- Copper is an earth abundant metal, and is therefore readily accessible and not prohibitively expensive. Copper (II) salts are commercially available with a variety of counterions, including chloride, acetate, nitrate and sulfate.
- Copper (II) centres can access multiple possible coordination geometries and thus may be synthetically more flexible than other alternatives.[27] This may facilitate incorporation of copper (II) into a TMS-POM cluster.
- Copper (II) centres possess an S=1/2 ground state which offers an ideal, relatively simple magnetic system for study. Compounds with odd numbers of copper (II) centres are particularly interesting as these represent spin-frustrated cluster entities, which cannot achieve an overall S=0 ground state *via* ferromagnetic coupling of the spin centres.[28–32]

Despite these apparent advantages, copper (II) substituted molybdates are relatively rare. In contrast to copper (II) tungstates, of which many examples exist,[33–36] traditional synthetic attempts to combine copper (II) with molybdate POMs tend to produce compounds where a terminal *oxo*- ligand on a POM unit acts as a loosely-bound ligand to a copper centre, rather than binding a copper centre into the POM core[37–41] (with the exception of some Anderson-type copper-molybdates[42–44]). The disassembly-reassembly technique, therefore, could potentially represent a plausible alternative route towards these interesting compounds.

Therefore, we set out to exploit our disassembly-reassembly approach to generate copper (II) cluster compounds by incorporating a copper (II) salt into a very similar reaction mixture that generated compounds **1**. Two compounds were isolated from this procedure, which shall be described over the next Chapter.

3.2) $[TBA]_2[Mo^{VI}_6Cu^{II}_4O_{16}(OH)_2(tBuPO_3)_4(py)_2(CH_3O)_4(H_2O)]$, (3)

$[TBA]_2[Mo^{VI}_6Cu^{II}_4O_{16}(OH)_2(t\text{BuPO}_3)_4(py)_2(CH_3O)_4(H_2O)]$, (**3**), where TBA represents tetrabutylammonium, *t*-Bu represents the *tert*-butyl moiety and py represents pyridine, was synthesised from the reaction of copper (II) acetate with *tert*-butylphosphonic acid and Lindqvist hexamolybdate in methanol in the presence of pyridine. After several weeks of slow solvent evaporation, pale blue plate-like crystals that contain **3** can be separated manually from the large green block crystals that form alongside them (these green crystals will be discussed in more detail later).

The pale blue crystals were subjected to single crystal X-ray diffraction and found to contain **3**, along with two constituent methanol molecules and one constituent water molecule, in the monoclinic crystal system in space group $P2_1/C$ (Table 3.2.1).

The cluster core in **3** contains four copper centres and six molybdenum centres. Formally, the structure can be conceptualised as two $\{Mo_3\}$ units encapsulating a $\{Cu_4\}$ core in a sandwich motif (Figure 3.2.1). The two $\{Mo_3\}$ units are stabilised by a total of sixteen *oxo*- ligands, in either terminal or bridging modes. The $\{Cu_4\}$ unit is bridged by two μ_3-OH hydroxyl moieties. The $\{Mo_3\}$ and $\{Cu_4\}$ units are bridged together by four μ_2-O bridging methoxy- ligands, as well as four fully deprotonated *tert*-butylphosphonate ligands which each coordinate to five metal centres each. The coordination spheres of the $\{Cu_4\}$ core are completed by two pyridine ligands and one water ligand.

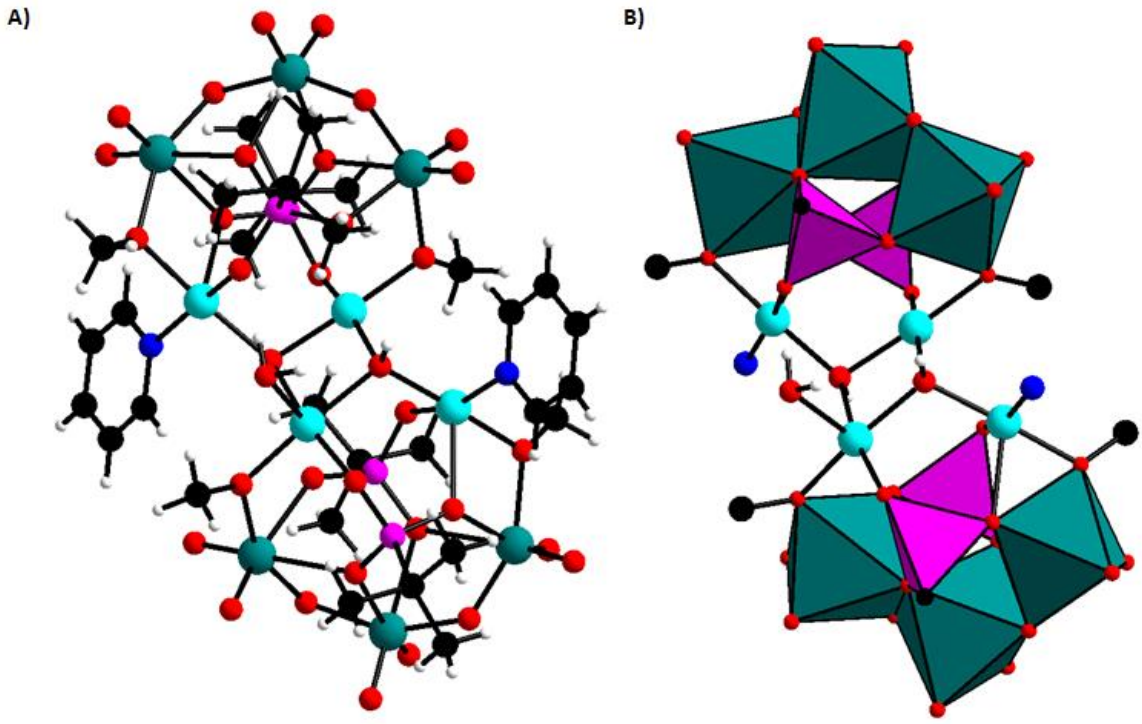

Figure 3.2.1 – A) Full representation of the $[Mo^{VI}_6Cu^{II}_4O_{16}(OH)_2(t\text{BuPO}_3)_4(py)_2(CH_3O)_4(H_2O)]^{2-}$ cluster in 3. B) Simplified representation of the same cluster - molybdate and phosphonate moieties are shown as polyhedra, pyridine and *tert*-butyl groups are reduced to single N and C atoms respectively, and H atoms are removed from the methoxy groups. Colour Scheme: Mo teal, Cu light blue, P pink, O red, N blue, C black, H white.

Identification code	**3**•2(MeOH)•(H_2O)
Empirical formula	$C_{64}H_{144}Cu_4Mo_6N_4O_{38}P_4$
Formula weight (g/mol)	2531.50
Temperature (K)	100(2)
Wavelength (Å)	0.71073
Crystal system	Monoclinic
Space group	$P2_1/c$
a (Å)	33.787(3)
b (Å)	13.6491(10)
c (Å)	22.4826(16)
α (°)	90
β (°)	105.0681(13)
γ (°)	90
Volume ($Å^3$)	10011.6(13)
Z	4
Calculated density ρ_{calc} (g/cm^3)	1.680
Absorption coefficient μ (mm^{-1})	1.698
F(000)	5152
Crystal size (mm^3)	0.160 x 0.120 x 0.060
2Θ range for data collection (°)	3.234 to 55.056
Index ranges	$-43 \leq h \leq 43$, $-17 \leq k \leq 17$, $-29 \leq l \leq 29$
Reflections collected	356699
Independent reflections	23014 [R_{int} = 0.0589]
Data/restraints/parameters	23014/10/1121
Goodness-of-fit on F^2	1.087
Final R indices [I>=2σ (I)]	R_1 = 0.0388, wR_2 = 0.0873
Final R indices [all data]	R_1 = 0.0554, wR_2 = 0.0951
Largest diff. peak and hole (e $Å^{-3}$)	1.801/-1.177

Table 3.2.1 – Crystallographic details for compound 3•2(MeOH)•(H_2O).

The two crystallographically distinct tetrabutylammonium cations both display crystallographic disorder. The N(3) cation is modelled as completely disordered over two positions with occupancy 67/33%. The N(4) cation is modelled with one carbon atom (C(59)) disordered over two positions with occupancy 55/45%.

{Mo_3} units

The {Mo_3} units in **3** can be conceptualised as three edge-sharing {MoO_6} distorted octahedra in a bend arrangement (Figure 3.2.2). Mo(1) is stabilised by three *oxo*- ligands, two of which are terminal, O(5) and O(6). The third *oxo*- ligand, O(7), and a bridging phosphonate O-donor, O(8), represent the shared edge with the Mo(2) octahedron. A bridging methoxy ligand O(3) and another bridging phosphonate O-donor O(4) bridge to the copper centre Cu(1). Mo(1), Mo(3), Mo(4) and Mo(6) all have equivalent coordination environments.

Mo(2) and Mo(5) are the central Mo centres of their respective {Mo_3} units, and so have equivalent environments to each other. They do not have any interactions with copper centres, with bridging interactions only taking place to other Mo centres. Mo(2) also possesses two terminal *oxo*- ligands, O(9) and O(10). The bridging *oxo*- ligand O(7) and bridging phosphonate O-donor O(8) form a shared edge with the Mo(1) octahedron while the bridging *oxo*- ligand O(11) and bridging phosphonate O-donor O(12) form a shared edge with the Mo(3) octahedron.

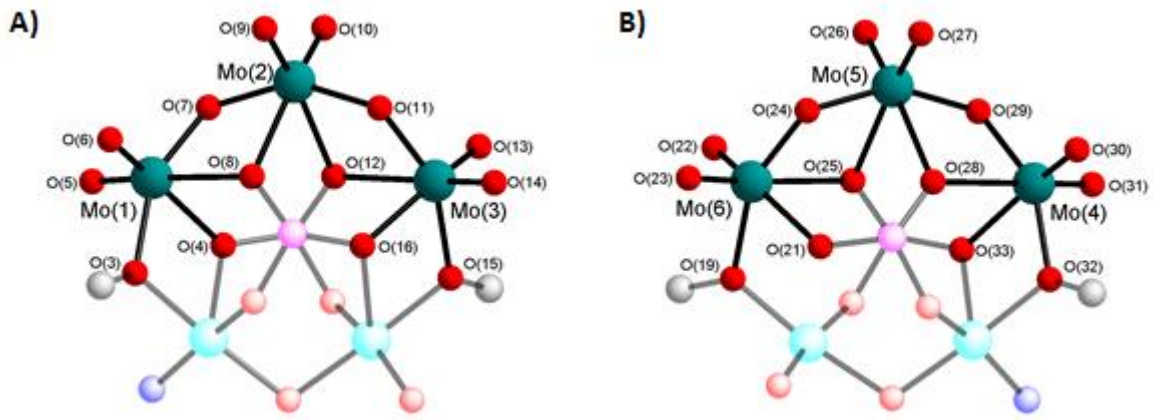

Figure 3.2.2 – The two {Mo_3} moieties in 3. A) Mo(1)-Mo(3). B) Mo(4)-Mo(6). Atoms outside the direct coordination spheres of the molybdenum atoms are partially faded out. Colour Scheme: Mo teal, Cu light blue, P pink, O red, N blue, C black.

In the previous Chapter, it was demonstrated that the Lindqvist hexamolybdate disassembles in methanol. There was some evidence for the existence of a [TBA][Mo_3O_{10}]$^-$ species in solution (*c.f.* Table 2.3.2), but the evidence was somewhat weak (*c.f.* Figure 2.3.13).

However, the presence of {$Mo_3O_8(OCH_3)_2$} moieties in **3** supports the hypothesis that {Mo_3O_{10}} species may exist in solution. The {$Mo_3O_8(OCH_3)_2$} moieties could arise from the {Mo_3O_{10}} species *via* substitution of two *oxo*- ligands with methoxy ligands.

Alternatively, the {$Mo_3O_8(OCH_3)_2$} moieties could arise from condensation reactions between mononuclear or dinuclear molybdate fragments.

Metal Atom	Bonded Atom	Bond Length (Å)	BVS	Oxidation State
Mo(1)	O(6)	1.700(3)	5.988	+VI
	O(5)	1.702(3)		
	O(7)	1.887(3)		
	O(3)	2.050(3)		
	O(4)	2.176(3)		
	O(8)	2.380(3)		
Mo(2)	O(10)	1.694(3)	6.016	+VI
	O(9)	1.704(3)		
	O(7)	1.920(3)		
	O(11)	1.937(3)		
	O(12)	2.306(3)		
	O(8)	2.373(3)		
Mo(3)	O(14)	1.703(3)	5.961	+VI
	O(13)	1.714(3)		
	O(11)	1.872(3)		
	O(15)	2.061(2)		
	O(16)	2.137(3)		
	O(12)	2.432(3)		
Mo(4)	O(27)	1.699(4)	6.009	+VI
	O(26)	1.701(3)		
	O(24)	1.922(3)		
	O(29)	1.936(3)		
	O(25)	2.329(3)		
	O(28)	2.341(2)		
Mo(5)	O(31)	1.670(3)	5.961	+VI
	O(30)	1.710(3)		
	O(29)	1.870(2)		
	O(32)	2.044(2)		
	O(33)	2.180(3)		
	O(28)	2.443(3)		
Mo(6)	O(23)	1.695(3)	5.981	+VI
	O(22)	1.712(3)		
	O(24)	1.881(3)		
	O(19)	2.052(3)		
	O(21)	2.157(3)		
	O(25)	2.412(3)		

Table 3.2.2 – Crystallographically-determined bond lengths for the molybdenum centres in 3, along with their oxidation state as determined by Bond Valence Sum (BVS) analysis.

The crystallographically determined Mo-O bond lengths in **3** range from 1.694(3) Å to 2.443(3) Å, depending on the type of O-donor (Table 3.2.2). Terminal *oxo*- ligands display Mo-O bond lengths of roughly 1.7 Å, bridging *oxo*- ligands display Mo-O bond lengths around 1.9 Å and bridging methoxy ligands display Mo-O bond lengths of around 2.0 Å. Phosphonate O-donors display more variation in Mo-O bond lengths, roughly in the range of 2.2 Å to 2.4 Å. All Mo-O bond lengths observed crystallographically in **3** are consistent with similar complexes observed in the literature.[45–48] When subjected to Bond Valence Sum (BVS) analysis, all bond lengths are consistent with Mo centres in oxidation state +VI.

Bond	Bond Angle (°)	Bond	Bond Angle (°)
O(7)-Mo(1)-O(8)	73.35(11)	O(7)-Mo(2)-O(8)	72.97(11)
O(3)-Mo(1)-O(4)	74.88(10)	O(11)-Mo(2)-O(12)	73.58(10)
O(4)-Mo(1)-O(8)	75.73(9)	O(12)-Mo(2)-O(8)	75.69(9)
O(7)-Mo(1)-O(4)	84.20(11)	O(11)-Mo(2)-O(8)	82.32(10)
O(3)-Mo(1)-O(8)	85.33(10)	O(7)-Mo(2)-O(12)	83.11(10)
O(6)-Mo(1)-O(8)	87.43(12)	O(9)-Mo(2)-O(8)	88.86(12)
O(6)-Mo(1)-O(3)	91.43(14)	O(10)-Mo(2)-O(12)	91.89(12)
O(5)-Mo(1)-O(4)	93.87(12)	O(9)-Mo(2)-O(11)	98.03(13)
O(5)-Mo(1)-O(3)	97.86(13)	O(9)-Mo(2)-O(7)	98.98(13)
O(5)-Mo(1)-O(7)	100.01(14)	O(10)-Mo(2)-O(7)	99.84(14)
O(6)-Mo(1)-O(7)	103.26(14)	O(10)-Mo(2)-O(11)	100.25(14)
O(6)-Mo(1)-O(5)	103.99(14)	O(10)-Mo(2)-O(9)	104.14(15)
Angle Variance (σ^2)	**120.2**	**Angle Variance (σ^2)**	**129.3**
Distortion Index	**0.102**	**Distortion Index**	**0.109**
O(11)-Mo(3)-O(12)	71.60(10)	O(29)-Mo(4)-O(28)	73.27(10)
O(15)-Mo(3)-O(16)	73.93(9)	O(24)-Mo(4)-O(25)	73.71(11)
O(16)-Mo(3)-O(12)	76.03(9)	O(25)-Mo(4)-O(28)	73.96(9)
O(11)-Mo(3)-O(16)	85.98(10)	O(29)-Mo(4)-O(25)	82.95(10)
O(15)-Mo(3)-O(12)	86.44(9)	O(24)-Mo(4)-O(28)	83.65(10)
O(13)-Mo(3)-O(12)	86.60(12)	O(27)-Mo(4)-O(28)	91.30(13)
O(13)-Mo(3)-O(15)	90.31(11)	O(26)-Mo(4)-O(25)	91.58(14)
O(14)-Mo(3)-O(16)	95.72(11)	O(26)-Mo(4)-O(29)	97.38(13)
O(14)-Mo(3)-O(15)	98.53(11)	O(27)-Mo(4)-O(24)	97.61(15)
O(14)-Mo(3)-O(11)	100.75(12)	O(27)-Mo(4)-O(29)	100.27(14)
O(13)-Mo(3)-O(11)	102.88(12)	O(26)-Mo(4)-O(24)	100.29(14)
O(14)-Mo(3)-O(13)	103.22(14)	O(27)-Mo(4)-O(26)	103.99(17)
Angle Variance (σ^2)	**126.74**	**Angle Variance (σ^2)**	**128.7**
Distortion Index	**0.103**	**Distortion Index**	**0.109**
O(29)-Mo(5)-O(28)	71.85(10)	O(24)-Mo(6)-O(25)	72.38(11)
O(32)-Mo(5)-O(33)	73.34(10)	O(19)-Mo(6)-O(21)	74.12(10)
O(33)-Mo(5)-O(28)	75.81(9)	O(21)-Mo(6)-O(25)	77.00(9)
O(32)-Mo(5)-O(28)	85.91(9)	O(22)-Mo(6)-O(25)	83.49(13)
O(29)-Mo(5)-O(33)	86.42(10)	O(24)-Mo(6)-O(21)	84.72(11)
O(30)-Mo(5)-O(28)	86.89(12)	O(19)-Mo(6)-O(25)	88.48(10)
O(30)-Mo(5)-O(32)	90.46(12)	O(22)-Mo(6)-O(19)	91.35(14)
O(31)-Mo(5)-O(33)	94.84(12)	O(23)-Mo(6)-O(19)	97.57(13)
O(31)-Mo(5)-O(32)	98.50(12)	O(23)-Mo(6)-O(21)	97.87(13)
O(31)-Mo(5)-O(29)	100.70(12)	O(23)-Mo(6)-O(24)	99.69(15)
O(30)-Mo(5)-O(29)	102.86(13)	O(22)-Mo(6)-O(24)	103.00(15)
O(31)-Mo(5)-O(30)	103.99(14)	O(23)-Mo(6)-O(22)	103.25(16)
Angle Variance (σ^2)	**129.0**	**Angle Variance (σ^2)**	**124.0**
Distortion Index	**0.099**	**Distortion Index**	**0.103**

Table 3.2.3 – Crystallographically-determined bond angles for the molybdenum centres in 3, along with their Angle Variance (σ^2) and Distortion Index (DI) values.

For metal centres with octahedral coordination geometries, the Bond Angle Variance (σ^2_{oct}) and the Distortion Index (DI) are two methods to quantify the extent of distortion away from the idealised octahedral geometry. The Bond Angle Variance is defined as:

$$\sigma^2_{oct} = \frac{1}{11}\sum_{i=1}^{12}(\alpha_i - 90°)^2$$

α represents a bond angle in the system (only the angles between *cis*- bonded ligands are considered).[49,50] σ^2_{oct} = 0 represents a perfect octahedron. The σ^2_{oct} values for Mo centres in compound **3** range from 120.2 to 129.3, indicating that the coordination octahedra in the system are highly distorted (Table 3.2.3).

The Distortion Index is defined as:

$$DI = \frac{1}{12\alpha_m}\sum_{i=1}^{12}|\alpha_i - \alpha_m|$$

α_i and α_m represent an individual bond angle and the average bond angle, respectively (again, considering only *cis*- bonded ligands).[51,52] Again DI = 0 reflects an undistorted coordination octahedron. The DI values are significantly higher, ranging from 0.099 to 0.109 (Table 3.2.3).

{Cu_4} units

The {Cu_4} unit consists of four copper (II) centres and two μ_3-OH hydroxyl moieties. Each hydroxyl ligand coordinates to three copper centres to form two fused triangles (Figure 3.2.3). The central copper atoms, Cu(2) and Cu(3), are coordinated by both O(1) and O(18), while the peripheral copper atoms Cu(1) and Cu(4) only coordinate to one hydroxyl ligand each (O(1) and O(18) respectively. This arrangement is common in the literature.[53–56]

All copper centres in **3** display square pyramidal coordination environments. For Cu(1) and Cu(4), the peripheral copper centres, these coordination spheres are {CuO_4N} environments, while for the central Cu(2) and Cu(3), the coordination sphere is {CuO_5}.

The base of the pyramid for Cu(1) is defined by pyridyl N-donor N(1), μ_3-OH hydroxyl ligand O(1), monodentate phosphonate O-donor O(2), and bridging methoxy ligand O(3). The apex of the pyramid is defined by bridging phosphonate O-donor O(4), which bridges to the same molybdenum centre as methoxy ligand O(3). The coordination environment for Cu(4) is equivalent.

The coordination environment for Cu(2) is very similar to that for Cu(1) and Cu(4), but with a hydroxyl O-donor in place of a pyridyl N-donor. The base of the pyramid is defined by two μ_3-OH hydroxyl donors O(1) and O(18), a monodentate phosphonate O-donor O(17) and bridging methoxy ligand O(15). The bridging phosphonate O-donor O(16) represents the apex of the pyramid.

Cu(3) is somewhat different to the other copper centres. The base of the pyramid is defined equivalently to that for Cu(2) – two μ_3-OH hydroxyl donors O(1) and O(18), one bridging methoxy ligand O(19), and one monodentate phosphonate O-donor O(20). However, Cu(3) recruits a water ligand to act as the apical ligand for its coordination sphere.

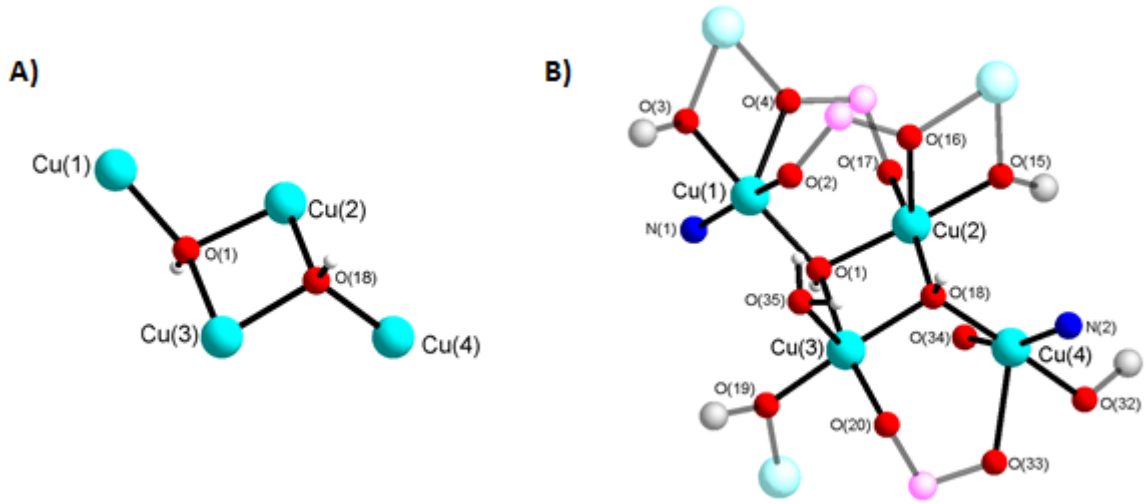

Figure 3.2.3 –A) The hydroxy-bonded {Cu_4} unit. B) This unit along with its peripheral supporting atoms. Atoms outside the direct coordination spheres of the copper atoms are partially faded out. Colour Scheme: Mo teal, Cu light blue, P pink, O red, N blue, C black, H white.

Metal Atom	Bonded Atom	Bond Length (Å)	BVS	Oxidation State
Cu(1)	O(2)	1.959(3)	2.028	+II
	O(3)	1.960(3)		
	O(1)	1.979(2)		
	N(1)	2.000(3)		
	O(4)	2.330(3)		
Cu(2)	O(17)	1.900(3)	1.953	+II
	O(18)	1.967(3)		
	O(15)	1.978(3)		
	O(1)	2.015(2)		
	O(16)	2.402(2)		
Cu(3)	O(19)	1.948(3)	1.923	+II
	O(20)	1.950(3)		
	O(18)	2.007(2)		
	O(1)	2.030(2)		
	O(35)	2.259(3)		
Cu(4)	O(34)	1.944(3)	2.102	+II
	O(32)	1.945(3)		
	O(18)	1.966(3)		
	N(2)	1.986(3)		
	O(33)	2.326(2)		

Table 3.2.4 – Crystallographically-determined bond lengths for the copper centres in 3, along with their oxidation state as determined by Bond Valence Sum (BVS) analysis.

The crystallographically identified copper-ligand bond lengths also depend on interaction type (Table 3.2.4). For the Cu-O or Cu-N bonds which represent the square bases of their respective pyramids, bond lengths range from 1.900(3) Å to 2.030(2) Å, depending on interaction. Bridging methoxy ligands and the monodentate phosphonate O-donors both display Cu-O bond lengths of around 1.9 Å. Bridging μ_3-OH units display Cu-O bond lengths of around 2.0 Å. The two Cu-N bond lengths are 1.986(3) Å and 2.000(3) Å. These are all in good agreement with literature bond lengths.[57–62]

The Cu-O bonds which represents the apexes of their respective pyramids are considerably longer than those which form the base of the pyramid. The copper-water bond Cu(3)-O(35) is 2.259(3) Å. The bridging phosphonate O-donor interactions Cu(1)-O(4), Cu(2)-O(16) and Cu(4)-O(33) is are 2.330(3) Å, 2.402(2) Å and 2.326(2) Å, respectively. This is consistent with square pyramidal copper (II) complexes reported previously.[57–62]

Bond	Bond Angle (°)	Bond	Bond Angle (°)
O(3)-Cu(1)-O(4)	73.07(11)	O(15)-Cu(2)-O(16)	69.64(9)
O(2)-Cu(1)-O(3)	86.01(11)	O(18)-Cu(2)-O(1)	82.57(10)
O(2)-Cu(1)-O(1)	88.15(10)	O(17)-Cu(2)-O(15)	88.68(11)
N(1)-Cu(1)-O(4)	92.43(12)	O(17)-Cu(2)-O(1)	92.30(11)
O(3)-Cu(1)-N(1)	92.68(13)	O(18)-Cu(2)-O(16)	92.47(9)
O(1)-Cu(1)-N(1)	93.02(12)	O(18)-Cu(2)-O(15)	97.23(10)
O(2)-Cu(1)-O(4)	100.08(10)	O(17)-Cu(2)-O(16)	101.19(9)
O(1)-Cu(1)-O(4)	107.94(10)	O(1)-Cu(2)-O(16)	106.72(9)
O(2)-Cu(1)-N(1)	166.43(13)	O(17)-Cu(2)-O(18)	166.29(10)
O(3)-Cu(1)-O(1)	174.17(11)	O(15)-Cu(2)-O(1)	176.35(10)
Geometry Index (τ_5)	**0.129**	**Geometry Index (τ_5)**	**0.167**
O(18)-Cu(3)-O(1)	81.25(10)	O(32)-Cu(4)-O(33)	71.86(10)
O(20)-Cu(3)-O(18)	90.77(11)	O(34)-Cu(4)-O(18)	85.03(10)
O(19)-Cu(3)-O(20)	92.11(12)	O(34)-Cu(4)-O(32)	91.46(11)
O(1)-Cu(3)-O(35)	92.11(10)	O(18)-Cu(4)-N(2)	91.80(12)
O(20)-Cu(3)-O(35)	92.82(11)	O(32)-Cu(4)-N(2)	91.90(12)
O(18)-Cu(3)-O(35)	93.68(10)	N(2)-Cu(4)-O(33)	96.70(11)
O(19)-Cu(3)-O(1)	94.95(11)	O(34)-Cu(4)-O(33)	102.92(10)
O(19)-Cu(3)-O(35)	96.63(11)	O(18)-Cu(4)-O(33)	107.76(10)
O(19)-Cu(3)-O(18)	169.14(11)	O(34)-Cu(4)-N(2)	160.17(12)
O(20)-Cu(3)-O(1)	170.87(11)	O(32)-Cu(4)-O(18)	176.30(11)
Geometry Index (τ_5)	**0.028**	**Geometry Index (τ_5)**	**0.268**

Table 3.2.5 – Crystallographically-determined bond angles for the copper centres in 3, along with their Geometry Index (τ_5) values.

For five-coordinate centres, the geometry index (τ_5) provides a metric to quantify the distortion from the idealised square planar geometry. The geometry index is defined as:

$$\tau_5 = \frac{\alpha_1 - \alpha_2}{60°}$$

α_1 and α_2 represent the largest and second largest bond angles in the system, respectively.[63] For an ideal square pyramid $\tau_5 = 0$ and for an ideal trigonal bipyramid $\tau_5 = 1$.

The Cu(3) centre displays closest to ideal square pyramidal geometry, at $\tau_5 = 0.028$ (Table 3.2.5). The water ligand O(35) may have been recruited into the Cu(3) coordination sphere in order to minimise the distortion from ideal geometry. However the other copper centres are unable to recruit such ancillary ligands, and so display more distorted environments, with τ_5 values ranging from 0.129 to 0.268.

Phosphonate binding modes

Two phosphonate binding modes are present in **3** (Figure 3.2.4). Three of the *tert*-butylphosphonate ligands bind to the cluster in η^1:η^2:η^2:μ_5 binding modes, bridging between two copper and three molybdenum centres. P(1) bridges between Mo(1) and Mo(2) with O-donor O(8), between Mo(3) and Cu(2) with O-donor O(16), and coordinates to Cu(1) *via* monodentate O-donor O(2). The monodentate donor O(2) forms part of the base of the Cu(1) pyramid, the bridging donor O(16) represents the apex of the Cu(2) pyramid. Phosphonates P(2) and P(3) coordinate in equivalent fashion.

Phosphonate P(4) coordinates in a η^1:η^1:η^2:μ_4 binding mode. Monodentate O-donor O(34) coordinates to Cu(4) and bridging O-donor O(28) coordinates to both Mo(4) and Mo(5). O(21) coordinates to only Mo(6).

These polydentate phosphonate ligands bear a striking resemblance to the ligands in **1** and **2**, which also display phosphonate ligands coordinating to five-membered ring-like systems. This may indicate that **3** forms due to the substitution of copper centres into a phosphonate-templated ring structure. This is consistent with the formation of phosphonate-templated Strandberg-type ring systems **1** and **2** *via* condensation between multiple metal units.

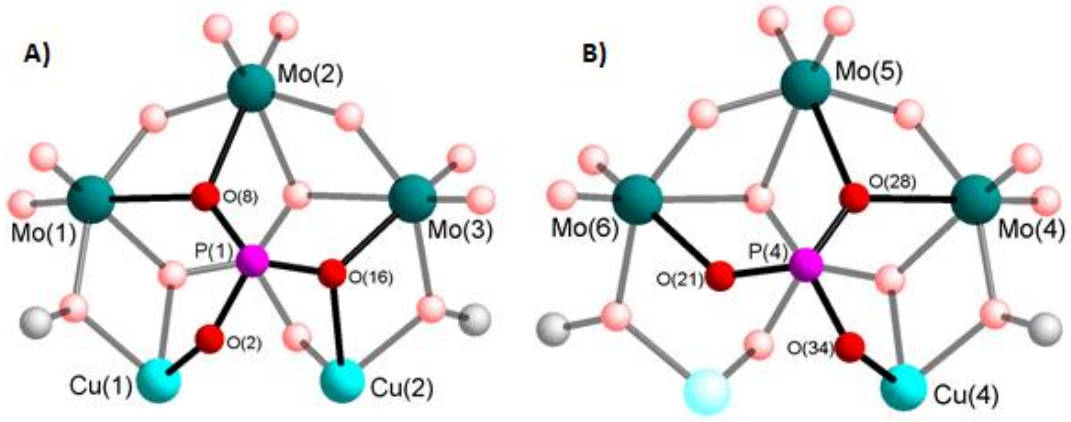

Figure 3.2.4 – The bonding motifs of phosphonate ligands A) P(1), representative of P(2) and P(3), which all bind in η^1:η^2:η^2:μ_5 binding modes. B) P(4), which binds in a η^1:η^1:η^2:μ_4 binding mode. *Tert*-butyl moieties are removed for clarity, and atoms not directly coordinated by the phosphonate ligands are partially faded out. Colour Scheme: Mo teal, Cu light blue, P pink, O red, N blue, C black.

Atom	Bond Valence Sum	Assignment
O(1)	1.025	μ_3-OH
O(18)	1.105	μ_3-OH
O(35)	0.173	H_2O

Table 3.2.6 – BVS values for oxygen atoms in 3, and their assigned protonation states.

Hydrogen positions for the O-donor ligands O(1), O(18) and O(35) are calculated. Bond Valence Sum (BVS) confirms the identities of these ligands as bridging hydroxides and monodentate water ligands, respectively (Table 3.2.6). BVS values for an oxygen atom in the approximate range 1.8-2.0 indicates *oxo*- ligands, 1.0-1.2 indicates hydroxo ligands, and values in the 0.2-0.4 range indicate water ligands.[64,65]

Crystal Packing

3 crystallises along with two constituent methanol molecules and one constituent water molecule. One of the methanol molecules is modelled as being disordered equally over two positions. The crystal packing is shown in Figure 3.2.5.

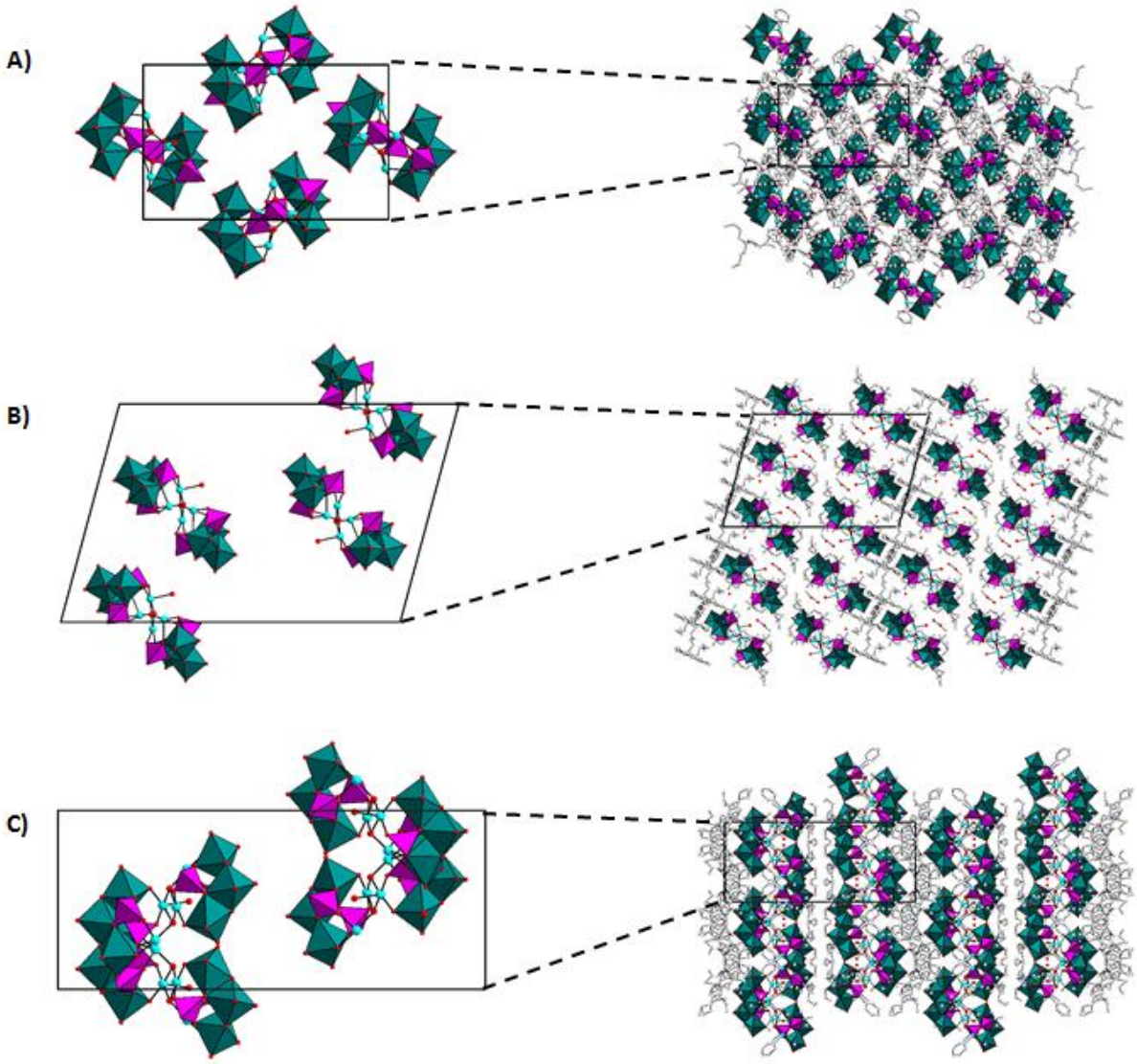

Figure 3.2.5 – Crystal packing diagrams for 3•2(MeOH)•(H_2O), as viewed down: A) The crystallographic *a*-axis, B) the crystallographic *b*-axis., C) the crystallographic *c*-axis. Colour Scheme: Mo teal, Cu light blue, P pink, O red, N blue, C black.

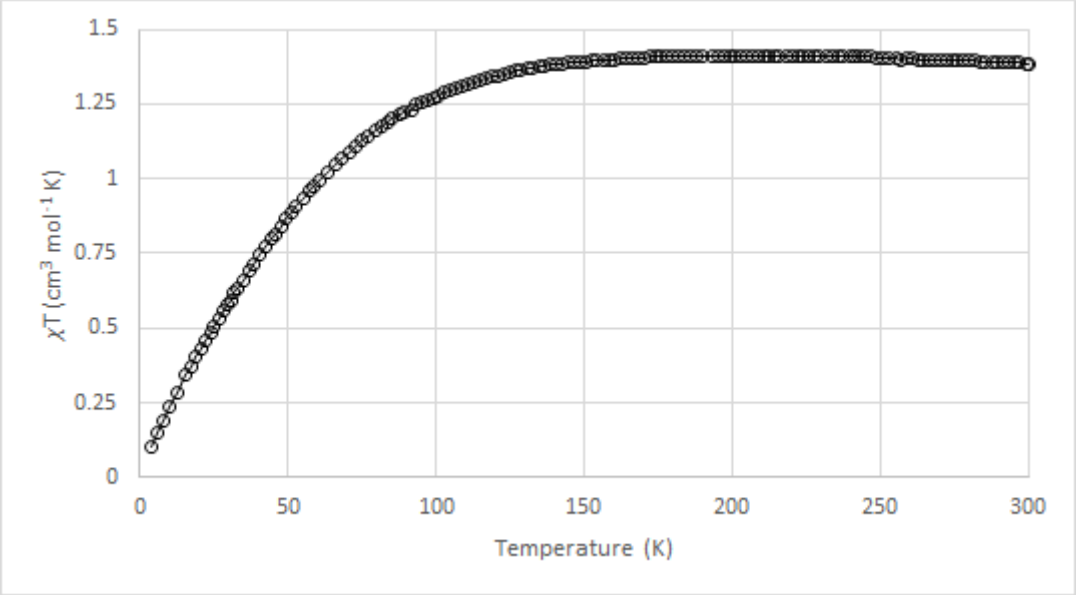

Figure 3.2.6 – Temperature dependence of the χT (magnetic susceptibility by temperature) product for 3 over the temperature range 4 – 300 K.

The temperature dependence of the magnetic susceptibility (χ) of **3** was measured over the temperature (T) range 4-300 K (Figure 3.2.6) at a constant magnetic field strength of 1.0 T. At temperatures above *c.* 150 K, the χT product is roughly constant at *c.* 1.4 cm^3 mol^{-1} K. This indicates paramagnetic behaviour (*i.e.* the spin centres are all decoupled from each other), which is described by the Curie Law:

$$C = \chi T = \frac{N\mu_B^2}{3k_b} g^2(S)(S+1)$$

Here C is the material-dependant Curie constant, μ_B is the Bohr magneton, k_b is Boltzmann's constant, and $\frac{N\mu_B^2}{3k_b}$ = 0.12505 cm^3 K mol^{-1}. g is the Land*é* g-factor and S is the spin state of a metal centre.[66] For the four S = ½ copper (II) spin centres in **3**, the expected value is therefore 1.5 cm^3 mol^{-1} K when g = 2, which is in reasonable agreement for the experimental values observed.

At lower temperatures, the χT product drops towards zero, reaching a minimum value of 0.105 cm^3 mol^{-1} K at T = 4 K. This is indicative of predominantly antiferromagnetic interactions between the four copper centres. Ferromagnetic coupling may still be present in the compound, but it is dominated by antiferromagnetic interactions. The χT product decreases towards zero, indicating a probable overall ground state of S_T = 0.

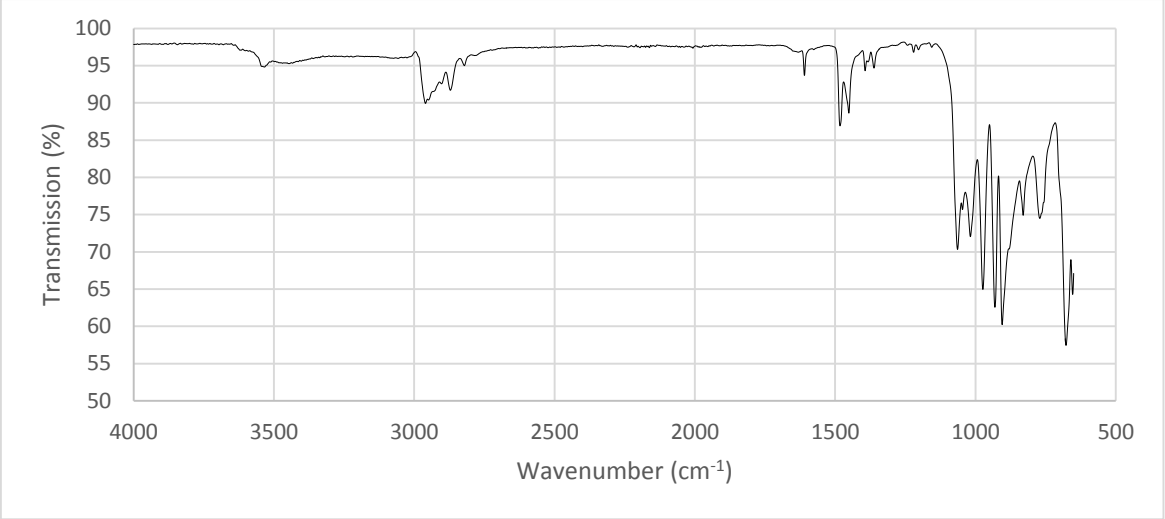

Figure 3.2.7 – The IR spectrum for 3•2(MeOH)•(H_2O).

The infrared (IR) spectrum for **3**•2(MeOH)•(H_2O) (Figure 3.2.7) is consistent with the structure as determined by XRD. The IR spectrum bares similarity to the spectra recorded for compounds **1** and **2**, which is unsurprising given the presence of similar ligands (especially *tert*-butylphosphonate and *oxo*- ligands in similar binding modes). The broad feature at 3448 cm^{-1} is due to hydrogen-bonding –OH moieties (methanol and water), while the distinctive feature at 2960 cm^{-1} is due to a combination of C-H vibrations in the organic ligands and TBA cations. The features in the 1300 – 1600 cm^{-1} region are additionally ascribed to the organic portion of the molecule, particularly C-C vibrations. By analogy with compounds **1** and **2**, the features in the *c*.950 – 1100 cm^{-1} region can be assigned as arising from P-O vibrations, with the features in the *c*.850 – 950 cm^{-1} region assigned to Mo=O terminal bonds. The P-O and M=O features have converged somewhat with respect to compounds **1** and **2**, which may indicate a shift in bonding character with respect to **1** and **2** (Figure 3.2.8). The feature at 678 cm^{-1} is assigned as a Mo-O bridging interaction.

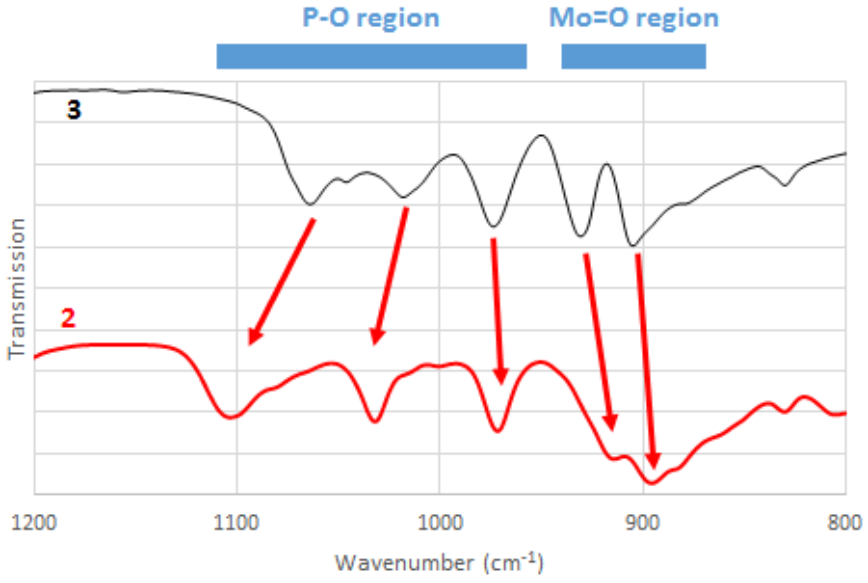

Figure 3.2.8 – Comparison of a portion of the IR spectrum for 2•0.6(MeOH) (red) and 3•2(MeOH)•(H_2O). (black).

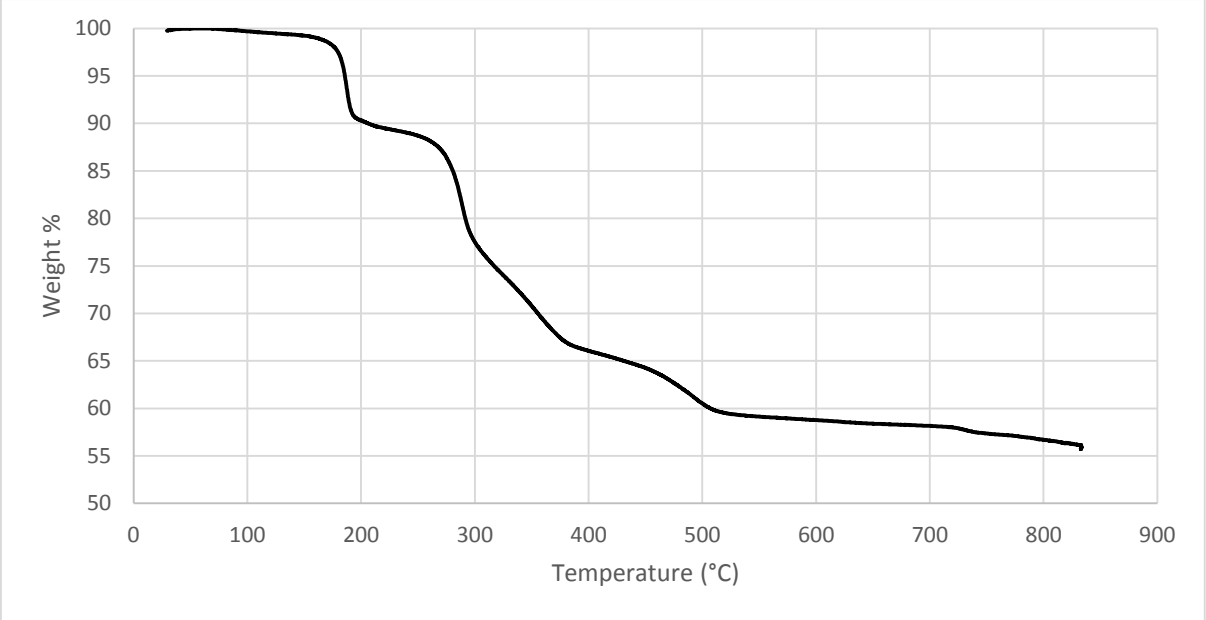

Figure 3.2.9 – Thermogravimetric Analysis (TGA) of 3 over the range 30-830°C.

Thermogravimetric analysis (TGA) for a dried sample of **3** indicates that the compound is stable in a nitrogen atmosphere up to *c.* 160 °C (Figure 3.2.9). A weight loss of 1.1% occurs up to this temperature, which is attributed to loss of solvent due to incomplete drying. The compound then undergoes a further weight loss of 8.6% centred around *c.* 180 °C, which likely corresponds to the loss of bound water and pyridine ligands (expected 7.9%). Further weight losses are observed beginning at *c.* 250 °C which likely correspond to ligand decomposition reactions. The gradual weight loss above *c.* 500 °C may correspond to oxide formation.

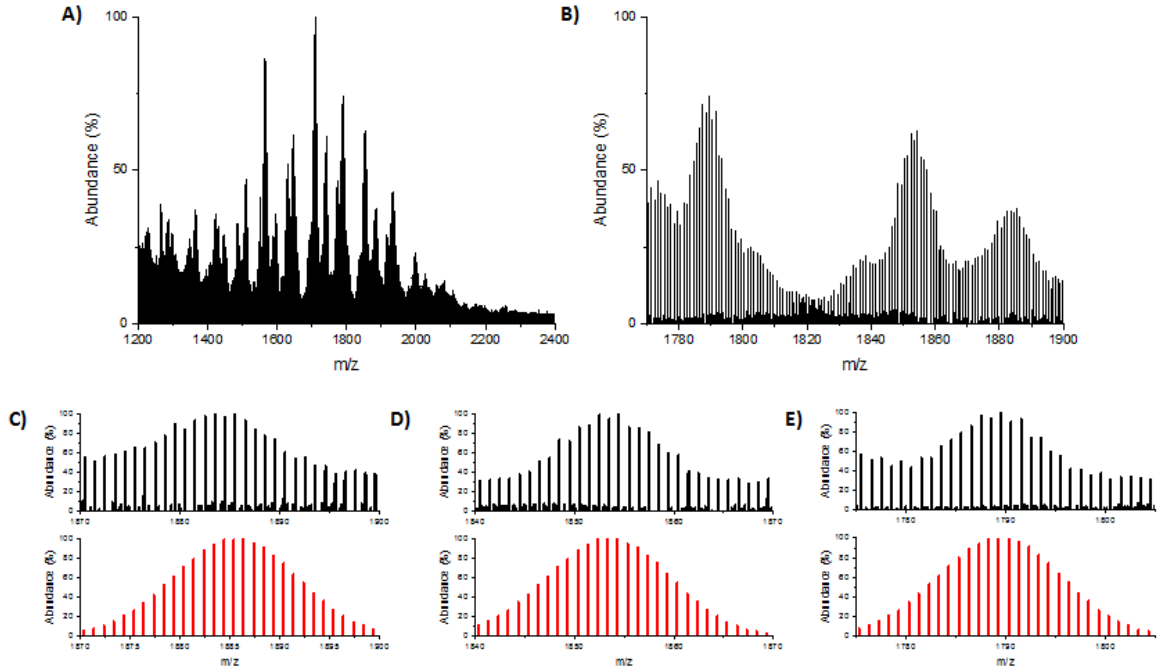

Figure 3.2.10 – A) Negative mode MALDI-MS analysis of 3 in methanol. B) Magnified portion of the spectrum. C-E) Experimental (black) and simulated (red) MALDI-MS signals for three possible molecular species observed in solution, $H[Mo^{VI}_6Cu^{II}_4O_{16}(t\text{BuPO}_3)_4(CH_3O)_4(OH)_2(CH_3OH)_3]^-$, $H[Mo^{VI}_6Cu^{II}_4O_{16}(t\text{BuPO}_3)_4(CH_3O)_4(OH)_2(CH_3OH)_2]^-$, and $H[Mo^{VI}_6Cu^{II}_4O_{16}(t\text{BuPO}_3)_4(CH_3O)_4(OH)_2]^-$, respectively.

The MALDI-MS analysis of a solution of **3** in methanol contains several signals, some of which can be tentatively assigned as molecular species (Figure 3.2.10 and Table 3.2.6). One signal is assigned as $H[Mo^{VI}_6Cu^{II}_4O_{16}(t\text{BuPO}_3)_4(CH_3O)_4(OH)_2(CH_3OH)_3]^-$ (expected mass 1886.49, observed mass 1886.35), which corresponds to the cluster core of **3** with the pyridine and water ligands replaced by methanol (which is not unexpected in a methanol solution). Two possible fragments of this species are also observed, $H[Mo^{VI}_6Cu^{II}_4O_{16}(t\text{BuPO}_3)_4(CH_3O)_4(OH)_2(CH_3OH)_2]^-$ and $H[Mo^{VI}_6Cu^{II}_4O_{16}(t\text{BuPO}_3)_4(CH_3O)_4\ (OH)_2]^-$, which correspond to the loss of one and three methanol ligands respectively from this species.

Species	*m/z calc.*	*m/z exp.*
$H[Mo^{VI}_6Cu^{II}_4O_{16}(t\text{BuPO}_3)_4(CH_3O)_4(OH)_2(CH_3OH)_3]^-$	*1886.49*	*1886.35*
$H[Mo^{VI}_6Cu^{II}_4O_{16}(t\text{BuPO}_3)_4(CH_3O)_4(OH)_2(CH_3OH)_2]^-$	*1854.47*	*1854.33*
$H[Mo^{VI}_6Cu^{II}_4O_{16}(t\text{BuPO}_3)_4(CH_3O)_4(OH)_2]^-$	*1789.50*	*1789.27*

Table 3.2.6 – Possible species observed in the MALDI-MS analysis of 3 in methanol.

*3.3) [TBA]$_2$[Mo$^{VI}_7$Cu$^{II}_7$O$_{19}$(OH)(CH$_3$O)$_7$(t*BuPO$_3$)$_6$(C$_5$H$_5$N)$_2$], (4)*

[TBA]$_2$[Mo$^{VI}_7$Cu$^{VI}_7$O$_{19}$(OH)(CH$_3$O)$_7$(*t*BuPO$_3$)$_6$(py)$_2$], **4**, where TBA represents tetrabutylammonium, *t*-Bu represents the *tert*-butyl moiety and py represents pyridine, was synthesised from the reaction of copper (II) acetate with *tert*-butylphosphonic acid and Lindqvist hexamolybdate in methanol in the presence of pyridine. After several weeks of slow solvent evaporation, green block-like crystals that contain **4** crystallise alongside the pale blue crystals containing **3** that were described in the previous section. The crystals containing **4** can be separated from the mixture manually.

The green block crystals were subjected to analysis by single crystal X-ray diffraction and found to contain **4**, along with six constituent methanol molecules, in the monoclinic crystal system in space group *C*2/C (Table 3.3.1).

The cluster core in **4** contains seven copper centres and seven molybdenum centres. Formally, the structure can be conceptualised as one {Mo$_3$} unit and two {Mo$_2$} units encapsulating a {Cu$_7$} core (Figures 3.3.1 and 3.3.2). The molybdate units are stabilised by a total of eighteen *oxo*- ligands, in either terminal or bridging modes. The {Cu$_7$} unit is stabilised by a combination of a central μ_4-O *oxo*- ligand, bridging phosphonate interactions, and two μ_3 ligands, O(10) and O(10'), which are disordered between μ_3-OH hydroxyl ligands and μ_3-OCH$_3$ methoxy ligands in a 50/50 ratio.

The molybdate units are bridged to the {Cu$_7$} core by a total of six μ_2-O bridging methoxy- ligands, as well as six fully deprotonated *tert*-butylphosphonate ligands. The coordination spheres of the {Cu$_7$} core are completed by two pyridine ligands. The cluster is C_2 symmetric, with the symmetry axis running through the central μ_4-O *oxo*- ligand, one copper centre, Cu(5), and one molybdenum centre, Mo(4).

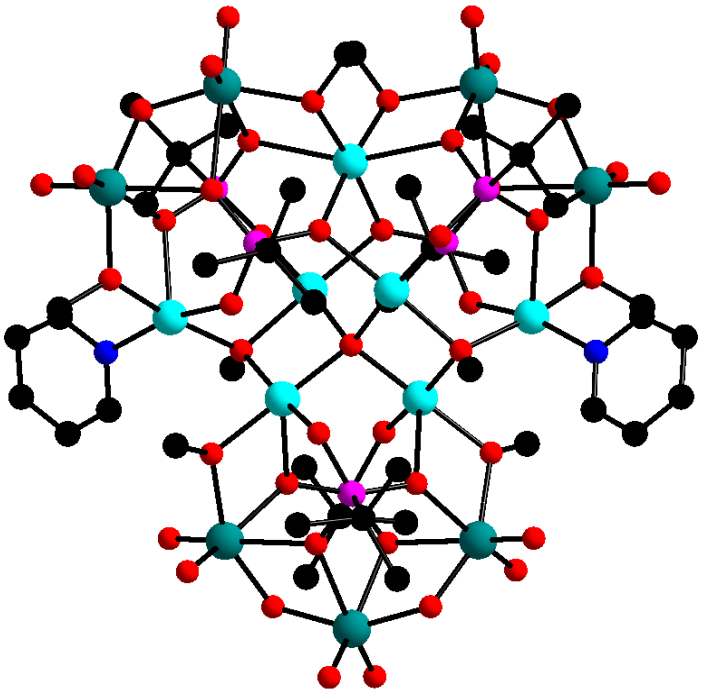

Figure 3.3.1 – Full representation of the [Mo$^{VI}_7$Cu$^{VI}_7$O$_{19}$(OH)(CH$_3$O)$_7$(*t*BuPO$_3$)$_6$(py)$_2$]$^{2-}$ cluster in 4. Colour Scheme: Mo teal, Cu light blue, P pink, O red, N blue, C black, H white.

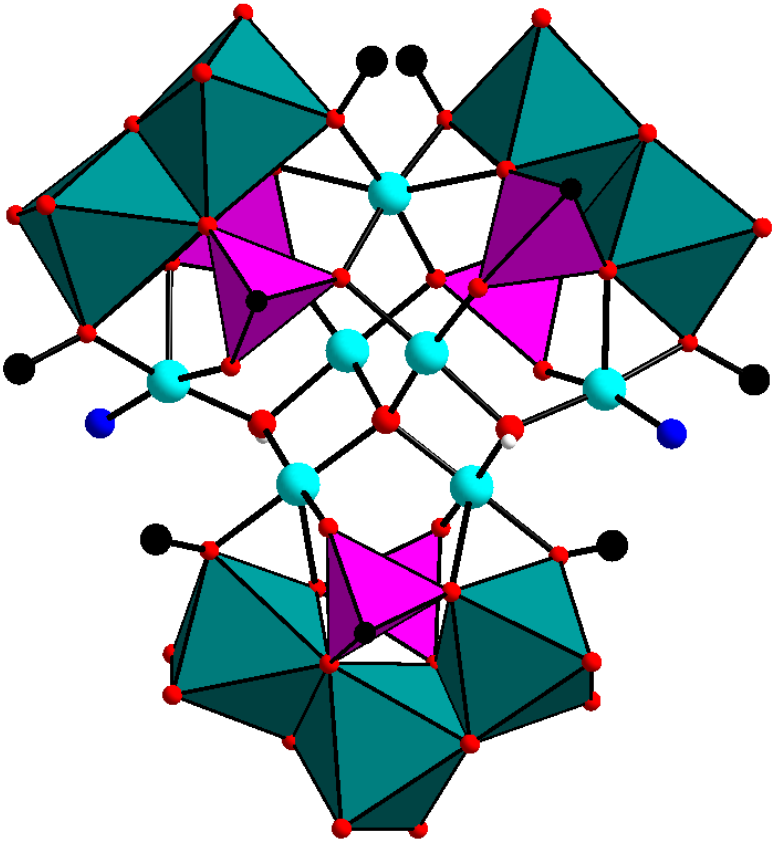

Figure 3.3.2 – Simplified representation of the $[Mo^{VI}_7Cu^{VI}_7O_{19}(OH)(CH_3O)_7(tBuPO_3)_6(py)_2]^{2-}$ cluster in 4. Molybdate and phosphonate moieties are shown as polyhedra, pyridine and *tert*-butyl groups are reduced to single N and C atoms respectively, and H atoms are removed from the methoxy groups, and the disordered methoxy/hydroxo ligands are shown as hydroxo ligands. Colour Scheme: Mo teal, Cu light blue, P pink, O red, N blue, C black, H white.

Identification code	**4**•6(MeOH)
Empirical formula	$C_{73}H_{158}Cu_7Mo_7N_4O_{45}P_6$
Formula weight (g/mol)	3114.20
Temperature (K)	100(2)
Wavelength (Å)	0.71073
Crystal system	Monoclinic
Space group	*C*2/c
a (Å)	18.3636(14)
b (Å)	35.236(3)
c (Å)	18.6488(14)
α (°)	90
β (°)	92.9173(13)
γ (°)	90
Volume (Å^3)	12051.1(16)
Z	4
Calculated density ρ_{calc} (g/cm^3)	1.716
Absorption coefficient μ (mm^{-1})	2.065
F(000)	6284
Crystal size (mm^3)	0.210 x 0.150 x 0.120
2Θ range for data collection (°)	3.182 to 52.854
Index ranges	$-22 \leq h \leq 22$, $-44 \leq k \leq 44$, $-23 \leq l \leq 23$
Reflections collected	193771
Independent reflections	12376 [R_{int} = 0.0339]
Data/restraints/parameters	12376/0/663
Goodness-of-fit on F^2	1.062
Final R indices [I>=2σ (I)]	R_1 = 0.0294, wR_2 = 0.0671
Final R indices [all data]	R_1 = 0.0369, wR_2 = 0.0721
Largest diff. peak and hole (e Å^{-3})	1.817/-1.751

Table 3.3.1 – Crystallographic details for compound 4•6(MeOH).

4 crystallises along with approximately six constituent methanol molecules. These molecules are not assigned crystallographic positions but were treated as a diffuse contribution to the overall crystal scattering using the SQUEEZE technique.

Molybdate units

The $\{Mo_3\}$ unit in **4** defined by metal centres Mo(3), Mo(4) and Mo(3'), is equivalent to the $\{Mo_3\}$ unit in **3** as described in the previous section (Figure 3.3.3).

The $\{Mo_2\}$ units can be described as pairs of edge-sharing $\{MoO_6\}$ octahedra. Both Mo(1) and Mo(2) are stabilised by two terminal *oxo*- ligands, one bridging *oxo*-, two bridging phosphonate O-donors, and one bridging methoxy ligand. Bridging *oxo*- ligand O(5) and bridging phosphonate O-donor O(4) represent the shared edge between the coordination octahedra. Mo(1) is bridged to Cu(5) by the bridging methoxy ligand O(14) and the bridging phosphonate donor O(3). Similarly Mo(2) is bridged to Cu(7) by the bridging methoxy ligand O(9) and the bridging phosphonate donor O(8).

The symmetry related Mo(1') and Mo(2') display equivalent coordination environments (Figure 3.3.3).

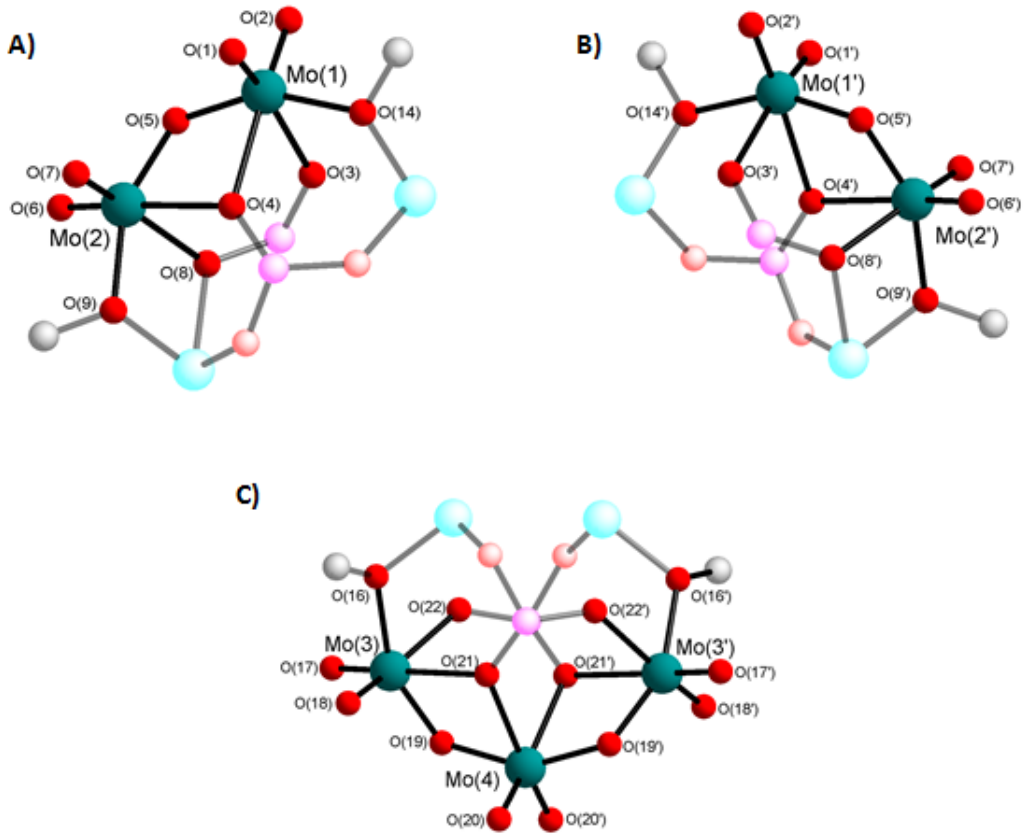

Figure 3.3.3 – The molybdate moieties in 4. A) Mo(1) and Mo(2). B) The symmetry-related Mo(1') and Mo(2'). C) Mo(3)-Mo(3'). Atoms outside the direct coordination spheres of the molybdenum atoms are partially faded out. Colour Scheme: Mo teal, Cu light blue, P pink, O red, N blue, C black.

As is the case for **3**, the $\{Mo_3O_8(OCH_3)_2\}$ moiety in **4** may arise either from $\{Mo_3O_{10}\}$ species or from condensation of mononuclear or dinuclear molybdates (see Table 2.3.2). Similarly, the $\{Mo_2O_5\}$ moieties in **4** may arise from the dinuclear species generated by the disassembly of the Lindqvist species. In particular, they may arise from the $[Mo^{VI}_2O_5(OCH_3)_3]^-$ species *via* loss of a methoxy ligand, from $[Mo^{VI}_2O_6(OCH_3)]^-$ *via* replacement of an *oxo*- ligand with a methoxy ligand, or from $[TBA][Mo^{VI}_2O_6(OCH_3)_2]^-$ *via* a combination of *oxo*- replacement and methoxy loss. The units could also arise from condensation of two mononuclear molybdates (see Table 2.3.2).

Metal Atom	Bonded Atom	Bond Length (Å)	BVS	Oxidation State
Mo(1)	O(2)	1.694(1)	5.981	+VI
	O(1)	1.706(1)		
	O(5)	1.902(1)		
	O(14)	2.015(1)		
	O(3)	2.202(1)		
	O(4)	2.392(2)		
Mo(2)	O(6)	1.702(1)	5.962	+VI
	O(7)	1.706(1)		
	O(5)	1.889(1)		
	O(9)	2.019(1)		
	O(8)	2.212(2)		
	O(4)	2.385(2)		
Mo(3)	O(17)	1.702(1)	5.963	+VI
	O(18)	1.705(1)		
	O(19)	1.886(1)		
	O(16)	2.064(1)		
	O(22)	2.157(1)		
	O(21)	2.385(2)		
Mo(4)	O(20)	1.702(1)	5.984	+VI
	O(20')	1.702(1)		
	O(19)	1.928(1)		
	O(19')	1.928(1)		
	O(21)	2.346(1)		
	O(21')	2.346(1)		

Table 3.2.2 – Crystallographically-determined bond lengths for the molybdenum centres in 4, along with their oxidation state as determined by Bond Valence Sum (BVS) analysis.

Similar to bond lengths observed in **3**, Mo-O bond lengths in **4** range from 1.694(1) Å to 2.392(2) Å, depending on the type of O-donor (Table 3.2.2). Bond lengths display similar trends as in **3** - terminal *oxo*- ligands display Mo-O bond lengths of roughly 1.7 Å, bridging *oxo*- ligands display Mo-O bond lengths around 1.9 Å and bridging methoxy ligands display Mo-O bond lengths of around 2.0 Å. Phosphonate O-donors bonds range from 2.2 Å to 2.4 Å. Bond lengths are consistent with those observed in the literature.[45–48] Bond Valence Sum (BVS) analysis indicates all Mo centres are in oxidation state +VI.

Bond	Bond Angle (°)	Bond	Bond Angle (°)
O(5)-Mo(1)-O(4)	74.06(8)	O(8)-Mo(2)-O(4)	73.46(7)
O(3)-Mo(1)-O(4)	74.63(7)	O(5)-Mo(2)-O(4)	74.46(8)
O(14)-Mo(1)-O(3)	75.53(8)	O(9)-Mo(2)-O(8)	74.65(8)
O(5)-Mo(1)-O(3)	83.10(8)	O(5)-Mo(2)-O(8)	84.80(9)
O(14)-Mo(1)-O(4)	83.92(7)	O(9)-Mo(2)-O(4)	85.62(8)
O(1)-Mo(1)-O(4)	87.39(9)	O(7)-Mo(2)-O(4)	89.44(10)
O(1)-Mo(1)-O(14)	92.98(9)	O(7)-Mo(2)-O(9)	93.61(11)
O(2)-Mo(1)-O(3)	95.35(10)	O(6)-Mo(2)-O(8)	93.79(10)
O(2)-Mo(1)-O(14)	97.66(9)	O(6)-Mo(2)-O(9)	95.90(10)
O(2)-Mo(1)-O(5)	101.10(10)	O(6)-Mo(2)-O(5)	99.96(10)
O(1)-Mo(1)-O(5)	101.76(10)	O(7)-Mo(2)-O(5)	101.36(11)
O(2)-Mo(1)-O(1)	103.16(11)	O(6)-Mo(2)-O(7)	104.00(12)
Angle Variance (σ^2)	**120.2**	**Angle Variance (σ^2)**	**116.7**
Distortion Index	**0.102**	**Distortion Index**	**0.099**
O(19)-Mo(3)-O(21)	72.55(10)	O(19)-Mo(4)-O(21)	72.82(10)
O(16)-Mo(3)-O(22)	74.90(9)	O(19')-Mo(4)-O(21')	72.82(10)
O(22)-Mo(3)-O(21)	77.43(9)	O(21)-Mo(4)-O(21')	74.63(12)
O(19)-Mo(3)-O(22)	85.87(10)	O(19)-Mo(4)-O(21')	84.14(9)
O(16)-Mo(3)-O(21)	86.61(9)	O(19')-Mo(4)-O(21)	84.14(9)
O(18)-Mo(3)-O(21)	87.23(11)	O(20)-Mo(4)-O(21)	91.47(12)
O(18)-Mo(3)-O(16)	90.61(11)	O(20')-Mo(4)-O(21')	91.47(12)
O(17)-Mo(3)-O(22)	93.56(12)	O(20')-Mo(4)-O(19)	97.70(13)
O(17)-Mo(3)-O(16)	97.44(11)	O(20)-Mo(4)-O(19')	97.71(13)
O(17)-Mo(3)-O(19)	100.59(12)	O(20)-Mo(4)-O(19)	100.11(12)
O(18)-Mo(3)-O(19)	102.82(12)	O(20')-Mo(4)-O(19')	100.11(12)
O(17)-Mo(3)-O(18)	103.03(14)	O(20)-Mo(4)-O(20')	103.4(2)
Angle Variance (σ^2)	**112.9**	**Angle Variance (σ^2)**	**127.5**
Distortion Index	**0.092**	**Distortion Index**	**0.107**

Table 3.3.3 – Crystallographically-determined bond lengths for the molybdenum centres in 4, along with their Angle Variance (σ^2) and Distortion Index (DI) values.

As is the case for **3**, the $\{MoO_6\}$ coordination environments in **4** are highly distorted from the ideal octahedral geometry, with σ^2_{oct} values ranging from 112.9 to 127.5, and DI values ranging from 0.092 to 0.107 (Table 3.3.3). σ^2_{oct} and DI are defined as:

$$\sigma^2_{oct} = \frac{1}{11}\sum_{i=1}^{12}(\alpha_i - 90°)^2$$

$$DI = \frac{1}{12\alpha_m}\sum_{i=1}^{12}|\alpha_i - \alpha_m|$$

α_i and α_m represent an individual bond angle and the average bond angle, respectively.[49–52]

{Cu_7} core

The {Cu_7} core of **4** is primarily aggregated by the μ_4-O ligand O(15) and the two μ_3-O ligands O(10) and O(10') (Figure 3.3.4). The μ_3-O ligand O(10) bridges between copper centres Cu(6), Cu(7) and Cu(8). The μ_4-O ligand O(15) bridges between Cu(6) and Cu(8) and their symmetry counterparts, Cu(6') and Cu(8'). Cu(6') and Cu(8') are then bridged to the Cu(7') by O(10'). The final copper centre, Cu(5), is connected to the rest of the {Cu_7} core *via* two bridging phosphonate O-donors, O(13) and O(13').

Three different coordination environments are seen for copper centres in **4**. Cu(5) displays a distorted octahedral coordination environment. In addition to O(13) and O(13'), Cu(5) is stabilised by bridging methoxy ligand O(14) and bridging phosphonate O-donor O(3), which both bridge to Mo(1), as well as their symmetry counterparts, O(14') and O(3').

Two centres adopt square planar coordination geometries, Cu(6) and Cu(6'). Cu(6) is coordinated by monodentate phosphonate O-donor O(12), bridging phosphonate O-donor O(13'), μ_3-O O(10) and μ_4-O O(15).

Cu(7), Cu(7'), Cu(8) and Cu(8') all display distorted square planar coordination geometry. Cu(7) is stabilised by one pyridyl N-donor N(1), one bridging methoxy O(9), one bridging phosphonate O(8), one monodentate phosphonate O-donor O(11), and μ_3-O ligand O(10). O(8) and O(9) both bridge to Mo(2). O(8) represents the apex of the square pyramidal coordination environment. Cu(8) is coordinated by μ_3-O O(10), μ_4-O O(15), monodentate phosphonate O-donor O(23), bridging methoxy O(16), and bridging phosphonate O(22). O(16) and O(22) bridge to Mo(3). O(22) represents the apex of the square pyramidal coordination environment.

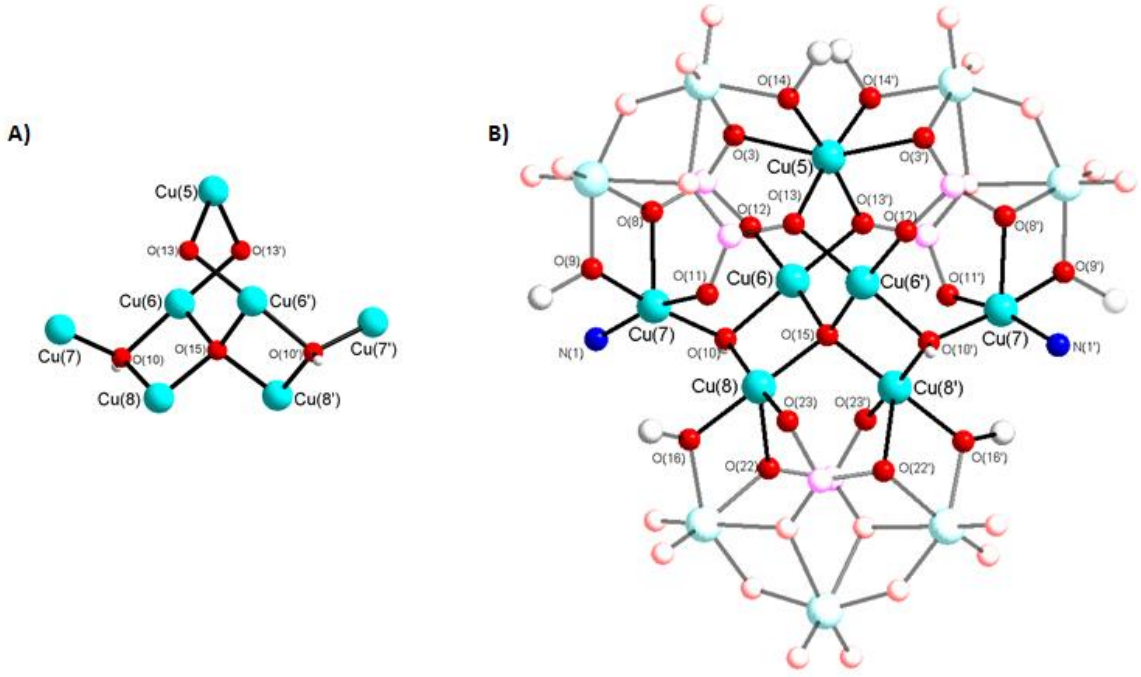

Figure 3.3.4 –A) The {Cu_7} core of 4. B) This unit along with its peripheral supporting atoms. Atoms outside the direct coordination spheres of the copper atoms are partially faded out. Colour Scheme: Mo teal, Cu light blue, P pink, O red, N blue, C black, H white.

Metal Atom	Bonded Atom	Bond Length (Å)	BVS	Oxidation State
Cu(5)	O(14)	1.942(1)	2.018	+II
	O(14')	1.942(1)		
	O(13)	2.014(1)		
	O(13')	2.014(1)		
	O(3)	2.401(1)		
	O(3')	2.401(2)		
Cu(6)	O(15)	1.892(1)	1.872	+II
	O(12)	1.898(1)		
	O(10)	2.002(1)		
	O(13)	2.041(1)		
Cu(7)	O(9)	1.939(1)	2.111	+II
	O(10)	1.957(1)		
	O(11)	1.970(1)		
	N(1)	2.001(1)		
	O(8)	2.243(1)		
Cu(8)	O(23)	1.912(1)	1.962	+II
	O(15)	1.941(1)		
	O(16)	1.968(1)		
	O(10)	2.008(1)		
	O(22)	2.484(1)		

Table 3.3.4 – Crystallographically-determined bond lengths for the copper centres in 4, along with their oxidation state as determined by Bond Valence Sum (BVS) analysis.

Copper bond lengths in **4** follow similar trends as in **3** (Table 3.3.4). Bridging methoxy ligands and the μ_4-O ligand display Cu-O bond lengths of about 1.9 Å. μ_3-O ligands display Cu-O bond lengths of around 2.0 Å. The Cu-N bond is 2.001 Å. Phosphonate ligands display a range of bond lengths up to 2.484 Å. The ligands which represent the apex of a square pyramid, O(22) and O(8), display much longer Cu-O bond lengths than their counterpart ligands. The O(3) and O(3') ligands to Cu(5) similarly display much longer Cu-O bond lengths than the other bonds to Cu(5), and may represent a Jahn-Teller axis on Cu(5).

All bond lengths observed are consistent with literature bond lengths.[57–62] Bond Valence Sum (BVS) analysis indicates that all copper centres are in oxidation state +II.

Bond	Bond Angle (°)	Bond	Bond Angle (°)
O(14)-Cu(5)-O(3')	72.09(8)		
O(14')-Cu(5)-O(3)	72.10(8)		
O(13)-Cu(5)-O(13')	83.35(11)		
O(14')-Cu(5)-O(13)	91.13(8)	O(15)-Cu(6)-O(10)	84.43(9)
O(14)-Cu(5)-O(13')	91.13(8)	O(12)-Cu(6)-O(10)	90.99(10)
O(13)-Cu(5)-O(3)	91.70(7)	O(12)-Cu(6)-O(13')	91.82(9)
O(13')-Cu(5)-O(3')	91.70(7)	O(15)-Cu(6)-O(13')	92.66(8)
O(14)-Cu(5)-O(3)	92.93(8)	O(15)-Cu(6)-O(12)	173.77(7)
O(14')-Cu(5)-O(3')	92.93(8)	O(10)-Cu(6)-O(13')	176.87(10)
O(14)-Cu(5)-O(14')	94.56(12)		
O(13')-Cu(5)-O(3)	104.63(7)		
O(13)-Cu(5)-O(3')	104.63(7)		
Angle Variance (σ^2)	**105.4**	**Geometry Index (τ_4)**	**0.066**
Distortion Index	**0.076**		
O(9)-Cu(7)-O(8)	75.46(8)	O(22)-Cu(8)-O(16)	69.34(3)
O(10)-Cu(7)-O(11)	83.20(10)	O(15)-Cu(8)-O(10)	83.01(7)
O(9)-Cu(7)-O(11)	87.62(10)	O(22)-Cu(8)-O(10)	85.77(4)
O(9)-Cu(7)-N(1)	93.05(11)	O(23)-Cu(8)-O(16)	89.60(11)
O(10)-Cu(7)-N(1)	96.39(11)	O(16)-Cu(8)-O(10)	93.01(10)
N(1)-Cu(7)-O(8)	97.11(10)	O(23)-Cu(8)-O(15)	94.91(7)
O(11)-Cu(7)-O(8)	97.75(8)	O(22)-Cu(8)-O(15)	106.62(4)
O(10)-Cu(7)-O(8)	103.54(9)	O(22)-Cu(8)-O(23)	107.75(4)
O(11)-Cu(7)-N(1)	164.80(11)	O(23)-Cu(8)-O(10)	170.43(10)
O(9)-Cu(7)-O(10)	170.56(10)	O(15)-Cu(8)-O(16)	174.61(9)
Geometry Index (τ_5)	**0.096**	**Geometry Index (τ_5)**	**0.070**

Table 3.3.5 – Crystallographically-determined bond angles for the copper centres in 4, along with their appropriate distortion parameters.

All copper coordination environments are distorted somewhat from their ideal geometries. The four coordinate geometry index τ_4 is defined as:

$$\tau_4 = \frac{360° - (\alpha_1 + \alpha_2)}{360° - 2\theta}$$

α_1 and α_2 represent the largest and second largest bond angles in the system, respectively. θ represents the ideal tetrahedral angle (*c.* 109.5°).[67] For an ideal square plane, $\tau_4 = 0$ and for an ideal tetrahedron $\tau_4 = 1$. A value of $\tau_4 = 0.066$ indicates a small amount of distortion from square planar.

The octahedral coordination geometry of metal centre Cu(5) displays similar levels of distortion to the octahedral coordination geometries of the Mo centres in **4** (Table 3.3.5). The centres with square planar coordination environments, Cu(7) and Cu(8), display moderately lower levels of distortion to the square planar environments in **3**.

σ^2_{oct}, DI and τ_5 are defined in the same way as previously.[49–52,63]

Phosphonate binding modes

Three phosphonate binding modes are present in **4**, representing the three crystallographically distinct phosphonate ligands present. All phosphonate ligands bind in η^1:η^2:η^2:μ_5 binding modes (Figure 3.3.5).

P(1) bridges between Mo(1) and Cu(5) *via* O-donor O(3), between Mo(2) and Cu(7) with O-donor O(8), and coordinates to Cu(6) *via* monodentate O-donor O(12). O(8) represents the apex of the Cu(7) pyramid, while O(3) occupies a Jahn-Teller axis on Cu(6).

P(2) also binds in a η^1:η^2:η^2:μ_5 binding mode. O(4) bridges between Mo(1) and Mo(2), O(13) bridges between Cu(5) and Cu(6'), and O(11) coordinates to Cu(7).

P(3) binds in a very similar fashion to phosphonate ligands in **3**. O(21) bridges between Mo(3) and Mo(4), O(22) bridges between Mo(3') and Cu(8'), and O(23) coordinates to Cu(8).

As with compounds **1-3**, the presence of five-membered phosphonate ring systems seems to be a significant structural factor in **4**, which may indicate a phosphonate templating effect in the formation of **4**.

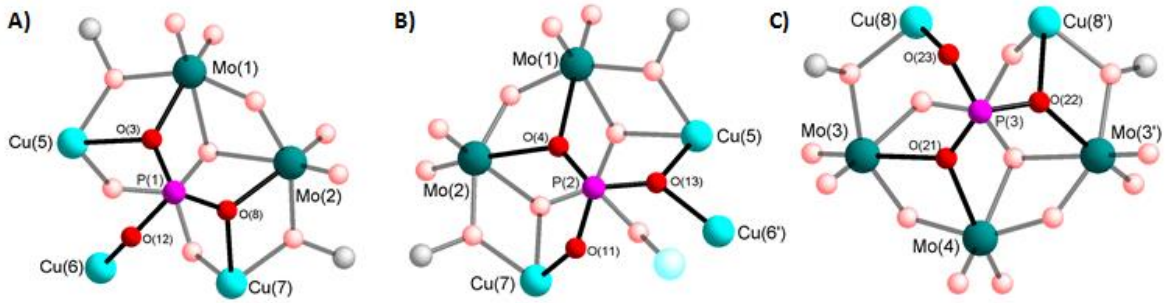

Figure 3.3.5 – The phosphonate ligands in 4, all of which bind in η^1:η^2:η^2:μ_5 binding modes. A) P(1). B) P(2). C) P(3). *Tert*-butyl moieties are removed for clarity, and atoms not directly coordinated by the phosphonate ligands are partially faded out. Colour Scheme: Mo teal, Cu light blue, P pink, O red, N blue, C black.

Atom	Bond Valence Sum	Assignment
O(10)	1.269	μ_3-OH
O(15)	2.074	μ_4-O

Table 3.3.6 – BVS values for oxygen atoms in 4, and their assigned protonation states.

The Bond Valence Sum (BVS) analysis confirms the identity of atom O(15) as an *oxo*- ligand. BVS values for an oxygen atom in the approximate range 1.8-2.0 indicates *oxo*- ligands, 1.0-1.2 indicates hydroxo ligands, and values in the 0.2-0.4 range indicate water ligands.[64,65]

BVS analysis for O(10) is consistent with a μ_3-OH ligand (Table 3.3.6). However, the presence of a partially occupied carbon atom C(13) indicates O(10) may be part of a methoxy ligand. Therefore O(10) is assigned as being disordered μ_3-OH hydroxyl ligands and μ_3-OCH_3 methoxy ligands at a 50/50 ratio. The hydrogen for the OH moiety could not be located crystallographically and was assigned a calculated position.

Crystal Packing

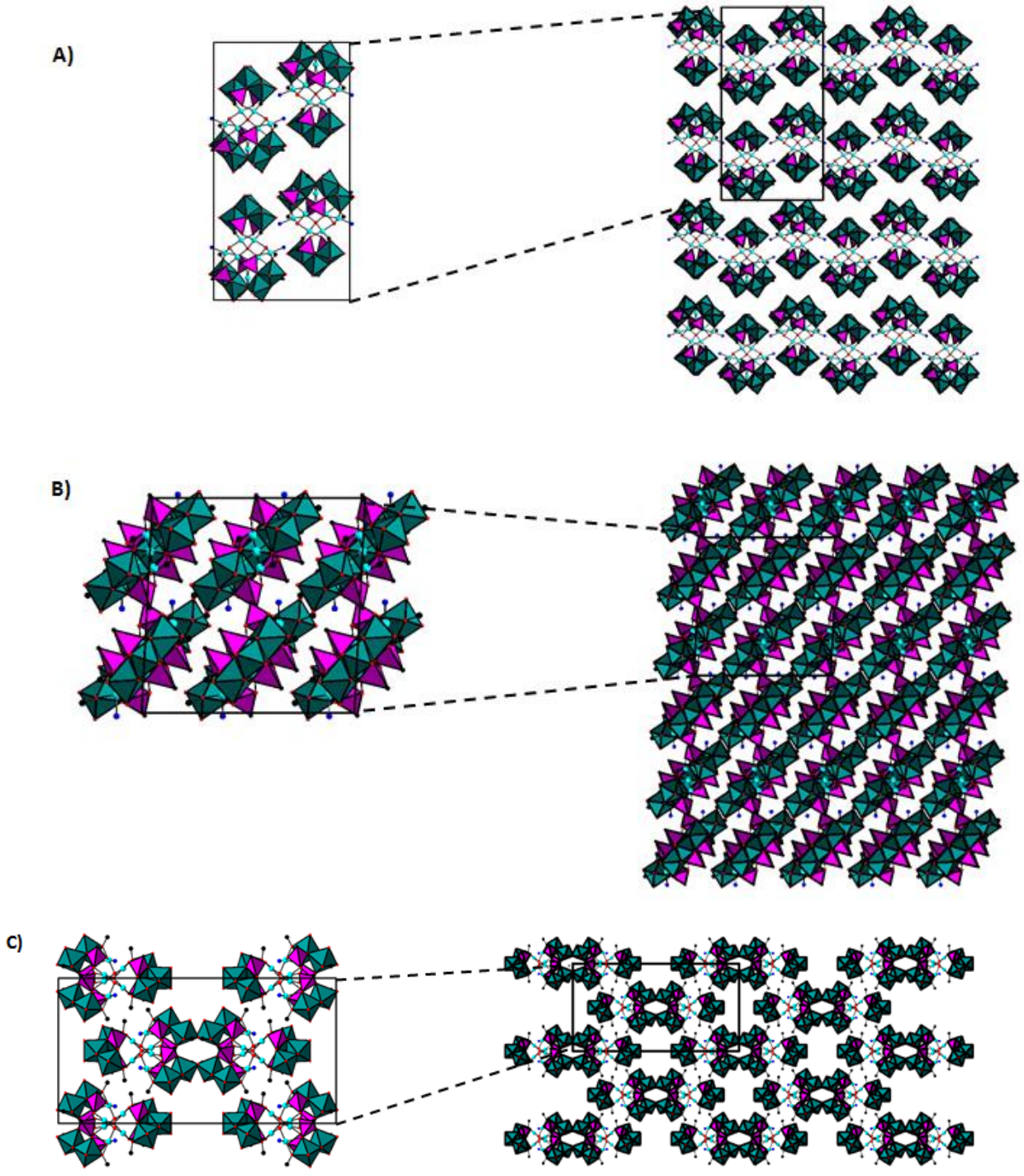

Figure 3.3.6 – Crystal packing diagrams for 4•6(MeOH), as viewed down : A) The crystallographic *a*-axis, B) the crystallographic *b*-axis. C) the crystallographic *c*-axis.
For clarity, solvent and cation molecules are removed and the cluster is shown in its simplified representation.
Colour Scheme: Mo teal, Cu light blue, P pink, O red, N blue, C black.

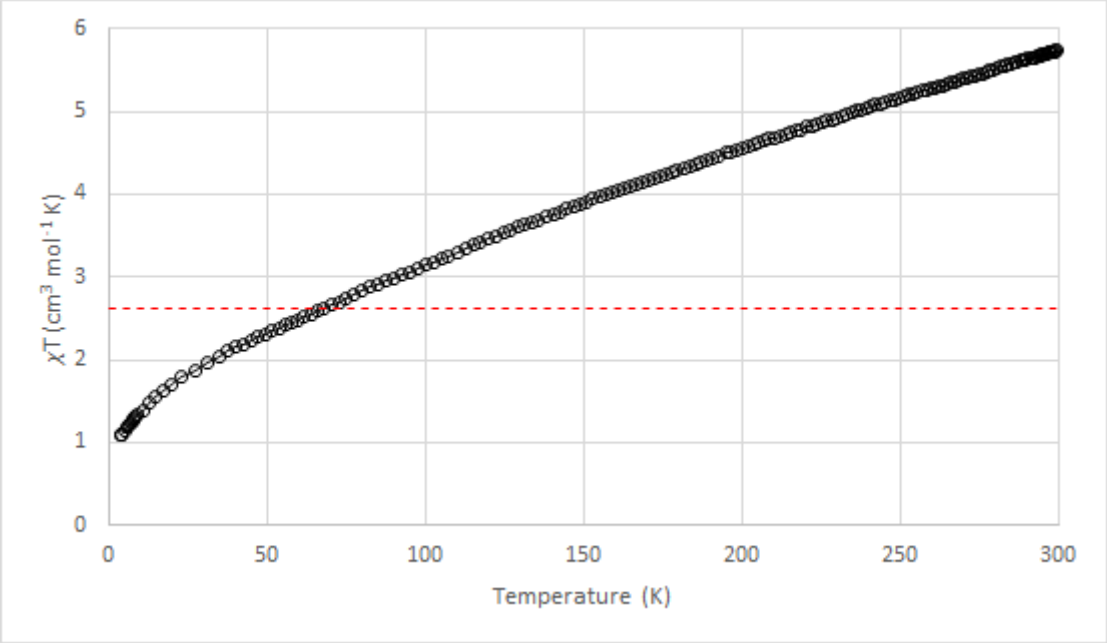

Figure 3.3.7 – Temperature dependence of the χT (magnetic susceptibility by temperature) product for 4 over the temperature range 4 – 300 K. The dotted red line indicates where the χT value was expected to plateau at higher temperatures, as predicted by the Curie Law.

The temperature dependence of the magnetic susceptibility (χ) of **4** was also measured over the temperature (T) range 4-300 K (Figure 3.3.7) at a constant magnetic field strength of 1.0 T. The behaviour is not quite as expected. It was expected that the behaviour of **4** would be broadly similar to that of **3**, *i.e.* at room temperature, thermal disorder was expected to overcome any interactions with spin centres and result in paramagnetic behaviour described by the Curie Law:

$$C = \chi T = \frac{N\mu_B^2}{3k_b} g^2(S)(S+1)$$

C is a material-specific Curie constant, μ_B is the Bohr magneton, k_b is Boltzmann's constant, and $\frac{N\mu_B^2}{3k_b}$ = 0.12505 cm^3 K mol^{-1}. g is the Landé g-factor and S is the spin state of a metal centre.[66] The expected χT value for seven S = ½ copper (II) spin centres is 2.625 cm^3 mol^{-1} K when g = 2. It is currently not clear why the χT value at high temperatures diverges so strongly from the expected behaviour.

At lower temperatures, the χT product does not drop to zero, reaching a minimum value of 1.09 cm^3 mol^{-1} K at T=4K. Again this deviates somewhat from the expected behaviour. As a compound with seven S = ½ spin centres, the compound was expected to display spin-frustrated behaviour with a ground state of S_T = ½, which should theoretically display a χT value of 0.375 cm^3 mol^{-1} K. Again, the reason for this discrepancy is not clear.

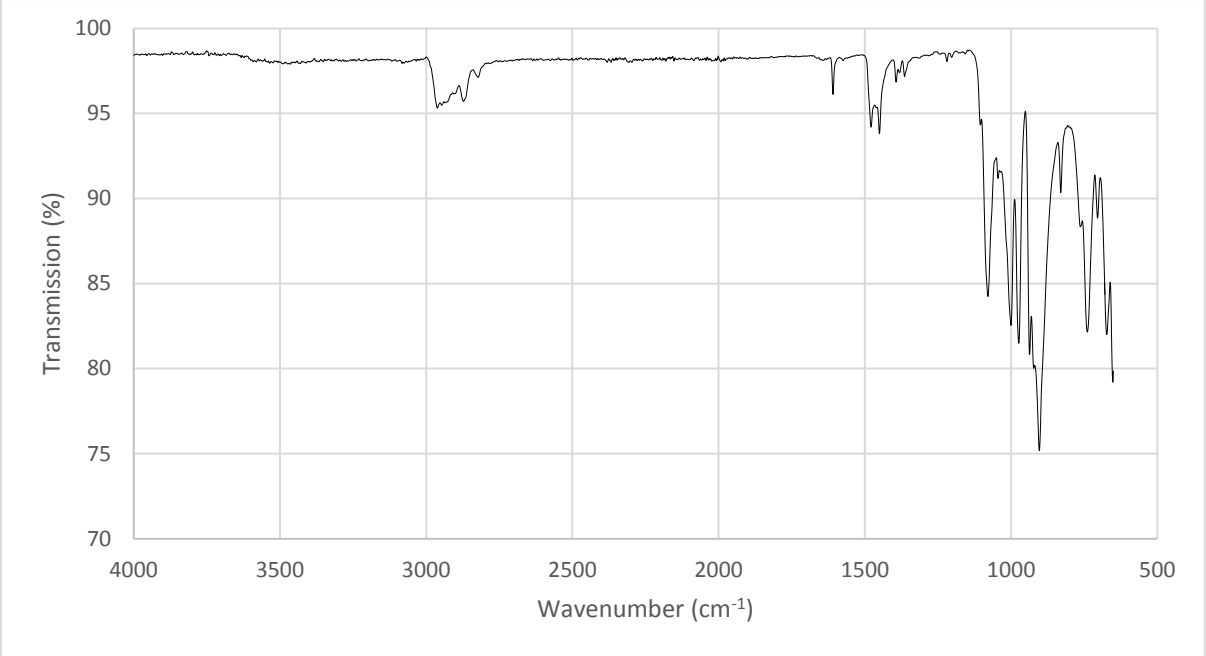

Figure 3.3.8 – The IR spectrum of 4•6(MeOH).

The infrared (IR) spectrum for **4**•6(MeOH) (Figure 3.3.8) is consistent with the structure as determined by XRD, and extremely similar to that for compound **3**•2(MeOH)•(H_2O). The feature at 2960 cm^{-1} is due to a combination of C-H vibrations in the organic ligands and TBA cations. The features in the 1300 – 1600 cm^{-1} region are additionally ascribed to the organic portion of the molecule, particularly C-C vibrations. Features in the *c.*950 – 1100 cm^{-1} region are assigned as P-O vibrations, with the features in the *c.*850 – 950 cm^{-1} region assigned to Mo=O terminal bonds. The feature at 678 cm^{-1} is assigned as a Mo-O bridging interaction.

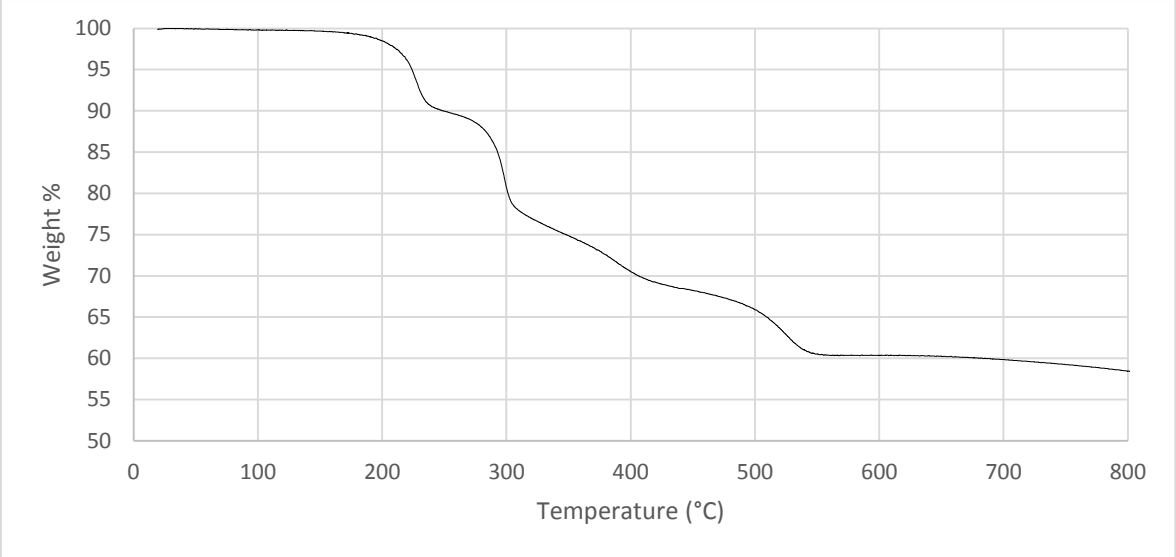

Figure 3.3.9– The TGA analysis of 4.

Thermogravimetric analysis (TGA) for a dried sample of **4** indicates that the compound is stable in a nitrogen atmosphere up to *c.* 200 °C (Figure 3.3.9). The compound then undergoes a further weight loss of 10.0% centred *c.* 220 °C. Further weight losses are observed beginning at *c.* 250 °C which likely correspond to ligand decomposition reactions, similar to those observed in the case of **3**. The gradual weight loss above *c.* 550 °C may correspond to oxide formation.

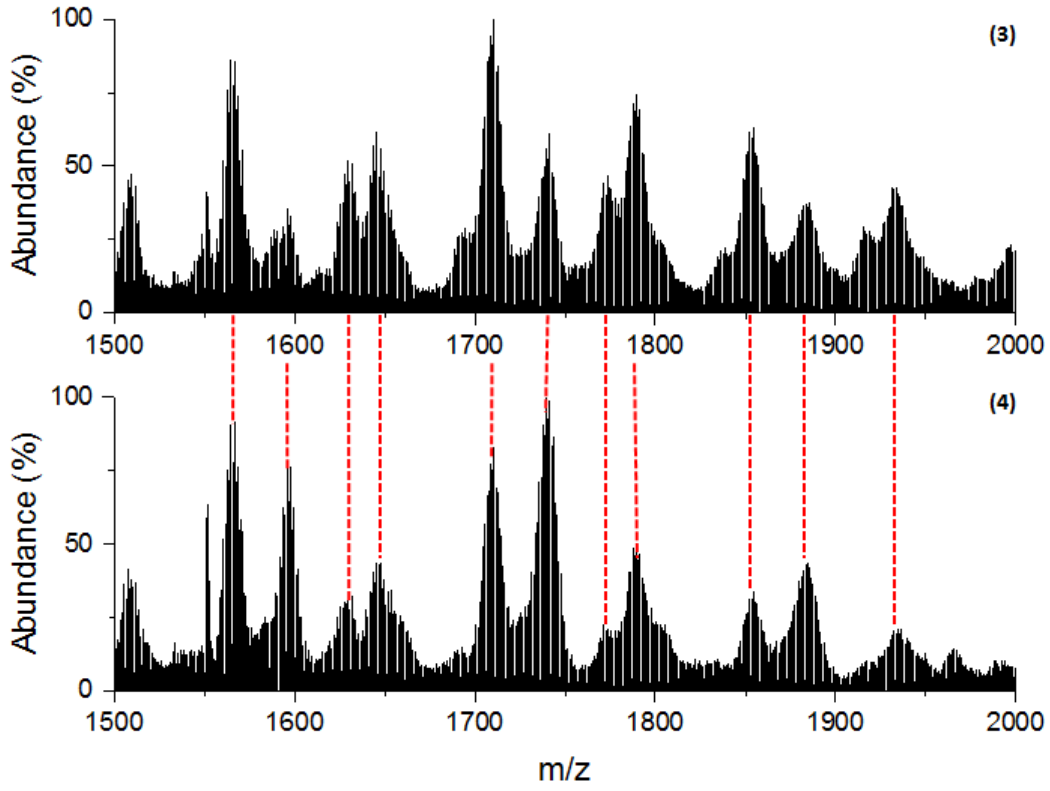

Figure 3.3.10 – The negative mode MALDI-MS spectra of 3 (top) and 4 (bottom) in methanol, with similarities between the spectra highlighted.

The MALDI-MS analysis of a solution of **4** in methanol (Figure 3.3.10) does not display any signals consistent with the structure of **4** as determined by XRD, indicating that **4** is likely not stable in solution. However, the analysis is almost identical to that of **3** (apart from shifts in the relative intensities of some signals), meaning that **4** may (at least partially) decompose to **3** in solution. This is not completely implausible, given the structural similarities between **3** and **4**.

3.4) Conclusions

In this Chapter, the "top down" synthetic method of assembly, disassembly and reassembly which was developed in Chapter 2 was extended to incorporate mixed metal systems. Copper (II) was identified as a suitable heterometal for this approach. The synthetic approach involved the disassembly of the Lindqvist hexamolybdate POM followed by subsequent reassembly with phosphonate ligands in the presence of a copper (II) salt to generate mixed-metal species stabilised by organic ligands.

Two new compounds were generated from this procedure, namely $[TBA]_2[Mo^{VI}_6Cu^{II}_4O_{16}(OH)_2(t\text{BuPO}_3)_4(py)_2(CH_3O)_4(H_2O)]$, (**3**), and $[TBA]_2[Mo^{VI}_7Cu^{VI}_7O_{19}(OH)(CH_3O)_7(t\text{BuPO}_3)_6(py)_2]$, (**4**), where TBA represents tetrabutylammonium, *t*Bu represents the *tert*-butyl moiety and py represents pyridine. These two compounds crystallise from the same reaction solution, and can be separated manually due to the distinct visual difference between the crystals of the two compounds (blue plates *vs.* green blocks respectively). The two compounds are both mixed-metal compounds stabilised by organic ligands (*i.e.* hybrid TMS-POMs).

The structures of these compounds were determined using single crystal X-ray crystallography, and supplemental characterisation techniques including IR spectroscopy and mass spectrometry.

These compounds contain $\{Mo_2O_5(OCH_3)_2\}$ and $\{Mo_3O_8(OCH_3)_2\}$ moieties (Figure 3.4.1), which we believe arose from the disassembly of the Lindqvist POM to produce molybdate oligomers including $[TBA][Mo^{VI}_2O_6(OCH_3)_2]^-$, $[Mo^{VI}_2O_5(OCH_3)_3]^-$ and $[Mo^{VI}_2O_6(OCH_3)]^-$ (see Chapter 2). We propose that the $\{Mo_2\}$ and $\{Mo_3\}$ moieties in **3** and **4** may have arisen directly from these fragments *via* ligand substitution, or from the condensation of multiple monomeric fragments which were also observed in the disassembly of the Lindqvist POM (see Chapter 2).

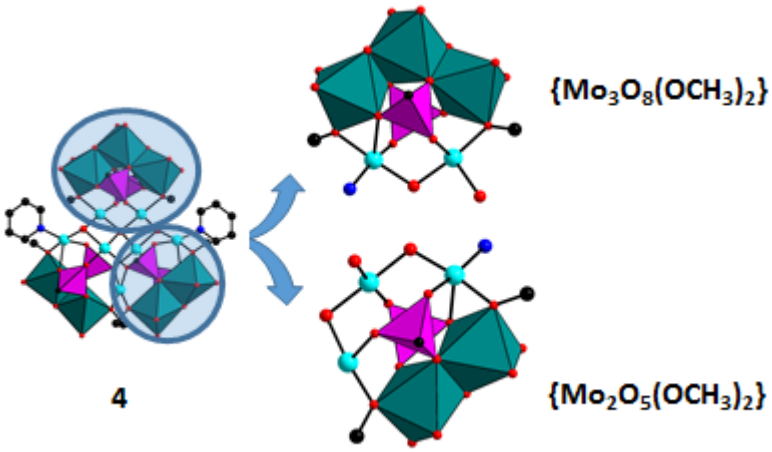

Figure 3.4.1 – The structure of compound 4, highlighting the $\{Mo_2O_5(OCH_3)_2\}$ and $\{Mo_3O_8(OCH_3)_2\}$ ring systems.

The compounds also contain five-coordinate phosphonate ligands, which bind to mixed-metal $\{Mo_2Cu_3\}$ and $\{Mo_3Cu_2\}$ ring systems. These mixed-metal ring systems bear striking similarity to the Strandberg-type $\{Mo_5\}$ ring systems **1** and **2** (see Chapter 2). We propose that the phosphonate ligands act as templating species for five-membered ring systems, which in a mixed solution of molybdate and copper species can lead to the assembly of $\{Mo_2Cu_3\}$ and $\{Mo_3Cu_2\}$ ring systems which ultimately lead to the formation of **3** and **4**.

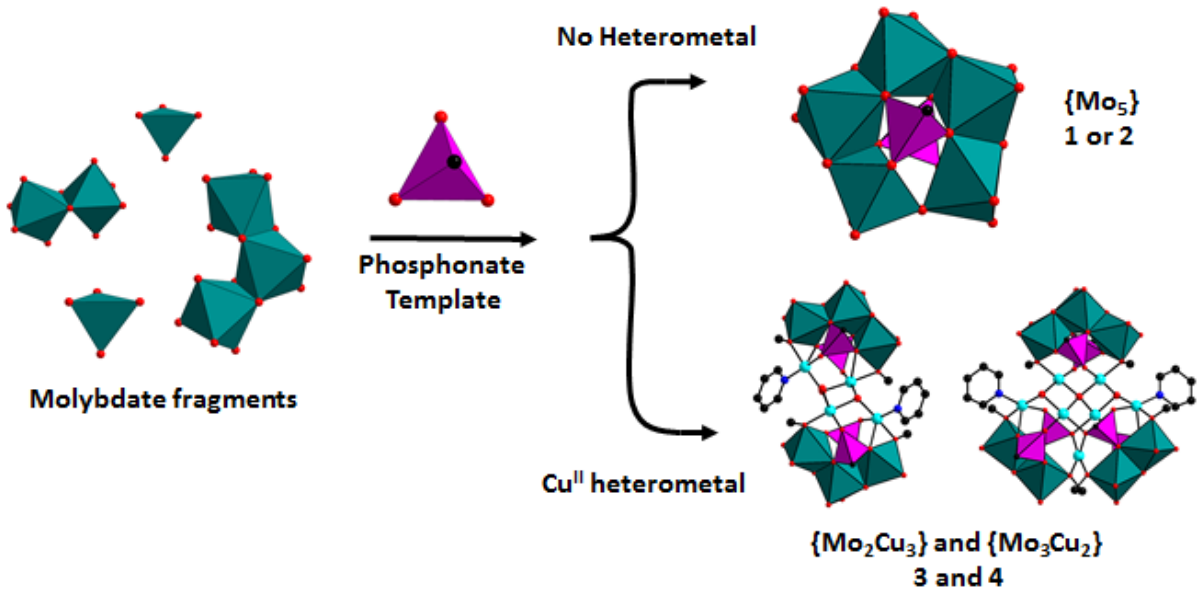

Figure 3.4.2 – The proposed templating effects of phosphonate ligands in molybdate reassembly; in the absence of heterometals, 5-membered Strandberg-type rings are generated, while in the presence of copper (II), mixed-metal $\{Mo_2Cu_3\}$ and $\{Mo_3Cu_2\}$ mixed-metal ring systems give rise to compounds 3 and 4.

The magnetic properties of **3** and **4** were also studied. **3** displays the expected paramagnetic Curie behaviour at room temperature, with predominantly antiferromagnetic interactions between the copper (II) centres dominating at low temperatures, leading to an overall ground state of $S_T = 0$. However, for reasons that remain unclear, the magnetic behaviour of **4** did not fit this expected pattern.

In conclusion, the assembly-disassembly-reassembly technique was exploited to generate new, hybrid TMS-POM species, $[TBA]_2[Mo^{VI}_6Cu^{II}_4O_{16}(OH)_2(t\text{BuPO}_3)_4(py)_2(CH_3O)_4(H_2O)]$, **3**, and $[TBA]_2[Mo^{VI}_7Cu^{VI}_7O_{19}(OH)(CH_3O)_7(t\text{BuPO}_3)_6(py)_2]$, **4**. The structures of the compounds were determined using single crystal XRD as well as supplemental techniques. The structural motifs were analysed, with the molybdate fragments observed in **3** and **4** proposed to arise from disassembly of the Lindqvist structure. Additionally, a probable template effect whereby the phosphonate ligands promote five-membered ring systems, ultimately leading to the formation of **3** and **4**, was proposed. Finally, the magnetic properties of **3** and **4** were examined.

3.5) References

1 J. M. Clemente-Juan, E. Coronado and A. Gaita-Arin, *Chem. Soc. Rev.*, 2012, **41**, 7464.

2 E. Coronado and P. Day, *Chem. Rev.*, 2004, **104**, 5419.

3 L. Bogani and W. Wernsdorfer, *Nature*, 2008, **7**, 179.

4 C. Chappert, A. Fert and F. N. Van Dau, *Nature*, 2007, **6**, 813.

5 W. Andra, U. Hafeli, R. Hergt and R. Misri, *Handbook of Magnetism and Advanced Magnetic Materials: Application of Magnetic Particles in Medicine and Biology*, 2007.

6 J. Ferrando-Soria, P. Serra-Crespo, M. De Lange, J. Gascon, F. Kapteijn, M. Julve, J. Cano, F. Lloret, J. Pasa and Y. Journaux, *J. Am. Chem. Soc.*, 2012, **134**, 15301.

7 E. Coronado and G. Minguez Espallargas, *Chem. Soc. Rev.*, 2013, **42**, 1525.

8 U. Kortz, A. Müller, J. van Slageren, J. Schnack, N. S. Dalal and M. Dressel, *Coord. Chem. Rev.*, 2009, **253**, 2315.

9 M. Ibrahim, Y. Lan, B. S. Bassil, Y. Xiang, A. Suchopar, A. K. Powell and U. Kortz, *Angew. Chem. Int. Ed.*, 2011, **50**, 4708.

10 M. Ibrahim, V. Mereacre, N. Leblanc, W. Wernsdorfer, C. E. Anson and A. K. Powell, *Angew. Chem. Int. Ed.*, 2015, **54**, 15574.

11 M. Ibrahim, A. Haider, Y. Lan, B. S. Bassil, A. M. Carey, R. Liu, G. Zhang, B. Keita, W. Li, G. E. Kostakis, A. K. Powell and U. Kortz, *Inorg. Chem.*, 2014, **53**, 5179.

12 A. Haider, M. Ibrahim, B. S. Bassil, A. M. Carey, A. N. Viet, X. Xing, W. W. Ayass, J. F. Min, R. Liu, G. Zhang, B. Keita, V. Mereacre, A. K. Powell, K. Balinski, A. T. N. Diaye, K. Ku, H. Chen, U. Stimming and U. Kortz, *Inorg. Chem.*, 2016, **55**, 2755.

13 A. Ben Khélifa, M. S. Belkhiria, G. Huang, S. Freslon, O. Guillou and K. Bernot, *Dalton Trans.*, 2015, **44**, 16458.

14 B. S. Bassil, S. Nellutla, U. Kortz, A. C. Stowe, J. Van Tol, N. S. Dalal, B. Keita and L. Nadjo, *Inorg. Chem.*, 2005, **44**, 2659.

15 I. M. Mbomekalle, B. Keita, M. Nierlich, U. Kortz, P. Berthet and L. Nadjo, 2003, **42**, 5143.

16 B. S. Bassil, M. Ibrahim, R. Al-Oweini, M. Asano, Z. Wang, J. Van Tol, N. S. Dalal, K. Choi, R. N. Biboum, B. Keita, L. Nadjo and U. Kortz, *Angew. Chem. Int. Ed.*, 2011, **50**, 5961.

17 U. Kortz, S. Isber, M. H. Dickman, D. Ravot, L. D. P. De Matie and R. V January, *Inorg. Chem.*, 2000, **34**, 2915.

18 U. Kortz, I. M. Mbomekalle, B. Keita, L. Nadjo, P. Berthet, *Inorg. Chem.*, 2002, **41**, 6412.

19 U. Kortz, S. Nellutla, A. C. Stowe, N. S. Dalal, U. Rauwald, W. Danquah and D. Ravot, *Inorg. Chem.*, 2004, **43**, 2308.

20 U. Kortz, Y. P. Jeannin, G. Herve, B. Street and P. O. Box, *Inorg. Chem.*, 1999, **38**, 3670.

21 L. Bi, U. Kortz, S. Nellutla, A. C. Stowe, J. Van Tol, N. S. Dalal, B. Keita and L. Nadjo, *Inorg. Chem.*, 2005, **44**, 896.

22 S. Nellutla, J. Van Tol, N. S. Dalal, L. Bi, U. Kortz, B. Keita, L. Nadjo, G. A. Khitrov and A. G. Marshall, 2005, **44**, 9795.

23 B. S. Bassil, U. Kortz, A. S. Tigan, J. M. Clemente-Juan, B. Keita, P. De Oliveira and L. Nadjo, *Inorg. Chem.*, 2005, **44**, 9360.

24 R. Al-Oweini, B. S. Bassil, T. Palden, B. Keita, Y. Lan, A. K. Powell and U. Kortz, *Polyhedron*, 2013, **52**, 461.

25 M. Ibrahim, Y. Xiang, B. S. Bassil, Y. Lan, A. K. Powell, P. De Oliveira, B. Keita and U. Kortz, *Inorg. Chem.*, 2013, **52**, 8399.

26 V. Singh, Z. Chen, P. Ma, D. Zhang, M. G. B. Drew, J. Niu and J. Wang, *Chem. Eur. J.*, 2016, **22**, 10983.

27 E. Garribba and G. Micera, *J. Chem. Educ.*, 2006, **83**, 1229.

28 I. Kuhne, G. E. Kostakis, C. E. Anson and A. K. Powell, *Chem. Commun.*, 2015, **51**, 2702.

29 E. T. Spielberg, A. Gilb, D. Plaul, D. Geibig, D. Hornig, D. Schuch, A. Buchholz, A. Ardavan and W. Plass, *Inorg. Chem.*, 2015, **54**, 3432.

30 A. Escuer, G. Vlahopoulou, F. Lloret and F. A. Mautner, *Eur. J. Inorg. Chem.*, 2014, 83.

31 M. J. Prushan, N. K. Privette, M. Zeller, A. D. Hunter, S. Lofland and S. D. Preite, *Inorg. Chem. Commun.*, 2007, **10**, 631.

32 P. Chaudhuri, I. Karpenstein, M. Winter, C. Butzlaff, E. Bill, X. Alfred, U. Florkec and H. Hauptc, *J. Chem. Soc. Chem. Commun.*, 1992, 321.

33 K. Kamata, S. Yamaguchi, M. Kotani, K. Yamaguchi and N. Mizuno, *Angew. Chem. Int. Ed.*, 2008, **47**, 2407.

34 T. Yamase, H. Ishikawa, H. Abe, K. Fukaya, H. Nojiri and H. Takeuchi, *Inorg. Chem.*, 2012, **51**, 4606.

35 K. Suzuki, M. Shinoe and N. Mizuno, *Inorg. Chem.*, 2012, **51**, 11574.

36 S. Reinoso, J. R. Galan-Mascaros and L. Lezama, *Inorg. Chem.*, 2011, **50**, 9587.

37 S. Roy, S. Sarkar, J. Pan, U. V Waghmare, R. Dhanya, C. Narayana and S. C. Peter, *Inorg. Chem.*, 2016, **55**, 3364.

38 G. Hou, L. Bi, B. Li and L. Wu, *Inorg. Chem.*, 2010, **49**, 6474.

39 J. Sha, J. Peng, H. Liu, J. Chen, A. Tian and P. Zhang, *Inorg. Chem.*, 2007, **46**, 11183.

40 Y. Ren, X. Kong, X. Hu, M. Sun, L. Long, R. Huang and L.-S. Zheng, *Inorg. Chem.*, 2006, **45**, 4016.

41 E. Burkholder, S. Wright, V. Golub, C. J. O. Connor and J. Zubieta, *Inorg. Chem.*, 2003, **42**, 7460.

42 Y. Wang, B. Li, H. Qian and L. Wu, *Inorg. Chem.*, 2016, **55**, 4271.

43 Q. He and E. Wang, *Inorg. Chem. Commun.*, 1999, **2**, 399.

44 J. Niu, J. Hua, X. Ma and J. Wang, *CrystEngComm*, 2012, **14**, 4060.

45 H. El Moll, A. Dolbecq, M. Mbomekalle, J. Marrot, P. Deniard, R. Dessapt and P. Mialane, *Inorg. Chem.*, 2012, **51**, 2291.

46 N. G. Armatas, D. G. Allis, A. Prosvirin, G. Carnutu, C. J. O. Connor, K. Dunbar and J. Zubieta, *Inorg. Chem.*, 2008, **47**, 832.

47 C. Sassoye, K. Norton and S. C. Sevov, *Inorg. Chem.*, 2003, **42**, 1652.

48 G. Cao, R. C. Haushalter and G. Karl, *Inorg. Chem.*, 1993, **32**, 127.

49 M. E. Fleet, *Mineral. Mag.*, 1976, **40**, 531.

50 R. M. Hazen, R. T. Downs and C. T. Prewitt, *Comp. Cryst. Chem.*, 1999.

51 M. Wildner, *Z. Krist.*, 1992, **202**, 51.

52 M. Hughes, F. Foit and E. Wright, *Can. Mineral.*, 2002, **40**, 153.

53 H. Miao, X. Xu, W. Ju, H. Wan, Y. Zhang, D. Zhu and Y. Xu, *Inorg. Chem.*, 2014, **53**, 2757.

54 J.-H. Zhou, R.-M. Cheng, Y. Song, Y.-Z. Li, Z. Yu, X.-T. Chen, Z.-L. Xue and X.-Z. You, *Inorg. Chem.*, 2005, **44**, 8011.

55 R. Murugavel, M. Sathiyendiran, R. Pothiraja, M. G. Walawalkar, T. Mallah and E. Rivie, *Inorg. Chem.*, 2004, **43**, 945.

56 L. Chen, L. K. Thompson and J. N. Bridson, *Inorg. Chem.*, 1993, **32**, 2938.

57 O. Oms, S. Yang, W. Salomon, J. Marrot, A. Dolbecq, E. Rivie, A. Bonnefont, L. Ruhlmann and P. Mialane, *Inorg. Chem.*, 2016, **55**, 1551.

58 V. Chandrasekhar, L. Nagarajan, S. Hossain, K. Gopal, S. Ghosh and S. Verma, *Inorg. Chem.*, 2012, **51**, 5605.

59 V. Chandrasekhar, L. Nagarajan, R. Cle, S. Ghosh, T. Senapati and S. Verma, *Inorg. Chem.*, 2008, **47**, 5347.

60 V. Chandrasekhar, P. Sasikumar, R. Boomishankar and G. Anantharaman, *Inorg. Chem.*, 2006, **45**, 3344.

61 S. Ushak, E. Spodine, E. Le Fur, D. Venegas-Yazigi, J. Pivan, W. Schnelle, R. Cardoso-Gil and R. Kniep, *Inorg. Chem.*, 2006, **45**, 5393.

62 S. Ciattini, F. Costantino, P. Lorenzo-luis, S. Midollini, A. Orlandini and A. Vacca, *Inorg. Chem.*, 2005, **44**, 4008.

63 A. W. Addison and T. N. Rao, *J. Chem. Soc. Dalton Trans.*, 1984, 1349.

64 T. C. Stamatatos, K. M. Poole, K. A. Abboud, W. Wernsdorfer, T. A. O. Brien and G. Christou, *Inorg. Chem.*, 2008, **47**, 5006.

65 C. Lampropoulos, C. Koo, S. O. Hill, K. Abboud and G. Christou, *Inorg. Chem.*, 2008, **47**, 11180.

66 R. Rennie, *A Dict. Chem.*, 2016, **7**.

67 L. Yang, D. R. Powell and R. P. Houser, *Dalton Trans.*, 2007, 955.

Chapter 4

Hybrid Cobalt-Polyoxomolybdates

4.1) Mixed-Metal POM Clusters - Cobalt

In the previous chapter, we demonstrated that the disassembly behaviour of the Lindqvist Hexamolybdate in methanol could be exploited in a disassembly-reassembly synthetic procedure to isolate mixed-metal hybrid POM systems by the addition of copper (II) salts into the reaction mixture. Having demonstrated the efficacy of this approach with copper (II) salts, we turned our attention to cobalt (II) salts.

Like copper(II), cobalt (II) centres possess a range of suitable properties that make them attractive synthetic targets for incorporation into a TMS-POM structure:

- Cobalt is a cheap, earth abundant metal, which is commercially available with a variety of counterions. Cobalt has been repeatedly flagged as an ideal metal to incorporate into TMS-POMs for this reason.[1–4]
- Cobalt (II) centres possess relatively flexible coordination geometries, which may facilitate synthesis of a TMS-POM cluster.
- Cobalt (II) centres are magnetically more versatile than the copper (II) centres explored in the previous chapter. Cobalt (II) centres can access both high spin (quartet) and low spin (doublet) electronic configurations, depending on the geometry around the metal centre and the strength of the associated ligand field. This has led cobalt (II) compounds to be investigated for their magnetic properties.[5–8]
- Cobalt is a redox active metal, which has led to a variety of applications in catalysis.[9–11] In particular, cobalt-containing POMs such as $[(Co_4(OH)_3PO_4)_4(XW_9O_{34})_4]^{n-}$ and $[Co_4(H_2O)_2(PW_9O_{34})_2]^{10-}$, have been reported as water oxidation catalysts.[12–15]

Cobalt (II) substituted molybdates have been reported previously.[16–18] Cobalt (II) (along with attendant ligands) can act as the central templating ion in the Keggin structure, the Anderson-Evans structure, and related molybdates.[19–23] A common motif in cobalt-molybdates is the $\{Mo_{12}Co\}$ motif $[H_{16}Co(PO_4)_8Mo_{12}O_{30}]$, where a single Co centre is sandwiched between two $\{Mo_6\}$-type rings.[24–27] Larger cobalt-molybdate clusters have also been reported, such as $[Co_9(en)_8(H_2O)_2Mo_{20}O_{76}]^{6-}$ and $[H_{31}Mo_{12}O_{24}Co_{12}(PO_4)_{23}(H_2O)_4]^{2-}$.[28,29] However, as with copper-molybdates, most of the examples reported in the literature feature the terminal *oxo*- ligand of a POM unit acting as a loosely-bound ligand to a cobalt centre.[30–35]

Therefore, we set out to extend our disassembly-reassembly approach to generate cobalt (II) cluster compounds. Several compounds were isolated from this procedure, which shall be described over the next chapter.

*4.2) [TBA]$_2$[Mo$^{VI}_{10}$Co$^{II}_6$O$_{12}$(μ-O)$_{14}$(μ$_3$-O)$_4$(t*BuPO$_3$)$_6$ (MeCOO)$_2$(py)$_2$(H$_2$O)$_6$], (5)*

In an extension of the disassembly-reassembly method towards hybrid TMS-POMs as discussed in the previous chapter, cobalt (II) acetate was combined with Lindqvist hexamolybdate and *tert*-butylphosphonic acid and in acetonitrile in the presence of pyridine. Pink-purple crystals were obtained from this reaction mixture after several days.

The crystals were subjected to single crystal X-ray diffraction and found to contain [TBA]$_2$[Mo$^{VI}_{10}$Co$^{II}_6$O$_{12}$(μ-O)$_{14}$(μ$_3$-O)$_4$(*t*BuPO$_3$)$_6$(MeCOO)$_2$(py)$_2$(H$_2$O)$_6$], **5**, where TBA represents tetrabutylammonium, *t*-Bu represents the *tert*-butyl moiety and py represents pyridine, along with three constituent acetonitrile molecules per formula unit. The crystals formed in the monoclinic crystal system in space group $P2_1/n$.

The cluster core in **5** can be conceptualised as two {Mo$_5$} units formally encapsulating a {Co$_6$} core in a sandwich motif (Figures 4.2.1 and 4.2.2). The two {Mo$_5$} units are stabilised by a total of thirty *oxo*- ligands, in either terminal or bridging modes. The {Mo$_5$} units are stabilised by phosphonate ligands, two of which support only molybdenum centres, and four of which bridge between the {Mo$_5$} units and the {Co$_6$} core. The {Co$_6$} core unit can be further subdivided into two sets of {Co$_2$} dimers and two isolated Co centres. Acetate ligands coordinate to the {Co$_2$} dimers in a *syn*-, *syn*- binding mode. The cobalt coordination environments are completed by water and pyridine ligands. The cluster is symmetrical to inversion through a point at the centre of the {Co$_6$} core.

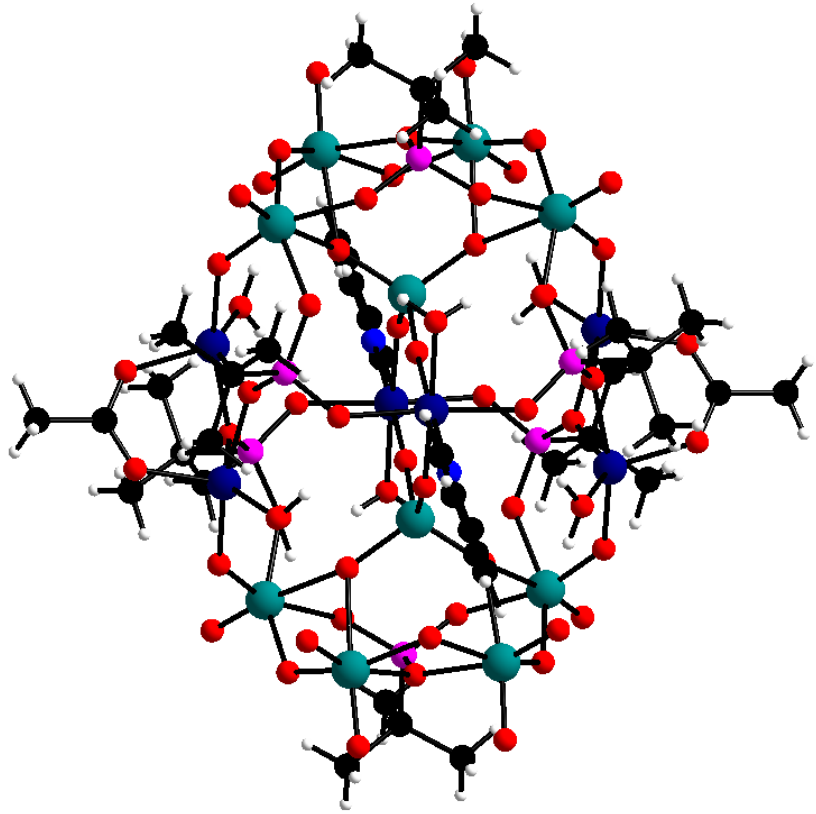

Figure 4.2.1 – Full representation of the [Mo$^{VI}_{10}$Co$^{II}_6$O$_{12}$(μ-O)$_{14}$(μ$_3$-O)$_4$(*t*BuPO$_3$)$_6$(MeCOO)$_2$(py)$_2$(H$_2$O)$_6$]$^{2-}$ cluster in 5. Colour Scheme: Mo teal, Co dark blue, P pink, O red, N blue, C black, H white.

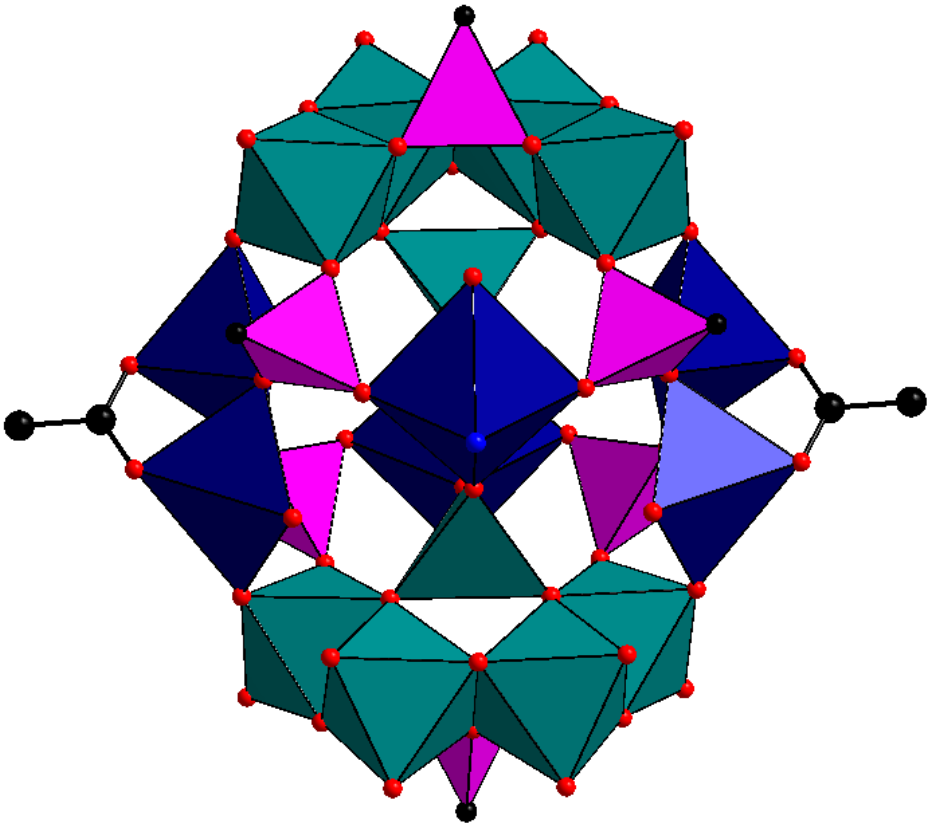

Figure 4.2.2 – Simplified representation of the $[Mo^{VI}_{10}Co^{II}_{6}O_{12}(\mu\text{-}O)_{14}(\mu_3\text{-}O)_4(t\text{BuPO}_3)_6(MeCOO)_2(py)_2(H_2O)_6]^{2-}$ cluster in 5 - molybdate and phosphonate moieties are shown as polyhedra, pyridine and *tert*-butyl groups are reduced to single N and C atoms respectively, and H atoms are removed from the water and acetate ligands. Colour Scheme: Mo teal, Co dark blue, P pink, O red, N blue, C black.

Identification code	**5**•3(MeCN)
Empirical formula	$C_{76}H_{163}Co_6Mo_{10}N_7O_{58}P_6$
Formula weight (g/mol)	3601.92
Temperature (K)	100(2)
Wavelength (Å)	0.71073
Crystal system	Monoclinic
Space group	$P2_1/n$
a (Å)	14.9997(4)
b (Å)	25.6304(7)
c (Å)	17.4332(5)
α (°)	90
β (°)	96.0101(11)
γ (°)	90
Volume (Å^3)	6665.3(3)
Z	2
Calculated density ρ_{calc} (g/cm^3)	1.794
Absorption coefficient μ (mm^{-1})	1.786
F(000)	3608
Crystal size (mm^3)	0.190 x 0.180 x 0.160
2Θ range for data collection (°)	2.836 to 68.958
Index ranges	$-23 \leq h \leq 23$, $-40 \leq k \leq 40$, $-27 \leq l \leq 27$
Reflections collected	274655
Independent reflections	28146 [R_{int} = 0.0416]
Data/restraints/parameters	28146/49/779
Goodness-of-fit on F^2	1.006
Final R indices [I>=2σ (I)]	R_1 = 0.0302, wR_2 = 0.0731
Final R indices [all data]	R_1 = 0.0483, wR_2 = 0.0779
Largest diff. peak and hole (e Å^{-3})	2.034/-1.301

Table 4.2.1 – Crystallographic details for compound 5•3(MeCN).

{Mo_5} units

The {Mo_5} units in **5** can be conceptualised as four edge-sharing {MoO_6} octahedra in a bend arrangement (Figure 4.2.3a), along with an additional {MoO_4} tetrahedron (Figure 4.2.3b). The {MoO_4} tetrahedron is in the interior of the cluster and occupies one face of the bend unit, while the other peripheral side is occupied by a phosphonate ligand. The unit is stabilised by a total of fifteen *oxo*-ligands; six of which are terminal, five of which bridge between molybdenum centres, and four of which bridge between molybdenum and cobalt centres.

Within the bend unit, Mo(1) is stabilised by two phosphonate O donors, O(9) and O(10), one terminal *oxo*-ligand O(8) and three bridging *oxo*- ligands, O(7), O(11) and O(12). O(11) and O(12) represent the shared edge of the Mo(1) and Mo(2) octahedra. Mo(3) is additionally stabilised by two terminal *oxo*- ligands, O(18) and O(19), a bridging *oxo*- ligand O(21) and a bridging phosphonate O(20). The latter two O donors represent the shared edge between the Mo(2) and Mo(3) octahedra. Mo(3) and Mo(4) display similar coordination environments to Mo(2) and Mo(1), respectively.

O(12) and O(24) are μ_3-O ligands which connect the bend arrangement to the {MoO_4} centre with tetrahedral geometry, Mo(5). The coordination sphere of Mo(5) is completed by two bridging *oxo*- ligands, O(13) and O(14), which connect to the {Co_6} core.

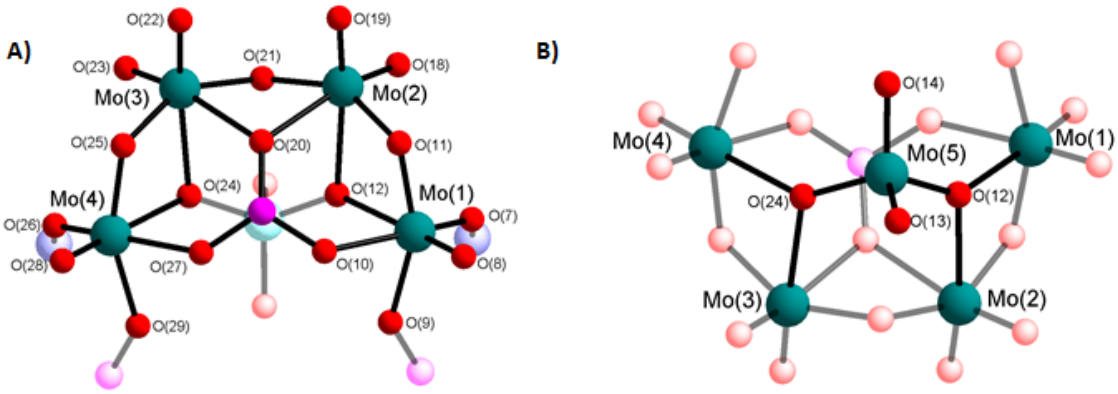

Figure 4.2.3 – The {Mo_5} units in 5. A) The bend unit, Mo(1)-Mo(4). B) The tetrahedral molybdenum centre, Mo(5), and its relationship to the bend unit. Atoms outside the direct coordination spheres of the relevant molybdenum atoms are partially faded out. Colour Scheme: Mo teal, Co dark blue, P pink, O red.

The {Mo_5} unit displays structural similarity to the Strandberg-type ring systems observed in the previous chapters. Breaking two Mo-O bonds in the {Mo_5} unit produces a {Mo_5O_{15}} unit with the same Mo-O connectivity as the Strandberg ring system (Figure 4.2.4, *c.f.* Figure 1.2.1.11).

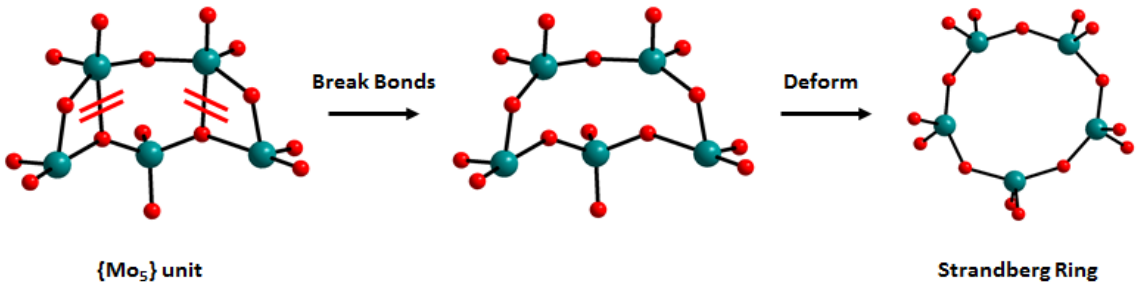

Figure 4.2.4 – The {Mo_5} units in 5 bares structural similarity to the Strandberg-type ring system.

Metal Atom	Bonded Atom	Bond Length (Å)	BVS	Oxidation State
Mo(1)	O(8)	1.688(2)	6.086	+VI
	O(7)	1.753(1)		
	O(11)	1.873(2)		
	O(9)	2.027(1)		
	O(10)	2.084(1)		
	O(12)	2.328(1)		
Mo(2)	O(19)	1.695(2)	5.985	+VI
	O(18)	1.717(2)		
	O(21)	1.920(1)		
	O(11)	1.923(1)		
	O(20)	2.308(1)		
	O(12)	2.382(1)		
Mo(3)	O(22)	1.694(2)	5.968	+VI
	O(23)	1.719(2)		
	O(21)	1.916(1)		
	O(25)	1.932(1)		
	O(20)	2.328(1)		
	O(24)	2.357(1)		
Mo(4)	O(28)	1.690(1)	6.063	+VI
	O(26)	1.748(1)		
	O(25)	1.878(1)		
	O(29)	2.034(2)		
	O(27)	2.085(1)		
	O(24)	2.328(1)		
Mo(5)	O(14)	1.721(1)	5.858	+VI
	O(13)	1.741(1)		
	O(12)	1.804(1)		
	O(24)	1.805(1)		

Table 4.2.2 – Crystallographically-determined bond lengths for the molybdenum centres in 5, along with their oxidation state as determined by Bond Valence Sum (BVS) analysis.

The crystallographically determined Mo-O bond lengths in **5** range from 1.688(2) Å to 2.382(1) Å, depending on the type of O-donor (Table 4.2.2). Terminal *oxo*- ligands display Mo-O bond lengths of roughly 1.7 Å, Mo-O-Co bridging *oxo*- ligands display Mo-O bond lengths around 1.7 Å while Mo-O-Mo bridging *oxo*- ligands display Mo-O bond lengths around 1.9 Å. Phosphonate O-donors display more variation in Mo-O bond lengths, roughly in the range of 2.0 Å to 2.35 Å. The μ_3-O ligands O(12) and O(24) display short bond lengths to Mo(5) (roughly 1.8 Å) and longer bonds to the other Mo centres (Mo(1)-Mo(4), roughly 2.35 Å).

All Mo-O bond lengths observed crystallographically in **5** are consistent with similar complexes observed in the literature.[36–39] When subjected to Bond Valence Sum (BVS) analysis, all bond lengths are consistent with Mo centres in oxidation state +VI.

Bond	Bond Angle (°)	Bond	Bond Angle (°)
O(11)-Mo(1)-O(12)	75.87(5)	O(21)-Mo(2)-O(20)	73.29(5)
O(10)-Mo(1)-O(12)	76.94(5)	O(11)-Mo(2)-O(12)	73.68(5)
O(9)-Mo(1)-O(10)	78.19(5)	O(20)-Mo(2)-O(12)	74.96(5)
O(9)-Mo(1)-O(12)	82.46(5)	O(21)-Mo(2)-O(12)	79.24(5)
O(7)-Mo(1)-O(12)	84.02(6)	O(11)-Mo(2)-O(20)	81.27(6)
O(11)-Mo(1)-O(10)	84.85(6)	O(18)-Mo(2)-O(12)	87.85(6)
O(7)-Mo(1)-O(9)	90.21(6)	O(19)-Mo(2)-O(20)	92.78(6)
O(8)-Mo(1)-O(10)	96.21(7)	O(18)-Mo(2)-O(21)	98.10(7)
O(7)-Mo(1)-O(11)	99.64(6)	O(18)-Mo(2)-O(11)	99.75(7)
O(8)-Mo(1)-O(9)	99.88(7)	O(19)-Mo(2)-O(11)	100.09(7)
O(8)-Mo(1)-O(11)	100.09(7)	O(19)-Mo(2)-O(21)	102.13(7)
O(8)-Mo(1)-O(7)	103.31(7)	O(19)-Mo(2)-O(18)	104.79(7)
Angle Variance (σ^2)	**103.4**	**Angle Variance (σ^2)**	**145.9**
Distortion Index	**0.100**	**Distortion Index**	**0.119**
O(21)-Mo(3)-O(20)	72.86(5)	O(25)-Mo(4)-O(24)	75.69(5)
O(25)-Mo(3)-O(24)	74.05(5)	O(27)-Mo(4)-O(24)	76.94(5)
O(20)-Mo(3)-O(24)	75.24(4)	O(29)-Mo(4)-O(27)	78.09(5)
O(21)-Mo(3)-O(24)	79.96(5)	O(29)-Mo(4)-O(24)	83.36(5)
O(25)-Mo(3)-O(20)	81.27(5)	O(26)-Mo(4)-O(24)	84.43(5)
O(23)-Mo(3)-O(24)	87.93(6)	O(25)-Mo(4)-O(27)	85.64(6)
O(22)-Mo(3)-O(20)	92.40(6)	O(26)-Mo(4)-O(29)	89.75(6)
O(22)-Mo(3)-O(25)	98.83(7)	O(28)-Mo(4)-O(27)	95.68(7)
O(23)-Mo(3)-O(21)	98.86(7)	O(28)-Mo(4)-O(29)	99.52(6)
O(23)-Mo(3)-O(25)	99.89(7)	O(28)-Mo(4)-O(25)	99.65(7)
O(22)-Mo(3)-O(21)	102.08(7)	O(26)-Mo(4)-O(25)	99.74(6)
O(22)-Mo(3)-O(23)	104.88(7)	O(28)-Mo(4)-O(26)	103.57(7)
Angle Variance (σ^2)	**143.2**	**Angle Variance (σ^2)**	**100.6**
Distortion Index	**0.118**	**Distortion Index**	**0.096**
O(14)-Mo(2)-O(24)	108.66(6)		
O(14)-Mo(2)-O(12)	109.09(6)		
O(13)-Mo(2)-O(12)	109.19(6)		
O(14)-Mo(2)-O(13)	109.47(6)		
O(13)-Mo(2)-O(24)	109.56(6)		
O(12)-Mo(2)-O(24)	110.85(6)		
Geometry Index (τ_4)	**0.990**		

Table 4.2.3 – Crystallographically-determined bond angles for the molybdenum centres in 5, along with their appropriate distortion parameters.

σ^2_{oct}, DI and τ_4 are defined in the same way as in the previous chapter.[40–44]

The σ^2_{oct} values for the Mo centres with octahedral coordination geometry in compound **5** range from 100.6 to 145.9, indicating that the coordination octahedra in the system are highly distorted, particularly for Mo(2) and Mo(3) (Table 4.2.3). This is in agreement with the distortion index values, which range from 0.096 to 0.119. The significant distortion in the octahedral coordination environments reflects the variety of O-donor ligands (terminal *O*- ligands, bridging μ-O and triply bridging μ_3-O ligands, monodentate phosphonates and bridging phosphonates).

In contrast, the tetrahedral coordination environment of Mo(5) is extremely close to an ideal tetrahedron (τ_4 = 0.990, where τ_4 = 1 represents an ideal tetrahedron). Mo centres with tetrahedral coordination geometries are rare in extended molybdate structures (one significant exception being the α-octamolybdate).[45–48] It is much more common for an Mo centre with tetrahedral geometry to expand its coordination sphere to octahedral when incorporated into an extended POM.[49–58]

Assembly and Templating Effects

The $\{Mo_5\}$ unit in **5** is the key structural unit, and formation of **5** probably depends on the self-assembly of this unit in solution. As is the case for the molybdate units in **1-4**, we propose that this molybdate unit self-assembled from condensation reactions between the molybdate oligomers that arose from the disassembly of the Lindqvist hexamolybdate.

As in the case of **1-4,** it seems reasonable to suggest that the phosphonate ligand acted as a template for the formation of this molybdate unit. Specifically, we highlight the similarities between the phosphonate-supported bend unit and the Strandberg ring system (Figure 4.2.5). The phosphonate-supported bend unit could reasonably self-assemble due to the templating effects of the phosphonate ligand. The opposite face of this unit could act either as a binding site for a second phosphonate ligands (*c.f.* Strandberg rings, Figure 1.2.1.11), or for a tetrahedral $\{MoO_4\}$ unit (*c.f* α-octamolybdate, Figure 1.2.1.10). These self-assembly events would likely be transient in the absence of any stabilising influence (*c.f.* Figure 2.5.1).

We propose that the phosphonate-supported $\{Mo_4\}$ bend unit could reversibly bind tetrahedral $\{MoO_4\}$ units to generate the $\{Mo_5\}$ unit in **5**. In the presence of cobalt (II) as a heterometal, this unit can assemble into the stable cluster **5** (Figure 4.2.5). In the absence of cobalt (II), this stable arrangement cannot be reached and the dominant product is therefore the Strandberg ring system (assuming the presence of a suitable cation, as in **1** or **2**).

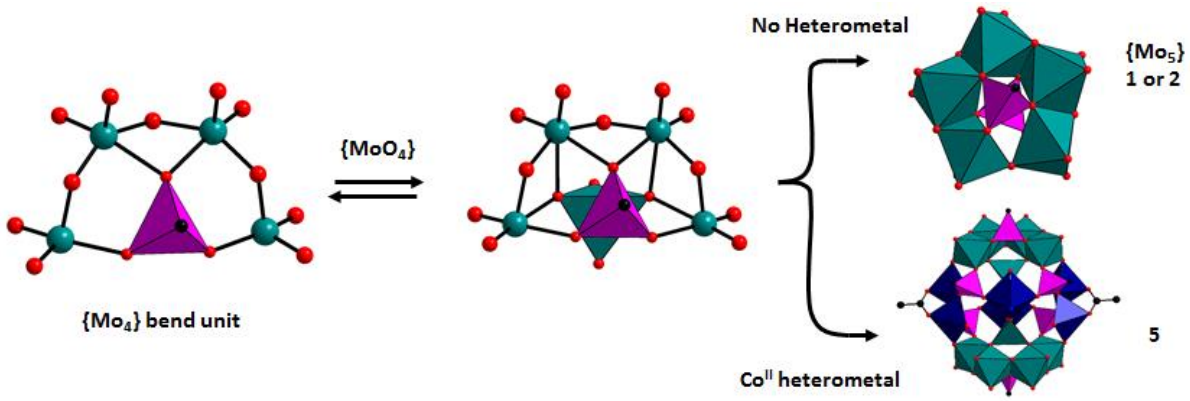

Figure 4.2.5 – The proposed templating effects of phosphonate ligands in molybdate reassembly. The proposed $\{Mo_4\}$ bend unit could reversibly bind $\{MoO_4\}$ units to generate a transient $\{Mo_5\}$ unit. In the absence of heterometals, the $\{MoO_4\}$ unit gets displaced by a second phosphonate and the Strandberg-type rings are generated. However in the presence of cobalt (II) the $\{Mo_5\}$ unit can be trapped into a stable architecture, forming the mixed-metal hybrid POM 5.

The trapping of a transient $\{Mo_5\}$ unit by cobalt (II) centres to generate **5** would be consistent with the presence of unusual $\{MoO_4\}$ tetrahedron in **5**. It is much more common for molybdenum centres to expand their coordination environments to octahedral upon incorporation into a POM unit. We propose that this unusual arrangement is due to the trapping of a transient $\{Mo_5\}$ species which would not normally be isolated.

{Co_6} units

The {Co_6} core of **5** can be further subdivided into two sets of dinuclear {Co_2} units, and two isolated Co centres.

Each {Co_2} unit consists of two Co centres with square pyramidal coordination geometries, bridged together by an acetate moiety and two phosphonate O donors (Figure 4.2.6a). The two O donors of the acetate ligand (O(2) and O(3)) represent the apexes of the respective pyramidal coordination polyhedra, while the two phosphonate O donors (O(4) and O(5)) represent the shared edge between the two pyramids. This carboxylate-bridged dimer arrangement is common in the literature.[59–65]

Each centre in the {Co_2} unit is additionally stabilised by one water ligand each (O(1) and O(6)), and one bridging *oxo*- ligand each (O(7) and O(26')). These latter bridging ligands connect to the molybdenum centres Mo(1) and Mo(4') in the two {Mo_5} units – in this way, the {Co_2} units act as a bridge between the {Mo_5} units.

The two remaining cobalt centres also bridge between the two {Mo_5} units (Figure 4.2.6b). Co(3) is connected to both of the {MoO_4} tetrahedra *via* two *cis*- μ-O ligand, O(14) and O(13'). Two phosphonate O-donors, O(16) and O(17), occupy *trans*- positions around the metal centre, while an additional water ligand O(15) and pyridine ligand N(2) on the periphery of the cluster core complete the {CoO_5N} coordination sphere.

Thus, the cobalt centres all play a role in bridging between the molybdate units. This bridging behaviour may have played a role in templating the structure, promoting the formation of **5**.

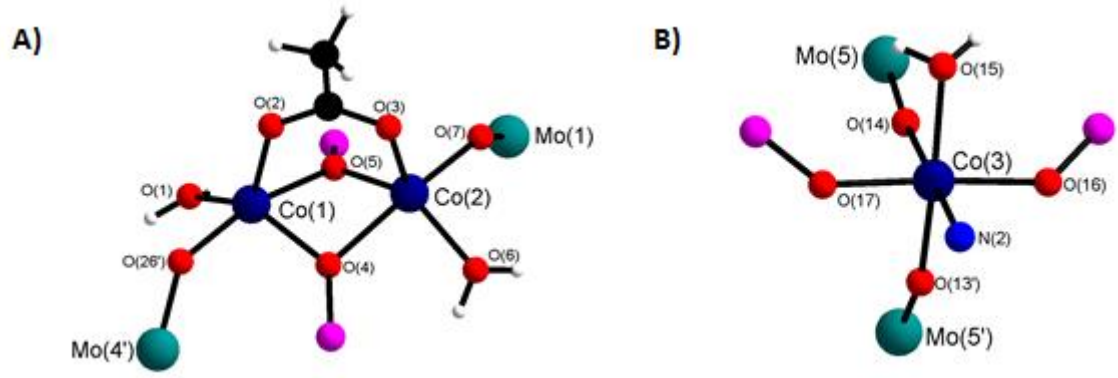

Figure 4.2.6 – The {Co_6} subunits in 5. A) The dinuclear unit, Co(1) and Co(2). B) The isolated Co centre, Co(3). Colour Scheme: Mo teal, Co dark blue, P pink, O red, N blue, C black, H white.

Metal Atom	Bonded Atom	Bond Length (Å)	BVS	Oxidation State
Co(1)	O(1)	1.975(1)	2.015	+II
	O(2)	1.982(2)		
	O(4)	1.988(1)		
	O(26')	2.047(1)		
	O(5)	2.189(2)		
Co(2)	O(6)	1.981(1)	2.005	+II
	O(3)	1.985(2)		
	O(5)	1.991(1)		
	O(7)	2.044(1)		
	O(4)	2.187(2)		
Co(3)	O(16)	2.051(1)	1.971	+II
	O(17)	2.054(1)		
	O(13')	2.069(1)		
	N(2)	2.140(3)		
	O(15)	2.143(1)		
	O(14)	2.190(1)		

Table 4.2.4 – Crystallographically-determined bond lengths for the cobalt centres in 5, along with their oxidation state as determined by Bond Valence Sum (BVS) analysis.

The Co-O bond lengths observed in **5** range from 1.975(1) Å to 2.190(1) Å, depending on the type of O-donor (Table 4.2.4). Co(1) and Co(2) in particular display very similar bond lengths to each other – their water and acetate ligands both display bond lengths of around 2.0 Å. The phosphonate O-donors are slightly skewed in the dimer unit – O(4) is about 0.2 Å closer to Co(1) than to Co(2), and *vice versa* for O(5). The bridging *oxo*-ligands display Co-O bond lengths of around 2.0 Å.

Co(3) displays slightly different bond lengths. The phosphonate O-donors display bond lengths of around 2.0 Å, with the water ligand displaying a bond length of around 2.2 Å. Again there is a slight asymmetry in the bond lengths – the bridging *oxo*- ligand O(13') is about 0.14 Å closer to Co(3) than the equivalent bridging *oxo*-ligand O(14). The Co-N bond length is 2.140(3) Å. These bond lengths are all consistent with similar complexes in the literature, and indicate that all Co centres in **5** are in oxidation state +II.[63–68]

Bond	Bond Angle (°)	Bond	Bond Angle (°)
O(4)-Co(1)-O(5)	81.05(5)	O(5)-Co(2)-O(4)	81.03(5)
O(1)-Co(1)-O(5)	85.57(5)	O(6)-Co(2)-O(4)	85.52(5)
O(2)-Co(1)-O(5)	89.98(6)	O(5)-Co(2)-O(7)	90.61(5)
O(4)-Co(1)-O(26')	90.60(6)	O(3)-Co(2)-O(4)	91.21(6)
O(1)-Co(1)-O(26')	93.46(6)	O(6)-Co(2)-O(7)	94.30(6)
O(2)-Co(1)-O(4)	95.85(6)	O(3)-Co(2)-O(5)	99.95(6)
O(2)-Co(1)-O(26')	102.02(6)	O(3)-Co(2)-O(7)	101.11(6)
O(1)-Co(1)-O(2)	123.65(7)	O(3)-Co(2)-O(6)	116.96(6)
O(1)-Co(1)-O(4)	138.23(6)	O(5)-Co(2)-O(6)	140.90(6)
O(5)-Co(1)-O(26')	166.08(6)	O(4)-Co(2)-O(7)	166.18(6)
Geometry Index (τ_5)	**0.464**	**Geometry Index (τ_5)**	**0.421**
O(15)-Co(3)-O(14)	83.06(5)		
O(17)-Co(3)-N(2)	84.9(2)		
O(13')-Co(3)-O(14)	87.27(5)		
O(16)-Co(3)-N(2)	87.8(2)		
O(13')-Co(3)-N(2)	88.37(18)		
O(16)-Co(3)-O(15)	90.08(5)		
O(17)-Co(3)-O(15)	90.22(5)		
O(17)-Co(3)-O(13')	90.23(5)		
O(16)-Co(3)-O(13')	90.72(5)		
O(17)-Co(3)-O(14)	92.60(5)		
O(16)-Co(3)-O(14)	94.80(5)		
N(2)-Co(3)-O(15)	101.29(18)		
Angle Variance (σ^2)	**22.5**		
Distortion Index	**0.035**		

Table 4.2.5 – Crystallographically-determined bond angles for the cobalt centres in 5, along with their appropriate distortion parameters.

The Co(1) and Co(2) coordination environments are quite distorted from their ideal square planar geometries (Table 4.2.5). Values of $\tau_5 = 0.464$ and $\tau_5 = 0.421$ are calculated for Co(1) and Co(2) respectively.[69]

The Co(3) coordination environment meanwhile is much closer to an idealised octahedral geometry, with an angle variance value of $\sigma^2_{oct} = 22.5$ and a distortion index value of DI = 0.035. σ^2_{oct} and DI are defined in the same way as previously.[40–43]

Phosphonate binding modes

Two phosphonate binding modes are present in **5**, with all three crystallographically distinct *tert*-butylphosphonate ligands binding to the cluster in $\eta^1{:}\eta^1{:}\eta^2{:}\mu_4$ binding modes (Figure 4.2.7).

P(1) bridges between the two metal centres Co(1') and Co(2') (*via* O(4')), coordinates to the Co(3) centre (*via* O(16)), and to the Mo(4) centre (*via* O(29)). Thus, P(1) bridges between the three significant structural features in **5**; an $\{Mo_5\}$ unit, a $\{Co_2\}$ dinuclear unit, and an isolated Co centre. P(2) coordinates in an equivalent fashion.

P(3) coordinates only to the molybdate unit, coordinating to one side of the $\{Mo_4\}$ bend unit. P(3) coordinates to Mo(1) and Mo(4) *via* O(10) and O(27) respectively, and bridges between Mo(2) and Mo(3) *via* O(20).

The prevalence of $\eta^1{:}\eta^1{:}\eta^2{:}\mu_4$ binding modes is consistent with the expected polydentate behaviour of the phosphonate ligands. In particular, the $\{Mo_4\}$ binding motif of P(3) is reminiscent of the $\{Mo_5\}$ binding motif displayed by the Strandberg-type compounds **1** and **2**. The $\{Mo_4\}$ binding motif displayed here may be related to an intermediate in the formation of the $\{Mo_5\}$ units in **1** and **2**. Additionally, the $\{Co_3Mo\}$ binding motifs of P(1) and P(2) are reminiscent of the mixed-metal ring systems in **3** and **4**, and may also have formed in a similar manner.

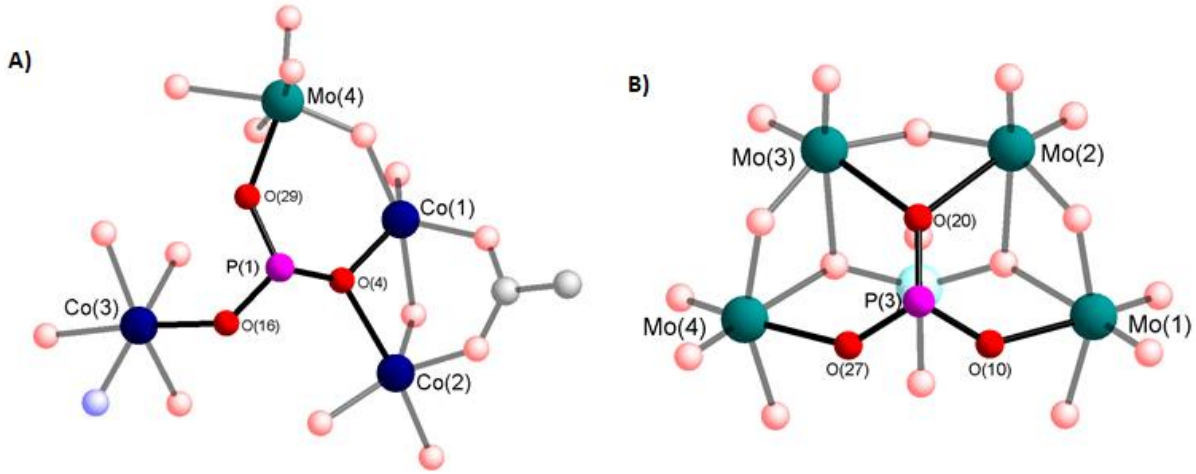

Figure 4.2.7 – The phosphonate binding modes in 5. A) P(1), which is representative of P(2). B) P(3). *Tert*-butyl moieties are removed for clarity, and atoms not directly coordinated by the phosphonate ligands are partially faded out. Colour Scheme: Mo teal, Co dark blue, P pink, O red, N blue, C black.

Intramolecular Hydrogen Bonding

Each face of the cluster core in 5 engages in a network of hydrogen-bonding interactions between the H-donor water molecules in the cluster (O(1), O(6), and O(15)) and a series of H-acceptor terminal *oxo*- ligands (O(18) and O(23)) and phosphonate oxygens (O(9), O(10), O(27), O(29), O(16) and O(17)). The interatomic distances and angles for the crystallographically observable atoms are consistent with "moderately weak" (*i.e.* mostly electrostatic) hydrogen bonding.[70–72] This network of weak H-O interactions may help stabilise the cluster core (distances and angles are consistent with bond energies *c.* 4-15 kcal mol^{-1}),[70] and could potentially play a role in templating the structure (Figure 4.2.8).

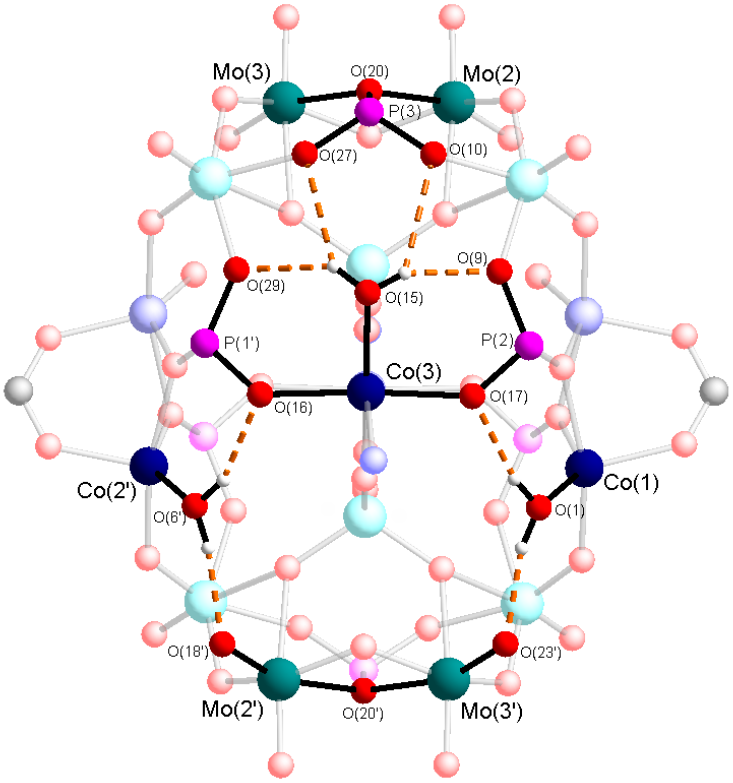

Figure 4.2.8 – The intramolecular hydrogen-oxygen interactions for one face of the cluster core in 5, with O-H…O interactions displayed as dotted lines. Atoms not directly involved in the network are partially faded out. *Tert*-butyl groups are removed and pyridine and carboxylate moieties reduced for clarity. Colour Scheme: Mo teal, Co dark blue, P pink, O red, N blue, C black, H white.

Atom	Bond Valence Sum	Assignment
O(1)	0.465	H_2O
O(6)	0.460	H_2O
O(15)	0.300	H_2O

Table 4.2.6 – BVS values for oxygen atoms in 5, and their assigned protonation states.

Bond Valence Sum (BVS) for the O-donor ligands O(1), O(6) and O(15) confirms the identities of these ligands as monodentate water ligands (Table 4.2.6). BVS values for an oxygen atom in the approximate range 1.8-2.0 indicates *oxo*- ligands, 1.0-1.2 indicates hydroxo ligands, and values in the 0.2-0.4 range indicate water ligands.[73,74] Hydrogen atoms could not be located crystallographically and so their positions are calculated.

Packing and Disorder

5 crystallises along with three constituent acetonitrile molecules in the monoclinic crystal system in space group $P2_1/n$. The crystal packing is shown in Figure 4.2.9.

One arm of the N(1) tetrabutlyammonium cation is crystallographically modelled as disordered over two positions with occupancy 50/50%. The pyridine ligand N(2) is crystallographically modelled as being disordered over three positions in a 30/40/30% ratio. Two solvent acetonitrile molecules, N(3) and N(4), are disordered over two positions each, with occupancy 50/50%.

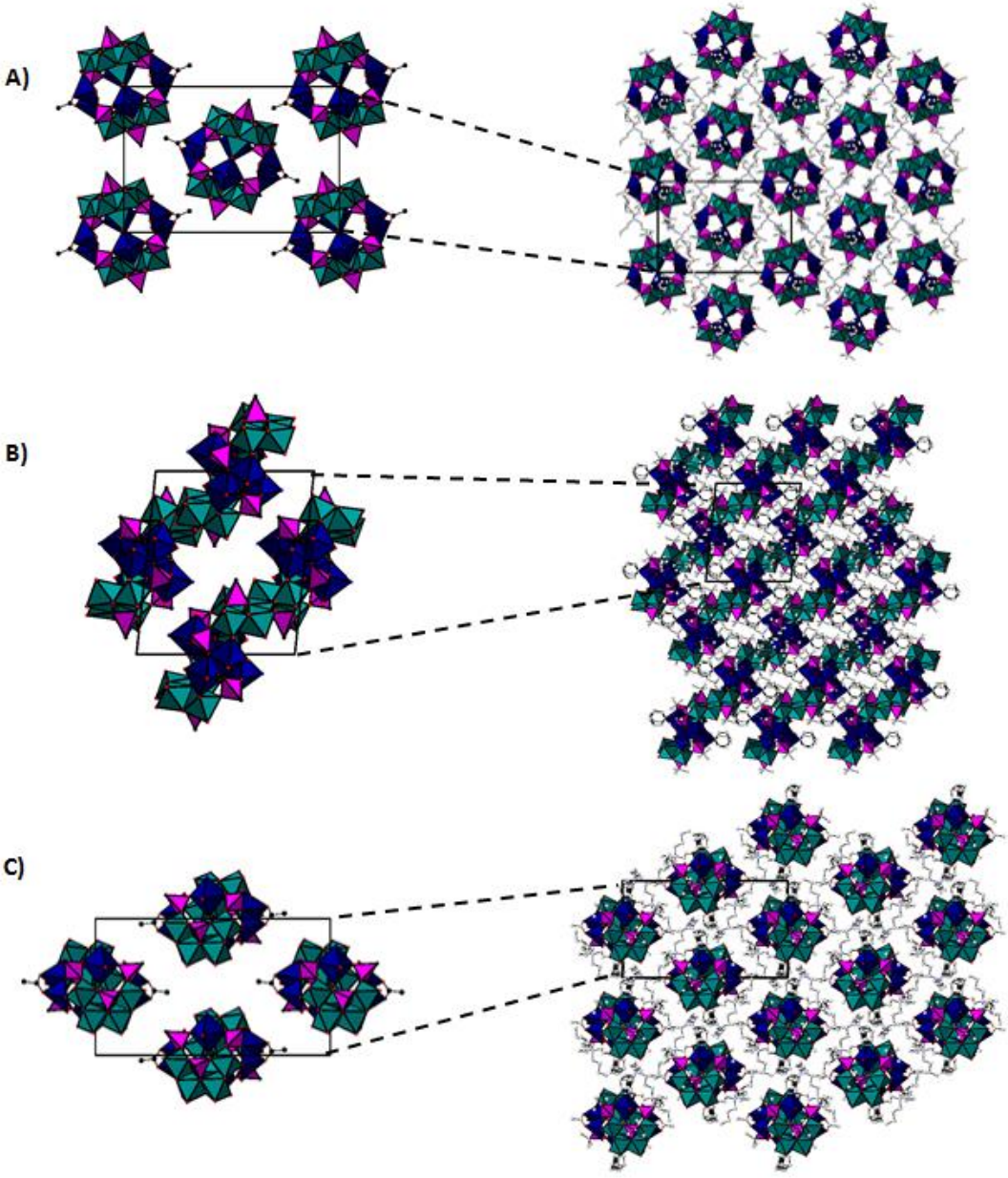

Figure 4.2.9 – Crystal packing diagrams for 5•3(MeCN), as viewed down : A) The crystallographic *a*-axis, B) the crystallographic *b*-axis. C) the crystallographic *c*-axis.
For clarity, solvent and cation molecules are removed and the cluster is shown in its simplified representation.
Colour Scheme: Mo teal, Cu light blue, P pink, O red, N blue, C black.

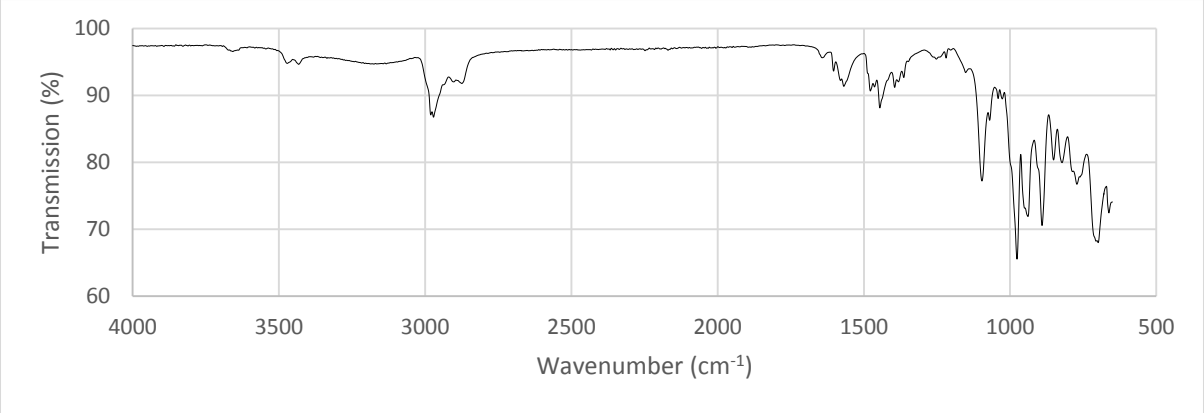

Figure 4.2.10 – A) The IR spectrum for 5•3(MeCN).

The infrared spectrum for **5**•3(MeCN) (Figure 4.2.10) is consistent with the crystallographic data presented above. The feature at 2964 cm^{-1} is assigned to the C-H organic backbones of the TBA cation and organic ligand groups. The features in the 1300 – 1600 cm^{-1} region are additionally ascribed to the organic portion of the molecule. The band at 1568 cm^{-1} and shoulder 1417 cm^{-1} are assigned as carboxylate symmetric and asymmetric stretches, respectively, with the difference between these two bands (Δ = 151 cm^{-1}) being consistent with the bidentate acetate bridging mode.[75] Three strong signals are observed in the *c.*950 – 1150 cm^{-1} region (at 1095 cm^{-1}, 977 cm^{-1} and 891 cm^{-1}), which are attributed to P-O vibrations by extension of the analyses in the previous two chapters (*c.f.* Figure 2.4.3). Similarly, features below 950 cm^{-1} probably arise from a combination of Mo-O and Co-O vibrations.

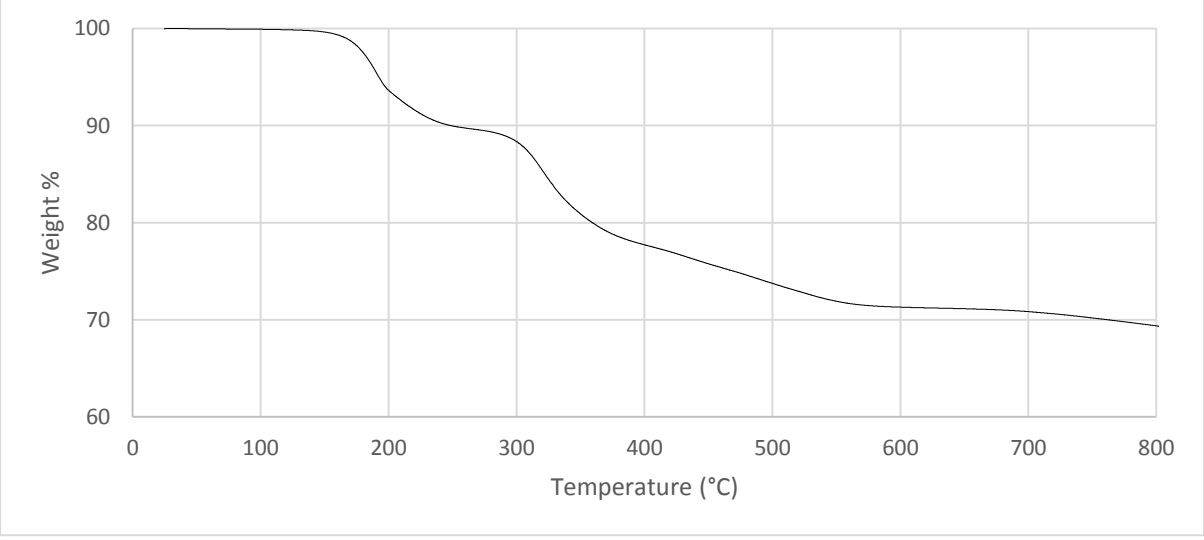

Figure 4.2.11 – TGA of compound 5.

The thermogravimetric analysis (TGA) for dried crystals of **5** is presented in Figure 4.2.11. No solvent loss is observed up to *c.* 150 °C. The weight loss centred on *c.* 200 °C probably corresponds to loss of water any pyridine ligands from the complex (expected 92.3%, observed 89.9%). The discrepancy in the observed and calculated values may be due to the partial incorporation of additional pyridine ligands (see Section 4.3). Subsequent weight loss features are attributed to a combination of ligand decomposition reactions (*c.* 300 °C - *c.* 700 °C) and oxide formation (> 700 °C).

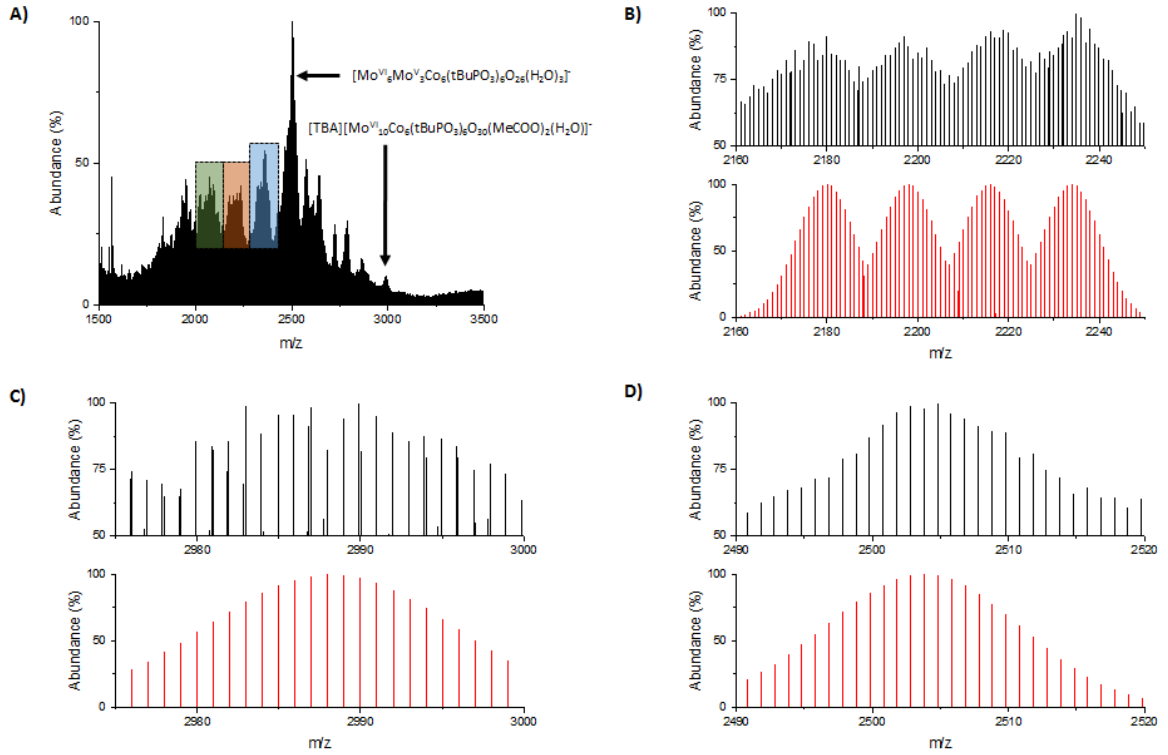

Figure 4.2.12 – A) Negative mode MALDI-MS of compound 5 in acetonitrile. B) Experimental (black) and simulated (red) spectra for the orange-shaded region in A. C) Experimental (black) and simulated (red) spectra for the [TBA][$Mo_{10}Co_6$(*t*BuPO_3)$_6O_{30}$(MeCOO)$_2$(H_2O)]$^-$ peak. D) Experimental (black) and simulated (red) spectra for the [$Mo^{VI}_6Mo^V_3Co_6$(*t*BuPO_3)$_6O_{26}$(H_2O)$_3$]$^-$ peak.

Several species can be seen in the MALDI-MS analysis of compound **5** in acetonitrile that are consistent with fragments of **5** (Figure 4.2.12 and Table 4.2.7). The largest observable species in the spectrum can be assigned as [TBA][$Mo_{10}Co_6$(*t*BuPO_3)$_6O_{30}$(MeCOO)$_2$(H_2O)]$^-$ (expected mass 2900.00, observed mass 2900.01), which corresponds to the loss of two pyridine and five water molecules from **5**. Interestingly, several decomposition products can be observed in the spectrum as the compound loses the peripheral ligands followed by a series of successive {MoO_x} fragments. The most intense peak observed in the spectrum is [$Mo^{VI}_6Mo^V_3Co_6$(*t*BuPO_3)$_6O_{26}$(H_2O)$_3$]$^-$, followed by a series of smaller fragments. These fragments come in clusters of four peaks, representing different protonation/charge states.

Species	*m/z calc.*	*m/z obs.*
$[TBA][Mo_{10}Co_6(t\text{BuPO}_3)_6O_{30}(MeCOO)_2(H_2O)]^-$	*2900.00*	*2900.01*
$[Mo^{VI}_6Mo^{V}_3Co_6(t\text{BuPO}_3)_6O_{26}(H_2O)_3]^-$	*2503.83*	*2503.79*
$[Mo^{VI}_8Mo^{V}Co_6(t\text{BuPO}_3)_6O_{27}]^-$	*2465.79*	*2465.80*
$[Mo^{VI}_5Mo^{V}_3Co_6(t\text{BuPO}_3)_6O_{23}(H_2O)_4]^-$	*2377.94*	*2377.87*
$[Mo^{VI}_5Mo^{V}_3Co_6(t\text{BuPO}_3)_6O_{23}(H_2O)_3]^-$	*2359.93*	*2359.89*
$[Mo^{VI}_5Mo^{V}_3Co_6(t\text{BuPO}_3)_6O_{23}(H_2O)_2]^-$	*2341.93*	*2341.88*
$[Mo^{VI}_5Mo^{V}_3Co_6(t\text{BuPO}_3)_6O_{23}(H_2O)]^-$	*2323.91*	*2323.89*
$[Mo^{VI}_3Mo^{V}_4Co_6(t\text{BuPO}_3)_6O_{20}(H_2O)_4]^-$	*2235.05*	*2234.97*
$[Mo^{VI}_3Mo^{V}_4Co_6(t\text{BuPO}_3)_6O_{20}(H_2O)_3]^-$	*2216.04*	*2216.00*
$[Mo^{VI}_3Mo^{V}_4Co_6(t\text{BuPO}_3)_6O_{20}(H_2O)_2]^-$	*2197.03*	*2196.96*
$[Mo^{VI}_3Mo^{V}_4Co_6(t\text{BuPO}_3)_6O_{20}(H_2O)_1]^-$	*2180.02*	*2179.98*
$[Mo^{IV}Mo^{V}_5Co_6(t\text{BuPO}_3)_6O_{15}(H_2O)_6]^-$	*2095.20*	*2095.02*
$[Mo^{IV}Mo^{V}_5Co_6(t\text{BuPO}_3)_6O_{15}(H_2O)_5]^-$	*2076.18*	*2076.02*
$[Mo^{IV}Mo^{V}_5Co_6(t\text{BuPO}_3)_6O_{15}(H_2O)_4]^-$	*2057.17*	*2057.01*
$[Mo^{IV}Mo^{V}_5Co_6(t\text{BuPO}_3)_6O_{15}(H_2O)_2]^-$	*2023.15*	*2023.03*

Table 4.2.7 – Possible species observed in the MALDI-MS analysis of 5 in acetonitrile.

4.3) Ligand Substitution of 5 – Pyridyl Substitution

As discussed in chapter 1, hybrid POM structures (ie. POM structures supported by organic ligands) are significant because they represent a synthetic handle for manipulation of the compound. Substitution of any particular organic ligand for another with an equivalent ligand allows the properties of the compound to be modified while retaining the same core structure. Electron withdrawing or donating substituents, for example, can be exploited to manipulate the electronic properties of metal centres. Moreover, the compound can be endowed with entirely new functionality (*e.g.* light harvesting ability or luminescence) by incorporating organic ligands with appropriate functional groups. In addition, polyfunctional ligands allow the dimensionality of the compounds to be manipulated, allowing zero dimensional clusters to be assembled into more sophisticated architectures like polymers or frameworks.

Compound **5** possesses a hybrid structure with three distinct classes of organic ligands supporting the cluster core - phosphonates, carboxylates and pyridyl ligands (in addition to water and oxo ligands). In this respect, compound **5** represents an ideal compound to explore the versatility of hybrid POM structures (Figure 4.3.1). Modifications of these three ligand classes are all synthetically feasible, allowing additional functionality to be incorporated. Moreover, the presence of multiple ligand classes was predicted to allow orthogonal substitution of any of the three ligand classes, while maintaining the integrity of the others.

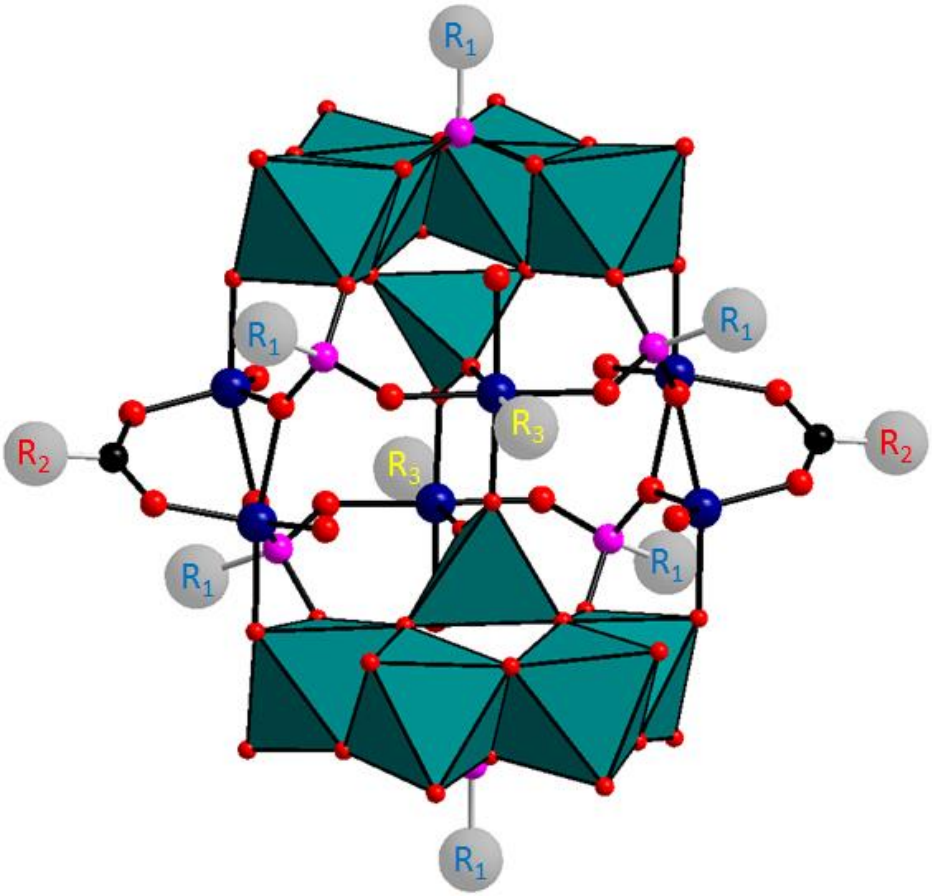

Figure 4.3.1 – The cluster core of 5, highlighting the three distinct ligand sites represented by the phosphonate ligands (R_1), carboxylate ligands (R_2) and pyridyl ligands (R_3).

To this end, a series of analogues of compound 5 were prepared by substituting one or more of the organic ligands found in 5 (Figure 4.3.2). In the first instance, the pyridyl ligands represented a relatively simple and straightforward target for substitution. Pyridyl ligands are monodentate by nature and therefore probably do not play a significant role in templating of the final structure, but allow the principle of ligand substitution to be demonstrated easily. Picoline was identified as a suitable substitution for pyridine, as it was deemed to be suitably similar in structure and reactivity to allow the reaction to proceed (as well as being reasonably straightforward to identify crystallographically).

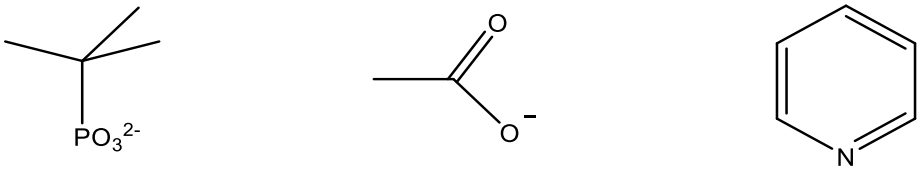

Figure 4.3.2 – The three organic ligands present in 5.

Therefore, cobalt (II) acetate, *tert*-butylphosphonic acid and Lindqvist hexamolybdate were combined in acetonitrile in the presence of picoline. The reaction mixture yielded pink-purple crystals after several days. The crystals were subjected to single crystal X-ray diffraction and found to contain $[TBA]_2[Mo^{VI}_{10}Co^{II}_6O_{12}(\mu\text{-}O)_{14}(\mu_3\text{-}O)_4(t\text{BuPO}_3)_6(\text{MeCOO})_2(\text{pic})_4(H_2O)_6]$, **6**. The crystals formed in the triclinic crystal system in the space group *P*-1, and also contained 4.4 constituent acetonitrile molecules per formula unit. TBA represents tetrabutylammonium, *t*-Bu represents the *tert*-butyl moiety and pic represents picoline (Figure 4.3.3).

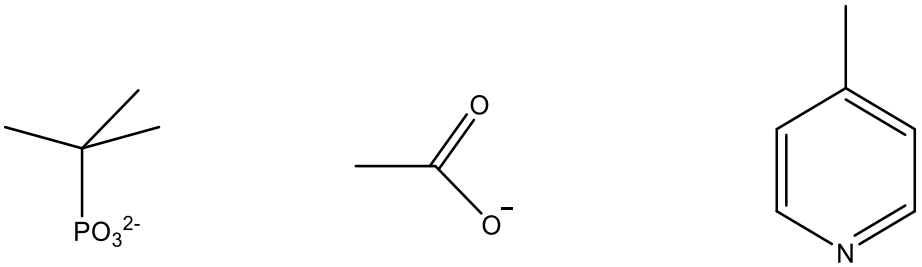

Figure 4.3.3 – The three organic ligands present in 6.

The core structure of **6** represents an analogue structure to **5**, but with pyridine ligands replaced by picoline ligands. There is one minor structural difference in **6** that is noteworthy – in **6**, one of the cobalt centres in the dinuclear units recruits an extra N-donor ligand (picoline) into its coordination sphere to generate a $\{CoO_5N\}$ environment (Figure 4.3.4). This simple substitution indicates that ligand modification of the core structure in **5** is indeed possible, encouraging the incorporation of more sophisticated ligand moieties onto the core of **5**.

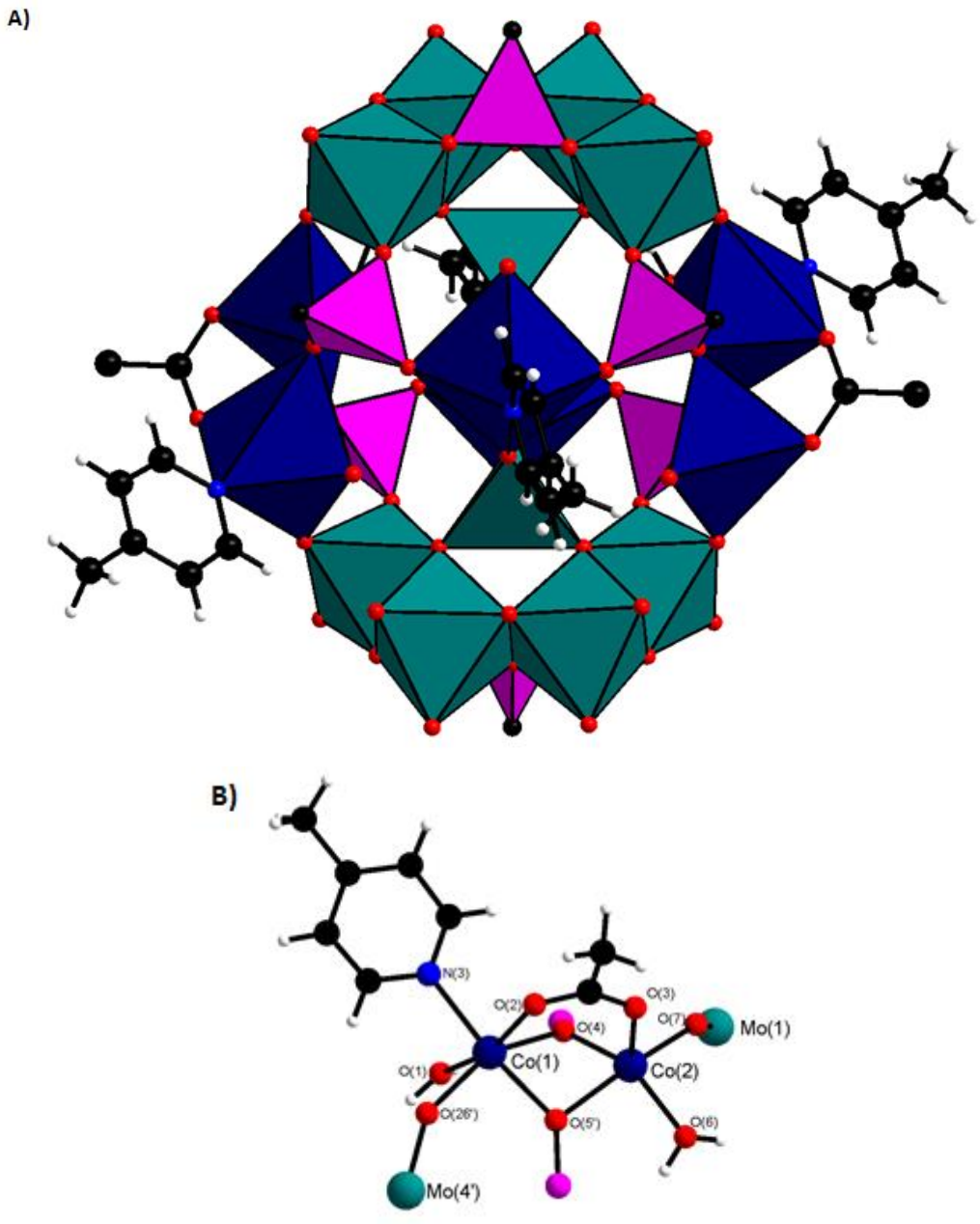

Figure 4.3.4 – A) Simplified representation of the cluster core in 6 showing the picoline ligands. B) The dinuclear cobalt unit in 6. Colour Scheme: Mo teal, Co dark blue, P pink, O red, N blue, C black, H white.

Identification code	**6**•4.4(MeCN)
Empirical formula	$C_{92.8}H_{185.2}Co_6Mo_{10}N_{10.4}O_{58}P_6$
Formula weight (g/mol)	3910.7
Temperature (K)	100(2)
Wavelength (Å)	0.71073
Crystal system	Triclinic
Space group	*P*-1
a (Å)	13.9147(6)
b (Å)	17.0418(7)
c (Å)	17.3781(7)
α (°)	74.8370(10)
β (°)	80.3310(10)
γ (°)	83.527(2)
Volume ($Å^3$)	3910.7(3)
Z	1
Calculated density ρ_{calc} (g/cm^3)	1.645
Absorption coefficient μ (mm^{-1})	1.529
F(000)	1951.0
Crystal size (mm^3)	0.11 x 0.1 x 0.09
2Θ range for data collection (°)	2.976 to 61.136
Index ranges	$-19 \leq h \leq 19$, $-24 \leq k \leq 24$, $-24 \leq l \leq 24$
Reflections collected	159269
Independent reflections	23891 [R_{int} = 0.0618]
Data/restraints/parameters	23891/41/923
Goodness-of-fit on F^2	1.093
Final R indices [I>=2σ (I)]	R_1 = 0.0460, wR_2 = 0.1089
Final R indices [all data]	R_1 = 0.0841, wR_2 = 0.1320
Largest diff. peak and hole (e $Å^{-3}$)	1.79/-1.21

Table 4.3.1 – Crystallographic details for compound 6•4.4(MeCN).

Crystallographically, two arms of the tetrabutylammonium cations are modelled as being disordered in 0.43:0.57 and 0.32:0.68 ratios, respectively. One crystallographically distinct acetonitrile molecule is disordered over three positions in a 0.5:0.25:0.25 ratio, while another is 0.2 occupied.

Metal Atom	Bonded Atom	Bond Length (Å)	BVS	Oxidation State
Co(1)	O(1)	2.037(3)	1.851	+II
	O(2)	2.078(3)		
	O(5)	2.092(3)		
	O(26')	2.147(4)		
	N(3)	2.159(4)		
	O(4)	2.352(4)		
Co(2)	O(6)	1.977(3)	1.980	+II
	O(3)	1.983(3)		
	O(4)	1.998(3)		
	O(7)	2.072(4)		
	O(5)	2.182(3)		
Co(3)	O(16)	2.035(3)	2.033	+II
	O(17)	2.038(3)		
	O(14)	2.101(3)		
	N(2)	2.126(3)		
	O(13')	2.145(3)		
	O(15)	2.155(4)		

Table 4.3.2 – Crystallographically-determined bond lengths for the cobalt centres in 6, along with their oxidation state as determined by Bond Valence Sum (BVS) analysis.

The cobalt bond lengths in **6** range from 1.977(3) Å to 2.352(4) Å, depending on the type of interaction (Table 4.3.2). The bond lengths for the cobalt centres Co(2) and Co(3) in **6** are extremely similar to their counterparts in **5**, as expected (*c.f.* Table 4.2.4).

However the incorporation of an extra N-donor ligand shifts bond lengths to slightly larger values in Co(1). The phosphonate O-donor O(4) in particular shifts significantly, from a bond length of *c.* 2.19 Å to *c.* 2.35 Å, resulting in a more significant asymmetry in the phosphonate O-donors than exists in **5**.

Interestingly, despite incorporating an extra ligand into its coordination sphere, the BVS value for Co(1) deviates more significantly from the expected value than the equivalent centre in **5**.

Bond	Bond Angle (°)	Bond	Bond Angle (°)
O(5')-Co(1)-O(4)	77.80(11)	O(13')-Co(3)-O(15)	82.93(11)
O(1)-Co(1)-O(4)	79.93(12)	O(17)-Co(3)-N(2)	84.93(13)
O(2)-Co(1)-N(3)	80.89(15)	O(17)-Co(3)-O(14)	86.27(11)
O(2)-Co(1)-O(5')	84.28(13)	O(16)-Co(3)-O(14)	89.05(12)
O(1)-Co(1)-N(3)	85.11(14)	O(14)-Co(3)-N(2)	89.13(12)
O(1)-Co(1)-O(26)	85.53(12)	O(17)-Co(3)-O(13')	90.29(11)
O(5')-Co(1)-O(26')	85.62(11)	O(16)-Co(3)-N(2)	91.82(13)
O(26')-Co(1)-N(3)	93.78(14)	O(16)-Co(3)-O(15)	91.87(12)
O(2)-Co(1)-O(4)	94.99(14)	O(13')-Co(3)-O(14)	92.01(11)
O(2)-Co(1)-O(26')	105.15(14)	O(13')-Co(3)-O(16)	93.06(11)
N(3)-Co(1)-O(4)	108.00(14)	O(13')-Co(3)-O(15)	93.07(12)
O(1)-Co(1)-O(5')	110.28(12)	N(2)-Co(3)-O(15)	95.85(12)
Angle Variance (σ^2)	**130.27**	**Angle Variance (σ^2)**	**14.1**
Distortion Index	**0.105**	**Distortion Index**	**0.033**
O(5')-Co(2)-O(4)	83.91(12)		
O(5')-Co(2)-O(6)	88.00(12)		
O(6)-Co(2)-O(7)	90.17(12)		
O(4)-Co(2)-O(7)	90.25(13)		
O(3)-Co(2)-O(5')	94.42(14)		
O(3)-Co(2)-O(7)	98.18(14)		
O(3)-Co(2)-O(4)	104.13(14)		
O(6)-Co(2)-O(3)	110.76(14)		
O(6)-Co(2)-O(4)	144.67(13)		
O(7)-Co(2)-O(5')	167.10(12)		
Geometry Index (τ_5)	**0.374**		

Table 4.3.3 – Crystallographically-determined bond angles for the cobalt centres in 6, along with the appropriate distortion parameters.

The cobalt centres in the dinuclear unit both display significant distortion away from their idealised geometries (Table 4.2.9). The octahedral environment around Co(1) is quite highly distorted, with σ^2_{oct} and DI values of 130.27 and 0.105, respectively. The Co(2) centre has a τ_5 value of 0.374, which is slightly smaller than (but still comparable to) the analogous τ_5 values in **5** (τ_5 = 0.464 and τ_5 = 0.421, *c.f.* Table 4.2.5). Given the extent of distortion in both **5** and **6**, it is somewhat unclear to what extent the incorporation of an additional N-donor ligand onto **6** offers any additional stabilisation over **5**.

The Co(3) coordination environment has very close to ideal octahedral geometry, with σ^2_{oct} and DI values of 14.1 and 0.033, respectively.

σ^2_{oct}, DI and τ_5 are defined in the same way as previously.[40–43,69]

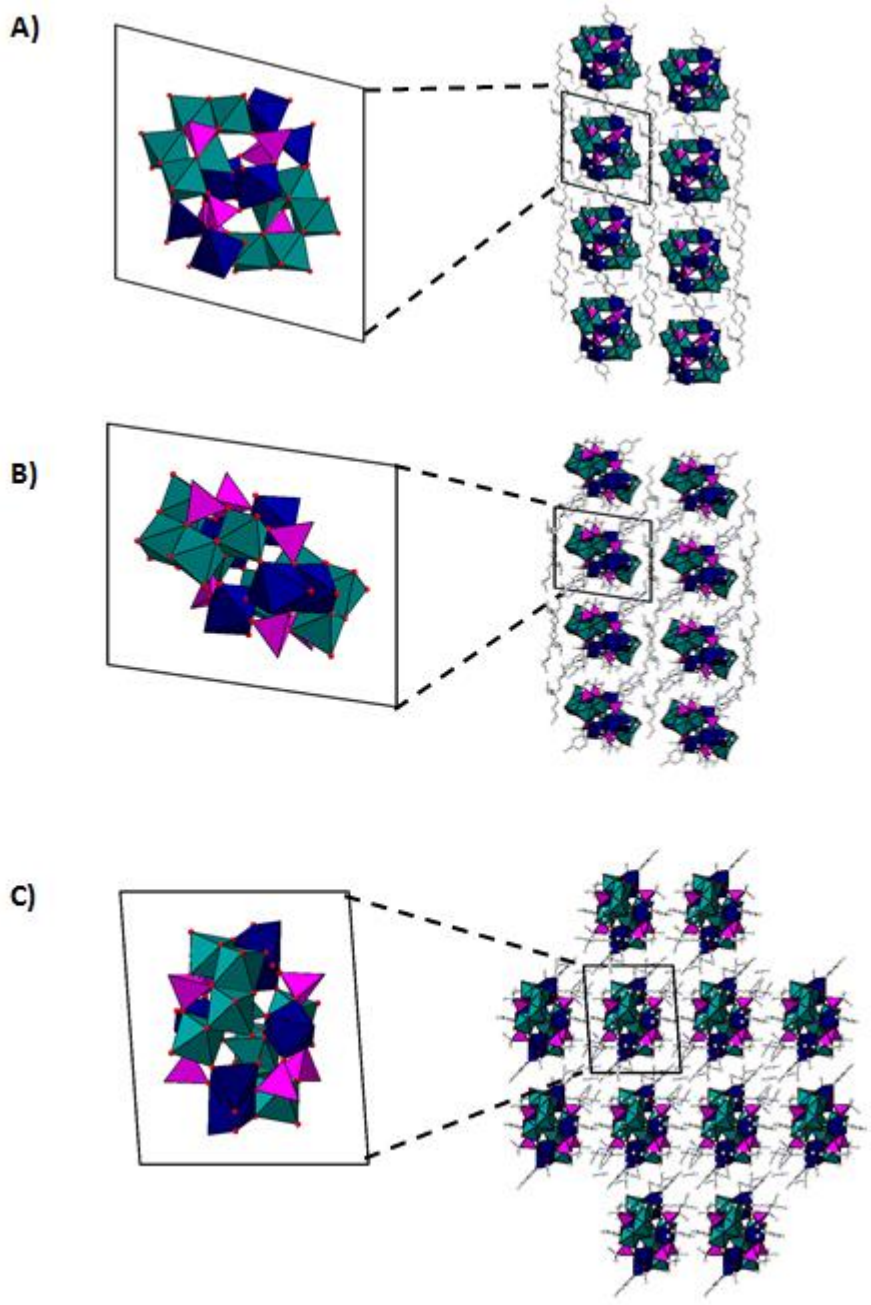

Figure 4.3.5 – Crystal packing diagrams for 6•4.4(MeCN), as viewed down : A) The crystallographic *a*-axis, B) the crystallographic *b*-axis. C) the crystallographic *c*-axis.

4.4) Ligand Substitution of 5 – Carboxylate Substitution

Having demonstrated the principle that pyridyl ligands on the cluster core of **5** can be replaced with analogous ligands, we decided to investigate the possibility of modifying the cluster core at the carboxylate position. Holding the phosphonate and pyridyl ligands constant, a series of substitutions were made by substituting different carboxylate ligands into the reaction mixture. Initially, carboxylate ligands bearing additional functional groups were avoided as the reactivity of the system was not yet fully understood.

In the first instance, benzoate ligands were targeted as a suitable substitution for the acetate ligands on the basis that the phenyl moiety was sufficiently rigid to be easily identifiable through crystallography, and on the basis that cobalt (II) benzoate was a readily available starting material.

Replacing cobalt (II) acetate with cobalt (II) benzoate and holding all other synthetic parameters constant yielded crystals of $[TBA]_2[Mo^{VI}_{10}Co^{II}_6O_{12}(\mu\text{-}O)_{14}(\mu_3\text{-}O)_4(t\text{BuPO}_3)_6(\text{PhCOO})_2(\text{py})_2(H_2O)_6]$, **7**, as pink-purple crystals after approximately one week of slow evaporation. TBA represents tetrabutylammonium, *t*-Bu represents the *tert*-butyl moiety, Ph represents a phenyl group and py represents pyridine. The crystals formed in the monoclinic crystal system in space group *C*2/c. No constituent solvent molecules were observed either crystallographically or through TGA analysis.

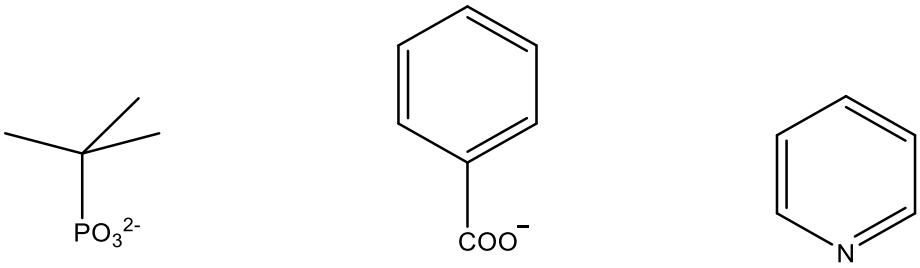

Figure 4.4.1 – The three organic ligands present in 7.

The structure of **7** represents an analogue of **5** with benzoate ligands substituted in place of the acetate ligands in **5** (Figures 4.4.1 and 4.4.2). The structure incorporates additional pyridine molecules onto the dinuclear unit like **6**. The structure indicates that the cobalt-molybdate core can accommodate both aromatic and aliphatic carboxylate supporting ligands into its structure. Moreover, the *para*- and *meta*- positions of the benzoate ligand are reasonably remote from the cluster core of **5**, and offering possibilities that functional groups could be incorporated at these positions without conflicting with the assembly of the cluster core.

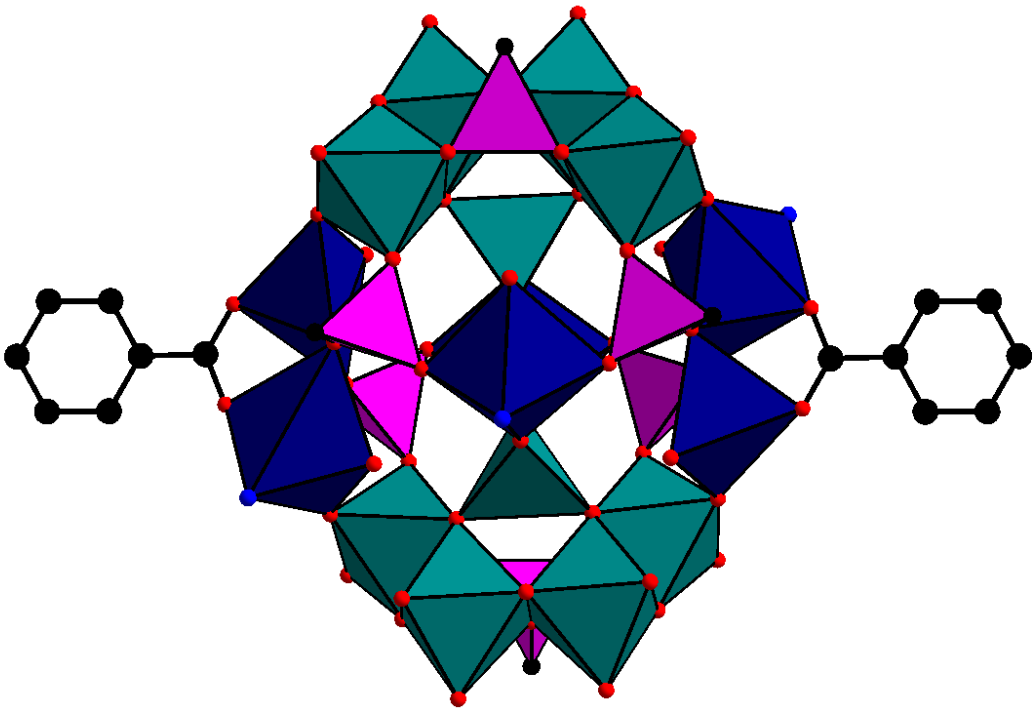

Figure 4.4.2 – Simplified representation of the cluster core in 7, showing the benzoate ligands. Colour Scheme: Mo teal, Co dark blue, P pink, O red, N blue, C black, H white.

Having successfully isolated **7**, the next target identified for incorporation onto the cluster core was the phenylacetate ligand. Similar to the benzoate ligand but incorporating an extra –CH_2– spacer, this represented a natural extension to the series.

The phenylacetate salt of cobalt (II) was not commercially available, but could be synthesised relatively easily. However, this proved an unnecessary synthetic step as cobalt (II) nitrate along with the free carboxylic acid could be used, generating the same product.

Therefore, cobalt (II) nitrate and phenylacetic acid were substituted into the synthetic procedure for **5** in place of cobalt (II) acetate. The reaction mixture yielded pink-purple crystals after approximately one week. The crystals were subjected to single crystal X-ray diffraction and found to contain $[TBA]_2[Mo^{VI}_{10}Co^{II}_6O_{12}(\mu\text{-}O)_{14}(\mu_3\text{-}O)_4(t\text{BuPO}_3)_6(\text{BzCOO})_2(py)_2(H_2O)_6]$ (**8**), along with 3.5 constituent acetonitrile molecules per formula unit in the monoclinic crystal system in space group $P2_1/n$. TBA represents tetrabutylammonium, *t*-Bu represents the *tert*-butyl moiety, Bz represents a benzyl group and py represents pyridine.

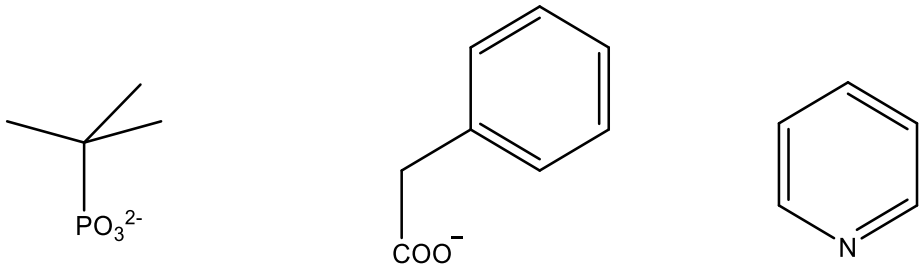

Figure 4.4.3 – The three organic ligands present in 8.

The structure of **8** represents an analogue of **5** with phenylacetate ligands substituted in place of the acetate ligands in **5** (Figures 4.4.3 and 4.4.4). Unlike **5**-**7**, the carboxylate ligand in **8** possesses rotational freedom of movement due to the –CH_2- (methylene) spacer. Nevertheless, the compound could be crystallised without any significant disorder being introduced into the crystal structure. The O-C-C-Ph torsion angle is 20.2° in the crystalline state, probably due to crystal packing considerations. This indicates that reasonably flexible ligands can be incorporated onto the cluster core of **5** without sacrificing the ability to characterise the compound crystallographically.

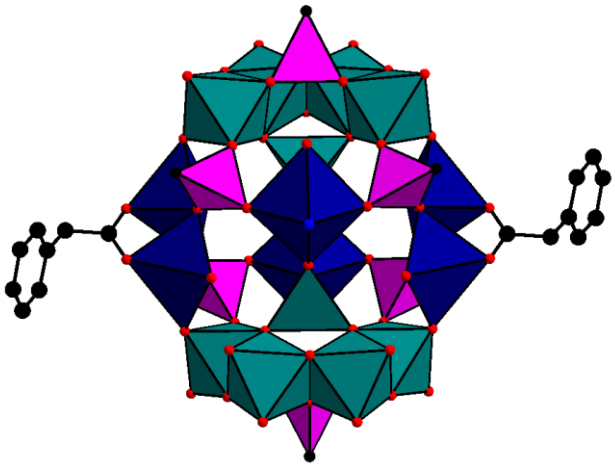

Figure 4.4.4 – Simplified representation of the cluster core in 8, showing the phenylacetate ligands. Colour Scheme: Mo teal, Co dark blue, P pink, O red, N blue, C black.

Having incorporated an aromatic carboxylate ligand onto the core of **7** and a rotationally flexible carboxylate ligand onto the core of **8**, we decided to investigate the addition of bulky aliphatic side groups at the carboxylate positions. Initially, pivalate substitutions of the cluster core were targeted, but these were unsuccessful (possibly due to the tendency of pivalate ligands to form cobalt cluster complexes under similar conditions[76]).

However, by substituting cobalt (II) nitrate and 1-adamantylcarboxylic acid into the synthesis of **5** in place of cobalt (II) acetate, $[TBA]_2[Mo^{VI}_{10}Co^{II}_6O_{12}(\mu\text{-}O)_{14}(\mu_3\text{-}O)_4(t\text{BuPO}_3)_6(\text{Ad-COO})_2(py)_2(H_2O)_6]$ (**9**) could be isolated. TBA represents tetrabutylammonium, *t*-Bu represents the *tert*-butyl moiety, Ad represents the adamantyl group and py represents pyridine. **9** crystallised overnight as pink-purple crystals in the monoclinic crystal system in space group *C2/c*. No constituent solvent molecules were observed crystallographically or through TGA analysis. The cluster incorporated additional pyridine ligands onto the dinuclear cobalt units, in the same manner as **6**.

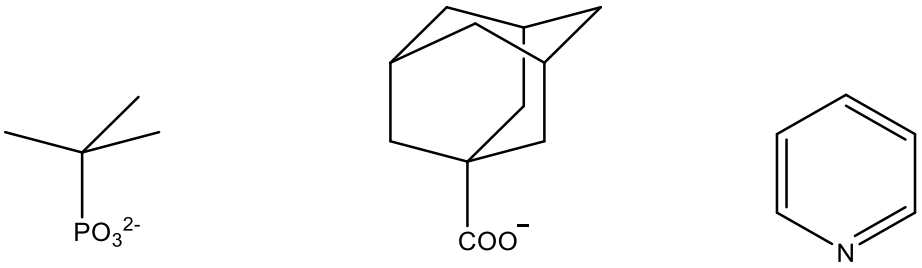

Figure 4.4.5 – The three organic ligands present in 9.

The structure of **9** represents an analogue of **5** with adamantylcarboxylate ligands substituted in place of the acetate ligands in **5** (Figures 4.4.5 and 4.4.6). The adamantyl group is quite a sterically bulky system of fused aliphatic rings, indicating the tolerance of the synthetic procedure towards bulky side groups.

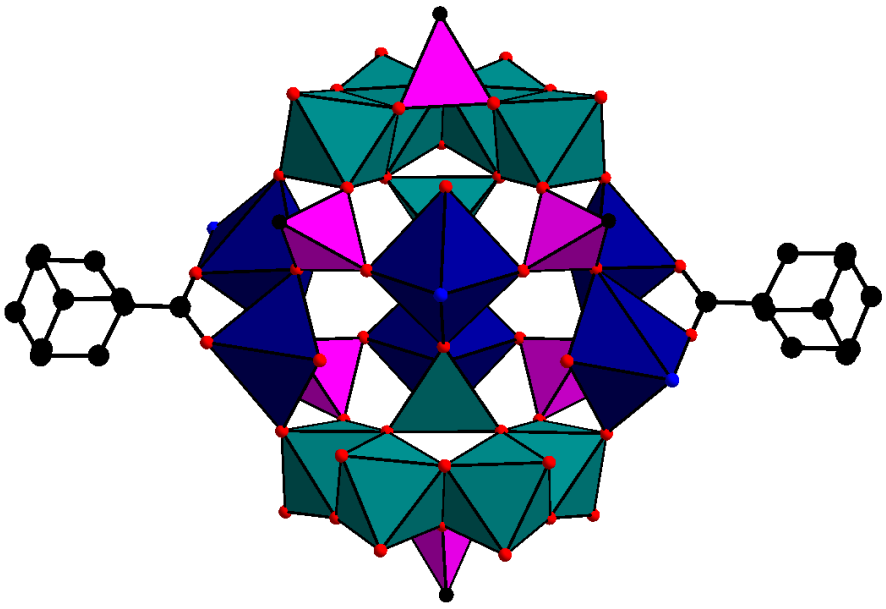

Figure 4.4.6 – Simplified representation of the cluster core in 9, showing the adamantylcarboxylate ligands. Colour Scheme: Mo teal, Co dark blue, P pink, O red, N blue, C black.

Identification code	**7**
Empirical formula	$C_{90}H_{167}Co_6Mo_{10}N_6O_{58}P_6$
Formula weight (g/mol)	3910.7
Temperature (K)	100(2)
Wavelength (Å)	0.71073
Crystal system	Monoclinic
Space group	C2/c
a (Å)	21.7038(18)
b (Å)	24.446(2)
c (Å)	28.467(3)
α (°)	90.00
β (°)	109.836(1)
γ (°)	90.00
Volume (Å^3)	14208(2)
Z	4
Calculated density ρ_{calc} (g/cm^3)	1.758
Absorption coefficient μ (mm^{-1})	1.680
F(000)	7544.0
Crystal size (mm^3)	0.18 × 0.12 × 0.04
2Θ range for data collection (°)	3.042 to 56.608
Index ranges	$-28 \leq h \leq 28$, $-32 \leq k \leq 31$, $-37 \leq l \leq 23$
Reflections collected	55974
Independent reflections	17629 [R_{int} = 0.0464]
Data/restraints/parameters	17629/17/671
Goodness-of-fit on F^2	1.079
Final R indices [I>=2σ (I)]	R_1 = 0.0615, wR_2 = 0.1584
Final R indices [all data]	R_1 = 0.1086, wR_2 = 0.1956
Largest diff. peak and hole (e Å^{-3})	1.93/-1.72

Table 4.4.1 – Crystallographic details for compound 7.

No solvent molecules or solvent-accessible voids were observed crystallographically. The pyridine ligands on Co(3) are modelled as disordered over two positions in 0.51:0.49 ratios. Reflections with I_{obs}-I_{calc}/σ greater than 10 were omitted.

Identification code	**8**•3.5(MeCN)
Empirical formula	$C_{89}H_{172.5}Co_6Mo_{10}N_{7.5}O_{58}P_6$
Formula weight (g/mol)	3773.82
Temperature (K)	100(2)
Wavelength (Å)	0.71073
Crystal system	Monoclinic
Space group	$P2_1/n$
a (Å)	15.6966(7)
b (Å)	19.5580(9)
c (Å)	23.4785(10)
α (°)	90.00
β (°)	97.587
γ (°)	90.00
Volume (Å^3)	7144.7(6)
Z	2
Calculated density ρ_{calc} (g/cm^3)	1.754
Absorption coefficient μ (mm^{-1})	1.671
F(000)	3788.0
Crystal size (mm^3)	0.176 × 0.108 × 0.068
2Θ range for data collection (°)	2.95 to 59.338
Index ranges	$-21 \leq h \leq 28$, $-27 \leq k \leq 27$, $-32 \leq l \leq 32$
Reflections collected	246867
Independent reflections	20165 [R_{int} = 0.0738]
Data/restraints/parameters	20165/32/866
Goodness-of-fit on F^2	1.193
Final R indices [I>=2σ (I)]	R_1 = 0.0514, wR_2 = 0.1041
Final R indices [all data]	R_1 = 0.0836, wR_2 = 0.1185
Largest diff. peak and hole (e Å^{-3})	2.03/-1.36

Table 4.4.2 – Crystallographic details for compound 8•3.5(MeCN).

The terminal methyl groups on two arms of the tetrabutlyammonium cations are modelled as being disordered over two positions in 0.3:0.7 and 0.4:0.6 ratios, respectively. One crystallographically distinct acetonitrile molecule is disordered over two positions in a 0.56:0.44 ratio, and the other is 0.75 occupied.

Identification code	**9**
Empirical formula	$C_{98}H_{176}Co_6Mo_{10}N_6O_{58}P_6$
Formula weight (g/mol)	3865.24
Temperature (K)	100(2)
Wavelength (Å)	0.71073
Crystal system	Monoclinic
Space group	*C*2/c
a (Å)	22.2697(15)
b (Å)	24.3823(17)
c (Å)	28.6484(18)
α (°)	90.00
β (°)	110.0166(17)
γ (°)	90.00
Volume (Å^3)	14616.1(17)
Z	4
Calculated density ρ_{calc} (g/cm^3)	1.757
Absorption coefficient μ (mm^{-1})	1.635
F(000)	7768
Crystal size (mm^3)	0.280 × 0.070 × 0.060
2Θ range for data collection (°)	3.300 to 55.052
Index ranges	$-21 \leq h \leq 28$, $-31 \leq k \leq 31$, $-37 \leq l \leq 37$
Reflections collected	179819
Independent reflections	16792 [R_{int} = 0.0692]
Data/restraints/parameters	16792/79/858
Goodness-of-fit on F^2	1.086
Final R indices [I>=2σ (I)]	R_1 = 0.0563, wR_2 = 0.1383
Final R indices [all data]	R_1 = 0.0906, wR_2 = 0.1627
Largest diff. peak and hole (e Å^{-3})	1.494/-1.542

Table 4.4.3 – Crystallographic details for compound 9.

The terminal methyl groups on two arms of the tetrabutlyammonium cations are modelled as being disordered over two positions in 0.44:0.56 and 0.41:0.59 ratios, respectively. One of the crystallographically distinct pyridine ligands is modelled as disordered over two positions in a 0.41:0.59 ratio. No solvent molecules or solvent-accessible voids were observed.

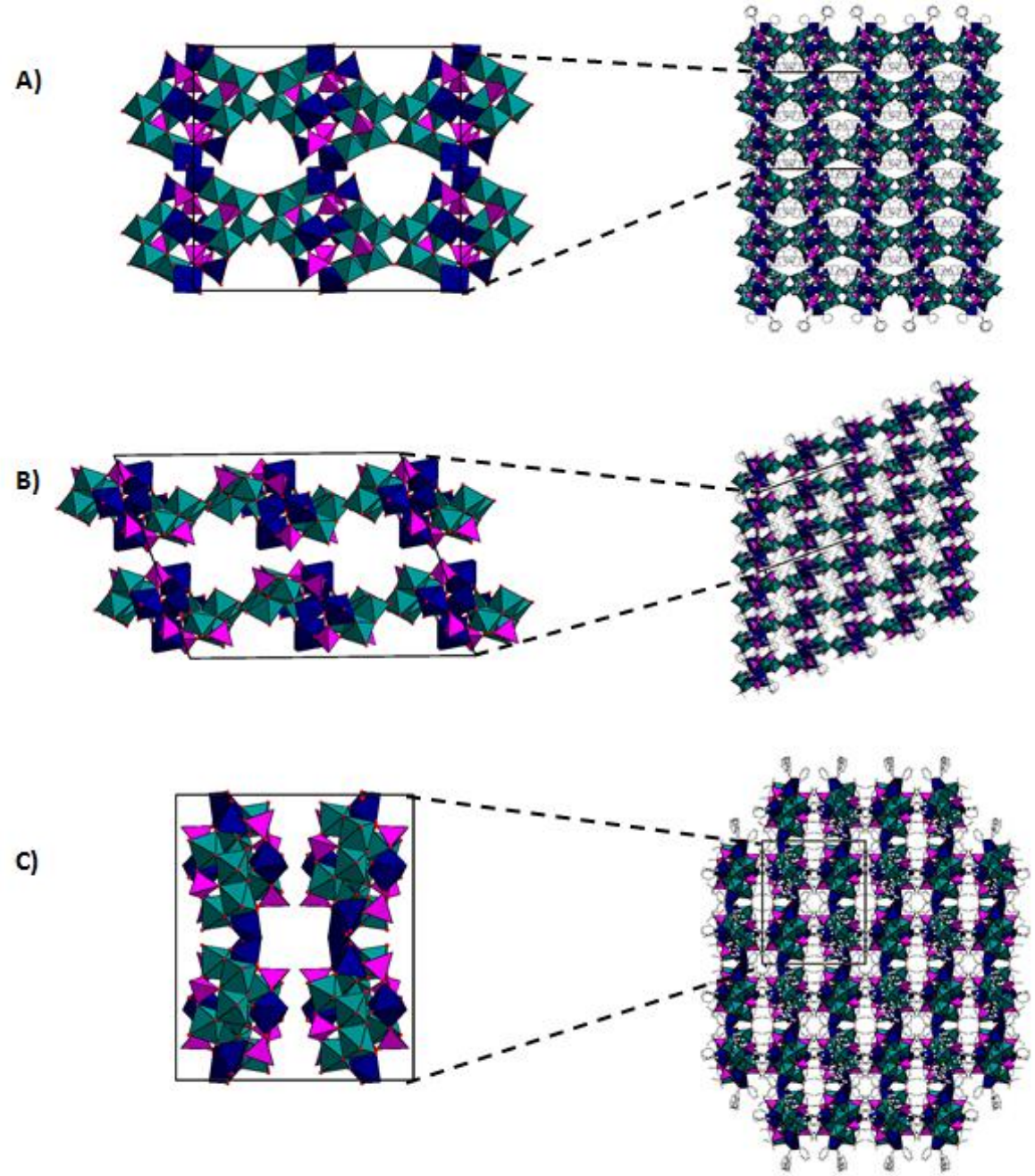

Figure 4.4.7 – Crystal packing diagrams for 7, as viewed down : A) The crystallographic *a*-axis, B) the crystallographic *b*-axis. C) the crystallographic *c*-axis.

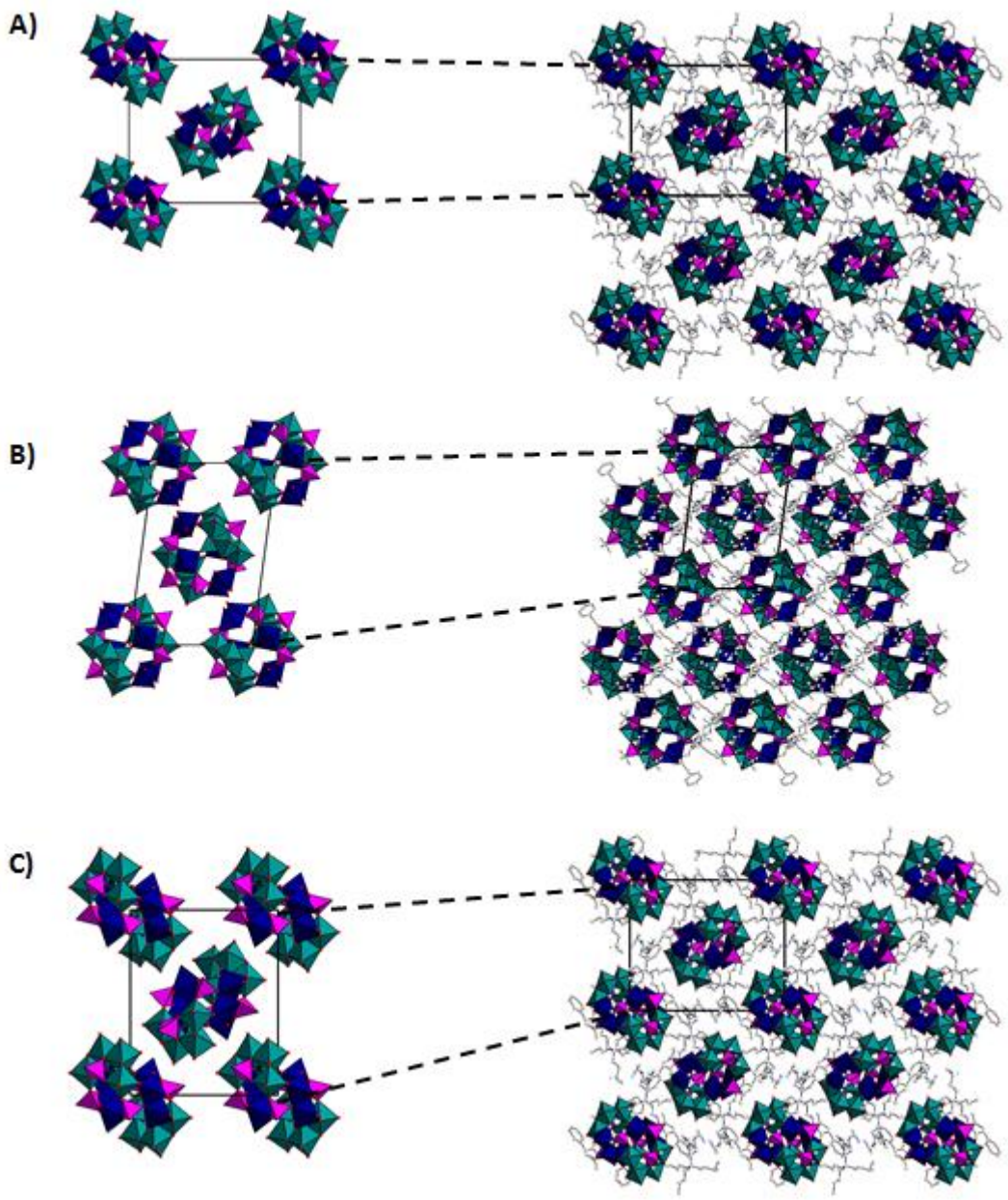

Figure 4.4.8 – Crystal packing diagrams for 8•3.5(MeCN), as viewed down : A) The crystallographic *a*-axis, B) the crystallographic *b*-axis. C) the crystallographic *c*-axis.

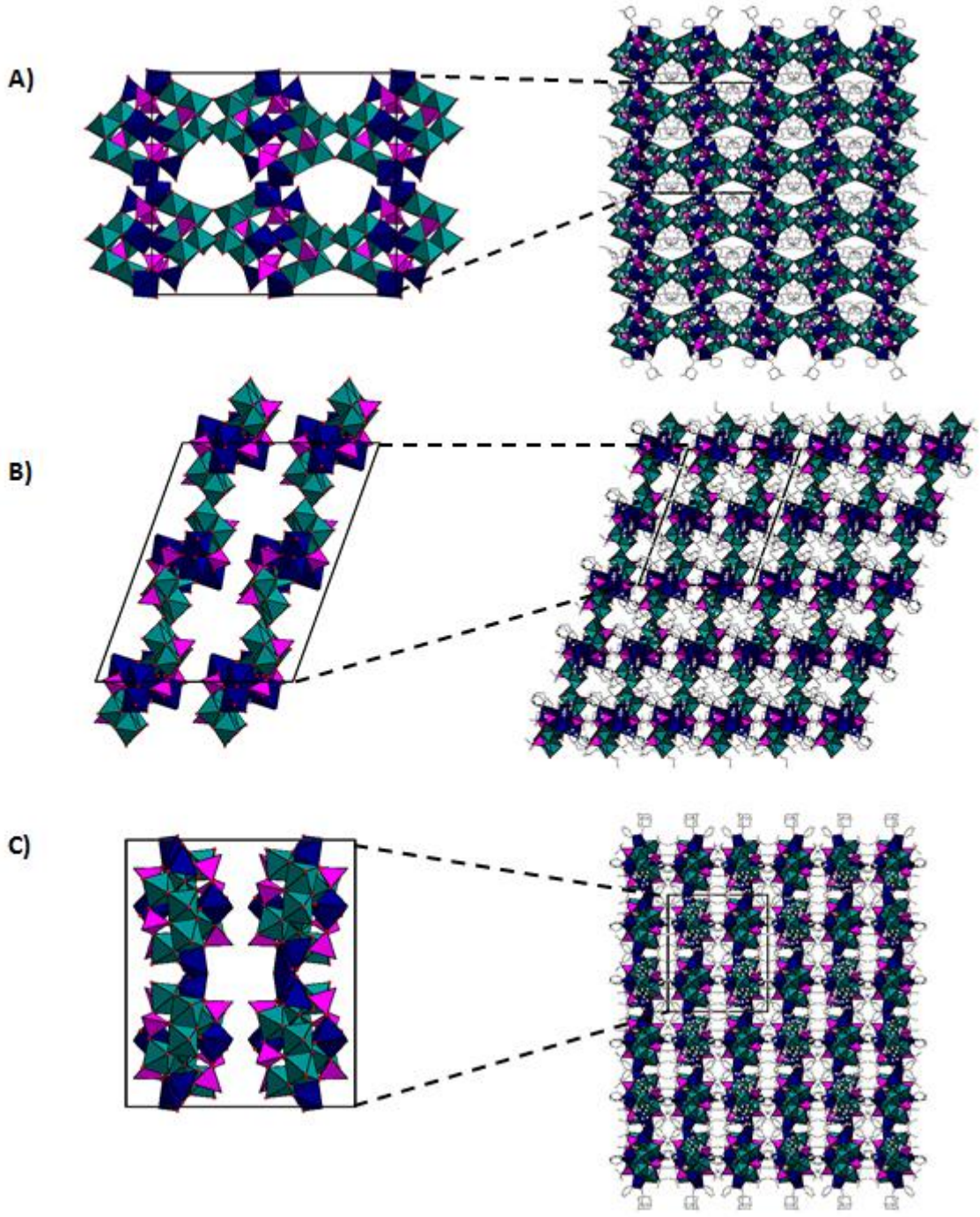

Figure 4.4.9 – Crystal packing diagrams for 9, as viewed down : A) The crystallographic *a*-axis, B) the crystallographic *b*-axis. C) the crystallographic *c*-axis.

4.5) Ligand Substitution of 5 – Phosphonate Substitution

Having successfully incorporated a range of simple aromatic and aliphatic ligands at the carboxylate positions, we turned our attention towards the phosphonate moieties. In particular, we were interested in generating an analogous series to **5**, **7**, **8** and **9** (which have different carboxylate ligands) by substituting different phosphonate ligands onto the structure.

Adamantylphosphonate was targeted as a suitable substitute to the *tert*-butylphosphonate used so far in this work. This ligand was identified as a suitable substitute as it is also contains a tertiary carbon centre, and therefore should display similar steric shielding effects in the early formation of the cluster core. Additionally, the adamantyl group is reasonably rigid and should therefore be amenable to crystallographic analysis.

Therefore, 1-adamantylphosphonic acid was incorporated into the synthesis of **5** in place of *tert*-butylphosphonic acid. The resulting reaction mixture yielded pink-purple crystals overnight. The crystals were subjected to single crystal X-ray diffraction and found to contain $[TBA]_2[Mo^{VI}_{10}Co^{II}_6O_{12}(\mu\text{-}O)_{14}(\mu_3\text{-}O)_4(AdPO_3)_6(MeCOO)_2(py)_2(H_2O)_6]$ (**10**), along with 9.5 constituent acetonitrile molecules per formula unit in the monoclinic crystal system in space group $P2_1/n$. TBA represents tetrabutylammonium, Ad represents the adamantyl group and py represents pyridine.

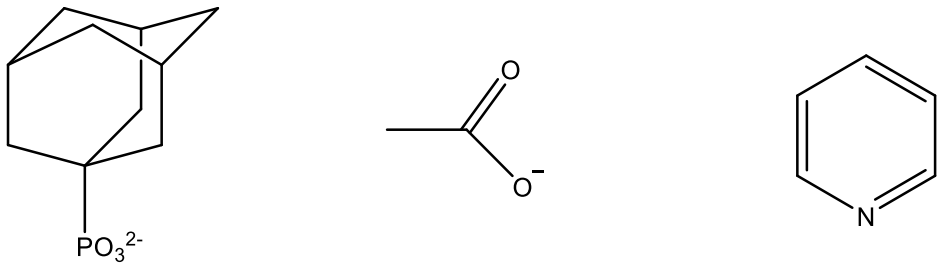

Fig 4.5.1 – The three organic ligands present in 10

The structure of **10** represents an adamantylphosphonate-substituted analogue of **5** (Figures 4.5.1 and 4.5.2). The isolation of **10** proves that substitution of **5** can also take place at the phosphonate positions. Moreover, **5** has now been modified at all three organic ligand positions – the phosphonate, carboxylate and pyridyl positions. Orthogonal ligand substitution in this manner is quite rare, and allows for a much higher degree of structural flexibility than is generally available in POM systems.

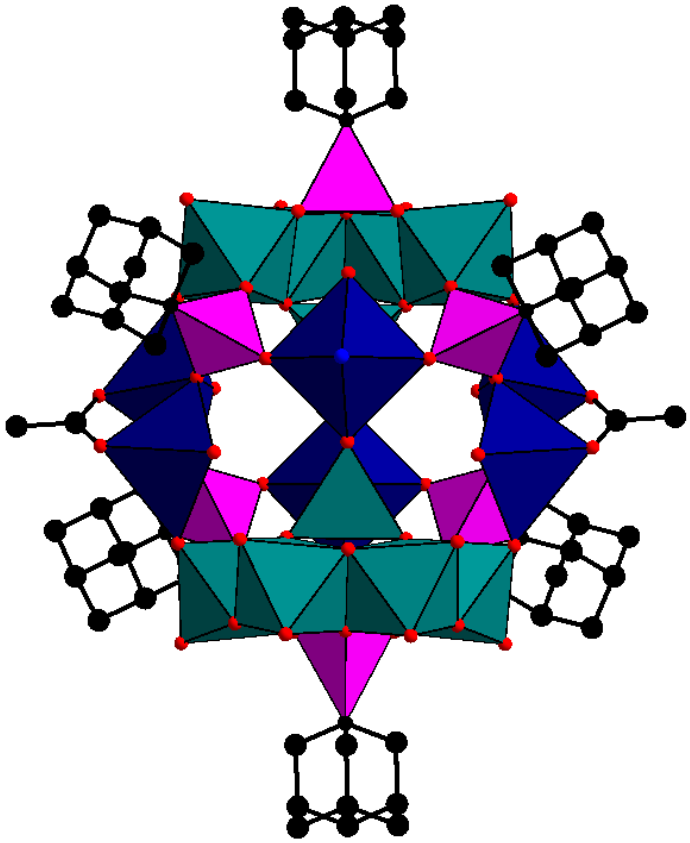

Figure 4.5.2 – Simplified representation of the cluster core in 10, showing the adamantyl backbones on the phosphonate ligands as well as the acetate ligands. Colour Scheme: Mo teal, Co dark blue, P pink, O red, N blue, C black.

Having demonstrated substitution of the phosphonate ligands in the case of **5**, a series of analogues were generated, corresponding to the adamantylphosphonate-substituted analogues of **7-9**. These compounds can equivalently be considered as adamantylphosphonate-substituted analogues of **7-9**, or carboxylate-substituted analogues of **10**. The compounds all display the same structural features as their substituted counterparts, demonstrating the orthogonality of the ligand substitution (Figures 4.5.3 and 4.5.4).

$[TBA]_2[Mo^{VI}_{10}Co^{II}_6O_{12}(\mu\text{-}O)_{14}(\mu_3\text{-}O)_4(AdPO_3)_6(PhCOO)_2(py)_2(H_2O)_6]$ (**11**), crystallised over one week along with two constituent acetonitrile molecules per formula unit. The crystals formed in the monoclinic crystal system in space group *C*2/m.

$[TBA]_2[Mo^{VI}_{10}Co^{II}_6O_{12}(\mu\text{-}O)_{14}(\mu_3\text{-}O)_4(AdPO_3)_6(Ph\text{-}CH_2\text{-}COO)_2(py)_3(H_2O)_6]$ (**12**), crystallised over two weeks along with five constituent acetonitrile molecules per formula unit. The crystals formed in the monoclinic crystal system in space group *P*-1.

$[TBA]_2[Mo^{VI}_{10}Co^{II}_6O_{12}(\mu\text{-}O)_{14}(\mu_3\text{-}O)_4(AdPO_3)_6(AdCOO)_2(py)_2(H_2O)_6]$ (**13**), crystallised overnight along with six constituent acetonitrile molecules per formula unit. The crystals formed in the triclinic crystal system in space group *P*-1.

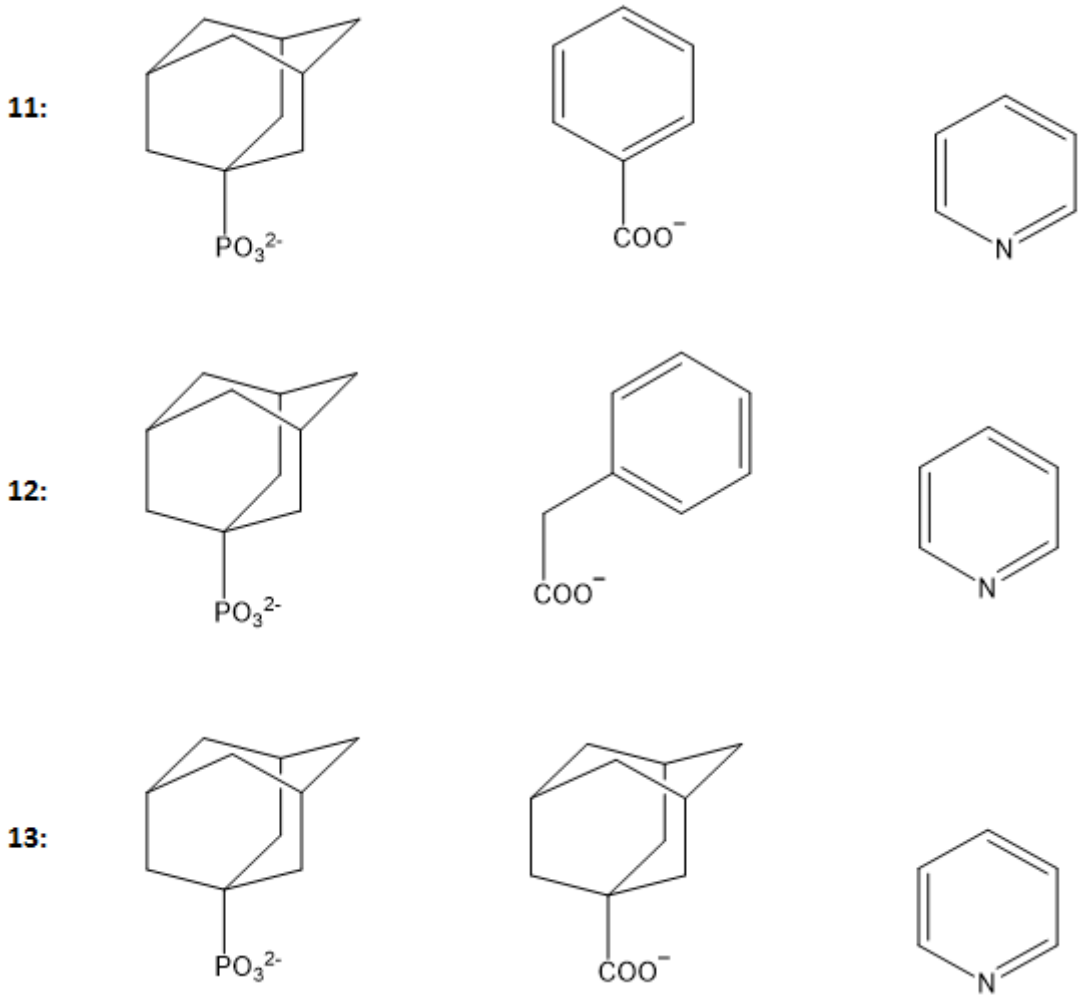

Figure 4.5.3 – The organic ligands present in 11-13.

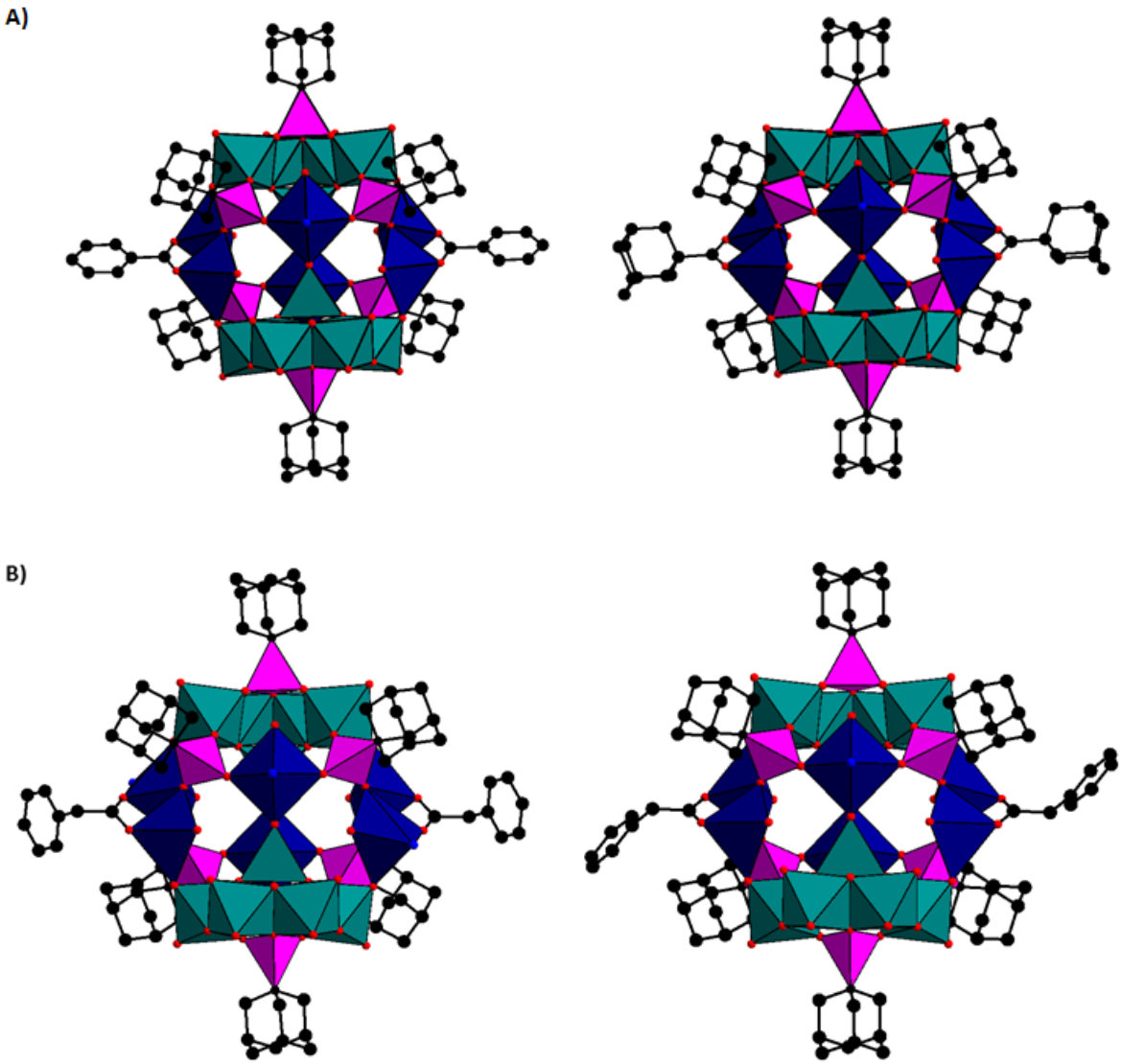

Figure 4.5.4 – A) Simplified representation of the cluster cores in 11 (left) and 13 (right), showing the adamantyl phosphonate moieties and carboxylate ligands. B) The two cluster units in 12, with four (left) and two (right) pyridine ligands per cluster unit. Colour Scheme: Mo teal, Co dark blue, P pink, O red, N blue, C grey.

The crystal structure for **12** contain two crystallographically distinct cluster units – one which incorporates two pyridine ligands in the manner of **5**, and one which incorporates four in the same manner as **6**. Hence the overall formula is given as containing three pyridine molecules per cluster unit.

This incorporation of pyridine ligands appears to affect the carboxylate torsion angle, O-C-C-Ph. In the case without the additional pyridine ligands on the dinuclear cobalt unit (*i.e.* equivalent to **5**), this torsion angle is 6.6°, while in the case with additional pyridine ligands (*i.e.* equivalent to **6**), the angle increases to 43.2° (Figure 4.5.4 B). This difference in torsion angle may simply be due to crystal packing constraints.

Identification code	**10**•9.5(MeCN)
Empirical formula	$C_{125}H_{218.5}Co_6Mo_{10}N_{13.5}O_{58}P_6$
Formula weight (g/mol)	4337.42
Temperature (K)	100(2)
Wavelength (Å)	0.71073
Crystal system	Monoclinic
Space group	$P2_1/n$
a (Å)	17.6667(8)
b (Å)	25.3666(12)
c (Å)	20.0291(9)
α (°)	90
β (°)	107.6720(10)
γ (°)	90
Volume (Å^3)	8552.3(7)
Z	2
Calculated density ρ_{calc} (g/cm^3)	1.684
Absorption coefficient μ (mm^{-1})	1.409
F(000)	4398.0
Crystal size (mm^3)	0.15 × 0.12 × 0.05
2Θ range for data collection (°)	2.67 to 52.234
Index ranges	$-21 \leq h \leq 21$, $-31 \leq k \leq 31$, $-24 \leq l \leq 24$
Reflections collected	104339
Independent reflections	16945 [R_{int} = 0.0909]
Data/restraints/parameters	16945/83/1006
Goodness-of-fit on F^2	0.889
Final R indices [I>=2σ (I)]	R_1 = 0.0356, wR_2 = 0.0643
Final R indices [all data]	R_1 = 0.0817, wR_2 = 0.0730
Largest diff. peak and hole (e Å^{-3})	1.04/-1.22

Table 4.5.1 – Crystallographic details for compound 10•9.5(MeCN).

Of the five crystallographically distinct acetonitrile molecules, two are fully occupied, one is modelled as disordered in a 0.72/0.28 ratio, one in a 0.75/0.25 ratio, and the fifth is modelled as being 0.75 occupied, split over two positions in a 0.25/0.5 ratio.

Identification code	**11**•2(MeCN)
Empirical formula	$C_{240}H_{354}Co_{12}Mo_{20}N_{12}O_{116}P_{12}$
Formula weight (g/mol)	8260.93
Temperature (K)	100(2)
Wavelength (Å)	0.71073
Crystal system	Monoclinic
Space group	*C*2/m
a (Å)	29.7884(13)
b (Å)	28.1953(12)
c (Å)	19.9483(8)
α (°)	90
β (°)	91.4630(10)
γ (°)	90
Volume (Å^3)	16749.0(12)
Z	2
Calculated density ρ_{calc} (g/cm^3)	1.638
Absorption coefficient μ (mm^{-1})	1.433
F(000)	8300.0
Crystal size (mm^3)	0.14 × 0.13 × 0.06
2Θ range for data collection (°)	2.736 to 51.566
Index ranges	-36 ≤ h ≤ 36, -34 ≤ k ≤ 34, -24 ≤ l ≤ 22
Reflections collected	157139
Independent reflections	16357 [R_{int} = 0.0738]
Data/restraints/parameters	16357/145/938
Goodness-of-fit on F^2	1.068
Final R indices [I>=2σ (I)]	R_1 = 0.0698, wR_2 = 0.1668
Final R indices [all data]	R_1 = 0.1279, wR_2 = 0.2192
Largest diff. peak and hole (e Å^{-3})	2.77/-2.14

Table 4.5.2 – Crystallographic details for compound 11•2(MeCN).

The pyridine ligands are modelled as disordered over two positions in a 50/50 ratio. The terminal carbon one arm of the tetrabutylammonium cation is modelled as disordered over two positions in a 0.61/0.39 ratio. Constraints (DFIX and DANG) were used on the adamantyl groups.

Identification code	**12**•5(MeCN)
Empirical formula	$C_{133}H_{203}Co_6Mo_{10}N_{10}O_{58}P_6$
Formula weight (g/mol)	4368.84
Temperature (K)	100(2)
Wavelength (Å)	0.71073
Crystal system	Triclinic
Space group	*P*-1
a (Å)	17.7506(7)
b (Å)	18.8983(8)
c (Å)	27.1892(12)
α (°)	75.8350(10)
β (°)	80.8820(10)
γ (°)	72.5210(10)
Volume (Å^3)	8399.5(6)
Z	2
Calculated density ρ_{calc} (g/cm^3)	1.727
Absorption coefficient μ (mm^{-1})	1.435
F(000)	4414.0
Crystal size (mm^3)	0.14 × 0.1 × 0.07
2Θ range for data collection (°)	2.748 to 52.994
Index ranges	$-22 \leq h \leq 22$, $-23 \leq k \leq 23$, $-34 \leq l \leq 34$
Reflections collected	202902
Independent reflections	34616 [R_{int} = 0.0895]
Data/restraints/parameters	34616/1/1956
Goodness-of-fit on F^2	1.009
Final R indices [I>=2σ (I)]	R_1 = 0.0439, wR_2 = 0.0957
Final R indices [all data]	R_1 = 0.0883, wR_2 = 0.1160
Largest diff. peak and hole (e Å^{-3})	1.94/-1.83

Table 4.5.3 – Crystallographic details for compound 12•5(MeCN).

Identification code	**13**•6(MeCN)
Empirical formula	$C_{136}H_{130}Co_6Mo_{10}N_{10}O_{58}P_6$
Formula weight (g/mol)	4331.29
Temperature (K)	100(2)
Wavelength (Å)	0.71073
Crystal system	Triclinic
Space group	*P*-1
a (Å)	16.9115(8)
b (Å)	17.8098(9)
c (Å)	18.2776(9)
α (°)	65.2690(10)
β (°)	64.0720(10)
γ (°)	84.8630(10)
Volume (Å^3)	4467.4(4)
Z	1
Calculated density ρ_{calc} (g/cm^3)	1.610
Absorption coefficient μ (mm^{-1})	1.349
F(000)	2152.0
2Θ range for data collection (°)	2.696 to 59.09
Index ranges	$-23 \leq h \leq 23$, $-24 \leq k \leq 24$, $-25 \leq l \leq 25$
Reflections collected	152064
Independent reflections	24963 [R_{int} = 0.0528]
Data/restraints/parameters	24963/4/971
Goodness-of-fit on F^2	1.022
Final R indices [I>=2σ (I)]	R_1 = 0.0622, wR_2 = 0.1622
Final R indices [all data]	R_1 = 0.0986, wR_2 = 0.1969
Largest diff. peak and hole (e Å^{-3})	2.95/-1.75

Table 4.5.4 – Crystallographic details for compound 13•6(MeCN).

The adamantyl groups on the carboxylate ligands are modelled as being rotationally disordered over two positions in a 0.59/0.41 ratio. Of the three crystallographically distinct acetonitrile molecules, two are modelled as fully occupied and the third is modelled as disordered over two positions with 50/50 occupancy.

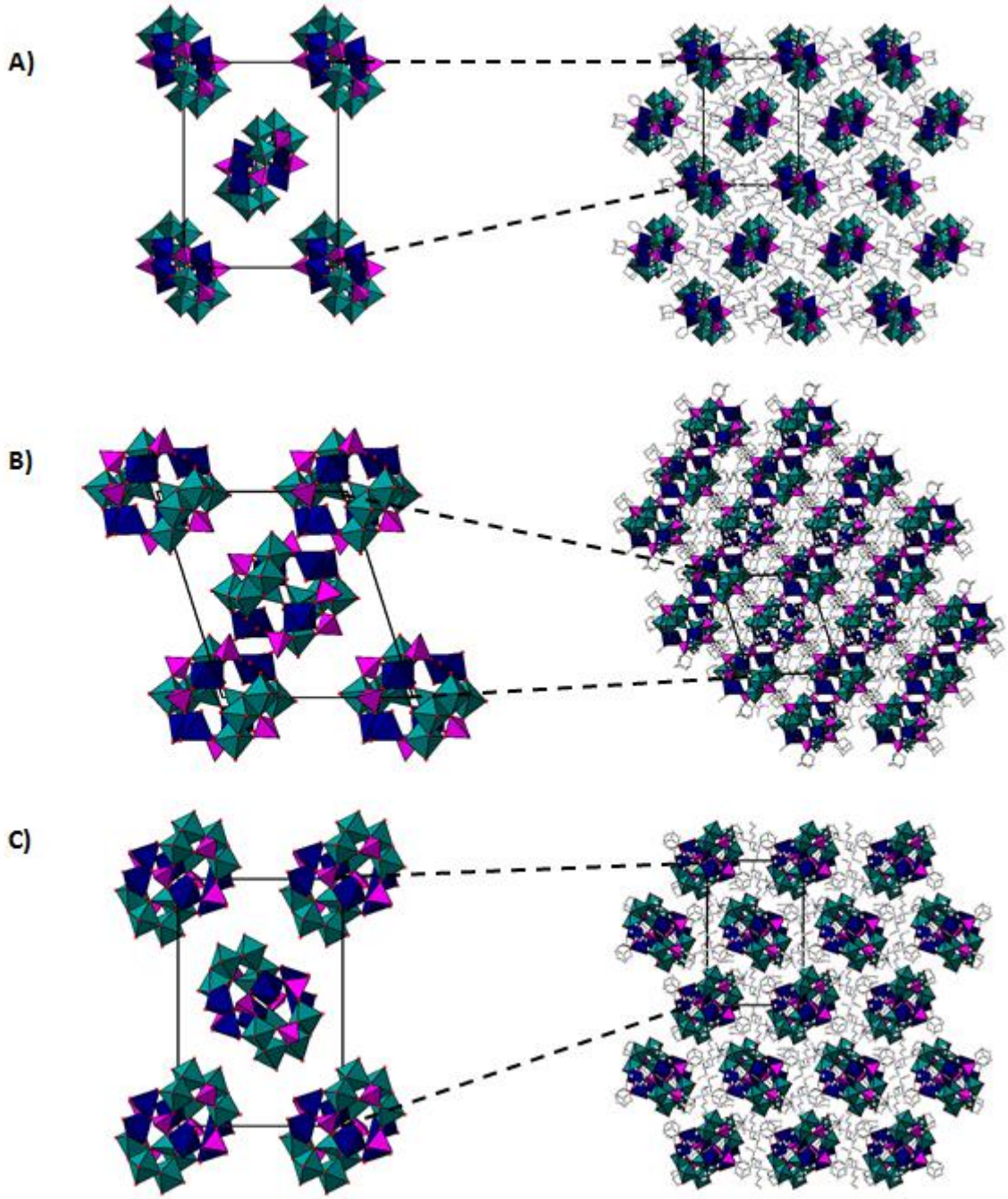

Figure 4.5.5 – Crystal packing diagrams for 10•9.5(MeCN), as viewed down: A) The crystallographic *a*-axis, B) the crystallographic *b*-axis. C) The crystallographic *c*-axis.

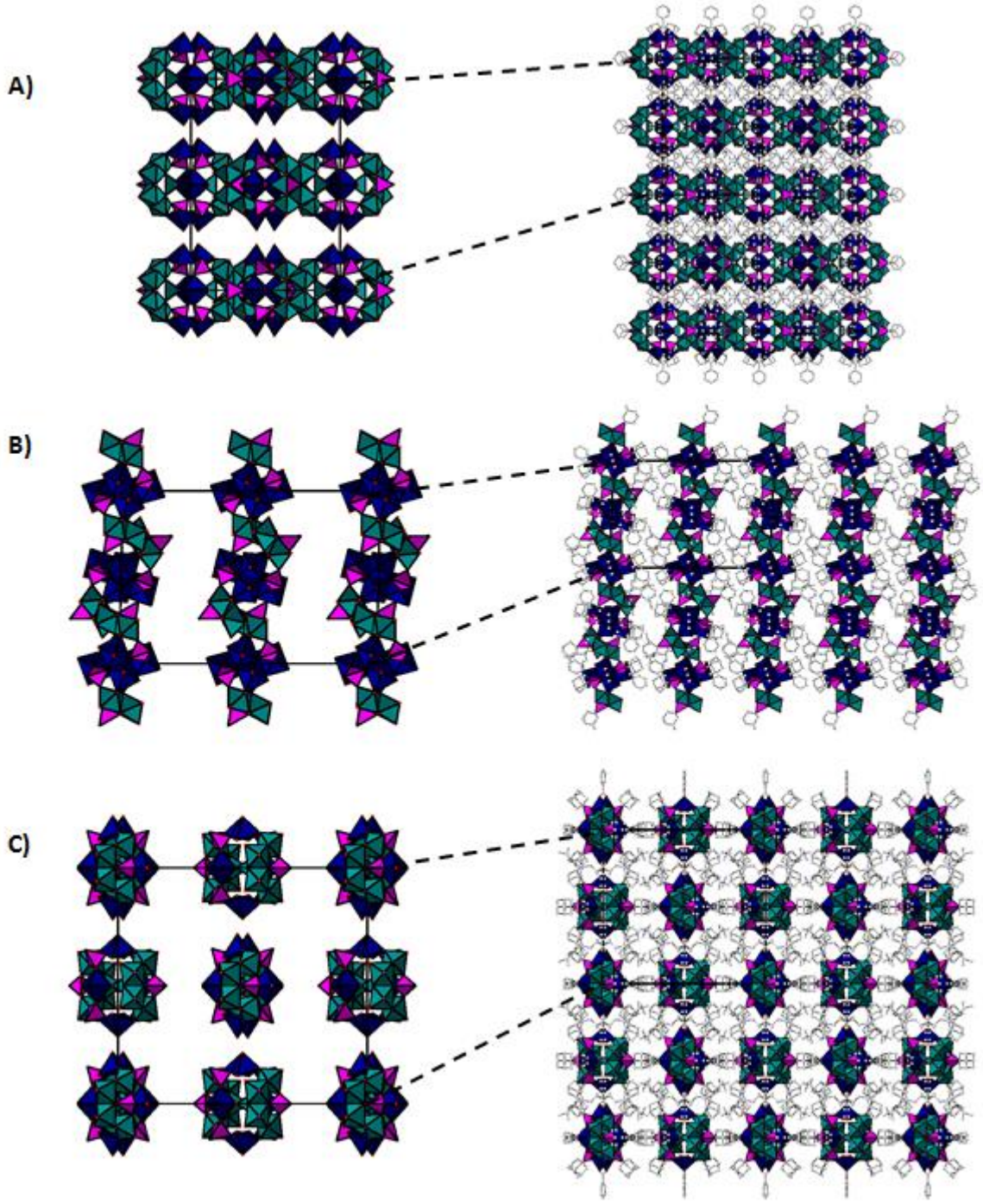

Figure 4.5.6 – Crystal packing diagrams for 11•2(MeCN), as viewed down: A) The crystallographic *a*-axis, B) the crystallographic *b*-axis. C) The crystallographic *c*-axis.

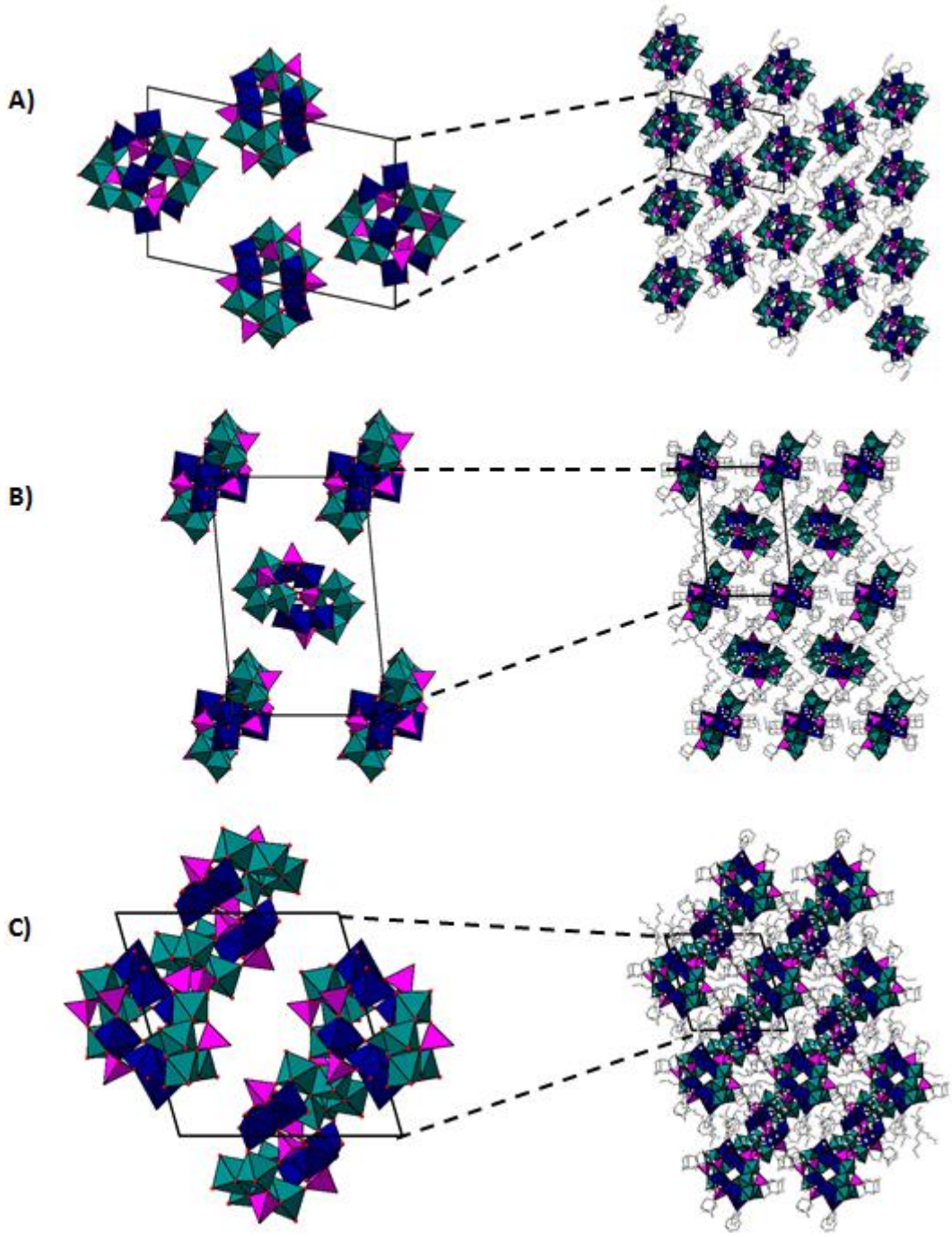

Figure 4.5.7 – Crystal packing diagrams for 12•5(MeCN), as viewed down: A) The crystallographic *a*-axis, B) the crystallographic *b*-axis. C) The crystallographic *c*-axis.

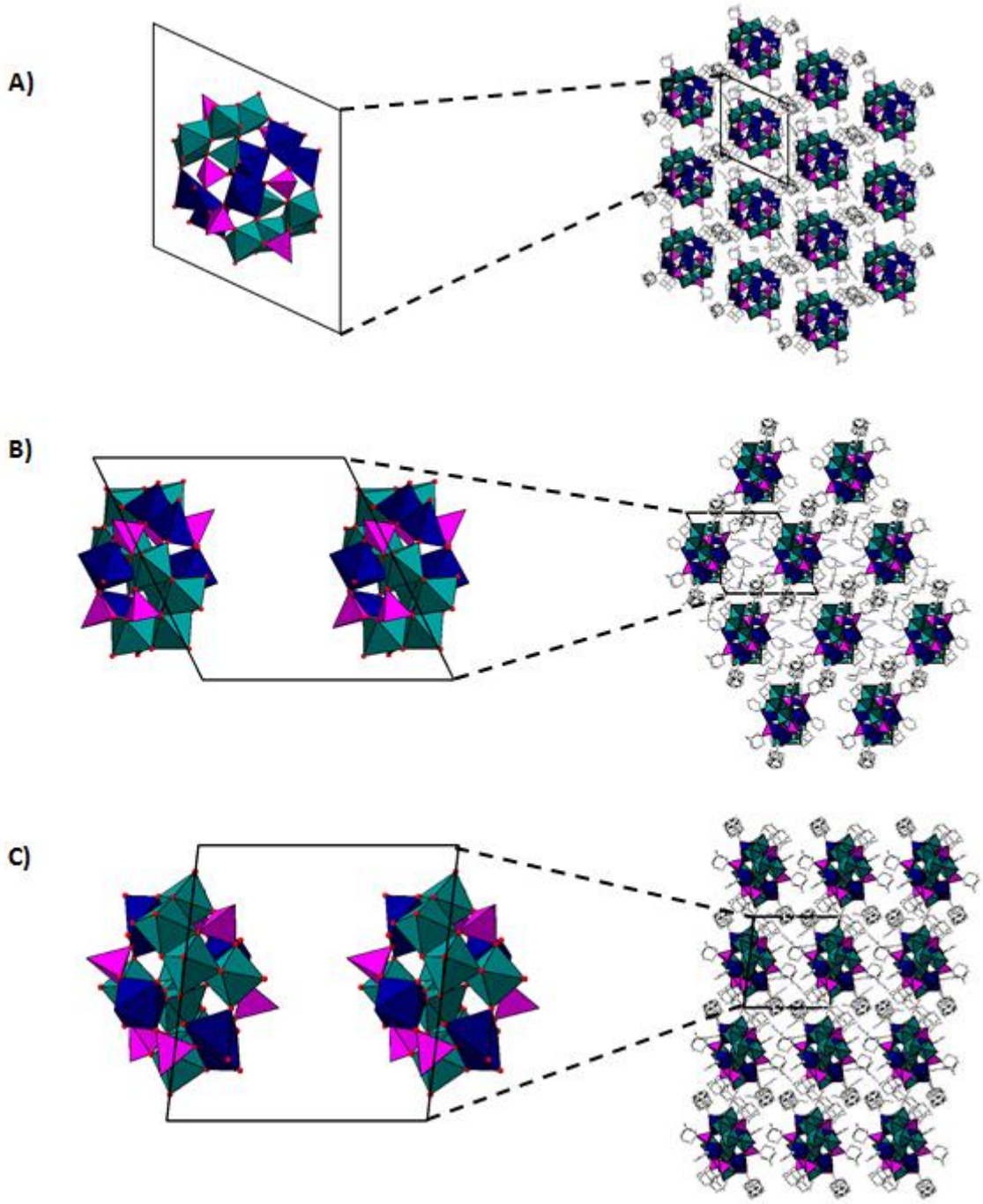

Figure 4.5.8 – Crystal packing diagrams for 13•6(MeCN), as viewed down: A) The crystallographic *a*-axis, B) the crystallographic *b*-axis. C) The crystallographic *c*-axis.

4.6) Ligand Substitution of 5 – Functional Groups

Having demonstrated that the pyridyl, carboxylate and phosphonate ligands on the core of **5** could be substituted with a range of other simple hydrocarbon backbones in an orthogonal manner, we then looked to incorporate functional moieties onto the cluster core. As discussed in Chapter 1, the incorporation of functional moieties into POM systems is highly desirable as it generates structural and functional diversity and allows modification of the physicochemical properties of the parent clusters (*c.f.* Sections 1.2.3 and 1.3).

The carboxylate moieties were chosen as the most suitable position to explore possible modifications of the cluster core. Specifically, we identified substituted benzoic acids as being particularly promising for functionalised cluster synthesis. Firstly, a wide range of functionalised benzoic acids are readily commercially available. As demonstrated with the synthesis of **8**, **9**, **12** and **13**, the free acids can be used directly in the synthesis in combination with cobalt (II) nitrate to generate the target clusters, making synthesis straightforward. The *meta*- and *para*- positions were particularly targeted as these positions were deemed to be sufficiently remote from the carboxylate that they were unlikely to interfere with templating effects at the carboxylate moiety (*e.g.* through chelation of a metal centre). They are also generally sufficiently rigid as to be amenable to crystallographic identification.

In the first instance, brominated benzoate ligands were targeted. *Bromo*- groups are known to exert a significant electronic influence on a phenyl ring system such as benzoate, but do not act as coordinating or donating groups to any significant extent. Therefore they should not interfere with templating effects (*e.g.* by competing for ligand binding sites). To this end, 4-bromobenzoic acid and 3,5-dibromobenzoic acid (BrPhCOOH and Br_2PhCOOH) were substituted into the reaction (Figure 4.6.1).

$[TBA]_2[Mo^{VI}_{10}Co^{II}_6O_{12}(\mu\text{-}O)_{14}(\mu_3\text{-}O)_4(t\text{BuPO}_3)_6(\text{BrPhCOO})_2(py)_2(H_2O)_6]$ (**14**) crystallised over approximately two weeks. XRD analysis indicates that the crystals were monoclinic, with cell parameters a = 21.48 Å, b = 14.06 Å, c = 25.39 Å and β = 100.47°. IR analysis confirms the identity of the compound (Figure 4.6.2), while TGA analysis indicates that the crystals also contained one constituent acetonitrile molecule per formula unit (Figure 4.6.3).

$[TBA]_2[Mo^{VI}_{10}Co^{II}_6O_{12}(\mu\text{-}O)_{14}(\mu_3\text{-}O)_4(t\text{BuPO}_3)_6(Br_2\text{PhCOO})_2(py)_2(H_2O)_6]$ (**15**) also crystallised over approximately two weeks. XRD analysis indicates that the crystals were monoclinic, with cell parameters a = 33.32 Å, b = 13.85 Å, c = 37.53 Å and β = 113.76°. IR analysis confirms the identity of the compound (Figure 4.6.2), while TGA analysis indicates that the crystals also contained 2.5 constituent acetonitrile molecules per formula unit (Figure 4.6.4).

These structures represent brominated analogues of compound **7**. The isolation of **14** and **15** was promising because it indicated that functional groups (outside of simple hydrocarbons) could be incorporated onto the cobalt-molybdate cluster core.

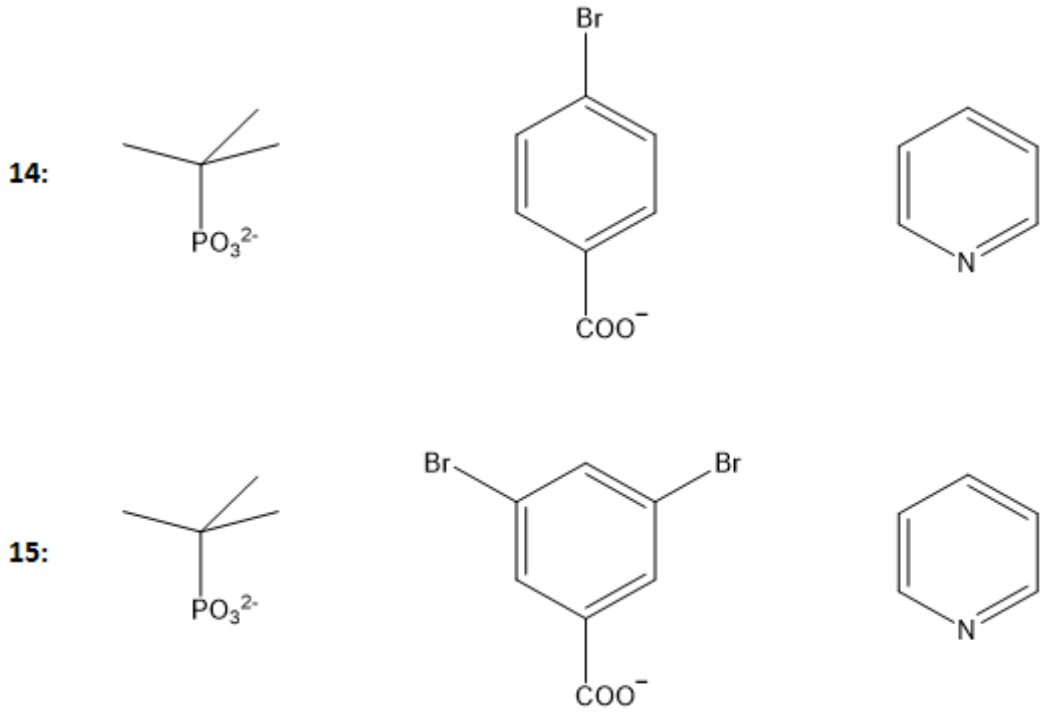

Figure 4.6.1 – The organic ligands present in 14-15.

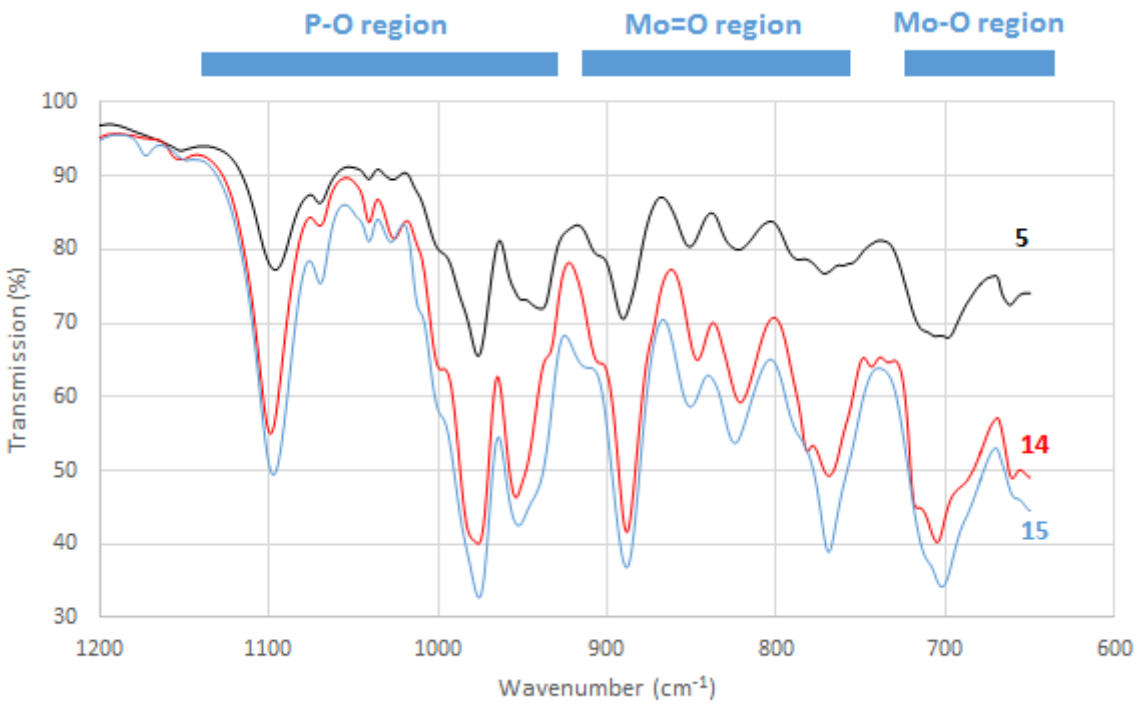

Figure 4.6.2 – Portion of the IR spectra for 5•3(MeCN) (black), 14•(MeCN) (red) and 15•2.5(MeCN) (blue), indicating that they have the same structure.

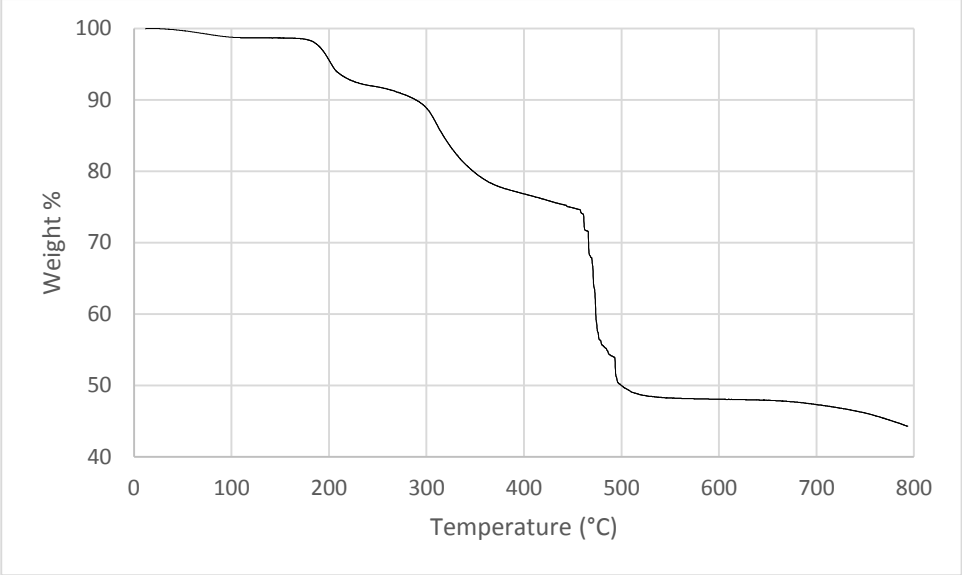

Figure 4.6.3 – TGA analysis for 14•(MeCN).

TGA analysis for **14** (Figure 4.6.3) shows the loss of one acetonitrile molecule per formula unit upon heating to *c.* 100 °C (calculated 98.9%, observed 98.7%). Further heating results in the loss of two pyridine and six water molecules per formula unit (calculated 91.9%, observed 91.8%), indicating that the dinuclear cobalt units do not incorporate additional pyridine ligands.

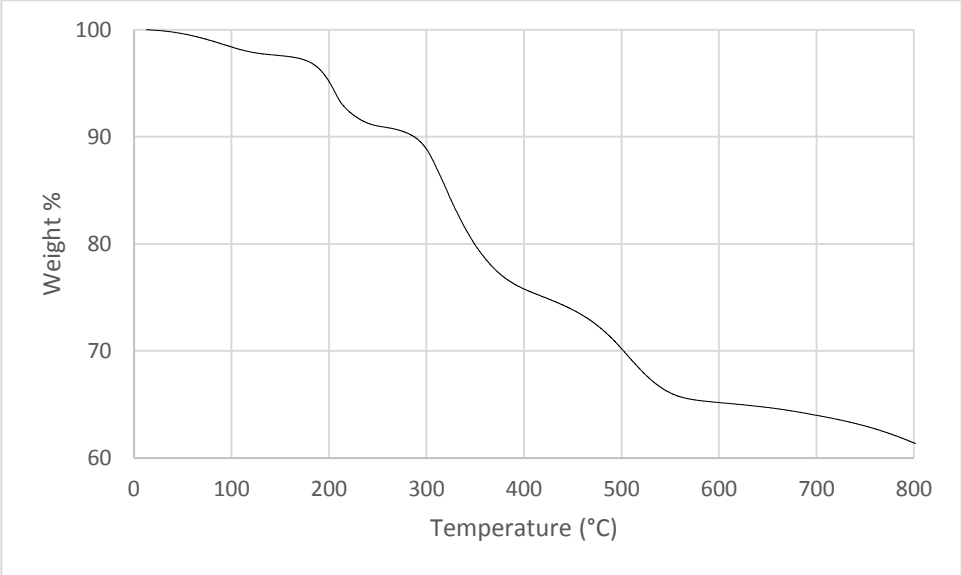

Figure 4.6.4 – TGA analysis for 15•2.5(MeCN).

TGA analysis for **15** (Figure 4.6.4) shows the loss of 2.5 acetonitrile molecules per formula unit upon heating to *c.* 100 °C (calculated 97.4%, observed 97.5%). Further heating results in the loss of two pyridine and six water molecules per formula unit (calculated 90.8%, observed 90.7%), indicating that the dinuclear cobalt units do not incorporate additional pyridine ligands.

Having successfully incorporated brominated ligands onto the cluster core, other electron-withdrawing and donating moieties were targeted. Like the *bromo-* groups, *nitro-* groups offered electronic modification of the benzoate ligand without incorporating strongly coordinating moieties that might interfere with templating effects. Therefore, 4-nitrobenzoic acid ($NO_2PhCOOH$) was incorporated into the reaction system.

$[TBA]_2[Mo^{VI}_{10}Co^{II}_6O_{12}(\mu\text{-}O)_{14}(\mu_3\text{-}O)_4(t\text{BuPO}_3)_6(NO_2PhCOO)_2(py)_4(H_2O)_6]$ (**16**) crystallised over two weeks. The crystals formed in the monoclinic crystal system in space group $P2_1/n$. As expected this compound was a *nitro*-substituted analogue of **7** (Figures 4.6.5 and 4.6.6). **16** incorporated additional pyridine ligands onto the dinuclear cobalt units in the same manner as **6**. No constituent solvent molecules or solvent-accessible voids were observed.

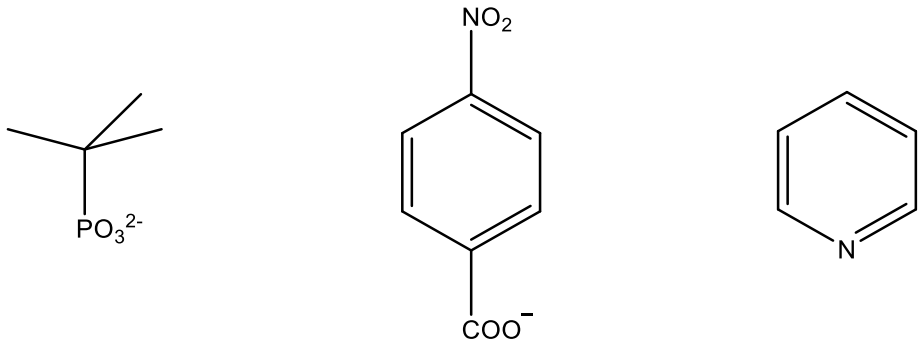

Figure 4.6.5 – The organic ligands present in 16.

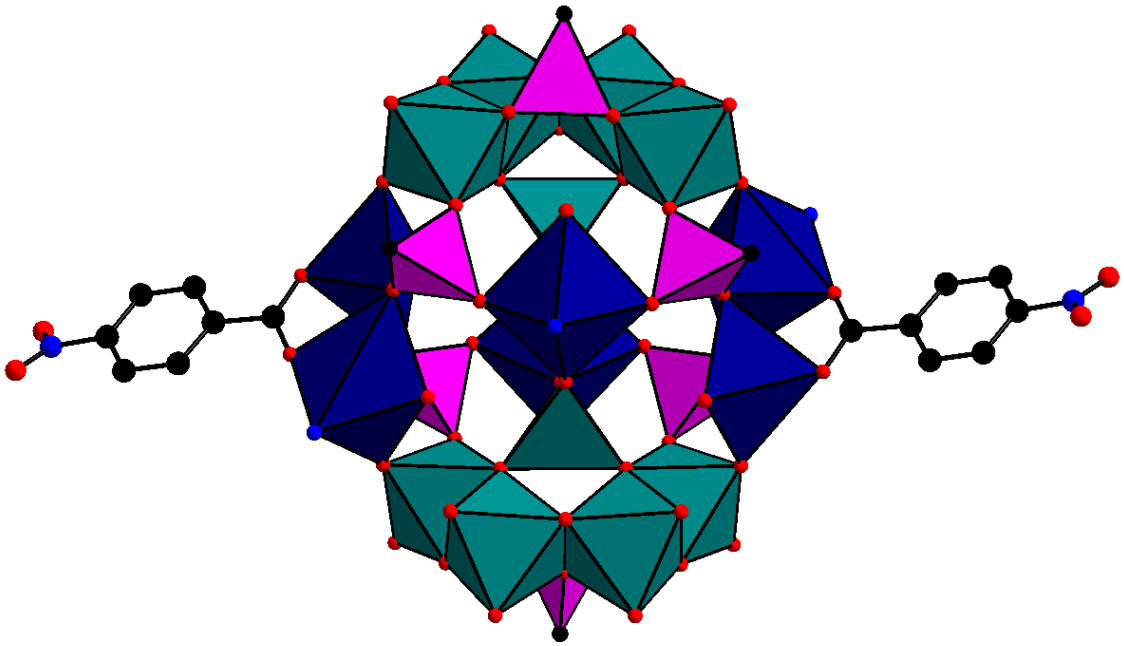

Figure 4.6.6 – Simplified representation of the cluster core in 16, showing the 4-nitrobenzoate ligands. Colour Scheme: Mo teal, Co dark blue, P pink, O red, N blue, C black.

Identification code	**16**
Empirical formula	$C_{90}H_{166}Co_6Mo_{10}N_8O_{62}P_6$
Formula weight (g/mol)	3851.10
Temperature (K)	100(2)
Wavelength (Å)	0.71073
Crystal system	Monoclinic
Space group	$P2_1/n$
a (Å)	15.8130(7)
b (Å)	27.6899(12)
c (Å)	15.8146(7)
α (°)	90
β (°)	99.1780(10)
γ (°)	90
Volume (Å^3)	6835.9(5)
Z	2
Calculated density ρ_{calc} (g/cm^3)	1.871
Absorption coefficient μ (mm^{-1})	1.750
F(000)	3860
Crystal size (mm^3)	0.040 x 0.300 x 0.473
2Θ range for data collection (°)	2.940 to 61.300
Index ranges	-22<=h<=22, -39<=k<=39, -22<=l<=22
Reflections collected	389959
Independent reflections	21105 [R_{int} = 0.0307]
Data/restraints/parameters	21105/0/834
Goodness-of-fit on F^2	1.091
Final R indices [I>=2σ (I)]	R_1 = 0.0239, wR_2 = 0.0584
Final R indices [all data]	R_1 = 0.0279, wR_2 = 0.0612
Largest diff. peak and hole (e Å^{-3})	1.787/-1.090

Table 4.6.1 – Crystallographic details for compound 16.

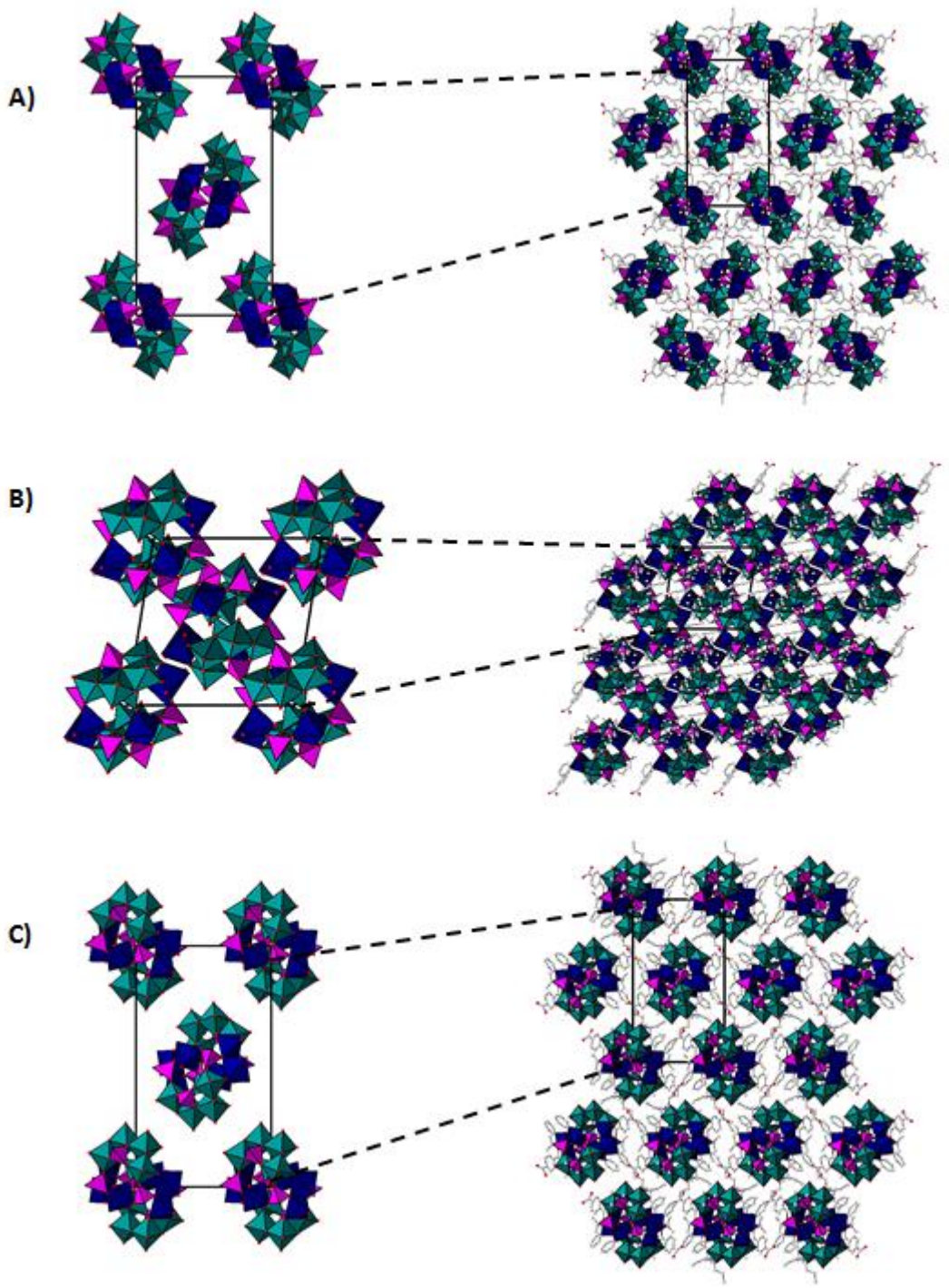

Figure 4.6.7 – Crystal packing diagrams for 16, as viewed down: A) The crystallographic *a*-axis, B) the crystallographic *b*-axis. C) The crystallographic *c*-axis.

Having incorporated electron-withdrawing functionalities, electron-donating functionalities were targeted next. Primary amine groups represent electron donating functionalities that are structurally and synthetically related to the *nitro*- groups present in **16**. Therefore, 4-aminobenzoic acid was incorporated reaction system (Figure 4.6.8).

$[TBA]_2[Mo^{VI}_{10}Co^{II}_6O_{12}(\mu\text{-}O)_{14}(\mu_3\text{-}O)_4(t\text{BuPO}_3)_6(NH_2\text{PhCOO})_2(py)_2(H_2O)_6]$ (**17**) crystallised over approximately two weeks. XRD analysis indicates that the crystals were monoclinic, with cell parameters a = 16.04 Å, b = 28.20 Å, c = 16.09 Å and β = 106.15°. IR analysis confirms the identity of the compound (Figure 4.6.9), while TGA analysis indicates that the crystals do not contain any constituent acetonitrile molecules (Figure 4.6.10).

Amino groups are particularly interesting functionalities to incorporate because they offer significant possibilities for facile post-synthetic modification of the cluster (*e.g.* through Schiff-base condensation reactions). However, **17** proved to be particularly insoluble, making post-synthetic modification difficult to achieve in practice.

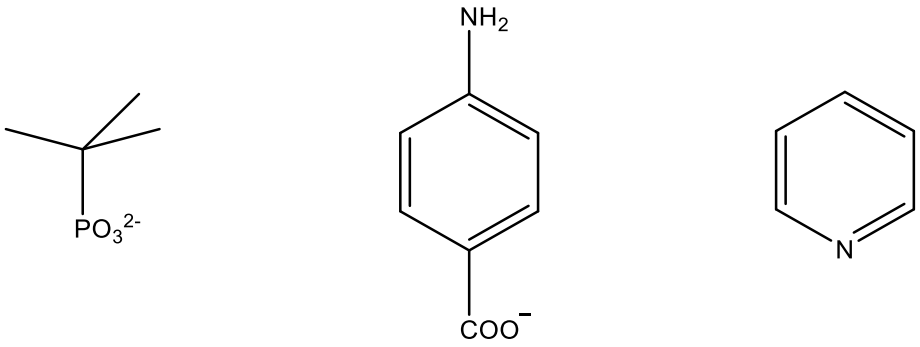

Figure 4.6.8 – The organic ligands present in 17.

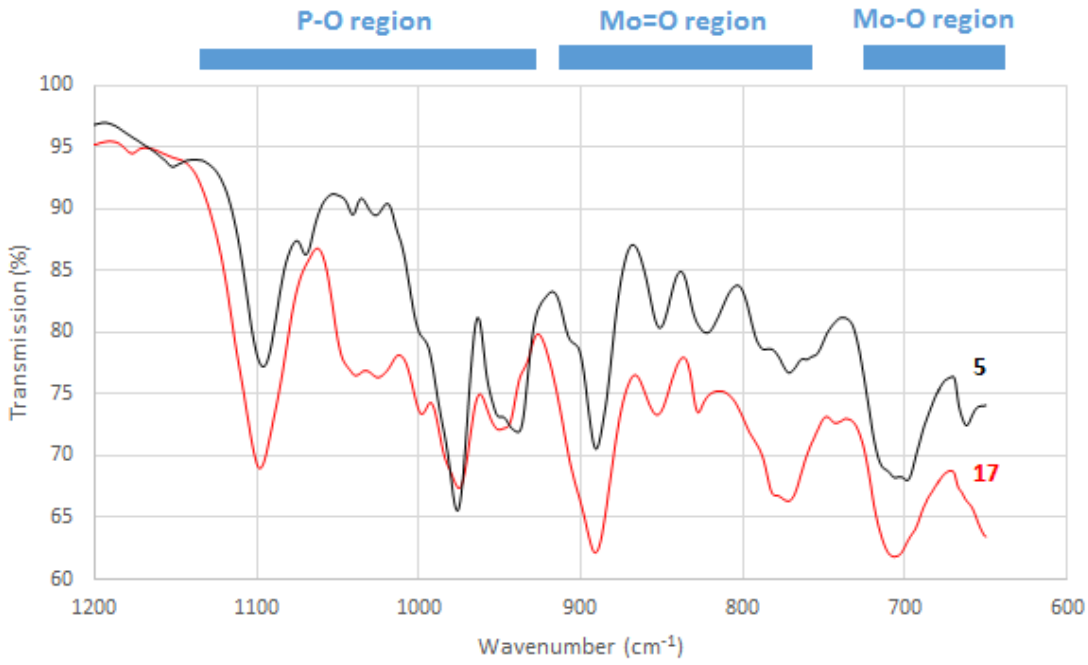

Figure 4.6.9 – Comparison of the IR spectrum for 5•3(MeCN) and 17.

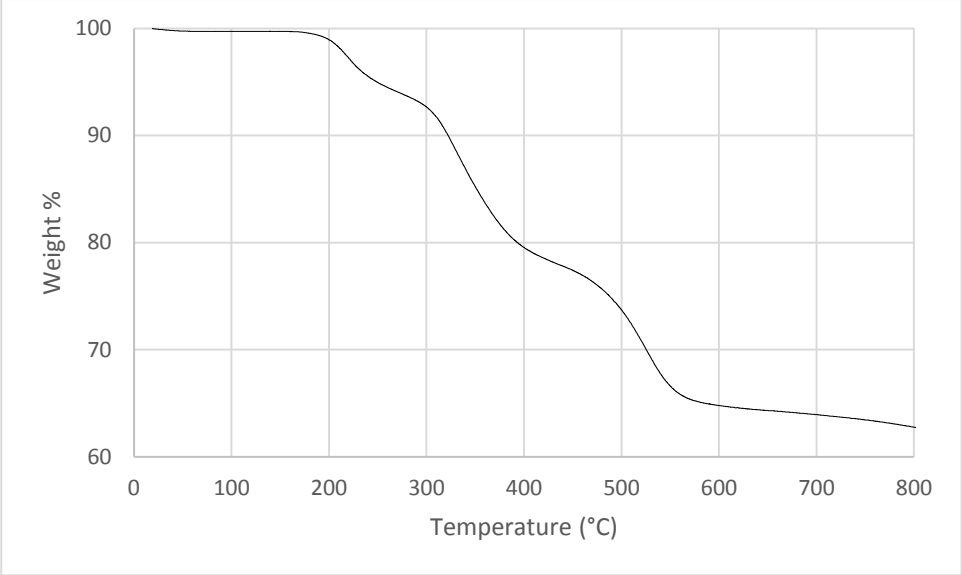

Figure 4.6.10 – TGA analysis for 17.

TGA analysis for **17** (Figure 4.6.10) shows no loss of solvent molecules up to a temperature of *c.* 180 °C (99.8%). Further heating to 300 °C results in the loss of two pyridine and six water molecules per formula unit (calculated 92.7%, observed 92.7%), indicating that the dinuclear cobalt units do not incorporate additional pyridine ligands. Further heating results in ligand decomposition reactions.

Another functional group with interesting potential applications in post-synthetic modification is the aldehyde moiety. This is an electron withdrawing group, and relatively sensitive to reaction conditions (*e.g.* oxidation or nucleophilic attack can occur). Nevertheless, the functionality could be incorporated onto the cluster core through incorporation of 4-formylbenzoic acid (CHOPhCOOH) into the reaction mixture (Figure 4.6.11).

$[TBA]_2[Mo^{VI}_{10}Co^{II}_6O_{12}(\mu\text{-}O)_{14}(\mu_3\text{-}O)_4(t\text{BuPO}_3)_6(\text{CHOPhCOO})_2(py)_2(H_2O)_6]$ (**18**) crystallised over approximately one week. XRD analysis indicates that the crystals were monoclinic, with cell parameters a = 20.67 Å, b = 24.35 Å, c = 28.18 Å and β = 109.75°. IR analysis confirms the identity of the compound (Figure 4.6.12), while TGA analysis indicates that the crystals do not contain any constituent solvent molecules (Figure 4.6.13).

This compound has significantly better solubility than **17**, making further reactions such as Schiff-base condensation reactions a promising avenue towards post-synthetic modification of the cluster.

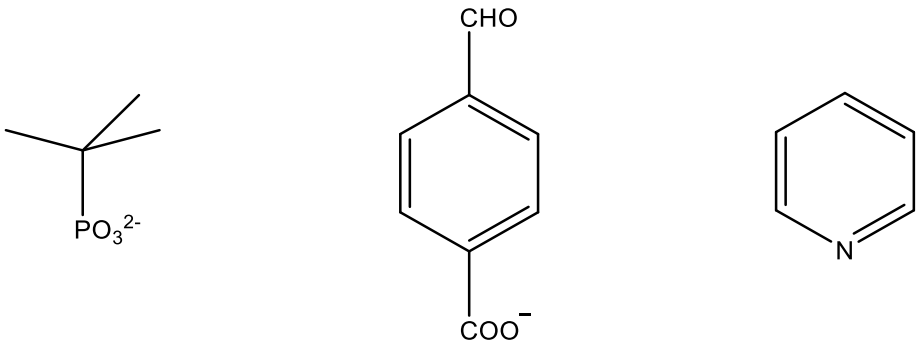

Figure 4.6.11 – The organic ligands present in 18.

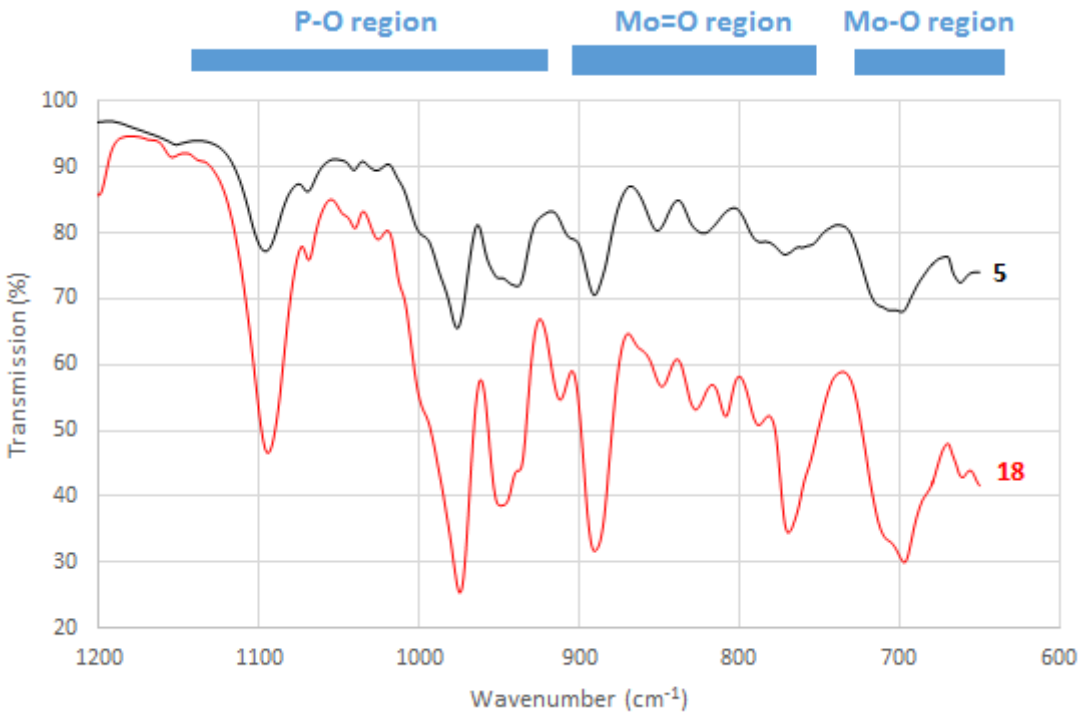

Figure 4.6.12 – Comparison of the IR spectrum for 5•3(MeCN) and 18.

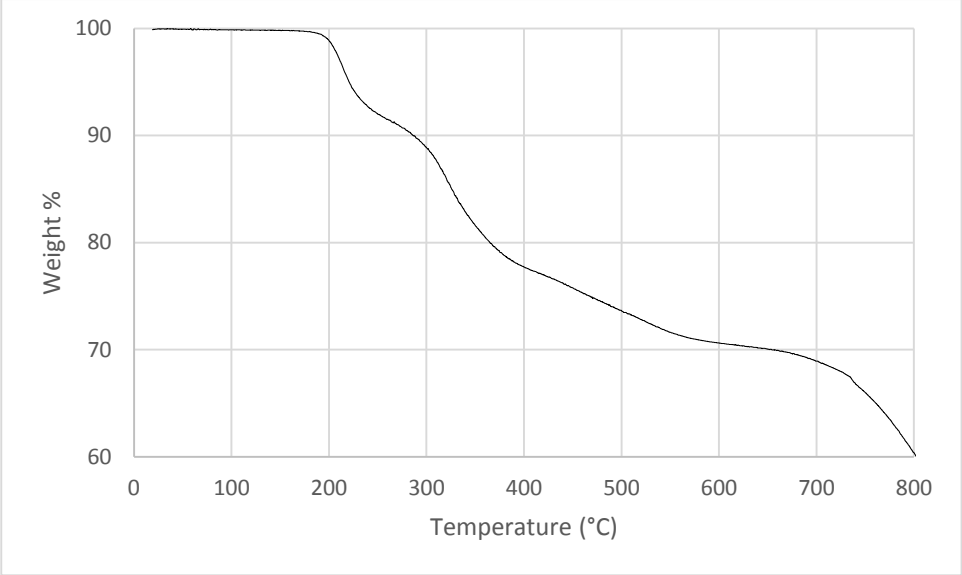

Figure 4.6.13 – TGA analysis for 18.

TGA analysis for **18** (Figure 4.6.13) shows no loss of solvent molecules up to a temperature of *c.* 180 °C (99.8%). Further heating to 240 °C results in the loss of two pyridine and six water molecules per formula unit (calculated 92.7%, observed 92.6%), indicating that the dinuclear cobalt units do not incorporate additional pyridine ligands. Further heating results in ligand decomposition reactions.

Finally, vanillic acid (vanCOOH) was investigated. Vanillic acid is a derivative of vanillin (a natural product) and consists of a substituted benzoate ligand with both alcohol (-OH) and ether (-OMe) substituents. Both of these substituents display electron donating effects. Moreover, the –OH and –OMe substituents are in the *ortho*- position relative to each other, offering a potential chelating site with which to bind heterometals (Figures 4.6.14 and 4.6.15).

$[TBA]_2[Mo^{VI}_{10}Co^{II}_6O_{12}(\mu\text{-}O)_{14}(\mu_3\text{-}O)_4(t\text{BuPO}_3)_6(\text{vanCOO})_2(\text{py})_2(H_2O)_6]$ (**19**) crystallised over two weeks along with six constituent acetonitrile molecules per formula unit. The crystals formed in the monoclinic crystal system in space group *C*2/c.

Other attempts to incorporate chelating sites onto the cluster core generally did not result in the formation of the intended cluster core (probably due to chelation of the cobalt metal at the chelating site, which resulted in the cobalt-chelate complex being sequestered out of solution before the POM core could form). However in this instance, the chelating site apparently did not offer a sufficiently attractive binding site to the cobalt metal, and so **19** was able to form. However, examples of metals binding at this chelating site are reported in the literature, and so this may represent another possible avenue towards post-synthetic modification of the cluster.

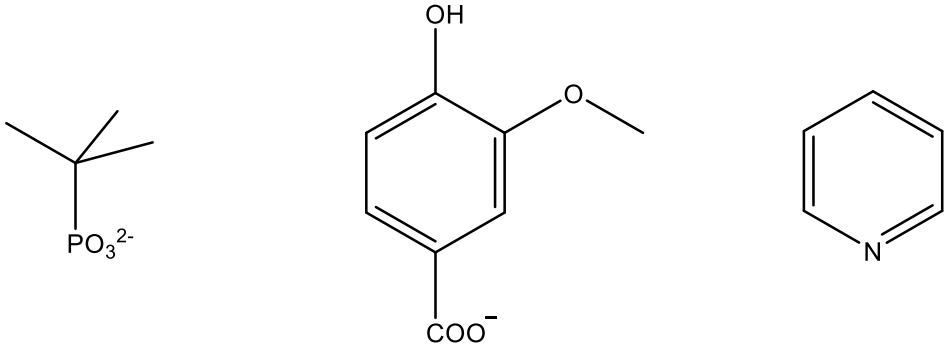

Figure 4.6.14 – The organic ligands present in 19.

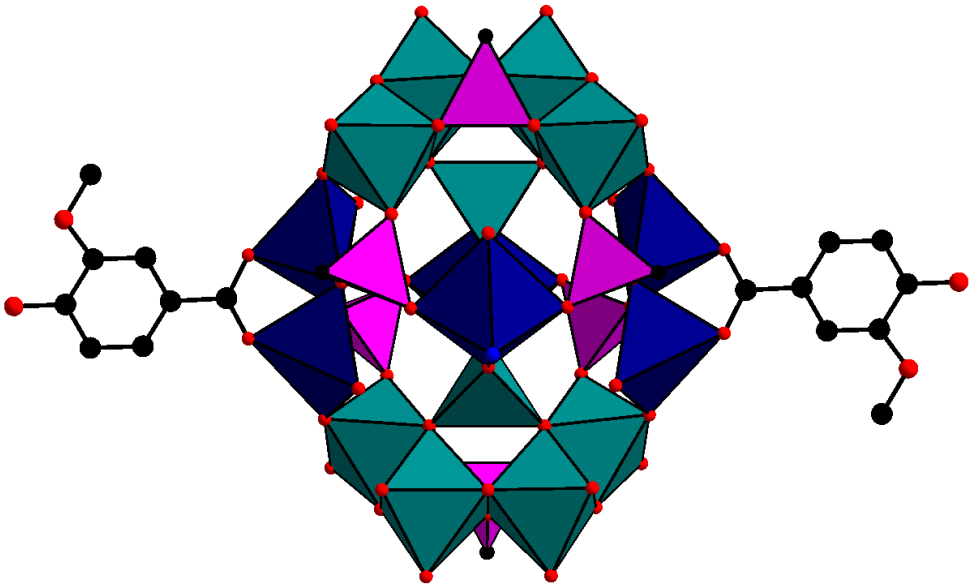

Figure 4.6.15 – Simplified representation of the cluster core in 19, showing the vanillic acid ligands. Colour Scheme: Mo teal, Co dark blue, P pink, O red, N blue, C black.

Identification code	**19**•6(MeCN)
Empirical formula	$C_{94}H_{178}Co_6Mo_{10}N_{10}O_{62}P_6$
Formula weight (g/mol)	3939.25
Temperature (K)	100(2)
Wavelength (Å)	0.71073
Crystal system	Monoclinic
Space group	*C*2/c
a (Å)	41.0011(10)
b (Å)	15.7446(4)
c (Å)	29.8657(13)
α (°)	90
β (°)	126.06
γ (°)	90
Volume (Å^3)	15585.7(9)
Z	4
Calculated density ρ_{calc} (g/cm^3)	1.679
Absorption coefficient μ (mm^{-1})	1.538
F(000)	7920.0
Crystal size (mm^3)	0.222 × 0.195 × 0.157
2Θ range for data collection (°)	2.940 to 61.300
Index ranges	-22<=h<=22, -39<=k<=39, -22<=l<=22
Reflections collected	2.934 to 70.106
Independent reflections	-66 ≤ h ≤ 66, -22 ≤ k ≤ 25, -46 ≤ l ≤ 48
Data/restraints/parameters	191248
Goodness-of-fit on F^2	34319 [R_{int} = 0.0321]
Final R indices [I>=2σ (I)]	34319/28/926
Final R indices [all data]	1.050
Largest diff. peak and hole (e Å^{-3})	R_1 = 0.0280, wR_2 = 0.0670

Table 4.6.2 – Crystallographic details for 19•6(MeCN).

Of the three crystallographically distinct acetonitrile molecules, two are modelled as being fully occupied and one is modelled as disordered over four positions with occupancy 0.25 each.

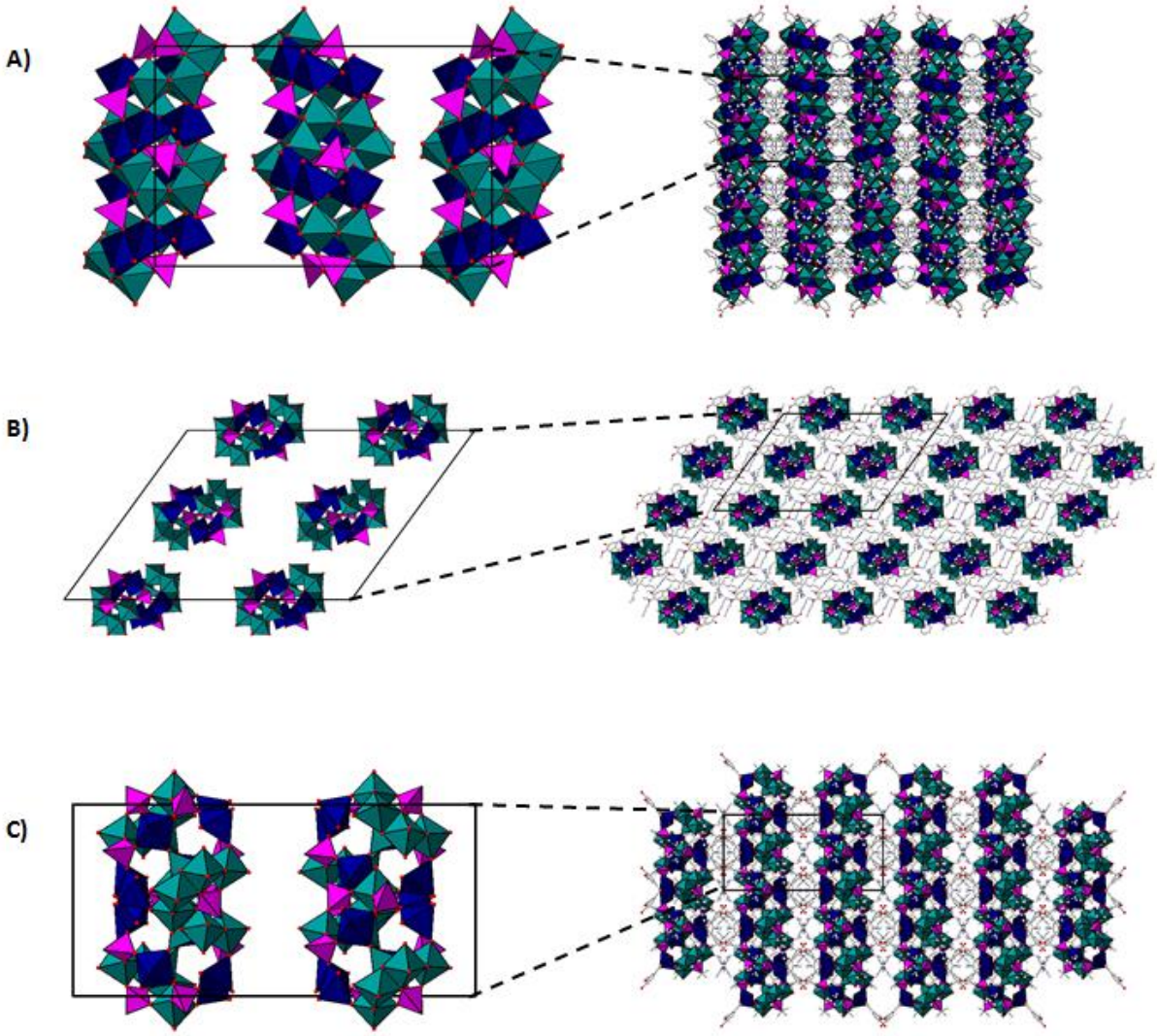

Figure 4.6.16 – Crystal packing diagrams for 19•6(MeCN), as viewed down : A) The crystallographic *a*-axis, B) the crystallographic *b*-axis. C) the crystallographic *c*-axis.

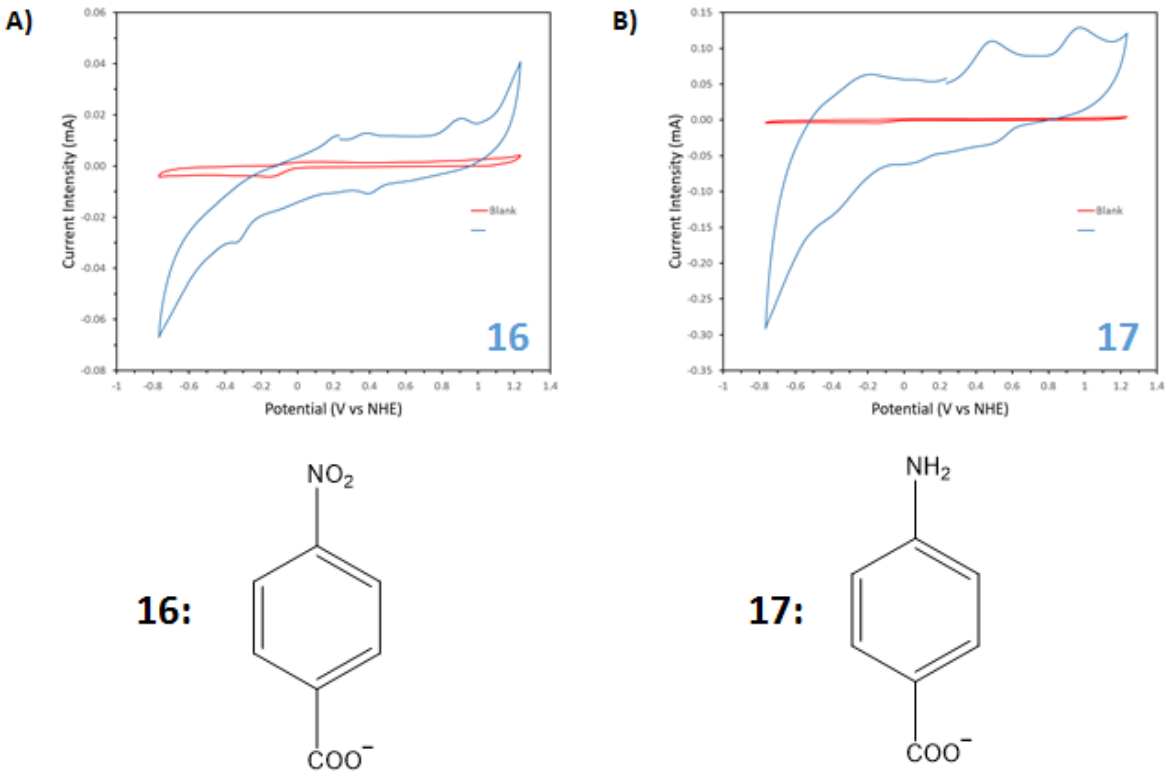

Figure 4.6.17 – Cyclic voltammagram sweeps for A) compound 16 and B) compound 17, which differ by an electron withdrawing (*nitro*-, 16) or donating (*amino*- 17) group on the carboxylate ligands.

Preliminary electrochemical analysis indicates that the electronic behaviour of the compounds is influenced by the presence of electron withdrawing or donating substituents on the cluster core. Comparison of **16** (which contains an electron withdrawing *nitro*- group) with **17** (which contains an electron donating *amino*- group) indicates a slight shift in oxidation potentials, with the first oxidation event shifting from *c.* 0.4 V vs. NHE (**16**) *c.* 0.45 V vs. NHE (**17**). This illustrates that the electronic properties of the cluster core can be manipulated by modifying the peripheral ligands.

When tested for electrocatalytic water oxidation, none of the compounds tested (**5**, **7**, **10**, **13**, **16** and **17**) demonstrated catalytic water oxidation.

4.7) Ligand Substitution of 5 – Photoactive Groups

Having incorporated several potentially reactive functional groups onto the cobalt-molybdate core, we then looked at optically active moieties. We decided to incorporate planar aromatic systems (Figure 4.7.1), as these tend to display significant UV absorption and luminescence capabilities.[77–80]

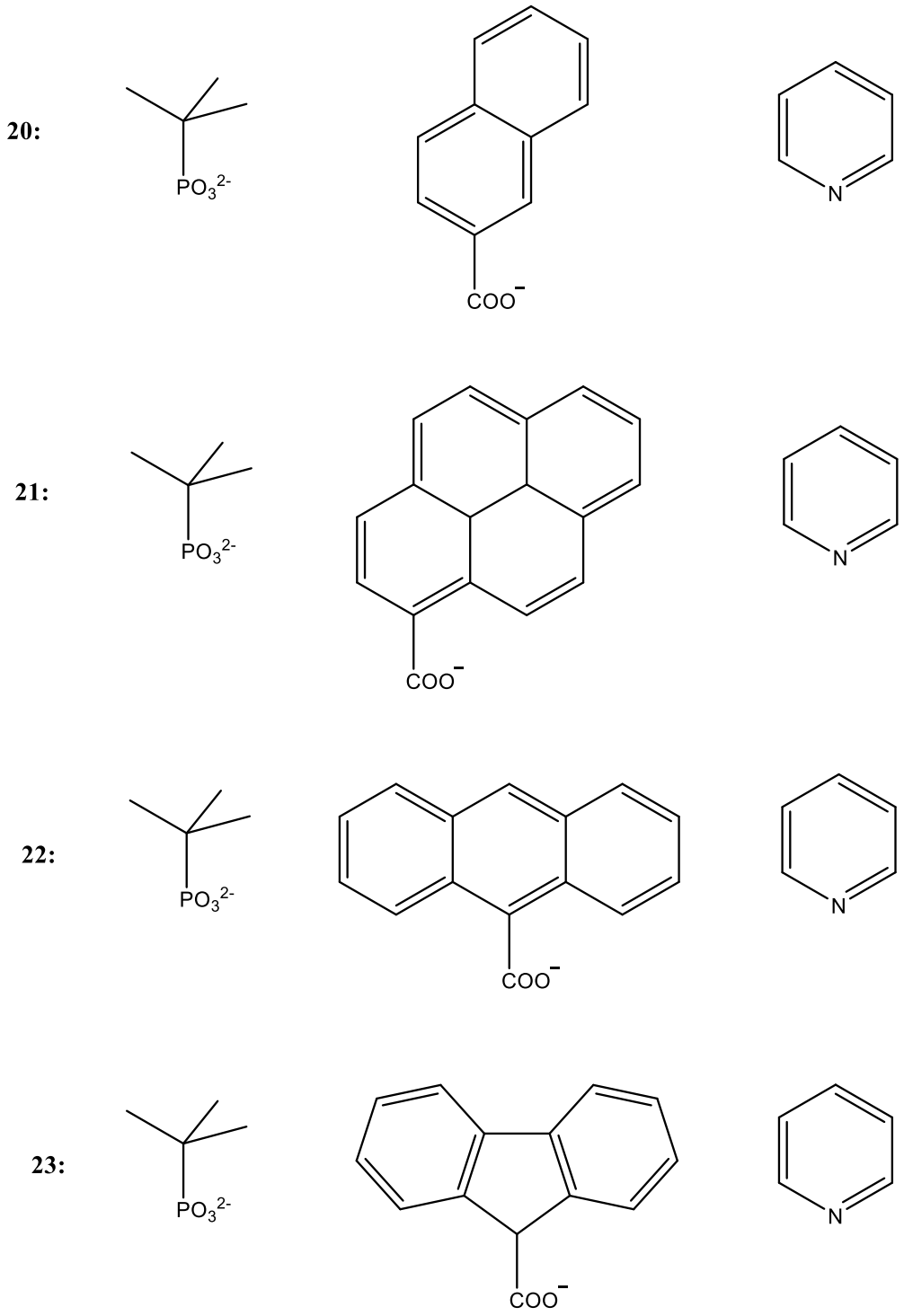

Figure 4.7.1 – The organic ligands present in 20-23.

$[TBA]_2[Mo^{VI}_{10}Co^{II}_6O_{12}(\mu\text{-}O)_{14}(\mu_3\text{-}O)_4(t\text{BuPO}_3)_6(\text{NapCOO})_2(\text{py})_2(H_2O)_6]$ (**20**) crystallised over two weeks along with two constituent acetonitrile molecules per formula unit (Figure 4.7.2). The crystals formed in the monoclinic crystal system in space group $P2_1/n$.

$[TBA]_2[Mo^{VI}_{10}Co^{II}_6O_{12}(\mu\text{-}O)_{14}(\mu_3\text{-}O)_4(t\text{BuPO}_3)_6(\text{pyrCOO})_2(\text{py})_2(H_2O)_6]$ (**21**) crystallised over four weeks along with 3.5 constituent acetonitrile molecules per formula unit (Figure 4.7.3). The crystals formed in the triclinic crystal system in space group *P*-1.

$[TBA]_2[Mo^{VI}_{10}Co^{II}_6O_{12}(\mu\text{-}O)_{14}(\mu_3\text{-}O)_4(t\text{BuPO}_3)_6(\text{anthCOO})_2(\text{py})_2(H_2O)_6]$ (**22**) crystallised over two weeks along with six constituent acetonitrile molecules per formula unit (Figure 4.7.4). The crystals formed in the monoclinic crystal system in space group *P*-1.

$[TBA]_2[Mo^{VI}_{10}Co^{II}_6O_{12}(\mu\text{-}O)_{14}(\mu_3\text{-}O)_4(t\text{BuPO}_3)_6(\text{fluoCOO})_2(\text{py})_2(H_2O)_6]$ (**23**) crystallised over two weeks along with 4.17 constituent acetonitrile molecules per formula unit. The crystals formed in the monoclinic crystal system in space group *P*-1.

Nap represents the 2-naphthyl moiety, pyr represents the 1-pyrene moiety, anth represents the 9-anthracene moiety, and fluo represents the 9-fluorene moiety.

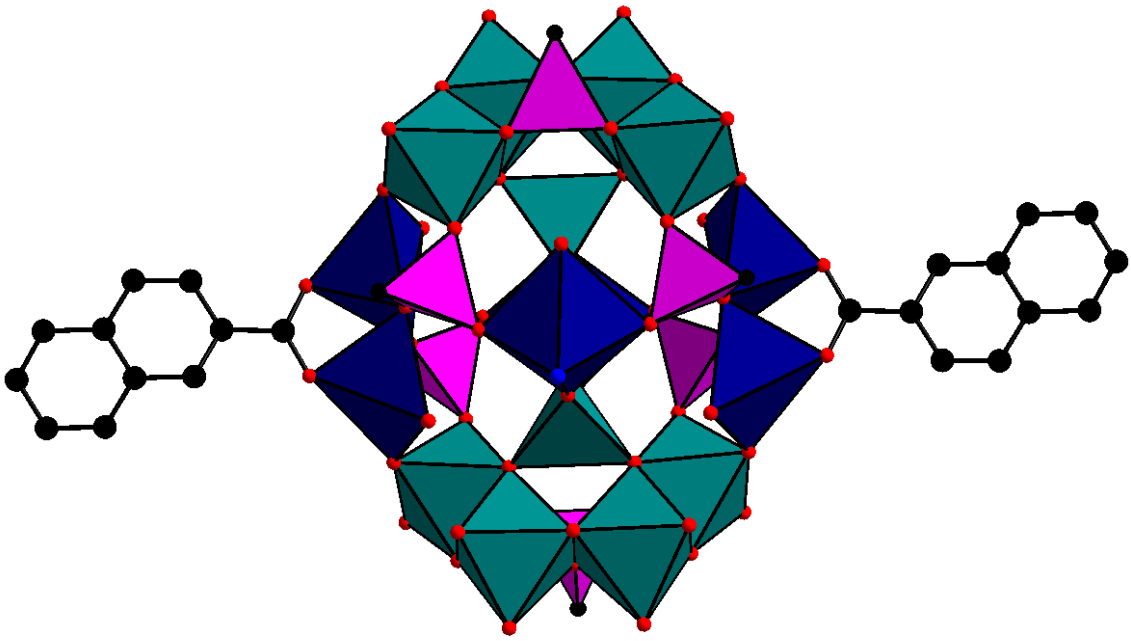

Figure 4.7.2 – Simplified representation of the cluster core in 20, showing the 2-naphthalene ligands. Colour Scheme: Mo teal, Co dark blue, P pink, O red, N blue, C black.

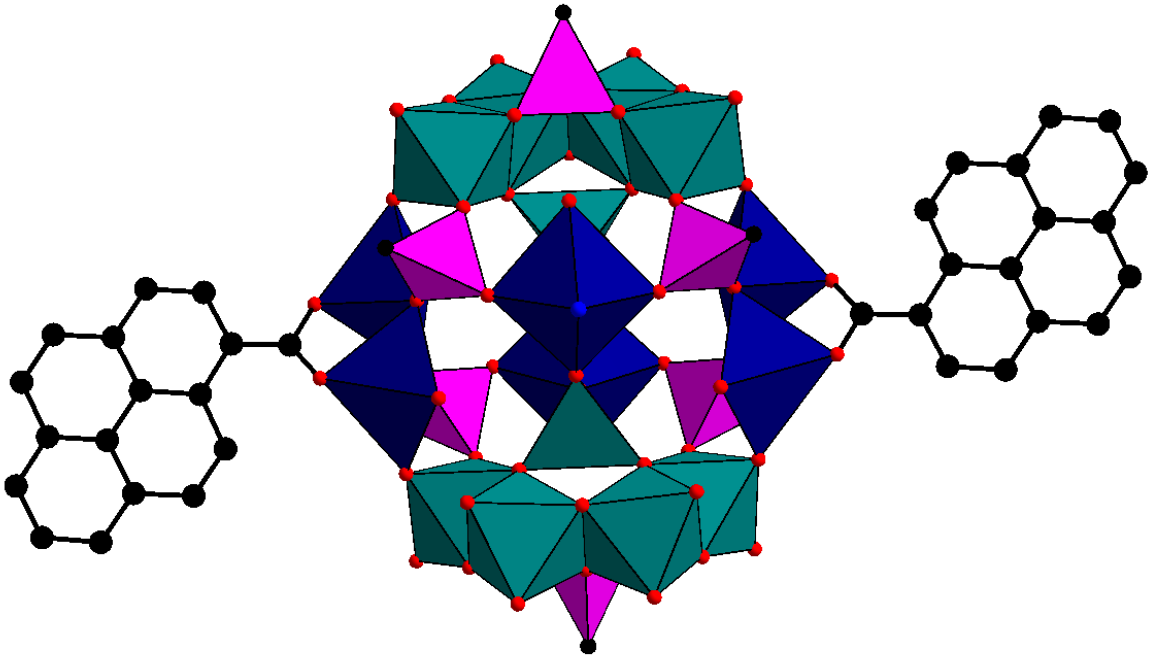

Figure 4.7.3 – Simplified representation of the cluster core in 21, showing the 1-pyrene ligands. Colour Scheme: Mo teal, Co dark blue, P pink, O red, N blue, C black.

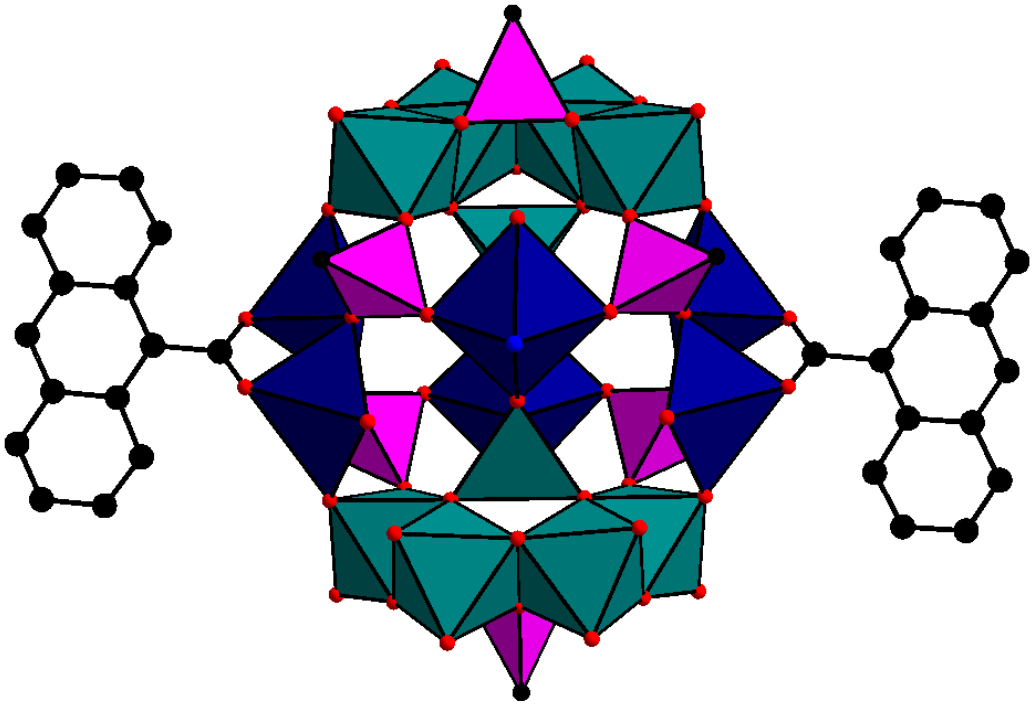

Figure 4.7.4 – Simplified representation of the cluster core in 22, showing the 9-anthracene ligands. Colour Scheme: Mo teal, Co dark blue, P pink, O red, N blue, C black.

The cluster core in **23** engages in π-π interactions between the flourerene moieties on adjacent cluster entities (Figure 4.7.5). The interplanar distance is approximately 3.3 Å, which is consistent with π-π interactions.[81] This stacking results in a one-dimensional pseudopolymer propagating through the crystal structure.

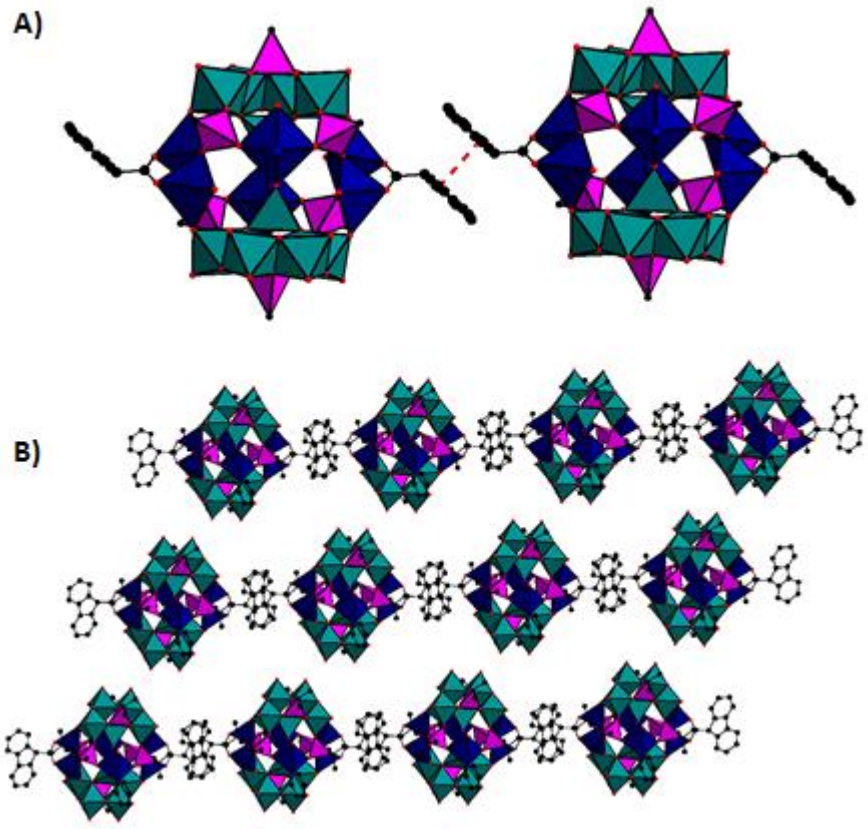

Figure 4.7.5 – A) π-π interactions between the fluorine moieties on adjacent cluster entities in crystals of 23•4(MeCN). B) These π-π interactions result in the formation of a one-dimensional pseudopolymer that propagates through the crystalline state. Colour Scheme: Mo teal, Co dark blue, P pink, O red, N blue, C black.

Identification code	**20**•2(MeCN)
Empirical formula	$C_{46}H_{84}Co_3Mo_5N_3O_{29}P_3$
Formula weight (g/mol)	1892.56
Temperature (K)	100(2)
Wavelength (Å)	0.71073
Crystal system	Monoclinic
Space group	$P2_1/n$
a (Å)	15.8891(16)
b (Å)	18.8429(19)
c (Å)	23.550(2)
α (°)	90
β (°)	90.414(2)
γ (°)	90
Volume (Å^3)	7050.6(12)
Z	4
Calculated density ρ_{calc} (g/cm^3)	1.783
Absorption coefficient μ (mm^{-1})	1.693
F(000)	3796.0
Crystal size (mm^3)	0.32 × 0.13 × 0.06
2Θ range for data collection (°)	3.352 to 63.068
Index ranges	$-23 \leq h \leq 23$, $-27 \leq k \leq 27$, $-34 \leq l \leq 34$
Reflections collected	184130
Independent reflections	23509 [R_{int} = 0.0447]
Data/restraints/parameters	23509/0/817
Goodness-of-fit on F^2	1.122
Final R indices [I>=2σ (I)]	R_1 = 0.0359, wR_2 = 0.0723
Final R indices [all data]	R_1 = 0.0535, wR_2 = 0.0786
Largest diff. peak and hole (e Å^{-3})	1.88/-0.92

Table 4.7.1 – Crystallographic details for compound 20•2(MeCN).

Identification code	**21**•3.5(MeCN)
Empirical formula	$C_{107}H_{166}Co_6Mo_{10}N_{7.5}O_{58}P_6$
Formula weight (g/mol)	3984.26
Temperature (K)	100(2)
Wavelength (Å)	0.71073
Crystal system	Triclinic
Space group	*P*-1
a (Å)	14.1248(4)
b (Å)	17.1990(4)
c (Å)	18.2808(4)
α (°)	115.5330(10)
β (°)	102.8840(10)
γ (°)	93.8560(10)
Volume ($Å^3$)	3838.43(17)
Z	1
Calculated density ρ_{calc} (g/cm^3)	1.724
Absorption coefficient μ (mm^{-1})	1.560
F(000)	1996.0
Crystal size (mm^3)	0.225 × 0.197 × 0.14
2Θ range for data collection (°)	2.572 to 82.756
Index ranges	$-26 \leq h \leq 26$, $-31 \leq k \leq 31$, $-33 \leq l \leq 33$
Reflections collected	489731
Independent reflections	51532 [R_{int} = 0.0412]
Data/restraints/parameters	51532/3/887
Goodness-of-fit on F^2	1.112
Final R indices [I>=2σ (I)]	R_1 = 0.0431, wR_2 = 0.1191
Final R indices [all data]	R_1 = 0.0639, wR_2 = 0.1324
Largest diff. peak and hole (e $Å^{-3}$)	4.12/-2.27

Table 4.7.2 – Crystallographic details for compound 21•3.5(MeCN).

The acetonitrile molecules are disordered with 0.5 or 0.25 occupancy.

Identification code	**22**•6(MeCN)
Empirical formula	$C_{108}H_{184}Co_6Mo_{10}N_{10}O_{58}P_6$
Formula weight (g/mol)	4049.44
Temperature (K)	100(2)
Wavelength (Å)	0.71073
Crystal system	Triclinic
Space group	*P*-1
a (Å)	13.7204(5)
b (Å)	17.4996(6)
c (Å)	18.0558(6)
α (°)	105.8800(10)
β (°)	106.5320(10)
γ (°)	100.2090(10)
Volume ($Å^3$)	3841.4(2)
Z	1
Calculated density ρ_{calc} (g/cm^3)	1.750
Absorption coefficient μ (mm^{-1})	1.561
F(000)	2038.0
Crystal size (mm^3)	0.22 × 0.18 × 0.13
2Θ range for data collection (°)	2.878 to 56.638
Index ranges	$-18 \leq h \leq 18$, $-23 \leq k \leq 23$, $-24 \leq l \leq 24$
Reflections collected	112190
Independent reflections	19102 [R_{int} = 0.0372]
Data/restraints/parameters	19102/0/911
Goodness-of-fit on F^2	1.052
Final R indices [I>=2σ (I)]	R_1 = 0.0260, wR_2 = 0.0547
Final R indices [all data]	R_1 = 0.0413, wR_2 = 0.0613
Largest diff. peak and hole (e $Å^{-3}$)	1.01/-0.59

Table 4.7.3 – Crystallographic details for compound 22•6(MeCN).

Identification code	**23**•4(MeCN)
Empirical formula	$C_{103.33}H_{176}Co_6Mo_{10}N_{8.17}O_{58}P_6$
Formula weight (g/mol)	3959.65
Temperature (K)	100(2)
Wavelength (Å)	0.71073
Crystal system	Triclinic
Space group	*P*-1
a (Å)	13.4626(10)
b (Å)	17.5362(13)
c (Å)	19.9202(15)
α (°)	112.340(2)
β (°)	108.453(2)
γ (°)	93.499(3)
Volume (Å^3)	4037.1(5)
Z	1
Calculated density ρ_{calc} (g/cm^3)	1.629
Absorption coefficient μ (mm^{-1})	1.483
F(000)	1989.0
Crystal size (mm^3)	0.185 × 0.163 × 0.116
2Θ range for data collection (°)	2.662 to 55.124
Index ranges	$-17 \leq h \leq 17$, $-22 \leq k \leq 22$, $-25 \leq l \leq 25$
Reflections collected	74772
Independent reflections	74772
Data/restraints/parameters	74772/54/907
Goodness-of-fit on F^2	1.058
Final R indices [I>=2σ (I)]	R_1 = 0.0545, wR_2 = 0.1397
Final R indices [all data]	R_1 = 0.0826, wR_2 = 0.1581
Largest diff. peak and hole (e Å^{-3})	1.52/-1.11

Table 4.7.4 – Crystallographic details for compound 23•4(MeCN).

Of the three crystallographically distinct acetonitrile molecules, one is disordered over two positions in a 50/50 ratio, another disordered in a 25/75 ratio, and the third is 1/3 occupied.

Packing Diagrams

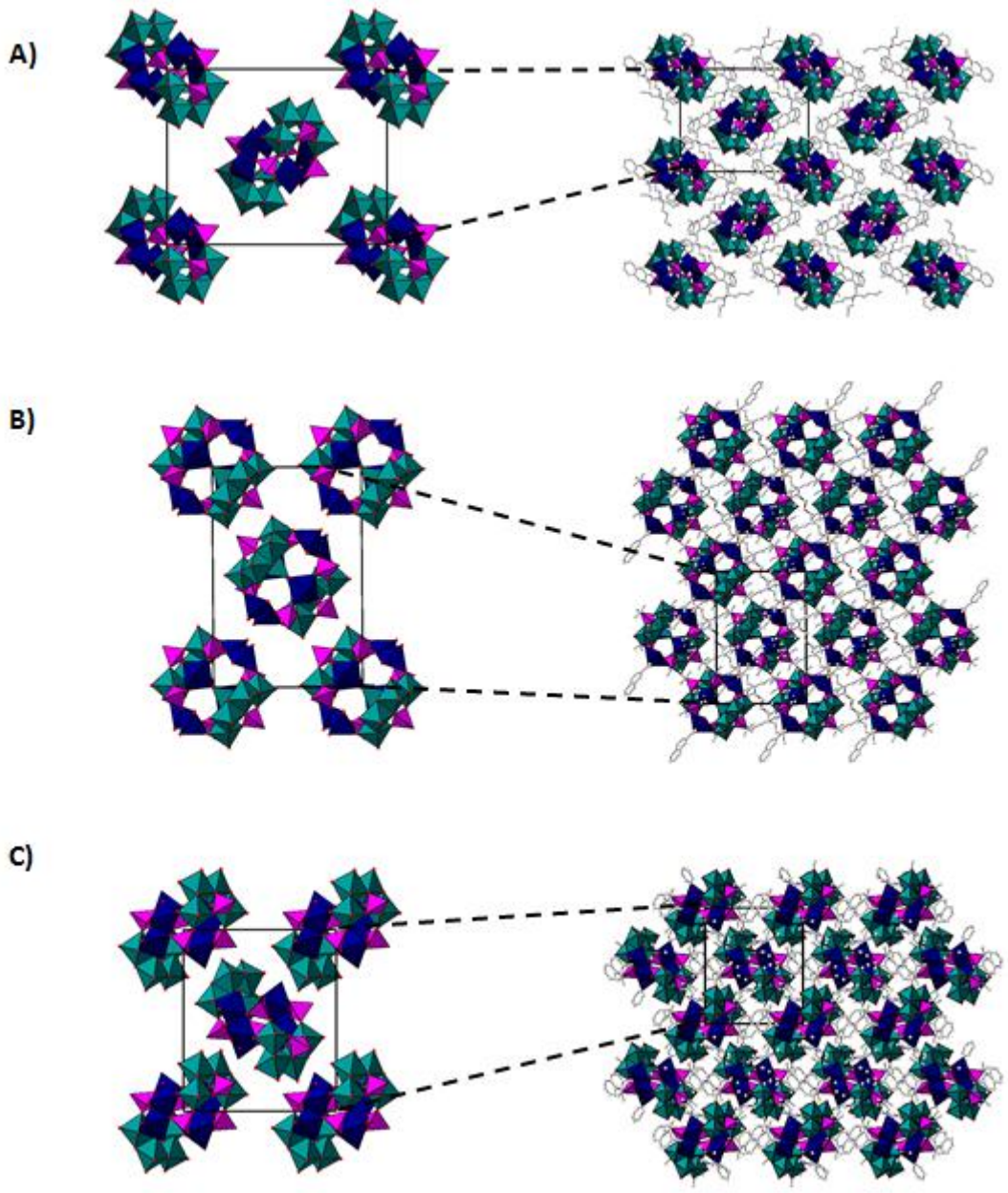

Figure 4.7.6 – Crystal packing diagrams for 20•2(MeCN), as viewed down: A) The crystallographic *a*-axis, B) the crystallographic *b*-axis. C) The crystallographic *c*-axis.

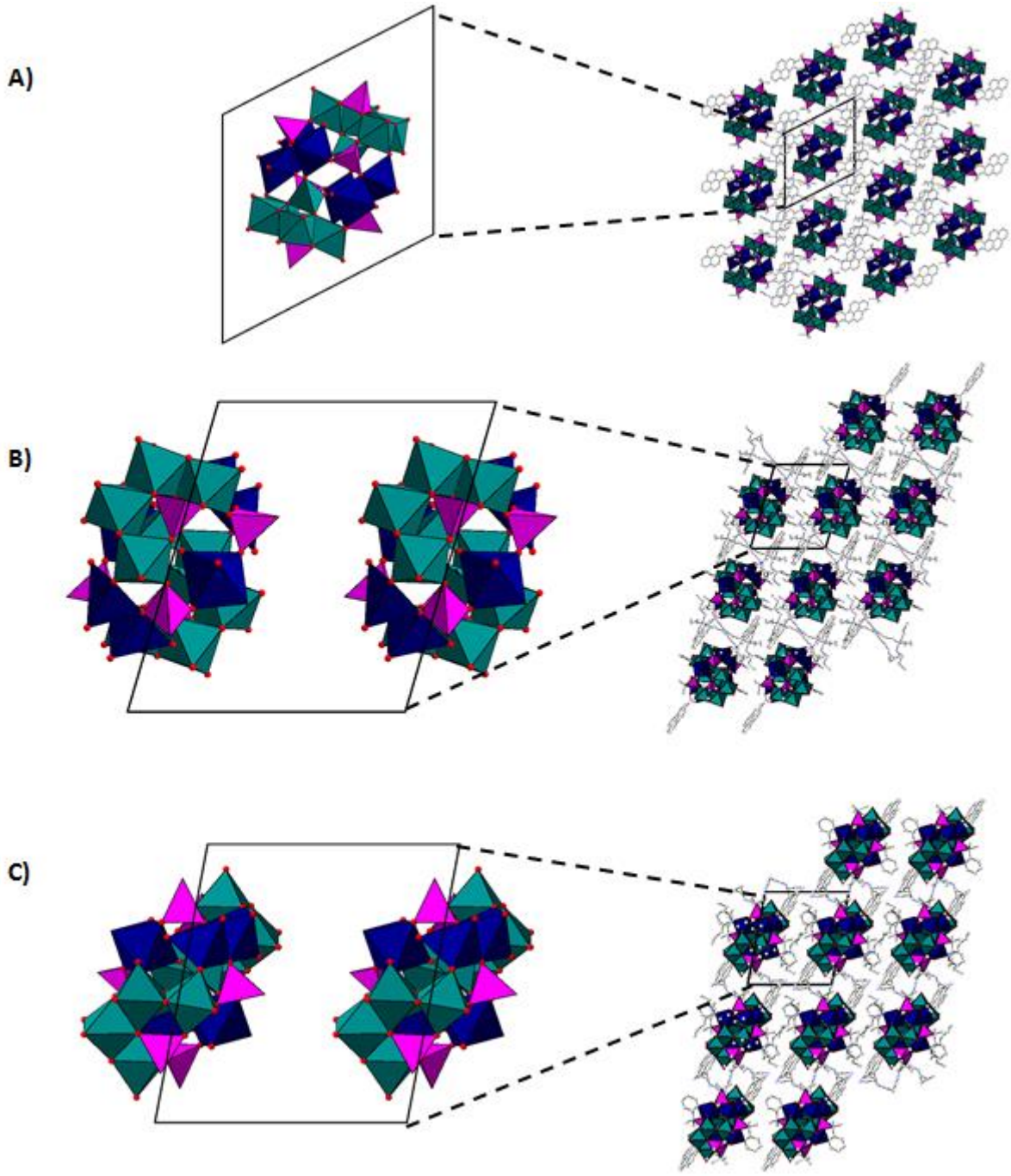

Figure 4.7.7 – Crystal packing diagrams for 21•3.5(MeCN), as viewed down: A) The crystallographic *a*-axis, B) the crystallographic *b*-axis. C) The crystallographic *c*-axis.

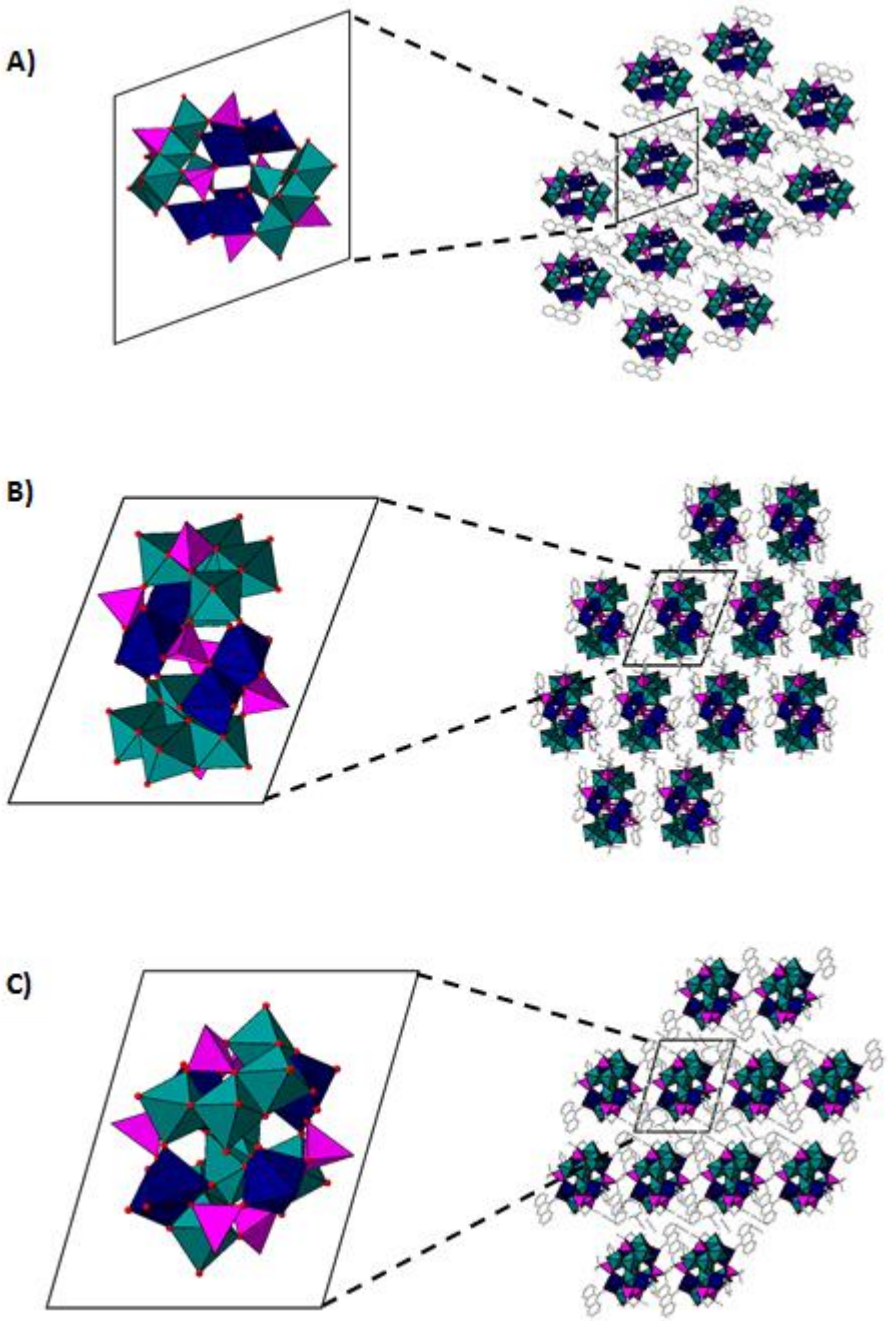

Figure 4.7.8 – Crystal packing diagrams for 22•6(MeCN), as viewed down: A) The crystallographic *a*-axis, B) the crystallographic *b*-axis. C) The crystallographic *c*-axis.

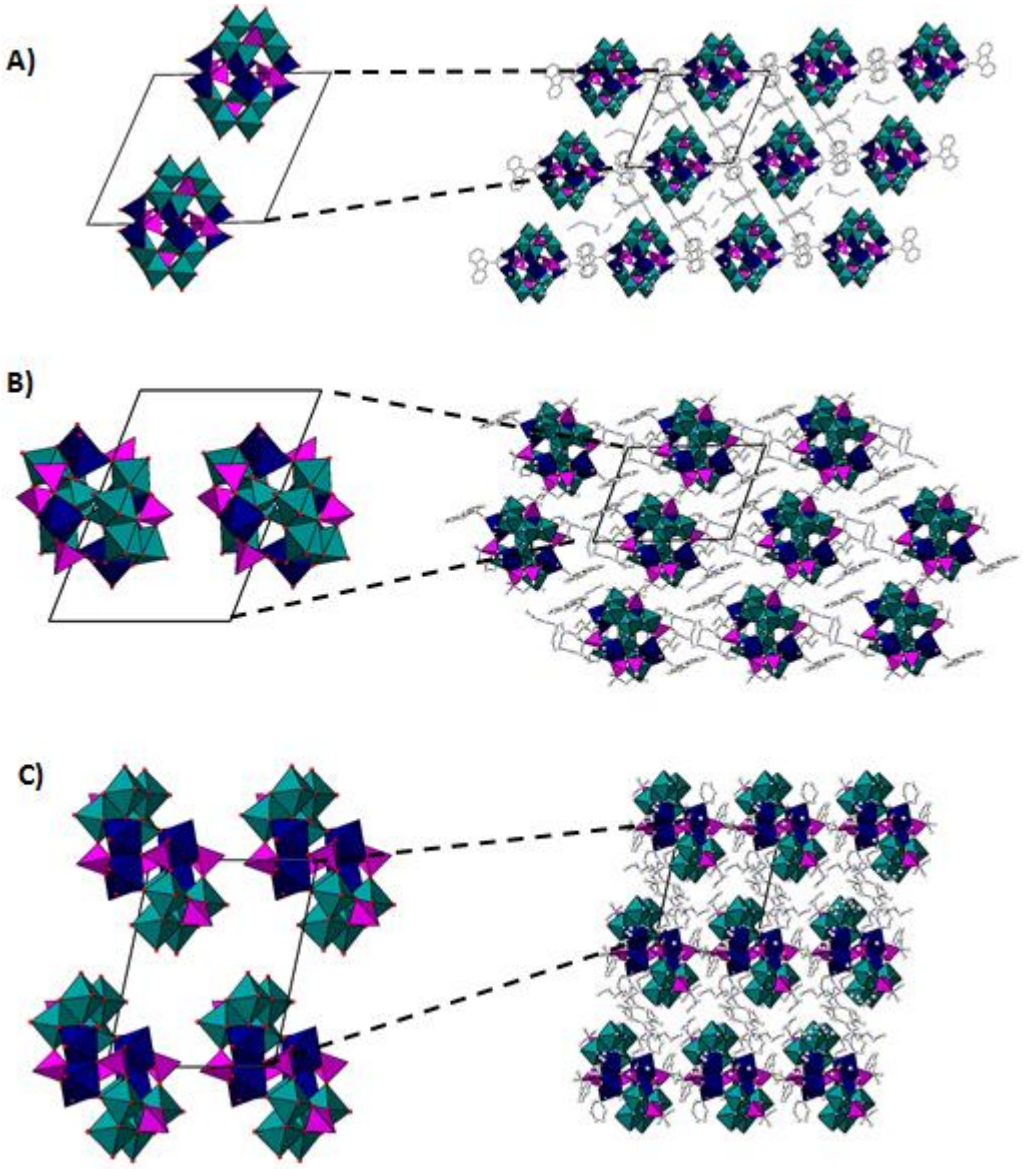

Figure 4.7.9 – Crystal packing diagrams for 23•4(MeCN), as viewed down: A) The crystallographic *a*-axis, B) the crystallographic *b*-axis. C) The crystallographic *c*-axis.

Photoactivity

To investigate the photophysical properties of the compounds, ultraviolet-visible (UV-Vis) absorption spectra were recorded for *c.* 30 μM samples of **20-23** in acetonitrile. Incorporation of the photoactive moieties significantly alters the ultraviolet absorbance of the compounds (Figure 4.7.10). In addition to a weak absorbance in the visible region (ε = 341 M^{-1} cm^{-1} at λ = 560 nm), compounds **21** and **22** show particularly strong absorbance in the *c.* 300-400 nm region, each showing multiple absorbance bands. The pyrene moieties in **21** absorb at *c.* 350 and 380 nm, while the anthracene moieties in **22** absorb at *c.* 350, 370 and 385 nm. Absorption coefficient (ε) values for these absorption bands are in the range 1.0x10^4 M^{-1} cm^{-1} (compound **21**, λ = 380 nm) to 4.0x10^4 M^{-1} cm^{-1} (compound **21**, λ = 350 nm). These ε values are consistent with organic π-π* transitions.

Compounds **20** and **23** do not absorb strongly in the near ultraviolet (*c.* 300-400 nm). Absorbance rises sharply below *c.* 300 nm for all of the compounds, probably due to Mo-O charge transfer bands, which dominate the spectra in this region.

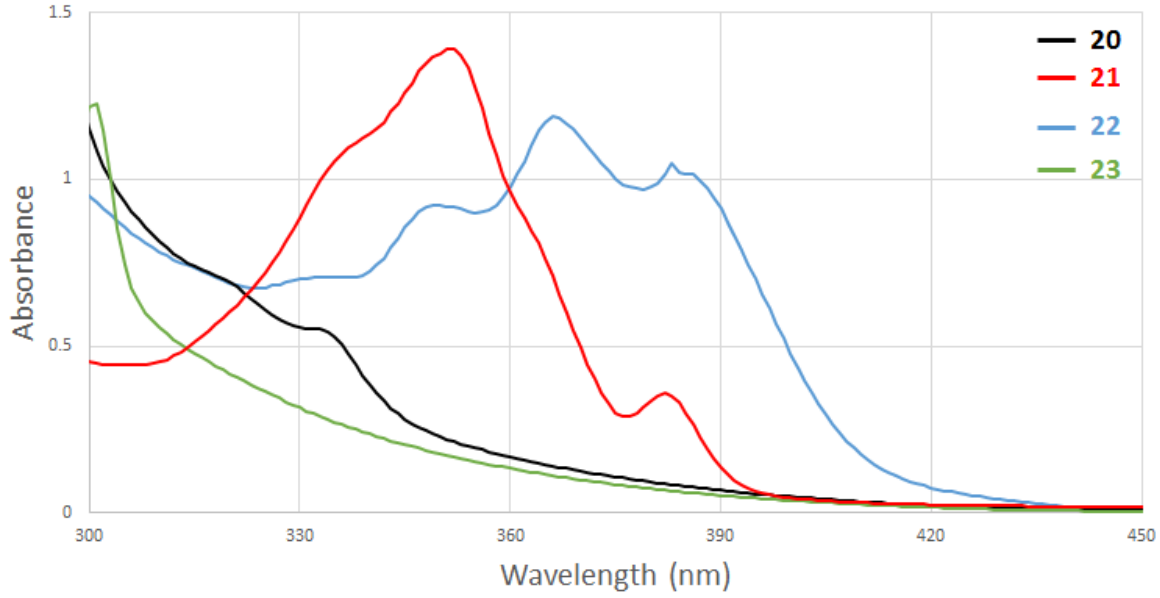

Figure 4.7.10 – Portion of the ultraviolet absorbance spectra for compounds 20-23 in acetonitrile.

Compounds **21** and **22** were selected for further photophysical studies, based on their strong absorbance in the near ultraviolet. The excitation wavelength was set at 350 nm, as both **21** and **22** display maxima in absorption around this wavelength. Under these conditions, both **21** and **22** display luminescent behaviour (Figure 4.7.11).

When excited at 350 nm, **21** luminesces with maxima in emission at 395 nm and 410 nm. When excited at the same wavelength, **22** emits over a broad range of visible wavelengths, with emission centred at 460 nm. This indicates that the photoexcited ligand states in these compounds are not quenched by interaction with the TMS-POM core, allowing luminescence to occur.

This behaviour is represented visually in Figure 4.7.11, showing compounds **20-23** under irradiation at 365 nm. Compound **21** luminesces blue under these conditions, while compound **22** luminesces blue-green. Compounds **20** and **23** do not display visible luminescence under these conditions.

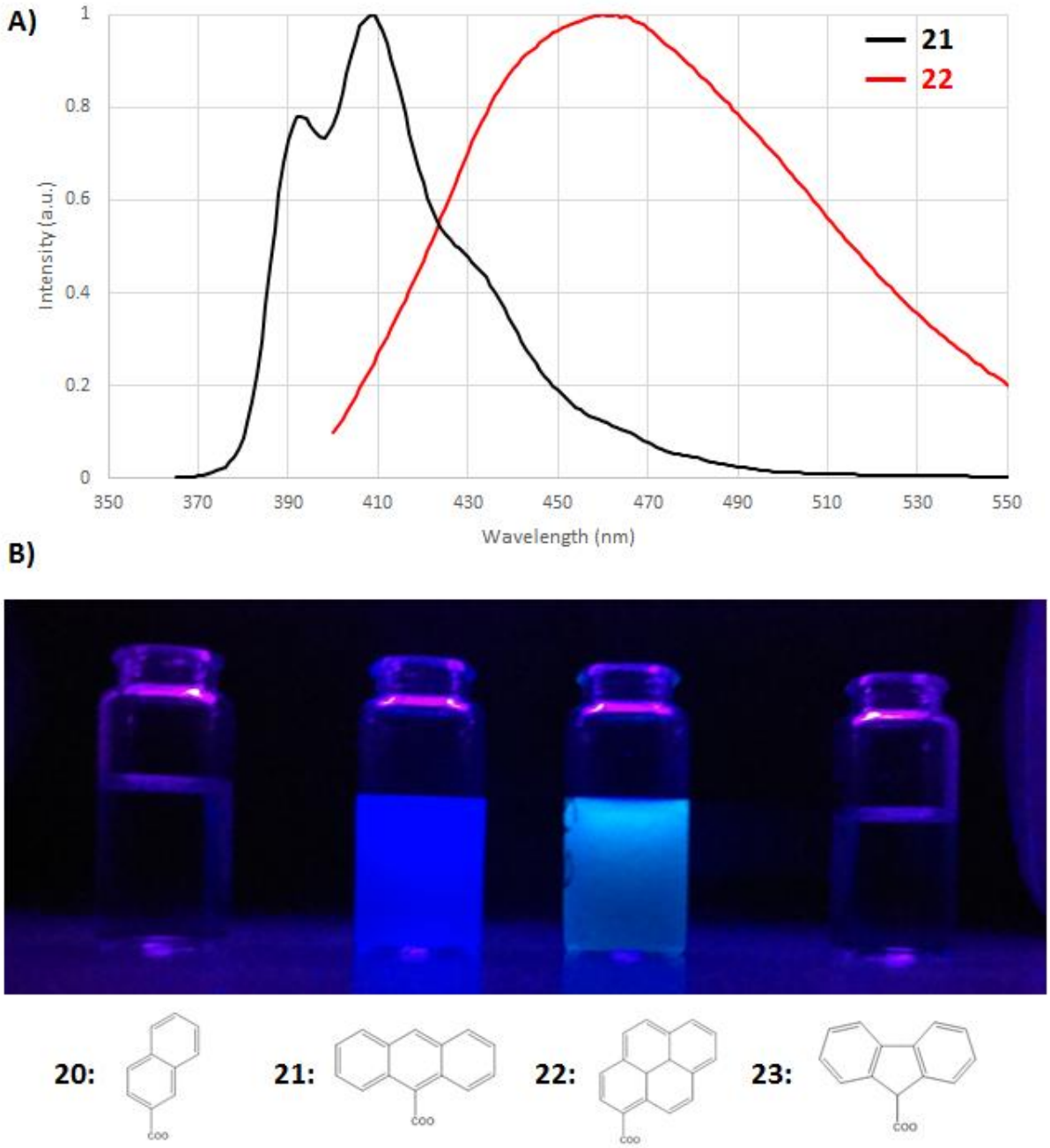

Figure 4.7.11 – A) Normalised photoluminescence spectra for *c.* 30 μM samples of 21 (black) and 22 (red) in acetonitrile when excited at λ = 350 nm. B) Samples of 20-23 (left-to-right) in acetonitrile under irradiation at 360 nm, showing visible luminescence of 21 and 22.

Thus, by incorporating photoactive ligands onto the cobalt-molybdate cluster core, we have significantly modified the absorption spectra of the compounds, as well as introducing colour-tuneable luminescence properties to the compounds.

Photodynamic Behaviour

In addition to the modification of the absorption and luminescence behaviour of the cobalt-molybdate core by the incorporation of photoactive moieties, photodynamic switching behaviour can also be introduced *via* supporting carboxylate ligands. The azobenzene moiety is well-known to undergo dynamic motion upon irradiation, switching from the *trans*- ground state to the *cis*- conformation upon irradiation at *c.* 360 nm.[82–85]

$[TBA]_2[Mo^{VI}_{10}Co^{II}_6O_{12}(\mu\text{-}O)_{14}(\mu_3\text{-}O)_4(t\text{BuPO}_3)_6(\text{azoCOO})_2(\text{py})_2(H_2O)_6]$ (**24**) was synthesised using 4-(phenylazo)benzoic acid (Figure 4.7.12 and 4.7.13). **24** crystallised over two weeks along with one constituent acetonitrile molecules per formula unit. The crystals formed in the monoclinic crystal system in space group $P2_1/n$.

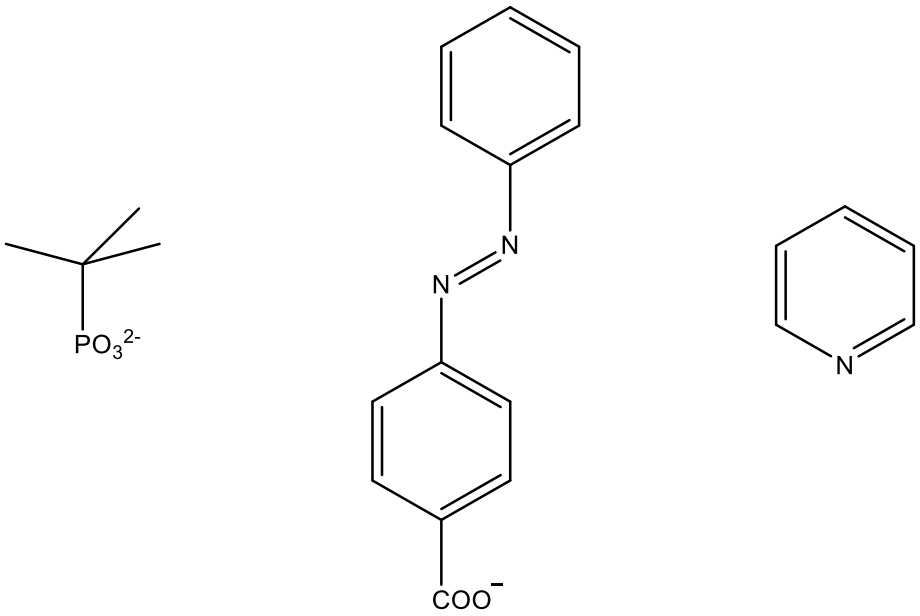

Figure 4.7.12 – The organic ligands present in 24.

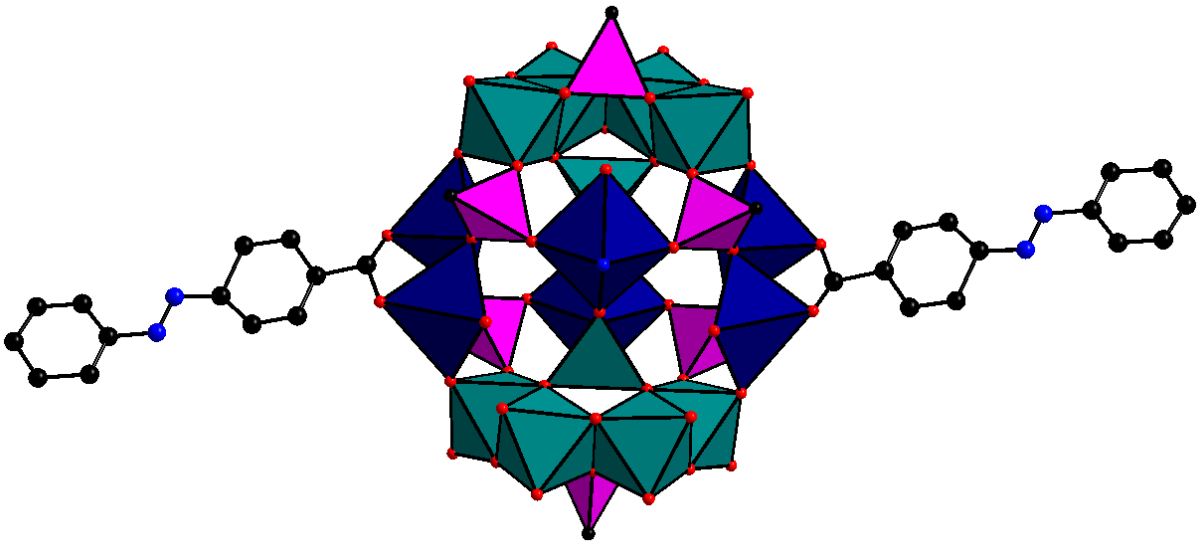

Figure 4.7.13 – Simplified representation of the cluster core in 24, showing the azobenzene moieties. Colour Scheme: Mo teal, Co dark blue, P pink, O red, N blue, C black.

As is the case for **23**, π-π interactions between the organic moieties direct the molecular stacking arrangement in the crystalline state (Figure 4.7.14). These π-π interactions results in a one-dimensional pseudopolymer propagating through the crystal structure. The interplanar distance is approximately 3.3 Å, which is consistent with π-π interactions.[81]

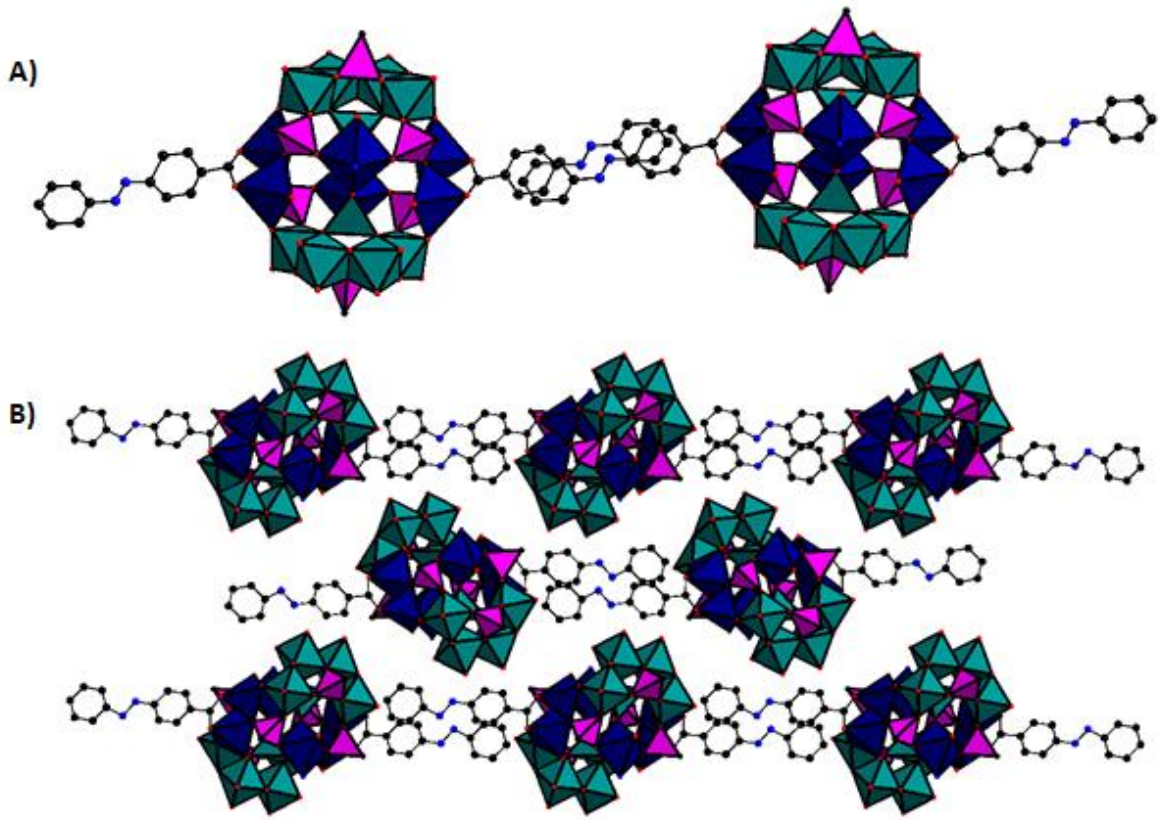

Figure 4.7.14 – A) π-π interactions between the azobenzene moieties on adjacent cluster entities in crystals of 24•(MeCN). B) These π-π interactions result in the formation of a one-dimensional pseudopolymer that propagates through the crystalline state. Colour Scheme: Mo teal, Co dark blue, P pink, O red, N blue, C black.

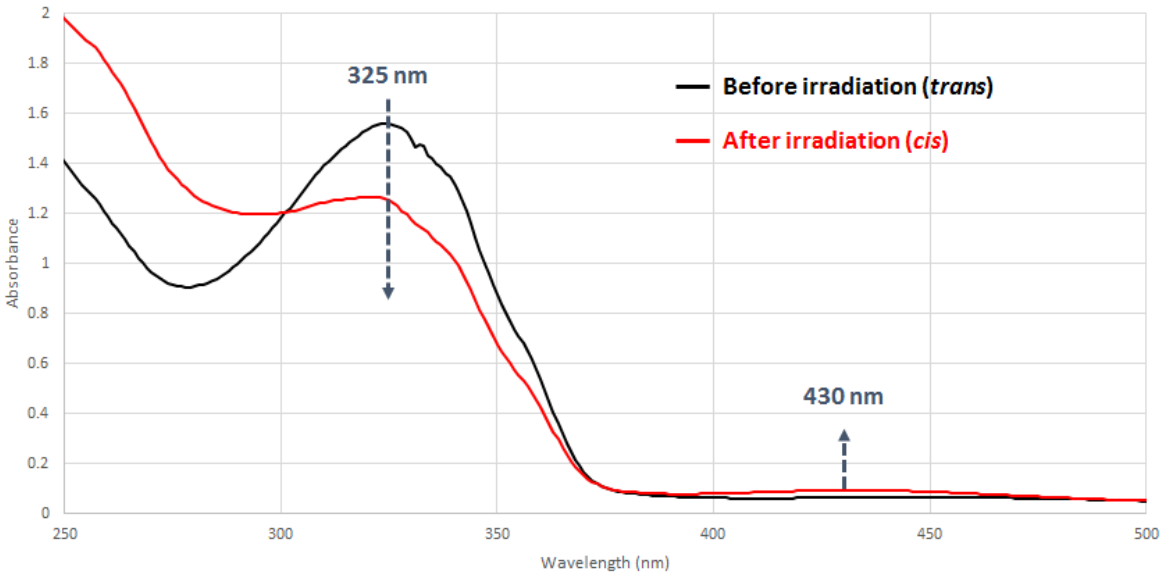

Figure 4.7.15 – UV-Vis absorption spectrum of 24 in acetonitrile, before and after irradiation at 360 nm.

Azobenzene moieties are well known to undergo *cis-trans* isomerisation under UV radiation. This dynamic process can be monitored using UV-Visible absorption spectroscopy (Figure 4.7.15).

When dissolved in acetonitrile, the UV-Vis absorption spectrum of **24** is dominated by an absorption band and 325 nm. Upon irradiation for 5 minutes at 360 nm, the absorption feature at 325 nm diminishes, along with the growth of a much smaller feature at 430 nm. This behaviour is consistent with *cis-trans* azobenzene isomerisation previously reported in the literature.[82–85]

Identification code	**24**•(MeCN)
Empirical formula	$C_{92}H_{154}Co_6Mo_{10}N_8O_{58}P_6$
Formula weight (g/mol)	3799.02
Temperature (K)	100(2)
Wavelength (Å)	0.71073
Crystal system	Monoclinic
Space group	$P2_1/n$
a (Å)	15.8651(12)
b (Å)	19.9490(15)
c (Å)	22.8883(17)
α (°)	90
β (°)	96.434(2)
γ (°)	90
Volume (Å^3)	7198.4(9)
Z	2
Calculated density ρ_{calc} (g/cm^3)	1.753
Absorption coefficient μ (mm^{-1})	1.659
F(000)	3796.0
Crystal size (mm^3)	0.12 × 0.11 × 0.06
2Θ range for data collection (°)	2.974 to 50.854
Index ranges	$-14 \leq h \leq 19$, $-24 \leq k \leq 24$, $-27 \leq l \leq 27$
Reflections collected	69588
Independent reflections	13142 [R_{int} = 0.1106]
Data/restraints/parameters	13142/0/554
Goodness-of-fit on F^2	1.003
Final R indices [I>=2σ (I)]	R_1 = 0.0940, wR_2 = 0.2252
Final R indices [all data]	R_1 = 0.1754, wR_2 = 0.2770
Largest diff. peak and hole (e Å^{-3})	3.32/-1.63

Table 4.7.5 – Crystallographic details for compound 24•(MeCN).

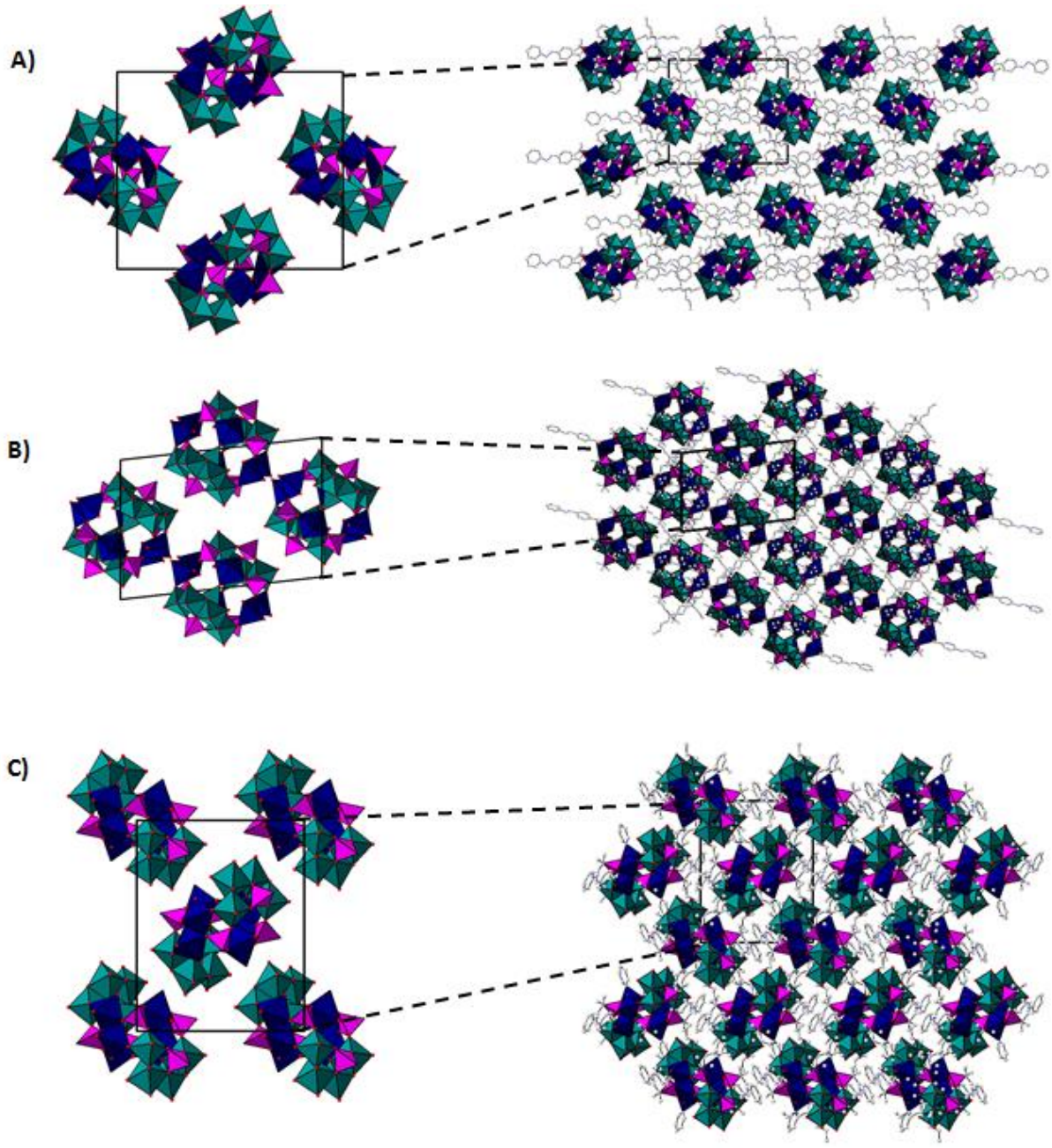

Figure 4.7.16 – Crystal packing diagrams for 24•(MeCN), as viewed down: A) The crystallographic *a*-axis, B) the crystallographic *b*-axis. C) The crystallographic *c*-axis.

4.8) Ligand Substitution of 5 – Polymeric Materials

One of the goals that we set out to achieve with this project was to generate extended materials (*i.e.* polymeric or framework materials). Given the success in generating numerous substituted analogues of **5**, the cobalt-molybdate reaction mixture seemed like an ideal system with which to attempt to generate polymeric materials using polytopic ligand systems.

Again, we decided to substitute the system at the carboxylate functionality, due to the easy availability of polytopic carboxylate ligands. Initial attempts using rigid polytopic carboxylates (*e.g.* terephthalate or trimesate) did not yield the target compounds, generally yielding amorphous cobalt compounds. These were not fully characterised but may represent cobalt-based coordination polymers of these ligands.[86–89] We hypothesised that these relatively short, rigid linkers might have constrained the system into an electrostatically unfavourable packing configuration (*c.f.* Figure 2.5.1).

Therefore, more flexible ligands were examined. Phenylenediacetic acid (PDA-H_2) is a rotationally flexible ditopic carboxylate, which bears similarity to the phenylacetate ligands used in **8** and **12**. **8** and **12** can accommodate rotational flexibility around the –CH_2– moieties in phenylacetate (*c.f.* Figure 4.5.2), potentially allowing the system flexibility to find a favourable packing arrangement. To this end, PDA-H_2 was incorporated into the reaction system (Figure 4.8.1).

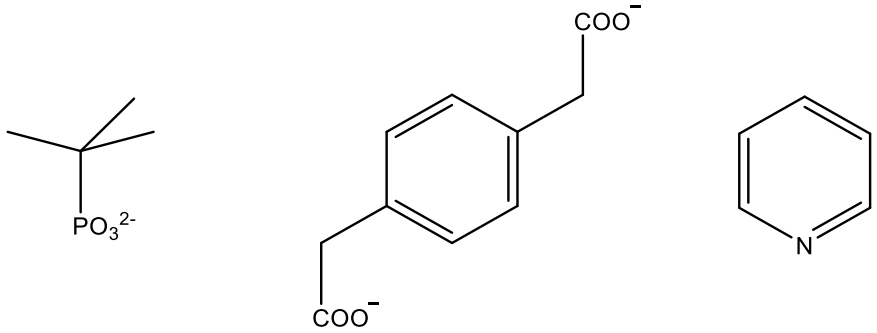

Figure 4.8.1 – The organic ligands present in 24.

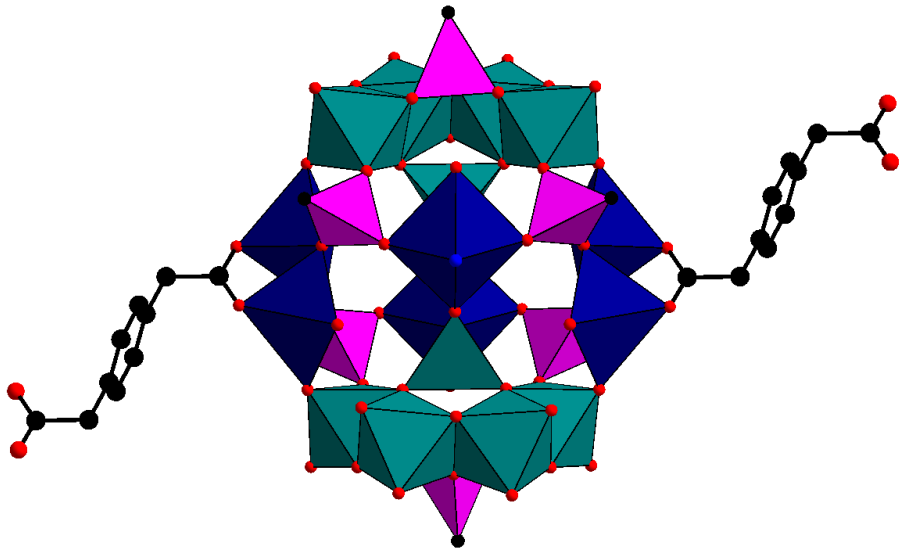

Figure 4.8.2 – Simplified representation of the cluster core in 25, showing the PDA moieties. Colour Scheme: Mo teal, Co dark blue, P pink, O red, N blue, C black.

$[TBA]_2[Mo^{VI}_{10}Co^{II}_6O_{12}(\mu\text{-}O)_{14}(\mu_3\text{-}O)_4(t\text{BuPO}_3)_6(PDA)(py)_2(H_2O)_6]$ (**25**) crystallised over the course of approximately one month (Figure 4.8.2). The crystals also contained 7.5 acetonitrile molecules per formula unit, and formed in the triclinic crystal system in space group *P*-1.

This compound has a polymeric structure, with one-dimensional hybrid polymer chains propagating throughout the crystal (Figure 4.8.3). The polymer chains propagate perpendicular to the crystallographic *c*-axis

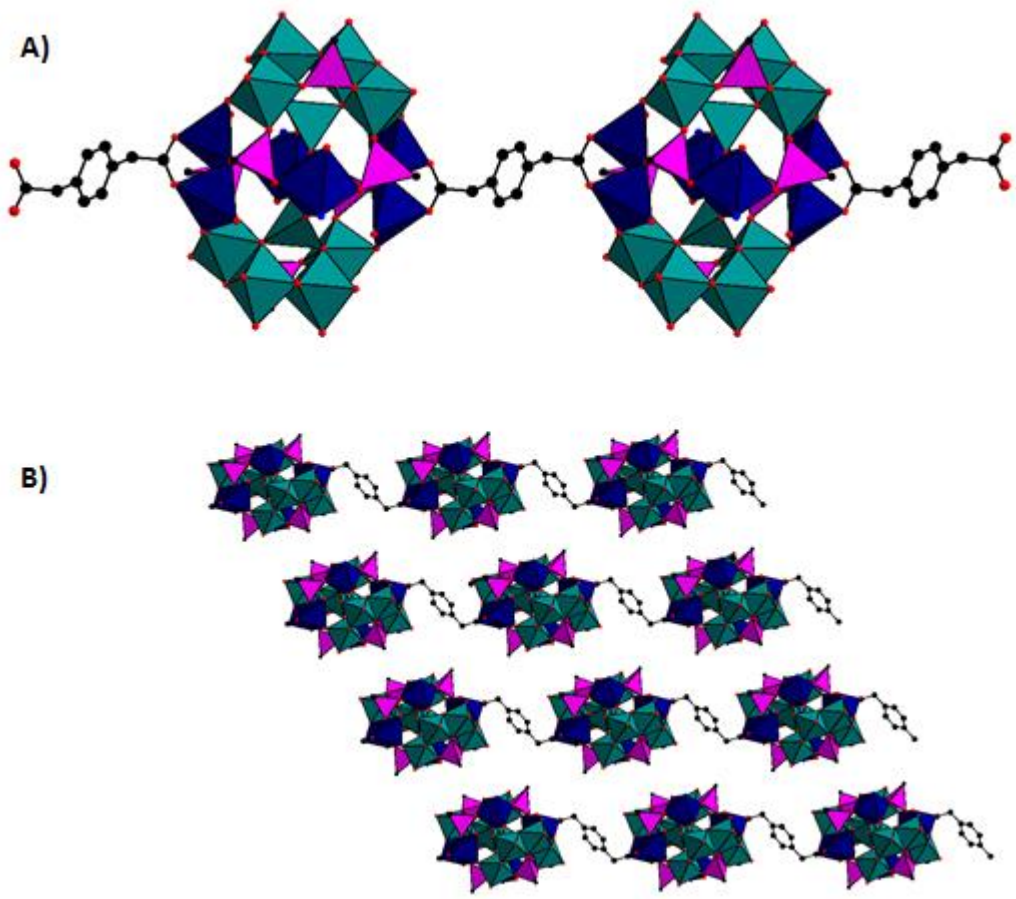

Figure 4.8.3 – A) Two repeat units of the polymer chain. B) The crystal structure of 25•7.5(MeCN) as viewed down the crystallographic *c*-axis, showing the parallel polymer chains propagating perpendicular to the *c*-axis. Colour Scheme: Mo teal, Co dark blue, P pink, O red, N blue, C black.

The torsion angle at the carboxylate site does seem to be significant, with the O-C-C-Ph angle increasing in this instance to be close to perpendicular (83°). The equivalent torsion angles in **8** and **12** were approximately in the range 0-45°. We attribute this difference to the different packing constraints on the polymer species.

Identification code	**25•**7.5(MeCN)
Empirical formula	$C_{45.5}H_{87.25}Co_3Mo_5N_{5.75}O_{29}P_3$
Formula weight (g/mol)	1928.36
Temperature (K)	100(2)
Wavelength (Å)	0.71073
Crystal system	Triclinic
Space group	*P*-1
a (Å)	13.7500(4)
b (Å)	16.8554(5)
c (Å)	17.1095(5)
α (°)	107.6320(10)
β (°)	95.0120(10)
γ (°)	101.6640(10)
Volume (Å^3)	3653.79(19)
Z	2
Calculated density ρ_{calc} (g/cm^3)	1.753
Absorption coefficient μ (mm^{-1})	1.636
F(000)	1937.0
Crystal size (mm^3)	0.131 × 0.076 × 0.04
2Θ range for data collection (°)	3.064 to 62.178
Index ranges	$-19 \leq h \leq 19$, $-24 \leq k \leq 22$, $-23 \leq l \leq 24$
Reflections collected	73920
Independent reflections	22705 [R_{int} = 0.0889]
Data/restraints/parameters	22705/8/848
Goodness-of-fit on F^2	1.002
Final R indices [I>=2σ (I)]	R_1 = 0.0544, wR_2 = 0.0903
Final R indices [all data]	R_1 = 0.1150, wR_2 = 0.1056
Largest diff. peak and hole (e Å^{-3})	1.64/-1.01

Table 4.8.1 – Crystallographic details for 25•7.5(MeCN).

Of the four crystallographically distinct acetonitrile solvent molecules, three are modelled as fully occupied and one is modelled with 0.75 occupancy.

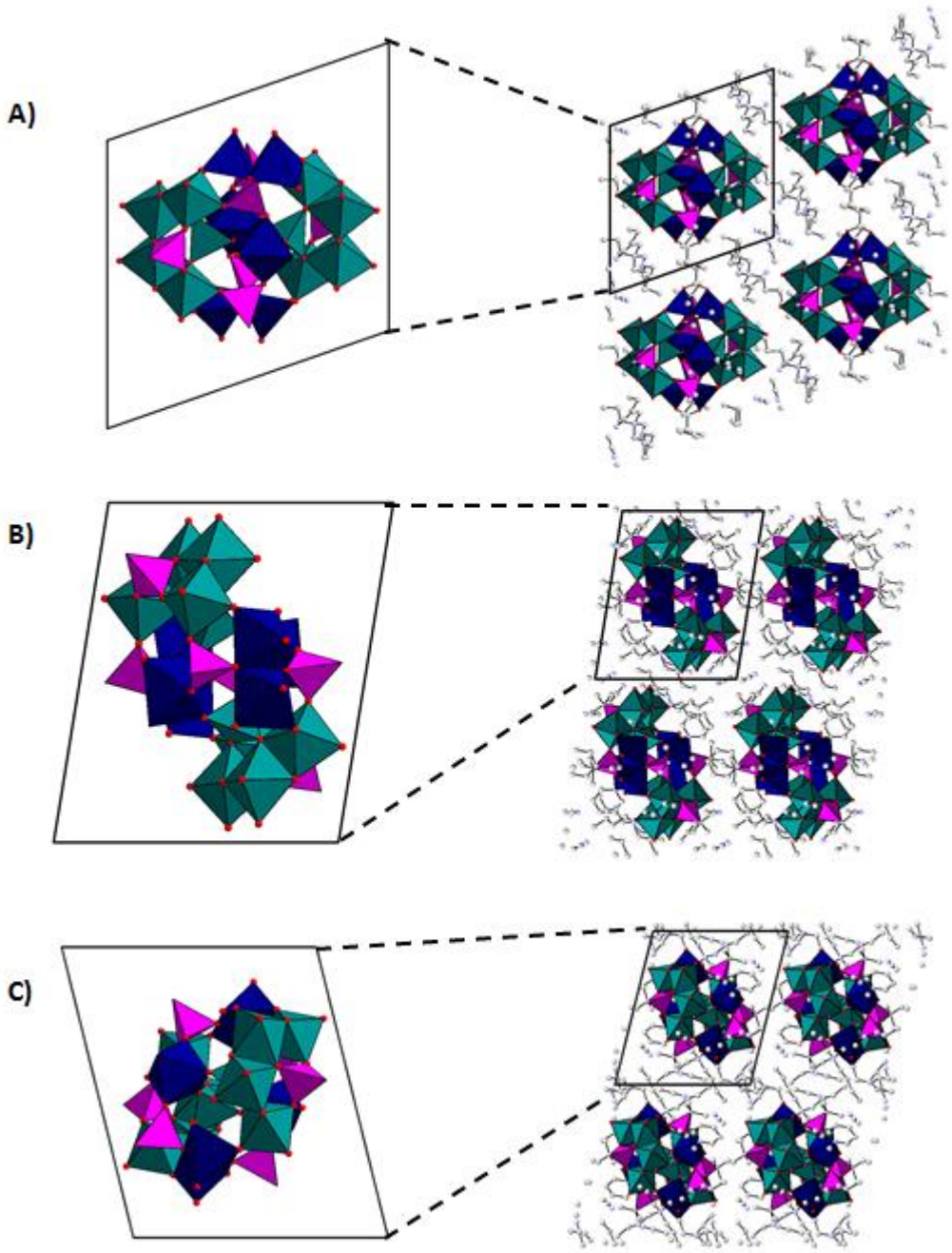

Figure 4.8.4 – Crystal packing diagrams for 25•7.5(MeCN), as viewed down: A) The crystallographic *a*-axis, B) the crystallographic *b*-axis. C) The crystallographic *c*-axis.

4.9) Conclusions

In summary, this chapter explored the extension of the assembly-disassembly-reassembly methodology developed over the previous two chapters to cobalt-molybdate systems. The disassembly of the Lindqvist hexamolybdate followed by reassembly in the presence of cobalt (II) generated a mixed-metal hybrid POM, $[TBA]_2[Mo^{VI}_{10}Co^{II}_6O_{12}(\mu\text{-}O)_{14}(\mu_3\text{-}O)_4(t\text{BuPO}_3)_6(\text{MeCOO})_2(\text{py})_2(H_2O)_6]$, **5**.

This compound contains two $\{Mo_5\}$ units capping a central $\{Co_6\}$ unit in a sandwich motif. The $\{Co_6\}$ core unit can be further subdivided into two sets of $\{Co_2\}$ dimers and two isolated Co centres. The compound is symmetric to inversion. Phosphonate templating effects and intramolecular hydrogen bonding appear to play a role in stabilising the structure. The compound was characterised by XRD as well as supplemental techniques including IR and mass spectrometry.

The $\{Mo_5\}$ units are believed to arise out of phosphonate-templated condensation reactions between molybdate oligomers. The phosphonate ligand may act as a template for the formation of an $\{Mo_4\}$ bend unit, which might reversibly bind $\{MoO_4\}$ units to generate the $\{Mo_5\}$ unit. In the presence of cobalt (II), this transient unit could be trapped into the stable structure **5**. In the absence of cobalt (II), the $\{MoO_4\}$ tetrahedron is displaced by a second phosphonate and the Strandberg-type rings in **1** or **2** become the dominant product (Figure 4.9.1).

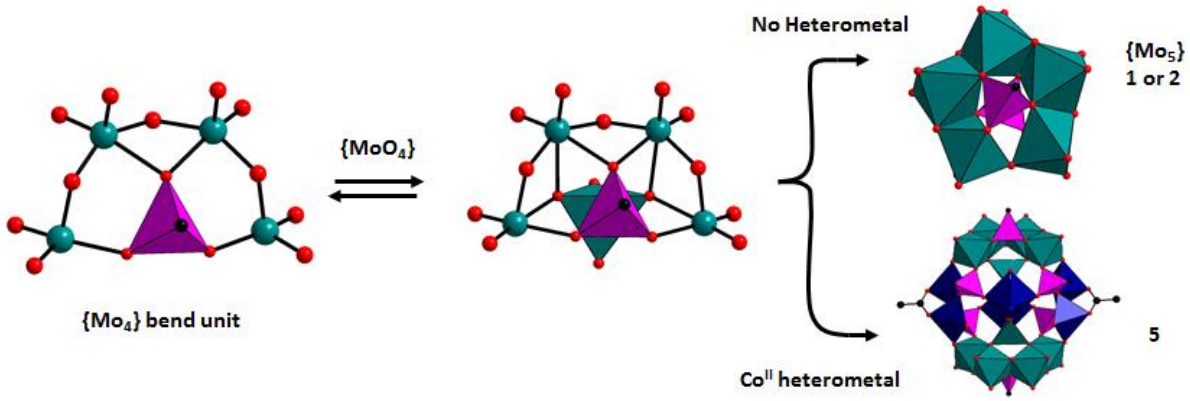

Figure 4.9.1 – The proposed templating effects of phosphonate ligands in molybdate reassembly. The proposed $\{Mo_4\}$ bend unit could reversibly bind $\{MoO_4\}$ units to generate a transient $\{Mo_5\}$ unit. In the absence of heterometals, the $\{MoO_4\}$ unit gets displaced by a second phosphonate and the Strandberg-type rings are generated. However in the presence of cobalt (II) the $\{Mo_5\}$ unit can be trapped into a stable architecture, forming the mixed-metal hybrid POM 5.

Significantly, the cluster core in **5** is supported by three distinct classes of organic ligand – phosphonates, carboxylates and pyridyl ligands. Substitution of any particular organic ligand for another with an equivalent ligand allows the properties of the compound to be modified while retaining the same core structure.

This concept was demonstrated with a series of analogous structures, **6-25**. $[TBA]_2[Mo^{VI}_{10}Co^{II}_6O_{12}(\mu\text{-}O)_{14}(\mu_3\text{-}O)_4(t\text{BuPO}_3)_6(\text{MeCOO})_2(\text{pic})_4(H_2O)_6]$, **6**, demonstrated the replacement of the pyridine ligands with picoline. **7-9** demonstrated the replacement of the acetate ligands with benzoate, phenylacetate and adamantylcarboxyalte ligands, respectively. **10-13** demonstrated the replacement of the *tert*-butylphosphonate ligands with adamantylphosphonate ligands. In the **10-13** series, adamantylphosphonate ligands were combined with acetate, benzoate, phenylacetate and adamantylcarboxyalte ligands respectively, demonstrating that the different ligand classes can be substituted in an orthogonal manner.

More sophisticated functional groups can also be introduced onto the cluster core of **5**. The series **14-19** introduced a series of functional groups at the carboxylate moiety by introducing benzoate ligands substituted at the *meta*- and/or *para*- positions. These substitutions included *bromo*-, *nitro*-, *amino*-, aldehyde-, alcohol- and ether-substituted benzoate ligands. These functional groups modify the electronic properties of the cluster core, as well as providing possible avenues for post-synthetic modification of the cluster core.

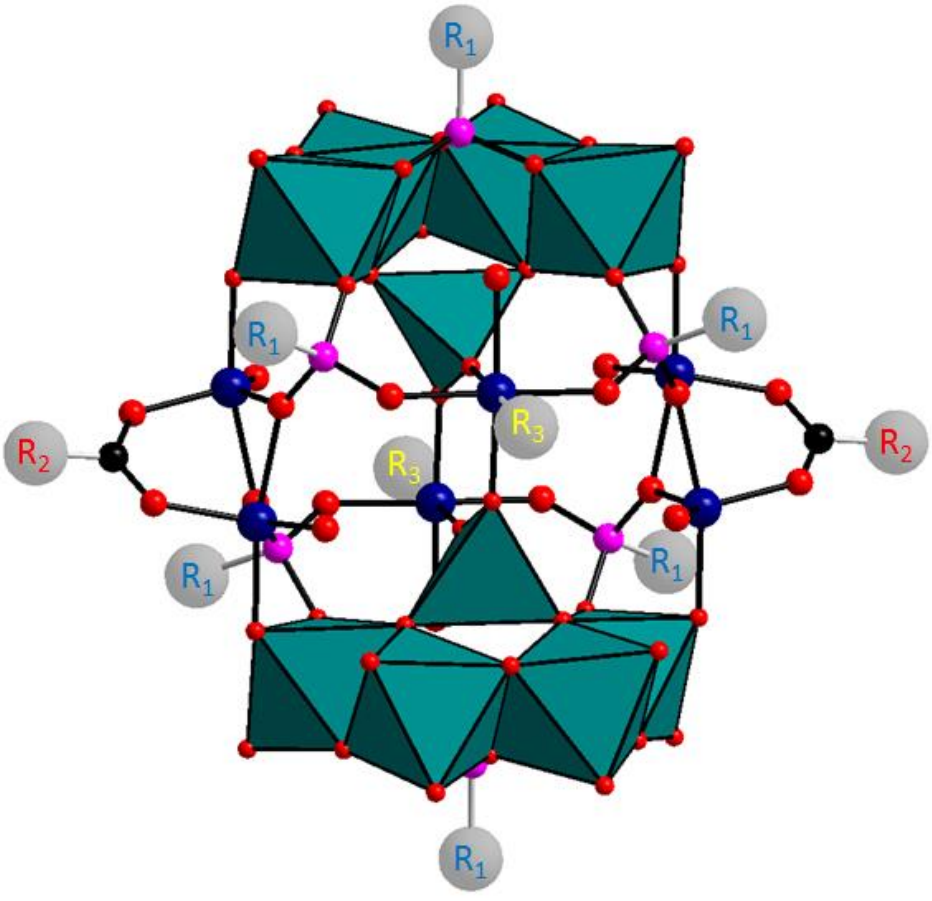

Figure 4.9.2 – The cluster core of 5, highlighting the three distinct ligand sites represented by the phosphonate ligands (R_1), carboxylate ligands (R_2) and pyridyl ligands (R_3).

The series **20**-**23** contained polyaromatic moieties at the carboxylate moiety, and were investigated for their photoactive properties. UV-Vis absorption spectroscopy demonstrated that the incorporation of these units significantly alters the ultraviolet absorption of the cluster core. Compounds **21** and **22** display visible luminescence when illuminated with UV light as a result of their organic ligands.

$[TBA]_2[Mo^{VI}_{10}Co^{II}_6O_{12}(\mu\text{-}O)_{14}(\mu_3\text{-}O)_4(t\text{BuPO}_3)_6(\text{azoCOO})_2(py)_2(H_2O)_6]$ (**24**) contains a photodynamic azobenzene moiety. This moiety was shown to undergo *cis-trans* isomerisation is solution under irradiation with UV light.

Finally, $[TBA]_2[Mo^{VI}_{10}Co^{II}_6O_{12}(\mu\text{-}O)_{14}(\mu_3\text{-}O)_4(t\text{BuPO}_3)_6(PDA)_2(py)_2(H_2O)_6]$ (**25**) is a polymeric compound, consisting of $\{Mo_{10}Co_6\}$ cluster units linked *via* polytopic phenylenediacetate ligands. These linker ligands connect the cluster units into one-dimensional chains that propagate through the crystal structure.

In conclusion, a series of cobalt-molybdate mixed metal hybrid POM clusters, **5**-**25**, was characterised and isolated. These compounds were all synthesised *via* the assembly-disassembly-reassembly technique. This series contains a variety of phosphonate, carboxylate and pyridyl ligand substitutions, allowing the structure to be modified by the substitution of the organic ligands. Any one organic unit (phosphonate, carboxylate or pyridyl ligand) can be substituted without affecting the other organic units. This allows distinct functional and steric groups to be incorporated into the cluster as desired.

4.10) References

1 V. Artero, M. Chavarot-Kerlidou and M. Fontecave, *Angew. Chem. Int. Ed.*, 2011, **50**, 7238.

2 J. M. Sumliner, H. Lv, J. Fielden, Y. V Geletii and C. L. Hill, *Eur. J. Inorg. Chem.*, 2014, 635.

3 Q. Yin, J. M. Tan, C. Besson, Y. V Geletii, D. G. Musaev, A. E. Kuznetsov, Z. Luo, K. I. Hardcastle and C. L. Hill, *Science*, 2010, **238**, 342.

4 M. Zhang, M. De Respinis and H. Frei, *Nat. Chem.*, 2014, **6**, 362.

5 H. A. Goodwin, *Spin Crossover in Transition Metal Compounds II*, Springer, 2004.

6 I. Krivokapic, M. Zerara, M. Lawson, A. Vargas, C. Enachescu, C. Ambrus, P. Tregenna-Piggott, N. Amstutz, E. Krausz and A. Hauser, *Coord. Chem. Rev.*, 2007, **251**, 364.

7 S. Hayami, Y. Komatsu, T. Shimizu, H. Kamihata and Y. H. Lee, *Coord. Chem. Rev.*, 2011, **255**, 1981.

8 S. Hayami, M. Nakaya, H. Ohmagari, A. S. Alao, M. Nakamura, R. Ohtani, R. Yamaguchi, T. Kuroda-Sowa and J. K. Clegg, *Dalton Trans.*, 2015, **44**, 9345.

9 H. Ohmiya, H. Yorimitsu and K. Oshima, *J. Am. Chem. Soc.*, 2006, **128**, 1886.

10 W. Hess, J. Treutwein and G. Hilt, *Synthesis*, 2008, **22**, 3537.

11 K. Gao and N. Yoshikai, *Acc. Chem. Res.*, 2014, **47**, 1208.

12 F. Song, Y. Ding, B. Ma, C. Wang, Q. Wang, X. Du, S. Fua and J. Song, *Energy Environ. Sci.*, 2013, **6**, 1170.

13 S. Tanaka, M. Annaka and K. Sakai, *Chem. Commun.*, 2012, **48**, 1653.

14 X. Han, Z. Zhang, T. Zhang, Y. Li, W. Lin, W. You, Z. Su and E. Wang, *J. Am. Chem. Soc.*, 2014, **136**, 5359.

15 H. Lv, J. Song, Y. V Geletii, J. W. Vickers, J. M. Sumliner, D. G. Musaev, P. Ko, P. F. Zhuk, J. Bacsa, G. Zhu and C. L. Hill, *J. Am. Chem. Soc.*, 2014, **136**, 9268.

16 G. Gao, F. Li, L. Xu, X. Liu and Y. Yang, *J. Am. Chem. Soc.*, 2008, **130**, 10838.

17 Y. Yang, L. Xu, G. Gao, F. Li, Y. Qiu, X. Qu and H. Liu, *Eur. J. Inorg. Chem.*, 2007, 2500.

18 Y. Huang, J. Chen, T. Lan, X. Lu, C. Wei, Z. Li and Z. Zhang, *J. Mol. Struct.*, 2006, **783**, 168.

19 G. Gao, L. Xu, W. Wang, X. Qu, H. Liu and Y. Yang, *Inorg. Chem.*, 2008, **47**, 2325.

20 F. Fei, H. An, T. Xu and C. Meng, *RSC Adv.*, 2016, **6**, 92092.

21 U. Lee, S. Jang, H. Joo and K. Park, *Acta Crystallogr. Sect. E*, 2003, **59**, 345.

22 J. Iijima, H. Naruke and H. Takiyama, *Acta Crystallogr. Sect. E*, 2013, **69**, 612.

23 K. Park, H. Joo and U. Lee, *Acta Crystallogr. Sect. E*, 2015, **71**, 1032.

24 X. He, P. Zhang, T.-Y. Song, Z.-C. Mu, J.-H. Yu, Y. Wang and J.-N. Xu, *Polyhedron*, 2004, **23**, 2153.

25 X. Zhang, J. X. Ã, J. Yu, J. Lu, Y. Xu, Y. Chen, T. Wang, X. Yu, Q. Yang and Q. Hou, *J. Solid State Chem.*, 2007, **180**, 1949.

26 Y. Ma, Y. Li, E. Wang, Y. Lu, X. Wang, D. Xiao and X. Xu, *Inorganica Chim. Acta*, 2007, **360**, 421.

27 X. Xu, Z. Xia, X. Liu, T. Sun and Y. Wang, *Transit. Met. Chem.*, 2009, **34**, 571.

28 N. Belai, P. N. Kapoor, M. H. Dickman, R. J. Butcher and M. T. Pope, *Eur. J. Inorg. Chem.*, 2009, 5215.

29 Y. Dong, G. Hu, H. Miao, X. He, M. Fang and Y. Xu, *Inorg. Chem.*, 2016, **55**, 11621.

30 J. Xu, R. Wang, G. Yang, Y. Xing, D. Li, W. Bu, L. Ye, Y.-G. Fan, G.-D. Yang, Y. Xing, Y.-H. Lind and H.-Q. Jia, *Chem. Commun.*, 1999, 983.

31 X. Gu, J. Peng, Z. Shi, Y. Chen, Z. Han, E. Wang, J. Ma and N. Hu, *Inorganica Chim. Acta*, 2005, **358**, 3701.

32 C. Tian, Z. Sun, J. Li, X. Zheng, H. Liang, L. Zhang, W. You and Z. Zhu, *Inorg. Chem. Commun.*, 2007, **10**, 757.

33 T. Arumuganathan, A. S. Rao and S. K. Das, *Cryst. Growth Des.*, 2010, **10**, 4272.

34 M. Singh and A. Ramanan, *Cryst. Growth Des.*, 2011, **11**, 3381.

35 X. Li, Y. Chen, C. Su, S. Zhou, Q. Tang and T. Shi, *Inorg. Chem.*, 2013, **52**, 11422.

36 H. El Moll, A. Dolbecq, M. Mbomekalle, J. Marrot, P. Deniard, R. Dessapt and P. Mialane, *Inorg. Chem.*, 2012, **51**, 2291.

37 N. G. Armatas, D. G. Allis, A. Prosvirin, G. Carnutu, C. J. O. Connor, K. Dunbar and J. Zubieta, *Inorg. Chem.*, 2008, **47**, 832.

38 C. Sassoye, K. Norton and S. C. Sevov, *Inorg. Chem.*, 2003, **42**, 1652.

39 G. Cao, R. C. Haushalter and G. Karl, *Inorg. Chem.*, 1993, **32**, 127.

40 M. E. Fleet, *Mineral. Mag.*, 1976, **40**, 531.

41 R. M. Hazen, R. T. Downs and C. T. Prewitt, *Comp. Cryst. Chem.*, 1999.

42 M. Wildner, *Z. Krist.*, 1992, **202**, 51.

43 M. Hughes, F. Foit and E. Wright, *Can. Mineral.*, 2002, **40**, 153.

44 L. Yang, D. R. Powell and R. P. Houser, *Dalton Trans.*, 2007, 955.

45 J. Fuchs and H. Hartl, *Angew. Chem. Int. Ed.*, 1976, **15**, 375.

46 A. J. Bridgeman, *J. Phys. Chem. A*, 2002, **106**, 12151.

47 M. L. Niven, J. J. Cruywagen and J. B. B. Heyns, *J. Chem. Soc. Dalton Trans.*, 1991, 2007.

48 W. G. Klemperer and W. Shum, *J. Am. Chem. Soc.*, 1976, **98**, 8291.

49 H. T. Evans, B. M. Gatehouse and P. Leverett, *J. Chem. Soc. Dalton Trans.*, 1975, 505.

50 A. Don and T. J. R. Weakley, *Acta Crystallogr. Sect. B*, 1981, **37**, 451.

51 T. Yamase and T. Ikawa, *Bull. Chem. Soc. Jpn.*, 1977, **50**, 746.

52 Y. Ohashi, K. Kanagi, Y. Sasada and T. Yamase, *Bull. Chem. Soc. Jpn.*, 1982, **55**, 1254.

53 I. Lindqvist, *Acta Crystallogr.*, 1952, **5**, 667.

54 S. Bartley, S. Bernstein and K. R. Dunbar, *Inorganica Chim. Acta*, 1993, **213**, 213.

55 P. A. Abramov, M. N. Sokolov, S. Floquet, M. Haouas, F. Taulelle, E. Cadot, E. V Peresypkina, A. V Virovets, C. Vicent, N. B. Kompankov, A. A. Zhdanov, O. V Shuvaeva and V. P. Fedin, *Inorg. Chem.*, 2014, **53**, 12791.

56 J. W. Illingworth and J. F. Keggin, *J. Chem. Soc.*, 1935, 575.

57 A. J. Bridgeman, *Chem. Phys.*, 2003, **287**, 55.

58 L. C. W. Baker and S. J. Figgis, *J. Am. Chem. Soc.*, 1970, **92**, 3794.

59 A. Tsohos, S. Dionyssopoulou, C. P. Raptopoulou, A. Terzis, E. G. Bakalbassis and S. P. Perlepes, *Angew. Chem. Int. Ed.*, 1999, **38**, 983.

60 E. K. Brechin, A. Graham, A. Parkin, S. Parsons, A. M. Seddon and R. E. P. Winpenny, *Dalton Trans.*, 2000, 3242.

61 D. A. Brown, W. K. Glass, N. J. Fitzpatrick, T. J. Kemp, W. Errington, G. J. Clarkson, W. Haase, F. Karsten and A. H. Mahdy, *Inorganica Chim. Acta*, 2004, **357**, 1411.

62 X. Tang, Q. Zhong, J. Xu, H. Li, S. Xu, X. Cui, B. Wei, Y. Ma and R. Yuan, *Inorganica Chim. Acta*, 2016, **442**, 195.

63 L. Cai, W. Xie, H. Mahmoud, Y. Hart, D. J. Wink, S. Li and C. J. O'Connor, *Inorganica Chim. Acta*, 1997, **263**, 231.

64 S. Kita, H. Furutachi and O. Hisashi, *Inorg. Chem.*, 1999, **38**, 4038.

65 K. Matsumoto, N. Sekine, K. Arimura, M. Ohba, H. Sakiyama and H. Okawa, *Bull. Chem. Soc. Jpn.*, 2004, **77**, 1343.

66 P. Ayyappan, O. R. Evans, Y. Cui, K. A. Wheeler and W. Lin, *Inorg. Chem.*, 2002, **41**, 4978.

67 Y.-S. Ma, W.-S. Cai, B. Chen, J.-Y. Chang, X.-Y. Tanga and R.-X. Yuan, *CrystEngComm*, 2013, **15**, 7615.

68 X. Sun, R. Ban, P. Ma, J. Wang, D. Zhang, J. Niu and J. Wang, *Synth. Met.*, 2017, **223**, 19.

69 A. W. Addison and T. N. Rao, *J. Chem. Soc. Dalton Trans.*, 1984, 1349.

70 T. Steiner, *Angew. Chem. Int. Ed.*, 2002, **41**, 48.

71 C. L. Perrin and J. B. Nielson, *Annu. Rev. Phys. Chem.*, 1997, **48**, 511.

72 G. R. Desiraju, *Acc. Chem. Res.*, 1991, **24**, 290.

73 T. C. Stamatatos, K. M. Poole, K. A. Abboud, W. Wernsdorfer, T. A. O. Brien and G. Christou, *Inorg. Chem.*, 2008, **47**, 5006.

74 C. Lampropoulos, C. Koo, S. O. Hill, K. Abboud and G. Christou, *Inorg. Chem.*, 2008, **47**, 11180.

75 V. Zelenak, Z. Vargova and K. Gyoryova, *Spectrochim. Acta Part A*, 2007, **66**, 260.

76 G. Aromì, A. S. Batsanov, P. Christian, M. Helliwell, A. Parkin, S. Parsons, A. A. Smith, G. A. Timco and R. E. P. Winpenny, *Chem. Eur. J.*, 2003, **9**, 5142.

77 K. Kalyanasundaram and J. K. Thomas, *J. Am. Chem. Soc.*, 1977, **99**, 2039.

78 J. C. del Valle, A. M. Turek, N. D. Tarkalanov and J. Saltiel, *J. Phys. Chem. A*, 2002, **106**, 5101.

79 S. A. Kurhuzenkau, A. W. Woodward, S. Yao, K. D. Belfield, Y. O. Shaydyuk, C. Sissa, M. V Bondar and A. Painelli, *Phys. Chem. Chem. Phys.*, 2016, **18**, 12839.

80 T. Nakahama, D. Kitagawa, H. Sotome, S. Ito, H. Miyasaka and S. Kobatake, *Photochem. Photobiol. Sci.*, 2016, **15**, 1254.

81 C. R. Martinez and B. L. Iverson, *Chem. Sci.*, 2012, **3**, 2191.

82 R. Lyndon, K. Konstas, B. P. Ladewig, P. D. Southon, C. J. Kepert and M. R. Hill, *Angew. Chem. Int. Ed.*, 2013, **52**, 3695.

83 N. Yanai, T. Uemura, M. Inoue, R. Matsuda, T. Fukushima, M. Tsujimoto, S. Isoda and S. Kitagawa, *J. Am. Chem. Soc.*, 2012, **134**, 4501.

84 J. Park, D. Yuan, K. T. Pham, J. Li, A. Yakovenko and H. Zhou, *J. Am. Chem. Soc.*, 2012, **134**, 99.

85 L. Heinke, M. Cakici, M. Dommaschk, S. Grosjean, R. Herges, S. Brase and C. Woll, *ACS Nano*, 2014, **8**, 1463.

86 M. Kurmoo, H. Kumagai, M. A. Green, B. W. Lovett, S. J. Blundell, A. Ardavan and J. Singleton, *J. Solid State Chem.*, 2001, **159**, 343.

87 X. Chen, H. Huang, M. Yang, L.-J. Chen and S. Lin, *Acta Crystallogr. Sect. C*, 2014, **70**, 488.

88 J. He, Y. Zhang, Q. Pan, J. Yu, H. Ding and R. Xu, *Micropor. Mesopor. Mater.*, 2006, **90**, 145.

89 C. Livage, N. Guillou, J. Marrot and G. Ferey, *Chem. Mater.*, 2001, **13**, 4387.

Chapter 5

Hybrid Manganese-Polyoxomolybdates

5.1) Manganese in POM Chemistry

In the previous chapter, we demonstrated that the assembly-disassembly-reassembly methodology can be exploited to produce hybrid TMS-POM species from Lindqvist Hexamolybdate and cobalt (II) salts. The presence of distinct organic ligands supporting the resulting cluster cores allowed for extensive manipulation of the structures to generate a series of analogous compounds. Having demonstrated the efficacy of this approach with cobalt (II) salts, we turned our attention to manganese (III) salts.

Like copper(II) and cobalt (II), manganese (III) centres possess a range of suitable properties that make them attractive synthetic targets for incorporation into a TMS-POM structure:

- Manganese is a cheap, earth abundant metal, which is commercially available with a variety of counterions.
- Manganese (III) centres display significant Jahn-Teller distortion, resulting in labile coordination sites with significant reactivity, which may facilitate synthesis of a TMS-POM cluster.
- Manganese centres of various oxidation states can access both high spin and low spin electronic configurations, leading manganese compounds to be investigated for their magnetic properties.[1–4] Some manganese compounds have also attracted considerable attention for their single molecule magnet behaviour.[5–8]
- Manganese is a redox active metal, which has led to a variety of applications in catalysis.[9–11] Manganese is present in a variety of biologically relevant redox active enzymes, including PSII.[12,13] This has led to significant efforts to emulate PSII synthetically, for example with the $[Mn_4O_3(CH_3COO)_3(A\text{-}\alpha\text{-}SiW9O_{34})]^{6-}$ and $[Mn_4V_4O_{17}(CH_3COO)_3]^{3-}$ TMS-POM clusters.[14,15]

Manganese substituted molybdates have been reported previously.[16–19] By far the most common structural motifs are for a manganese (II) centre to serve as the central heteroatom in an Anderson-Evans molybdate (often with *tris*-alkoxide supporting organic ligands)[20–27] or for a manganese (II) centre to be sandwiched between two $\{Mo_6\}$ rings in a $\{Mo_{12}Mn\}$ motif, $[H_{16}Mn(PO_4)_8Mo_{12}O_{30}]$.[28–34] Some substituted Keggin structures are also known.[35–37] However it is common for the terminal *oxo*- ligand of a POM unit to act as a loosely-bound ligand to a manganese centre instead of incorporating the manganese centre into the body of a POM cluster.[38–40]

Therefore, we set out to extend our disassembly-reassembly approach to generate manganese-substituted TMS-POM cluster compounds. Several compounds were isolated from this procedure, which shall be described over the next chapter.

*5.2) [TBA]$_2$[Mo$^{VI}_{10}$Mn$^{II}_6$O$_{12}$(μ-O)$_{14}$(μ$_3$-O)$_4$(t*BuPO$_3$)$_6$ (MeCOO)$_2$(py)$_4$(H$_2$O)$_6$], (26)*

In an extension of the disassembly-reassembly method towards hybrid TMS-POMs as discussed in the previous two chapters, manganese (III) acetylacetonate was combined with Lindqvist hexamolybdate and *tert*-butylphosphonic acid and in acetonitrile in the presence of pyridine.[19] The resulting dark brown solution was left to stand for one week, over which time it gradually decolourised to a pale yellow colour. Yellow-orange crystals were obtained from this solution after one week.

The crystals were subjected to single crystal X-ray diffraction and found to contain [TBA]$_2$[Mo$^{VI}_{10}$Mn$^{II}_6$O$_{12}$(μ-O)$_{14}$(μ$_3$-O)$_4$(*t*BuPO$_3$)$_6$(MeCOO)$_2$(py)$_4$(H$_2$O)$_6$], **26**, where TBA represents tetrabutylammonium, *t*Bu represents the *tert*-butyl moiety and py represents pyridine. The crystals formed in the monoclinic crystal system in space group $P2_1/c$, and also contained six acetonitrile molecules per formula unit.

The cluster core in **26** is a manganese (II) analogue of the cluster cores of compounds **5-25**. It can be conceptualised as two {Mo$_5$} units formally encapsulating a {Mn$_6$} core in a sandwich motif (Figures 5.2.1 and 5.2.2). The two {Mo$_5$} units are stabilised by a total of thirty *oxo*- ligands, in either terminal or bridging modes. The {Mo$_5$} units are stabilised by phosphonate ligands, two of which support only molybdenum centres, and four of which bridge between the {Mo$_5$} units and the {Mn$_6$} core. The {Mn$_6$} core unit can be further subdivided into two sets of {Mn$_2$} dimers and two isolated Mn centres. Acetate ligands coordinate to the {Mn$_2$} dimers in a *syn*-, *syn*- binding mode. The cobalt coordination environments are completed by water and pyridine ligands. The cluster is symmetrical to inversion through a point at the centre of the {Mn$_6$} core.

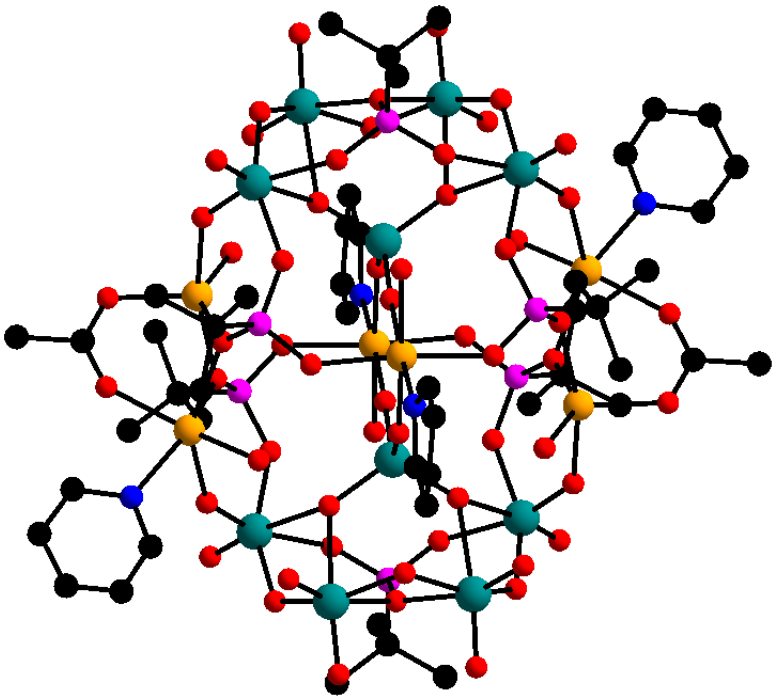

Figure 5.2.1 – Full representation of the [Mo$^{VI}_{10}$Mn$^{II}_6$O$_{12}$(μ-O)$_{14}$(μ$_3$-O)$_4$(*t*BuPO$_3$)$_6$ (MeCOO)$_2$(py)$_4$(H$_2$O)$_6$]$^{2-}$ cluster in 5. Colour Scheme: Mo teal, Mn orange, P pink, O red, N blue, C black. H atoms omitted for clarity.

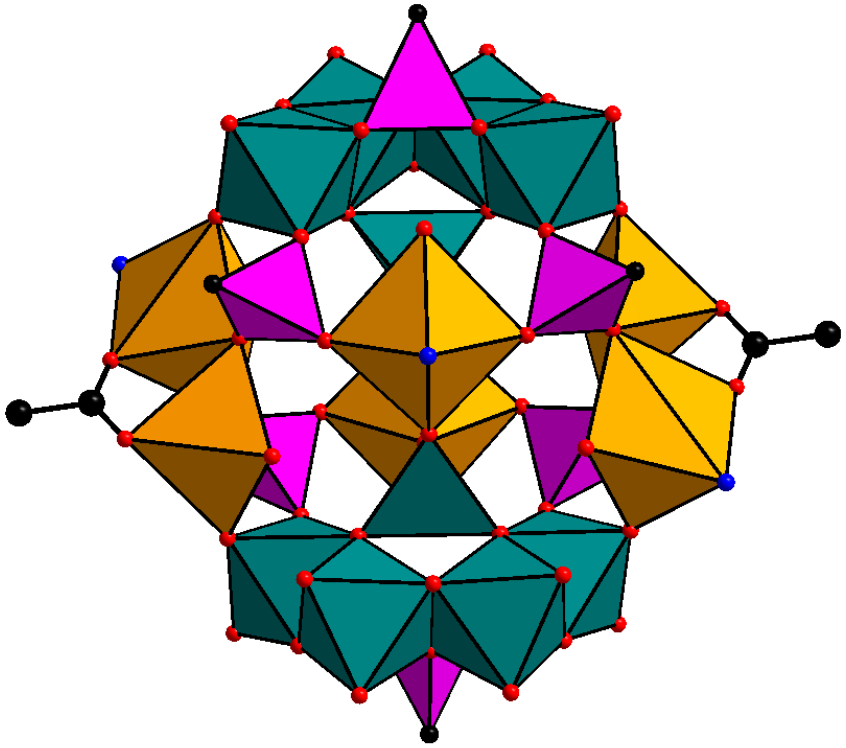

Figure 5.2.2 – Simplified representation of the $[Mo^{VI}_{10}Mn^{II}_{6}O_{12}(\mu\text{-}O)_{14}(\mu_3\text{-}O)_4(t\text{BuPO}_3)_6(MeCOO)_2(py)_4(H_2O)_6]^{2-}$ cluster in 26 – molybdate, manganese and phosphonate moieties are shown as polyhedra, pyridine and *tert*-butyl groups are reduced to single N and C atoms respectively, and H atoms are removed from the water and acetate ligands. Colour Scheme: Mo teal, Mn orange, P pink, O red, N blue, C black.

Due to the similarities between the **26** and the cobalt systems described in the previous chapter, we propose that similar templating effects occur in the two systems (*c.f.* Figure 4.2.5). We propose that the $\{Mo_5\}$ unit is templated primarily by a phosphonate ligand, and that this transient unit is trapped into a stable architecture by assembly into the $\{Mo_{10}Mn_6\}$ cluster core.

Identification code	**26**•6(MeCN)
Empirical formula	$C_{92}H_{184}Mn_6Mo_{10}N_{12}O_{58}P_6$
Formula weight (g/mol)	3861.36
Temperature (K)	100(2)
Wavelength (Å)	0.71073
Crystal system	Monoclinic
Space group	$P2_1/c$
a (Å)	14.638(3)
b (Å)	24.750(5)
c (Å)	23.287(7)
α (°)	90
β (°)	120.03(2)
γ (°)	90
Volume (Å^3)	7304(3)
Z	2
Calculated density ρ_{calc} (g/cm^3)	1.756
Absorption coefficient μ (mm^{-1})	1.475
F(000)	3887
Crystal size (mm^3)	0.16 x 0.112 x 0.10
2Θ range for data collection (°)	3.26 to 50.00
Index ranges	$-17 \leq h \leq 17, -29 \leq k \leq 29, -27 \leq l \leq 25$
Reflections collected	63245
Independent reflections	12855 [R_{int} = 0.0339]
Data/restraints/parameters	12855/3/804
Goodness-of-fit on F^2	0.997
Final R indices [I>=2σ (I)]	R_1 = 0.0443, wR_2 = 0.1365
Final R indices [all data]	R_1 = 0.0584, wR_2 = 0.1529
Largest diff. peak and hole (e Å^{-3})	2.89/-1.09

Table 5.2.1 – Crystallographic details for compound 26•6(MeCN).

Due to the similarities between **26** and the cobalt analogues **2-25** discussed in the previous chapter, the structure of **26** will not be discussed in as much detail. The molybdate moieties, phosphonate binding modes, and intramolecular hydrogen bonding are all extremely similar in this structure to the analogues discussed in section 4.2.2. The manganese coordination environments (Figure 5.2.3) are also extremely similar to the examples discussed in the previous chapter. **26** incorporates additional N-donors onto the dinuclear manganese unit, in a similar fashion to **6**.

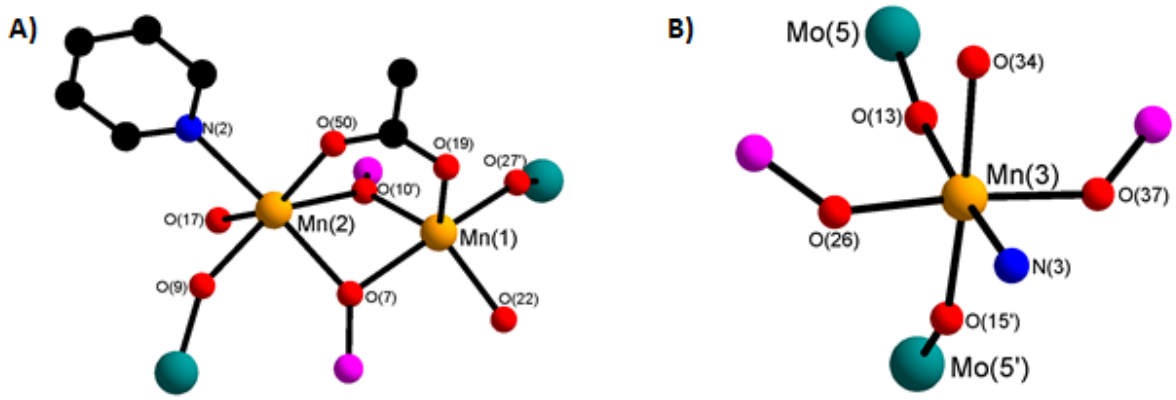

Figure 5.2.3 – Manganese centres in 26. A) The dinuclear unit. B) The isolated Mn centre. Colour Scheme: Mo teal, Mn orange, P pink, O red, N blue, C black.

Metal Atom	Bonded Atom	Bond Length (Å)	BVS	Oxidation State
Mn(1)	O(19)	2.054(4)	2.145	+II
	O(10')	2.084(4)		
	O(22)	2.096(4)		
	O(27')	2.125(3)		
	O(7)	2.167(3)		
Mn(2)	O(17)	2.127(4)	1.933	+II
	O(50)	2.136(4)		
	O(9)	2.179(3)		
	O(7)	2.208(4)		
	N(2)	2.323(5)		
	O(10')	2.335(3)		
Mn(3)	O(26)	2.105(3)	2.114	+II
	O(37)	2.109(3)		
	O(15')	2.154(3)		
	O(34)	2.231(3)		
	O(13)	2.261(5)		
	N(3)	2.276(7)		

Table 5.2.2 – Crystallographically-determined bond lengths for the manganese centres in 26, along with their oxidation state as determined by Bond Valence Sum (BVS) analysis.

The manganese bond lengths in **26** range from 2.054(4) Å to 2.335(3) Å, depending on the type of interaction (Table 5.2.2 and Figure 5.2.3). The bond lengths tend to be slightly longer than for the equivalent cobalt centres (*c.f.* Table 4.2.8). On the dinuclear unit, acetate, water and bridging *oxo*- ligands display bond lengths of around 2.1 Å. The phosphonate O-donors display a wider range of bond lengths, from 2.084(4) Å to 2.335(3) Å. There is an asymmetry in the phosphonate O-donors, with both O(7) and O(10') being closer to Mn(1) than Mn(2). The Mn(2)-N(2) distance is 2.335(3). The isolated Mn centre displays short phosphonate bonds (*c.* 2.1 Å) and long water and pyridine bonds (*c.* 2.3 Å). The bridging *oxo*- ligands are asymmetric, with O(15') displaying a *c.* 0.1 Å shorter bond distance than O(13).

All bond lengths are consistent with manganese (II) compounds reported in the literature, and BVS analysis indicates that all Mn centres are in oxidation state +II.[41–43] As the starting material was a manganese (III) salt, this indicates redox activity in the synthesis of **26**. This will be discussed in more detail in section 5.5.

Bond	Bond Angle (°)	Bond	Bond Angle (°)
O(10')-Mn(2)-O(7)	75.49(12)	O(13)-Mn(3)-O(34)	81.94(15)
O(17)-Mn(2)-O(10')	79.69(12)	N(3)-Mn(3)-O(37)	86.92(13)
N(2)-Mn(2)-O(50)	79.98(16)	N(3)-Mn(3)-O(26)	87.42(13)
O(9)-Mn(2)-O(7)	81.84(12)	O(15')-Mn(3)-O(26)	88.57(11)
O(10')-Mn(2)-O(50)	84.49(14)	O(15')-Mn(3)-O(37)	89.32(11)
N(2)-Mn(2)-O(9)	84.7(13)	O(15')-Mn(3)-O(13)	90.09(16)
N(2)-Mn(2)-O(17)	85.6(17)	O(34)-Mn(3)-O(26)	90.83(11)
O(50)-Mn(2)-O(7)	87.82(12)	O(34)-Mn(3)-O(37)	92.07(11)
O(17)-Mn(2)-O(9)	88.59(13)	O(13)-Mn(3)-O(37)	92.23(12)
O(17)-Mn(2)-O(7)	115.47(16)	N(3)-Mn(3)-O(34)	93.12(20)
O(50)-Mn(2)-O(9)	119.06(14)	O(13)-Mn(3)-O(26)	93.64(11)
N(2)-Mn(2)-O(10')	124.8(14)	N(3)-Mn(3)-O(15')	94.86(20)
Angle Variance (σ^2)	**297.51**	**Angle Variance (σ^2)**	**12.7**
Distortion Index	**0.108**	**Distortion Index**	**0.030**
O(10')-Mn(1)-O(7)	81.76(13)		
O(10')-Mn(1)-O(27')	88.33(13)		
O(22)-Mn(1)-O(7)	89.61(13)		
O(22)-Mn(1)-O(27')	90.77(13)		
O(19)-Mn(1)-O(27')	96.46(13)		
O(19)-Mn(1)-O(7)	98.40(13)		
O(19)-Mn(1)-O(10')	108.05(16)		
O(19)-Mn(1)-O(22)	109.34(15)		
O(22)-Mn(1)-O(10')	142.46(13)		
O(7)-Mn(1)-O(27')	164.12(12)		
Geometry Index (τ_5)	**0.361**		

Table 5.2.3 – Crystallographically-determined bond angles for the manganese centres in 26, along with the appropriate distortion parameters.

The manganese centres in the dinuclear unit of **26** display significant distortion away from their idealised geometries (Table 5.2.3). The pentacoordinate centre Mn(1) has a geometry index $\tau_5 = 0.361$, which is a similar level of distortion as displayed by the cobalt analogues discussed in the previous chapter (*c.f.* Tables 4.2.5 and 4.2.9). The hexacoordinate Mn(2) centre, however, displays significant distortion away from the ideal octahedral coordination geometry, with σ^2_{oct} and DI values of 297.51 and 0.108, respectively.

The Mn(3) centre, however, displays very close to ideal geometry, with σ^2_{oct} and DI values of 12.7 and 0.030, respectively.

σ^2_{oct}, DI and τ_5 are defined in the same way as previously.[44–48]

Packing

26 crystallises along with six constituent acetonitrile molecules in the monoclinic crystal system in space group $P2_1/c$. The crystal packing is shown in Figure 5.2.4. The packing in the system is not dissimilar to the packing seen in the analogous cobalt compound (*c.f.* Figure 4.2.7).

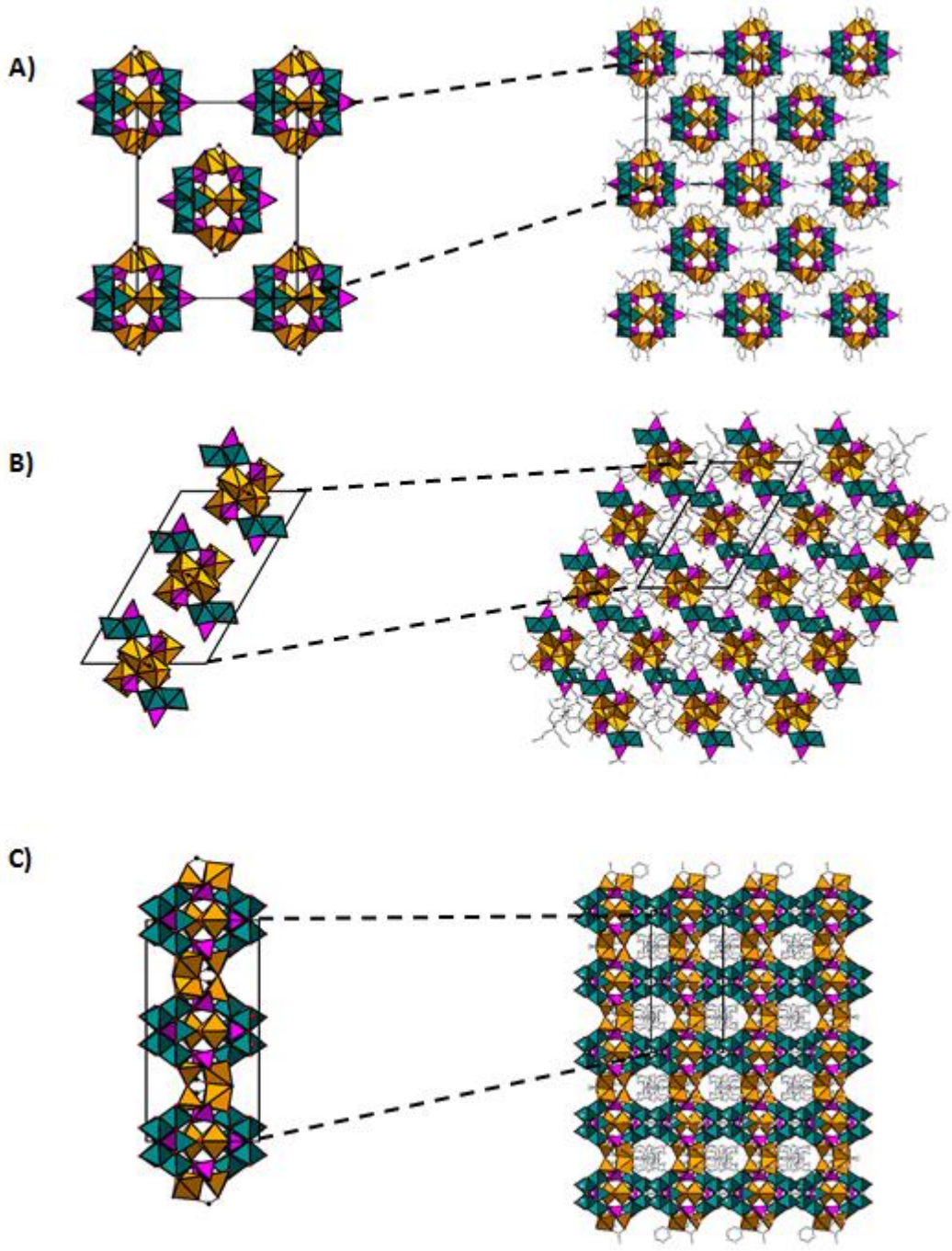

Figure 5.2.4 – Crystal packing diagrams for 26•6(MeCN), as viewed down: A) The crystallographic *a*-axis, B) the crystallographic *b*-axis. C) The crystallographic *c*-axis. Colour Scheme: Mo teal, Mn orange, P pink, O red, N blue, C grey.

5.3) Ligand Substitution of 26

When the synthesis of **26** was repeated using methanol in place of acetonitrile as a solvent, yellow-orange crystals were formed over several days. When subjected to XRD analysis, the crystals were found to contain $[TBA]_2[Mo^{VI}_{10}Mn^{II}_6O_{12}(\mu\text{-}O)_{14}(\mu_3\text{-}O)_4(t\text{BuPO}_3)_6(MeCOO)_2(MeOH)_4(H_2O)_6]$, **27**, where TBA represents tetrabutylammonium and *t*Bu represents the *tert*-butyl moiety. The crystals formed in the monoclinic space group $P2_1/n$. The crystals also contained five methanol molecules per formula unit.

27 is analogous to **26**, with methanol ligands replacing the pyridine ligands in **26**, binding to both the dinuclear units and the isolated manganese centres (Figure 5.3.1).

This substitution of pyridine for methanol ligands is fairly trivial, but it indicates that for the manganese compounds at least, the cluster core can be generated in either methanol or acetonitrile (*c.f.* compounds **1** and **2**). This supports the hypothesis that similar synthetic intermediates (disassembly oligomers) form in both acetonitrile and methanol.

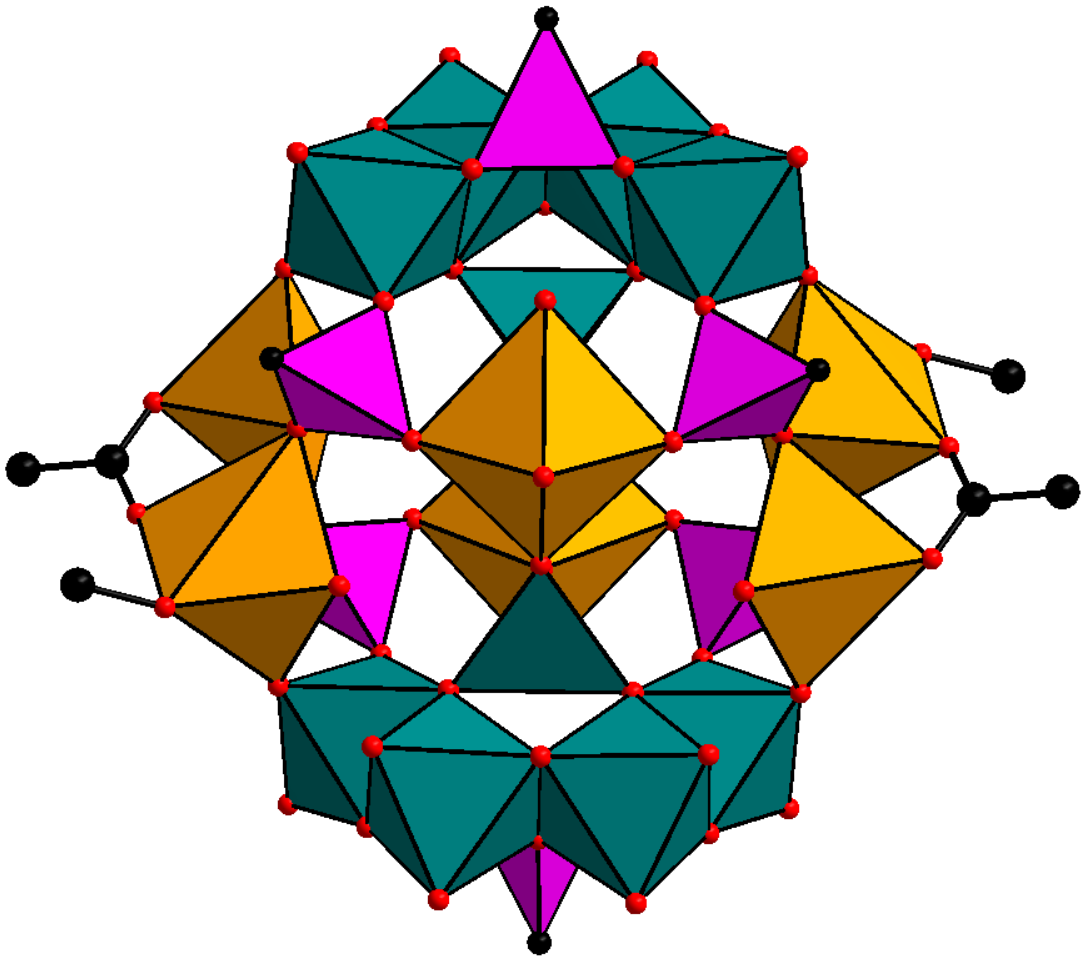

Figure 5.3.1 – Simplified representation of the cluster core in 27, showing the methanol ligands on the dinuclear units. Colour Scheme: Mo teal, Mn orange, P pink, O red, N blue, C black, H white.

Identification code	**27**•5(MeOH)
Empirical formula	$C_{34.5}H_{80}Mn_3Mo_5NO_{34.5}P_3$
Formula weight (g/mol)	1800.44
Temperature (K)	100(2)
Wavelength (Å)	0.71073
Crystal system	Monoclinic
Space group	$P2_1/n$
a (Å)	16.5333(13)
b (Å)	25.282(2)
c (Å)	17.6221(14)
α (°)	90
β (°)	97.443(2)
γ (°)	90
Volume (Å^3)	7303.9(10)
Z	4
Calculated density ρ_{calc} (g/cm^3)	1.637
Absorption coefficient μ (mm^{-1})	1.472
F(000)	3608.0
Crystal size (mm^3)	0.32 × 0.25 × 0.21
2Θ range for data collection (°)	2.834 to 52.894
Index ranges	$-20 \leq h \leq 20$, $-31 \leq k \leq 31$, $-22 \leq l \leq 22$
Reflections collected	347085
Independent reflections	15018 [R_{int} = 0.0759]
Data/restraints/parameters	15018/11/647
Goodness-of-fit on F^2	1.098
Final R indices [I>=2σ (I)]	R_1 = 0.0971, wR_2 = 0.2155
Final R indices [all data]	R_1 = 0.1550, wR_2 = 0.2703
Largest diff. peak and hole (e Å^{-3})	1.92/-1.65

Table 5.3.1 – Crystallographic details for compound 27•5(MeOH).

Packing

27 crystallises along with five methanol molecules in the monoclinic crystal system in space group $P2_1/n$. The crystal packing is shown in Figure 5.3.2.

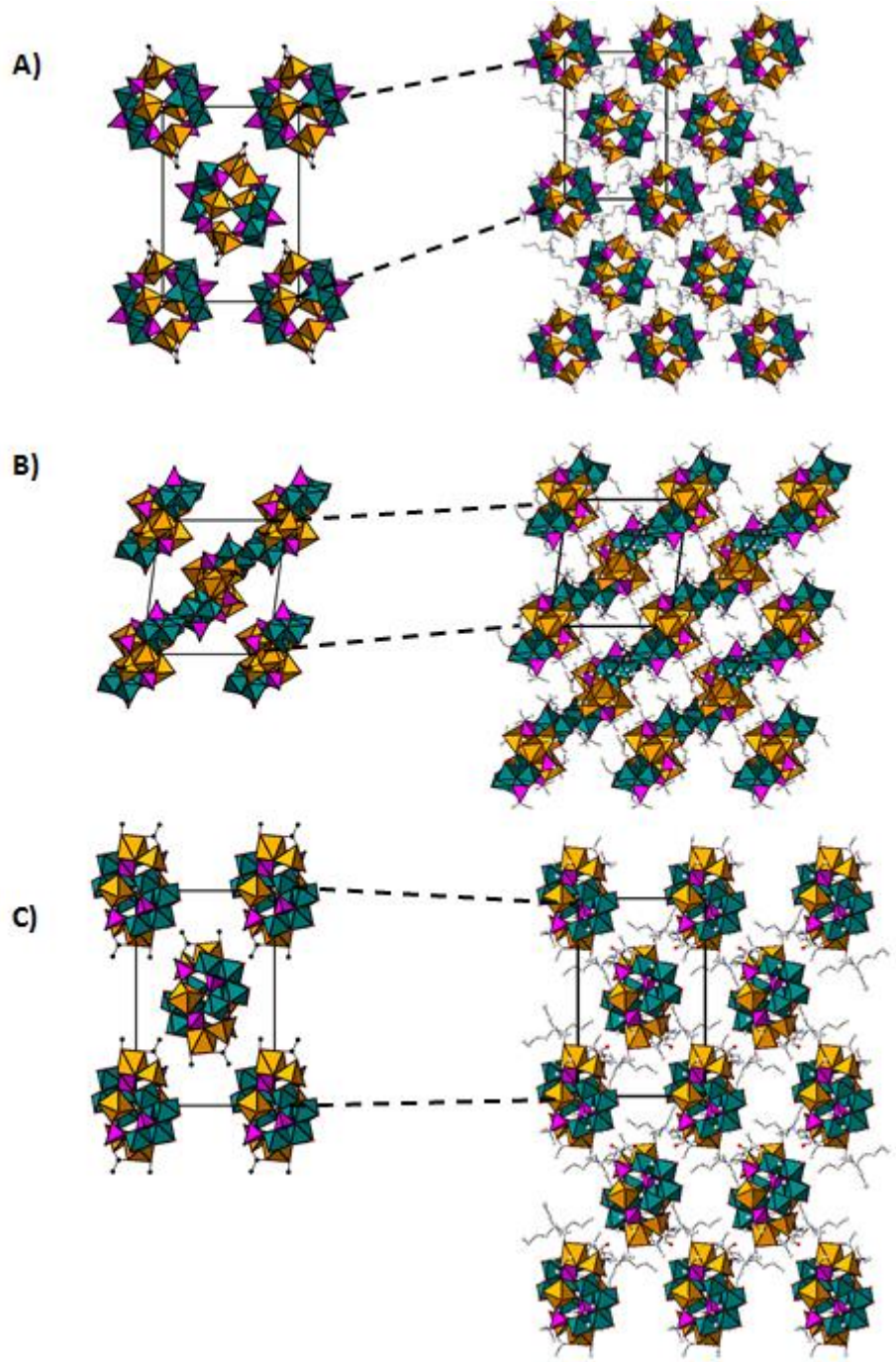

Figure 5.3.2 – Crystal packing diagrams for 27•5(MeOH), as viewed down: A) The crystallographic *a*-axis, B) the crystallographic *b*-axis. C) The crystallographic *c*-axis. Colour Scheme: Mo teal, Mn orange, P pink, O red, N blue, C grey.

When the synthesis of **26** was repeated using adamantylphosphonic acid in place of *tert*-butylphosphonic acid, yellow-orange crystals were formed after one week. When subjected to XRD analysis, the crystals were found to contain $[TBA]_2[Mo^{VI}_{10}Mn^{II}_6O_{12}(\mu\text{-}O)_{14}(\mu_3\text{-}O)_4(AdPO_3)_6(MeCOO)_2(py)_4(H_2O)_6]$, **28**, where TBA represents tetrabutylammonium, Ad represents the adamantly group and py represents pyridine. The crystals formed in the triclinic space group *P*-1.

This compound is the adamantylphosphonate analogue of **26**, or alternatively, the manganese (II) analogue of compound **10** (Figure 5.3.3). This indicates that the same orthogonal ligand substitution performed in the series **5**-**25** can also be performed here.

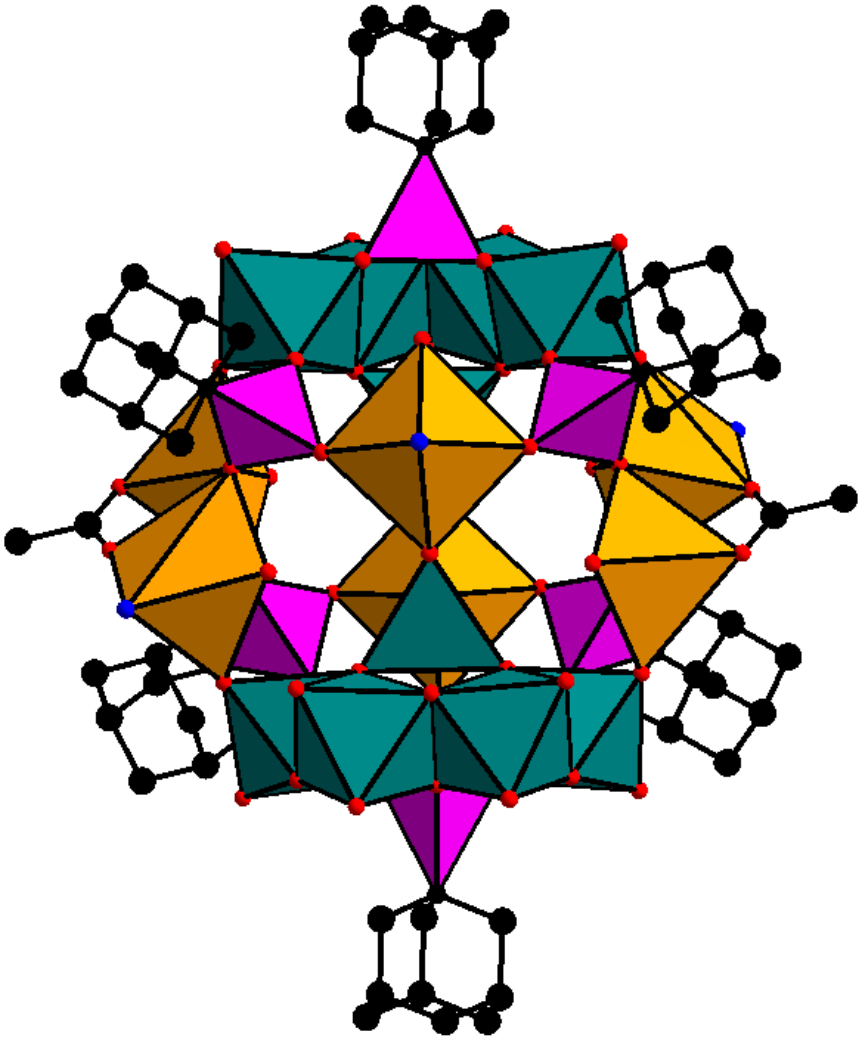

Figure 5.3.3 – Simplified representation of the cluster core in 28, showing the adamantyl backbones on the phosphonate ligands. Colour Scheme: Mo teal, Mn orange, P pink, O red, N blue, C black.

Identification code	**28**•3(MeCN)
Empirical formula	$C_{232}H_{400}Mn_{12}Mo_{20}N_{12}O_{116}P_{12}$
Formula weight (g/mol)	8341.68
Temperature (K)	100(2)
Wavelength (Å)	0.71073
Crystal system	Triclinic
Space group	*P*-1
a (Å)	15.1276(5)
b (Å)	20.2822(7)
c (Å)	27.5272(9)
α (°)	89.5500(10)
β (°)	85.2160(10)
γ (°)	84.3200(10)
Volume (Å^3)	8375.2(5)
Z	1
Calculated density ρ_{calc} (g/cm^3)	1.654
Absorption coefficient μ (mm^{-1})	1.294
F(000)	4236.0
2Θ range for data collection (°)	1.484 to 57.514
Index ranges	$-20 \leq h \leq 20$, $-27 \leq k \leq 27$, $-37 \leq l \leq 37$
Reflections collected	254326
Independent reflections	43465 [R_{int} = 0.0332]
Data/restraints/parameters	43465/0/1561
Goodness-of-fit on F^2	1.412
Final R indices [I>=2σ (I)]	R_1 = 0.0558, wR_2 = 0.1586
Final R indices [all data]	R_1 = 0.0665, wR_2 = 0.1664
Largest diff. peak and hole (e Å^{-3})	6.78/-2.93

Table 5.3.2 – Crystallographic details for compound 28•3(MeCN).

Packing

28 crystallises along with three acetonitrile molecules in the triclinic crystal system in space group *P*-1. The crystal packing is shown in Figure 5.4.2.

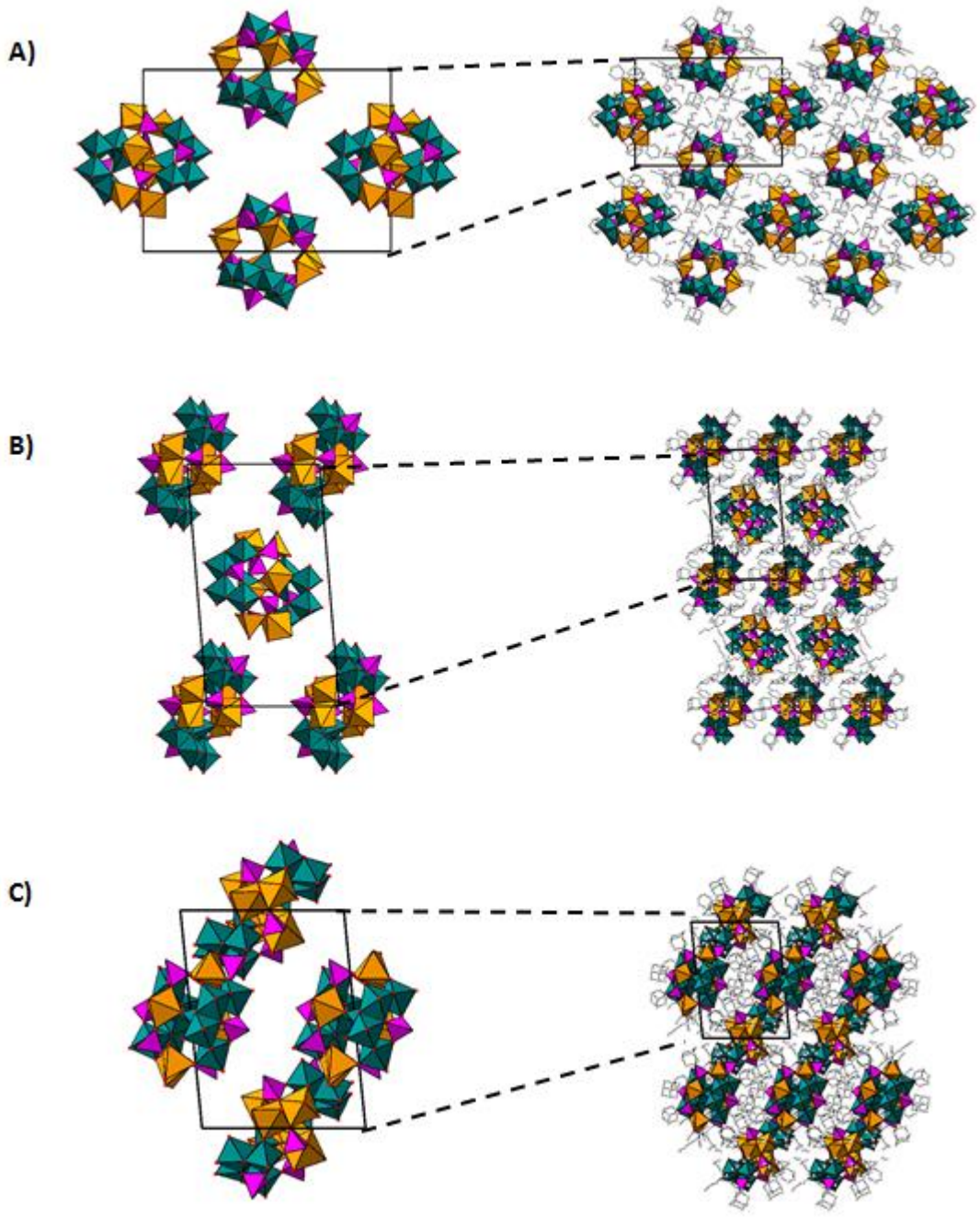

Figure 5.3.4 – Crystal packing diagrams for 28•3(MeCN), as viewed down: A) The crystallographic *a*-axis, B) the crystallographic *b*-axis. C) The crystallographic *c*-axis. Colour Scheme: Mo teal, Mn orange, P pink, O red, N blue, C grey.

5.4) C-C Bond Cleavage by Manganese Compounds

Compounds **26**-**28** all contain acetate ligands which bridge between the manganese centres in the dinuclear units. This acetate ligand must arise from *in situ* ligand generation, as no acetate source was included in any of the reaction mixtures. It was hypothesised that the acetate may have been generated *via in situ* cleavage of the acetylacetonate (acac) counterions to the manganese (III) starting material.[49–53] (Hydrolysis of the acetonitrile solvent was also proposed after the isolation of compound **26**,[19] but was ruled out by the isolation of compound **27** in the absence of acetonitrile).

To validate this hypothesis, the syntheses were repeated using an alternative manganese (III) starting material, 2,2,6,6-tetramethylheptan-(3,5)-dionato manganese (III), ($Mn(TMH)_3$) (Figure 5.4.1). Like acac, TMH is the enolate of a 1,3-diketone, and should therefore in principle engage in similar reactivity. Assuming that the acac is being cleaved into acetate ligands, this *tert*-butyl-substituted compound should generate pivalate-substituted analogues of compounds **26**-**28**.

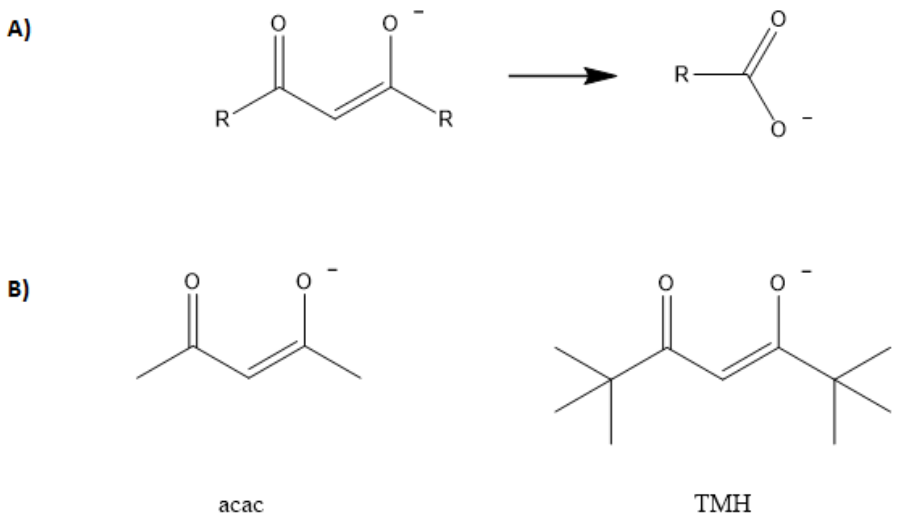

Figure 5.4.1 – A) The C-C bond cleavage reaction that was proposed to generate the acetate ligands in compounds 25-27. B) The structures of the acac and TMH anions.

When the synthesis of **27** was repeated using $Mn(TMH)_3$ in place of $Mn(acac)_3$, yellow-orange crystals were formed after one week. When subjected to XRD analysis, the crystals were found to contain $[TBA]_2[Mo^{VI}_{10}Mn^{II}_6O_{12}(\mu\text{-}O)_{14}(\mu_3\text{-}O)_4(t\text{BuPO}_3)_6(t\text{BuCOO})_2(MeOH)_4(H_2O)_6]$, **29**, where TBA represents tetrabutylammonium and *t*Bu represents the *tert*-butyl moiety. The crystals formed in the monoclinic space group $P2_1/n$ and also contained six methanol molecules.

This compound is the pivalate-substituted analogue of **27**, as predicted. This indicates that the carboxylate ligands in **26**-**28** do indeed arise from the cleavage of acetylacetonate-type ligands (Figure 5.4.2).

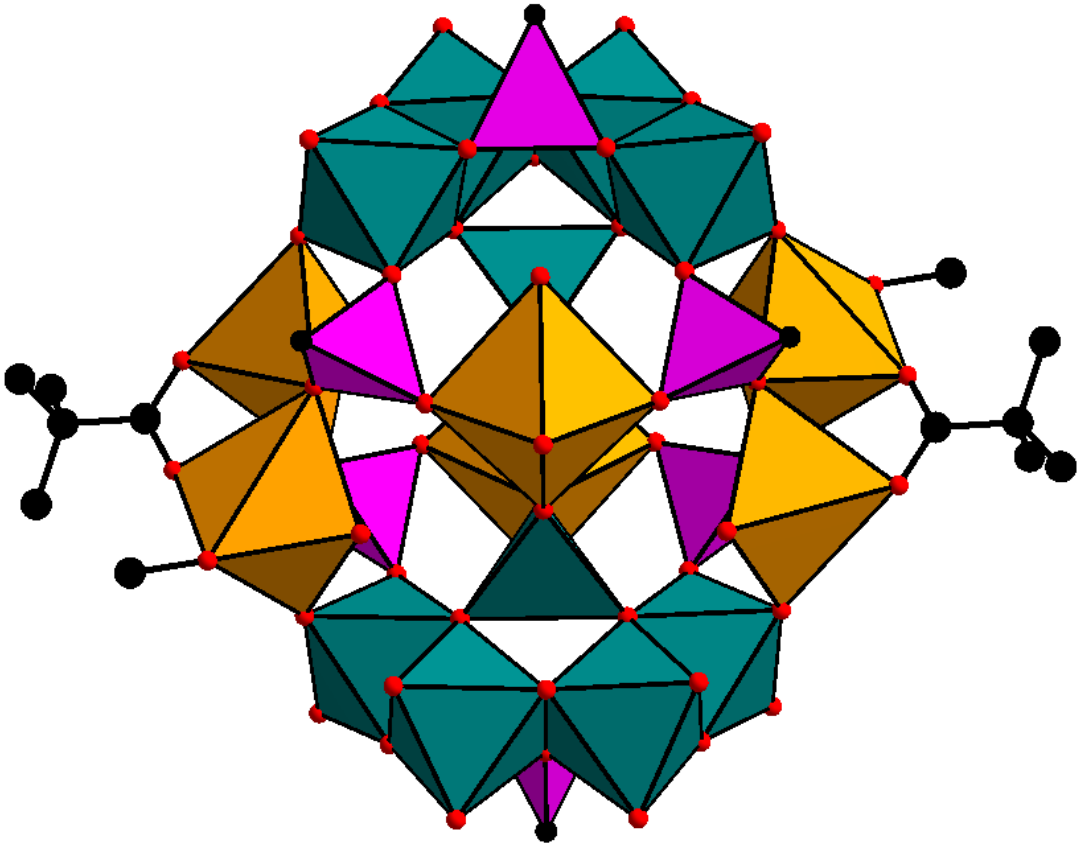

Figure 5.4.2 – Simplified representation of the cluster core in 29, showing the *tert*-butyl side groups on the carboxylate ligands. These ligands can only have arisen *via* the *in situ* cleavage of acetylacetonate-type ligands. Colour Scheme: Mo teal, Mn orange, P pink, O red, N blue, C black.

Identification code	**29**•6(MeOH)
Empirical formula	$C_{76}H_{192}Mn_6Mo_{10}N_2O_{68}P_6$
Formula weight (g/mol)	3697.16
Temperature (K)	100(2)
Wavelength (Å)	0.71073
Crystal system	Monoclinic
Space group	$P2_1/n$
a (Å)	16.980(3)
b (Å)	24.374(4)
c (Å)	17.930(3)
α (°)	90
β (°)	102.289(4)
γ (°)	90
Volume (Å^3)	7251(2)
Z	2
Calculated density ρ_{calc} (g/cm^3)	1.693
Absorption coefficient μ (mm^{-1})	1.485
F(000)	3732
2Θ range for data collection (°)	2.860 to 52.254
Index ranges	-21≤h≤20, -30≤k≤30, -15≤l≤22
Reflections collected	108539
Independent reflections	14317 [R_{int} = 0.0418]
Data/restraints/parameters	14317/3/785
Goodness-of-fit on F^2	1.149
Final R indices [I>=2σ (I)]	R_1 = 0.0512, wR_2 = 0.1341
Final R indices [all data]	R_1 = 0.0771, wR_2 = 0.1647
Largest diff. peak and hole (e Å^{-3})	1.648/-2.092

Table 5.4.1 – Crystallographic details for compound 29•6(MeOH).

The solvent molecules were modelled as being disordered over six positions with partial occupancies (93, 66, 50, 41, 30 and 20%), with constraints (DFIX) applied to some of these molecules. The coordinated methanol molecule O(5) was modelled as disordered over three positions with 39/33/28% occupancy. The carbon atom in this ligand was held isotropic.

Packing

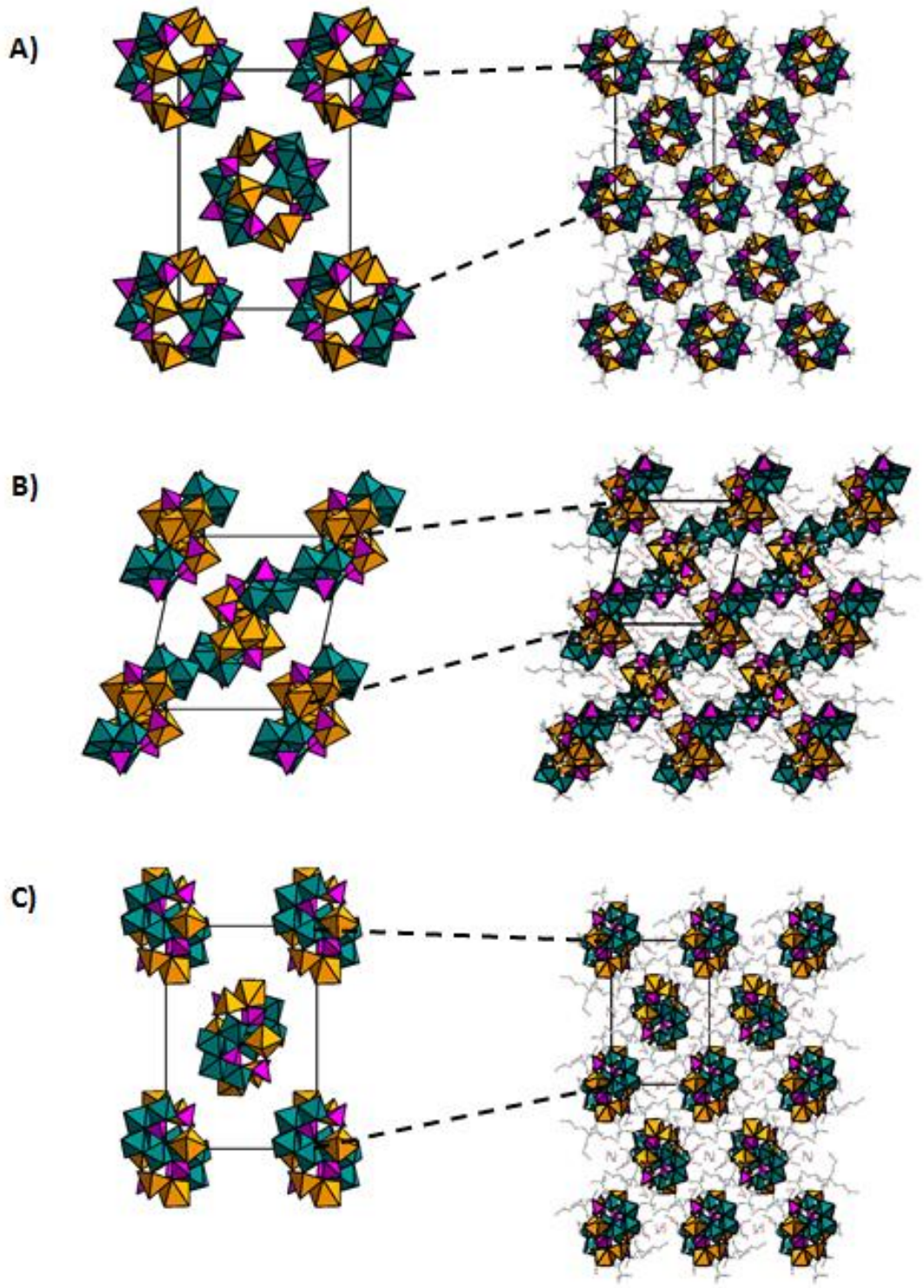

Figure 5.4.3 – Crystal packing diagrams for 29•6(MeOH), as viewed down: A) The crystallographic *a*-axis, B) the crystallographic *b*-axis. C) The crystallographic *c*-axis. Colour Scheme: Mo teal, Mn orange, P pink, O red, N blue, C black.

Carbon-carbon bond cleavage of this type could potentially proceed *via* oxidative or hydrolytic processes.[54–56] The most likely oxygen sources for this bond cleavage are the *oxo*-cluster, water and atmospheric oxygen.[57–62] It would be expensive and difficult to rule out either of the first two potential sources with any certainty (*e.g.* through isotope labelling experiments), but atmospheric oxygen can be excluded from the reaction mixture with relative ease. To this end, the synthesis of **26** was repeated under a nitrogen atmosphere, using solvent that had been previously degassed (*via* the freeze-pump-thaw method), and the resulting solution was stored in an airtight container under nitrogen atmosphere.

In contrast to the reaction performed under an oxygenated atmosphere, which decolourised over the course of about one week, this solution retained its dark brown colour for an extended period of time (at least six months, Figure 5.4.4). After six months under an inert atmosphere, the dark brown solution was subsequently exposed to the atmosphere, after which it decolourised over the course of one week and produced crystals containing **26**. This provides fairly strong evidence that molecular oxygen is indeed necessary for the production of **26** and its analogues. While this does not conclusively demonstrate that the oxygen in the carboxylate ligands originates from the atmosphere (*e.g.* molecular oxygen may play a role in activating some other species rather than being inserted into the carbon-carbon bond), it does provide support for the hypothesis that the carbon-carbon bond cleavage seen in these compounds proceeds *via* an oxidative mechanism with atmospheric molecular oxygen as the oxygen source.

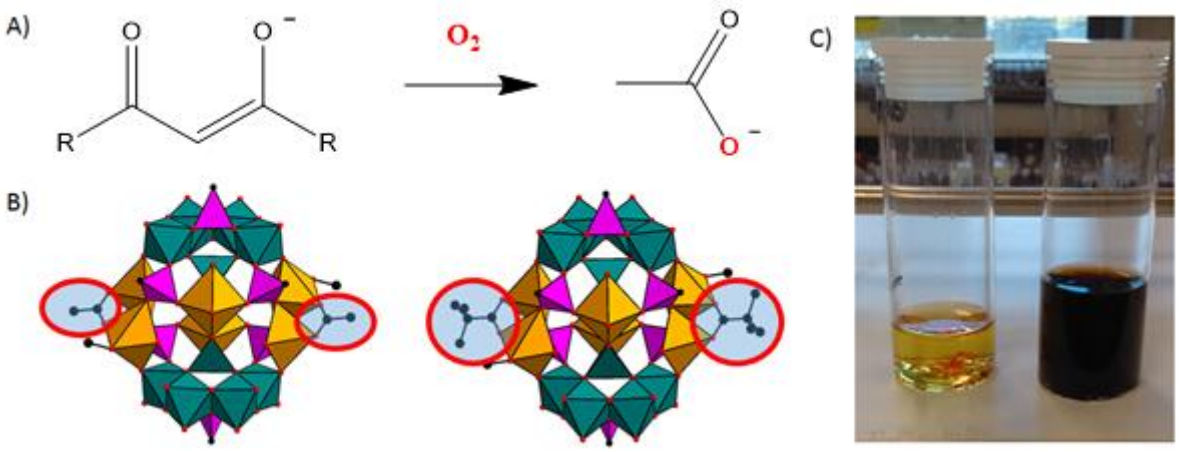

Figure 5.4.4 –A) The hypothesised *in situ* cleavage of acac-type ligands to produce carboxylates. B) Simplified structures of 27 and 29 as determined by XRD, highlighting the different carboxylate ligands that were formed *via* this C-C bond cleavage. C) The reaction mixtures for 26 when exposed to air for one week (left) and when stored under nitrogen for 6 months (right), indicating that atmospheric oxygen may play a role in the cleavage of the acac-type ligands.

Of course, the active species in this reaction is not **26** itself but presumably is some precursor to **26**. This active species has not yet been identified.

5.5) Polymeric Manganese Compounds

One of the objectives for this research project as set out in chapter 1 was to generate extended structures (*i.e.* polymer or framework-type materials with repeating organic and inorganic units with an extended architecture). To this end, the synthesis of compound **26** was repeated in the presence of PDA-H_2, in a similar manner to the synthesis of compound **25** in the previous chapter.

After one week, orange crystals were obtained from the reaction mixture, which were found to contain $[TBA]_2[Mo^{VI}_{10}Mn^{II}_6O_{12}(\mu\text{-}O)_{14}(\mu_3\text{-}O)_4(t\text{BuPO}_3)_6(PDA)(py)_4(H_2O)_6]$, **30**, where TBA is the tetrabutylammonium cation, *t*Bu represents the *tert*-butyl moiety, PDA represents phenylenediacetate, and py represents pyridine. The crystals also contain two acetonitrile molecules per formula unit, and crystallise in the triclinic space group *P*-1.

As expected, the compound is a polymeric analogue of **26**, or alternatively is a manganese (II) analogue of compound **25** (Figure 5.5.1).

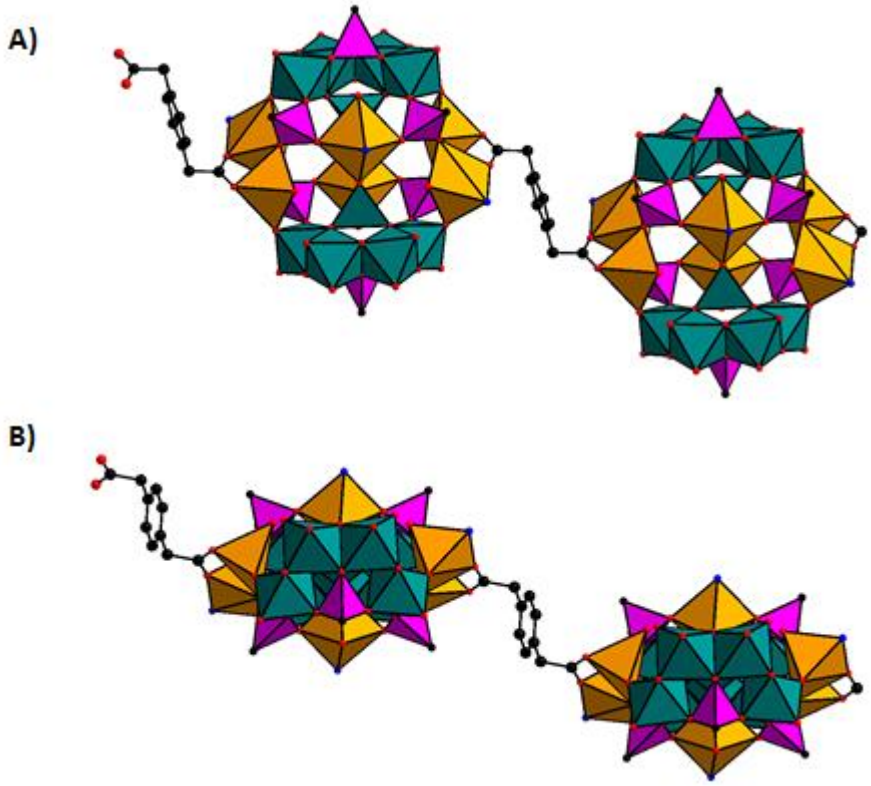

Figure 5.5.1 –A) Side-on and B) top-down views of two units of the polymer chain in $[TBA]_2[Mo^{VI}_{10}Mn^{II}_6O_{12}(\mu\text{-}O)_{14}(\mu_3\text{-}O)_4(t\text{BuPO}_3)_6(PDA)(py)_4(H_2O)_6]$, 30. The $\{Mn_6Mo_{10}\}$ units are held together by PDA ligands. Colour scheme: Mo teal, Mn orang, P pink, O red, N blue, C black.

The O-C-C-Ph torsion angle in **30** (71°) is comparable to the equivalent torsion angle in **25** (83°), indicating that there may be similar packing constraints in the two compounds.

Identification code	**30**•2(MeCN)
Empirical formula	$C_{90}H_{172}Mn_6Mo_{10}N_8O_{58}P_6$
Formula weight (g/mol)	3769.22
Temperature (K)	100(2)
Wavelength (Å)	0.71073
Crystal system	Triclinic
Space group	*P*-1
a (Å)	13.9591(6)
b (Å)	17.0195(6)
c (Å)	17.5948(6)
α (°)	100.782(2)
β (°)	100.743(2)
γ (°)	103.585(2)
Volume (Å^3)	3873.6(3)
Z	1
Calculated density ρ_{calc} (g/cm^3)	1.616
Absorption coefficient μ (mm^{-1})	11.465
F(000)	1891.0
2Θ range for data collection (°)	7.398 to 132.188
Index ranges	$-15 \leq h \leq 9$, $-19 \leq k \leq 19$, $-20 \leq l \leq 20$
Reflections collected	30325
Independent reflections	12691 [R_{int} = 0.0453]
Data/restraints/parameters	12691/0/821
Goodness-of-fit on F^2	0.719
Final R indices [I>=2σ (I)]	R_1 = 0.0371, wR_2 = 0.0981
Final R indices [all data]	R_1 = 0.0451, wR_2 = 0.1062
Largest diff. peak and hole (e Å^{-3})	1.29/-0.97

Table 5.5.2 – Crystallographic details for compound 30•2(MeCN).

Packing

The crystal packing diagrams for compound **30**•2(MeCN) are shown in Figure 5.5.2. The polymer chains propagate in a direction perpendicular to the *a*- and *c*-axes.

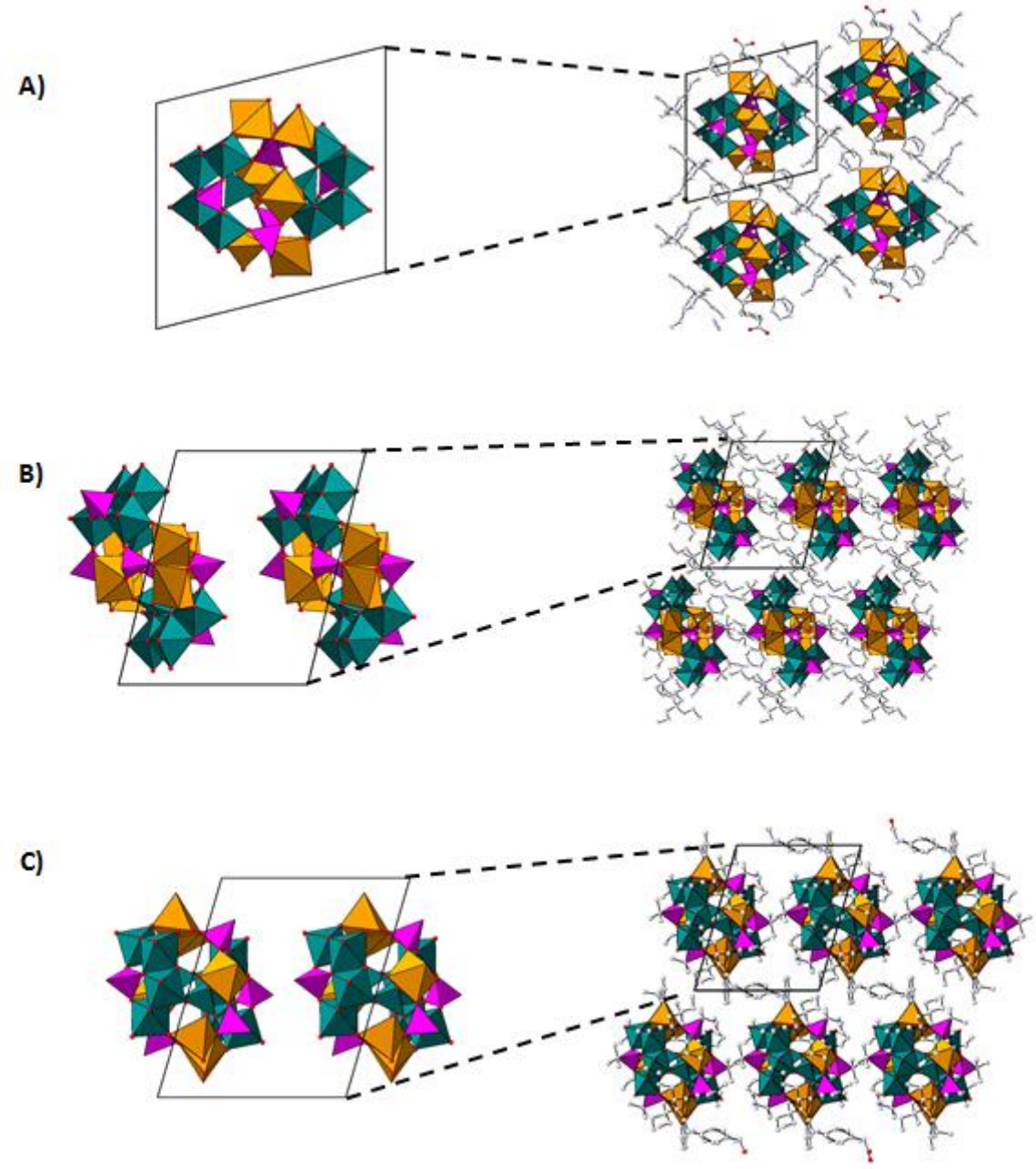

Figure 5.5.2 – Crystal packing diagrams for 30•2(MeCN), as viewed down: A) The crystallographic *a*-axis, B) the crystallographic *b*-axis. C) The crystallographic *c*-axis. Colour Scheme: Mo teal, Mn orange, P pink, O red, N blue, C grey.

*5.6) [Cl⊂Mn$^{III}_6$(t*BuPO$_3$*)$_8$(py)$_6$] [Mo$^{VI}_2$Mn$^{III}_{11}$O$_2$(μ-O)$_4$(μ$_4$-O)$_6$(μ-OH)$_2$(t*BuPO$_3$*)$_{10}$(py)$_4$], (31)*

In light of the successful isolation of compound **30**, it was hypothesised that an analogous polymer compound could be formed using a shorted organic linker, terephthalate. To this end, manganese (III) acetylacetonate was combined with Lindqvist hexamolybdate and *tert*-butylphosphonic acid in acetonitrile in the presence of pyridine and terephthalic acid. The intended compound did not form; however, serendipitously, small brown crystals were obtained from the reaction mixture after 2 days.

The crystals were subjected to analysis by XRD and found to contain [Cl⊂Mn$^{III}_6$(*t*BuPO$_3$)$_8$(py)$_6$][Mo$^{VI}_2$Mn$^{III}_{11}$O$_2$(μ-O)$_4$(μ$_3$-O)$_4$(μ$_4$-O)$_2$(μ-OH)$_2$(*t*BuPO$_3$)$_{10}$(py)$_4$], **31**, where *t*Bu represents the *tert*-butyl moiety and py represents pyridine. The crystals also contained 4.5 acetonitrile molecules per formula unit, and formed in the monoclinic space group $P2_1/c$. The crystal structure contained two distinct phosphonate-supported cluster entities, both of which are analogues of compounds previously reported by the Schmitt group (Figures 5.6.1 and 5.6.2).[63,64]

Firstly, **31** contains a cationic {Mn$_6$} species, [Cl⊂Mn$^{III}_6$(*t*BuPO$_3$)$_8$(py)$_6$]$^+$. This cluster consists of a cage of six manganese (III) centres in around a central, encapsulated chloride ion. Eight *tert*-butylphosphonate ligands support the cluster, each binding to three manganese centres. Six pyridine ligands also support the cluster, one binding to each metal centre. The cluster is symmetric to inversion through the chloride ion.

The second cluster is an anionic {Mn$_{11}$Mo$_2$} cluster, [Mo$^{VI}_2$Mn$^{III}_{11}$O$_2$(μ-O)$_4$(μ$_3$-O)$_4$(μ$_4$-O)$_2$(μ-OH)$_2$(*t*BuPO$_3$)$_{10}$(py)$_4$]$^-$. The cluster can be conceptualised as a three-layered structure. The central layer consists of a hexagonal {Mn$_7$} moiety supported by six multiply-bridging (μ$_3$-O and μ$_4$-O) *oxo*-. The top and bottom layers both consist of {MoMn$_2$} units, each of which can be further subdivided into an isolated {MoO$_6$} octahedron and a hydroxo- and phosphonate-bridged dinuclear manganese unit. These components are connected *via* a total of four bridging (μ-O) *oxo*- ligands and ten fully deprotonated *tert*-butylphosphonate ligands (five of which bridge between the middle and top layers, the other five of which bridge between the middle and bottom layers). The structure is symmetric to inversion through the central manganese atom.

Samples of **31** generated by the method described above (using Mn(acac)$_3$ as a manganese (III) source) were contaminated by crystals containing **26**. However by modifying the reaction procedure to generate manganese (III) *via* the comproportionation of potassium permanganate and manganese (II) chloride, samples of **31** could be generated without the possibility of generating **26** (*via in situ* cleavage of the acac ligand).

Interestingly, although this compound contains only isolated molybdate centres, it does not appear to form when the Lindqvist species is substituted by monomeric molybdate, [MoO$_4$]$^{2-}$.

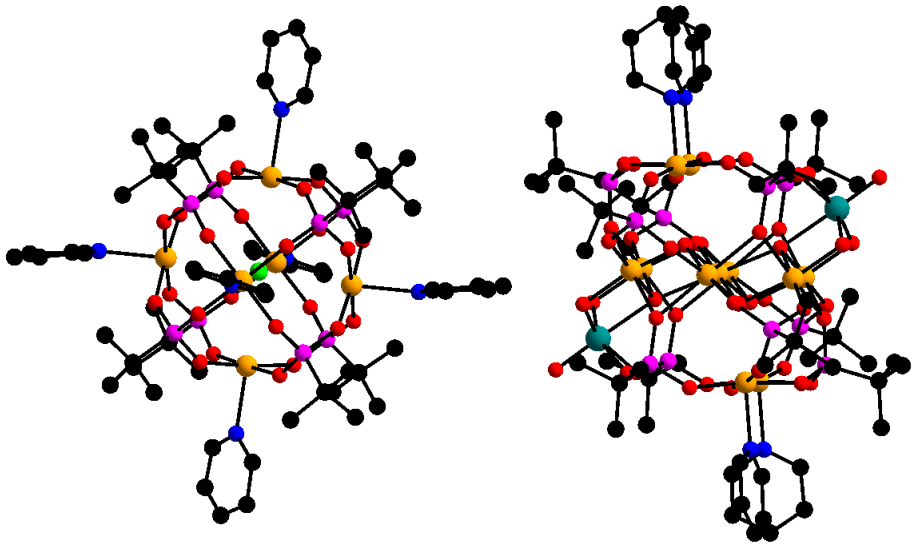

Figure 5.6.1 – Full representation of the two cluster entities in compound 31, $[Cl\subset Mn^{III}_6(t\text{BuPO}_3)_8(py)_6]^+$ and $[Mo^{VI}_2Mn^{III}_{11}O_2(\mu\text{-O})_4(\mu_3\text{-O})_4(\mu_4\text{-O})_2(\mu\text{-OH})_2(t\text{BuPO}_3)_{10}(py)_4]^-$. Colour Scheme: Mo teal, Mn orange, Cl light green, P pink, O red, N blue, C black. H atoms omitted for clarity.

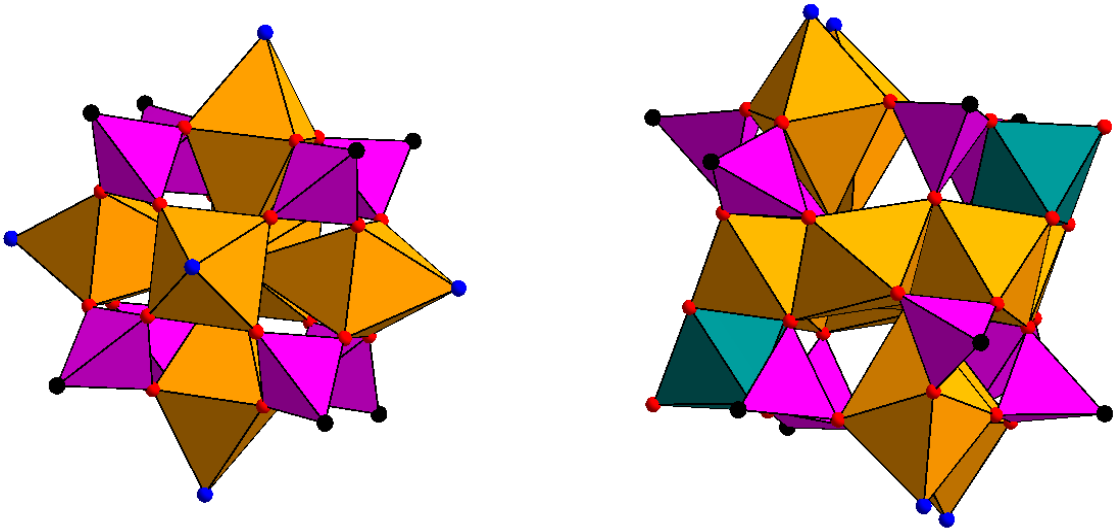

Figure 5.6.2 – Simplified representation of the cluster entities in 31, $[Cl\subset Mn^{III}_6(t\text{BuPO}_3)_8(py)_6]^+$ and $[Mo^{VI}_2Mn^{III}_{11}O_2(\mu\text{-O})_4(\mu_3\text{-O})_4(\mu_4\text{-O})_2(\mu\text{-OH})_2(t\text{BuPO}_3)_{10}(py)_4]^-$. Molybdate, manganese and phosphonate moieties are shown as polyhedra, while pyridine and *tert*-butyl groups are reduced to single N and C atoms respectively. Colour Scheme: Mo teal, Mn orange, Cl light green, P pink, O red, N blue, C black.

Identification code	**31**•4.5(MeCN)
Empirical formula	$C_{131}H_{225.5}ClMn_{17}Mo_2N_{14.5}O_{68}P_{18}$
Formula weight (g/mol)	4810.52
Temperature (K)	100(2)
Wavelength (Å)	0.71073
Crystal system	Monoclinic
Space group	$P2_1/c$
a (Å)	24.9217(8)
b (Å)	16.7635(5)
c (Å)	26.4380(8)
α (°)	90
β (°)	112.200(2)
γ (°)	90
Volume (Å^3)	10226.4(6)
Z	2
Calculated density ρ_{calc} (g/cm^3)	1.562
Absorption coefficient μ (mm^{-1})	11.316
F(000)	4906.0
Crystal size (mm^3)	0.13 × 0.09 × 0.02
2Θ range for data collection (°)	3.83 to 120.196
Index ranges	$-28 \leq h \leq 27$, $-18 \leq k \leq 18$, $-29 \leq l \leq 27$
Reflections collected	93826
Independent reflections	15014 [R_{int} = 0.1760]
Data/restraints/parameters	15014/12/1112
Goodness-of-fit on F^2	1.034
Final R indices [I>=2σ (I)]	R_1 = 0.0878, wR_2 = 0.2248
Final R indices [all data]	R_1 = 0.1606, wR_2 = 0.2710
Largest diff. peak and hole (e Å^{-3})	1.48/-0.75

Table 5.6.1 – Crystallographic details for compound 31•4.5(MeCN)

The {Mn_6} cation

The cationic {Mn_6} cluster entity, $[Cl\subset Mn^{III}_6(t\text{BuPO}_3)_8(py)_6]^+$, has been previously reported by the Schmitt group.[63] In the previous report, the cluster entity was also generated using picoline, methanol, water, and pyridinecarboxaldehyde ligands (or mixtures thereof) in place of the pyridine ligands, but is otherwise identical. Figure 5.6.3 compares the {Mn_6} cluster entity in **31** to the picoline analogue.[63]

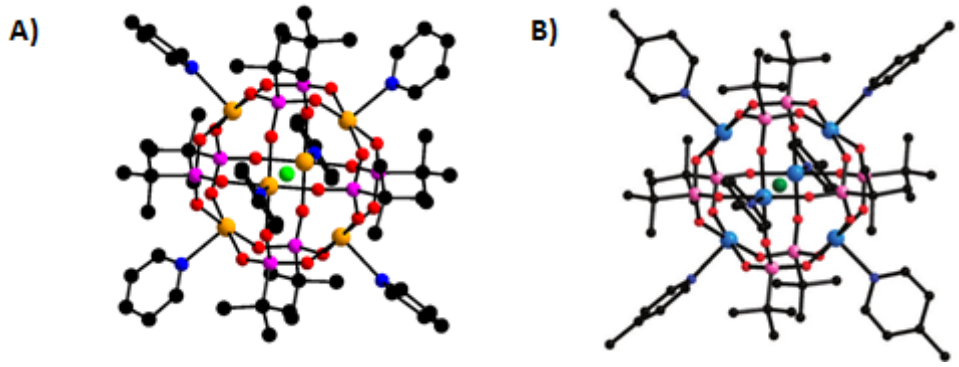

Figure 5.6.3 –A) The {Mn_6} cluster entity in 31, $[Cl\subset Mn^{III}_6(t\text{BuPO}_3)_8(py)_6]^+$. Colour Scheme: Mn orange, Cl light green, P pink, O red, N blue, C black. B) An analogous previously reported {Mn_6} cluster entity, $[Cl\subset Mn^{III}_6(t\text{BuPO}_3)_8(pic)_6]^+$. Colour Scheme: Mn blue, Cl green, P pink, O red, N blue, C black. Reproduced from reference 63.

The chloride ion in the {Mn_6} cluster sits at the centre of an octahedron of Mn^{III} centres (in this way, the cluster represents an inversion of the familiar octahedral coordination environments of metal centres surrounded by donating ligands). Each of the faces of this octahedron are capped by one of eight *tert*-butylphosphonate ligands (Figure 5.6.4). Each phosphonate ligand coordinates to three manganese centres in a $\eta^1{:}\eta^1{:}\eta^1{:}\mu_3$ binding mode. The coordination environments of each manganese centre is completed by one pyridine N-donor.

Each manganese centre is Jahn-Teller distorted (axially elongated), as expected for manganese (III) centres. The distorted axis for each centre is the Br-N axis, perpendicular to the {MnO_4} phosphonate O-donor plane.

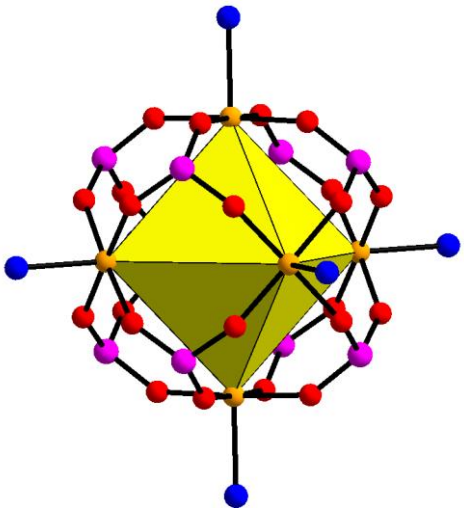

Figure 5.6.4 – The {Mn_6} cluster entity in 31, $[Cl\subset Mn^{III}_6(t\text{BuPO}_3)_8(py)_6]^+$, represented as an octahedron centred on the central Cl ion. Phosphonate ligands cap the eight faces of this octahedron, while pyridine ligands coordinate at the six vertices. Colour Scheme: Mn orange, P pink, O red, N blue.

Metal Atom	Bonded Atom	Bond Length (Å)	BVS	Oxidation State
Mn(1)	O(1)	1.839(11)	3.460	+III
	O(10')	1.860(12)		
	O(2)	1.865(12)		
	O(3)	1.8772(11)		
	N(1)	2.2255(12)		
	Cl(1)	3.097(9)		
Mn(2)	O(11')	1.843(12)	3.418	+III
	O(5)	1.860(11)		
	O(4)	1.873(11)		
	O(12')	1.875(11)		
	N(2)	2.244(11)		
	Cl(1)	3.112(8)		
Mn(3)	O(6)	1.860(14)	3.325	+III
	O(8)	1.867(15)		
	O(9)	1.875(10)		
	O(7)	1.885(10)		
	N(3)	2.2667(11)		
	Cl(1)	3.125(10)		

Table 5.6.2 – Crystallographically-determined bond lengths for the metal centres in the {Mn_6} unit in 31, along with their oxidation state as determined by Bond Valence Sum (BVS) analysis.

All three crystallographically distinct manganese centres in the {Mn_6} unit in **31** display axially elongation along their respective Cl-Mn-N axes (Table 5.6.2). This is consistent with Jahn-Teller distortion, common in manganese (III) metal centres.

The Mn-O distances in the {Mn_6} unit are all fairly consistent at *c.* 1.85 Å. This reflects the high symmetry of the system. Mn-N bond distances are consistent with Jahn-Teller distorted Mn(III)-pyridine bond lengths in the literature at *c.* 2.2 Å.[65–69] The Mn-Cl bond lengths are quite long, at over 3 Å. This is also consistent with Jahn-Teller distorted Mn(III)-halide bond lengths in the literature.[63,70,71]

Bond	Bond Angle (°)	Bond	Bond Angle (°)
O(3)-Mn(1)-N(1)	88.0(4)	Cl(1)-Mn(2)-O(11')	88.2(5)
Cl(1)-Mn(1)-O(1)	88.0(4)	O(5)-Mn(2)-O(4)	88.2(6)
Cl(1)-Mn(1)-O(2)	88.8(4)	Cl(1)-Mn(2)-O(4)	88.6(5)
Cl(1)-Mn(1)-O(3)	88.9(4)	Cl(1)-Mn(2)-O(5)	88.9(5)
O(1)-Mn(1)-O(2)	89.1(6)	O(4)-Mn(2)-N(2)	89.3(4)
O(1)-Mn(1)-O(2)	89.9(7)	O(11')-Mn(2)-O(12')	89.3(5)
O(1)-Mn(1)-O(10')	90.0(6)	Cl(1)-Mn(2)-O(12')	89.4(5)
O(2)-Mn(1)-O(3)	90.4(6)	O(5)-Mn(2)-N(2)	89.4(6)
O(10')-Mn(1)-O(3)	90.5(7)	O(11')-Mn(2)-O(4)	91(5)
O(10')-Mn(1)-N(1)	90.6(5)	O(5)-Mn(2)-O(12')	91.4(6)
O(2)-Mn(1)-N(1)	90.8(5)	O(12')-Mn(2)-N(2)	92.7(6)
O(1)-Mn(1)-N(1)	95.0(4)	O(11')-Mn(2)-N(2)	93.5(6)
Angle Variance (σ^2)	**3.4**	**Angle Variance (σ^2)**	**3.1**
Distortion Index	**0.013**	**Distortion Index**	**0.016**
Cl(1)-Mn(3)-O(8)	87.3(6)		
O(8)-Mn(3)-O(9)	87.7(6)		
O(6)-Mn(3)-O(7)	88.5(6)		
Cl(1)-Mn(3)-O(7)	88.5(5)		
Cl(1)-Mn(3)-O(6)	88.8(5)		
O(7)-Mn(3)-N(3)	89.1(5)		
Cl(1)-Mn(3)-O(9)	89.3(5)		
O(6)-Mn(3)-N(3)	91.4(4)		
O(6)-Mn(3)-O(9)	91.5(6)		
O(8)-Mn(3)-O(7)	92.1(7)		
O(8)-Mn(3)-N(3)	92.6(5)		
O(9)-Mn(3)-N(3)	93.1(4)		
Angle Variance (σ^2)	**4.1**		
Distortion Index	**0.020**		

Table 5.6.3 – Crystallographically-determined bond angles for the metal centres in the {Mn_6} unit in 31, along with their appropriate distortion parameters.

The manganese centres in the {Mn_6} unit display very little distortion away from the ideal octahedral coordination environments (axially elongation aside), with all bond angles close to 90° (Table 5.6.3). σ^2_{oct} and DI values are very low, ranging from 3.4-4.1 and 0.013-0.020, respectively.

σ^2_{oct} and DI are defined in the same way as previously.[44–47]

The {$Mn_{11}Mo_2$} anion

This {$Mn_{11}Mo_2$} cluster, [$Mo^{VI}_2Mn^{III}_{11}O_2(\mu\text{-}O)_4(\mu_3\text{-}O)_4(\mu_4\text{-}O)_2(\mu\text{-}OH)_2(t\text{BuPO}_3)_{10}(py)_4]^-$, is also an analogue of a previously reported compound from the Schmitt group (Figure 5.6.5). This cluster is a molybdate-substituted analogue of an {Mn_{13}} cluster, formulated as [$(Mn^{II}_{0.5}Mn^{III}_{0.5})Mn^{III}_{12}(\mu_4\text{-}O)_6(\mu\text{-}OH)_2(\mu\text{-}MeO)_4(t\text{BuPO}_3)_{10}(MeOH)_2(pic)_4]^{0.5+}$.[64] The {$Mn_{11}Mo_2$} cluster replaces two manganese centres in the {Mn_{13}} cluster with molybdate moieties.

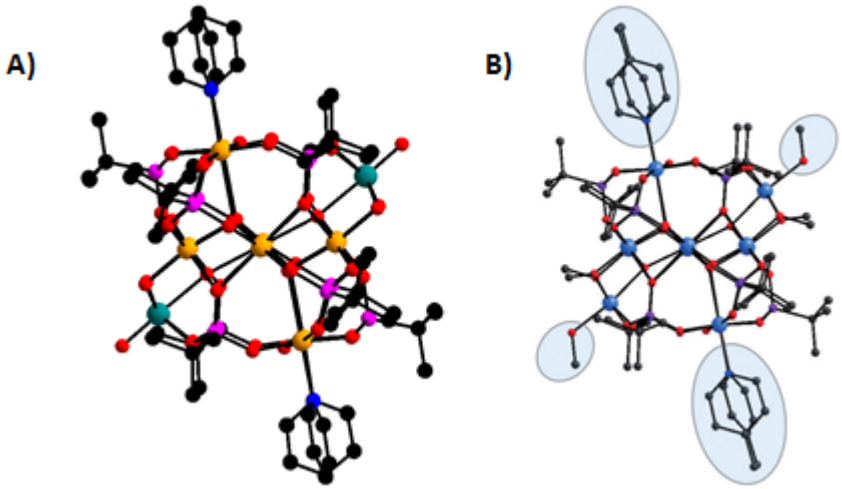

Figure 5.6.5 –A) The {$Mn_{11}Mo_2$} cluster entity in 31, [$Mo^{VI}_2Mn^{III}_{11}O_2(\mu\text{-}O)_4(\mu_3\text{-}O)_4(\mu_4\text{-}O)_2(\mu\text{-}OH)_2(t\text{BuPO}_3)_{10}(py)_4]^-$. Colour Scheme: Mo teal, Mn orange, P pink, O red, N blue, C black. B) An analogous previously reported {Mn_{13}} cluster entity, [$(Mn^{II}_{0.5}Mn^{III}_{0.5})Mn^{III}_{12}(\mu_4\text{-}O)_6(\mu\text{-}OH)_2(\mu\text{-}MeO)_4(t\text{BuPO}_3)_{10}(MeOH)_2(pic)_4]^{0.5+}$. Colour Scheme: Mn blue, P pink, O red, N blue, C black. Reproduced from reference 64.

The {$Mn_{11}Mo_2$} cluster in **31** can be subdivided into three layers, a {Mn_7} "middle" layer, and two {$MoMn_2$} layers (Figure 5.6.6) . The top and bottom layers can each be further subdivided into an isolated Mo centre and a dinuclear manganese unit. The structure is held together by bridging phosphonate and *oxo*- ligands.

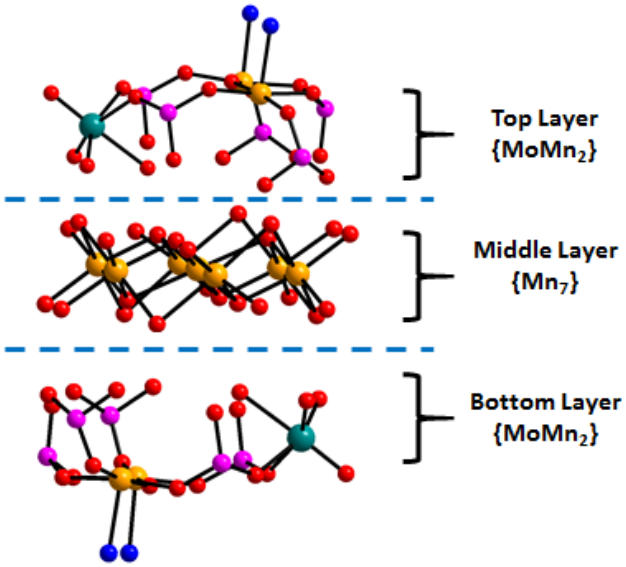

Figure 5.6.6 –The {$Mn_{11}Mo_2$} cluster entity in can be divided into three distinct layers. Colour Scheme: Mo teal, Mn orange, P pink, O red, N blue.

Middle {Mn_7} layer

The middle layer of the cluster core in **31** is described as a {Mn_7O_6} structure with C_3 symmetry. Taken along with the supporting phosphonate and *oxo*- ligands, the middle layer is overall a {Mn_7O_{24}} unit, which bares structural similarity to the $[XM_6O_{24}]^{n-}$ Anderson POM structure (Figure 5.6.7, *c.f.* Figure 1.2.1.7). All of the manganese centres in this unit display highly distorted (axially elongated) {MnO_6} coordination environments, as expected for Mn^{III} centres.

The {Mn_7O_6} structure is supported by six internal bridging *oxo*- ligands. All of these *oxo*- ligands are multiply-bridging μ_4-O ligands, each of which bridge between three manganese centres in the {Mn_7} layer, and additionally coordinate to one metal centre in either the top or bottom layers. O(15) and O(15') bridge between the {Mn_7} layer and the molybdate units, while each of O(13), O(13'), O(14) and O(14') bridge between the {Mn_7} layer and one of the manganese centres in the dinuclear units in the top and bottom layers (Figure 5.6.8).

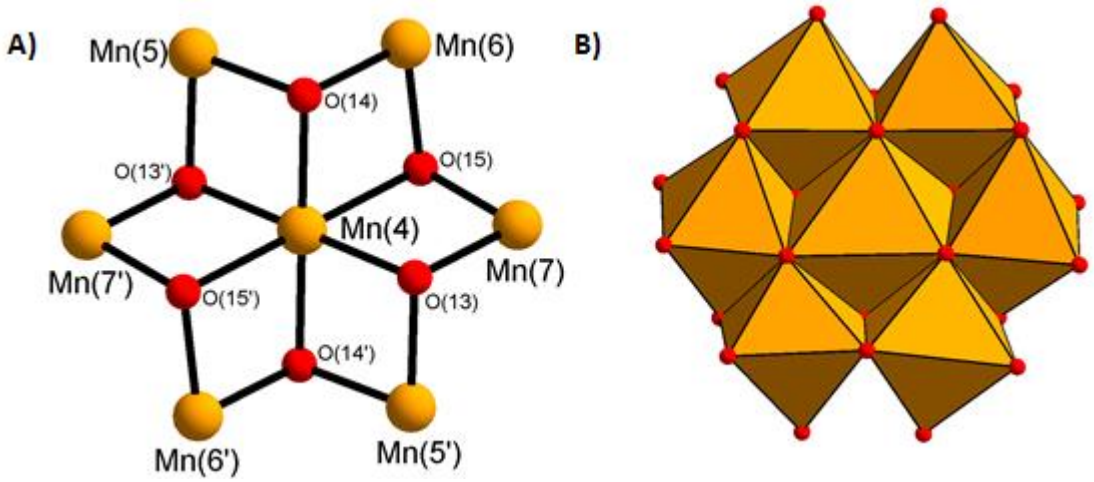

Figure 5.6.7 – A) The {Mn_7O_6} unit in the middle layer of the {$Mn_{11}Mo_2$} cluster. B) The {Mn_7O_6} unit including the supporting phosphonate and *oxo*- ligands, generating an overall {Mn_7O_{24}} unit. Colour Scheme: Mn orange, O red.

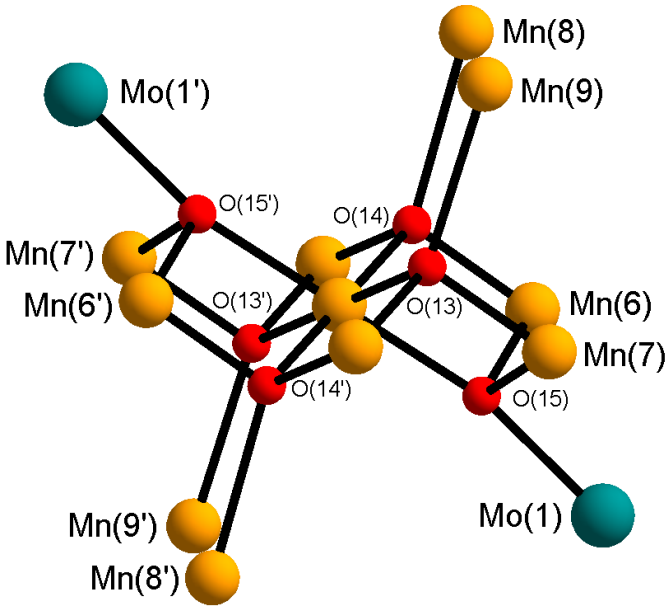

Figure 5.6.8 – Bridging *oxo*- ligands connect the {Mn_7} unit to the metal centres in the top and bottom layers of the cluster. Colour Scheme: Mo teal, Mn orange, O red.

Dinuclear manganese unit

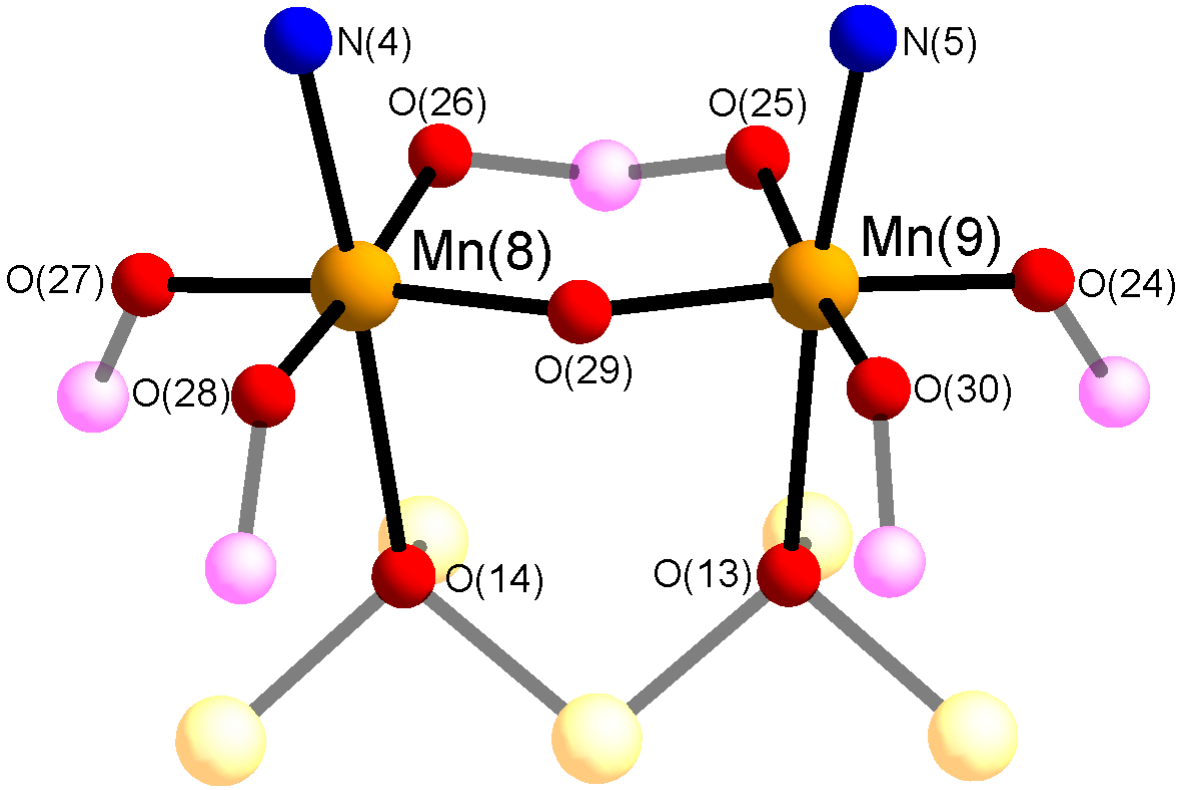

Figure 5.6.9 – The dinuclear manganese units in the {$Mn_{11}Mo_2$} cluster. Colour Scheme: Mn orange, P pink, O red, N blue.

The manganese centres in the dinuclear unit are both described by highly distorted (axially elongated) {MnO_5N} coordination environments (Figure 5.6.9). The unit is bridged together by a shared hydroxo ligand O(29), and by a phosphonate ligand which binds to each centre in a monodentate fashion *via* O(26) and O(25). The unit is additionally stabilised by four monodentate phosphonate O-donors (O(24), O(27), O(28) and O(30)). Each centre is connected to the {Mn_7} layer by a μ_4-O ligand, O(13) or O(14). The coordination environments of each metal centre are completed by pyridine ligands (N(4) and N(5)). The distorted axis for each metal centre is defined by the pyridine - μ_4-O axis, *i.e.* N(4)-O(14) and N(5)-O(13), respectively.

Molybdate units

The isolated Mo centres in the $\{Mn_{11}Mo_2\}$ cluster are supported by two phosphonate and four *oxo*-ligands. The two phosphonate O-donors O(32) and O(33) coordinate in a monodentate fashion. The two μ-O *oxo*-ligands O(19) and O(20) and the μ_4-O *oxo*-ligand O(15) all connect the molybdenum centre to the central $\{Mn_7\}$ layer. The molybdenum coordination environment is completed by the terminal *oxo*- ligand O(21).

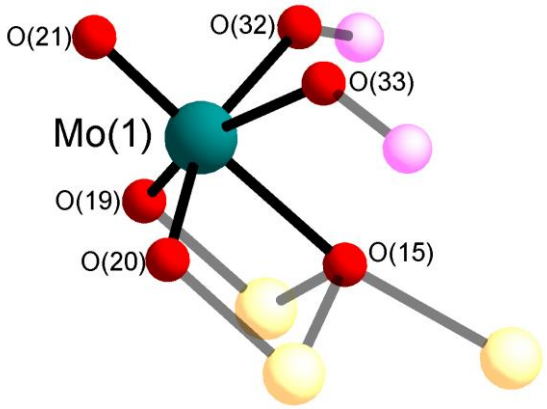

Figure 5.6.10 – The molybdenum centre in the $\{Mn_{11}Mo_2\}$ cluster. Colour Scheme: Mo teal, Mn orange, P pink, O red.

The substitution of a molybdate unit in the $\{Mn_{11}Mo_2\}$ cluster in place of a manganese (III) centre in the $\{Mn_{13}\}$ cluster[64] results in significant differences between the two clusters. The monoanionic bridging methoxy ligands in $\{Mn_{13}\}$ are replaced by dianionic bridging *oxo*- ligands, while the neutral terminal methanol ligand is replaced by a dianionic terminal *oxo*- ligand. This results in two significant changes in **31** with respect to $\{Mn_{13}\}$:

- A labile coordination site (terminal methanol) is now replaced by a strongly bound *oxo*- ligand, effectively blocking coordination from occurring at this site (Figure 5.6.11).
- There is an overall difference in charge in the cluster; the $\{Mn_{13}\}$ cluster was overall cationic while the $\{Mn_{11}Mo_2\}$ cluster is anionic (Figure 5.6.11)

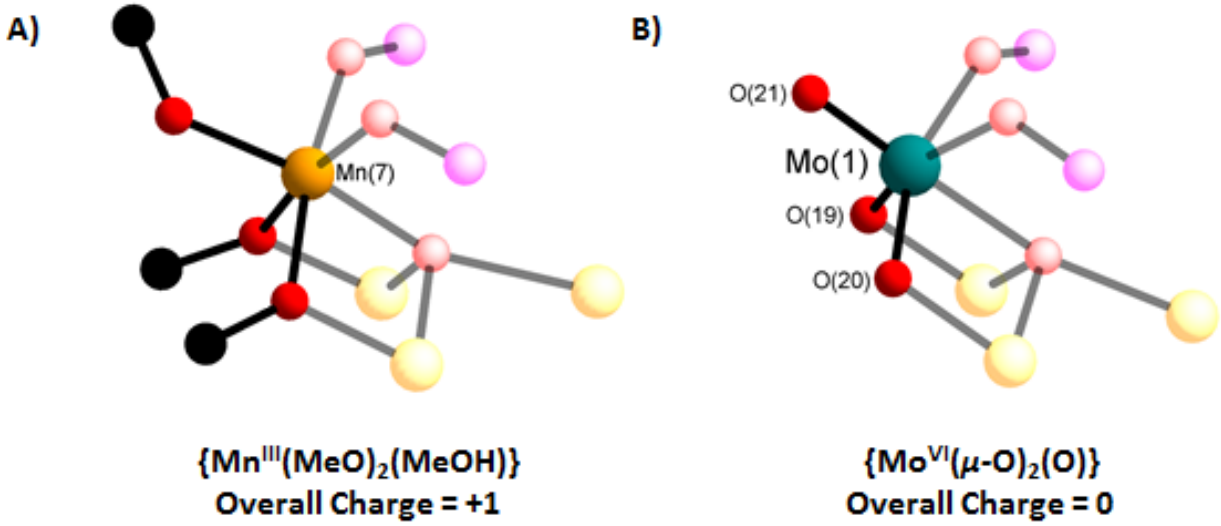

Figure 5.6.11 – A) The $\{Mn(MeO)_2(MeOH)\}$ unit in the $\{Mn_{13}\}$ cluster. B) The equivalent $\{MoO_3\}$ unit in the $\{Mn_{11}Mo_2\}$ cluster. Colour Scheme: Mo teal, Mn orange, P pink, O red, C black.

{$Mn_{11}Mo_2$} bond lengths

Metal Atom	Bonded Atom	Bond Length (Å)	BVS	Oxidation State
Mn(4)	O(13)	1.994(7)	2.609	+III
	O(13')	1.994(7)		
	O(14)	2.022(9)		
	O(14')	2.022(9)		
	O(15)	2.230(7)		
	O(15')	2.230(7)		
Mn(5)	O(17)	1.937(10)	2.994	+III
	O(23')	1.940(7)		
	O(14)	1.948(7)		
	O(13')	1.960(10)		
	O(16)	2.208(7)		
	O(31')	2.233(8)		
Mn(6)	O(15)	1.917(9)	3.109	+III
	O(18)	1.930(10)		
	O(14)	1.951(7)		
	O(19)	1.956(8)		
	O(31')	2.182(7)		
	O(34)	2.187(7)		
Mn(7)	O(15)	1.908(7)	3.080	+III
	O(22)	1.925(8)		
	O(20)	1.967(9)		
	O(13)	1.971(9)		
	O(16')	2.181(9)		
	O(34)	2.194(9)		
Mn(8)	O(26)	1.876(7)	3.130	+III
	O(28)	1.878(7)		
	O(27)	1.898(11)		
	O(29)	1.959(9)		
	N(4)	2.2653(10)		
	O(14)	2.608(10)		
Mn(9)	O(25)	1.874(10)	3.157	+III
	O(30)	1.883(8)		
	O(24)	1.910(8)		
	O(29)	1.942(8)		
	N(5)	2.240(10)		
	O(13)	2.594(10)		
Mo(1)	O(21)	1.730(9)	5.808	+VI
	O(20)	1.805(9)		
	O(19)	1.825(9)		
	O(33)	2.080(10)		
	O(32)	2.086(9)		
	O(15)	2.259(7)		

Table 5.6.4 – Crystallographically-determined bond lengths for the metal centres in the {$Mn_{11}Mo_2$} unit in 31, along with their oxidation state as determined by Bond Valence Sum (BVS) analysis.

As expected for Jahn-Teller distorted (axially elongated) Mn^{III} centres, all of the manganese centres in **31** display four short bonds in the plane (*c.* 1.9 Å) and two longer bonds which define the Jahn-Teller axis for the metal centre. The Mn(2)-O(18) and Mn(3)-O(17) bonds are particularly elongated at *c.* 2.6 Å, but this is still in the reported range for Mn^{III} centres reported in the literature.[72–75]

BVS analysis deviates somewhat from the expected values in this case, but the BVS results are mostly in good agreement with +III oxidation states, with the possible exception of the Mn(4) centre, which displays a BVS value of 2.609. The equivalent Mn centre in the previously reported $\{Mn_{13}\}$ compound displayed a similar BVS value, and in that example was assigned as being 50/50 disordered between +II and +III oxidation states.[64] Here however, it is assigned as being fully in the +III oxidation state due to charge-balance considerations. It is not clear why this metal centre displays such a large deviation from the expected BVS value.

Bond	Bond Angle (°)	Bond	Bond Angle (°)
O(14)-Mn(4)-O(15)	76.8(3)	O(14)-Mn(5)-O(31')	83.0(3)
O(14')-Mn(4)-O(15')	76.8(3)	O(13')-Mn(5)-O(16)	83.3(3)
O(13)-Mn(4)-O(15)	77.1(3)	O(14)-Mn(5)-O(13')	83.7(3)
O(13')-Mn(4)-O(15')	77.1(3)	O(13')-Mn(5)-O(31')	87.1(3)
O(13)-Mn(4)-O(14')	81.0(3)	O(23')-Mn(5)-O(16)	87.3(3)
O(13')-Mn(4)-O(14)	81.0(3)	O(17)-Mn(5)-O(31')	87.4(3)
O(13)-Mn(4)-O(14)	99.0(3)	O(14)-Mn(5)-O(16)	87.9(3)
O(13')-Mn(4)-O(14')	99.0(3)	O(17)-Mn(5)-O(23')	90.2(3)
O(13)-Mn(4)-O(15')	102.9(3)	O(17)-Mn(5)-O(14)	92.8(3)
O(13')-Mn(4)-O(15)	102.9(3)	O(23')-Mn(5)-O(13')	93.7(3)
O(14)-Mn(4)-O(15')	103.2(3)	O(23')-Mn(5)-O(31')	101.4(3)
O(14')-Mn(4)-O(15)	103.2(3)	O(17)-Mn(5)-O(16)	101.8(3)
Angle Variance (σ^2)	**153.3**	**Angle Variance (σ^2)**	**41.0**
Distortion Index	**0.130**	**Distortion Index**	**0.056**
O(15)-Mn(6)-O(34)	83.0(3)	O(15)-Mn(7)-O(34)	83.0(3)
O(14)-Mn(6)-O(31')	84.3(3)	O(13)-Mn(7)-O(16')	83.7(3)
O(15)-Mn(6)-O(19)	84.3(3)	O(15)-Mn(7)-O(20)	84.1(3)
O(15)-Mn(6)-O(14)	86.4(3)	O(15)-Mn(7)-O(13)	85.8(3)
O(15)-Mn(6)-O(31')	86.8(3)	O(15)-Mn(7)-O(16')	86.6(3)
O(19)-Mn(6)-O(34)	88.9(3)	O(20)-Mn(7)-O(34)	88.1(3)
O(19)-Mn(6)-O(31')	89.9(3)	O(22)-Mn(7)-O(16')	91.1(3)
O(18)-Mn(6)-O(31')	91.5(3)	O(20)-Mn(7)-O(16')	91.1(3)
O(18)-Mn(6)-O(14)	93.2(3)	O(22)-Mn(7)-O(13)	92.9(3)
O(14)-Mn(6)-O(34)	95.2(3)	O(13)-Mn(7)-O(34)	95.3(3)
O(18)-Mn(6)-O(19)	95.9(4)	O(22)-Mn(7)-O(20)	96.9(4)
O(18)-Mn(6)-O(34)	98.6(3)	O(22)-Mn(7)-O(34)	99.3(3)
Angle Variance (σ^2)	**26.1**	**Angle Variance (σ^2)**	**29.9**
Distortion Index	**0.047**	**Distortion Index**	**0.051**
O(14)-Mn(8)-O(27)	85.4(3)	O(30)-Mn(9)-N(5)	86.1(4)
O(28)-Mn(8)-N(4)	86.2(3)	O(13)-Mn(9)-O(24)	86.4(3)
O(26)-Mn(8)-O(27)	87.5(3)	O(25)-Mn(9)-N(5)	87.1(4)
O(26)-Mn(8)-N(4)	88.1(3)	O(25)-Mn(9)-O(24)	87.3(4)
O(14)-Mn(8)-O(29)	88.1(3)	O(13)-Mn(9)-O(29)	87.8(3)
O(28)-Mn(8)-O(29)	88.5(3)	O(24)-Mn(9)-N(5)	88.2(4)
O(14)-Mn(8)-O(28)	90.9(3)	O(30)-Mn(9)-O(29)	88.5(3)
O(28)-Mn(8)-O(27)	91.7(3)	O(30)-Mn(9)-O(24)	91.7(4)
O(27)-Mn(8)-N(4)	92.4(3)	O(13)-Mn(9)-O(30)	92.3(3)
O(26)-Mn(8)-O(29)	92.9(3)	O(25)-Mn(9)-O(29)	93.2(3)
O(29)-Mn(8)-N(4)	94.1(3)	O(13)-Mn(9)-O(25)	94.5(3)
O(14)-Mn(8)-O(26)	94.8(3)	O(29)-Mn(9)-N(5)	97.4(4)
Angle Variance (σ^2)	**9.9**	**Angle Variance (σ^2)**	**13.4**
Distortion Index	**0.030**	**Distortion Index**	**0.035**

Table 5.6.5 – Crystallographically-determined bond angles for the manganese centres in the {$Mn_{11}Mo_2$} unit in 31, along with their distortion parameters.

Bond	Bond Angle (°)
O(19)-Mo(1)-O(15)	78.4(3)
O(20)-Mo(1)-O(15)	78.6(3)
O(32')-Mo(1)-O(15)	81.7(3)
O(33')-Mo(1)-O(32')	81.8(3)
O(33')-Mo(1)-O(15)	82.4(3)
O(19)-Mo(1)-O(32')	86.1(3)
O(20)-Mo(1)-O(33')	88.1(3)
O(21)-Mo(1)-O(33')	96.0(4)
O(20)-Mo(1)-O(19)	97.2(4)
O(21)-Mo(1)-O(32')	97.3(4)
O(21)-Mo(1)-O(20)	102.2(4)
O(21)-Mo(1)-O(19)	103.1(4)
Angle Variance (σ^2)	**85.3**
Distortion Index	**0.091**

Table 5.6.6 – Crystallographically-determined bond angles for the molybdenum centre in the {$Mn_{11}Mo_2$} unit in 31, along with distortion parameters.

The manganese centres in the {$Mn_{11}Mo_2$} largely display relatively undistorted octahedral coordination environments (Table 5.7.5). Vales of σ^2_{oct} are in the 0-40 range and DI values in the 0.030-0.060 range. The central Mn(4) is an exception to this, displaying significantly higher σ^2_{oct} and DI values (153.3 and 0.130, respectively).

The molybdenum centre also displays a mildly distorted coordination environment, with σ^2_{oct} and DI values of 85.3 and 0.091, respectively (Table 5.7.6).

σ^2_{oct} and DI are defined in the same way as previously.[44–47]

Phosphonate Binding Modes

The structure of **31** contains 9 crystallographically distinct phosphonate ligands.

Four of these (P(1) to P(4)) are associated with the $\{Mn_6\}$ cation. These all display equivalent coordination modes, coordinating to three distinct manganese centres in a $\eta^1{:}\eta^1{:}\eta^1{:}\mu_3$ binding mode (Figure 5.6.12).

The remaining five are associated with the $\{Mn_{11}Mo_2\}$ anion. P(5) connects the central $\{Mn_7\}$ layer to the dinuclear unit (Mn(8)) in a $\eta^1{:}\eta^1{:}\eta^1{:}\mu_3$ binding mode, coordinating through O(27), O(18) and O(17). P(8), P(5') and P(8') coordinate in an equivalent fashion (Figure 5.7.13). P(6) connects the $\{Mn_7\}$ layer, the dinuclear unit and the isolate molybdenum centre. P(6) coordinates in a $\eta^1{:}\eta^1{:}\eta^2{:}\mu_4$ binding mode through O(16) (bidentate, supporting the $\{Mn_7\}$ layer), O(28) (monodentate, supporting the dinuclear unit Mn(8)) and O(33) (monodentate, supporting the molybdenum centre. P(7), P(6') and P(7') coordinate in an equivalent fashion. Finally, P(9) supports both centres in the dinuclear unit, and connects this unit to the central $\{Mn_7\}$ layer. P(9) coordinates in a monodentate fashion through O(25) and O(26) to the dinuclear unit metal centres Mn(9) and Mn (8), respectively. P(9) further supports the $\{Mn_7\}$ unit in a bidentate fashion through O(34), which coordinates to Mn(7) and Mn(6). P(9') coordinates in an equivalent fashion.

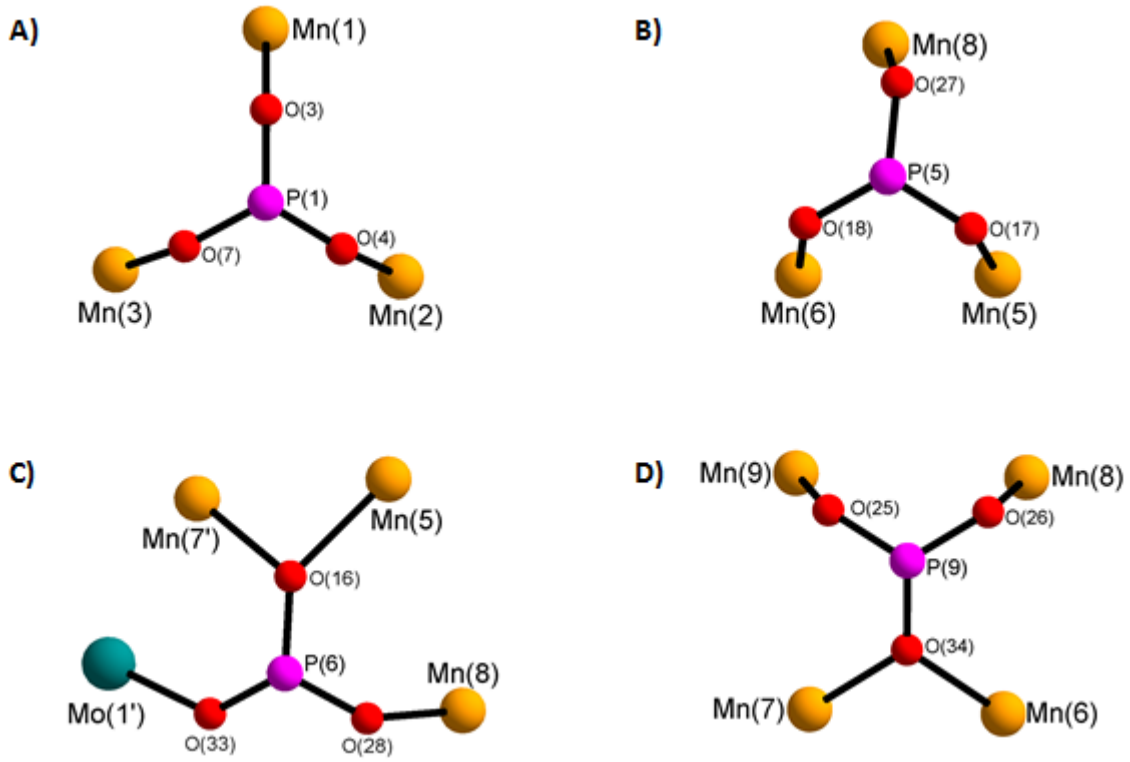

Figure 5.6.12 – The phosphonate binding modes in 31. Colour Scheme: Mo teal, Mn orange, P pink, O red. *Tert*-butyl groups are removed for clarity.

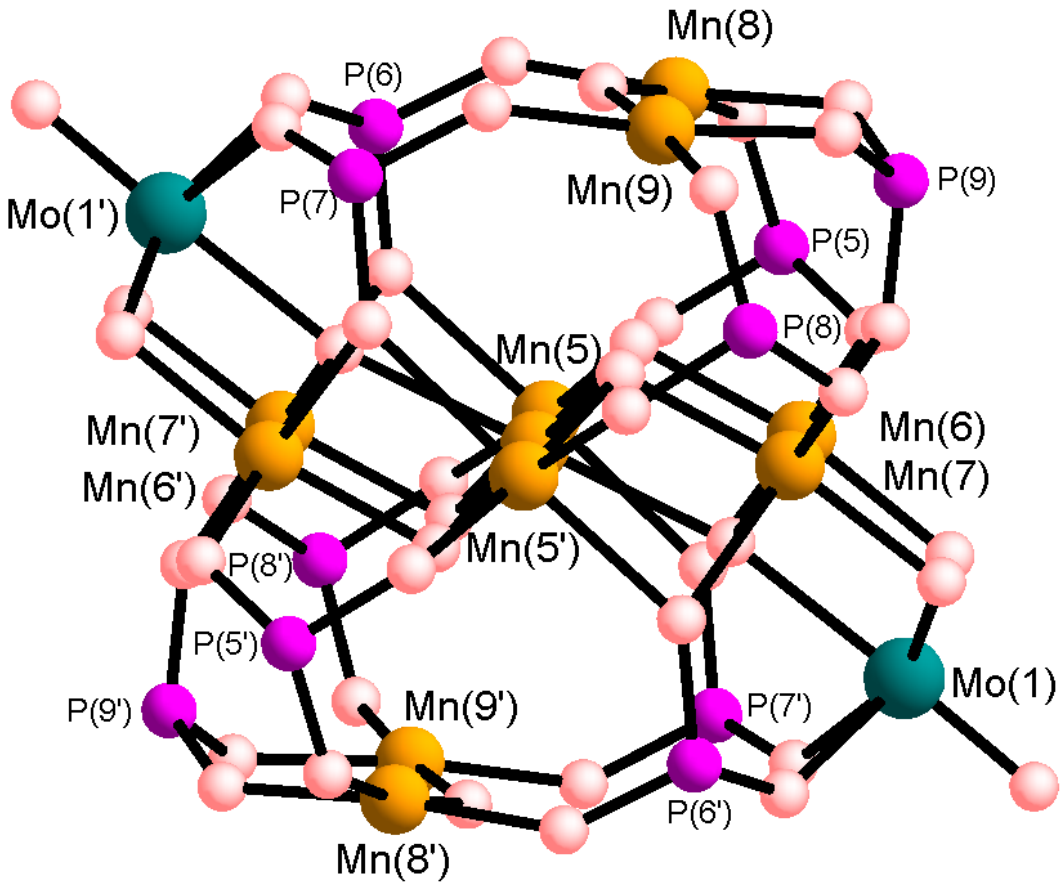

Figure 5.6.13 – The phosphonate binding modes in the {$Mn_{11}Mo_2$} anion in 31. Colour Scheme: Mo teal, Mn orange, P pink, O red. *Tert*-butyl groups and pyridine ligands are removed for clarity.

In combination, the ten phosphonate ligands in the {$Mn_{11}Mo_2$} anion in **31** all connect the middle {Mn_7} layer to either the manganese or molybdenum metal centres in the top or bottom layers (Figure 5.6.13).

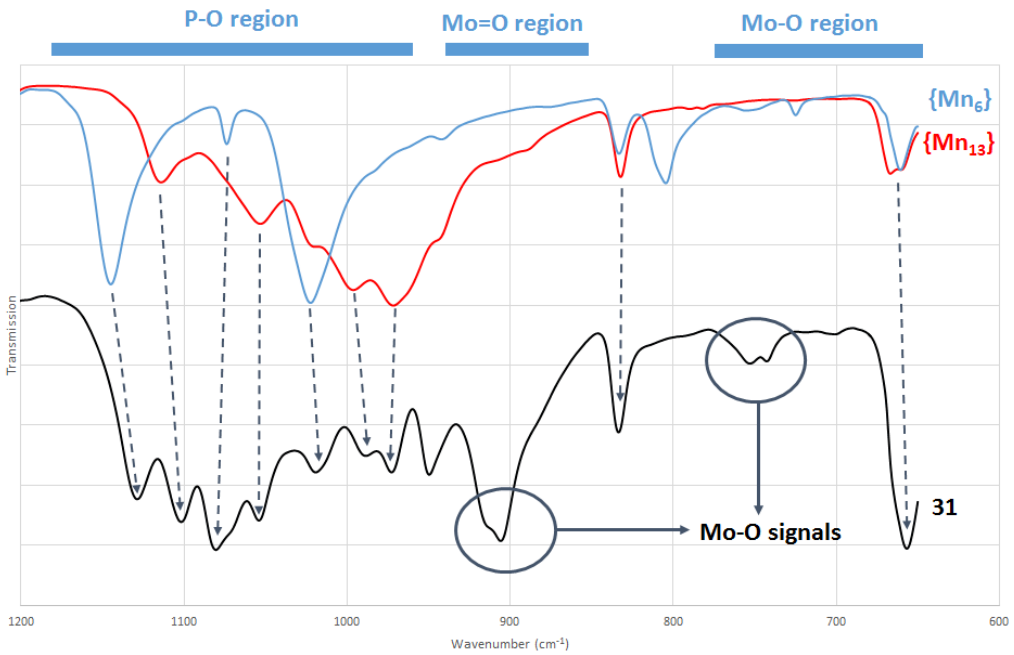

Figure 5.6.14 – Comparison of the IR spectrum for 31•4.5(MeCN) (black) with the IR spectra for the previously reported {Mn_6} (blue) and {Mn_{13}} (red) compounds.[63,64]

IR spectroscopy of compound **31** is consistent with the structure as described above. The P-O region is quite crowded, which is consistent with the multiple phosphonate coordination modes (Figure 5.6.14). Comparison of the spectrum of **31** with the previously reported {Mn_6} and {Mn_{13}} allows these signals to be assigned as arising from either the {Mn_6} cation or the {$Mn_{11}Mo_2$} anion.[63,64] As expected, additional signals arise in **31** which are assigned to the molybdenum-*oxo* bonds – the signal at 905 cm^{-1} is assigned to the terminal Mo=O bond and the signal at 742 cm^{-1} is assigned to the bridging Mo-O bonds (based on assignments by Kwak *et al.*, *c.f.* Table 2.4.1).[76]

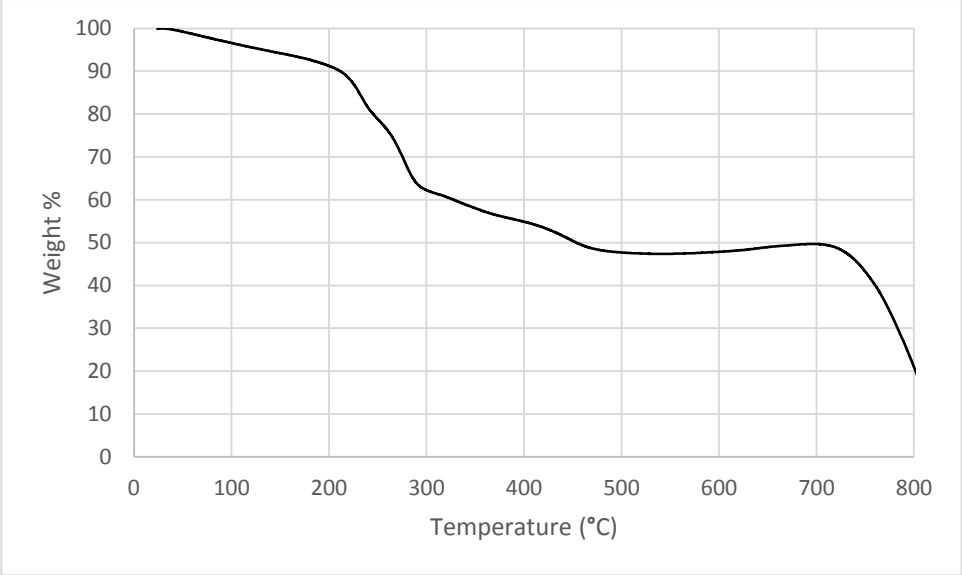

Figure 5.6.16 – TGA for compound 31•4.5(MeCN).

The TGA of compound **31**•4.5(MeCN) is presented in Figure 5.6.15. The weight loss up to 100 °C is consistent with the loss of 4.5 acetonitrile molecules per formula unit (expected 96.2%, observed 96.3%). Further heating to 250 °C is consistent with the loss of a further 10 bound pyridine ligands (expected 79.8%, observed 79.9%).

5.7) Modifications of compound 31

Having isolated and characterised compound **31**, we decided to investigate modifications to the compound. We were interested in retaining the $\{Mn_{11}Mo_2\}$ cluster, as it represents an intriguing analogue to the previously reported $\{Mn_{13}\}$ compound. Therefore, we set out to generate the $\{Mn_{11}Mo_2\}$ cluster with different cationic species balancing the charge.

To this end, the reaction procedure which generated **31** was repeated, replacing the manganese (II) chloride with other manganese (II) halide salts. The idea was to modify the characteristics of the $\{Mn_6\}$ cation while retaining the characteristics of the $\{Mn_{11}Mo_2\}$ cluster. However, the fluoride and iodide analogues of the reaction did not produce phase-pure products.

However, when manganese (II) bromide combined with potassium permanganate, Lindqvist hexamolybdate and *tert*-butylphosphonic acid were combined in acetonitrile, brown crystals were obtained from the reaction mixture after two days. These crystals contained $[Br\subset Mn^{III}_6(t\text{BuPO}_3)_8(py)_6][Mo^{VI}_2Mn^{III}_{11}O_2(\mu\text{-O})_4(\mu_3\text{-O})_4(\mu_4\text{-O})_2(\mu\text{-OH})_2(t\text{BuPO}_3)_{10}(py)_4]$, **32**, along with 4.5 acetonitrile molecules per formula unit.

This compound is analogous to compound **31**, but with a bromide-centred $\{Mn_6\}$ cation instead of a chloride-centred $\{Mn_6\}$ cation.

The crystals were found to possess the same unit cell as **31•4.5(MeCN)**, forming in the monoclinic crystal system with cell parameters a = 24.96 Å, b = 16.77 Å, c = 26.38 Å and β = 112.09°. Therefore we can assume similar solid-state packing arrangements, *etc.* Supplemental characterisation confirms the identity of compound **32** (Figure 5.7.1).

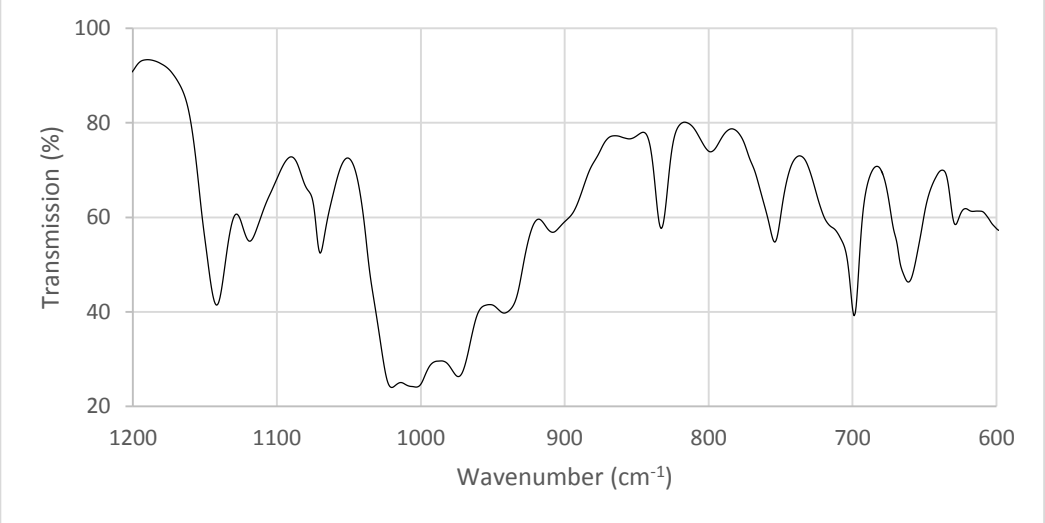

Figure 5.7.1 – IR spectrum for compound 32•4.5(MeCN).

While **32** demonstrates that the structure of **31** can be modified, we were particularly interested in investigating the catalytic properties of the $\{Mn_{11}Mo_2\}$ cluster. This cluster represents an intriguing analogue to the previously reported $\{Mn_{13}\}$ compound, and therefore comparisons of their reactivity could be enlightening. However, **31** and **32** both represent challenges to the catalytic study of the $\{Mn_{11}Mo_2\}$ cluster, as any reactivity from the $\{Mn_6\}$ cation would have to be disentangled from the reactivity of **31** or **32**.

To this end, the synthesis of **31** and **32** was repeated but with all halide ions replaced by nitrate ions. The principle was that the $\{Mn_6\}$ cation would be unable to form without a central templating halide species. Excess tetrabutylammonium hexafluorophosphate was additionally added to the system, to promote the formation of the tetrabutylammonium salt.

An amorphous brown powder was produced. IR analysis indicates that this solid contained $[TBA][Mo^{VI}_2Mn^{III}_{11}O_2(\mu\text{-}O)_4(\mu_3\text{-}O)_4(\mu_4\text{-}O)_2(\mu\text{-}OH)_2(t\text{BuPO}_3)_{10}(py)_4]$, **33**. This compound represents the tetrabutylammonium salt of the $\{Mn_{11}Mo_2\}$ species (Figure 5.7.2). IR signals at 1144 cm^{-1} and 1021 cm^{-1} associated with the $\{Mn_6\}$ cation have disappeared (*c.f.* Figure 5.6.14) and TGA indicates that this powder also contains 1.5 constituent solvent molecules per formula unit (Expected 97.5%, observed 97.4%, Figure 5.8.3).

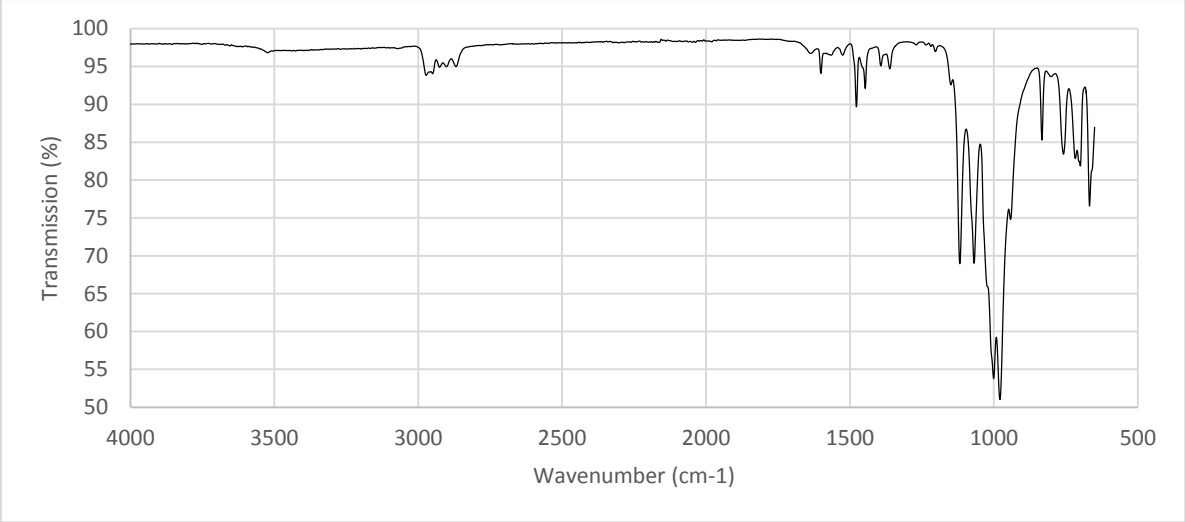

Figure 5.7.2 – IR spectrum for compound 33•1.5(MeCN).

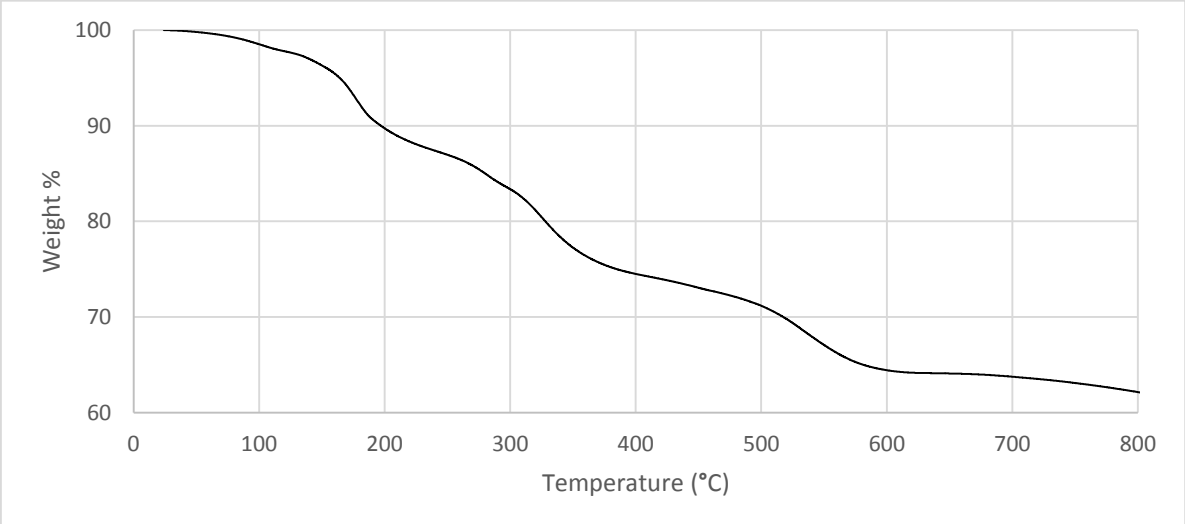

Figure 5.7.3 – TGA for compound 33•1.5(MeCN).

5.8) Water Oxidation Catalysis by 33

Compound **33** represented an intriguing synthetic target as the $\{Mn_{11}Mo_2\}$ cluster entity bares strong similarity to the previously reported $\{Mn_{13}\}$ cluster, but with two important differences – two of the labile ligand binding sites have been effectively blocked off by terminal *oxo*- ligands, and the overall charge of the cluster is now anionic instead of cationic as before (*c.f.* Figure 5.6.11). Therefore, we set out to compare the catalytic activity of **33** with respect to water oxidation, and to compare it to the $\{Mn_{13}\}$ analogue.[64]

A dried sample of **33** was tested as a catalyst for photochemical water oxidation in the presence of a sacrificial oxidant. A 6.2 nM solution of **33** in a phosphate buffer at *p*H = 7 was combined in solution with a ruthenium *tris*(bipyridine) photosensitiser and an excess of sodium persulfate, a sacrificial electron acceptor. The solution was placed in a sealed container, protected from ambient light and allowed to come to thermal equilibrium with a water bath (25 °C). The solution was subsequently irradiated with a blue LED light ($\lambda = 470$ nm, incident power estimated as 9.6 mW/cm^2). Oxygen concentration was monitored using a Clarke electrode.

Oxygen evolution was observed immediately (Figure 5.8.1), plateauing after about 100 seconds with a turnover number (TON) of about 14 (*i.e.* 14 molecules of oxygen were produced for each molecule of catalyst present).

Interestingly, the $\{Mn_{13}\}$ analogue, when tested under equivalent conditions, demonstrated similar behaviour, but with a TON of about 20, indicating that the $\{Mn_{13}\}$ analogue may be more catalytically active than the $\{Mn_{11}Mo_2\}$ analogue.

The reason for this difference is not yet completely clear. We hypothesise that since the time required for the two catalysts to deactivate is similar (*c.* 100 s), the two compounds may undergo similar deactivation pathways with similar kinetics. The difference in activity over this time might therefore be simply attributed to the fact that one potential water binding site is blocked off by an *oxo*- ligand on the $\{Mn_{11}Mo_2\}$ species, rendering it less active over the course of the measurement. However, more detailed evidence is required to confirm or refute this hypothesis.

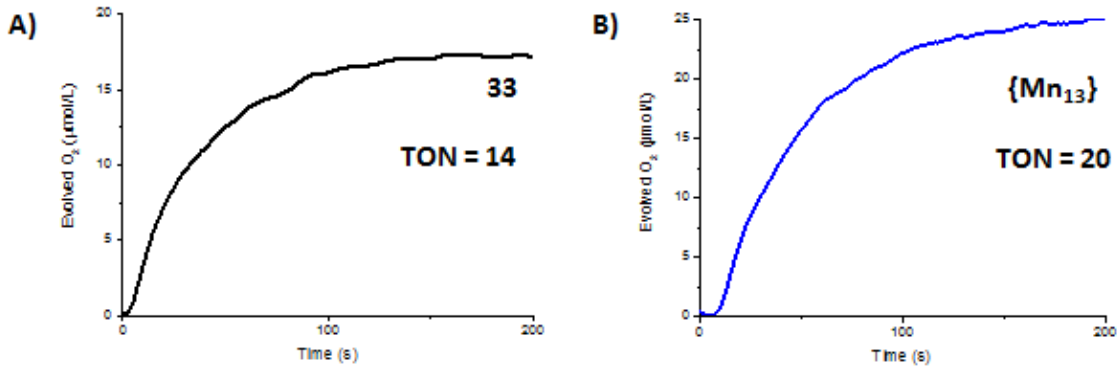

Figure 5.8.1 – A) Photochemical oxygen evolution by 33. B) Photochemical oxygen evolution by $\{Mn_{13}\}$.[64]

The catalysis data presented in Figure 5.9.1 is still a relatively preliminary result. As noted in Chapter 1, identification of the active catalyst in water oxidation reactions is not always trivial. Further studies are required to demonstrate if the proposed compounds are indeed the true catalytic species, or if decomposition to an active catalytic species in solution can be observed. More detailed kinetic studies would also be valuable for elucidation of the catalytic mechanism. Further studies of this apparent catalytic behaviour will be undertaken.

5.9) Conclusions

In conclusion, this chapter demonstrated the extension of the assembly-disassembly-reassembly methodology to manganese-molybdenum mixed-metal compounds.

The disassembly of the Lindqvist hexamolybdate followed by reassembly in the presence of manganese (III) generated a mixed-metal hybrid POM, $[TBA]_2[Mo^{VI}_{10}Mn^{II}_6O_{12}(\mu\text{-}O)_{14}(\mu_3\text{-}O)_4(t\text{BuPO}_3)_6(MeCOO)_2(py)_4(H_2O)_6]$, **26**. This compound was structurally characterised to be analogous to the cobalt compounds discussed in the previous chapter, **5**-**25**. The compound contains two $\{Mo_5\}$ units capping a central $\{Mn_6\}$ unit in a sandwich motif. The $\{Mn_6\}$ core unit can be further subdivided into two sets of $\{Mn_2\}$ dimers and two isolated Mn centres. Phosphonate templating effects and intramolecular hydrogen bonding probably play a similar role in stabilising the structure as they did in the cobalt examples (*c.f.* Figure 4.9.1).

The ligand substitution procedures developed for the cobalt analogues can also be applied to **26**, generating pyridyl- and phosphonate-substituted analogues $[TBA]_2[Mo^{VI}_{10}Mn^{II}_6O_{12}(\mu\text{-}O)_{14}(\mu_3\text{-}O)_4(t\text{BuPO}_3)_6(MeCOO)_2(MeOH)_4(H_2O)_6]$, **27**, and $[TBA]_2[Mo^{VI}_{10}Mn^{II}_6O_{12}(\mu\text{-}O)_{14}(\mu_3\text{-}O)_4(Ad\text{PO}_3)_6(MeCOO)_2(py)_4(H_2O)_6]$, **28**.

Intriguingly, the reaction system was demonstrated to display significant C-C bond cleavage ability. Some unidentified precursor to **26** is capable of cleaving acetylacetonate-type ligand species to generate carboxylate ligands. Atmospheric oxygen appears to play some role in this system, possibly as an oxygen source. This feature of the reaction system was exploited to generate a carboxylate-substituted analogue of **26**, $[TBA]_2[Mo^{VI}_{10}Mn^{II}_6O_{12}(\mu\text{-}O)_{14}(\mu_3\text{-}O)_4(t\text{BuPO}_3)_6(t\text{BuCOO})_2(MeOH)_4(H_2O)_6]$, **29**.

A polymer analogue of this $\{Mo_{10}Mn_6\}$ sandwich motif could also be obtained by incorporating PDA ligands to generate $[TBA]_2[Mo^{VI}_{10}Mn^{II}_6O_{12}(\mu\text{-}O)_{14}(\mu_3\text{-}O)_4(t\text{BuPO}_3)_6(PDA)(py)_4(H_2O)_6]$, **30**. This polymer compound bears significant similarity to the cobalt analogue, compound **25**.

Modification of this reaction system produced a series of compounds not based on the $\{Mo_{10}Mn_6\}$ sandwich motif. $[Cl\subset Mn^{III}_6(t\text{BuPO}_3)_8(py)_6][Mo^{VI}_2Mn^{III}_{11}O_2(\mu\text{-}O)_4(\mu_3\text{-}O)_4(\mu_4\text{-}O)_2(\mu\text{-}OH)_2(t\text{BuPO}_3)_{10}(py)_4]$, **31**, is a compound of two manganese-containing cluster units, both of which are supported by phosphonate and pyridine ligands. The cationic $\{Mn_6\}$ entity is a chloride-centred octahedron of manganese (III) ions, with each face of the octahedron capped by a *tert*-butylphosphonate ligand, and each vertex occupied by a pyridine ligand. This cation has been previously reported.[63] The anionic $\{Mn_{11}Mo_2\}$ cluster is a mixed-metal hybrid species, which is analogous to a previously reported $\{Mn_{13}\}$ compound.[64] This cluster consists of a central $\{Mn_7\}$ *oxo*-layer, which is connected to two dinuclear manganese units and two isolated molybdenum centres by bridging *oxo*- and phosphonate ligands.

The $\{Mn_6\}$ cation could be modified to form the bromide-centred analogue in $[Br\subset Mn^{III}_6(t\text{BuPO}_3)_8(py)_6][Mo^{VI}_2Mn^{III}_{11}O_2(\mu\text{-}O)_4(\mu_3\text{-}O)_4(\mu_4\text{-}O)_2(\mu\text{-}OH)_2(t\text{BuPO}_3)_{10}(py)_4]$, **32**, or replaced with tetrabutylammonium in $[TBA][Mo^{VI}_2Mn^{III}_{11}O_2(\mu\text{-}O)_4(\mu_3\text{-}O)_4(\mu_4\text{-}O)_2(\mu\text{-}OH)_2(t\text{BuPO}_3)_{10}(py)_4]$, **33**.

This last compound appears to be a competent water oxidation catalyst, photochemically oxidising water to generate oxygen with a turnover number (TON) of 14. We postulate that the activity of the $\{Mn_{11}Mo_2\}$ species is lower than that of the $\{Mn_{13}\}$ equivalent (TON = 20) because the *oxo*- groups effectively block some of the reactive sites, although further experiments are necessary to elucidate the details of this reaction.

In conclusion, a series of mixed-metal hybrid manganese-molybdenum compounds were generated using the assembly-disassembly-reassembly technique. One set of these is analogous to the cobalt compounds discussed in the previous chapter. The reaction mixture from which these compounds are generated is capable of cleaving C-C bonds in acac-type ligands, apparently through reaction with atmospheric oxygen. This effect was exploited to generate carboxylate ligands *in situ*. A second set of compounds was analogous to previously reported $\{Mn_6\}$ and $\{Mn_{13}\}$ compounds. One of these appears to be active as a photochemical water oxidation catalyst.

5.10) References

1 Z. Liu, S. Liang, X. Di and J. Zhang, *Inorg. Chem. Commun.*, 2008, **11**, 783.

2 S. I. Klokishner, M. A. Roman and O. S. Reu, *Inorg. Chem.*, 2011, **50**, 11394.

3 J. Sirirak, D. J. Harding, P. Harding, K. S. Murray, B. Moubaraki, L. Liu and S. G. Telfer, *Eur. J. Inorg. Chem.*, 2015, 2534.

4 S. Amabilino and R. J. Deeth, *Inorg. Chem.*, 2017, **56**, 2602.

5 A. M. Ako, I. J. Hewitt, V. Mereacre, R. Clérac, W. Wernsdorfer, C. E. Anson and A. K. Powell, *Angew. Chem. Int. Ed.*, 2006, **45**, 4926.

6 C. J. Milios, A. Vinslava, W. Wernsdorfer, S. Moggach, S. Parsons, S. P. Perlepes, G. Christou and E. K. Brechin, *J. Am. Chem. Soc.*, 2007, **129**, 2754.

7 R. Sessoli, D. Gatteschi, A. Caneschi and M. A. Novak, *Nature*, 1999, **365**, 141.

8 A. J. Tasiopoulos, A. Vinslava, W. Wernsdorfer, K. A. Abboud and G. Christou, *Angew. Chem. Int. Ed.*, 2004, **43**, 2117.

9 T. Katsuki, *Coord. Chem. Rev.*, 1995, **140**, 189.

10 E. M. McGarrigle and D. G. Gilheany, *Chem. Rev.*, 2005, **105**, 1564.

11 H. Dau, C. Limberg, T. Reier, M. Risch, S. Roggan and P. Strasser, *ChemCatChem*, 2010, **2**, 724.

12 M. Suga, F. Akita, K. Hirata, G. Ueno, H. Murakami, Y. Nakajima, T. Shimizu, K. Yamashita, M. Yamamoto, H. Ago and J. Shen, *Nature*, 2014, **517**, 99.

13 M. Wiechen, M. M. Najafpour, S. I. A. De and L. Spiccia, *Energy Environ. Sci.*, 2014, **7**, 2203.

14 R. Al-Oweini, A. Sartorel, B. S. Bassil, M. Natali, S. Berardi, F. Scandola, U. Kortz and M. Bonchio, *Angew. Chem. Int. Ed.*, 2014, **53**, 11182.

15 B. Schwarz, J. Forster, M. K. Goetz, D. Yucel, C. Berger, T. Jacob and C. Streb, *Angew. Chem. Int. Ed.*, 2016, **55**, 6344.

16 Y. Yang, L. Xu, G. Gao, F. Li, X. Liu and W. Guo, *Eur. J. Inorg. Chem.*, 2009, 1460.

17 Y. Yang, L. Xu, G. Gao, F. Li, X. Qu and W. Guo, *J. Mol. Struct.*, 2008, **886**, 85.

18 P. Gong, Y. Li, C. Zhai, J. Luo, X. Tian, L. Chen and J. Zhao, *CrystEngComm*, 2017, **19**, 834.

19 L. Zhang, R. Clérac, C. I. Onet, C. Healy and W. Schmitt, *Eur. J. Inorg. Chem.*, 2013, **2013**, 1654.

20 B. Hasenknopf, R. Delmont, P. Herson and P. Gouzerh, *Eur. J. Inorg. Chem.*, 2002, 1081.

21 P. R. Marcoux, B. Hasenknopf, J. Vaissermann and P. Gouzerh, *Eur. J. Inorg. Chem.*, 2003, 2406.

22 Y. Song, D. Long and L. Cronin, *Angew. Chem. Int. Ed.*, 2007, **46**, 3900.

23 Y. Song, D. Long, S. E. Kelly and L. Cronin, *Inorg. Chem.*, 2008, **47**, 9137.

24 J. Zhang, Y. Song, L. Cronin and T. Liu, *J. Am. Chem. Soc.*, 2008, **130**, 14408.

25 J. Fuchs and I. Brudgam, *Z. Naturforsch, Tl. B*, 1977, **32**, 403.

26 R. Delmont, A. Proust, F. Robert, P. Herson and P. Gouzerh, *C. R. Acad. Sci. Paris*, 2000, **3**, 147.

27 Y. Song, N. McMillan, D. Long, S. Kane, J. Malm, M. O. Riehle, C. P. Pradeep, N. Gadegaard and L. Cronin, *J. Am. Chem. Soc.*, 2009, **131**, 1340.

28 L. Xu, Y. Sun, E. Wang, E. Shen, Z. Liu, C. Hu, Y. Xing, Y. Lin and H. Jia, *New J. Chem.*, 1999, **23**, 1041.

29 M. Yuan, E. Wang, Y. Lu, Y. Li, C. Hu, N. Hu and H. Jia, *Inorg. Chem. Commun.*, 2002, **5**, 505.

30 H. Guo, X. Li and W. Weng, *Inorg. Chem. Commun.*, 2010, **13**, 909.

31 M. Zhu, J. Peng, A. Tian, H. Pang, P. Zhang, Y. Chen, D. Wang and Y. Wang, *Solid State Sci.*, 2010, **12**, 1051.

32 D. Yan, J. Fu, L. Zheng, Z. Zhang, Y. Xu, X. Zhu and D. Zhu, *CrystEngComm*, 2011, **13**, 5133.

33 W. Zhang, Y. Yang, Y. Liu, H. Zhang, G. Zhang, H. Dong, H. Hu, F. Zhao and Z. Kang, *Dalton Trans.*, 2013, **42**, 1760.

34 K. Gong, Y. Liu, W. Wang, T. Fang, C. Zhao, Z. Han and X. Zhai, *Eur. J. Inorg. Chem.*, 2015, 5351.

35 C. Zhang, H. Pang, Q. Tang and Y. Chen, *Dalton Trans.*, 2012, **41**, 9365.

36 C. Zhang, N. Huang, D. Yang, Y. Chen and H. Pang, *Solid State Sci.*, 2014, **35**, 33.

37 Y. Wang, N. Jiang, F. Li, Y. Zheng, L. Xu and M. Sun, *Dalton Trans.*, 2014, **43**, 16147.

38 B. Dong and Q. Xu, *Cryst. Growth Des.*, 2009, **9**, 2776.

39 H. An, X. Liu, H. Chen, Z. Han, H. Zhanga and Z. Chena, *CrystEngComm*, 2011, **13**, 5384.

40 X. Meng, C. Qin, X-L Wang, Z.-M. Su, B. Lib and Q.-H. Yang, *Dalton Trans.*, 2011, **40**, 9964.

41 M. Shanmugam, G. Chastanet, T. Mallah, R. Sessoli, S. J. Teat, G. A. Timco and R. E. P. Winpenny, *Chem. Eur. J.*, 2006, **12**, 8777.

42 S. Maheswaran, G. Chastanet, S. J. Teat, T. Mallah, R. Sessoli, W. Wernsdorfer and R. E. P. Winpenny, *Angew. Chem. Int. Ed.*, 2005, **44**, 5044.

43 Y. Ma, Y. Song, Y. Li and L. Zheng, *Inorg. Chem.*, 2007, **46**, 5459.

44 M. E. Fleet, *Mineral. Mag.*, 1976, **40**, 531.

45 R. M. Hazen, R. T. Downs and C. T. Prewitt, *Comp. Cryst. Chem.*, 1999.

46 M. Wildner, *Z. Krist.*, 1992, **202**, 51.

47 M. Hughes, F. Foit and E. Wright, *Can. Mineral.*, 2002, **40**, 153.

48 A. W. Addison and T. N. Rao, *J. Chem. Soc. Dalton Trans.*, 1984, 1349.

49 C. Hauser, F. Swamer and B. Ringler, *J. Am. Chem. Soc.*, 1948, **70**, 4023.

50 S. W. Ashford and K. C. Grega, *J. Org. Chem.*, 2001, **66**, 1523.

51 P. Saikia, S. Gogoi and R. C. Boruah, *J. Org. Chem.*, 2015, **80**, 6885.

52 Y. Yuan, X. Ji and D. Zhao, *Eur. J. Org. Chem.*, 2010, 5274.

53 Y. Zhang, J. Jiao and R. a Flowers, *J. Org. Chem.*, 2006, **71**, 4516.

54 L. Souillart and N. Cramer, *Chem. Rev.*, 2015, **115**, 9410.

55 Z. Nairoukh, M. Cormier and I. Marek, *Nat. Rev. Chem.*, 2017, **1**, 35.

56 G. Fumagalli, S. Stanton and J. F. Bower, *Chem. Rev.*, 2017, **117**, 9404.

57 B. C. T. Walsh and Y. J. Chen, *Angew. Chem. Int. Ed.*, 1988, **27**, 333.

58 G. Brink, I. W. C. E. Arends and R. A. Sheldon, *Chem. Rev.*, 2004, **104**, 4105.

59 O. Fukuda, S. Sakaguchi and Y. Ishii, *Tetrahedron Lett.*, 2001, **42**, 3479.

60 F. Minisci, F. Recupero, F. Fontana, H.-R. Bjorsvik and L. Liguori, *Synlett*, 2002, **4**, 610.

61 F. Minisci, F. Recupero, G. Franco and M. Lucarini, *J. Mol. Cat.*, 2003, **205**, 63.

62 V. R. Chumbhale, S. A. Paradhy, M. Anilkumar, S. T. Kadam and V. V Bokade, *Chemical Engineering Research and Design*, 2005, **83**, 75.

63 L. Zhang, B. Marzec, R. Clérac, Y. Chen, H. Zhang and W. Schmitt, *Chem. Commun.*, 2013, **108**, 66.

64 L. Zhang, R. Clérac, C. I. Onet, M. Venkatesan, P. Heijboer and W. Schmitt, *Chem. Eur. J.*, 2012, **18**, 13984.

65 A. R. E. Baikie, M. B. Hursthouse, L. New, P. Thornton and R. G. White, *J. Chem. Soc. Chem. Commun.*, 1980, 684.

66 R. A. Reynolds and D. Coucouvanis, *J. Am. Chem. Soc.*, 1998, **120**, 209.

67 M. Tabatabaee, H. Mahmoodikhah, G. Ahadiat, M. Dusek and M. Pojarova, *Monatsh. Chem.*, 2013, **144**, 621.

68 Y. Miao, S. Li, J. Liu, F. Guo and M. Tong, *Inorg. Chem. Commun.*, 2015, **52**, 77.

69 J. C. Axelson, M. I. Gonzalez, K. R. Meihaus, C. J. Chang and J. R. Long, *Inorg. Chem.*, 2016, **55**, 7527.

70 L. Zhang, T. Chimamkpam, C. I. Onet, N. Zhu, R. Clérac and W. Schmitt, *Dalton Trans.*, 2016, **45**, 17705.

71 L. Zhang, R. Clérac, P. Heijboer and W. Schmitt, *Angew. Chem. Int. Ed.*, 2012, **51**, 3007.

72 V. Viossat, P. Lemoine, E. Dayan, N. Dung and B. Viossat, *Polyhedron*, 2003, **22**, 1461.

73 E. Fursova, V. Ovcharenko, K. Nosova, G. Romanenko and V. Ikorskii, *Polyhedron*, 2005, **24**, 2084.

74 N. Shaikh, S. Goswami, A. Panja, H. Sun, F. Pan, S. Gao and P. Banerjee, *Inorg. Chem.*, 2005, **44**, 9714.

75 Y. Lu, W. Zhao, Y. Liu, B. Liu, X. Feng, J. Tan, X. Li and X. Yang, *J. Solid State Chem.*, 2012, **192**, 144.

76 W. Kwak, M. T. Pope and T. F. Scully, *J. Am. Chem. Soc.*, 1975, **97**, 5737.

Chapter 6

Disassembly and Reassembly of Metal-Organic Frameworks

6.1) Metal-Organic Frameworks

As discussed in the introductory chapter, extended systems such as Metal-Organic Frameworks exhibit interesting physicochemical properties which have garnered them significant attention over the past few decades. Chief among these is the tendency towards highly porous materials, which gives rise to range of host-guest applications, including separation, storage and catalysis.[1–10]

However, it was also noted in the introduction that many of these host-guest processes rely fundamentally on diffusion, which is frequently a relatively slow process.[11–13] Guest molecules diffusing either into or out of a host MOF matrix can do so over a period of multiple days in some instances (Figure 6.1.1).[11] Of course, this may be desirable depending on the intended application (*e.g.* drug delivery applications),[12–14] but in many cases fast uptake or release can be desirable.

For example, MOFs have attracted attention for potential carbon capture and storage applications. The principle is that MOFs would (ideally selectively) absorb CO_2 from waste gases, allowing it to be sequestered and stored elsewhere.[15–17] However, practical considerations would require the framework to be evacuated in a reasonable timescale at controlled intervals, so that the host matrix could be reused for further carbon capture cycles (Figure 6.1.2).[18–21] For gas-uptake systems, release of the guest molecule from the host matrix is generally achieved by applying (often very significant) temperature or pressure differences. [18–21] In a real-world scenario, applying these relatively harsh stimuli might not be a practical way to regenerate the host matrix.

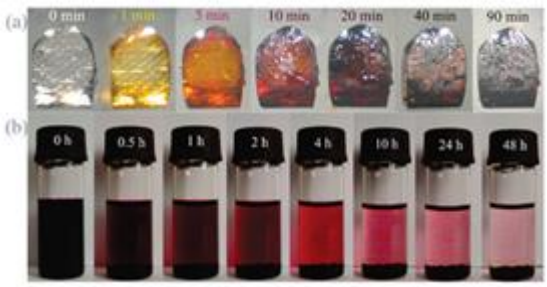

Figure 6.1.1 – An example of slow diffusion in MOF systems, showing the capture of iodine from solution over the course of 48 hours. Reproduced from reference 11.

To this end, several strategies exist to essentially modify the release behaviour of a host, allowing host matrices to be recycled (Figure 6.1.2).[22,23] The following strategies have been explored:

- Applying decreased pressure to the host MOF (typically to extract gaseous guests)[18,19]
- Applying increased pressure to the host MOF (to induce a phase change which forces guests from their host pores)[24,25]
- Heating the host MOF (effectively increasing the rate of diffusion)[26–28]
- Embedding magnetic nanoparticles into the host MOF (effectively allowing localised heating upon application of alternating magnetic fields)[29,30]
- Cation exchange (to displace guests)[31,32]
- Applying light to light-sensitive MOFs (*e.g.* MOFs containing azobenzene-type constituents, which undergo structural changes under irradiation)[33–35]

These systems all have advantages and disadvantages depending on their intended use. While they all represent promising developments in the manipulation of MOF host-guest behaviour, controllable release of guest molecules still represents somewhat of a barrier to the widespread practical application of MOFs.

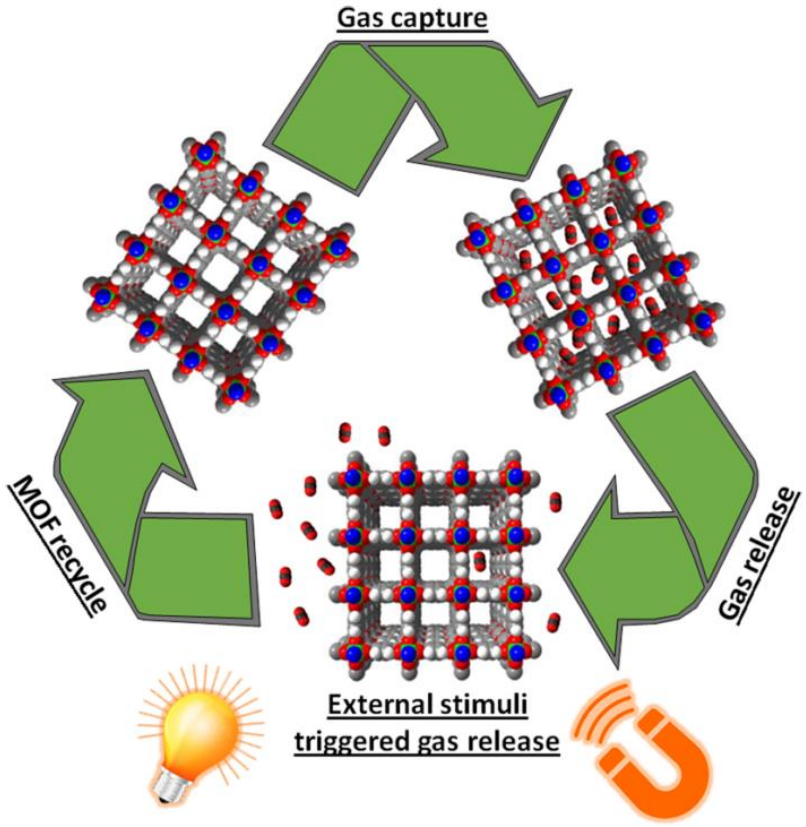

Figure 6.1.2 – An example of slow diffusion in MOF systems, showing the capture of iodine from solution over the course of 48 hours. Reproduced from reference 22.

Therefore, we were interested in exploring methods for fast, controllable, and reliable uptake and release of guest molecules in MOF-type host matrices. In light of our work on disassembly in POM systems, we considered applying some of the disassembly-reassembly concepts to this challenge. We hypothesised that by breaking apart the bonds holding a MOF together (*i.e.* disassembling the MOF), release of the guest molecules could be achieved. In principle this could be achieved in a stimulus-responsive way, so that disassembly (and concomitant release of guest molecules) could be achieved in a controllable manner.

This methodology has some precedent in the literature. One example exploited the addition of chelating ligands to the system in order to trigger partial decomposition of an iron-terephthalate MOF, MIL88(Fe), in order to release a guest molecule.[36] The MOF was loaded with an anti-biofilm agent, 5-(4-chlorophenyl)-N-(2-isobutyl)-2-aminoimidazole. Addition of iron-chelating ligands such as citrate would result in partial degradation of the MOF, and consequently the release of the anti-biofilm agent.

Neatly, it was demonstrated that iron-scavenging microorganisms would achieve the same effect, effectively triggering the release of the anti-biofilm agent whenever biofilms began to form (Figure 6.1.3).[36]

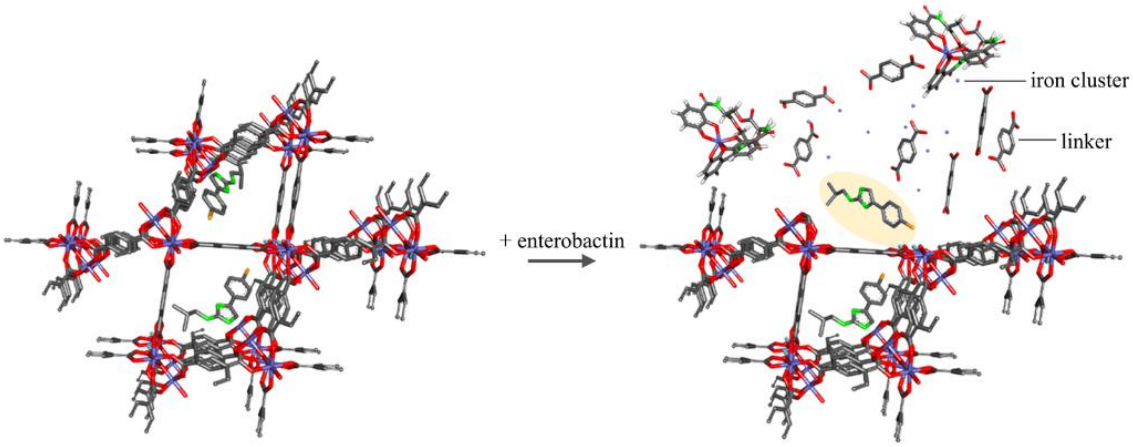

Figure 6.1.3 – Disassembly of an iron MOF, MIL88(Fe), can be triggered by naturally occurring iron-scavenging microorganisms, resulting in release of an anti-biofilm agent. Reproduced from reference 36.

This report clearly demonstrates that partial MOF disassembly can be beneficial, depending on the intended application. In this example, MOF disassembly was relatively slow (occurring over *c.* 24 hours), and the MOF was only partly disassembled at any given step.[36] This was beneficial for the desired application (gradual release on a similar timescale to biofilm formation), but many applications might require fast release (*e.g.* sensing applications).

In a sensing example where fast release of a guest was desirable, an adenine-zinc MOF, $[Zn_8(adeninate)_4(terephthalate)_6O]$,[31,32] was loaded with ruthenium (II) *tris*(bipyridine) cation guests.[37] Subsequent addition of mercury ions to the system resulted in displacement of photosensitiser cations, resulting in localised charge-imbalances that rendered the framework unstable.[37] Addition of mercury was demonstrated to completely disintegrate the parent MOF, not simply release the photosensitiser through cation exchange. This disassembly was exploited as a visible sensor for the presence of mercury ions, as the disassembly of the framework released the red-orange ruthenium (II) *tris*(bipyridine) cations into solution (Figure 6.1.4).[37]

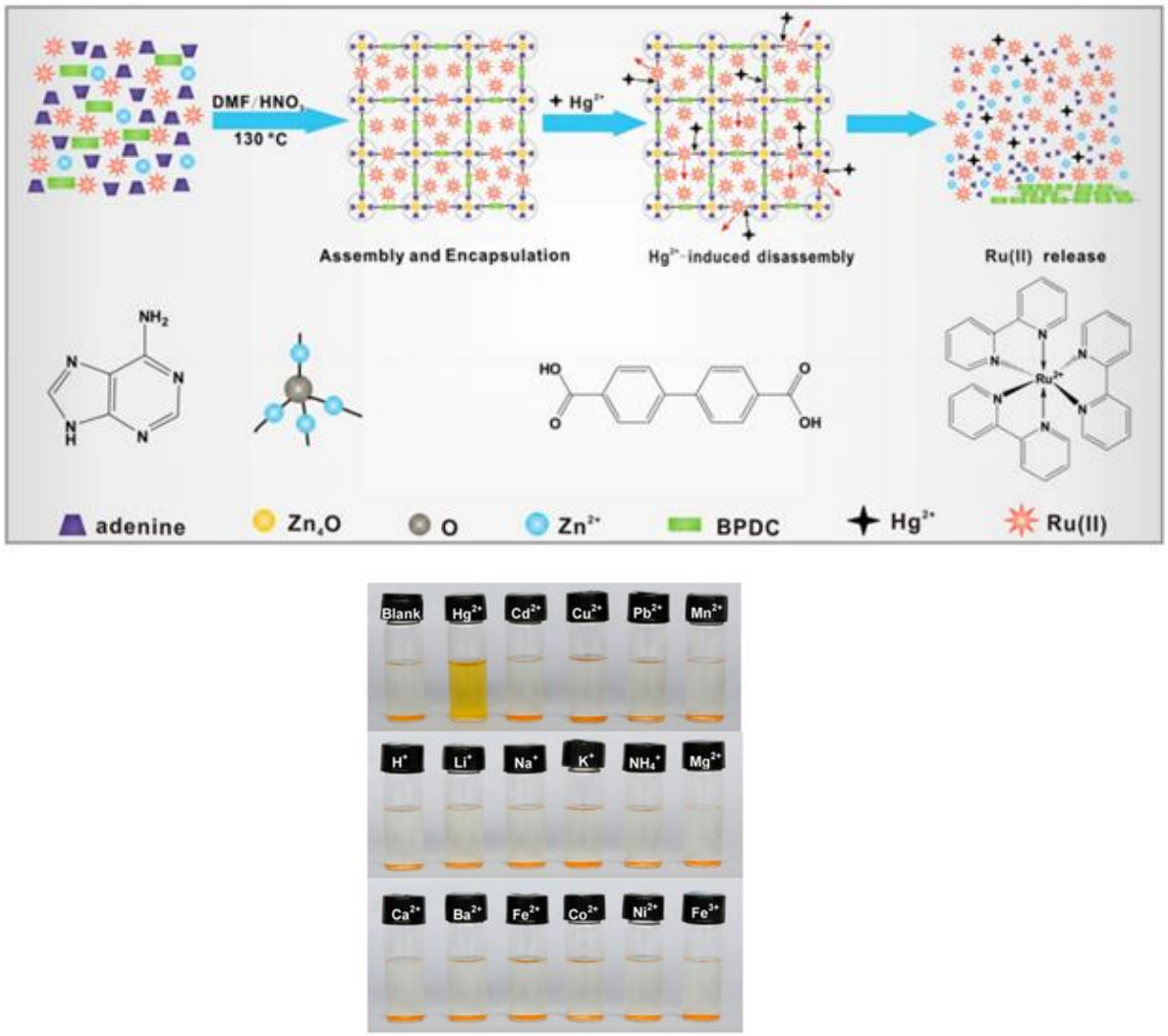

Figure 6.1.4 – A) Disassembly of a zinc MOF $[Zn_8(adeninate)_4(terephthalate)_6O]$ can be triggered by the addition of mercury ions Hg^{2+}, resulting in release of a ruthenium dye. B) This stimulus-responsive disassembly was exploited as a selective sensor for Hg^{2+} ions. Reproduced from reference 37.

In many scenarios, disassembly of the MOF would only be of practical use if the MOF could be subsequently reassembled. In the previous two examples, disassembly-induced release of guest molecules was beneficial, but reassembly was not demonstrated.[36,37] Reassembly would have allowed the MOF to be recovered, and subsequently reused for further practical cycles.

Disassembly of a MOF followed by reassembly also has precedent in the literature. In one example, the archetypal framework MOF-5[38–40] was disassembled by reaction with water (a known decomposition pathway of MOF-5)[41,42] to generate a non-porous material. However, the constituent parts could subsequently be reassembled into a pristine MOF (Figure 6.1.5) by the addition of strong acids (to force the constituent components into solution) followed by strong bases (to deprotonate the linker molecules and allow them to re-bind as ligand species).[43] The physicochemical properties of the MOF (gas uptake, surface area, diffraction pattern, *etc.*) were unaffected by the disassembly-reassembly process, although modification of the reaction conditions allowed control over the morphology of the crystals.[43] This paper was concerned with the recovery of degraded MOF samples, and so only examined the effects of disassembly and reassembly on a host matrix and did not consider the effects of disassembly on the release of guests (Figure 6.1.5).[43]

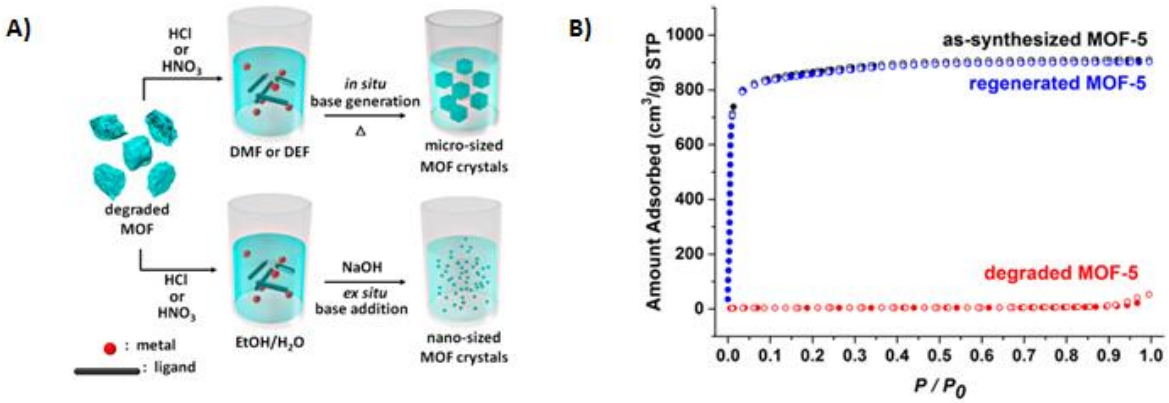

Figure 6.1.5 – A) MOF-5 can be degraded to a non-porous form, and subsequently reassembled from solution by manipulating *p*H conditions. B) The regenerated MOF samples display identical physical properties (gas uptake) as the Reproduced from reference 43.

This example demonstrates the principle of disassembly-reassembly quite well, although the conditions used are quite harsh. This somewhat limits the range of practical applications for disassembly-reassembly as a method to controllably release guest molecules. Under harsh disassembly-reassembly conditions, the guest molecule must be resilient towards chemical degradation. Harsh procedures also raise practical considerations, as circumstances may constrain what is practical or safe for a given application.

Taking these considerations into account, we set out to design a MOF-type structure which could be disassembled into its constituent parts (releasing any guest molecules in the process), and subsequently reassembled from solution, all under mild conditions. Ideally, these disassembly and reassembly steps should be stimulus-responsive.

In order to achieve this, it would be necessary to design a framework where the framework is maintained by reasonably labile bonds. We hypothesised that, in such a system, the difference in stability between the parent framework and its constituent parts would be sufficiently small that a mild external stimulus could shift the balance towards the one system or the other, as desired (Figure 6.1.6). In this way, disassembly and reassembly (along with release of guest molecules) could be achieved under mild conditions.

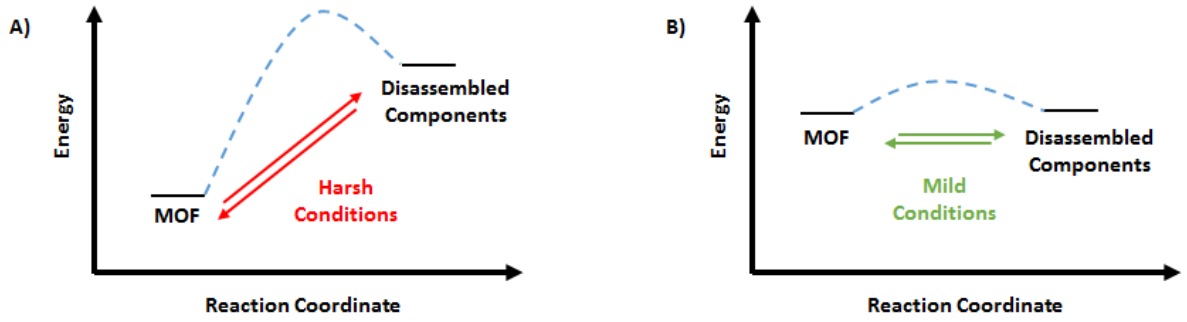

Figure 6.1.6 – Hypothetical energy diagrams for A) A strongly-bound MOF, where harsh conditions are necessary to shift between assembled and disassembled states, and B) A labile MOF which could shift between assembled and disassembled states upon application of a mild stimulus.

We reasoned that a simple ligand-exchange mechanism would generate the desired effect. If only bridging ligands are present in the system, bridging interactions should dominate and the framework material should be the dominant structure. However, if the bridging ligands were displaced by suitable terminal ligands, the system should disassemble into its constituent building blocks. Therefore, simply adding or removing a competing terminal ligand to the system should, in theory, shift the system from the (heterogeneous) parent framework to the (homogenous) building-blocks and back again, in principle indefinitely (Figure 6.1.7).

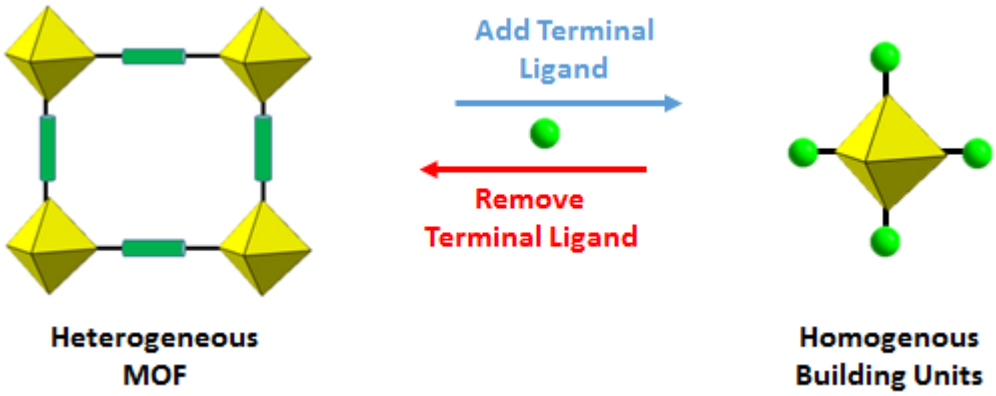

Figure 6.1.7 – Hypothetical model of the disassembly-reassembly methodology applied to MOF structures. Addition of a terminal ligand should displace the bridging ligands, promoting a disassembled MOF (homogenous building units in solution). Removal of this ligand should concurrently promote the reassembly of a MOF structure. Yellow octahedra represent MOF nodes, Green balls terminal ligands, green tubes ditopic linkers.

MOF frameworks with labile bonds are generally rare, as robust networks are generally highly prized (*e.g.* to survive the harsh, low-pressure conditions of gas sorption analysis). Therefore we set out to identify a suitable metal building unit from which a weakly-bound framework could be assembled.

The metal building unit in question would require the following characteristics:

- Ligand binding sites available in a suitable geometry that could generate a two- or three-dimensional framework. A highly symmetric building unit would be ideal.
- Weakly bound terminal ligands present on these units, such that they could be reasonably easy to displace.

The linker units should possess complementary characteristics:

- Multiple binding sites present in a geometry that would complement the geometry of the metal unit to generate stable topologies. Again, high symmetry is valuable.
- Reasonably mild ligand behaviour (for example, chelating ligands would probably be unsuitable as these would be comparatively difficult to displace).

Consideration should also be given to the guest molecule when designing a labile framework. If the framework structure is weakly-bound, care should be taken that any guest molecules should not interfere with the disassembly-reassembly process (*i.e.* a guest with significant ligand character could displace linker molecules if the linker molecules are sufficiently labile).

Re-capture of the guest molecule upon reassembly should also be considered, depending on the application. Two regimes should be considered:

- First, where the guest molecule is being released in order to free the host matrix to capture more guest molecules (*i.e.* where the intention is to reuse the host matrix, for example in CO_2 capture systems).
- Second, where the guest molecule is required for the intended application (*e.g.* the example demonstrated in Figure 6.1.3, where the guest molecule is the active sensing component. Reassembly of the parent MOF while leaving the guest molecules free in solution would not allow further cycles to be exploited in this case).

In the first regime, guest molecules should have no particular impetus to return to the host matrix upon reassembly (*i.e.* it should have more affinity for the solution in which disassembly-reassembly takes place than for the framework system). In the second regime, however, there should be some significant affinity between the guest molecule and host matrix (*e.g.* electrostatic/charge balancing interactions, hydrogen bonding, or other supramolecular interactions).

Taking all of these considerations into account, we identified the $\{Mn_6\}$ species present in compound **31**, $[Cl\subset Mn^{III}_6(t\text{BuPO}_3)_8(py)_6]^+$, to be a suitable building unit from which to construct a MOF-type framework that would be susceptible to disassembly (Figure 6.1.8).[44] The unit possesses the following beneficial characteristics:

- The unit is highly symmetric and well characterised.
- The unit possesses six terminal ligands in a simple octahedral arrangement. Combination of this octahedral arrangement with simple linear linkers should in principle generate a simple cubic framework.
- The six terminal ligands are all on the Jahn-Teller distorted (elongated) axes of their respective manganese (III) ions. Coordination bonds along these distorted axes are generally quite labile, and so the terminal ligands should be susceptible to displacement.
- The unit has been characterised with many different monodentate ligands in the terminal positions, including pyridine, picoline, methanol, water and pyrdinecarboxaldehyde, including mixtures thereof. This indicates that ligand substitution reactions at these positions are synthetically reasonable.[44]
- A one-dimensional polymer chain containing this building unit linked by 4,4'-bipyridine ligands has been previously characterised using single crystal XRD, $[Cl\subset Mn^{III}_6(t\text{BuPO}_3)_8(py)_4(bpy)]Cl$,. This synthesis used combinations of terminal and bridging ligands, but it indicates that extended structures containing this unit are synthetically achieveable.[44]
- The unit is cationic. This lends the system to applications where guest recapture would be desirable, as the framework will not reassemble without a charge-balancing anion.
- The central chloride ion can be replaced with bromide ions (as in compound **32**). This indicates that structural modifications of the unit are possible. Moreover, this chloride ion occupies the Jahn-Teller axis for all six manganese centres in the unit. Replacement of this chloride with bromide could in principle effect the lability of the terminal ligands, potentially providing a measure of synthetic control over the system.

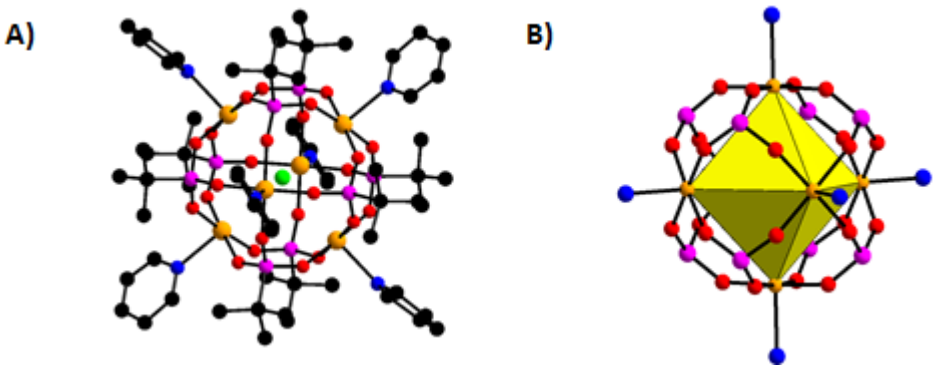

Figure 6.1.8 – The $[Cl\subset Mn^{III}_6(t\text{BuPO}_3)_8(py)_6]^+$ cation, $\{Mn_6\}$, in A) its full form and B) a reduced form, emphasising the octahedral symmetry of the pyridyl N-donors (blue). Colour Scheme: Mn orange, Cl green, P pink, O red, N blue, C black. H atoms omitted for clarity.

Therefore, we set out to generate MOF-type structures using the $\{Mn_6\}$ species and rigid linear linkers. The products resulting from these reactions will be described in the next section.

6.2) MOF Compounds from {Mn_6}

The {Mn_6} structure was previously prepared by the comproportionation of manganese (II) chloride with potassium permanganate to generate manganese (III) ions in the presence of *tert*-butylphosphonic acid and a monodentate ligand (typically a pyridyl-type ligand). 1,4-phenylenediacetic acid (PDA-H_2) was also added to the reaction mixture – it is unclear what role this plays in the reaction, as it does not form part of the final product, but it does appear to promote the formation of the {Mn_6} compound over the formation of the {Mn_{13}} compound that forms under similar conditions.[44,45]

To generate a MOF-type structure using this building unit, this reaction was simply repeated with the terminal pyridyl ligand replaced by the ditopic equivalent, 4,4'-bipyridine. This resulted in the formation of a brown solid, [Cl⊂Mn^{III}_6(*t*BuPO_3)$_8$(bpy)$_3$]Cl, **34**, where bpy represents 4,4'-bipyridine. Unfortunately, crystals suitable for analysis by XRD were not obtained, but supplemental chacterisation techniques are consistent with the assigned formula.

We postulate that this compound consists of {Mn_6} units linked together by bpy linker ligands in three dimensions to form a simple cubic network (Figure 6.2.1, *c.f.* MOF-5). In this configuration, each cubic pore should be occupied by one charge-balancing chloride ion.

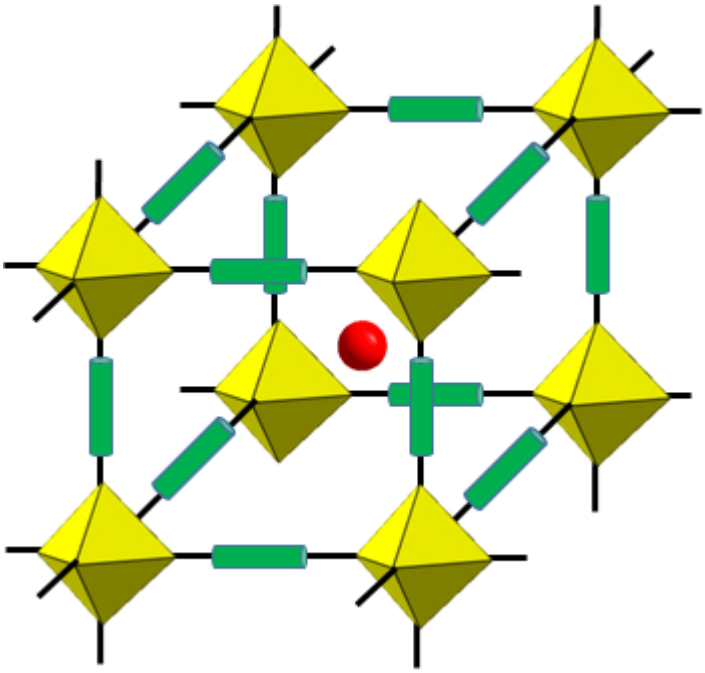

Figure 6.2.1 – Hypothesised structure of [Cl⊂Mn^{III}_6(*t*BuPO_3)$_8$(bpy)$_3$]Cl, 34. Yellow octahedra represent the {Mn_6} nodes, green rods represent the bipyridine linkers, and the red ball represents the chloride ion.

A cubic structure of this nature would be expected to be highly symmetric (*P*-43m space group). Based on crystallographic data, for the {Mn_6} cluster and for 4,4'-bipyridine ligands, the length of any given side should be approximately 17.65 Å.

By comparison with the previously-reported {Mn_6} compounds, IR spectroscopy (Figure 6.2.2) indicates that the {Mn_6} core forms and is present in **34**. It seems reasonable to conclude that if the {Mn_6} core is present that it should be linked by bipyridyl ligands, in some arrangement.

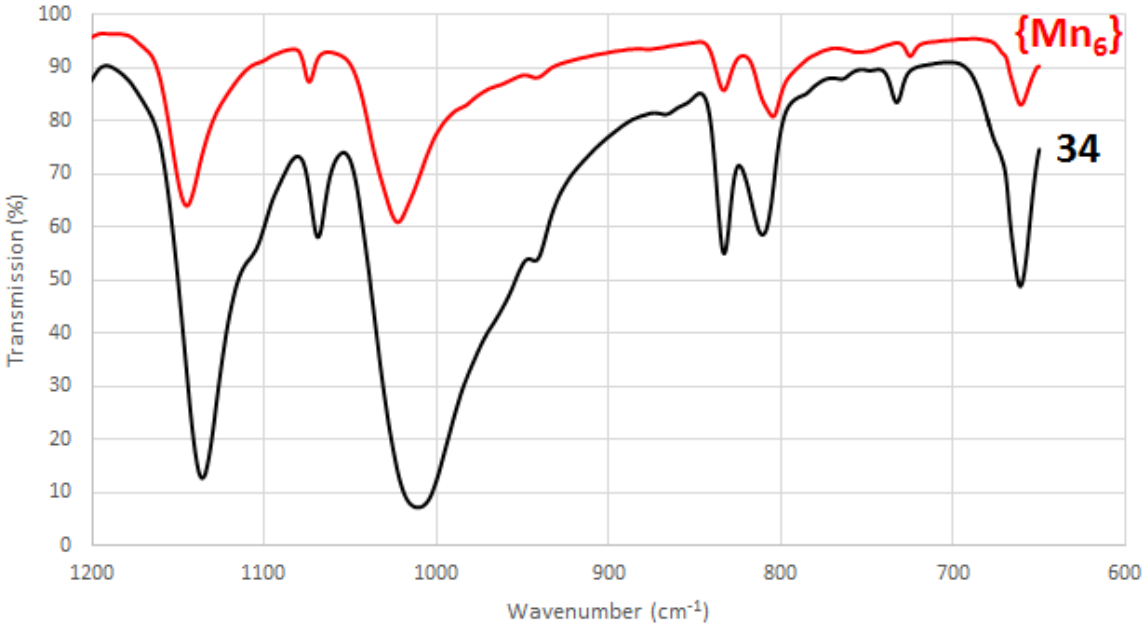

Figure 6.2.2 – Portion of the IR spectrum of compound 34, compared to that of the previously reported {Mn_6} core.[44]

Powder X-ray Diffraction (PXRD) indicates that the obtained powder is crystalline (*i.e.* locally ordered) (Figure 6.2.3). This is consistent with a locally ordered arrangement, as expected for the highly symmetric and rigid building units.

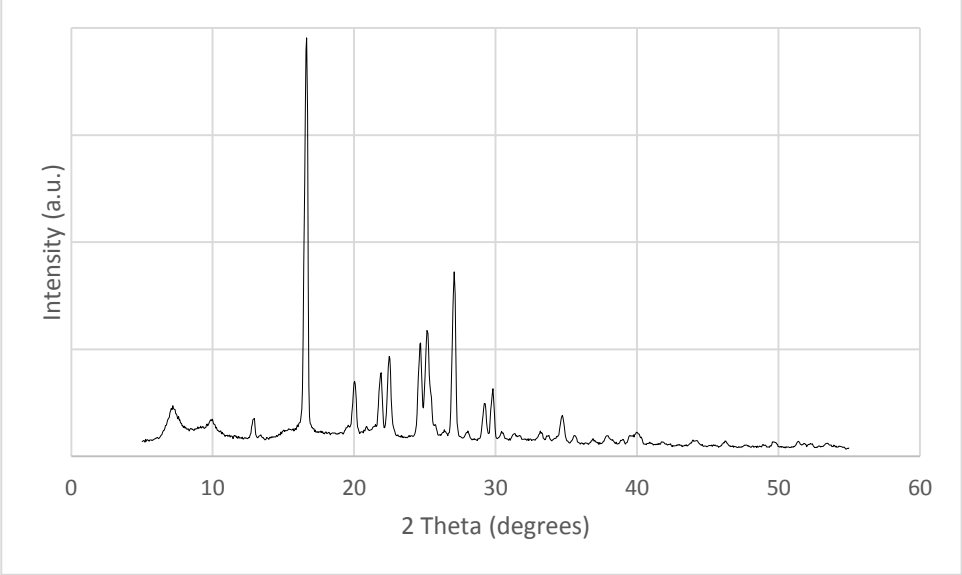

Figure 6.2.3 – PXRD spectrum of compound 34.

TGA analysis indicates that the compound does not contain any constituent solvent molecules, showing no weight loss upon heating to *c.* 140 °C (Figure 6.2.4). This may indicate the absence of accessible voids in the structure (possibly due to a combination of the bulky *tert*-butyl groups and chloride counterions, which could potentially block solvents from accessing the pores). The compound appears to be reasonably unstable compared to other MOFs, undergoing significant thermal decomposition beginning at *c.* 140 °C.

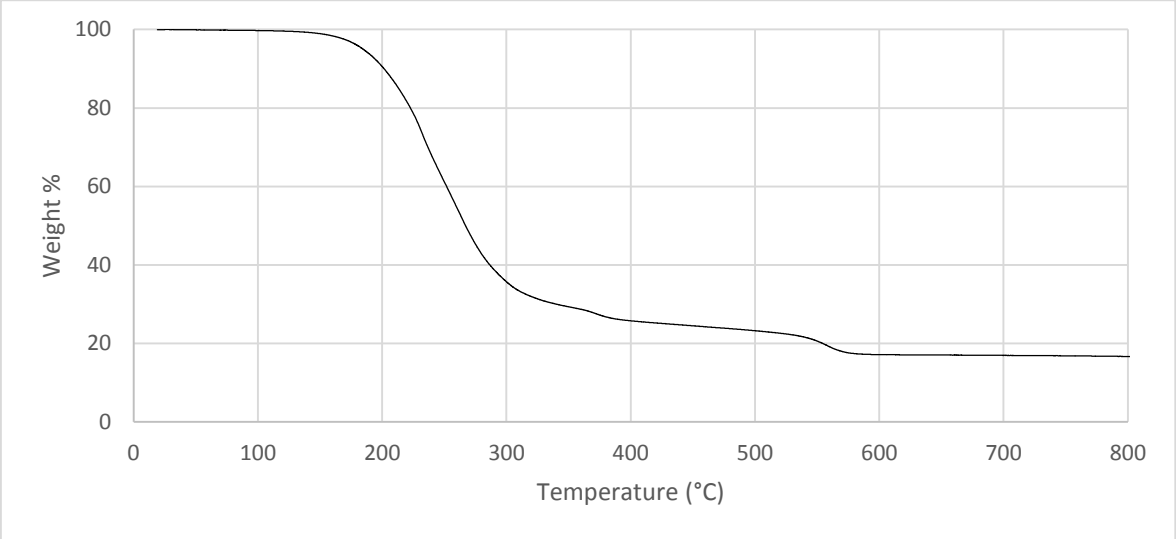

Figure 6.2.4 – TGA analysis of compound 34.

Finally, gas sorption analysis was performed (Figure 6.2.5). Unfortunately, this analysis does not show any significant porosity. This is consistent with the TGA analysis, which does not appear to display any solvent-accessible void volume. This is tentatively assigned to a combination of the bulky *tert*-butyl groups and chloride counterions occupying the otherwise-accessible void space. Gas-sorption analysis indicates a surface area of 130 m^2/g by the BET method.

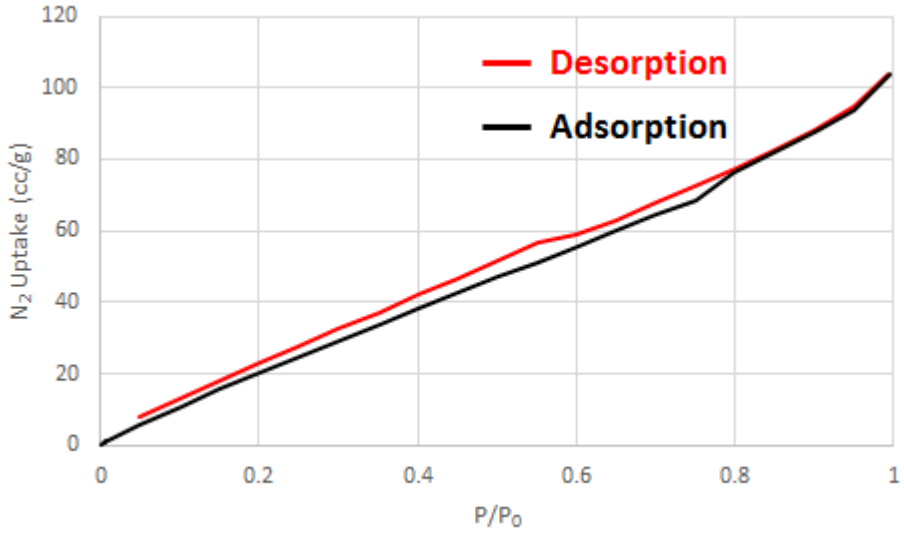

Figure 6.2.5 – Gas sorption analysis of compound 34.

Interestingly, modification of the reaction conditions to include 2/3 the amount of bpy produces a related compound, $[Cl\subset Mn^{III}_6(t\text{BuPO}_3)_8(\text{bpy})_2(H_2O)_2]Cl$, **35**. In contrast to **34**, this compound probably has a two-dimensional, sheet-like structure (Figure 6.2.6), with bpy ligands linking the $\{Mn_6\}$ building units in one plane with axial ligands occupied by water ligands. In this arrangement, the chloride counterions would probably intercalate between these sheets.

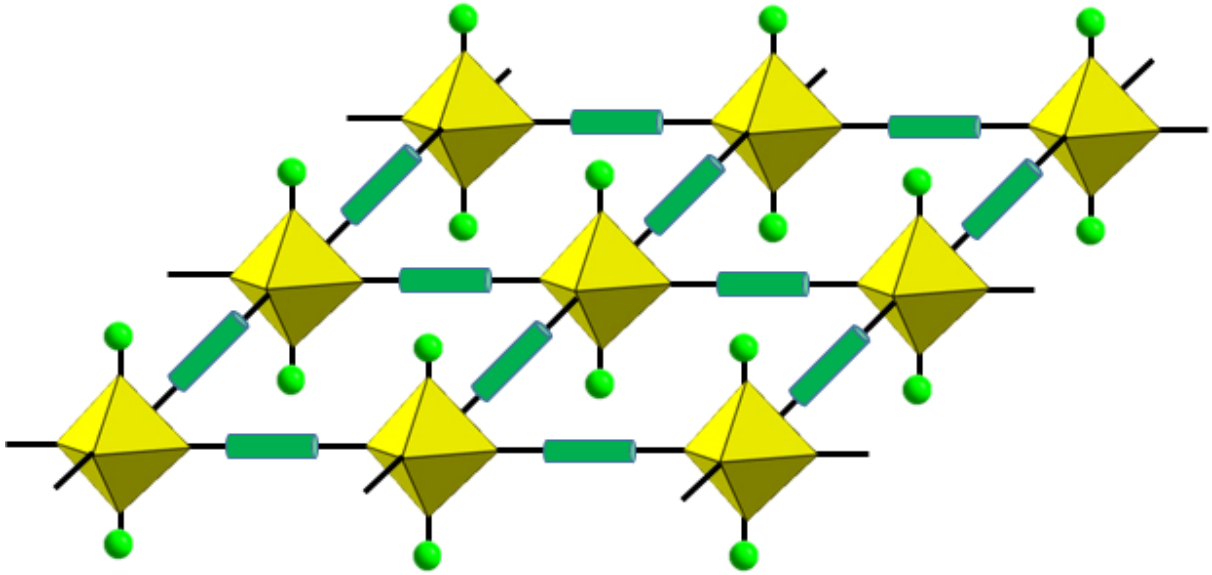

Figure 6.2.6 – Hypothesised sheet structure of compound 35. Yellow octahedra represent the $\{Mn_6\}$ nodes, green rods represent the bipyridine linkers, and the green balls represents terminal water ligands.

The water ligands in this structure are assigned as taking up *trans*- positions relative to each other on the $\{Mn_6\}$ core, with the bpy ligands all occupying the same equatorial plane on the $\{Mn_6\}$ core. This is consistent with the previously reported crystal structures of the $\{Mn_6\}$ core with mixed supporting ligands, $[Cl\subset Mn^{III}_6(t\text{BuPO}_3)_8(\text{MeOH})_4(H_2O)_2]^+$ and $[Cl\subset Mn^{III}_6(t\text{BuPO}_3)_8(\text{pyridinecarboxaldehyde})_4(H_2O)_2]^+$.[44] In these systems, the water ligands were demonstrated by XRD to occupy mutually *trans*- positions, indicating that this substitution pattern may be more favourable.

Of course, disorder is entirely possible in this system. Water ligands could potentially coordinate to mutually *cis*- coordination site. Additionally, $\{Mn_6\}$ units could be "twisted" so that two of their bpy ligands could point out of the plane, connecting the system in three dimensions but in a disordered way. However, the compound is presented in the configuration most likely to be the thermodynamic minimum – two dimensional sheets, with water ligands occupying *trans*- positions on either side of the sheet.

In this configuration, hydrogen bonding interactions between these terminal water ligands could potentially play a role in the stacking interactions between the sheets.

As with the previous compound, IR spectroscopy (Figure 6.2.7) indicates that the {Mn_6} core forms and is present in **35**. It seems reasonable to conclude that if the {Mn_6} core is present that it should be linked by bipyridyl ligands, in some arrangement.

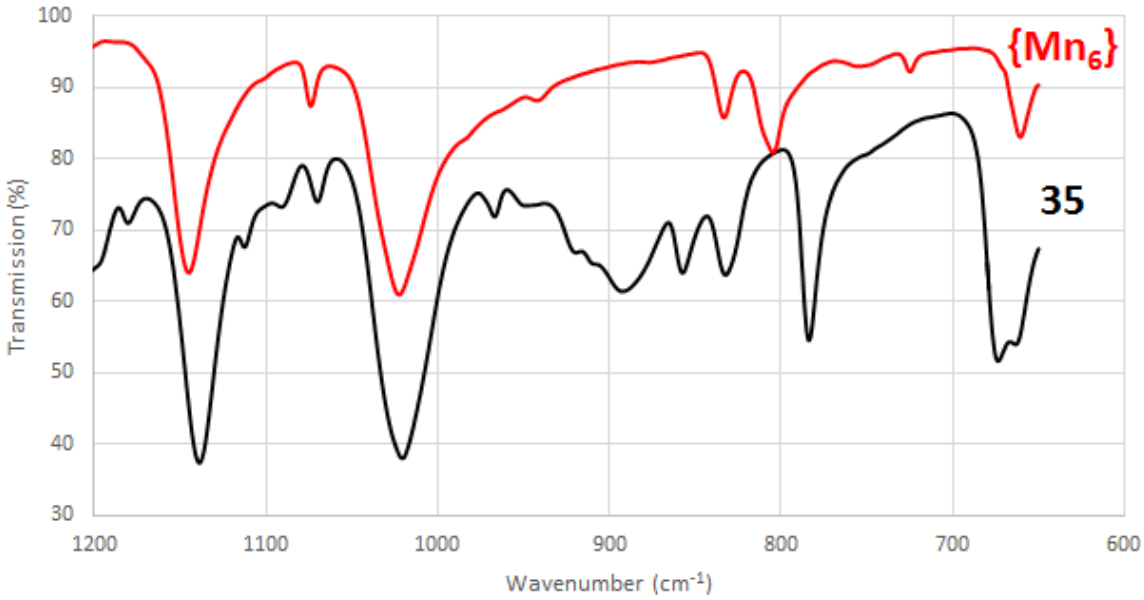

Figure 6.2.7 – IR spectrum of compound 35, compared to that of the previously reported {Mn_6} core.[44]

Powder X-ray Diffraction (PXRD) indicates that the obtained powder is (at least locally) crystalline (Figure 6.2.8). However the pattern is different from **34**, indicating that some different local arrangement of the building units is present.

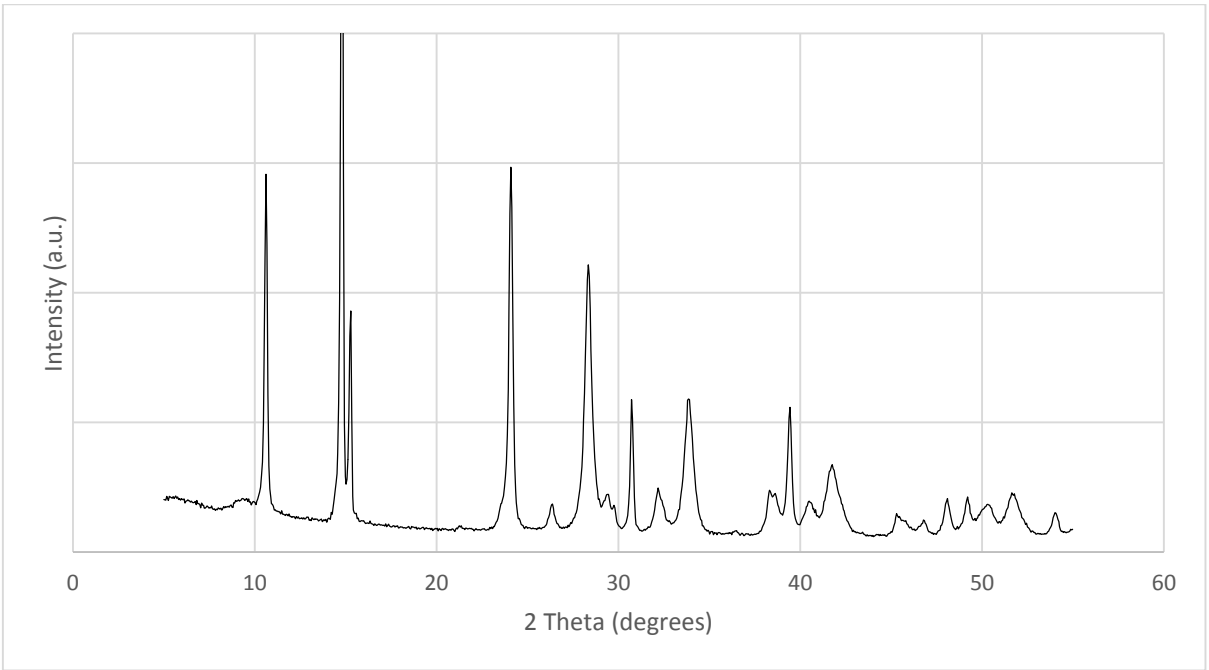

Figure 6.2.8 – PXRD spectrum of compound 35.

TGA analysis indicates that the compound does not contain any constituent solvent molecules (Figure 6.2.9). Again, this may indicate the absence of accessible voids in the structure (possibly due to a combination of the bulky *tert*-butyl groups and chloride counterions, which could potentially block solvents from accessing the pores).

The thermal behaviour of **35** is quite different to that of **34**. Compound **35** appears to be more stable than its three dimensional counterpart **34**, undergoing a more gradual weight decrease up to a temperature of *c.* 400 °C before significant decomposition takes place.

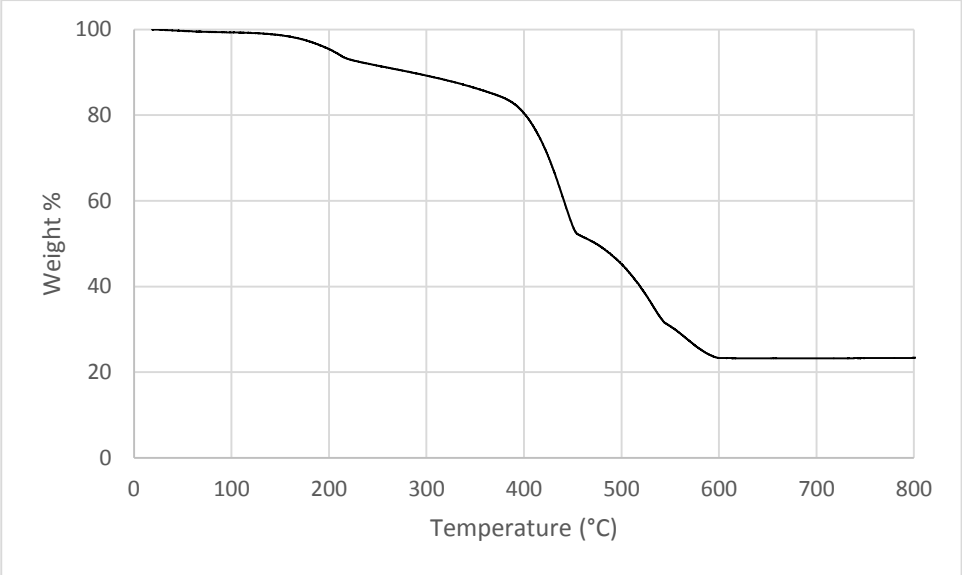

Figure 6.2.9 – TGA analysis of compound 35.

Finally, gas sorption analysis was performed (Figure 6.2.10). Unfortunately, this analysis does not show any significant porosity. This is consistent with the TGA analysis, which does not appear to display any solvent-accessible void volume. This is tentatively assigned to a combination of the bulky *tert*-butyl groups and chloride counterions occupying the otherwise-accessible void space. Gas-sorption analysis indicates a surface area of 125 m^2/g by the BET method.

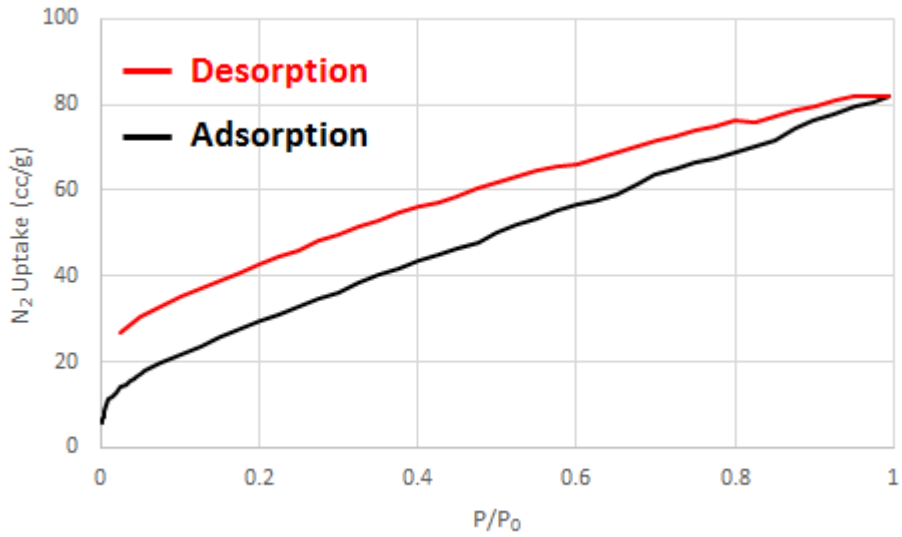

Figure 6.2.10– Gas sorption analysis of compound 35.

Bromide Analogue

As mentioned in Section 6.1, bromide analogues of the {Mn_6} unit can be generated (*c.f.* compound **32**). Therefore, we set out to generate a bromine-substituted analogue of compound **34**, [Br⊂Mn^{III}_6(*t*BuPO_3)$_8$(bpy)$_3$]Br, **36**. This analogue was generated simply by exchanging the chloride salt for the bromide salt of manganese (II).

36 has an analogous structure to **34** (*c.f.* Figures 6.2.1), but with chloride ions replaced by bromide ions (both in the centre of the {Mn_6} unit, and as the external counterion). IR analysis indicates that the {Mn_6} structure is intact in the bromide analogue. (Figure 6.2.11).

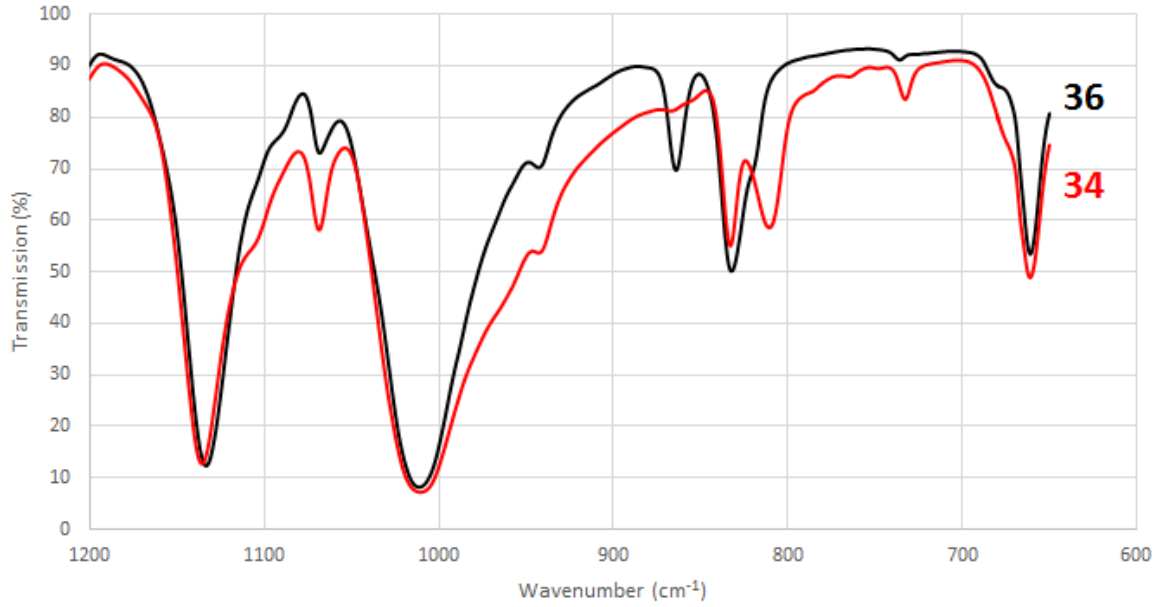

Figure 6.2.11 – Portion of the IR spectra of compounds 36 and 34.

Replacement of the external halide ion indicates that the encapsulated "guest" anions in the structures **34**-**36** could potentially be replaced with more exotic anions. As guest molecules, simple halides do not offer significant functionality to the reaction system, but other anionic species could potentially occupy the charge-balancing role of the external halide ions. If these anionic species possessed their own interesting properties (*e.g.* catalytic activity, photoactivity, sensing capability, *etc.*), then in principle, these molecules could be released into solution upon disassembly of the parent framework material, and re-sequestered upon reassembly of the framework.

Additionally, the central halide occupies the Jahn-Teller distorted axes of all six manganese (III) centres in the {Mn_6} unit. As such, this halide ion could potentially significantly affect the ligand behaviour of the pyridyl-type ligands. In principle, this chloride-halide substitution could affect the stability of the parent frameworks, and the amount of impetus required to disassemble the framework.

6.3) MOF Disassembly and Reassembly

Having generated the MOF-type compounds **34-36**, we set out to investigate if the disassembly-reassembly procedure outlined in Section 6.1 could be applied to these systems. The idea is that addition of competitor ligands to these systems should result in the displacement of the bridging ligands, causing the MOF to disassemble into its constituent parts (*c.f.* Figure 6.1.7).

This was demonstrated in preliminary experiments using compound **34** (Figure 6.3.1). A sample of **34** (*c.* 20 mg in 20 ml acetonitrile) was stirred at room temperature for *c*. 24 hours. There is no evidence of MOF disassembly after this time, and the MOF remains entirely heterogeneous.

However addition of pyridine to the system results in gradual disassembly of the MOF framework, resulting in the disassembly of the framework. The brown solid **34** disappears, along with the appearance of an orange-brown colour to the solution (Figure 6.3.2). The $\{Mn_6\}$ core is shown to be still intact in solution by mass spectrometry (Figure 6.3.3).

As a reasonably volatile liquid, the pyridine can be easily removed from the system simply by placing the system under reduced pressure. The resulting evaporation of pyridine (along with the supporting acetonitrile solvent) results in the precipitation of a brown solid in quantitative yield. This brown powder is identical to the original sample of **34** by both IR and PXRD (Figures 6.3.4 and 6.3.5).

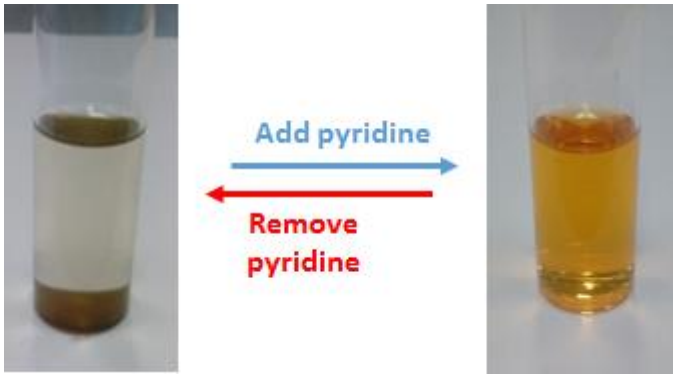

Figure 6.3.1 – A sample of 34 does not dissolve in pure acetonitrile (left), but addition of pyridine (a competitor ligand) to the system results in dissolution of the component parts of 34 (right). The competitor ligand can be removed under reduced pressure, regenerating 34.

We propose that addition of pyridine to the system displaces the bipyridine linker ligands in **34**, resulting in disassembly of the framework. This exploits the labile nature of the Jahn-Teller distorted manganese-bipyridine bonds, allowing the framework-maintaining bonds to be disrupted under mild conditions, without degrading the constituent parts of the framework.

The constituent parts of the framework are then free components in solution. Excess pyridine is required in order to maintain the equilibrium point in this homogenous phase. However, the pyridine can be easily removed under reduced pressure. Analysis indicates that the resulting brown powder is identical to the original sample **34**. Thus, stimulus-responsive reassembly of the framework was achieved, again under mild conditions.

Additionally, the "guest" chloride ion is released into solution upon disassembly of the framework. Moreover, reassembly of the framework results in the re-capture of the chloride guest into the framework (no other anionic species is present, and charge-balance is required for the framework to form). Thus, we have achieved the aim of releasing a guest molecule from its host matrix as well as recapturing it, in a stimulus-responsive manner, by means of a disassembly-reassembly mechanism.

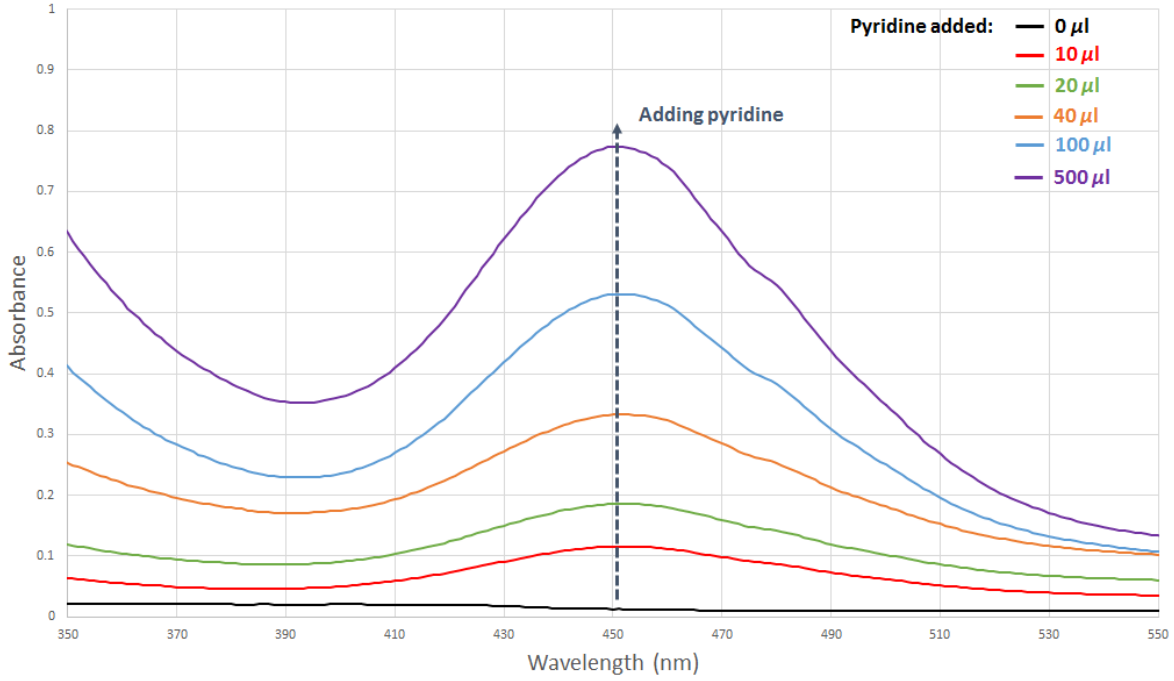

Figure 6.3.2 – Absorption spectra showing the gradual disassembly of 34 upon addition of aliquots of pyridine.

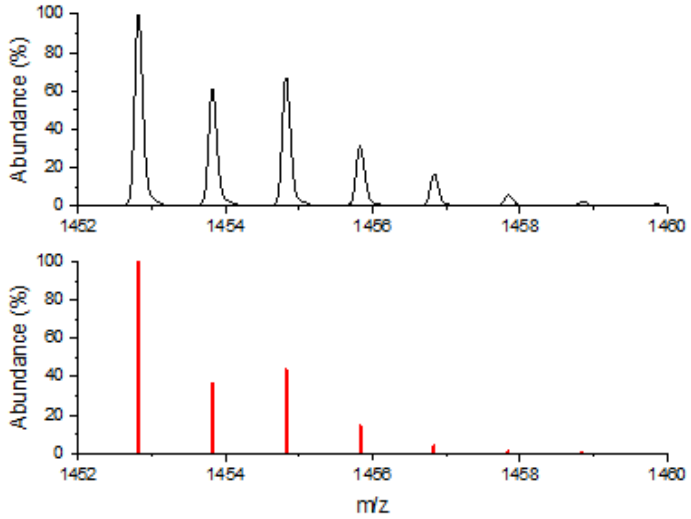

Figure 6.3.3 – Mass spectrum of the disassembly solution, showing the experimental data (black) and the simulated spectrum for $[ClMn_6(t\text{BuPO}_3)_8]^+$ (corresponding to the loss of six pyridyl ligands), demonstrating that the $\{Mn_6\}$ unit stays intact in solution.

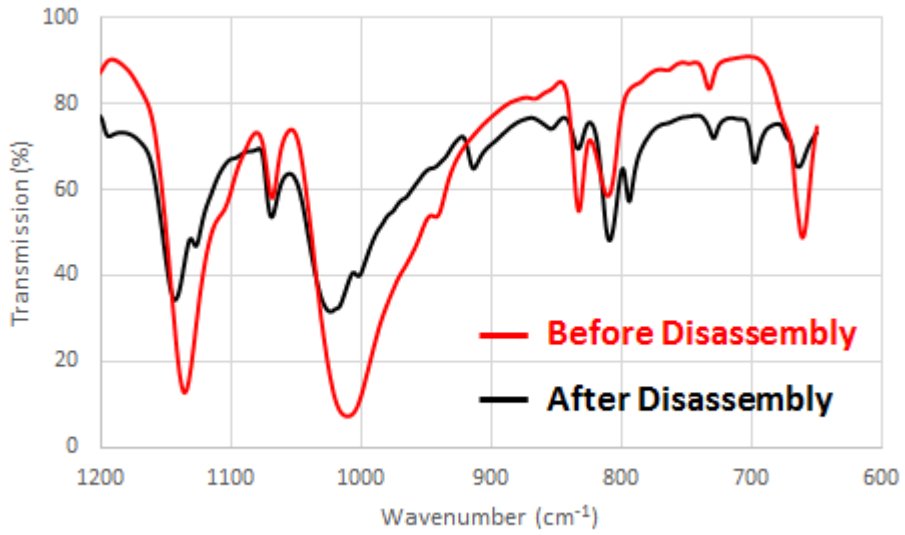

Figure 6.3.4 – Comparison of the IR spectra for 34 before and after applying the disassembly-reassembly procedure.

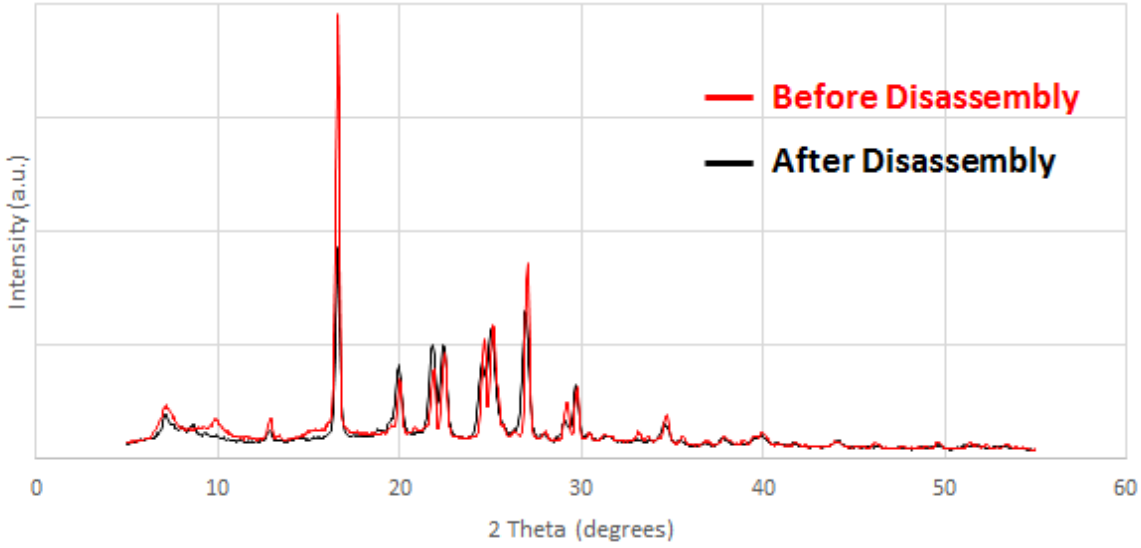

Figure 6.3.5– Comparison of the PXRD spectra for 34 before and after applying the disassembly-reassembly procedure.

6.4) Conclusions and Outlook

In conclusion, we have generated three new MOF-type compounds based on the {Mn_6} unit seen in the previous chapter; [Cl⊂Mn^{III}_6(*t*BuPO_3)$_8$(bpy)$_3$]Cl, **34**, [Cl⊂Mn^{III}_6(*t*BuPO_3)$_8$(bpy)$_2$(H_2O)$_2$]Cl, **35,** and [Br⊂Mn^{III}_6(*t*BuPO_3)$_8$(bpy)$_3$]Br, **36**.

34 and **36** are probably three-dimensional frameworks, with {Mn_6} nodes connected by bipyrdine linker ligands in a simple cubic network. Each pore of the network is occupied by a chloride or bromide counterion.

35 is probably a two-dimensional network, with {Mn_6} nodes connected in a continuous sheet by bipyrdine linker ligands, and water ligands occupying the coordination sites on either side of the sheets. The chloride counterions intercalate between the sheets.

Importantly, it was demonstrated that **34** could be reversibly disassembled and reassembled in a stimulus-responsive manner (Figure 6.4.1). Addition of pyridine caused the disassembly of the framework **34** by displacing the bipyridine linker units, resulting in the components of the framework dissolving into solution. Subsequent removal of the pyridine under reduced pressure regenerated the framework.

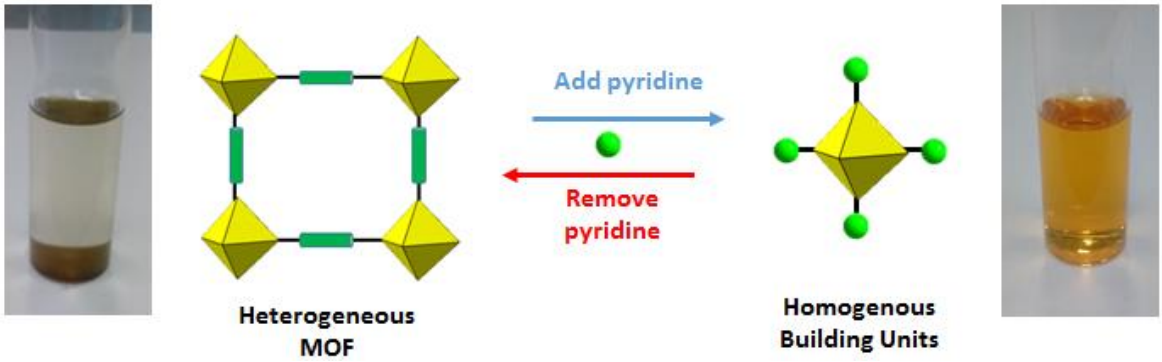

Figure 6.4.1 - Summary of the disassembly-reassembly procedure, as applied to 34.

These results represent an intriguing insight into the disassembly and reassembly of MOF structures, but this work is very much still in its preliminary stages. Many questions remain to be answered about the behaviour of the system. These questions include:

- Can the system be modified further, and if so, how far?
- Could alternative linker units be employed?
- Can more exotic anions be introduced into these structures, in place of the chloride and bromide ions explored so far?
- If such anions could be introduced to the structure, would the disassembly-reassembly methodology allow them to be selectively released into and captured back out of solution?
- Would they retain their useful physicochemical properties in solution?
- Can the disassembly-reassembly behaviour be quantified? If so could we use this information to fine-tune the strength of the framework?
- Can alternative competitor ligands be employed?
- Are there morphological differences (*e.g.* particle size) between the samples (particularly before and after the disassembly-reassembly technique is applied)?

Many promising candidates could be used to generate additional MOF structures. In particular, we are interested in extended versions of the linear bipyrdine ligands, as these could generate structures with the same topology but with larger pore sizes. This strategy was successful in the case of MOF-5 and its analogues (*c.f.* Figure 1.4.1.2)[40], and if applied here could potentially separate the nodes sufficiently to generate guest-accessible pores. Linker units with other topologies are also possible (*e.g.* tripodal pyridyl ligands), which could generate alternative topologies (Figure 6.4.2).

Non-pyridyl ligands also represent an interesting alternative. We know that O-donor ligands can coordinate to the {Mn_6} node, including water and methanol ligands.[44] These should display different binding strengths compared to the N-donor pyridyl ligands, which could offer an avenue towards fine-tuning the disassembly-reassembly behaviour.

Additionally, functionality could be introduced at the linker unit. For example, fluorescent linker units could be employed (*e.g.* substituted naphthalenes or coumarins, which are employed elsewhere as fluorescent sensors). If possible, this offers an interesting and simple avenue towards introducing functionality to the system.

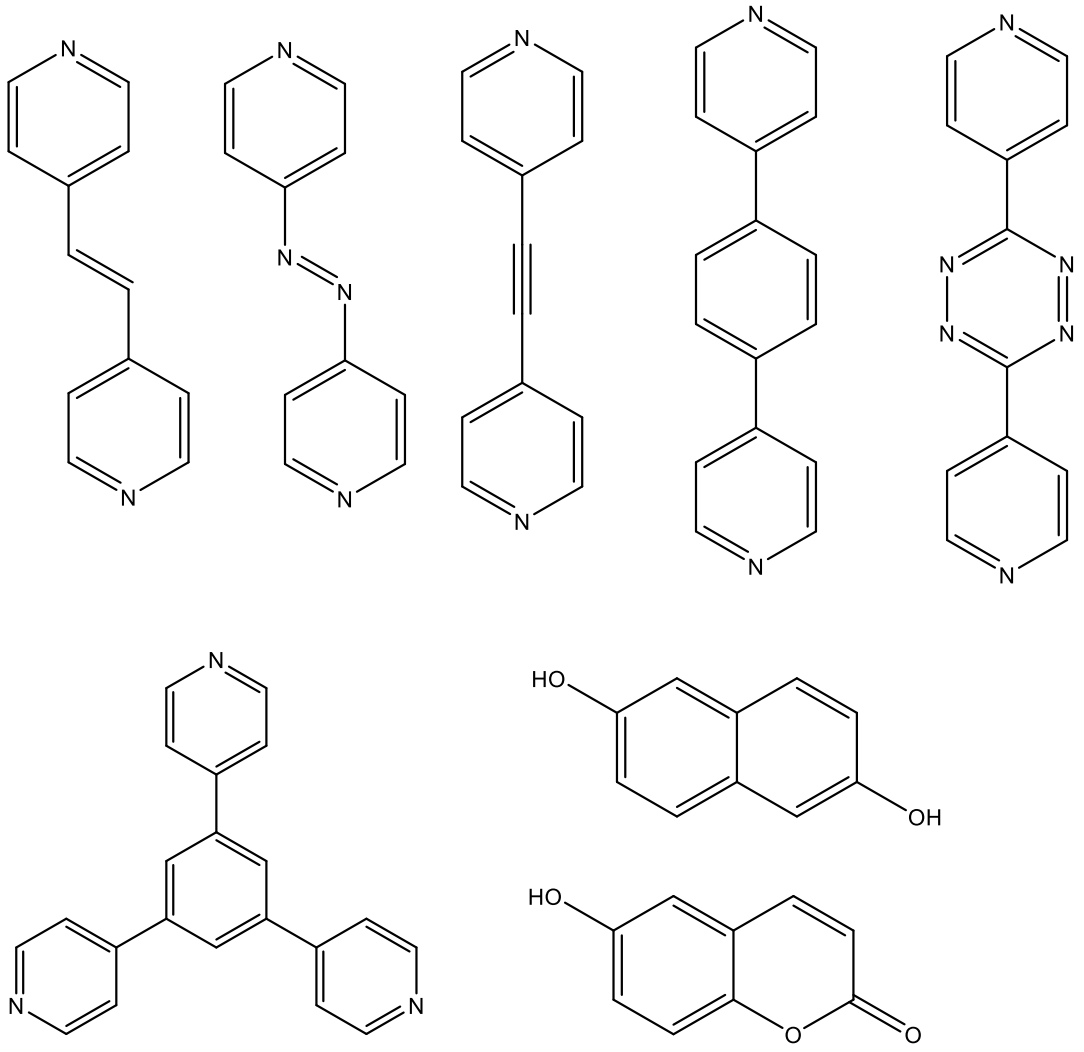

Figure 6.4.2 – Polytopic linker units that could potentially generate new structures along with the {Mn_6} node.

Additionally, many promising anions could be incorporated into the pores of the MOF-structures. Chlorides and bromides have been incorporated so far, indicating that substitution might be possible, but it is still unclear how far the system could be modified.

Simple anions such as hexafluorophosphate or hexafluorosilicate are ideal candidates for initial study of anion exchange behaviour (Figure 6.4.3). These are both relatively hydrophobic and possess octahedral symmetry, which should in principle complement the hydrophobic, cubic pores of the three dimensional frameworks. Additionally, these anions have relatively poor ligand character, and so would be unlikely to interfere with ligand binding interactions. In principle, these anions could be incorporated into the structures by simple ligand exchange procedures (*e.g.* soaking the framework in a near-saturated solution of the target anion).

As hexafluorosilicate is dianionic, it would represent an interesting comparison to the monoanionic hexafluorophosphate. Assuming no significant changes to the structure occur, incorporation of dianions should leave every other pore unoccupied due to charge balance considerations, potentially opening up more accessible pore volume to guest molecules.

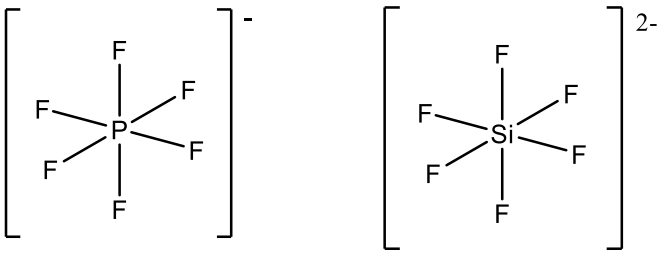

Figure 6.4.3 – Simple anions that could potentially be incorporated into the system.

In principle, increasingly large anions could be incorporated in order to increase accessible void volume, although this strategy could run into steric problems as the anions increase in size. Increasingly large anions may require increasingly long linker ligands in order to accommodate their size.

Moreover, much more exotic ions could be incorporated into the system. For example, photoactive or luminescent species could introduce interesting functionality to the frameworks. However, we are particularly interested in incorporating catalytically active anions into the system. Many examples of catalytically active POM species could be introduced to the system (*c.f.* Section 1.2.2).

The end goal of incorporating catalytic entities into the MOF would be to exploit the disassembly-reassembly behaviour to controllably shift the catalytically active species between homogenous and heterogeneous states. The catalyst could be stored in its host matrix until desired, released into solution upon disassembly, used to perform some homogenous catalytic transformation, and then trapped back into the heterogeneous state and easily removed from the system (Figure 6.4.4).

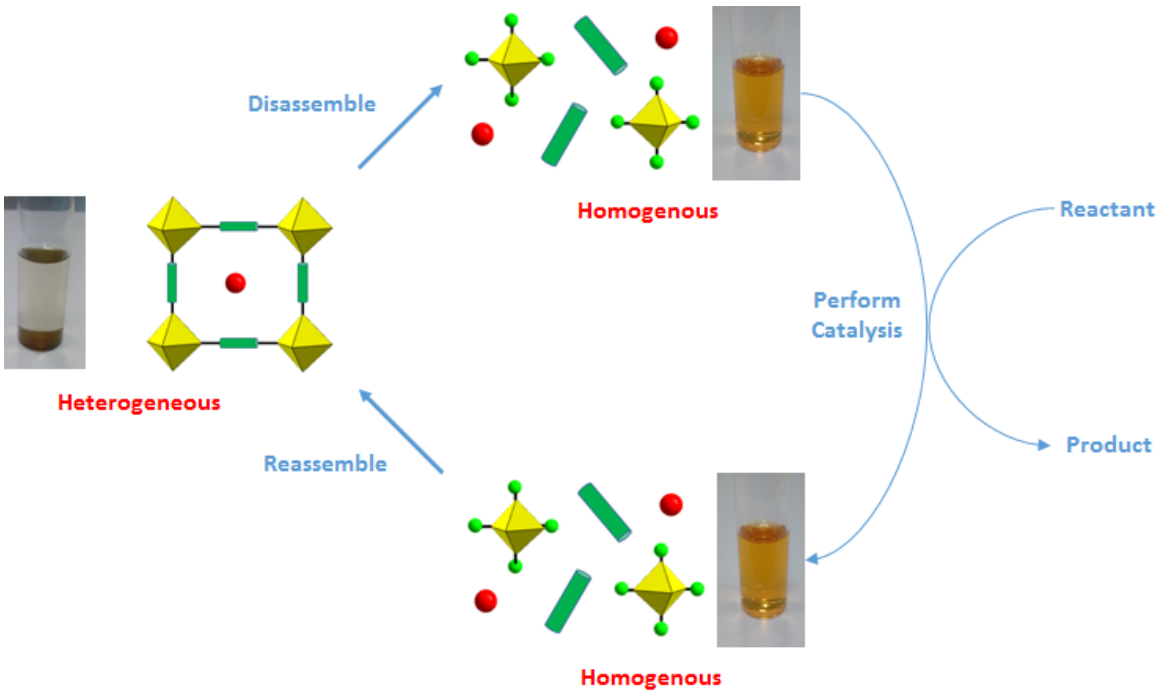

Figure 6.4.4 – Hypothetical end goal of incorporating catalytically active anions into the MOF structure. The catalyst could be released into solution to perform the reaction, then sequestered into the solid MOF structure when the reaction is complete.

This disassembly-reassembly catalytic cycle is the end goal of this avenue of research. In order to achieve this goal, several conditions must be met - the catalyst must be resilient towards the disassembly conditions, while the framework components (the $\{Mn_6\}$ nodes and linker ligands) must be resilient towards the catalytic conditions. We are currently in the process of identifying suitable candidate catalysts, substrates and conditions for this hypothetical application, and hope to make progress towards realising this goal in the near future.

6.5) References

1 O. M. Yaghi, G. Li and H. Li, *Nature*, 1995, **378**, 703.

2 J. Ren, H. W. Langmi, B. C. North and M. Mathe, *Int. J. Energy Res.*, 2015, **39**, 607.

3 N. L. Rosi, J. Eckert, M. Eddaoudi, D. Vodak, J. Kim, M. O. Keeffe and O. M. Yaghi, *Science*, 2003, **300**, 1127.

4 J. Vitillo, B. Smit and L. Gagliardi, *Chem. Rev.*, 2017, **117**, 9521.

5 M. Mohamedali, D. Nath and H. Ibrahim, *Greenh. Gases*, 2016, 116.

6 A. H. Chughtai, N. Ahmad, H. A. Younus, A. Laypkovc and F. Verpoort, *Chem. Soc. Rev.*, 2015, **44**, 6804.

7 A. Dhakshinamoorthy, A. M. Asiri and H. Garcia, *Chem. Eur. J.*, 2016, **22**, 8012.

8 B. J. S. Johnson, S. A. Geers, W. W. Brennessel, V. G. Young and A. Stein, *Dalton Trans.*, 2003, 4678.

9 J. Sha, J. Sun, C. Wang, G. Li, P. Yan and M. Li, *Cryst. Growth Des.*, 2012, **12**, 2242.

10 Z. Zhang, T. Zhang, C. Wang, Z. Lin, L. Long and W. Lin, *J. Am. Chem. Soc.*, 2015, **137**, 3197.

11 M. Zeng, Q. Wang, Y. Tan, S. Hu, H. Zhao and L. Long, *J. Am. Chem. Soc.*, 2010, **132**, 2561.

12 M. Yu, D. You, J. Zhuang, S. Lin, L. Dong, S. Weng, B. Zhang, K. Cheng, W. Weng and H. Wang, *ACS Appl. Mater. Interfaces*, 2017, **9**, 19698.

13 M. A. Chowdhury, *Rev. J. Chem.*, 2017, **7**, 1.

14 P. Horcajada, C. Serre, G. Maurin, N. A. Ramsahye, F. Balas, M. Sebban, F. Taulelle and G. Ferey, *J. Am. Chem. Soc.*, 2008, **130**, 6774.

15 T. M. McDonald, W. R. Lee, J. A. Mason, B. M. Wiers, C. S. Hong and J. R. Long, *J. Am. Chem. Soc.*, 2012, **134**, 7056.

16 P. Nugent, Y. Belmabkhout, S. D. Burd, A. J. Cairns, R. Luebke, K. Forrest, T. Pham, S. Ma, B. Space, L. Wojtas, M. Eddaoudi and M. J. Zaworotko, *Nature*, 2013, **495**, 80.

17 A. Ziaee, D. Chovan, M. Lusi, J. J. Perry, M. Zaworotko and S. A. M. Tofail, *Cryst. Growth Des.*, 2016, **16**, 3890.

18 M. S. Ray, *Sep. Sci. Technol.*, 1986, **21**, 1.

19 C. A. Grande, *ISRN Chem. Eng.*, 2012, **2012**, 100.

20 E. Adatoz, A. K. Avci and S. Keskin, *Sep. Purif. Technol.*, 2015, **152**, 207.

21 K. Sumida, D. L. Rogow, J. A. Mason, T. M. McDonald, E. D. Bloch, Z. R. Herm, T. Bae and J. R. Long, *Chem. Rev.*, 2012, **112**, 724.

22 H. Li and M. R. Hill, *Acc. Chem. Res.*, 2017, **50**, 778.

23 S. Horike, S. Shimomura and S. Kitagawa, *Nat. Chem.*, 2009, **1**, 695.

24 A. Schneemann, V. Bon, I. Schwedler, I. Senkovska, S. Kaskel and R. A. Fischer, *Chem. Soc. Rev.*, 2014, **43**, 6062.

25 A. J. Graham, D. R. Allan, A. Muszkiewicz, C. A. Morrison and S. A. Moggach, *Angew. Chem. Int. Ed.*, 2011, **50**, 11138.

26 H. Kim, S. Yang, S. R. Rao, S. Narayanan, E. A. Kapustin, H. Furukawa, A. S. Umans, O. M. Yaghi and E. N. Wang, *Science*, 2017, **356**, 430.

27 J. A. Mason, K. Sumida, Z. R. Herm, R. Krishna and J. R. Long, *Energy Environ. Sci.*, 2011, **4**, 3030.

28 Y. Labreche, Y. Fan, R. P. Lively, C. W. Jones and W. J. Koros, *J. Appl. Polym. Sci.*, 2015, 41845.

29 H. Li, M. M. Sadiq, K. Suzuki, R. Ricco, C. Doblin, A. J. Hill, S. Lim, P. Falcaro and M. R. Hill, *Adv. Mater.*, 2016, **28**, 1839.

30 H. Li, M. M. Sadiq, K. Suzuki, ChristianDoblin, S. Lim, P. Falcaro, A. J. Hill and M. R. Hill, *J. Mater. Chem. A*, 2016, **4**, 18757.

31 J. An, S. J. Geib and N. L. Rosi, *J. Am. Chem. Soc.*, 2009, **131**, 8376.

32 J. An and N. L. Rosi, *J. Am. Chem. Soc.*, 2010, **132**, 5578.

33 R. Lyndon, K. Konstas, B. P. Ladewig, P. D. Southon, C. J. Kepert and M. R. Hill, *Angew. Chem. Int. Ed.*, 2013, **52**, 3695.

34 N. Yanai, T. Uemura, M. Inoue, R. Matsuda, T. Fukushima, M. Tsujimoto, S. Isoda and S. Kitagawa, *J. Am. Chem. Soc.*, 2012, **134**, 4501.

35 J. Park, D. Yuan, K. T. Pham, J. Li, A. Yakovenko and H. Zhou, *J. Am. Chem. Soc.*, 2012, **134**, 99.

36 B. Claes, T. Boudewijns, L. Muchez, G. Hooyberghs, E. V. Van Der Eycken, J. Vanderleyden, H. P. Steenackers and D. E. De Vos, *ACS Appl. Mater. Interfaces*, 2017, **9**, 4440.

37 X. Lin, F. Luo, L. Zheng, G. Gao and Y. Chi, *Anal. Chem.*, 2015, **87**, 4864.

38 H. Li, M. Eddaoudi, M. O'Keeffe and O. M. Yaghi, *Nature*, 1999, **402**, 276.

39 R. L. Martin, L. Lin, K. Jariwala, B. Smit and M. Haranczyk, *J. Phys. Chem. C*, 2013, **117**, 12159.

40 M. Eddaoudi, J. Kim, N. Rosi, D. Vodak, J. Wachter, M. O. Keeffe and O. M. Yaghi, *Science*, 2002, **295**, 469.

41 J. A. Greathouse and M. D. Allendorf, *J. Am. Chem. Soc.*, 2006, **128**, 10678.

42 P. Guo, D. Dutta, A. G. Wong-Foy, D. W. Gidley and A. J. Matzger, *J. Am. Chem. Soc.*, 2015, **137**, 2651.

43 S. Han and M. S. Lah, *Cryst. Growth Des.*, 2015, **15**, 5568.

44 L. Zhang, B. Marzec, R. Clérac, Y. Chen, H. Zhang and W. Schmitt, *Chem. Commun.*, 2013, **108**, 66.

45 L. Zhang, R. Clérac, C. I. Onet, M. Venkatesan, P. Heijboer and W. Schmitt, *Chem. Eur. J.*, 2012, **18**, 13984.

Chapter 7

Experimental Details

7.1) Methods and Materials

Reagents

All chemicals were of reagent grade and were purchased from Sigma-Aldrich, Alfa Aesar or Acros Organics, and were used as received without further purification. Solvents were supplied by in-house solvent suppliers, and were used as received without further purification. Methanol was of technical grade quality and acetonitrile was of HPLC quality, except where otherwise noted. Water was deionised before use, except where otherwise noted.

Mass Spectrometry

MS samples were prepared using either HPLC grade methanol or HPLC grade acetonitrile. Samples for analysis were added to the solvent (*c.* 0.5 mg/ml) and sonicated for *c.* 15 minutes before being passed through a Teflon filter (pore size *c.* 200 μm) to remove any solid particles. Samples were then analysed by either Dr. Martin Feeney or Dr. Gary Hessman.

MALDI spectra were acquired using a Waters Maldi Q-Tof Premier in negative mode using DCTB (trans-2-[3-4-tert-butylphenyl)-2-methyl-2-propenylidene]malononitrile) as a MALDI matrix. The laser operated at 337 nm. The instrument was calibrated using PEG and the internal lock mass used was [Glu] Fibrinopetide B. MassLynx 4.1 software and mMass software were used to carry out the analysis.

ESI mass spectra were acquired using a Micromass time of flight mass spectrometer (tof), interfaced to a Waters 2690 HPLC. The instrument was operated in positive or negative mode as required. Leucine Enkephalin was used as an internal lock mass. Masses were recorded over the range 100-1000 m/z. The bath gas was nitrogen. MassLynx 4.0 software and mMass software were used to carry out the analysis.

For ESI-MS analyses, the following operating conditions were used: ESI capillary voltage 2500V, cone voltage 25V, desolvation temperature 300^{o}C, source temperature 100^{o}C. For CV variation experiments, all other parameters were held constant, and the cone voltage varied to 10 V, 30 V, 50 V and 75 V.

Single Crystal XRD

Single crystal X-ray Diffraction data were collected by Dr. Brendan Twamley, Dr. Tom McCabe, Dr. Amal Cherian Kathalikkattil, Dr. Lauren Macreadie, Friedrich Steuber or Paul Wix.

Analyses were performed using a Bruker APEX2 Duo diffractometer equipped with a Mo-Kα source (λ = 0.71073 Å) and a Cu-Kα source (λ = 1.5418 Å). Data was gathered using a Bruker SMART APEX2 area detector. Structures were solved using Bruker APEX v2011.8-0 software and refined using OLEX 2 software. H positions were calculated using a riding model. Where appropriate, the SQUEEZE routine was used to model disordered solvent molecules.

Powder XRD

Powder diffraction data was gathered using a Bruker D2 Phaser using a low-background silicon sample holder. Data were gathered between 2θ = 5 ° and 2θ = 55 °, with the sample rotating at 1 rotation per minute.

Infrared Spectroscopy (IR)

Infrared data in the 4000-650 cm^{-1} region were obtained using a PerkinElmer Spectrum One FT-IR spectrometer with a universal Attenuated Total Reflectance (ATR) sampling accessory. The following symbols were used to describe the spectra: w weak, m medium, s strong, sh shoulder, b broad.

Thermogravimetric Analyses (TGA)

Thermogravimetric analyses were performed using a Perkin Elmer Pyriss 1 TGA instrument that had been previously calibrated using nickel and iron standards. Approximately 5 mg of the samples were heated in a ceramic crucible under a nitrogen atmosphere, from room temperature to *c.* 800˚ C, at a rate of 10˚ C/min.

CHN Elemental Analyses

Elemental analyses were performed by the Microanalysis Lab of the School of Chemistry and Chemical Biology in University College Dublin using an Exeter Analytical CE 440 instrument.

UV-Vis Absorption Spectroscopy

UV-Vis absorption spectra were recorded using a Lambda 35 spectrometer from Perkin Elmer using a pair of matched Quartz cuvettes (path length 10mm) at room temperature. Analysis was performed using UVWinlab software. Samples were *c.* 30 μM in acetonitrile.

Photoluminescence Spectroscopy

Luminescence spectra were recorded using a FluoroMax-4 spectrofluorometer using a Quartz cuvette (cell length 10mm) at room temperature. Analysis was performed using FluorEssence v 3.5 software. Samples were *c.* 30 μM in acetonitrile.

Magnetic Susceptibility Measurements

Magnetic susceptibility measurements were performed by Dr. Munuswamy Venkatesan using a 5 T MPMS SQUID from Quantum Design. Temperature dependence of magnetization was measured in temperature range 2-300 K in an applied magnetic field of 0.1 T.

Water Oxidation Measurements

Water oxidation measurements were performed by Dr. Amal Cherian Kathalikkattil and Rory Elliott a needle-mounted Clarke electrode from Unisense (OX-NP-7041) and a blue LED LED (λ = 470, incident power estimated as 9.6 mW/cm).

Gas Sorption Analyses

Nitrogen gas sorption analyses were performed by Debobroto Sensharma using a Quantachrome Autosorb-iQ. The temperature was maintained at 77 K using a liquid nitrogen bath. The samples were activated at 80 ˚C for eight hours under secondary vacuum prior to the measurements and the mass of the samples was measured after the activation. The N_2 and He gas cylinders in CP grade were obtained from BOC Gases Ireland.

7.2) Synthesis

Organic Ligands

Adamantylphosphonic acid ($AdPO_3H_2$)

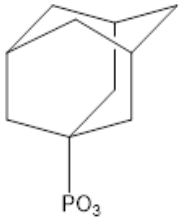

Adamantylphosphonic acid was prepared by a modification of literature procedure for other tertiary phosphonic acids.[1] Solid 1-bromoadamantane (5.4 g, 25 mmol) and aluminium trichloride (3.33 g, 25 mmol) were combined at 0 °C, followed by slow addition of excess phosphorus trichloride (10 ml) at 0 °C. After standing at room temperature overnight, the solid was dispersed in chloroform (100 ml) and poured over a mixture of ice (100 g) and hydrochloric acid (35 %, 50 ml) and stirred vigorously for *c.* 15 minutes, adding more ice as required. The chloroform layer was allowed to separate, and the aqueous layer extracted again with chloroform. The combined chloroform solutions were dried using $MgSO_4$ and evaporated under reduced pressure. Without further purification, the resulting solid was added to a concentrated aqueous KOH (50 ml) solution at 0 °C before refluxing overnight. The solution was subsequently neutralised with ice-cold HCl at 0 °C, resulting in a white precipitate that was washed with copious amounts of water and dried under vacuum. Yield: 3.5 g, 65 %. NMR: δ_H ($CDCl_3$) 1.8 (6H, d), 1.7 (3H, m), 1.6 (6H, d).

Metal Complexes

Lindqvist Hexamolybdate $[TBA]_2[Mo_6O_{19}]$

The Lindqvist Hexamolybdate species $[TBA]_2[Mo_6O_{19}]$ was prepared by literature procedure.[2] Sodium molybdate (2.5 g, 10.3 mmol) was dissolved in 10 ml of water and acidified drop-wise with hydrochloric acid (35 %, 1.75 ml). A solution of TBA bromide (1.2 g, 3.75 mmol in 2 ml water) was added, producing a white precipitate. The slurry was refluxed overnight, turning yellow. The yellow solid was filtered off and washed with water and diethyl ether before air-drying for one hour. The solid was then recrystallized from boiling acetone (*c.* 100 ml) by cooling overnight at -20 °C. The large yellow crystals were isolated by filtration, washed with diethyl ether and air dried. Yield: 1.62 g, 69.1%. FT-IR υ_{max} (cm^{-1}): 2962 (w), 2873 (w), 1468 (m), 951 (Mo=O) (s), 789 (Mo-O bridging) (s).

Strandberg Ring Structures (Chapter 2):

$[TBA]_2[Mo_6O_{19}]$ (0.137 g, 0.1 mmol), *tert*-butylphosphonic acid (0.067 g, 0.5 mmol) and either piperazine (**1**) or trimethylenedipyridine (**2**) (0.5 mmol) were combined in methanol (25 ml) and stirred at room temperature. The yellow crystals of $[TBA]_2[Mo_6O_{19}]$ gradually disappeared along with the concomitant production of a white precipitate over the course of one hour. The white solid was isolated by filtration, washed with hot acetonitrile and diethyl ether and left to air dry.

$[pip\text{-}H_2]_2[Mo_5O_{15}(tBuPO_3)_2]$•2(MeOH), 1•2(MeOH):

Yield: 0.085 g, 58.0% based on Mo. FT-IR (ATR) υ_{max} (cm^{-1}): 3400 (w, b), 2970 (w, b), 2732 (w, b), 2441 (w, b), 1602 (m), 1456 (m), 1397 (w), 1317 (w), 1205 (w), 1087 (P-O) (m), 1032 (P-O) (m), 976 (P-O) (m), 919 (Mo=O) (sh), 892 (Mo=O) (s), 654 (Mo-O) (s).

$[TDP\text{-}H_2]_2[Mo_5O_{15}(tBuPO_3)_2]$•0.6(MeOH), 2•0.6(MeOH)

Yield: 0.080 g, 47.3% based on Mo. FT-IR (ATR) υ_{max} (cm^{-1}): 3463 (w, b), 3067 (w), 2860 (w), 1636 (m), 1503 (m), 1393 (w), 1361 (w), 1207 (w), 1102 (P-O) (m), 1034 (P-O) (m), 973 (P-O) (m), 906 (Mo=O) (sh), 894 (Mo=O) (s), 657 (Mo-O) (s).

Copper-Molybdate Structures (Chapter 3):

$[TBA]_2[Mo_6O_{19}]$ (0.137 g, 0.1 mmol), *tert*-butylphosphonic acid (0.067 g, 0.5 mmol), copper (II) acetate monohydrate (0.100 g, 0.5 mmol) and tetrabutylammonium bromide (0.322 g, 1 mmol) were combined in methanol (25 ml). Pyridine (80 μl, 1 mmol) was added. The solution was stirred at room temperature for four hours. The blue-green solution was filtered and left to evaporate slowly. Pale blue, plate-like crystals of **3**•2(MeOH)•(H_2O) and large, green, block-like crystals of **4**•6(MeOH) formed from the same solution over the course of one week. The crystals were separated manually based on appearance before being washed with diethyl ether and air dried.

$[TBA]_2[Mo^{VI}_6Cu^{II}_4O_{16}(OH)_2(tBuPO_3)_4(py)_2(CH_3O)_4(H_2O)]$•2(MeOH)•($H_2O$), 3•2(MeOH)•($H_2O$)

Yield: 0.098 g, 31.0% based on Cu. FT-IR (ATR) υ_{max} (cm^{-1}): 3570 (vw), 2967 (w) (C-H), 2879 (w) (C-H), 1613 (vw), 1486 (w), 1480 (w), 1069 (P-O) (m), 1023 (P-O) (m), 977 (m) (P-O), 934 (m) (Mo=O), 932 (m) (Mo=O), 778 (m) (Mo-O). CHN Analysis for $Mo_6Cu_4P_4O_{38}N_4C_{64}H_{144}$; Expected C% 30.23, H% 5.71, N% 2.20; Found C% 29.12, H% 5.20, N% 1.89. MALDI-MS for $Mo_6Cu_4P_4O_{35}C_{23}H_{63}$ calculated *m/z* 1886.49, observed *m/z* 1886.35

$[TBA]_2[Mo^{VI}_7Cu^{VI}_7O_{19}(OH)(CH_3O)_7(tBuPO_3)_6(py)_2]$•6(MeOH), 4•6(MeOH)

Yield: 0.143 g, 41.5% based on Cu. FT-IR (ATR) υ_{max} (cm^{-1}): 2967 (w) (C-H), 2879 (w) (C-H), 1610 (w), 1452 (w), 1082 (m) (P-O), 1000 (m) (P-O), 975 (m) (P-O), 905 (s) (Mo=O), 742 (m) (Mo-O). CHN Analysis for $Mo_7Cu_7P_6O_{53}N_4C_{78}H_{182}$; Expected C% 28.06, H% 5.05, N% 1.68; Found C% 28.06, H% 4.82, N% 1.70.

Cobalt-Molybdate Structures (Chapter 4)

Method A: $[TBA]_2[Mo_6O_{19}]$ (0.137 g, 0.1 mmol), the appropriate cobalt (II) carboxylate salt (0.5 mmol), *tert*-butylphosphonic acid or 1-adamantlyphosphonic acid (0.5 mmol) and tetrabutylammonium bromide (0.322 g, 1 mmol) were combined in acetonitrile (25 ml). Pyridine or picoline (1 mmol) was added. The solution was stirred at room temperature for four hours. The (generally purple) solution was filtered and left to evaporate slowly until crystalline material formed. The crystals were isolated by filtration, washed with diethyl ether and air dried.

Method B: $[TBA]_2[Mo_6O_{19}]$ (0.068 g, 0.05 mmol), cobalt (II) nitrate (0.072 g, 0.25 mmol), *tert*-butylphosphonic acid or 1-adamantlyphosphonic acid (0.5 mmol), the appropriate carboxylic acid (0.5 mmol) and tetrabutylammonium bromide (0.161 g, 0.5 mmol) were combined in acetonitrile (25 ml). Pyridine (40 μl, 0.5 mmol) was added. The solution was stirred at room temperature for four hours. The (generally purple) solution was filtered and left to evaporate slowly until crystalline material formed. The crystals were isolated by filtration, washed with diethyl ether and air dried.

$[TBA]_2[Mo^{VI}_{10}Co^{II}_6O_{12}(\mu\text{-}O)_{14}(\mu_3\text{-}O)_4(t\text{BuPO}_3)_6(\text{MeCOO})_2(\text{py})_2(H_2O)_6]\bullet 3(\text{MeCN})$, 5•3(MeCN)

Method A. Yield: 0.152 g, 68.8% based on Mo. FT-IR (ATR) υ_{max} (cm^{-1}): 3460 (w), 3425 (w), 3147 (b), 2964 (w) (C-H), 2873 (w) (C-H), 1644 (w), 1600 (w), 1568 (ν_{sym}) (m), 1479 (m), 1445 (m), 1417 (sh) (ν_{asym}) (Δ = 151), 1396 (w), 1097 (s) (P-O), 975 (s) (P-O), 956 (s) (P-O), 891 (s) (Mo=O), 771 (s), 699 (s) (Mo-O). CHN Analysis for $Mo_{10}Co_6P_6O_{58}N_8C_{81}H_{168}$; Expected C% 26.42, H% 4.60, N% 3.04; Found C% 26.45, H% 4.35, N% 2.85. UV-Vis λ_{max}/nm (ε_{max}/M^{-1} cm^{-1}): 560 (341). MALDI-MS for $Mo_{10}Co_6P_6O_{53}N_1C_{44}H_{98}$ (loss of 1 TBA, 2 py, 5 H_2O) calculated *m/z* 2900.00, observed *m/z* 2900.01.

$[TBA]_2[Mo^{VI}_{10}Co^{II}_6O_{12}(\mu\text{-}O)_{14}(\mu_3\text{-}O)_4(t\text{BuPO}_3)_6(\text{MeCOO})_2(\text{pic})_4(H_2O)_6]\bullet 4.4(\text{MeCN})$, 6•4.4(MeCN)

Method A. Yield 0.096 g, 51.7% based on Mo. FT-IR (ATR) υ_{max} (cm^{-1}): 3469 (w), 3432 (w), 3171 (b), 2964 (w) (C-H), 2874 (w) (C-H), 1639 (w), 1602 (m), 1562 (ν_{sym}) (m), 1486 (m), 1446 (m), 1383 (w) (ν_{asym}) (Δ = 179), 1098 (s) (P-O), 968 (s) (P-O), 948 (s) (P-O), 886 (s) (Mo=O), 850 (s), 823 (s), 765 (s), 699 (s) (Mo-O). MALDI-MS for $Mo_{10}Co_6P_6O_{53}N_1C_{44}H_{98}$ (loss of 1 TBA, 4 pic, 5 H_2O) calculated *m/z* 2900.00, observed *m/z* 2900.01.

$[TBA]_2[Mo^{VI}_{10}Co^{II}_6O_{12}(\mu\text{-}O)_{14}(\mu_3\text{-}O)_4(t\text{BuPO}_3)_6(\text{PhCOO})_2(\text{py})_2(H_2O)_6]$, 7

Method A. Yield: 0.120 g, 55.5% based on Mo. FT-IR (ATR) υ_{max} (cm^{-1}): 3487 (w), 3441 (w), 3240 (b), 2970 (w) (C-H), 2869 (w) (C-H), 1738 (m), 1602 (m), 1564 (ν_{sym}) (m), 1538 (m), 1479 (m), 1405 (m) (ν_{asym}) (Δ = 159), 1215 (w), 1096 (s) (P-O), 973 (s) (P-O), 938 (s) (P-O), 890 (s) (Mo=O), 768 (s), 707 (s) (Mo-O). MALDI-MS for $Mo_{10}Co_6P_6O_{52}N_1C_{54}H_{100}$ (loss of 1 TBA, 2 py, 6 H_2O) calculated *m/z* 3094.02, observed *m/z* 3094.16.

$[TBA]_2[Mo^{VI}_{10}Co^{II}_6O_{12}(\mu\text{-}O)_{14}(\mu_3\text{-}O)_4(t\text{BuPO}_3)_6(\text{BzCOO})_2(\text{py})_2(H_2O)_6]\bullet 3.5(\text{MeCN})$, 8•3.5(MeCN)

Method B. Yield: 0.045 g, 39.7% based on Mo. FT-IR (ATR) υ_{max} (cm^{-1}): 3469 (w), 3432 (w), 3171 (b), 2964 (w) (C-H), 2874 (w) (C-H), 1639 (w), 1602 (m), 1560 (ν_{sym}) (m), 1478 (m), 1396 (m) (ν_{asym}) (Δ = 164), 1293 (w), 1096 (s) (P-O), 975 (s) (P-O), 953 (s) (P-O), 891 (s) (Mo=O), 850 (s), 823 (s), 770 (s), 700 (s) (Mo-O). CHN Analysis for $Mo_{10}Co_6P_6O_{58}N_4C_{82}H_{162}$; Expected C% 27.12, H% 4.49, N% 1.54; Found C% 27.04, H% 4.41, N% 1.26. MALDI-MS for $Mo_{10}Co_6P_6O_{52}N_1C_{56}H_{104}$ (loss of 1 TBA, 2 py, 6 H_2O) calculated *m/z* 3122.05, observed *m/z* 3122.05.

$[TBA]_2[Mo^{VI}_{10}Co^{II}_6O_{12}(\mu\text{-}O)_{14}(\mu_3\text{-}O)_4(t\text{BuPO}_3)_6(\text{AdCOO})_2(\text{py})_2(H_2O)_6]$, 9

Method B. Yield 0.034 g, 40.3% based on Mo. FT-IR (ATR) υ_{max} (cm^{-1}): 3478 (w), 3155 (b), 2903 (w) (C-H), 1640 (w), 1602 (m), 1535 (ν_{sym}) (m), 1479 (m), 1445 (m), 1395 (sh) (ν_{asym}) (Δ = 140), 1312 (w), 1097 (s) (P-

O), 973 (s) (P-O), 947 (s) (P-O), 912 (s), 890 (s) (Mo=O), 850 (s), 826 (s), 770 (s), 699 (s) (Mo-O). CHN Analysis for $Mo_{10}Co_6P_6O_{58}N_4C_{88}H_{178}$; Expected C% 28.41, H% 4.82, N% 1.50; Found C% 28.72, H% 4.71, N% 1.39. MALDI-MS for $Mo_{10}Co_6P_6O_{50}C_{35}H_{69}$ (loss of 2 TBA, 1 AdCOO, 2 py, 6 H_2O) calculated *m/z* 2790.79, observed *m/z* 2790.82.

$[TBA]_2[Mo^{VI}_{10}Co^{II}_6O_{12}(\mu\text{-}O)_{14}(\mu_3\text{-}O)_4(AdPO_3)_6(MeCOO)_2(py)_2(H_2O)_6]$•9.5(MeCN), 10•9.5(MeCN)

Method A. Yield 0.032 g, 17.3% based on Mo. FT-IR (ATR) υ_{max} (cm^{-1}): 3189 (b), 2903 (w) (C-H), 2850 (w) (C-H), 1604 (m), 1562 (ν_{sym}) (m), 1486 (m), 1446 (m), 1383 (w) (ν_{asym}) (Δ = 179), 1098 (s) (P-O), 968 (s) (P-O), 948 (s) (P-O), 886 (s) (Mo=O), 850 (s), 823 (s), 765 (s), 699 (s) (Mo-O). CHN Analysis for $Mo_{10}Co_6P_6O_{58}N_4C_{106}H_{196}$; Expected C% 32.25, H% 4.85, N% 1.42; Found C% 28.94, H% 4.09, N% 0.92. MALDI-MS for $Mo_{10}Co_6P_6O_{56}N_1C_{80}H_{140}$ (loss of 1 TBA, 2 py, 2 H_2O) calculated *m/z* 3511.32, observed *m/z* 3511.34.

$[TBA]_2[Mo^{VI}_{10}Co^{II}_6O_{12}(\mu\text{-}O)_{14}(\mu_3\text{-}O)_4(AdPO_3)_6(PhCOO)_2(py)_2(H_2O)_6]$•2(MeCN), 11•2(MeCN)

Method A. Yield 0.024 g, 9.6% based on Mo. FT-IR (ATR) υ_{max} (cm^{-1}): 3456 (w), 3167 (b), 2903 (w) (C-H), 2850 (w) (C-H), 1640 (w), 1601 (m), 1535 (ν_{sym}) (m), 1484 (m), 1446 (m), 1407 (m) (ν_{asym}) (Δ = 128), 1097 (s) (P-O), 970 (s) (P-O), 952 (s) (P-O), 887 (s) (Mo=O), 827 (s), 768 (s), 697 (s) (Mo-O). CHN Analysis for $Mo_{10}Co_6P_6O_{58}N_4C_{116}H_{194}$; Expected C% 34.22, H% 4.80, N% 1.37; Found C% 33.87, H% 4.68, N% 1.64. MALDI-MS for $Mo_{10}Co_6P_6O_{56}N_1C_{90}H_{144}$ (loss of 1 TBA, 2 py, 2 H_2O) calculated *m/z* 3634.35, observed *m/z* 3634.43.

$[TBA]_2[Mo^{VI}_{10}Co^{II}_6O_{12}(\mu\text{-}O)_{14}(\mu_3\text{-}O)_4(AdPO_3)_6(BzCOO)_2(py)_3(H_2O)_6]$•5(MeCN), 12•5(MeCN)

Method B. Yield 0.027 g, 20.5% based on Mo. FT-IR (ATR) υ_{max} (cm^{-1}): 3431 (w), 3167 (b), 2903 (w) (C-H), 2850 (w) (C-H), 1567 (ν_{sym}) (m), 1485 (m), 1446 (m), 1407 (m) (ν_{asym}) (Δ = 160), 1098 (s) (P-O), 978 (s) (P-O), 950 (s) (P-O), 888 (s) (Mo=O), 851 (s), 824 (s), 771 (s), 701 (s) (Mo-O). CHN Analysis for $Mo_{10}Co_6P_6O_{58}N_4C_{118}H_{198}$; Expected C% 34.60, H% 4.87, N% 1.36; Found C% 32.97, H% 4.62, N% 1.12. MALDI-MS for $Mo_{10}Co_6P_6O_{52}N_1C_{92}H_{140}$ (loss of 1 TBA, 2 py, 5 H_2O) calculated *m/z* 3591.34, observed *m/z* 3591.37.

$[TBA]_2[Mo^{VI}_{10}Co^{II}_6O_{12}(\mu\text{-}O)_{14}(\mu_3\text{-}O)_4(AdPO_3)_6(AdCOO)_2(py)_2(H_2O)_6]$•6(MeCN), 13•6(MeCN)

Method B. Yield 0.031 g, 23.3% based on Mo. FT-IR (ATR) υ_{max} (cm^{-1}): 3181 (b), 2903 (w) (C-H), 1602 (w), 1534 (ν_{sym}) (m), 1480 (m), 1446 (m), 1421 (m) (ν_{asym}) (Δ = 113), 1097 (s) (P-O), 973 (s) (P-O), 947 (s) (P-O), 890 (s) (Mo=O), 851 (s), 829 (s), 771 (s), 699 (s) (Mo-O). CHN Analysis for $Mo_{10}Co_6P_6O_{58}N_4C_{124}H_{214}$; Expected C% 35.56, H% 5.15, N% 1.33; Found C% 31.89, H% 4.41, N% 1.62. MALDI-MS for $Mo_{10}Co_6P_6O_{52}N_1C_{98}H_{156}$ (loss of 1 TBA, 2 py, 6 H_2O) calculated *m/z* 3678.48, observed *m/z* 3678.47.

$[TBA]_2[Mo^{VI}_{10}Co^{II}_6O_{12}(\mu\text{-}O)_{14}(\mu_3\text{-}O)_4(t\text{BuPO}_3)_6(BrPhCOO)_2(py)_2(H_2O)_6]$•(MeCN), 14•(MeCN)

Method B. Yield 0.056 g, 51.5% based on Mo. FT-IR (ATR) υ_{max} (cm^{-1}): 3435 (w), 3169 (b), 2964 (w) (C-H), 2873 (w) (C-H), 1587 (w), 1542 (ν_{sym}) (m), 1477 (m), 1446 (m), 1407 (m) (ν_{asym}) (Δ = 135), 1097 (s) (P-O), 975 (s) (P-O), 952 (s) (P-O), 888 (s) (Mo=O), 850 (s), 824 (s), 769 (s), 702 (s) (Mo-O). CHN Analysis for $Mo_{10}Co_6P_6O_{58}N_4C_{80}H_{156}Br_2$; Expected C% 25.54, H% 4.18, N% 1.48; Found C% 25.59, H% 4.01, N% 1.11. MALDI-MS for $Mo_{10}Co_6P_6O_{52}N_1C_{54}H_{98}Br_2$ (loss of 1 TBA, 2 py, 6 H_2O) calculated *m/z* 3251.84, observed *m/z* 3251.60.

$[TBA]_2[Mo^{VI}_{10}Co^{II}_6O_{12}(\mu\text{-}O)_{14}(\mu_3\text{-}O)_4(t\text{BuPO}_3)_6(Br_2\text{PhCOO})_2(py)_2(H_2O)_6]\bullet 2.5(MeCN)$, 15•2.5(MeCN)

Method B. Yield 0.069 g, 57.2% based on Mo. FT-IR (ATR) υ_{max} (cm^{-1}): 3432 (w), 3160 (b), 2965 (w) (C-H), 2874 (w) (C-H), 1585 (w), 1544 (ν_{sym}) (m), 1478 (m), 1446 (m), 1432 (m), 1396 (m) (ν_{asym}) (Δ = 148), 1376 (m), 1098 (s) (P-O), 976 (s) (P-O), 953 (s) (P-O), 888 (s) (Mo=O), 846 (s), 821 (s), 769 (s), 705 (s) (Mo-O). CHN Analysis for $Mo_{10}Co_6P_6O_{58}N_{6.5}C_{85}H_{161.5}Br_4$; Expected C% 25.38, H% 4.04, N% 2.26; Found C% 25.53, H% 4.08, N% 1.28. MALDI-MS for $Mo_{10}Co_6P_6O_{52}N_1C_{54}H_{96}Br_4$ (loss of 1 TBA, 2 py, 6 H_2O) calculated *m/z* 3410.66, observed *m/z* 3410.47.

$[TBA]_2[Mo^{VI}_{10}Co^{II}_6O_{12}(\mu\text{-}O)_{14}(\mu_3\text{-}O)_4(t\text{BuPO}_3)_6(NO_2\text{PhCOO})_2(py)_4(H_2O)_6]$, 16

Method B. Yield 0.043 g, 37.2% based on Mo. FT-IR (ATR) υ_{max} (cm^{-1}): 3416 (w), 3257 (b), 2961 (w) (C-H), 2871(w) (C-H), 1571 (m), 1529 (ν_{sym}) (m), 1479 (m), 1445 (m), 1411 (m), 1347 (m) (ν_{asym}) (Δ = 182), 1087 (s) (P-O), 977 (s) (P-O), 943 (s) (P-O), 898 (s) (Mo=O), 854 (s), 816 (s), 790 (s), 757 (s), 702 (s) (Mo-O). Analysis for $Mo_{10}Co_6P_6O_{62}N_8C_{90}H_{166}$; Expected C% 28.07, H% 4.34, N% 2.90; Found C% 27.76, H% 4.29, N% 2.69. MALDI-MS for $Mo_{10}Co_6P_6O_{56}N_3C_{54}H_{98}$ (loss of 1 TBA, 4 py, 6 H_2O) calculated *m/z* 3251.84, observed *m/z* 3251.60.

$[TBA]_2[Mo^{VI}_{10}Co^{II}_6O_{12}(\mu\text{-}O)_{14}(\mu_3\text{-}O)_4(t\text{BuPO}_3)_6(NH_2\text{PhCOO})_2(py)_2(H_2O)_6]$, 17

Method B. Yield 0.062 g, 56.9% based on Mo. FT-IR (ATR) υ_{max} (cm^{-1}): 3439 (w), 3190 (b), 2906 (w) (C-H), 1698 (m), 1591 (m), 1551 (m) (ν_{sym}), 1478 (m), 1447 (m), 1409 (m), (ν_{asym}) (Δ = 133), 1276 (m), 1098 (s) (P-O), 975 (s) (P-O), 951 (s) (P-O), 891 (s) (Mo=O), 877 (s), 800 (s), 772 (s), 708 (s) (Mo-O).

$[TBA]_2[Mo^{VI}_{10}Co^{II}_6O_{12}(\mu\text{-}O)_{14}(\mu_3\text{-}O)_4(t\text{BuPO}_3)_6(CHOPhCOO)_2(py)_2(H_2O)_6]$, 18

Method B. Yield 0.024 g, 21.9% based on Mo. FT-IR (ATR) υ_{max} (cm^{-1}): 3437 (w), 3170 (b), 2968 (w) (C-H), 2871 (w) (C-H), 1677 (w), 1603(w), 1548 (m) (ν_{sym}), 1479 (m), 1448 (m), 1409 (m), (ν_{asym}) (Δ = 139), 1201 (m), 1095 (s) (P-O), 978 (s) (P-O), 949 (s) (P-O), 890 (s) (Mo=O), 770 (s), 697 (s) (Mo-O).

$[TBA]_2[Mo^{VI}_{10}Co^{II}_6O_{12}(\mu\text{-}O)_{14}(\mu_3\text{-}O)_4(t\text{BuPO}_3)_6(vanCOO)_2(py)_4(H_2O)_6]\bullet 6(MeCN)$, 19•6(MeCN)

Method B. Yield 0.055g, 47.3% based on Mo. FT-IR (ATR) υ_{max} (cm^{-1}): 3416 (w), 3257 (b), 2961 (w) (C-H), 2871(w) (C-H), 1571 (m), 1529 (ν_{sym}) (m), 1479 (m), 1445 (m), 1411 (m), 1347 (m) (ν_{asym}) (Δ = 182), 1087 (s) (P-O), 977 (s) (P-O), 943 (s) (P-O), 898 (s) (Mo=O), 854 (s), 816 (s), 790 (s), 757 (s), 702 (s) (Mo-O).

$[TBA]_2[Mo^{VI}_{10}Co^{II}_6O_{12}(\mu\text{-}O)_{14}(\mu_3\text{-}O)_4(t\text{BuPO}_3)_6(napCOO)_2(py)_2(H_2O)_6]\bullet 2(MeCN)$, 20•2(MeCN)

Method B. Yield 0.044 g, 38.1% based on Mo. FT-IR (ATR) υ_{max} (cm^{-1}): 3437 (w), 3170 (b), 2968 (w) (C-H), 2871 (w) (C-H), 1677 (w), 1603(w), 1548 (m) (ν_{sym}), 1479 (m), 1448 (m), 1409 (m), (ν_{asym}) (Δ = 139), 1201 (m), 1095 (s) (P-O), 978 (s) (P-O), 949 (s) (P-O), 890 (s) (Mo=O), 770 (s), 697 (s) (Mo-O). CHN Analysis for $Mo_{10}Co_6P_6O_{58}N_4C_{88}H_{162}$; Expected C% 28.54, H% 4.41, N% 1.51; Found C% 28.22, H% 4.38, N% 1.27. UV-Vis λ_{max}/nm (ε_{max}/M^{-1} cm^{-1}): 560 (340). MALDI-MS for $Mo_{10}Co_6P_6O_{52}N_1C_{62}H_{104}$ (loss of 1 TBA, 2 py, 6 H_2O) calculated *m/z* 3193.05, observed *m/z* 3193.10.

$[TBA]_2[Mo^{VI}_{10}Co^{II}_6O_{12}(\mu\text{-}O)_{14}(\mu_3\text{-}O)_4(t\text{BuPO}_3)_6(pyrCOO)_2(py)_2(H_2O)_6]\bullet 3.5(MeCN)$, 21•3.5(MeCN)

Method B. Yield 0.035 g, 29.2% based on Mo. FT-IR (ATR) υ_{max} (cm^{-1}): 3432 (w), 3174 (b), 2962 (w) (C-H), 2873 (w) (C-H), 1640 (w), 1602(w), 1585 (m), 1559 (m) (ν_{sym}), 1531 (m), 1476 (m), 1445 (m), 1412 (m), (ν_{asym}) (Δ = 147), 1403 (m), 1363 (w), 1318 (w), 1099 (s) (P-O), 974 (s) (P-O), 947 (s) (P-O), 890 (s) (Mo=O), 850 (s), 820 (s), 767 (s), 699 (s) (Mo-O). CHN Analysis for $Mo_{10}Co_6P_6O_{58}N_4C_{90}H_{166}$; Expected C% 31.19, H% 4.34, N% 1.45, Found C% 29.98, H% 4.29, N% 1.17. UV-Vis λ_{max}/nm (ε_{max}/M^{-1} cm^{-1}): 350 ($4.0x10^4$), 380

($1.0x10^4$), 560 (340). MALDI-MS for $Mo_{10}Co_6P_6O_{52}N_1C_{74}H_{108}$ (loss of 1 TBA, 2 py, 6 H_2O) calculated *m/z* 3343.09, observed *m/z* 3343.13.

$[TBA]_2[Mo^{VI}_{10}Co^{II}_6O_{12}(\mu\text{-}O)_{14}(\mu_3\text{-}O)_4(t\text{BuPO}_3)_6(\text{anthCOO})_2(py)_2(H_2O)_6]\bullet 6(MeCN)$, 22•6(MeCN)

Method B. Yield 0.032 g, 26.3% based on Mo. FT-IR (ATR) υ_{max} (cm^{-1}): 3463 (w), 3150 (b), 2963 (w) (C-H), 2874 (w) (C-H), 1601 (w), 1548 (m) (ν_{sym}), 1476 (m), 1445 (m), 1423 (m), 1392 (m) (ν_{asym}) (Δ = 156), 1316 (w), 1276 (w), 1098 (s) (P-O), 974 (s) (P-O), 948 (s) (P-O), 890 (s) (Mo=O), 848 (s), 822 (s), 758 (s), 700 (s) (Mo-O). CHN Analysis for $Mo_{10}Co_6P_6O_{58}N_4C_{96}H_{166}$; Expected C% 30.31, H% 4.39, N% 1.47, Found C% 30.23, H% 4.30, N% 1.16. UV-Vis λ_{max}/nm (ε_{max}/M^{-1} cm^{-1}): 350 ($2.7x10^4$), 370 ($3.4x10^4$), 385 ($2.8\ x10^4$), 560 (340). MALDI-MS for $Mo_{10}Co_6P_6O_{52}N_1C_{70}H_{108}$ (loss of 1 TBA, 2 py, 6 H_2O) calculated *m/z* 3294.08, observed *m/z* 3293.96.

$[TBA]_2[Mo^{VI}_{10}Co^{II}_6O_{12}(\mu\text{-}O)_{14}(\mu_3\text{-}O)_4(t\text{BuPO}_3)_6(\text{fluoCOO})_2(py)_2(H_2O)_6]\bullet 4(MeCN)$, 23•4(MeCN)

Method B. Yield 0.034 g, 28.8% based on Mo. FT-IR (ATR) υ_{max} (cm^{-1}): 3437 (w), 3170 (b), 2968 (w) (C-H), 2871 (w) (C-H), 1677 (w), 1603(w), 1548 (m) (ν_{sym}), 1479 (m), 1448 (m), 1409 (m), (ν_{asym}) (Δ = 139), 1201 (m), 1095 (s) (P-O), 978 (s) (P-O), 949 (s) (P-O), 890 (s) (Mo=O), 770 (s), 697 (s) (Mo-O). CHN Analysis for $Mo_{10}Co_6P_6O_{58}N_4C_{94}H_{164}$; Expected C% 29.89, H% 4.37, N% 1.48, Found C% 29.82, H% 4.32, N% 1.20. UV-Vis λ_{max}/nm (ε_{max}/M^{-1} cm^{-1}) : 300 ($3.3x10^4$), 560 (340). MALDI-MS for $Mo_{10}Co_6P_6O_{52}N_1C_{72}H_{106}$ (loss of 1 TBA, 2 py, 6 H_2O) calculated *m/z* 3272.09, observed *m/z* 3272.55.

$[TBA]_2[Mo^{VI}_{10}Co^{II}_6O_{12}(\mu\text{-}O)_{14}(\mu_3\text{-}O)_4(t\text{BuPO}_3)_6(\text{azoCOO})_2(py)_2(H_2O)_6]\bullet 1(MeCN)$, 24•1(MeCN)

Method B. Yield 0.029 g, 24.8% based on Mo. FT-IR (ATR) υ_{max} (cm^{-1}): 3431 (w), 3162 (b), 2965 (w) (C-H), 2874 (w) (C-H), 1639 (w), 1593(w), 1541 (m) (ν_{sym}), 1478 (m), 1446 (m), 1408 (m), (ν_{asym}) (Δ = 133), 1201 (m), 1095 (s) (P-O), 978 (s) (P-O), 949 (s) (P-O), 890 (s) (Mo=O), 770 (s), 697 (s) (Mo-O). CHN Analysis for $Mo_{10}Co_6P_6O_{58}N_8C_{92}H_{166}$; Expected C% 28.99, H% 4.39, N% 2.94, Found C% 28.27, H% 4.31, N% 2.83. MALDI-MS for $Mo_{10}Co_6P_6O_{52}N_5C_{66}H_{108}$ (loss of 1 TBA, 2 py, 6 H_2O) calculated *m/z* 3303.10, observed *m/z* 3303.16.

$[TBA]_2[Mo^{VI}_{10}Co^{II}_6O_{12}(\mu\text{-}O)_{14}(\mu_3\text{-}O)_4(t\text{BuPO}_3)_6(PDA)(py)_2(H_2O)_6]\bullet 7.5(MeCN)$, 25•7.5(MeCN)

Method B. Yield 0.022 g, 19.0% based on Mo. FT-IR (ATR) υ_{max} (cm^{-1}): 3435 (w), 3159 (b), 2964 (w) (C-H), 2872 (w) (C-H), 1566 (m) (ν_{sym}), 1477 (m), 1446 (m), 1401 (m) (ν_{asym}) (Δ = 165), 1096 (s) (P-O), 974 (s) (P-O), 949 (s) (P-O), 890 (s) (Mo=O), 853 (s), 825 (s), 769 (s), 700 (s) (Mo-O). CHN Analysis for $Mo_{10}Co_6P_6O_{58}N_8C_{92}H_{166}$; Expected C% 25.69, H% 4.42, N% 1.57, Found C% 25.46, H% 4.30, N% 1.28.

Manganese-Molybdate Structures (Chapter 5):

$[TBA]_2[Mo^{VI}_{10}Mn^{II}_6O_{12}(\mu\text{-}O)_{14}(\mu_3\text{-}O)_4(t\text{BuPO}_3)_6(MeCOO)_2(py)_4(H_2O)_6]\bullet 6(MeCN)$, 26•6(MeCN)

$[TBA]_2[Mo_6O_{19}]$ (0.137 g, 0.1 mmol), manganese (III) acetylacetonate (0.175 g, 0.5 mmol), *tert*-butylphosphonic acid (0.068 g, 0.5 mmol) and tetrabutylammonium bromide (0.322 g, 1 mmol) were combined in acetonitrile (25 ml). Pyridine (80 µL, 1 mmol) was added. The solution was stirred at room temperature for four hours. The dark brown-red solution was filtered and left to evaporate slowly. Orange crystals formed over the course of one week with decolourisation of the solution. The crystals were isolated by filtration, washed with diethyl ether and air dried. Yield 0.136 g, 58.7% based on Mo. FT-IR (ATR) υ_{max} (cm^{-1}): 3442 (w), 3262 (b), 2964 (w) (C-H), 2872 (w) (C-H), 1635 (w), 1597 (w), 1565 (m) (ν_{sym}), 1478 (m), 1443 (m), 1400 (m) (ν_{asym}) (Δ = 165), 1101 (s) (P-O), 972 (s) (P-O), 947 (s) (P-O), 893 (s) (Mo=O), 848 (s), 796 (s), 767 (s), 701 (s) (Mo-O). CHN Analysis for $Mo_{10}Mn_6P_6O_{58}N_4C_{70}H_{154}$; Expected C% 24.33, H% 4.49, N% 1.62, Found C% 24.32, H% 4.55, N% 1.62. MALDI-MS for $Mo_{10}Mn_6P_6O_{53}N_1C_{44}H_{98}$ (loss of 1 TBA, 4 py, 5 H_2O) calculated *m/z* 2964.08, observed *m/z* 2964.00.

$[TBA]_2[Mo^{VI}_{10}Mn^{II}_6O_{12}(\mu\text{-}O)_{14}(\mu_3\text{-}O)_4(t\text{BuPO}_3)_6(MeCOO)_2(MeOH)_4(H_2O)_6]\bullet 5(MeOH)$, 27•5(MeOH)

The procedure for **26•6(MeCN)** was repeated using methanol in place of acetonitrile. Yield 0.105 g, 48.8% based on Mo. FT-IR (ATR) υ_{max} (cm^{-1}): 3440 (w), 3266 (b), 2966 (w) (C-H), 2873 (w) (C-H), 1630 (w), 1568 (m) (ν_{sym}), 1478 (m), 1433 (m) (ν_{asym}) (Δ = 135), 1104 (s) (P-O), 972 (s) (P-O), 951 (s) (P-O), 889 (s) (Mo=O), 848 (s), 793 (s), 763 (s), 704 (s) (Mo-O). CHN Analysis for $Mo_{10}Mn_6P_6O_{60}N_2C_{62}H_{152}$; Expected C% 22.15, H% 4.55, N% 0.83, Found C% 21.32, H% 4.39, N% 0.53. MALDI-MS for $Mo_{10}Mn_6P_6O_{54}N_1C_{44}H_{100}$ (loss of 1 TBA, 4 MeOH, 4 H_2O) calculated *m/z* 9282.04, observed *m/z* 2981.99.

$[TBA]_2[Mo^{VI}_{10}Mn^{II}_6O_{12}(\mu\text{-}O)_{14}(\mu_3\text{-}O)_4(Ad\text{PO}_3)_6(MeCOO)_2(py)_4(H_2O)_6]\bullet 3(MeCN)$, 28•3(MeCN)

The procedure for **26•6(MeCN)** was repeated using Adamantylphosphonic acid in place of *tert*-butylphosphonic acid. Yield 0.028 g, 11.1% based on Mo. FT-IR (ATR) υ_{max} (cm^{-1}): 3443 (w), 2903 (m) (C-H), 2849 (w) (C-H), 1631 (w), 1568 (m) (ν_{sym}), 1478 (m), 1433 (m) (ν_{asym}) (Δ = 135), 1100 (s) (P-O), 967 (s) (P-O), 948 (s) (P-O), 892 (s) (Mo=O), 845 (s), 797 (s), 766 (s), 701 (s) (Mo-O). CHN Analysis for $Mo_{10}Mn_6P_6O_{58}N_4C_{106}H_{190}$; Expected C% 32.45, H% 4.88, N% 1.42, Found C% 32.77, H% 4.64, N% 1.49. MALDI-MS for $Mo_{10}Mn_6P_6O_{54}N_1C_{80}H_{136}$ (loss of 1 TBA, 4 py, 4 H_2O) calculated *m/z* 3450.32, observed *m/z* 3450.26.

$[TBA]_2[Mo^{VI}_{10}Mn^{II}_6O_{12}(\mu\text{-}O)_{14}(\mu_3\text{-}O)_4(t\text{BuPO}_3)_6(t\text{BuCOO})_2(MeOH)_4(H_2O)_6]\bullet 3(MeCN)$, 29•6(MeOH)

The procedure for **27•5(MeOH)** was repeated using adamantylphosphonic acid in place of *tert*-butylphosphonic acid. Yield 0.062 g, 22.4% based on Mo. FT-IR (ATR) υ_{max} (cm^{-1}): 3525 (w), 2967 (w) (C-H), 2869 (w) (C-H), 1601 (w), 1599 (m), 1566 (w) (ν_{sym}), 1522 (w), 1477 (m), 1392 (w), 1360 (w), 1117 (s), 1068 (s) (P-O), 978 (s) (P-O), 940 (s) (P-O), 894 (s) (Mo=O), 832 (s), 799 (s), 757 (s), 700 (s) (Mo-O). CHN Analysis for $Mo_{10}Mn_6P_6O_{62}N_2C_{70}H_{172}$; Expected C% 23.96, H% 4.94, N% 0.79, Found C% 24.02, H% 4.32, N% 0.87.

$[TBA]_2[Mo^{VI}_{10}Mn^{II}_6O_{12}(\mu\text{-}O)_{14}(\mu_3\text{-}O)_4(t\text{BuPO}_3)_6(PDA)(py)_4(H_2O)_6]\bullet 2(MeCN)$, 30•2(MeCN)

The procedure for **26•6(MeCN)** was repeated, adding phenylenediacetic acid (0.097 g, 0.5 mmol) to the reaction mixture. Yield 0.012 g, 5.4% based on Mo. . FT-IR (ATR) υ_{max} (cm^{-1}): 3443 (w), 2903 (m) (C-H), 2849 (w) (C-H), 1631 (w), 1568 (m) (ν_{sym}), 1478 (m), 1433 (m) (ν_{asym}) (Δ = 135), 1100 (s) (P-O), 967 (s) (P-O), 948 (s) (P-O), 892 (s) (Mo=O), 845 (s), 797 (s), 766 (s), 701 (s) (Mo-O).

[Cl⊂Mn^{III}_6(*t*BuPO_3)$_8$(py)$_6$][$Mo^{VI}_2Mn^{III}_{11}O_2$(*μ*-O)$_4$(*μ*$_3$-O)$_4$(*μ*$_4$-O)$_2$(*μ*-OH)$_2$(*t*BuP$O_3$)$_{10}(py)_4$]•4.5(MeCN), 31•4.5(MeCN)

Method A: [TBA]$_2$[Mo_6O_{19}] (0.137 g, 0.1 mmol), manganese (III) acetylacetonate (0.175 g, 0.5 mmol), *tert*-butylphosphonic acid (0.068 g, 0.5 mmol), tetramethylammonium chloride (0.110 g, 1 mmol) and terephthalic acid (0.083 g, 0.5 mmol) were combined in acetonitrile (25 ml). Pyridine (80 μL, 1 mmol) was added. The solution was stirred at room temperature for four hours. The dark brown solution was filtered and left to evaporate slowly. Brown crystals formed over the course of a few days. The crystals were separated manually from orange crystals of **26•6(MeCN)**, washed with diethyl ether and air dried.

Method B: [TBA]$_2$[Mo_6O_{19}] (0.137 g, 0.1 mmol), potassium permanganate (0.016 g, 0.1 mmol), manganese (II) chloride dihydrate (0.161 g, 1 mmol), *tert*-butylphosphonic acid (0.068 g, 0.5 mmol) and tetramethylammonium chloride (0.110 g, 1 mmol) were combined in acetonitrile (25 ml). Pyridine (80 μL, 1 mmol) was added. The solution was stirred at room temperature for four hours. The dark brown solution was filtered and left to evaporate slowly. Brown crystals formed over the course of a few days. The crystals were isolated by filtration, washed with diethyl ether and air dried.

Yield (Method B) 0.075 g, 44.2% based on Mn. FT-IR (ATR) υ_{max} (cm^{-1}): 3375 (b), 2963 (w) (C-H), 2869 (w) (C-H), 1574 (w), 1484 (m), 1390 (m), 1206 (m), 1129 (s) (P-O), 1102 (s) (P-O), 1081 (s) (P-O), 1054 (s) (P-O), 1020 (s) (P-O), 973 (s) (P-O), 950 (s), 906 (s) (Mo=O), 833 (s), 754 (s) (Mo-O), 657 (s).

[Br⊂Mn^{III}_6(*t*BuPO_3)$_8$(py)$_6$][$Mo^{VI}_2Mn^{III}_{11}O_2$(*μ*-O)$_4$(*μ*$_3$-O)$_4$(*μ*$_4$-O)$_2$(*μ*-OH)$_2$(*t*BuP$O_3$)$_{10}(py)_4$]•4.5(MeCN), 32•4.5(MeCN)

Method B for **31•4.5(MeCN)** was repeated using manganese (II) bromide tetrahydrate in place of manganese (II) chloride dihydrate and tetrabutylammonium bromide for tetramethylammonium chloride. Yield 0.040 g, 23.5% based on Mn. FT-IR (ATR) υ_{max} (cm^{-1}): 3434 (b), 2970 (w) (C-H), 2866 (w) (C-H), 1576 (w), 1477 (m), 1447 (m), 1390 (m), 1202 (m), 1142 (s) (P-O), 1119 (s) (P-O), 1070 (s) (P-O), 1020 (s) (P-O), 974 (s) (P-O), 942 (s), 907 (s) (Mo=O), 833 (s), 754 (s) (Mo-O), 699 (s), 661 (s).

[TBA][$Mo^{VI}_2Mn^{III}_{11}O_2$(*μ*-O)$_4$(*μ*$_3$-O)$_4$(*μ*$_4$-O)$_2$(*μ*-OH)$_2$(*t*BuP$O_3$)$_{10}(py)_4$]•1.5(MeCN), 33•1.5(MeCN)

Method B for **31•4.5(MeCN)** was repeated using manganese (II) nitrate tetrahydrate in place of manganese (II) chloride dehydrate and tetrabutylammonium hexafluorophosphate in place of tetramethylammonium chloride. Yield 0.052 g, 31.7% based on Mn. FT-IR (ATR) υ_{max} (cm^{-1}): 2972 (w) (C-H), 2868 (w) (C-H), 1567 (w), 1478 (m), 1447 (m), 1118 (s) (P-O), 1068 (s) (P-O), 1000 (s) (P-O), 979 (s) (P-O), 942 (s), 907 (s) (Mo=O), 833 (s), 759 (s) (Mo-O), 700 (s), 668 (s).

MOF Structures (Chapter 6):

$[Cl\subset Mn^{III}_6(t\text{BuPO}_3)_8(bpy)_3]Cl$, 34

Potassium permanganate (0.032 g, 0.2 mmol), manganese (II) chloride dihydrate (0.161 g, 1 mmol), *tert*-butylphosphonic acid (0.136 g, 1 mmol), 4,4'-bipyridine (0.093 g, 0.6 mmol) and 1,4-penylenediacetic acid (0.193g, 1 mmol) were combined in acetonitrile (25 ml). The mixture was stirred at room temperature for four hours. The brown precipitate was isolated by filtration, washed with acetonitrile, water and diethyl ether and air dried. Yield: 0.280 g, 71.5% based on Mn. FT-IR (ATR) υ_{max} (cm^{-1}): 2969 (w) (C-H), 1656 (s), 1605 (m), 1447 (m), 1388 (m), 1137 (s) (P-O), 1041 (m) (P-O), 1013 (s) (P-O), 833 (s), 811 (s), 733 (s), 661 (s).

$[Cl\subset Mn^{III}_6(t\text{BuPO}_3)_8(bpy)_2(H_2O)_2]Cl$, 35

The procedure for **35** was repeated using 0.062 g (0.4 mmol) of 4,4'-bipyridine. Yield: 0.220 g, 59.9% based on Mn. FT-IR (ATR) υ_{max} (cm^{-1}): 2969 (w) (C-H), 1691 (s), 1408 (m), 1340 (m), 1234 (m), 1202 (m), 1138 (s) (P-O), 1070 (m) (P-O), 1021 (s) (P-O), 894 (s), 858 (s), 832 (s), 784 (s), 673 (s).

$[Cl\subset Mn^{III}_6(t\text{BuPO}_3)_8(bpy)_2(H_2O)_2]Cl$, 35

The procedure for **35** was repeated using manganese (II) bromide tetrahydrate in place of manganese (II) chloride dihydrate. Yield: 0.250 g, 61.1% based on Mn. FT-IR (ATR) υ_{max} (cm^{-1}): 2968 (w) (C-H), 1680 (s), 1607 (m), 1478 (m), 1134 (s) (P-O), 1068 (m) (P-O), 1010 (s) (P-O), 864 (s), 832 (s), 661 (s).

7.3) Experimental Procedures

Water Oxidation Procedure (Compound 33):

A $6.3x10^{-9}$ molar stock solution of **33•1.5(MeCN)** (stock **A)** was prepared in pH 7, 0.01 M phosphate buffer, and a second stock solution of 10 mM $Na_2S_2O_8$ was also prepared in pH 7, 0.01 M phosphate buffer (11.9mg/mL, stock **B)**. A 7mL glass vial containing a stir bar was loaded with 2 mg $[Ru(bpy)_2(deeb)](PF_6)_2$ (resulting in 0.5 mM photosensitizer in the whole reaction mixture). It was then crimped with butyl septum cap, foiled to protect from light and was clamped to the setup. Stirring was set at 500 rpm, and the bath temperature at 25 °C. 4mL of stock A and 1mL of stock B were injected through the septum to the vial. Clark electrode for O_2 sensing (Unisense) and the ground cable were inserted, after which the real time values are monitored. The setup was then degassed with a flow of N_2 injected and left for a few minutes to obtain a constant level of O_2 just above zero. Further, the foil was unwrapped, blue LED (470 nm wavelength light) was shown at power = 1 at a distance of 1cm from the sample (incident power estimated as 9.6 mW/cm^2), and the O_2 evolution was recorded continuously.

MOF disassembly procedure (Compound 34):

Compound **34** (20 mg, 1 μmol) was added to 20 ml acetonitrile. Aliquots of pyridine were added (up to 500 μl, 6 mmol). After each addition, the sample was stirred for 10 minutes. Before absorption spectra were obtained, the sample was centrifuged (5000 rpm for 5 minutes) to aggregate any solid particles at the bottom of the sample vial and a sample was removed from the top of the vial for analysis. After analysis the samples were combined and further aliquots added. The resulting solution was diluted with acetonitrile for analysis by mass spectrometry.

Reassembly procedure:

The solution was evaporated under reduced pressure using a rotary evaporator (60 °C, 200 mbar), producing a brown powder. Additional acetonitrile was added and the procedure was repeated twice more to remove additional pyridine.

7.4) References

1 P. C. Crofts and G. M. Kosolapoff, *J. Am. Chem. Soc.*, 1953, **75**, 3379.

2 N. J. Hur, W. G. Klemperer and R. C. Wang, *Inorg. Synth.*, 1990, **27**, 77.

Chapter 8

Conclusions and Outlook

Summary

In summary of the work in presented in this thesis, we have developed a synthetic strategy to generate new examples of advanced materials which contain multiple chemically distinct components. In contrast to the more traditional "bottom-up" approaches to these materials, the methodology employed in this work uses distinct assembly, disassembly, and reassembly processes to access these materials. In particular, we have applied this synthetic methodology to generate three classes of materials:

- *Organic-Inorganic Hybrid Materials* (Compounds **1**-**33**)
- *TMS-POMs* (Compounds **3**-**33**)
- *Extended Materials* (Compounds **25**, **30**)

In order to achieve these synthetic goals, the following strategy was applied:

- The Lindqvist hexamolybdate species was identified as a suitable material to undergo disassembly and reassembly under mild synthetic conditions.
- Using ESI-MS analysis, the Lindqvist hexamolybdate was demonstrated to undergo disassembly in solution under ambient conditions, generating a series of mononuclear and polynuclear molybdate fragments (Figure 8.1). CV variation experiments were carried out to demonstrate that these fragments are really present in solution and are not the result of instrumental effects.

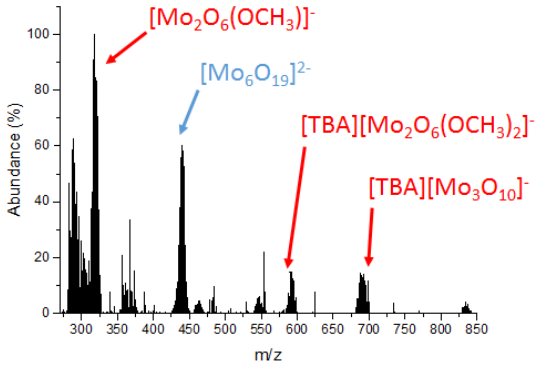

Figure 8.1 – ESI-MS of the Lindqvist hexamolybdate in methanol, showing the parent cluster (blue) and disassembled molybdate fragments (red).

- Phosphonate ligands were used to reassemble these fragments into hybrid {Mo_5} Strandberg-type compounds, **1** and **2** (Figure 8.2). The templating effects of the phosphonate ligand were shown to be important for the success of the disassembly-reassembly methodology.

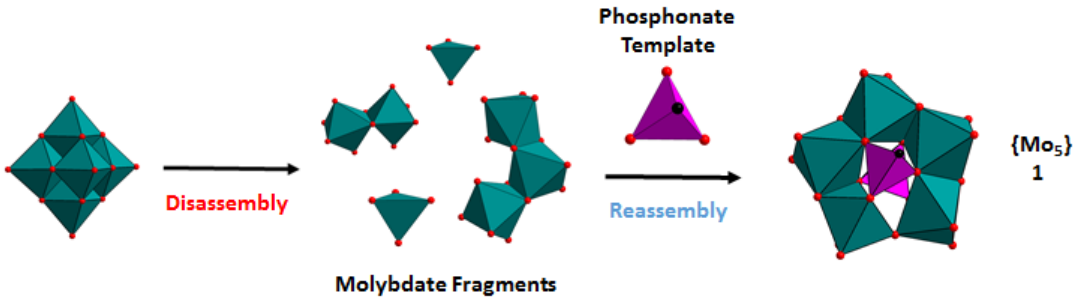

Figure 8.2 – Proposed disassembly of the hexamolybdate into molybdate fragments, followed by phosphonate-templated reassembly into Strandberg-type {Mo_5} species.

- The methodology was extended to mixed metal systems, starting with copper (II)-molybdates **3** and **4**. The phosphonate templating effects that governed the formation of **1** and **2** were also shown to be significant in the formation of **3** and **4** (Figure 8.3).

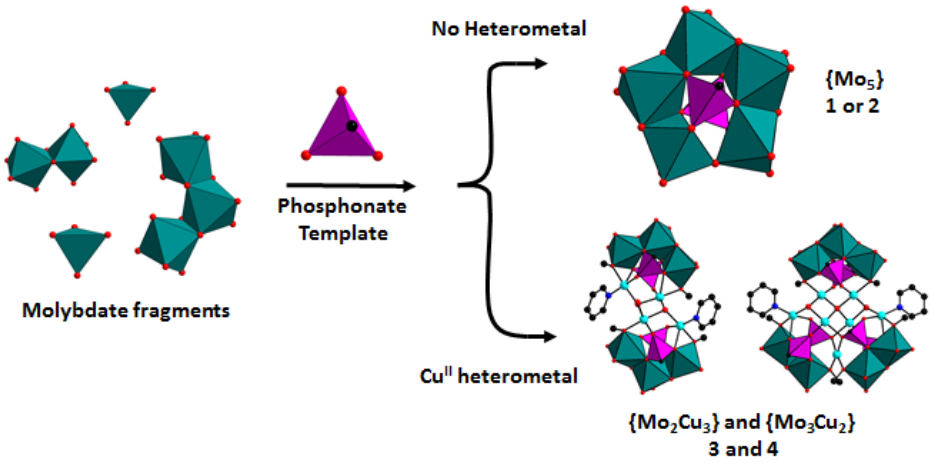

Figure 8.3 – Proposed reassembly of the disassembled molybdate fragments in the presence of copper (II) ions to generate compounds 3 and 4.

- The methodology was further extended to cobalt (II)-molybdates. Related phosphonate templating effects were also demonstrated in the formation of $\{Mo_{10}Co_6\}$ compound **5** (Figure 8.4).

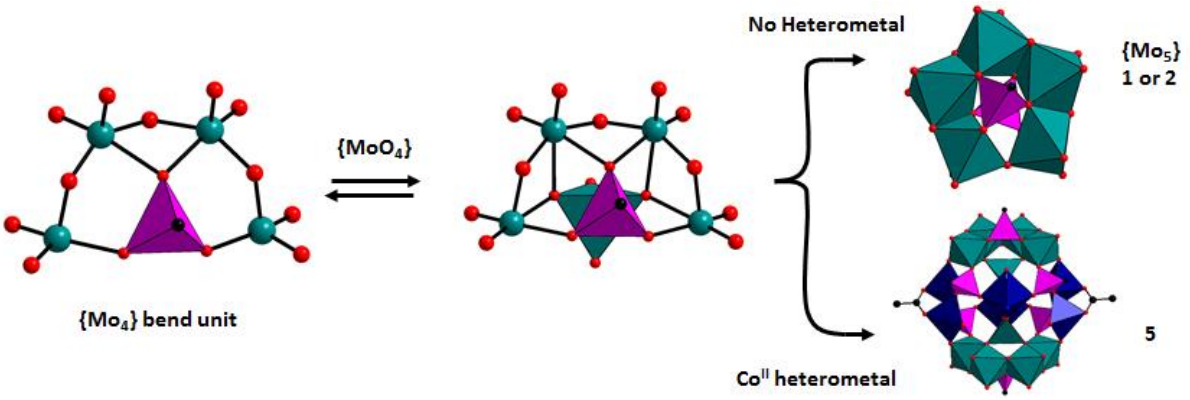

Figure 8.4 – Proposed phosphonate-templated reassembly of the $\{Mo_5\}$ units in 5, which in the presence of cobalt (II) ions can generate compound 5.

- The hybrid nature of **5** was exploited to generate a series of analogous compounds, **6-25**, through a series of ligand-exchange syntheses (Figure 8.5).

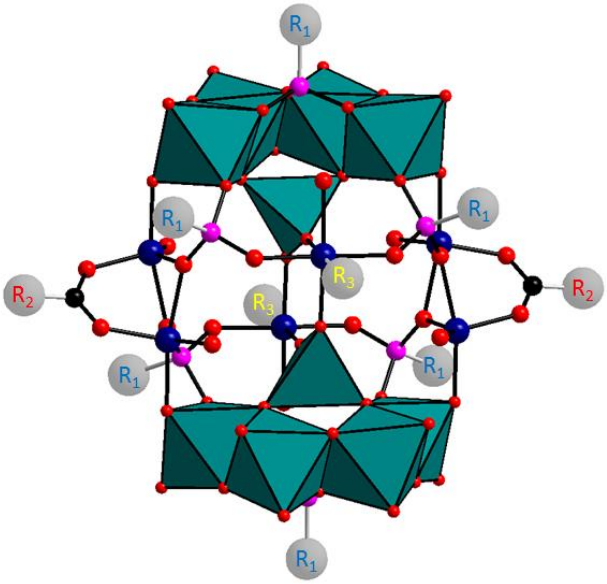

Figure 8.5 – The cluster core of 5, highlighting the three distinct ligand sites represented by the phosphonate ligands (R_1), carboxylate ligands (R_2) and pyridyl ligands (R_3). Modifications at these positions generate compounds 5-25.

- The methodology was then extended to manganese systems. $\{Mo_{10}Mn_6\}$ compounds **26-30** were manganese (II) analogues of compound **5** (Figure 8.6).
- The reaction system was modified to generate compound **31**, a mixed system containing a $\{Mn_6\}$ cation and a $\{Mn_{11}Mo_2\}$ anion. The system was further modified to replace the $\{Mn_6\}$ cation to generate compounds **32** and **33**.

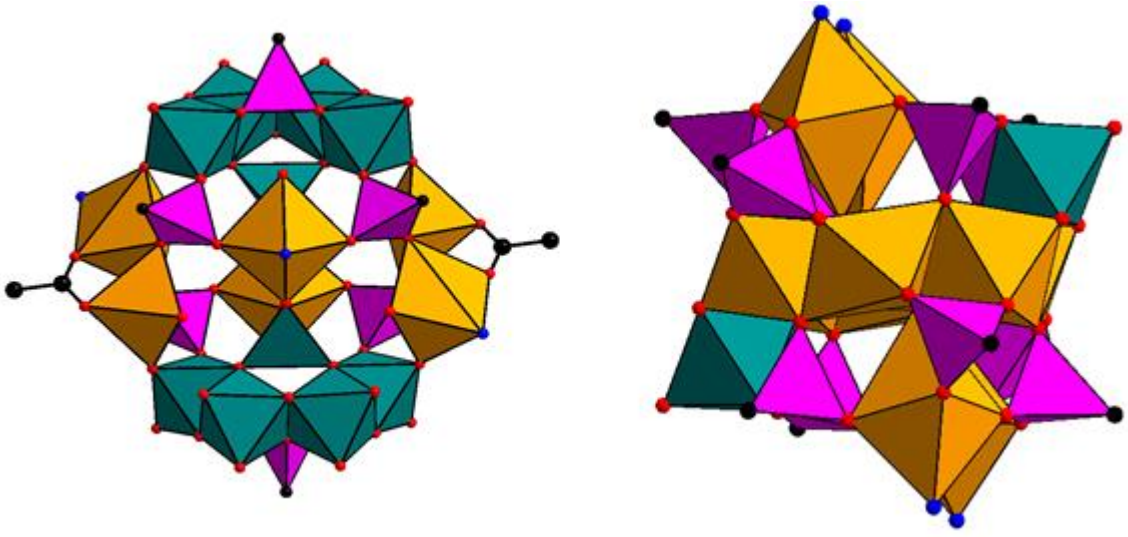

Figure 8.6 – Simplified representations of the $\{Mo_{10}Mn_6\}$ (left) and $\{Mn_{11}Mo_2\}$ (right) cluster entities in compounds 26-30 and 31-33, respectively.

- Polymeric compounds **25** and **30** were generated by incorporation of bridging carboxylate ligands into the disassembly-reassembly reactions (Figure 8.7).

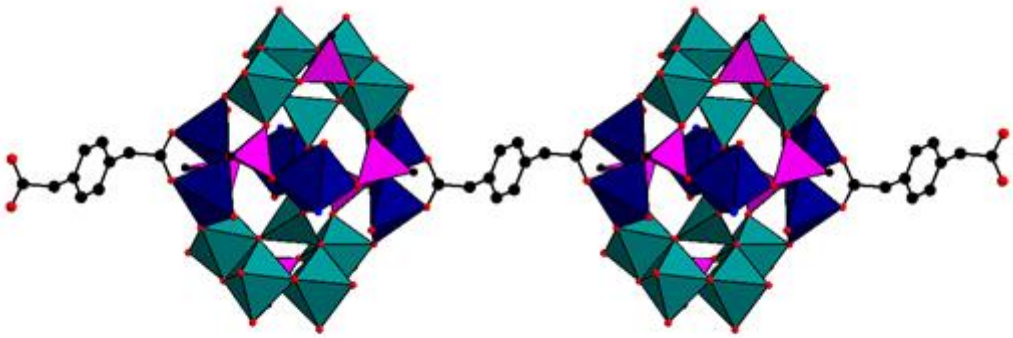

Figure 8.7 – Simplified representations of the polymeric compound 25, generated from polytopic carboxylate ligands.

- These compounds were all characterised by single crystal XRD where possible, and by supplementary characterisation techniques including IR, TGA and mass spectrometry as appropriate.

Having synthesised and characterised these compounds, we set out to investigate their structure-dependant physicochemical properties:

- Compounds **3** and **4** were investigated for their magnetic properties. Predominantly antiferromagnetic coupling interactions between the copper (II) spin centres in **3** were identified, although the magnetic properties of **4** are not understood (Figure 8.8).

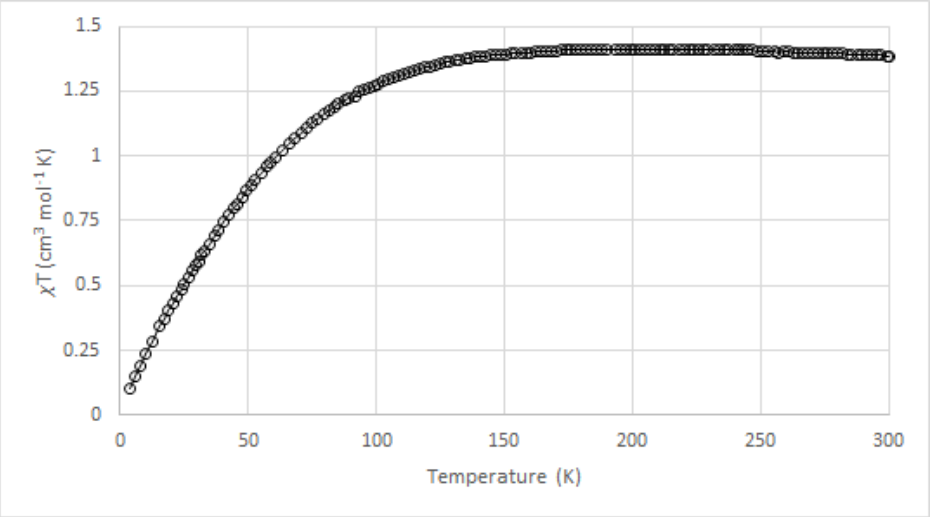

Figure 8.8 – Temperature dependence of the χT (magnetic susceptibility by temperature) product for compound 3.

- The effects of electron withdrawing and electron donating substituents on the electronic properties of the metal centres in hybrid TMS-POMs were investigated in the case of *nitro*- (electron withdrawing) and *amino*- (electron donating) substituted cobalt compounds, **16** and **17** (Figure 8.9).

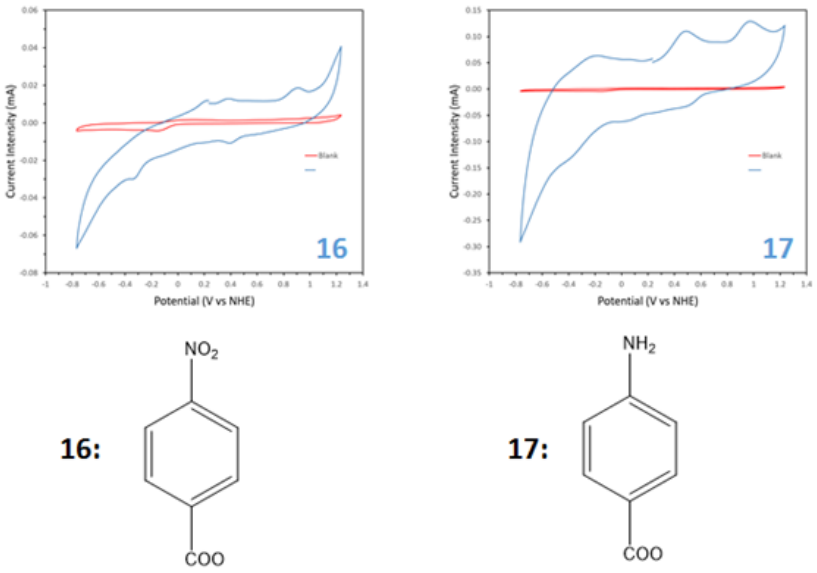

Figure 8.9 – Cyclic voltammagrams for compounds 16 and 17, containing electron withdrawing and donating substituents, respectively.

- The effects of UV-absorbing substituents on the photophysical properties of the compounds was investigated for the series of aromatic-substituted TMS-POMs **20**-**23**. Compounds **21** and **22** were shown to display visible luminescence when irradiated with UV light (Figure 8.10).

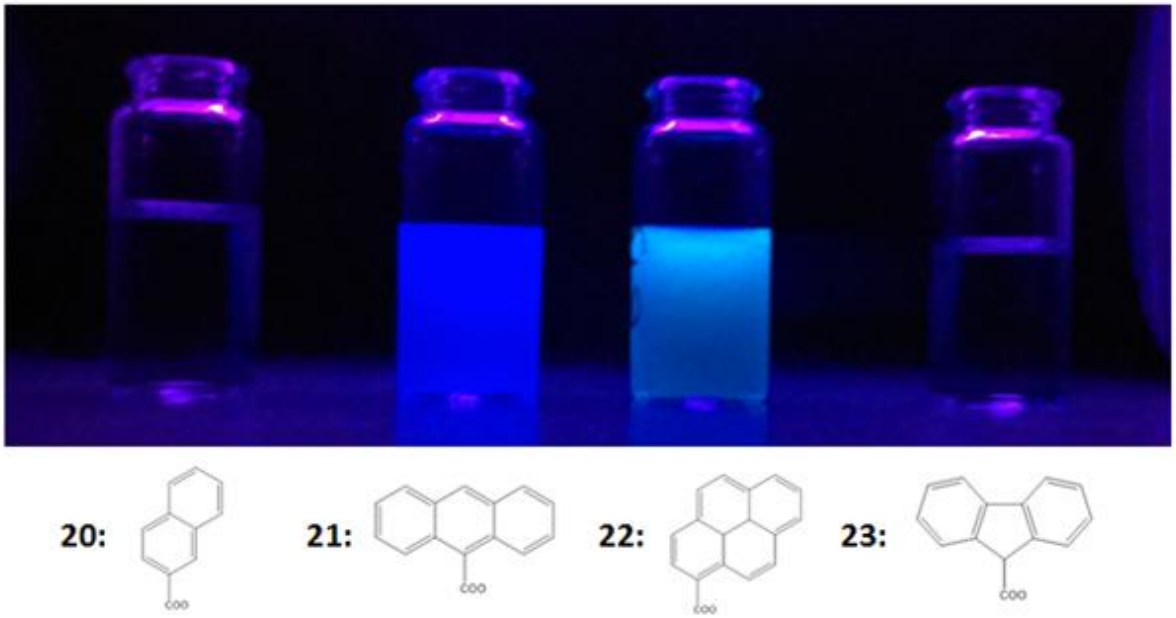

Figure 8.10 - Samples of 20-23 (left-to-right) in acetonitrile under irradiation at 360 nm, showing visible luminescence of 21 and 22.

- The azobenzene-containing TMS-POM **24** was shown to undergo dynamic *cis*-*trans* isomerisation under UV irradiation (Figure 8.11).

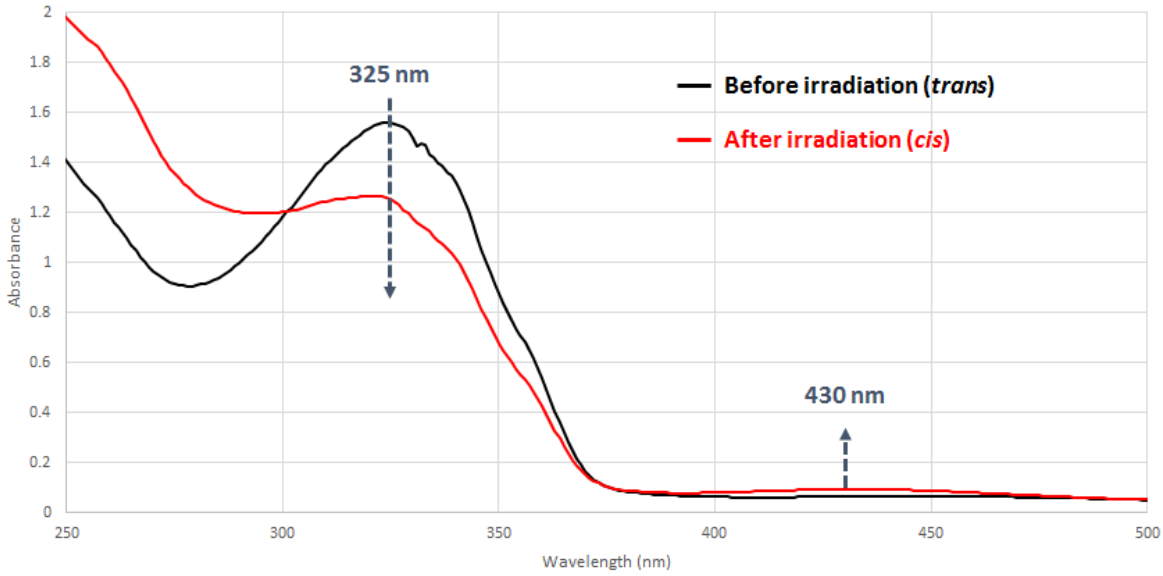

Figure 8.11 – Absorption spectrum of 24 in acetonitrile before and after irradiation, indicating *cis*-*trans* isomerisation of the azobenzene moieties.

Chemical reactivity was also investigated, where possible:

- The reaction systems that generated the manganese-molybdate compounds **26**-**30** were demonstrated to be capable of cleaving C-C bonds. This was exploited to generate carboxylate ligands *in situ* from the cleavage of acac-type ligands. The active compound is an unidentified precursor to compounds **26**-**30**. It was demonstrated that the reaction requires atmospheric oxygen to proceed (Figure 8.12)

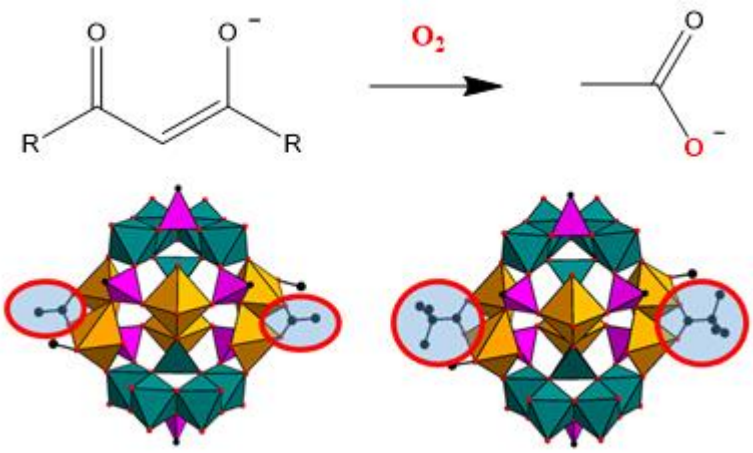

Figure 8.12 – The reaction systems that generate compounds 26-30 are capable of cleaving C-C bonds, which was exploited to generate acetate and pivalate ligands *in situ*.

- The $\{Mn_{11}Mo_2\}$ compound **33** was investigated for photochemical water oxidation (Figure 8.13). The compound appears to catalyse the reaction, with a TON of 14. Comparison with an analogous $\{Mn_{13}\}$ compound (TON = 20) indicates that the substitution of two Mn centres for two Mo centres lowers the activity of the compound. This is tentatively attributed to the blocking of potential reaction sites by relatively inert *oxo*- ligands in the $\{Mn_{11}Mo_2\}$ case, although further analysis is required.

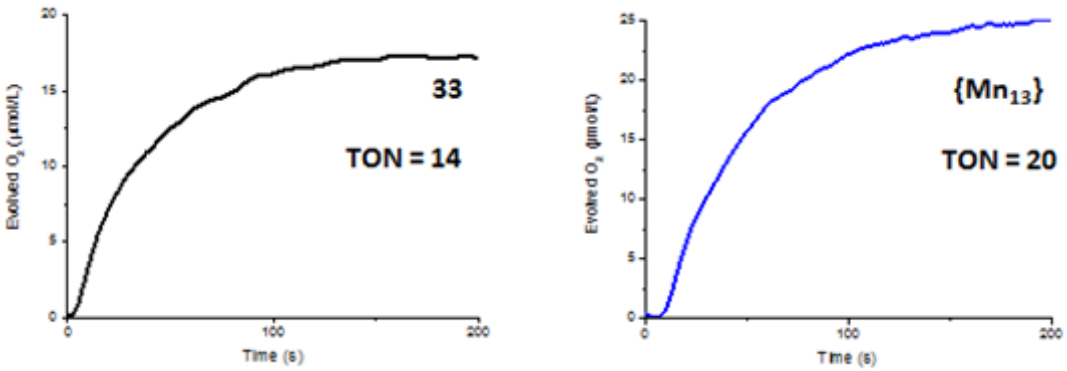

Figure 8.13 – Photochemical oxygen evolution by 33 and by a related $\{Mn_{13}\}$ compound.

Having exploited the assembly-disassembly-reassembly technique to generate novel compounds **1-33**, the principles of disassembly and reassembly were applied to MOF-type compounds. Three MOF-type compounds were generated from the $\{Mn_6\}$ cation units in compounds **31** and **32** connected *via* 4,4'-bipyridine ligands. These compounds are tentatively assigned as three dimensional and two dimensional framework structures, **34-36**.

In the case of **34**, it was demonstrated that the addition of a competitor ligand (pyridine) could displace the bridging bipyridine ligands, resulting in the disassembly of the framework into its constituent components. The $\{Mn_6\}$ nodes were demonstrated to remain intact in solution upon disassembly of the framework. It was also demonstrated that removal of the competitor pyridine ligand under reduced pressure resulted in the reassembly of the parent framework **34** (Figure 8.14).

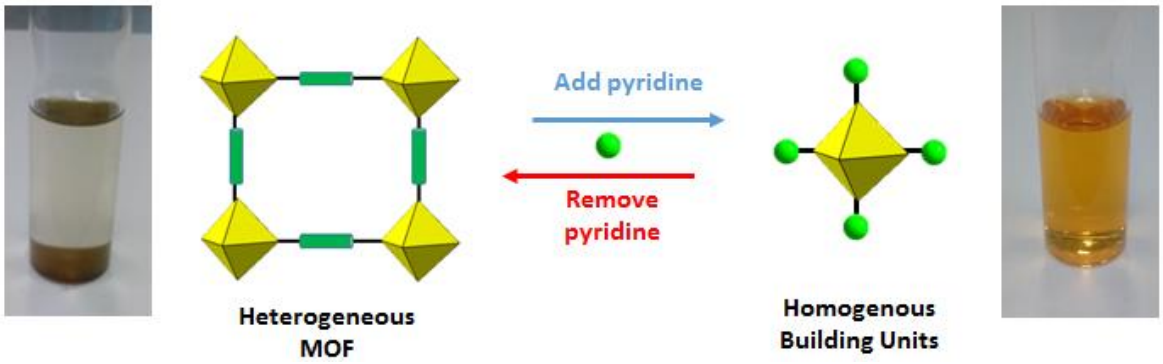

Figure 8.14 - Summary of the disassembly-reassembly procedure, as applied to 34.

Future Work

The success (so far) of the assembly-disassembly-reassembly methodology for the production of hybrid POMs, TMS-POMs and extended materials indicates that the methodology may be a valuable tool in the generation of new compounds. However, the compounds presented in this thesis probably represents only a small subset of the possible compounds that could be generated from this technique. Possible avenues for future work include:

- *Chemical reactivity.* So far, we have only explored a few examples of chemical reactivity using the compounds generated in this thesis. However many catalytically active TMS-POMs are known (*c.f.* Section 1.2.2). The advantage of hybrid POMs with respect to catalysis is that reactivity can be tuned by modification of the steric and electronic attributes of the organic ligands. Investigation of the chemical activity of the compounds generated so far would be interesting in this regard. We are particularly interested in investigating the activity of our compounds with respect to water splitting reactions, but many other redox processes are promising candidates for catalytic studies.
- *Different POM precursors.* Modification of the synthetic procedures explored so far is potentially fertile ground for generating new compounds. For example, replacing the hexamolybdate with heptamolybdate or octamolybdate could in principle generate different oligomeric intermediates, which could influence the final product.
- *Different POM metals.* This thesis only considered the molybdates, but vanadates and tungstates could behave in a similar manner.
- *Different heterometals.* The first-row transition metal heterometals considered in this thesis represent only a small subset of possible heterometals which could be included. For example, heavier metals such as ruthenium or iridium could introduce interesting chemical functionality into the materials. Lanthanide heterometals could introduce interesting magnetic and photochemical properties. Heterometals with restricted coordination geometries such as platinum or palladium could modify the geometries of the materials.
- *Different heterometal ligands.* The examples of the assembly-disassembly-reassembly methodology examined so far all used hydrated carboxylate or nitrate heterometal salts. However including different ligands with the heterometal could generate different compounds – for example, incorporating chelating ligands onto the heterometal could restrict possible coordination environments, thus modifying the template effect.
- *Polynuclear heterometal assemblies.* In all of the cases explored in this thesis, mononuclear heterometals were included. However, pre-ordered polynuclear assemblies would respond differently to templating effects, possibly generating different compounds.
- *Different ligands.* Phosphonates, carboxylates and monodentate ligands such as pyridine or methanol were all demonstrated to be suitable ligands for the assembly-disassembly-reassembly approach. Substitution of any of these ligands was shown to generate modifications of the product clusters. Moreover, the organic ligands clearly have a strong templating effect – therefore modification of the template should generate different products. This is already demonstrated by the disassembly-reassembly approaches towards hybrid Anderson-type POMs, where *tris*(alkoxide) ligands (in combination with a suitable heterometal) template an Anderson ring structure.

- *Different polytopic ligands.* The generation of compounds **25** and **30** indicates that extended structures can be formed using the assembly-disassembly-reassembly method, but only one dimensional polymers have been explored so far. Different linker ligands (*e.g.* triangular or tetrahedral linker ligands) could generate network structures. This is particularly interesting in the case of the cobalt and manganese compounds **5**-**30**, as these possess phosphonate, carboxylate and pyridyl ligands – in principle these different ligand sites could all be used to generate extended structures.
- *Different reaction conditions.* All of the synthesis described in this thesis take place at ambient conditions (room temperature, atmospheric pressure, under air). Modification of these conditions could generate different compounds.
- *Different solvent systems.* Methanol and acetonitrile are known to be favourable solvents for the assembly-disassembly-reassembly method, but many other solvents are possible.
- *Post-synthetic modification.* Many of the compounds described in Chapter 4 contain functional groups that might be amenable to post-synthetic modification. For example, the amine functionality in **16** or the aldehyde functionality in **18** are both good candidates for post-synthetic modification of their respective cluster compounds through Schiff-base condensation reactions. These could be exploited to introduce additional functionality or to incorporate the clusters into extended networks.
- *Disassembly and reassembly of MOFs.* Much work remains to be done on the disassembly and reassembly of MOF compounds – this is discussed in more detail in Section 6.4.